Inertial Wave Attractors, Resonances, and Wave Excitation by Libration

– Direct Numerical Simulations and Theory –

Von der Fakultät für Umwelt und Naturwissenschaften
der Brandenburgischen Technischen Universität Cottbus - Senftenberg
zur Erlangung des akademischen Grades eines

doctor rerum naturalium (Dr. rer. nat.)

genehmigte Dissertation

vorgelegt von

Diplom-Physiker
Marten Klein

aus Bad Muskau

1. Gutachter: Prof. Dr. Christoph Hinz
2. Gutachter: Prof. Dr. Leo R. M. Maas
Tag der mündlichen Prüfung: 6. Dezember 2016

Abstract

Resonance phenomena are ubiquitous in Nature. Resonance means that a system can accumulate large amounts of kinetic energy. In rotating flows inertial waves provide a mechanism for resonance by redistributing momentum, kinetic energy and helicity. Kinetic energy and helicity are linked to the velocity amplitudes, whereas helicity also depends on the velocity gradients (shear) in the flow. Large values of the kinetic energy and the helicity can thus lead to instability and turbulence.

In order to investigate inertial waves a Taylor–Couette system was investigated which consists of a homogeneous liquid confined between two coaxial cylinders and two rigid lids. The inner cylinder is slightly conical (frustum) to break the vertical mirror symmetry. Inertial waves were excited by two different forcing configurations: the frustum in libration and the lids together with the outer cylinder in libration. Libration means that the rotation rate of the wall is modulated with a frequency ω and an amplitude $\varepsilon\Omega_0$, in which ε is the dimensionless libration amplitude and Ω_0 the mean rotation rate. Direct numerical simulations (DNS) were conducted with a numerical solver in terrain-following coordinates.

DNS results reveal that inertial wave excitation is localised at the edges of the confinement, which is in very good agreement with recent laboratory measurements of Seelig (2014, PhD thesis, BTU Cottbus - Senftenberg). A model of the wave excitation mechanism was developed with the aid of boundary layer theory. The model suggests that a difference in the boundary layer mass flux (Ekman flux) excites the waves by driving an excess Ekman pumping velocity w_E at the edges. The DNS results exhibit this flux difference, and the simulated kinetic energy spectra of the waves exhibit the frequency dependency $K(\omega) \propto w_\mathrm{E}^2(\omega)$, which was predicted by the model.

However, DNS results also exhibit helical vortices at the edges which are not part of the model. Conservation properties suggest that these vortices are merely a compensating phenomenon which tends to stabilise the boundary layer flow. The details of this flow, however, appear less important for the wave excitation.

Response spectra of the kinetic energy, the dissipation rate, the helicity, and the quality factor were computed in order to assess resonance conditions. Simulated resonance peaks were as narrow as $\Delta\omega/\Omega_0 \approx 0.05$. At these peaks, the kinetic energy was found to increase by a factor 10–50 even though viscous forces were still rather large (Ekman number $E = \nu\Omega_0^{-1}(\Delta r)^{-2} \sim 10^{-5}$ with the kinematic viscosity ν and the typical radial gap width Δr).

The flow patterns found at those resonances were investigated and found to be in very good agreement with the spatial patterns obtained by laboratory measurements and geometric ray tracing. The DNS results suggest that there are two types of resonance in rotating flows: modes and wave attractors. In contrast to a mode, a wave attractor exhibits net focusing of wave energy and occupies a finite frequency band. DNS results show that the wave attractor resonance frequency adjusts within the frequency band which suggests that wave attractor resonances complement ‘classical’ mode resonances and may, thus, be relevant in various applications.

Keywords: direct numerical simulations, rotating flows, resonance, inertial waves, boundary layers

Kurzfassung

In der Natur sind Resonanzphänomene allgegenwärtig. Resonanz bedeutet, dass ein System eine große Menge an kinetischer Energie akkumulieren kann. In rotierenden Strömungen stellen Trägheitswellen einen Resonanzmechanismus bereit, indem sie den Impuls, die kinetische Energie und die Helizität umverteilen. Die Kinetische Energie und die Helizität hängen von den Geschwindigkeitsamplituden ab, die Helizität zudem von den Geschwindigkeitsgradienten. Hohe Werte der kinetischen Energie und der Helizität können deshalb zu Instabilität und schließlich auch turbulentem Strömungsverhalten führen.

Um Trägheitswellen zu untersuchen, wurde ein Taylor–Couette-System betrachtet. Dieses besteht aus zwei koaxialen Zylindern, zwei Deckeln und einer darin eingeschlossenen Flüssigkeit. Der innere Zylinder ist konisch geformt (Kegelstumpf), um die vertikale Spiegelsymmetrie zu brechen. Zwei Konfigurationen wurden zur Wellenanregung genutzt: Die Libration des Kegelstumpfs und die Libration der Deckel zusammen mit dem Außenzylinder. Libration bedeutet, dass die Drehzahl der Wand mit einer Frequenz ω und einer Amplitude $\varepsilon\Omega_0$ moduliert wird. Dabei ist ε die dimensionslose Librationsamplitude und Ω_0 die mittlere Drehzahl. Die Direkten Numerischen Simulationen (DNS) wurden in geländefolgenden Koordinaten durchgeführt.

Die DNS-Ergebnisse zeigen, dass die Wellenanregung an den Kanten des Behälters lokalisiert ist. Dies deckt sich mit den Messergebnissen von Seelig (2014, Doktorarbeit, BTU Cottbus - Senftenberg). Mit Hilfe der Grenzschichttheorie wurde ein Modell der Wellenanregung entwickelt. Das Modell legt nahe, dass eine Differenz des Massenstroms in der Grenzschicht (Ekman-Fluss) maßgeblich für die Wellenanregung ist, indem das Ekman-Pumpen w_E an den Kanten verstärkt wird. Die DNS-Ergebnisse weisen diese Massenstromdifferenz auf und die Frequenzabhängigkeit der kinetischen Energie der Wellen, $K(\omega) \propto w_\mathrm{E}^2(\omega)$, deckt sich mit der Vorhersage des Modells.

Die DNS-Ergebnisse weisen außerdem helikale Wirbel an den Kanten des Taylor–Couette-Systems auf. Die vorgelegten Untersuchungsergebnisse legen jedoch nahe, dass diese Wirbel ein kompensierendes Phänomen darstellen um die Grenzschicht nahe den Kanten zu stabilisieren. Die Wellenanregung selbst scheint nur unwesentlich von den Details dieser Wirbel abzuhängen.

Um Resonanzen zu untersuchen, wurden Spektren der Energie, der Dissipationsrate, der Helizität und des Gütefaktors berechnet. Die Resonanzen in den DNS-Ergebnissen haben eine minimale Breite von $\Delta\omega/\Omega_0 \approx 0.05$ und sind durch eine Zunahme der Energie um einen Faktor 10–50 gekennzeichnet, trotz recht großer Viskosität (Ekman-Zahl $E = \nu\Omega_0^{-1}(\Delta r)^{-2} \sim 10^{-5}$ mit der kinematischen Viskosität ν und der mittleren Spaltbreite Δr).

Die simulierten Strömungsmuster stimmen sehr gut mit den räumlichen Mustern der Referenzmessungen im Labor und der Strahlverfolgung überein. Die DNS-Ergebisse legen nahe, dass in rotierenden Strömungen zwei Arten von Resonanz existieren: Moden und Wellenattraktoren. Im Gegensatz zu einer Mode existiert ein Wellenattraktor in einem Frequenzband. DNS-Ergebnisse zeigen, dass sich die Resonanzfrequenz in diesem variabel einstellen kann, wodurch Wellenattraktor-Resonanzen, ergänzend zu den ‘"klassischen'Moden-Resonanzen, für viele Anwendungen relevant sein können.

Schlagworte: Direkte Numerische Simulationen, rotierende Strömungen, Resonanz, Trägheitswellen, Grenzschichten

für Sindy, Corina und Olaf

Contents

List of figures

List of tables

List of symbols

Abbreviations

BC	boundary condition
BL	boundary layer
BTU C-S	Brandenburg University of Technology Cottbus - Senftenberg
CN	Crank–Nicolson (scheme)
DFT	discrete Fourier transform
DNS	direct numerical simulation
EVP	eigenvalue problem
FD	finite-difference (scheme)
FT	Fourier transform
FFT	fast Fourier transform
LONO	low-order neutral orbit
LOWA	low-order wave attractor
n-D	n-dimensional
ODE	ordinary differential equation
PDE	partial differential equation
PIV	particle image velocimetry
PSD	power spectral density
RK	Runge–Kutta (scheme)
RT	ray tracing

Sub- and superscripts

i, j, k, ...	Cartesian tensor indices (upper and lower position)
$(\cdot)_{i,j,k}$	array indices due to spatial discretisation
$(\cdot)^n$, $(\cdot)^m$	time level, sub-time level
$(\cdot)^{\mathrm{T}}$	transposed matrix
$(\cdot)_\lambda$, $(\cdot)_\mu$, $(\cdot)_\nu$, ...	covariant tensor indices (w.r.t. curvilinear basis)
$(\cdot)^\lambda$, $(\cdot)^\mu$, $(\cdot)^\nu$, ...	contravariant tensor indices (w.r.t. curvilinear basis)
$(\cdot)_\sigma$	filtered at the frequency σ
$(\cdot)^\dagger$	complex conjugate

Lower case Roman symbols

$\mathrm{e} = 2.71828\ldots$, e^x	Euler number, exponential function
$\mathrm{i} = \sqrt{-1}$	imaginary number
l	harmonic of the libration frequency
m, n, k	wave number components (axial, radial, azimuthal)
f, f_*	Coriolis parameter, effective Coriolis parameter
h	height
p	pressure
q_μ, $q^\mu = Ju^\mu$	co-, contravariant volume flux components
r	radius
s	(normalised) arc coordinate
t, Δt	time, time step
u_μ, u^μ	co-, contravariant velocity components
v_i, v^i	Cartesian velocity components
u	zonal velocity in a local Cartesian frame
v	local wall-tangential velocity in a local Cartesian frame
w	local wall-normal velocity in a local Cartesian frame
w_E, w'_E	Ekman pumping velocity (lid, frustum)
x^1, x^2, x^3	global Cartesian coordinates
x, y, z	local Cartesian coordinates
$\boldsymbol{a}_\mu$, $\boldsymbol{a}^\mu$	co-, contravariant basis vector
$\boldsymbol{c}_\mathrm{p}$, $\boldsymbol{c}_\mathrm{g}$	vectors of the phase and group velocity
$\boldsymbol{e}$	unit vector
$\boldsymbol{e}_i = \boldsymbol{e}^i$	Cartesian basis vector
$\boldsymbol{f}$	mass-specific force vector
$\boldsymbol{g}$	gravitational acceleration on Earth
$\boldsymbol{k}$	wave vector
$\boldsymbol{n}$	surface normal
$\boldsymbol{q} = q^\mu \boldsymbol{a}_\mu$	volume flux vector (Einstein's summation convention)
$\boldsymbol{r} = x^i \boldsymbol{e}_i = \xi^\mu \boldsymbol{a}_\mu$	position vector (Einstein's summation convention)
$\boldsymbol{v} = v^i \boldsymbol{e}_i = u^\mu \boldsymbol{a}_\mu$	velocity vector (Einstein's summation convention)
$(c^i_{\ \mu}) = \dfrac{\partial(x^1, x^2, x^3)}{\partial(\xi^1, \xi^2, \xi^3)}$	Jacobi matrix
$g_{\mu\nu}$, $g^{\mu\nu}$	co-, contravariant metric tensor components

Upper case Roman symbols

A, B, C, ...	point label
$\mathrm{Im}(\cdot)$	imaginary part of a complex number
$\mathrm{Re}(\cdot)$	real part of a complex number
A, B	amplitude parameter
C	Courant number
D	dissipation rate; wall-tangential divergence
E	Ekman number
H	total helicity
I	definite integral
$J = \det(c^i_\mu)$	Jacobian of a coordinate transformation
K	total kinetic energy
L	length scale
M	number of complete libration periods
N	numerical resolution (number of grid cells)
Q	quality factor
R	Rossby number
S	surface area
T	temperature; time scale; time interval
U	velocity scale
V	volume
∂V	volume boundary (closed surface)
W	complex amplitude
Z	total enstrophy; complex amplitude
$\boldsymbol{A}$	vector potential
$\boldsymbol{Q}_\mathrm{E}$, $\boldsymbol{Q}'_\mathrm{E}$	Ekman flux (lid, frustum)

Greek symbols

$\pi = 3.14159\ldots$	Ludolph's constant
α, β, γ, ...	angles; quadrature weights; scalar coefficients
α	wall inclination angle; apex half-angle
δ	boundary layer thickness
κ	wave number
ε	libration amplitude
ν	kinematic viscosity
ω, $\Delta\omega$, $\delta\omega$	libration frequency, frequency resolution, frequency interval
ρ	density
φ	azimuth angle
ϕ	scalar field
σ	inertial wave frequency parameter
θ	phase (relative to the phase of libration ωt)
ϑ	angle between the inertial wave vector and the rotation axis
ψ	stream function; scalar field
ξ^1, ξ^2, ξ^3	generalised curvilinear coordinates (contravariant components)
$\Delta\xi^1$, $\Delta\xi^2$, $\Delta\xi^3$	curvilinear increments
Δ	error
Ω, Ω_0	angular velocity, mean angular velocity
Φ	dissipation function; scalar potential
$\boldsymbol{\zeta}$	vorticity vector
$\boldsymbol{\tau}$	rate of strain tensor
δ^ν_μ	Kronecker symbol
$\varepsilon_{\lambda\mu\nu}$	Levi-Civita tensor
$\epsilon^{\lambda\mu\nu} \equiv J^{-1}\epsilon_{\lambda\mu\nu}$	contravariant Levi-Civita tensor
$(\gamma^\mu_i) = J\left[\dfrac{\partial(x^1,x^2,x^3)}{\partial(\xi^1,\xi^2,\xi^3)}\right]^{-1}$	J-scaled inverse Jacobi matrix
$\Lambda^{\mu\nu} = Jg^{\mu\nu}$	J-scaled contravariant metric tensor

Tensor operations

$\boldsymbol{A}\cdot\boldsymbol{B}=A_\mu B^\mu$	scalar product (Einstein's summation convention)
$\boldsymbol{A}\times\boldsymbol{B}=\boldsymbol{a}_\mu\epsilon^{\mu\nu\rho}A_\nu B_\rho$	cross / vector product (Einstein's summation convention)
$\boldsymbol{A}\circ\boldsymbol{B}=(A_\mu B_\nu)$	dyadic product

Operators and operator matrices

$\mathrm{d}/\mathrm{d}x$	total derivative
$\partial/\partial x\equiv\partial_x$	partial derivative
$\partial/\partial\xi^\mu\equiv\partial_\mu$	covariant derivative
$\partial/\partial\xi_\mu\equiv\partial^\mu$	contravariant derivative
$\boldsymbol{\nabla}=\boldsymbol{e}^i\,\partial/\partial x^i$	nabla operator (Einstein's summation convention)
$\mathbf{1}$	identity operator (unit matrix)
$\mathcal{C}$	cross-product operator (matrix)
$\mathcal{D}$	divergence operator (matrix)
$\mathcal{G}$	gradient operator (matrix)
$\mathcal{L}$	linear operator (matrix)
$\mathcal{N}$	non-linear operator (matrix)

Other decoration symbols

$\lvert\cdot\rvert$	absolute value; Euclidean vector norm
$\lvert\lvert\cdot\rvert\rvert$	spatial norm
$\overline{(\cdot)}$	temporal average over integer libration periods ($T=2\pi M/\omega$)
$\hat{c}$	complex amplitude

Acknowledgements

I would like to thank Prof. E. Schaller[†]for giving me the opportunity to do my doctorate in a fundamental fluid-dynamical research topic, his valuable input at the in-house seminars and his patience. I thank Prof. C. Hinz for taking over the responsibility and guiding this piece of work to a good end. I am also very grateful to Prof. L. R. M. Maas for acting as the second reviewer and for carefully reading and commenting on the manuscript.

I am indebted to Dr. A. Will, for his guidance, fruitful discussions, and—most importantly—for giving me the freedom to develop own ideas to make the research topic my own. He provided the documented channel code version which cut down the time of code development. This thesis would not have been possible without his critical remarks, ideas, and continued motivation.

I am grateful to Prof. U. Harlander who suggested to look into the wave excitation mechanism. Grounded in geophysics, he hinted at relevant articles and asked critical questions, which helped to set the tone.

I express my gratitude to Prof. M. V. Kurgansky for fruitful discussion and sharing his intuition on the analytical approach during his visits of the BTU Cottbus - Senftenberg between 2011 and 2014. A similar level of understanding would not have been achieved without his insight.

Thanks go to the colleagues involved in the 'QBO project': MSc A. Ghasemi V. for lively discussions on inertial waves, for his contributions to the code and critical examinations of my own developments that helped to find some bugs; Dr. I. D. Borcia for contributing with intensive ray tracing simulations; Dr. T. Seelig for discussions and performing the lab experiments, which started out a bit earlier than numerics and marked some interesting points in the parameter space.

For maintaining a stable computing infrastructure I would like to thank Dr. A. Krebs and Dipl.-Ing. W. Christoph. Refreshing coffee breaks with Dr. M. Nawdiyal, Dr. J. Ogaja and Dipl.-Met. S. Weiher are kindly acknowledged, not to forget a couple of road bike rides with Drs. K. Keuler and K. Radtke. I acknowledge the organising abilities of S. Printschitsch regarding seminars, formalities and group events.

Funding by the German Science Foundation (DFG) under project *'Mischung und Grundstromanregung durch propagierende Trägheitswellen'* is also kindly acknowledged.

All software tools used for the finalisation of results are freely available or under public license. A hat-tip to the Linux, LaTeX, Numpy, Matplotlib, SciPy and ParaView developers.

Last but not least, I thank all my family and friends for their moral support and their curiosity in *what* I am actually doing.

[†]Who left us unfortunately before the disputation date.

1 Introduction

The flows taking place in Earth's atmosphere are of immediate relevance for humans by affecting the daily weather and the climate. The conditions in the atmosphere are constantly changing and wind speeds, for example, range from a light breeze on a bright sunny day up to several hundred kilometres per hour in storms and the jet stream (e.g. Lindzen, 1990). Besides the atmosphere there are other flows taking place in the Earth system which are less obvious. For instance, the oceanic circulation (e.g. Pedlosky, 1987) and even flows below the surface in the liquid mantle and the liquid outer core (e.g. Aldridge & Lumb, 1987; Noir *et al.*, 2009). One indicator for the existence of such geophysical subsurface flows is volcanic activity. Another one is Earth's magnetic field. The magnetic field is believed to be of hydrodynamic origin and caused by the so-called geodynamo mechanism for which rotation of the Earth is an important property (e.g. Malkus, 1968; Tilgner, 2008). Life as we know it would certainly not be possible without the magnetic field due to the absence of the magnetic 'shield' against cosmic radiation. Weakening of the geodynamo and, hence, of the magnetic field would have immense consequences for life even if it happened slowly over many decades. There is no foreseeable option for humans to counteract any such changes. The least we can do is obtain a comprehensive understanding of the Earth system, in particular, the flows on Earth.

For the applications mentioned it is of interest to understand the natural variability in order to be able to answer if and how the system properties may change drastically. This happens usually when high velocities are reached in a fluid due to which a flow can become unstable and break down into turbulence. Large velocity amplitudes can be the consequence of *resonance*. Resonance can be defined as the state with the (kinetic) energy stored in the system being much larger than the amount of energy dissipated (converted into heat) during a typical time interval. This can result in *resonance failure* when the system is unable to bear the resulting load imposed. In a rigid structure resonance failure would be due to excessively high stress that results in breaking of beams, possibly already during the non-equilibrium oscillation build-up phase. In a fluid system *turbulent collapse* is more likely to be observed instead.

For such a scenario a mechanism is required by which kinetic energy and momentum are accumulated in the system. This storage mechanism is provided by *waves*. Waves with the longest wavelengths exhibit small velocity gradients which means less shear and less dissipation. In that way large amounts of kinetic energy can be stored in the system. This yields large-scale oscillating flow structures, as will be discussed in more detail later.

Sound waves, gravity waves and inertial waves occur in geo- and astrophysical flows and are therefore potentially relevant for resonance as described above. Sound waves are restored by the pressure gradient force which is relevant in compressible media (like the atmosphere), but less in liquids (e.g. Lighthill, 1978, pp. xiv, 5, 439). Focussing on liquids, say applications in the ocean and subsurface flows, means that the effects of compressibility and sound waves will be neglected in the following. By contrast, gravity waves and inertial waves owe their existence to restoring forces that result from stratification effects. Gravity waves, on the one hand, are

restored by the buoyancy force which is due to a stratification of temperature[1]. Inertial waves, on the other hand, are restored by the Coriolis force which is due to a stratification of angular momentum in rotating fluids (e.g. Høiland, 1962; Salmon, 1998, pp. 68). Interestingly, both types of waves exhibit huge similarities in their mathematical treatment (e.g. Seelig, 2014). Both waves may therefore be investigated individually and results can be taken over almost identically. However, the difference is that gravity waves are two-dimensional (2-D) and without any swirling motions, whereas inertial waves are three-dimensional[2] (3-D). This renders inertial waves closer to turbulence which is known to possess a complicated 3-D structure of the velocity and vorticity fields (e.g. Campagne *et al.*, 2015). Therefore *inertial waves* are in the focus of this study realised by considering a system rotating with uniform mean angular velocity Ω_0. Gravity waves are removed entirely by assuming an approximately homogeneous fluid density, a uniform temperature distribution and by using a rigid container.

This brings us to the key questions to be addressed by this thesis. First, how and how efficiently can inertial waves be excited by a geophysically relevant forcing? Second, what are the spatial structures in the flow related to inertial waves? Third, what are the resonance conditions in a confined rotating fluid, and how are they related to inertial waves? Fourth, does the anomalous reflection law of inertial waves result in a different resonance mechanism than that of a 'classical' eigenmode resonance?

Current state of research

Inertial waves are known since the late 19th century, when Lord Kelvin (1880) formulated a mathematical model for small velocity fluctuations in a rotating fluid. About 60 years passed before the importance of inertial oscillations for the planetary-scale atmospheric flows has been recognised by means of Rossby waves (2-D planetary waves; see Rossby, 1939).

In the 1960s and 1970s the 3-D structure of rotating flows has moved into the focus. Analytical efforts concentrated on the existence of continuous solutions (e.g. Høiland, 1962; Wood, 1966) and non-continuous solutions (e.g. Bretherton, 1964; Stewartson & Rickard, 1969). According to analytical feasibility idealised flow experiments have been designed. A very successful example of that time is the sliced cylinder with differential rotation. Pedlosky & Greenspan (1967) developed a complete analytical solution for the wave propagation (Rossby waves) and the boundary layer currents, which was confirmed by a laboratory experiment (see Greenspan, 1969, pp. 59, 78, 81, 85–91, 118–124). However, not only the waves themselves, but also instability, intermittency and the route to turbulence have been addressed (e.g. McEwan, 1970). Unfortunately, computers available at that time have not been powerful enough to help out with numerical simulations and measurement equipment could not yet make use of laser light illumination, so that inertial waves seem to have fallen into hibernation.

Whatever the reasons might be, since the 1990s inertial waves have received an increasing attention again thanks to improved measurement equipment, new analytical approaches and advances in computing power which allowed to tackle open questions on the relevance of inertial waves for geophysical flows. Henderson & Aldridge (1992), for example, computed a few inertial

[1] In a liquid, stratification by temperature T is in fact a stratification by density ρ, where the density is assumed to depend on temperature but *not* on pressure. This is known as the Boussinesq approximation in which temperature variations ΔT and density variations $\Delta\rho$ are proportional, that is

$$\frac{\Delta T}{T} = \frac{\Delta\rho}{\rho}.$$

[2] More precisely, inertial waves are helical as will be shown later.

eigenmodes of an asymmetric annulus numerically. These eigenmodes are solutions to the linearised Navier–Stokes equations (linearised around the state of rigid body rotation). A sensitive dependency of the spatial patterns on the frequency eigenvalue was observed which suggests that the full solution will depend crucially on the forcing frequency applied in an experiment. It is quite surprising that Henderson & Aldridge (1992) were able to compute such eigenmodes since in the frustum singular solutions are more generic which indicates that there is a 'residual symmetry' of the straight annulus in the frustum geometry (we shall discuss the various properties in more detail in chapter 2.4).

However, even the linearised system of equations is still too expensive to be solved many hundred times for the various combinations of system parameters so that a more efficient model would be desirable. It has been recognised a few years later that the simpler method of *ray tracing* can be used if one is only interested in the spatial patterns related to the waves (e.g. Maas & Lam, 1995). By ray tracing the path along which wave energy propagates can be constructed by a repeated application of the wave reflection law. It can happen that a unique spatial pattern emerges independently of source point—a so-called *wave attractor* (e.g. Maas *et al.*, 1997; Rieutord & Valdettaro, 1997). Existence of a wave attractor implies that all the wave energy of a particular frequency is focused into a tiny fraction of the fluid volume but which extends also through the fluid volume. The velocity gradients steepen along the wave attractor so that the overall dissipation rate increases.

It has been argued further, for example by Rieutord *et al.* (2001) and Ogilvie (2005), that the dissipation rate will reach a finite value under the presence of a wave attractor. This may be counter-intuitive, but the reasoning is based on the notion that a steepening of velocity gradients is counteracted by a simultaneous reduction of the volume that is affected by the wave. Since energy dissipation means heating, it can be speculated that the volcanic activity of Earth, Io, Enceladus, Triton and Europa[3] might in fact be the result of a wave attractor-based internal heating mechanism. However, it could be that the flow undergoes turbulent collapse when the rotation rate has become high enough. Greenspan (1969, p. 185) noted that it makes a difference if first the viscous and then the inertial forces become small compared to the Coriolis force. Current models for the internal heating rates might thus overestimate the heating rates by neglecting turbulent collapse. Moreover, they also imply that inertial waves are excited *somehow*.

The mechanisms responsible for inertial wave excitation are not yet very well understood. In experiments a wave maker can be used (e.g. Messio *et al.*, 2008) or it is argued that a local 'eruption' of the boundary layer perturbs the flow (e.g. Kerswell, 1995). This circumstance indicates a fundamental problem in atmospheric, oceanographic and other system models. There are no wave makers and the boundary layers are typically not resolved but modelled by wall functions. It is very likely that inertial waves and related effects are therefore missing or underrepresented[4].

Low frequency and large scale forcing mechanisms are usually considered the ones most relevant for geophysical applications. Earth's tidal bulges, for example, provide a quasi-semi-diurnal forcing for the ocean and the subsurface liquid layers. This, however, requires a notably ellipsoidal confinement geometry to work efficiently. Alternatively, also time dependent rotation rates can be used to excite waves which works independently of the confinement geometry. This

[3] Volcanoes in the solar system, NASA, `http://spaceplace.nasa.gov/volcanoes`, last accessed: Sep. 18, 2015.

[4] This suggests that not only inertial waves but also gravity waves are underrepresented in state-of-the-art system models.

type of forcing is external, which means it is imposed on the system under consideration. Two different mechanisms of that type have been discussed in literature.

The first mechanism is *precession*, which is believed to affect the flow in rapidly rotating massive objects, for example, giant stars or giant gas planets due to the non-uniform distribution of mass in their interior. Precession can be parametrised in the lab or in the simulations by letting the main rotation axis revolve around another axis (the precession axis). Hence, there are two angular frequencies: the mean rotation rate Ω_0 and the precession frequency ω_p. In the system revolving with the mean rotation rate, say averaged over integer precession periods, precession manifests itself by an effective body force due to which the non-axisymmetric spin-over mode (an inertial mode with azimuthal wave number $k = 1$) can be driven efficiently (e.g. Hollerbach & Kerswell, 1995; Noir *et al.*, 2001; Tilgner & Busse, 2001). Therefore, precession has been used in recent studies to address triadic interactions of normal modes in simple geometry (e.g. Albrecht *et al.*, 2015; Lopez & Marques, 2015).

The second mechanism is (longitudinal) *libration*, which is believed to affect the dynamics of subsurface liquid layers of smaller celestial objects like planets or moons nearby a massive star or planet (see e.g. Comstock & Bills, 2003). In fact, many librating planets or moons are believed to possess a liquid core like Earth's moon, or liquid layers in the form of subsurface oceans like Saturn's moons Titan and Enceladus (e.g. Noir *et al.*, 2012, 2009). In the case of librational forcing the axis of rotation remains fixed but the rotation rate of the wall varies in time. Libration can be parametrised by two angular frequencies: the mean rotation rate Ω_0 and the libration frequency ω. In contrast to precession, libration does not yield a body force in the frame of reference attached to the mean rotation rate when the geometry is axisymmetric.

In a viscous fluid, however, the oscillating boundary layer over the librating wall exhibits shear and can thus drive a flow or might excite waves by turn unstable under certain conditions. It has therefore been debated whether libration can drive inertial waves efficiently to be relevant in applications. Recent studies suggest that this is the case but it depends on the geometry and the flow regime how efficient this is (e.g. Klein *et al.*, 2014; Koch *et al.*, 2013; Noir *et al.*, 2012; Sauret *et al.*, 2012).

In addition, it has been observed that inertial waves are excited locally at edges or corners. Beardsley (1970), for example, observed that characteristic shear layers originate from the edges of his librating cone configuration. About 40 years later localised wave excitation has been rediscovered (e.g. Boisson *et al.*, 2012; Sauret *et al.*, 2012; Swart *et al.*, 2010) but no quantitative model has been developed yet.

In order to obtain a better understanding of the processes at work, many numerical simulations have been conducted to obtain more information about the flow than can be acquired by state-of-the-art laboratory experiments. Focusing on particular processes comprising wave excitation, resonance and wave interactions, various geometries have been studied: spherical shells (e.g. Calkins *et al.*, 2010; Hollerbach & Kerswell, 1995; Noir *et al.*, 2009; Tilgner, 2007) and full spheres (e.g. Sauret *et al.*, 2013; Zhang *et al.*, 2013), but also other geometries like cylinders (e.g. Lopez & Marques, 2015; Mason & Kerswell, 1999; Noir *et al.*, 2010; Sauret *et al.*, 2012), annular confinements (e.g. Borcia *et al.*, 2014; Ghasemi V., 2016), and boxes (e.g. Boisson *et al.*, 2012; Jouve & Ogilvie, 2014).

It is worth to emphasise that numerical solutions do not yield realistic solutions *per se*. First, it is commonly assumed that fluid dynamical problems are well-described mathematically by the Navier–Stokes equations, which are a set of differential equations for the continuous flow variables pressure and velocity. Second, solutions to the Navier–Stokes equations cannot be obtained analytically in most cases. Therefore, an approximating algebraic problem is solved instead with the flow variables defined at a few distinct points. Viscosity ensures that the

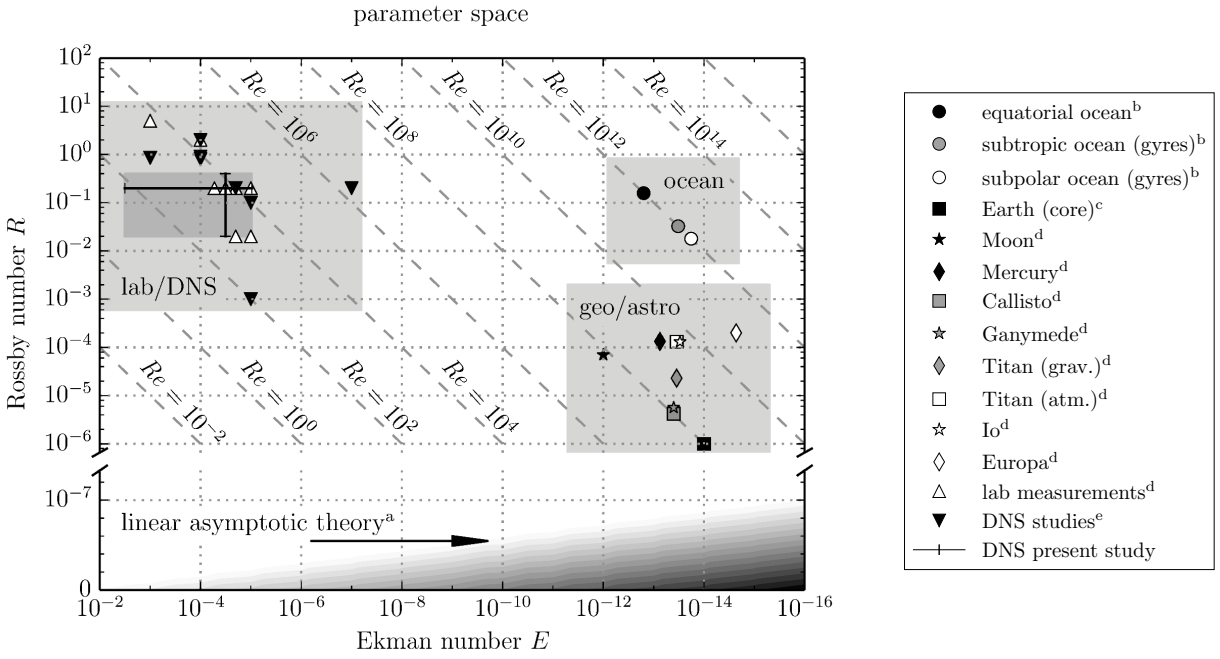

[a] Rieutord *et al.* (2001), Ogilvie (2005)

[b] Pedlosky (1987, pp. 254–257)

[c] Davidson (2014)

[d] Noir *et al.* (2009, and references therein)

[e] Koch *et al.* (2013)

[f] Beardsley (1970), Boisson *et al.* (2012), Maas (2001)

[g] Seelig (2014)

[h] Sauret *et al.* (2013)

[i] Calkins *et al.* (2010)

[j] Lopez & Marques (2011, 2014), Sauret *et al.* (2012)

[k] Borcia *et al.* (2014), Ghasemi V. (2016)

Figure 1.1: The parameter space in terms of the Rossby (R), Ekman (E) and Reynolds (Re) numbers investigated in this work in comparison to a few geo- and astrophysical flows (geo/astro, ocean), laboratory experiments and numerical studies (lab/DNS), as well as linear theory (lower panel). Linear theory is strictly valid only in the limit $R = 0$ which would correspond to inertial waves of infinitesimal amplitude. DNS results discussed in this work are marked by a black cross which corresponds to the ranges $2 \times 10^{-2} \leqslant R \leqslant 4 \times 10^{-1}$ and $10^{-5} \leqslant E \leqslant 3 \times 10^{-3}$.

solution is smooth on a microscopic scale. Therefore, the spatial resolution of the numerical approximation does not need to be reduced below the Kolmogorov micro-scale (Kolmogorov, 1941) in pure hydrodynamic problems. One can only be sure that an *accurate* numerical solution has been obtained if all scales of the flow down to the viscous length scale have been resolved. The method of computing accurate numerical solutions is known as *direct numerical simulation* (DNS). Which means DNS does not make any assumptions beyond the mathematical model formulation, here the Navier–Stokes equations (for a review on DNS see Moin & Mahesh, 1998).

DNS of an actual planetary flow is not possible[5] which means that only highly idealised configurations can be studied numerically and in the lab. Even for these idealised flows the parameters accessible remain far from reality.

Figure 1.1 shows the parameter space of various flows in terms of the Rossby (R), Ekman (E) and Reynolds ($Re = R/E$) numbers which are introduced later in equations (2.8) and (2.9). The Rossby number measures the strength of inertial forces relative to the Coriolis force, the Ekman number the viscous forces relative to the Coriolis force, and the Reynolds number the inertial forces relative to the viscous forces. The non-dimensional numbers are defined following the literature using the basin dimension as length scale and the inverse rotation rate of the system as time scale. This is somewhat inconsistent from the perspective of similarity theory but cannot be resolved since we do not know any details about the scales of the various flows. At the very least, the parameter space defined in that way gives an impression how far away theory and experiments (numerical and in the lab) are from actual applications.

The upper part of figure 1.1 contains state-of-the-art experiments in comparison to Earth's ocean currents and other geo- and astrophysical flows. Parameters of the DNS results discussed in the following chapters are highlighted (accessible parameters are estimated in section 3.3). It can be seen that experiments are orders of magnitude away from the parameters of the applications and that the DNS conducted for this work are of a similar order as those published.

The lower part of figure 1.1 illustrates the parameter space corresponding to the (asymptotic) linear theory of Rieutord *et al.* (2001) and Ogilvie (2005), where black shading means the theory is applicable and white that it is not. Strictly, the linear theory is valid only for $R = 0$, but finite Rossby numbers corresponding to finite amplitude inertial waves are believed to be permissible as long as the flow remains stable.

The configuration used in this work

The snapshot of Jupiter shown in figure 1.2 suggests that spherical geometry is a necessity to study planetary flows. However, this is not strictly the case as a second look at Jupiter reveals: the dynamics are organised in bands. All of the bands appear roughly similar so that an annular configuration is actually sufficient. In fact, this has been recognised several times, for instance, by Greenspan (1969, p. 294) regarding Earth's mid latitudes and, more recently, also by Seelig (2014, pp. 25) regarding Earth's near equator region. Therefore, an annular configuration has been selected for this study in order to simplify the confinement geometry as much as possible and to address the problem of localised wave excitation, wave propagation and focusing separately.

Figure 1.3 shows a schematic drawing of the geometry. The annular configuration consists of a liquid confined between two concentric cylinders. In the lab, the vessel mounted in upright

[5]DNS of Earth's mantle, for example, requires to resolve at least the viscous boundary layer δ, which is of the order of meters ($\delta \sim 1$ m), for the basin scale L of the order 1000 km (see Noir *et al.*, 2009). One needs about $(L/\delta)^3 \sim 10^{18}$ grid points to fully resolve the flow. For comparison, the simulations conducted in this work used up to 10^7 grid points, which is 11 orders of magnitude less.

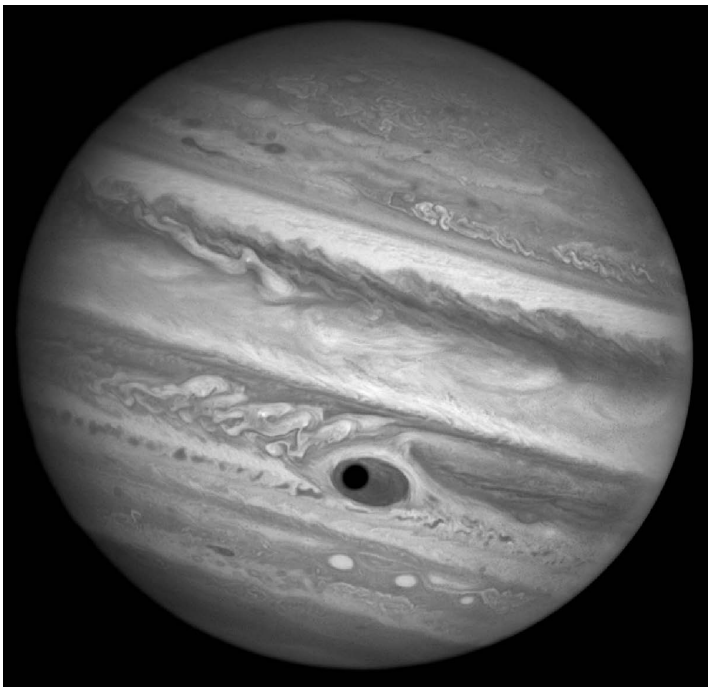

Figure 1.2: Banded atmospheric cloud patterns on Jupiter. Hubble image WFPC3/UVIS, April 21, 2014. (`http://hubblesite.org/newscenter/archive/releases/2014/31/image/c/`, last accessed: Feb. 28, 2015)

position wherefore all flow visualisations following will be presented for the symmetry axis (z-axis) pointing upward as indicated. Similar to standard Taylor–Couette systems the cylinders can rotate independently around their common symmetry axis which is indicated by the two rotation rates Ω_1 and Ω_2. Rigid lids close the annular gap at the top and bottom. The inner cylinder has been modified into a truncated cone (so-called frustum) in order to break the vertical mirror symmetry and to yield focusing and wave attractors (to be explained later). The radius $r_1\,(z|\alpha)$ of the inner wall is a function of height z and depends on the inclination angle α so that

$$r_1\,(z|\alpha) = r_1(0) - z\tan\alpha. \tag{1.1}$$

The physical dimensions of the table-top experiment (see Seelig, 2014) are given by the height $h = 500$ mm, the outer radius $r_2 = 200$ mm and the height-dependent inner radius $50\text{ mm} \leqslant r_1 \leqslant 100$ mm with an inclination angle of $\alpha = 5.71°$. Hence, the gap width varies between $100\text{ mm} \leqslant r_2 - r_1 \leqslant 150$ mm. Seelig (2014) has used water as working fluid, which has a kinematic viscosity of $\nu = 1.0018\,\mathrm{mm^2\,s^{-1}}$ at 20 °C (Grigull *et al.*, 1990). The temperature was also held constant during his experiments so that stratification is negligible and the flow is considered approximately incompressible. The laboratory experiment allows mean rotation rates $\Omega_0 \leqslant 100$ rpm, which corresponds to circumferential velocities of $v_\varphi \leqslant 2\,\mathrm{m\,s^{-1}}$.

Wall libration is used in numerical simulations (this thesis) and laboratory experiments (Seelig, 2014) to facilitate a 1-to-1 comparison of the flow induced. A small sinusoidal modulation is imposed on a uniform mean rotation rate Ω_0, that is,

$$\Omega(t) = \Omega_0\big[1 + \varepsilon\sin(\omega t)\big], \tag{1.2}$$

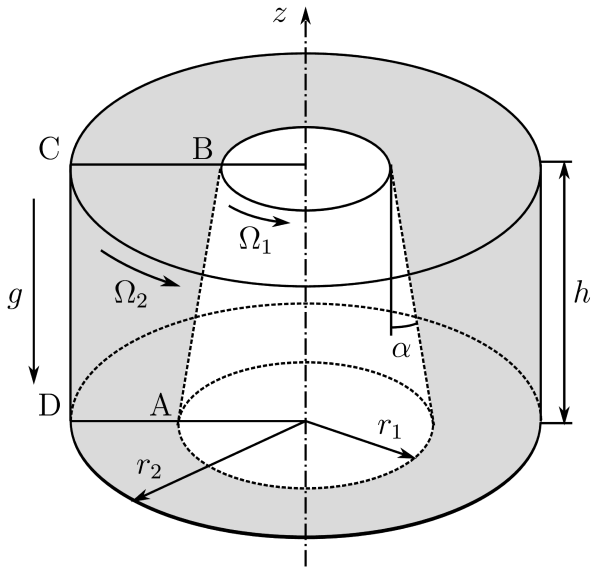

Figure 1.3: Schematic drawing of the annular geometry used in this study. Two concentric cylinders with radii r_1, r_2 and height h can rotate independently as indicated by the rotation rates Ω_1 and Ω_2. Lids at the top and bottom are attached to the outer cylinder, that is, all grey parts rotate with Ω_2 and the conical inner part (white) with Ω_1. Waves are excited by libration, which means by a modulation of the rotation rates. (From M. Klein *et al.* (2014). 'Inertial wave excitation and focusing in a liquid bounded by a frustum and a cylinder'. *J. Fluid Mech.*, **751**, pp. 258, reproduced with permission.)

where $\Omega(t)$ is the momentary rotation rate of the wall, ω is the libration frequency, and ε is the non-dimensional libration amplitude (similar to Maas, 2001; Seelig, 2014; Swart *et al.*, 2010). In the axisymmetric confinement shown in figure 1.3, libration provides a basin-scale axisymmetric perturbation. Equation (1.2) shows that libration yields a perturbation velocity scale $v' \sim \varepsilon\, r_{\mathrm{lib}}$ relative to the co-rotating frame of reference which is of the order r_{lib}, the distance of the librating wall from the axis of rotation. In the laboratory experiments of Seelig (2014) libration amplitudes of $\varepsilon \leqslant 0.5$ could be realised, which is also the upper limit investigated in the numerical study. We will see later that the flow induced by libration is significantly slower than the underlying mean rotation and that libration affects only a thin boundary layer directly.

Two complementary forcing configurations are studied throughout this work. With $\Omega(t)$ given by equation (1.2) the two configurations are as follows:

(i) the case of frustum in libration (the shaded part in figure 1.3), which means $\Omega_1 = \Omega(t)$ and $\Omega_2 = \Omega_0$;

(ii) the case of lids together with the outer cylinder in libration (the inner white part in figure 1.3), which means $\Omega_1 = \Omega_0$ and $\Omega_2 = \Omega(t)$.

Both configurations correspond precisely to the laboratory experiments of Seelig (2014) and provide a certain level of redundancy to evaluate hypotheses regarding wave excitation and resonance.

Outline of this thesis

In chapter 2 all theoretical foundations are collected. In section 2.1 the general mathematical description of the incompressible, rotating flow of interest is given in non-dimensional form. In section 2.2 the libration boundary conditions are introduced, in particular for the rotating annulus. In section 2.3 the properties of inertial waves are discussed including the frequency band of existence, the reflection law, wave propagation, their helicity, and viscous damping / broadening. In section 2.4 the method of geometric ray tracing is introduced and applied to inertial waves in the annular confinement. The method is used to obtain approximately a spectrum of frequency eigenvalues in terms of a bifurcation diagram of a map. Furthermore, the relevance of re-tracing ray orbits is discussed. The correspondence between ray orbits, wave attractors and normal modes is considered in more detail.

In chapter 3 the technical details of the numerical solver used for this study are given. In section 3.1 the transformed equations of motion are derived for terrain-following coordinates and contravariant volume fluxes in order to treat the frustum accurately. In section 3.2 the spatial discretisation is discussed. In section 3.3 the accuracy of the discretisation scheme is considered and the limits of DNS are addressed for the librating annulus. Accuracy and spatial convergence are addressed by the geometric conservation law and by a validation of the generalised curl implementation which has been added to the solver as part of this work. The limits of DNS are addressed by estimating the Rossby (R), Ekman (E) and Reynolds (Re) numbers reachable with the current implementation on state-of-the-art high-performance computers. In that way the working configuration is defined in terms of R and E as anticipated by figure 1.1. In section 3.4 the fractional-step method is described which ensures mass conservation and has been tied into the semi-implicit time-integration scheme used. An accurate implementation requires care in the selection of quadrature weights due to which the time integration scheme is discussed in detail. In section 3.5 the solution method for the Poisson equation for the pressure is explained since it is needed to complete the fractional step.

In chapter 4 the low-order inertial wave attractors and normal modes in the rotating annulus are investigated by DNS. Numerical solutions obtained are compared to reference laboratory experiments of Seelig (2014) and geometric ray tracing. In section 4.1 the rhomboidal wave attractor is discussed in detail for the case of forcing by frustum libration. In section 4.2 a normal mode is discussed for the case of forcing by lids plus outer cylinder libration. In section 4.3 the frequency-filter has been applied to the velocity field from which amplitude and phase have been obtained, as well as the time mean distribution of kinetic energy and dissipation rate associated with a given oscillation frequency. In sections 4.4 and 4.5 the sensitivity of the flow patterns and the frequency spectra with respect to the Rossby and Ekman numbers within the ranges $0.02 \leqslant R \lesssim 0.4$ and $3 \times 10^{-3} \leqslant E \leqslant 10^{-5}$ are investigated.

In chapter 5 the mechanism of localised inertial wave excitation due to wall libration is investigated. In section 5.1 the corner flow responsible for inertial wave emission is investigated by DNS. In section 5.2 laminar boundary layer theory is applied to the librating annulus. The local solutions obtained are compared to DNS results. In section 5.3 a quantitative model of the wave excitation mechanism is derived by making use of the local analytical solutions.

In chapter 6 the excitation efficiency of inertial wave attractors and normal modes is discussed. In section 6.1 the kinetic energy in the bulk and the boundary layer for different libration frequencies is compared to the prediction of the model for non-resonant wave excitation. The spectrum of resonance frequencies is compared to the reference spectrum of frequency eigenvalues that has been estimated by geometric ray tracing. In section 6.2 the kinetic energy at harmonics of the forcing frequency is considered to elucidate the non-linear excitation of

inertial waves. In section 6.3 the Q factor (quality factor) is introduced as ratio of the energy contained in the system *versus* the energy passing through the system over one libration period. The Q factor quantifies the strength of a resonance. In section 6.4 representative resonance peaks are selected and discussed in more detail by showing integral values of the kinetic energy, the dissipation rate, the Q factor, and the helicity.

In chapter 7 the main results of this thesis regarding inertial wave excitation and resonance conditions are summarised and discussed.

Appendix A gives an overview of the history of the numerical solver used and collects additional technical details relevant for reproduction of the numerical results, namely the smoothing function for the frustum wall and an outline of the frequency filter.

2 Fundamentals

The purpose of this chapter is to formulate the governing equations of a rotating flow and to clarify inertial waves. First, the equations of motions are introduced in the co-rotating frame of reference. Relevant properties of the equations are discussed in order to be clear about the mathematical model, the underlying assumptions, and the limitations. Second, plane inertial waves are obtained for an unbounded fluid and their properties are discussed in detail. Third, geometric ray tracing is used to study inertial waves in a confinement without actually solving the equations of motion. Finally, ray tracing is applied to the annulus which exhibits inertial wave attractors. The wave attractors are indexed for later reference.

2.1 Equations of motion for an incompressible fluid with rotation

The motion of a fluid is described mathematically by the Navier–Stokes equations (see, for example, Batchelor, 1967; Landau & Lifshitz, 1987). We restrict our attention to incompressible and homogeneous fluids in line with the applications outlined in the introduction. The fluid density ρ is assumed to be constant and uniform throughout the volume that rotates with the angular velocity $\boldsymbol{\Omega}$. Inertia is assumed more important than compressibility and rotation is assumed to be rapid such that Coriolis force is stronger than buoyancy.

The fluid velocity field $\boldsymbol{v} = \boldsymbol{v}(\boldsymbol{r}, t)$ is measured relative to the co-rotating frame of reference. The Navier–Stokes equations for a rotating, incompressible, Newtonian fluid simplify to (e.g. Greenspan, 1969, p. 6)

$$\partial_t \boldsymbol{v} + (\boldsymbol{v} \cdot \boldsymbol{\nabla})\, \boldsymbol{v} = -2\boldsymbol{\Omega} \times \boldsymbol{v} - \boldsymbol{\nabla}\phi - \nu \boldsymbol{\nabla} \times (\boldsymbol{\nabla} \times \boldsymbol{v}) \qquad \text{momentum eq.,} \tag{2.1}$$

$$0 = \boldsymbol{\nabla} \cdot \boldsymbol{v} \qquad \text{continuity eq.,} \tag{2.2}$$

with the time t, the fluid's constant kinematic viscosity ν, and the excess pressure $\phi = \phi(\boldsymbol{r}, t)$ (Lighthill, 1978, p. 438).

One should note the rotational form of the viscous term in equation (2.1). In general, viscous stresses yield the acceleration field $\rho^{-1}\boldsymbol{\nabla} \cdot (\mu \boldsymbol{\nabla} \circ \boldsymbol{v})$, which collapses to the momentum diffusion term $\nu \nabla^2 \boldsymbol{v}$ since ρ, ν and the dynamic viscosity $\mu = \rho\nu$ are constant. With the aid of the continuity equation Bronstein *et al.* (and the vector identity (3.258) in 2005, p. 190), we obtain the viscous term in rotational form as $-\nu \boldsymbol{\nabla} \times (\boldsymbol{\nabla} \times \boldsymbol{v})$. The rotational form highlights the importance of vortical motions in the fluid, since the vorticity vector $\boldsymbol{\zeta} = \boldsymbol{\nabla} \times \boldsymbol{v}$ now enters the momentum equations directly. Hence, spatial variations in the vortical motions—which is always the case in wall-bounded flows—will always lead to viscous losses. This is the foundation to be able to simulate actual geophysical and technical flows by modelling the unresolved scales by an additional turbulent viscosity, which constitutes the Boussinesq eddy viscosity approximation (Boussinesq, 1877) that is used in many state-of-the-art numerical solvers. In direct numerical simulations, the equations of motion (2.1) remain unaltered in order to capture the intricate interplay between dispersion related to momentum advection and momentum diffusion by molecular motions.

The excess pressure ϕ collects the potentials of the conservative forces. Here, these are the pressure gradient force, $-\boldsymbol{\nabla} p$, and the centrifugal force, $-\boldsymbol{\Omega} \times (\boldsymbol{\Omega} \times \boldsymbol{r})$, with $\boldsymbol{r}$ the position vector with the coordinate origin located on the rotational axis. The corresponding potentials are the hydrodynamic pressure p and the centrifugal potential $-\rho \left|\boldsymbol{\Omega} \times \boldsymbol{r}\right|^2 /2$, for which division by the constant density yields

$$\phi = \frac{p}{\rho} - \frac{\left|\boldsymbol{\Omega} \times \boldsymbol{r}\right|^2}{2}. \tag{2.3}$$

The rational behind this is as follows: a conservative force exerts surface normal stress on the fluid parcels and, thus, tries to change the fluid volume. This is, of course, not possible for an incompressible fluid and the pressure needs to develop in such a way that any compressing or expanding forces are balanced locally by the pressure gradient force. It is straightforward to include external conservative forces, $\boldsymbol{f}_\mathrm{c} = -\boldsymbol{\nabla}\Phi_\mathrm{c}$, by adding the corresponding potential Φ_c/ρ to the right hand side of equation (2.3). Consider, for example, the gravitational potential $\Phi_\mathrm{c} = -\rho \boldsymbol{g} \cdot \boldsymbol{r}$, where $\boldsymbol{g}$ is the local gravitational acceleration (on Earth). Pressure p needs to change accordingly such that ϕ remains unchanged. Using ϕ in the momentum equation reminds us of the unknown 'excess accelerations' that arise from the evolution of the velocity field.

The excess pressure ϕ can be viewed as Hodge potential of an irrotational-solenoidal decomposition (Helmholtz–Hodge decomposition; see, for example, Arfken & Weber, 2005, pp. 97) of the accelerations $\partial_t \boldsymbol{v}$. The continuity equation (2.2) yields solenoidal accelerations ($\partial_t \boldsymbol{v} = 0$). A substitution of the momentum equation (2.1) provides us with the Poisson equation for the excess pressure,

$$\nabla^2 \phi = -\boldsymbol{\nabla} \cdot (\boldsymbol{v} \cdot \boldsymbol{\nabla})\, \boldsymbol{v} + 2\boldsymbol{\Omega} \cdot \boldsymbol{\zeta}, \tag{2.4}$$

where $\boldsymbol{\Omega}$ is assumed uniform and constant and $\boldsymbol{\zeta} \equiv \boldsymbol{\nabla} \times \boldsymbol{v}$ is the vorticity (vector) for the velocity in the co-rotating frame. The sources are given by inertial terms, namely the divergence of the momentum transport and the vorticity component in the direction of the background rotation. The Poisson equation (2.4) reflects that the excess pressure reacts instantaneously in order to counteract any change of the fluid volume.

It is also worth noting that the mathematical model given by equations (2.1) and (2.2) is inconsistent at the very moment. The presence of friction implies that energy conversion can take place and turns mechanical energy into heat. Basically, this requires to formulate the internal energy equation and to take into account temperature-dependent viscosity and density (see, for example, Batchelor, 1967, pp. 151–156).

Dissipation rates and heating rates are generally inhomogeneous, which leads to the development of temperature and density gradients. This can be a severe problem when dissipation remains localised at a few 'hot spots' due to which instability or thermal convection might be caused. However, equations (2.1) and (2.2) are acceptable if the fluid remains in the vicinity of thermodynamic equilibrium at all times. This is a strong assumption and requires a heat sink that prevents the temperature from growing indefinitely. In applications, heat is extracted by radiation (e.g. planets, moons) or additional cooling (e.g. laboratory experiments, technical flows). We may assume dissipative heating to be small, the heat capacity to be large, and thermal conductivity to be high compared to the dynamical transport so that temperature gradients are generally small and disperse quickly. For the sake of simplicity, let us restrict the attention to the fluid in thermodynamic equilibrium throughout this study.

Scaling and non-dimensional formulation

Dimensional analysis (due to Buckingham, 1914) is one of the most powerful tools in fluid mechanics. The flow variables are scaled such that leading-order terms are $O(1)$. Consequently, the equations of motion receive dimensionless parameters. The dimensionless parameters are believed to control the solution. The Reynolds number, for example regarding the flow around an aerofoil, is such a dimensionless parameter. A smaller model of the aerofoil can be studied in the laboratory and it is believed to exhibit the same properties as the real aerofoil when the Reynolds numbers are the same in both cases. Mathematically, the scaled Navier–Stokes equations need to be solved only once. The solution exhibits turbulence for high Reynolds numbers and needs to be obtained numerically. The numerical solutions also benefit from proper scaling due to a minimisation of truncation errors that arise from the limited number representation and other discretisation errors (see, for example, Goldberg, 1991).

Let us return to rotating flow. Equations (2.1) and (2.2) are scaled by a typical fluid velocity U, a typical length scale L, and a typical time scale T. U and L need to be determined later in dependence on the problem. The time scale is typically fixed at $T = \Omega^{-1}$ with Ω the magnitude of the system's rotation rate. Without loss of generality, let $\boldsymbol{\Omega} = \Omega \boldsymbol{e}_z$ point along the z-direction with the unit vector $\boldsymbol{e}_z$. We use

$$\boldsymbol{v} = U\boldsymbol{v}^*, \quad \phi = UL\Omega\phi^*, \quad \boldsymbol{\nabla} = L^{-1}\boldsymbol{\nabla}^*, \quad \boldsymbol{r} = L\boldsymbol{r}^*, \quad t = \Omega t^* \tag{2.5}$$

and drop the asterisk '$*$' immediately after substitution into equations (2.1) and (2.2), which yields the scaled equations of motion (see Greenspan, 1969, p. 7)

$$\partial_t \boldsymbol{v} = -R\,(\boldsymbol{v}\cdot\boldsymbol{\nabla})\,\boldsymbol{v} - 2\boldsymbol{e}_z \times \boldsymbol{v} - \boldsymbol{\nabla}\phi - E\boldsymbol{\nabla}\times(\boldsymbol{\nabla}\times\boldsymbol{v})\,, \tag{2.6}$$

$$0 = \boldsymbol{\nabla}\cdot\boldsymbol{v}. \tag{2.7}$$

The dimensionless parameters are given by the Rossby number and the Ekman number, that is,

$$R := \frac{U}{\Omega L}, \qquad E := \frac{\nu}{\Omega L^2}. \tag{2.8}$$

The Rossby number measures the strength of momentum advection compared to Coriolis force, whereas the Ekman number measures the strength of viscous forces compared to Coriolis force. The Reynolds number measures momentum advection in comparison to the viscous forces,

$$Re := \frac{UL}{\nu} = \frac{R}{E}. \tag{2.9}$$

The non-dimensional numbers R, E, Re used in this study are computed with respect to the boundary condition, that is, from the libration-induced velocity perturbation and the basin geometry known *a priori*. A different scaling is possible but would require knowledge of the solution which is not accessible at that point. The specific definitions of R and E will be given together with the boundary conditions. Beforehand, the dimensionless formulation of the governing equations will be discussed since it does not depend on a specific choice of the dimensionless numbers.

Non-dimensional equations in Cartesian and cylindrical coordinates

The governing equations (2.6) and (2.7) are given in coordinate independent form. In order to interpret results and for the development of simplified theories it is often helpful to consider

the projections on particular coordinate axes. Cartesian coordinates (x, y, z) with the velocity components $\boldsymbol{v} = (u, v, w)$ are frequently encountered. In chapter 5, for example, we will make use of the Cartesian projections to elaborate on wave excitation. The dimensionless equations with respect to the Cartesian basis read (e.g. Pedlosky, 1987, p. 184, for the Coriolis parameter $f = 2$)

$$\left.\begin{aligned}
\frac{\partial u}{\partial t} =& - R\left(u\frac{\partial u}{\partial x} + v\frac{\partial u}{\partial y} + w\frac{\partial u}{\partial z}\right) + 2v - \frac{\partial \phi}{\partial x} + E\left(\frac{\partial^2 u}{\partial x^2} + \frac{\partial^2 u}{\partial y^2} + \frac{\partial^2 u}{\partial z^2}\right), \\
\frac{\partial v}{\partial t} =& - R\left(u\frac{\partial v}{\partial x} + v\frac{\partial v}{\partial y} + w\frac{\partial v}{\partial z}\right) - 2u - \frac{\partial \phi}{\partial y} + E\left(\frac{\partial^2 v}{\partial x^2} + \frac{\partial^2 v}{\partial y^2} + \frac{\partial^2 v}{\partial z^2}\right), \\
\frac{\partial w}{\partial t} =& - R\left(u\frac{\partial w}{\partial x} + v\frac{\partial w}{\partial y} + w\frac{\partial w}{\partial z}\right) - \frac{\partial \phi}{\partial z} + E\left(\frac{\partial^2 w}{\partial x^2} + \frac{\partial^2 w}{\partial y^2} + \frac{\partial^2 w}{\partial z^2}\right),
\end{aligned}\right\} \tag{2.10}$$

$$0 = \frac{\partial u}{\partial x} + \frac{\partial v}{\partial y} + \frac{\partial w}{\partial z}. \tag{2.11}$$

Rotating flows are naturally anisotropic due to the circular motion of the fluid volume (the underlying rigid body rotation). The preferred axis is given by the mean rotation $\boldsymbol{\Omega}$, which we have chosen to point in the vertical direction $\boldsymbol{e}_z$. In chapter 4, for example, we will use cylindrical velocity components to visualise the flow excited by libration. The cylindrical coordinates are denoted (r, φ, z) with the corresponding velocity components $\boldsymbol{v} = (v_r, v_\varphi, v_z)$. The governing equations (2.6) and (2.7) can be written with respect to the cylindrical basis by the aid of a polar coordinate transformation (e.g. Bronstein *et al.*, 2005, pp. 669, 680), so that

$$\left.\begin{aligned}
\frac{\partial v_r}{\partial t} =& - R\left(v_r\frac{\partial v_r}{\partial r} + \frac{v_\varphi}{r}\frac{\partial v_r}{\partial \varphi} - \frac{v_\varphi^2}{r} + v_z\frac{\partial v_r}{\partial z}\right) + 2v_\varphi - \frac{\partial \phi}{\partial r} \\
&+ E\left(\frac{1}{r}\frac{\partial}{\partial r}\left[r\frac{\partial v_r}{\partial r}\right] - \frac{v_r}{r^2} + \frac{1}{r^2}\frac{\partial^2 v_r}{\partial \varphi^2} - \frac{2}{r^2}\partial_\varphi v_\varphi + \frac{\partial^2 v_r}{\partial z^2}\right), \\
\frac{\partial v_\varphi}{\partial t} =& - R\left(v_r\frac{\partial v_\varphi}{\partial r} + \frac{v_\varphi}{r}\frac{\partial v_\varphi}{\partial \varphi} + \frac{v_r v_\varphi}{r} + v_z\frac{\partial v_\varphi}{\partial z}\right) - 2v_r - \frac{1}{r}\frac{\partial \phi}{\partial \varphi} \\
&+ E\left(\frac{1}{r}\frac{\partial}{\partial r}\left[r\frac{\partial v_\varphi}{\partial r}\right] - \frac{v_\varphi}{r^2} + \frac{1}{r^2}\frac{\partial^2 v_\varphi}{\partial \varphi^2} + \frac{2}{r^2}\partial_\varphi v_r + \frac{\partial^2 v_\varphi}{\partial z^2}\right), \\
\frac{\partial v_z}{\partial t} =& - R\left(v_r\frac{\partial v_z}{\partial r} + \frac{v_\varphi}{r}\frac{\partial v_z}{\partial \varphi} + v_z\frac{\partial v_z}{\partial z}\right) - \frac{\partial \phi}{\partial z} \\
&+ E\left(\frac{1}{r}\frac{\partial}{\partial r}\left[r\frac{\partial v_z}{\partial r}\right] + \frac{1}{r^2}\frac{\partial^2 v_z}{\partial \varphi^2} + \frac{\partial^2 v_z}{\partial z^2}\right),
\end{aligned}\right\} \tag{2.12}$$

$$0 = \frac{1}{r}\frac{\partial\left(r v_r\right)}{\partial r} + \frac{1}{r}\frac{\partial v_\varphi}{\partial \varphi} + \frac{\partial v_z}{\partial z}. \tag{2.13}$$

The advective accelerations (with a factor R) and the viscous accelerations (with a factor E) in equations (2.12) and (2.13) exhibit additional terms compared to the Cartesian components in equations (2.10) and (2.11). The additional terms originate from the coordinate transformation

by the orientation of the orthonormal cylindrical basis dependent on the position. One needs to keep track of changes in the basis orientation in order to keep the flow physics unchanged.

Note that the Coriolis force does not yield any additional terms or factors in the momentum equation, which is due to the transformation in a plane perpendicular to the rotation axis $\boldsymbol{e}_z$. This shows that only the fluid moving perpendicular to $\boldsymbol{e}_z$ is always accelerated towards the left by the Coriolis force.

2.2 Boundary conditions

All incompressible rotating flows are modelled by the (dimensionless) equations (2.6) and (2.7). In order to predict or study the flow in a specific application (e.g. liquid planet interiors) we need to make our mathematical model more specific by imposing boundary conditions to the governing equations.

On the one hand, we need initial conditions that define the state at time $t = 0$ in the whole fluid volume V. For an incompressible fluid it is sufficient to know the initial velocity field, $\boldsymbol{v}_0(\boldsymbol{r})$, from which a consistent initial condition for the excess pressure, $\phi_0(\boldsymbol{r})$, can be obtained via the Poisson equation (2.4). For simplicity, let the fluid be in rigid body rotation initially, which means $\boldsymbol{v}_0 = \boldsymbol{0}$ and $\phi_0 = 0$ relative to the co-rotating frame of reference.

On the other hand, boundary values for $\boldsymbol{v}$ and ϕ are needed along the domain boundary ∂V as time progresses. An inhomogeneous boundary condition forces a flow by an injection of energy and momentum into the fluid domain. In fact, there are no other forces in the equations (2.6) and (2.7) that could drive a flow. In principle, any value may be prescribed on the boundary provided that the boundary condition is compatible with the momentum equation and mass conservation. The latter demands that there is no net inflow or outflow across the domain boundary ∂V.

Let us limit our attention to a confined flow excited by motions of the bounding wall. It is relatively easy to motivate and formulate boundary conditions for the velocity field or the stresses (e.g. Batchelor, 1967, pp. 148–151). We follow common practice and assume that near-wall molecules stick to the wall such that the outermost fluid layer follows the wall motions exactly. In effect, the velocity vector is prescribed at the boundary which is known as the *no-slip boundary condition*,

$$\boldsymbol{v}|_{\partial V} = \boldsymbol{v}_\mathrm{w} \qquad \text{with} \quad \boldsymbol{n} \cdot \boldsymbol{v}_\mathrm{w} = 0. \tag{2.14}$$

The wall velocity $\boldsymbol{v}_\mathrm{w}$ is a function of time restricted only by the impermeability condition on the right which reflects that the shape of the confinement remains constant. The flow is forced by the wall moving in lateral direction (perpendicular to the surface normal $\boldsymbol{n}$ on ∂V) and power input results from the action of viscous stresses (for a discussion of the wall shear stress see, for example, Pope, 2000, pp. 264–271). Impermeability of the wall requires Neumann boundary conditions for the excess pressure, say $\boldsymbol{n} \cdot \boldsymbol{\nabla}\phi = G_\mathrm{w}(\boldsymbol{r}, t)$ for $\boldsymbol{r} \in \partial V$. To be more precise, Robin boundary conditions apply due to the skew-derivative, but these details of the gradient function G_w will not be so important for the formulation of the numerical algorithm. Instead, the excess pressure can be interpreted as a 'kinematic potential' for which an analysis of the boundary conditions (see chapter 3) will show that the specification of G_w is not needed for the computation of the velocity solution. For further details on the pressure boundary conditions see, for example, Gresho & Sani (1987).

We proceed with the libration boundary conditions used for the annular confinement (figure 1.3). The annulus is installed such that it rotates around its axis pointing in the direction

$\boldsymbol{e}_z$. Libration given by equation (1.2) means that the rotation rate is modulated but the rotation axis remains fixed. Using cylindrical coordinates (r, φ, z) yields that the velocity components v_r and v_z need to vanish at the confinement walls, that is

$$v_r = v_z = 0 \qquad \text{at} \quad z = 0, h \quad \text{and} \quad r = r_1(z), r_2. \tag{2.15}$$

Hence, the flow is excited only by the azimuthal velocity component v_φ. In the co-rotating frame of reference, the scaled wall velocity consistent with equations (2.6) and (2.7) reads

(i) in the case of frustum libration

$$v_\varphi(r, z, t) = \begin{cases} \dfrac{r}{r_1(0)} \sin(\omega t) & \text{for} \quad r = r_1(z), \\ 0 & \text{otherwise;} \end{cases} \tag{2.16}$$

(ii) in the case of lids plus outer cylinder libration

$$v_\varphi(r, z, t) = \begin{cases} \dfrac{r}{r_2} \sin(\omega t) & \text{for} \quad z = 0, h \quad \text{and} \quad r = r_2, \\ 0 & \text{otherwise.} \end{cases} \tag{2.17}$$

The height-dependent radius $r_1(z)$ defines the shape of the inner frustum wall, for example $r_1(z|\alpha) = r_1(0) - z \tan\alpha$ with α the wall inclination as given earlier by equation (1.1).

The velocity scale relative to the co-rotating frame of reference is $U_{(\mathrm{i})} = \varepsilon\Omega_0 r_1(0)$ in case (i), but $U_{(\mathrm{ii})} = \varepsilon\Omega_0 r_2$ in case (ii), in order to yield a comparable Rossby number R as defined in equation (2.8). The two velocity scales differ by the radius ratio, that is, $U_{(\mathrm{ii})}/U_{(\mathrm{i})} = r_2/r_1(0) = 2$ for the specifications of the laboratory experiment (see Seelig, 2014). The Ekman number E, also defined in equation (2.8), is fixed by selecting an appropriate length scale. In this study we will use the minimum gap width, $L = r_2 - r_1(0)$, measured at the bottom lid (or $L = 100$ mm for the specifications of the laboratory experiment described by Seelig, 2014).

Note that the azimuthal direction is periodic for $\varphi \in [0, 2\pi)$. Hence, periodic Dirichlet conditions are used for both the velocity field $\boldsymbol{v}$ and the excess pressure field ϕ.

2.3 Inertial waves

Sound and light waves are widely known to people from daily life experience. The propagation and reflection of these wave types can be visualised, for example, by the aid of laser pointers. Wave crests, kinetic energy and momentum propagate in the direction of the wave vector, which is perpendicular to the crests (phase fronts) and defines the direction along which the wavelength is measured. Sound and light waves reflect like a billiard ball by conserving the angle between the propagation direction and the surface normal (Snell's law, see e.g. Lighthill, 1978, p. 323). Conservation of energy and momentum require that the speed of a billiard ball or the wavelength for that matter does not change by a reflection.

By contrast, inertial wave propagation and reflection is significantly different from the daily life experience. Energy and momentum of an inertial wave propagates perpendicular to the wave crests. Moreover, inertial waves reflect by conserving the angle between the propagation direction and the rotation axis which can result in geometric focusing. Kinetic energy is compressed into a tiny fraction of the fluid volume and a so-called wave attractor may emerge (e.g. Maas *et al.*, 1997). In the following, relevant properties of inertial waves are repeated from

literature and streamlined notation. More emphasize is put on the 3-D structure of inertial waves and their helicity which, in particular, is only rarely discussed but will prove useful later in this study.

The simplest setting exhibiting inertial waves is a rapidly rotating, unbounded fluid subject to small velocity perturbations. The scaled equations (2.6) and (2.7) in the co-rotating frame of reference are linearised around the state of rigid body rotation simply by setting $R = 0$. Since there are no boundaries, let us also neglect viscosity by setting $E = 0$, hence

$$\partial_t \boldsymbol{v} = -\boldsymbol{\nabla}\phi - 2\boldsymbol{e}_z \times \boldsymbol{v}, \qquad \boldsymbol{\nabla} \cdot \boldsymbol{v} = 0. \tag{2.18}$$

Consequently, the Poisson equation (2.4) reduces to

$$\nabla^2 \phi = 2\zeta_z \tag{2.19}$$

with sources due to the vertical vorticity ζ_z in the direction $\boldsymbol{e}_z$ of the rotational axis and the vorticity vector given by $\boldsymbol{\zeta} \equiv \boldsymbol{\nabla} \times \boldsymbol{v}$.

The excess pressure ϕ can be removed from the governing equations by taking the curl of equation (2.18), which yields the vorticity equation (compare to Greenspan, 1969; Névir & Blender, 1993)

$$\partial_t \boldsymbol{\zeta} = (2\boldsymbol{e}_z \cdot \boldsymbol{\nabla})\, \boldsymbol{v}. \tag{2.20}$$

Note that the vorticity is solenoidal ($\boldsymbol{\nabla} \cdot \boldsymbol{\zeta} = 0$) by construction. This is a direct consequence of the vanishing divergence of the curl, that is, $\boldsymbol{\nabla} \cdot (\boldsymbol{\nabla} \times \boldsymbol{A}) \equiv 0$ for any vector field $\boldsymbol{A}$. Consequently, the vector identity for the double curl (e.g. Bronstein *et al.*, 2005, pp. 190, equation (3.258)) of the velocity or the vorticity of an incompressible flow reduces to

$$\boldsymbol{\nabla} \times (\boldsymbol{\nabla} \times \boldsymbol{A}) = -\nabla^2 \boldsymbol{A} \qquad \text{for} \quad \boldsymbol{A} = \boldsymbol{v}, \boldsymbol{\zeta}. \tag{2.21}$$

By the aid of the latter equation one can show that every flow variable obeys a Poincaré equation. Following Cartan (1922), one has

$$\mathcal{L}\phi = 0, \quad \mathcal{L}\boldsymbol{v} = \boldsymbol{0}, \quad \mathcal{L}\boldsymbol{\zeta} = \boldsymbol{0} \qquad \text{with} \quad \mathcal{L} \equiv \left[\partial_t^2 \nabla^2 + 4\partial_z^2\right], \tag{2.22}$$

where $\mathcal{L}$ is the so-called Poincaré operator.

Without boundary conditions, the Poincaré equation (2.22) has plane *inertial wave* (or Poincaré wave) solutions

$$(p, \boldsymbol{v}, \boldsymbol{\zeta})^{\mathrm{T}} \propto \exp\left(\mathrm{i}\boldsymbol{k} \cdot \boldsymbol{r} - \mathrm{i}\sigma t\right) \tag{2.23}$$

with σ the wave frequency and $\boldsymbol{k}$ the wave vector. The Poincaré equations show that the restoring force for inertial waves is the Coriolis force.

Insertion of the plane wave solution into the Poincaré equation yields the *dispersion relation* (e.g. Lighthill, 1978, pp. 437–439)

$$\sigma = \pm 2\frac{k_z}{k} = 2\cos\vartheta \qquad \text{with} \quad 0 < \sigma < 2, \tag{2.24}$$

where $k \equiv |\boldsymbol{k}|$. The angle ϑ takes values in $(0, \pi/2)$ and is measured between the wave vector $\boldsymbol{k}$ and the rotation axis $\boldsymbol{e}_z$. The sign in equation (2.24) needs to be selected in accord with $\operatorname{sgn}(k_z) = \pm 1$ to yield only positive frequencies. The propagation direction of inertial waves is

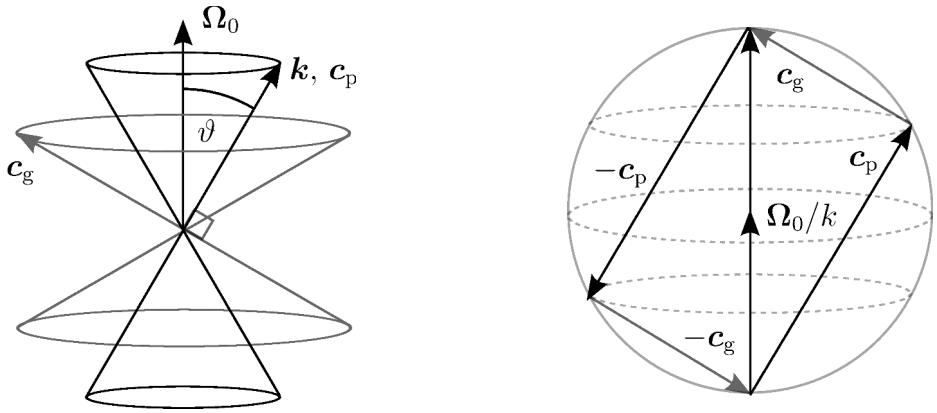

(a) (b)

Figure 2.1: Panel (a) visualises the anisotropic dispersion relation (2.24) by the double cone. It shows the geometrical constrains of the wave vector $\boldsymbol{k}$, phase velocity $\boldsymbol{c}_\mathrm{p}$ and group velocity $\boldsymbol{c}_\mathrm{g}$ when the frequency σ and the wavelength $\lambda = 2\pi k^{-1}$ are fixed. Panel (b) gives a geometric interpretation of the interdependent $\boldsymbol{c}_\mathrm{p}$ and $\boldsymbol{c}_\mathrm{g}$ constrained to the surface of a $2\Omega_0/k$-sphere (diameter $2\Omega_0/k$).

determined by the wave frequency, which is quite different from light or sound waves, commonly referred to as anisotropic dispersion.

The dispersion relation is visualised in figure 2.1(a) by the so-called double cone (e.g. Manders & Maas, 2003), where $\boldsymbol{c}_\mathrm{p}$ and $\boldsymbol{c}_\mathrm{g}$ denote the phase and group velocity respectively. Crests and troughs propagate with $\boldsymbol{c}_\mathrm{p}$, whereas wave energy propagates with $\boldsymbol{c}_\mathrm{g}$ (e.g. Lighthill, 1978, pp. 312). Following Greenspan (1969, pp. 185–188), phase and group velocity read

$$\boldsymbol{c}_\mathrm{p} = \pm\frac{2k_z\boldsymbol{k}}{k^3}, \qquad \boldsymbol{c}_\mathrm{g} = \mp\frac{\boldsymbol{k}\times(\boldsymbol{k}\times 2\boldsymbol{e}_z)}{k^3} \qquad \text{with} \quad \boldsymbol{c}_\mathrm{p}+\boldsymbol{c}_\mathrm{g} = \pm\frac{2}{k}\,\boldsymbol{e}_z. \tag{2.25}$$

The equation on the right is an invariant for a fixed wavelength $\lambda = 2\pi k^{-1}$. The geometric interpretation is shown in figure 2.1(b) by the $2\Omega_0/k$-sphere. Phase and group velocity are perpendicular to each other. Inertial wave energy hence propagates parallel to the wave crests but perpendicular to the phase.

Note in this respect that phase and group velocity need to have common parallel or anti-parallel projections on the rotational axis so that kinetic energy and phase propagate upward (+1) or downward (−1) *together*. Therefore one has for the phase and group velocity projections on the rotation axis

$$\boldsymbol{e}_z\cdot\boldsymbol{c}_\mathrm{p} = \pm\frac{2}{k^3}k_z^2, \qquad \boldsymbol{e}_z\cdot\boldsymbol{c}_\mathrm{g} = \pm\frac{2}{k^3}\left(\boldsymbol{e}_z\times\boldsymbol{k}\right)^2. \tag{2.26}$$

Inertial waves are transverse waves which is a consequence of the continuity equation (2.7). The full solution exhibits a phase lag between the velocity components in a plane perpendicular to $\boldsymbol{k}$ (see Greenspan, 1969, p. 187). In complex notation, with $\hat{\boldsymbol{v}}$ the complex velocity amplitude, one has

$$\boldsymbol{v} = \hat{\boldsymbol{v}}\,\exp\left(\mathrm{i}\boldsymbol{k}\cdot\boldsymbol{r} - \mathrm{i}\sigma t\right). \tag{2.27}$$

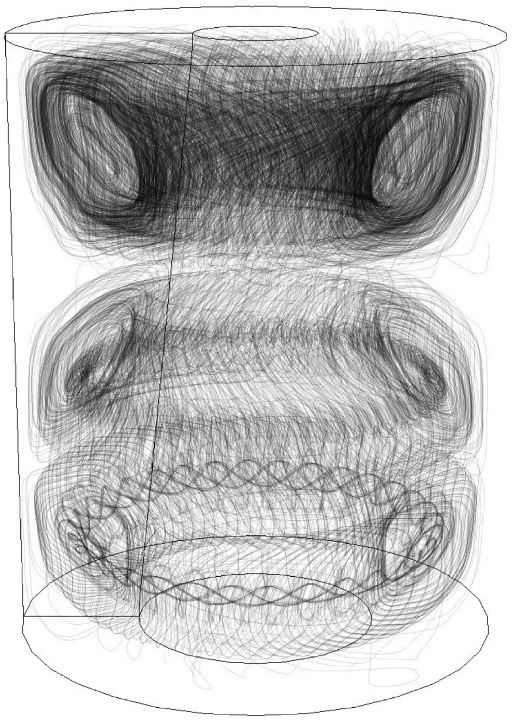

Figure 2.2: The helical structure of inertial waves in the rotating annulus obtained by DNS and visualised by 3-D streamlines in a 'frozen' flow field. Each streamline has been integrated up to a length of 50 minimum gap widths starting from 100 random points in the radial-axial section illustrated. In this example inertial waves are excited by libration of the conical inner wall (frustum) with the non-dimensional frequency $\omega = 1.18$ and the non-dimensional parameters $R = 0.2$, $E = 3.19 \times 10^{-5}$. The selected libration frequency excites the so-called $(1, 3)$ wave attractor, which is axisymmetric and is accompanied by three large helical vortices (toroids) in the fluid bulk. The wave attractor classification and their realisation in the DNS will be discussed further in section 2.4 and chapter 4.

Substitution into the vorticity equation (2.20) and an exploit of the dispersion relation (2.24) yields

$$-\mathrm{i}\sigma\hat{\boldsymbol{\zeta}} = (2\boldsymbol{e}_z \cdot \boldsymbol{k})\,\mathrm{i}\hat{\boldsymbol{v}} \qquad \Rightarrow \qquad \hat{\boldsymbol{\zeta}} = \mp k\hat{\boldsymbol{v}}. \tag{2.28}$$

The vorticity equation removes the freedom in the phase (e.g. Davidson, 2013, p. 54), which means

$$\boldsymbol{k} \times \mathrm{i}\hat{\boldsymbol{v}} = \mp k\hat{\boldsymbol{v}}. \tag{2.29}$$

Equation (2.29) shows that velocity and vorticity are in phase and inertial waves are circularly polarised. More precisely, inertial waves are *helical*. Helicity quantifies the handedness and strength of screw-like structures in a vector field (see Kurgansky, 2002, pp. 26).

Figure 2.2 illustrates the helical (spiral) structures in the velocity field by computing streamlines in a 'frozen' velocity field. The flow has been excited by libration of the conical inner wall (frustum) of the rotating annulus[1] and is dominated by inertial waves[2]. The streamlines reveal the presence of distinct spatial structures in the bulk flow consisting of three toroids. The flow is obviously axisymmetric, which is due to the symmetry of the forcing and the weak Rossby

[1] Details of the waves excited in the rotating annulus are postponed to chapter 4.

[2] We will discuss the excitation and dominance of inertial waves in chapter 5.

number used ($R = 0.2$). Each toroid is revealed by a bunch of spiralling streamlines which directly hint at helical structures in the velocity field.

Note that the visualisation by streamlines is possible only because of the cylindrical geometry which enforces a recurrence of streamlines along the periodic azimuthal coordinate. Here, the flow is axisymmetric and waves travel in the axial-radial direction exclusively. Surfaces of constant phase are therefore concentric cones. In the case of a plane inertial wave the 'frozen' velocity field would be composed of parallel sheets (surfaces of constant phase) in each of which the velocity vector points in a unique direction (see Messio *et al.*, 2008). It is due to the action of the Coriolis force that the velocity vector has to point in different directions in neighbouring sheets. The streamlines in this scenario would be straight, extending from minus to plus infinity, and would not be parallel between neighbouring sheets. However, a helical structure is present as well. This helical structure is revealed when looking along the axis defined by the wave vector $\boldsymbol{k}$, which is perpendicular to the surfaces of constant phase. The analogue of planar sheets in annular configuration are conical surfaces with the wave vector lying in the axial-radial plane. So, we demand a quantity that measures the presence of helical structures independently of the selected geometry. This can be achieved by the aid of helicity.

Inertial waves possess non-zero helicity independent of the selected coordinate system. The time-averaged helicity density, for example of a plane inertial wave, can be obtained straightforwardly by the aid of the complex vorticity and velocity representation given above. One has

$$\overline{\mathrm{Re}\,(\boldsymbol{v}) \cdot \mathrm{Re}\,(\boldsymbol{\zeta})} = \mp k \left|\hat{\boldsymbol{v}}\right|^2, \tag{2.30}$$

where $\overline{(\cdot)}$ denotes the temporal average. The wave vector and velocity magnitudes are positive, $k > 0$ and $|\hat{\boldsymbol{v}}|^2 > 0$, due to which the sign of the helicity in equation (2.30) needs to be reversed compared to that in the dispersion relation given in equation (2.24). Waves propagating upward (downward) have negative (positive) helicity. Upward (downward) propagation means $\boldsymbol{e}_z \cdot \boldsymbol{c}_\mathrm{g} > 0$ ($\boldsymbol{e}_z \cdot \boldsymbol{c}_\mathrm{g} < 0$) such that helicity is transported by inertial waves. It depends on the problem, though, if this yields mixing or de-mixing of helicity Davidson (e.g. 2013, pp. 54). The helicity can be important for the coupling of hydrodynamics to the magnetic field in an electrically conducting fluid wherefore inertial waves have received an increasing attention over the past years in the field of magnetohydrodynamics (MHD), in particular in the context of wave-driven dynamos (e.g. Davidson, 2014).

Inertial waves are also present in viscous fluids. We still assume small amplitude perturbations and remain in the linear limit ($R = 0$), but allow the Ekman numbers to be finite ($E > 0$). Equation (2.18) receives the viscous term $E\nabla^2\boldsymbol{v}$ from equation (2.6). Consequently, the vorticity equation (2.20) receives the viscous term $E\nabla^2\boldsymbol{\zeta}$. According to Phillips (1963), an inviscid plane wave solution given by equations (2.27) and (2.29) remains intact except for the attenuation factor

$$a_k(t) = \exp\left(-Ek^2 t\right) \tag{2.31}$$

due to which the wave amplitude decays exponentially with time.

Cortet *et al.* (2010) have shown how to adapt Phillips' solution for a stationary boundary value problem with sinusoidal forcing at some point in space. They consider a local frame of reference attached to the wave that propagates with $|\boldsymbol{c}_\mathrm{g}| \equiv c_\mathrm{g}$ away from the source. The local axes is indicated by primed variables and aligned such that $\boldsymbol{e}'_y \parallel \boldsymbol{c}_\mathrm{g}$, $\boldsymbol{e}'_z \parallel \boldsymbol{k}$, and $\boldsymbol{e}_z \cdot \boldsymbol{e}'_z = \cos\vartheta$. The offset ξ between the wave source and the origin of the local frame of reference is given by

$$\xi(t) = c_\mathrm{g} t = \frac{2\sin\vartheta}{k} t, \tag{2.32}$$

which makes use of the geometric property shown in figure 2.1(b) and the wave propagation direction ϑ. Substituting equation (2.32) and the dispersion relation (2.24) into equation (2.31) yields the attenuation factor of a propagating inertial wave as

$$a'_k(\xi) = \exp\left(-k^3\delta^2\xi\right) \qquad \text{with} \quad \delta \equiv \sqrt{\frac{E}{\sigma\tan\vartheta(\sigma)}}. \tag{2.33}$$

Here, δ is the viscous length scale of the stationary problem and is constant for any wave number of the same frequency σ.

The interesting point with respect to the spatial attenuation $a'_k(\xi)$ (equation (2.33)) in comparison to the temporal attenuation $a_k(t)$ (equation (2.33)) is as follows: in the case of a continuously driven inertial wave one can express the elapsed time by a distance with the aid of the dispersion relation (2.24). Hence, the attenuation of the stationary wave is known *a priori* for every point along the wave path and can be computed from the specified wave frequency σ, a typical wave number k corresponding roughly to the inverse size of the wave source, and the Ekman number E.

2.4 Wave attractors in the annulus obtained by ray tracing

Inertial waves in an unbounded domain are merely an academic problem. Hence, the question is what will happen in a confinement? In short, one is faced with inertial eigenmodes of the rotating vessel. The spectrum of eigenmodes, however, may be difficult or at least expensive to compute and most likely requires numerical techniques. In order to learn more about inertial waves in confinements nevertheless, let us proceed by reducing the problem further. First, the method of ray tracing is introduced with an eye on cylindrical geometry and we discuss in which sense it is an efficient method to study inertial waves. Second, ray tracing is applied to the annulus (see figure 1.3) in order to get an overview of the possible wave attractors. Third, relevant properties of wave attractors are discussed and bifurcations due to frequency variation are studied. Finally, we will organise the wave attractors and ray orbits exhibited by the annulus shown in figure 1.3.

Ray tracing in the annulus

We start from the linearised, inviscid equations (2.18) and separate time by looking for oscillatory solutions $\propto \exp(-\mathrm{i}\sigma t)$ (see Cartan, 1922). In the latter, σ denotes the frequency of an inviscid inertial eigenmode of the confinement. Inserting the ansatz into equation (2.22) yields the transformed Poincaré operator

$$\mathcal{L}' \equiv \left[\nabla^2 - \frac{4}{\sigma^2}\frac{\partial^2}{\partial z^2}\right]. \tag{2.34}$$

Due to the coupling of the variables ϕ, $\boldsymbol{v}$, $\boldsymbol{\zeta}$, it is sufficient to consider only the scalar excess pressure ϕ, which we assume complex in the following. Without loss of generality but in anticipation of the annular confinement we may use cylindrical coordinates which yields the Poincaré equation as (e.g. Borcia & Harlander, 2012)

$$\frac{\partial^2\phi}{\partial r^2} + \frac{1}{r}\frac{\partial\phi}{\partial r} + \frac{1}{r^2}\frac{\partial^2\phi}{\partial\varphi^2} - \left(\frac{4}{\sigma^2} - 1\right)\frac{\partial^2\phi}{\partial z^2} = 0. \tag{2.35}$$

Equation (2.35) is hyperbolic for any frequency $\sigma \in (0, 2)$, which means oscillatory solutions are inertial modes in the same frequency band as plane inertial waves.

Geometry comes into play via the pressure boundary condition which, in the linear inviscid limit, is obtained by requiring impermeable walls $\boldsymbol{n} \cdot \boldsymbol{v}|_{\partial V} = 0$. For the geometry in figure 1.3 with an inner frustum described by equation (1.1), one can obtain the following pressure boundary conditions (see Borcia & Harlander, 2012)

$$\left.\begin{aligned} \frac{\partial \phi}{\partial z} &= 0 \qquad \text{at} \quad z = 0, h, \\ \mathrm{i}\sigma \left[\frac{\partial \phi}{\partial r} - \left(\frac{4}{\sigma^2} - 1 \right) \frac{\partial \phi}{\partial z} \tan\alpha \right] + \frac{2}{r} \frac{\partial \phi}{\partial \varphi} &= 0 \qquad \text{at} \quad r = r_1(0) - z \tan\alpha, \\ \mathrm{i}\sigma \frac{\partial \phi}{\partial r} + \frac{2}{r} \frac{\partial \phi}{\partial \varphi} &= 0 \qquad \text{at} \quad r = r_2. \end{aligned}\right\} \tag{2.36}$$

Furthermore, considering librational forcing as introduced in section 2.2 yields purely axisymmetric perturbations to the rigid body rotation. Assuming that the flow remains stable, it seems reasonable to restrict our attention to purely axisymmetric solutions by letting $\partial_\varphi \phi = 0$ in equations (2.34), (2.35) and (2.36). Consequently, it remains to solve the second-order PDE

$$\frac{\partial^2 \phi}{\partial r^2} - \left(\frac{4}{\sigma^2} - 1 \right) \frac{\partial^2 \phi}{\partial z^2} + \frac{1}{r} \frac{\partial \phi}{\partial r} = 0, \tag{2.37}$$

with the axisymmetric boundary conditions

$$\left.\begin{aligned} \frac{\partial \phi}{\partial z} &= 0 \qquad \text{at} \quad z = 0, h, \\ \mathrm{i}\sigma \left[\frac{\partial \phi}{\partial r} - \left(\frac{4}{\sigma^2} - 1 \right) \frac{\partial \phi}{\partial z} \tan\alpha \right] &= 0 \qquad \text{at} \quad r = r_1(0) - z \tan\alpha, \\ \frac{\partial \phi}{\partial r} &= 0 \qquad \text{at} \quad r = r_2. \end{aligned}\right\} \tag{2.38}$$

A solution to the eigenvalue problems (EVPs), equation (2.35) or (2.37), is feasible only in simple geometry, like a sphere (e.g. Greenspan, 1969, pp. 63), an untiled box (e.g. Maas, 2003), a cylinder (e.g. Sauret *et al.*, 2012), or a straight annulus (e.g. Borcia *et al.*, 2014). In general, solving is a complicated undertaking due to the emergence of singularities (see, for example, Harlander, 2008; Harlander & Maas, 2007). One option is to re-introduce the viscous term but to keep the impermeable stress-free boundary condition $\boldsymbol{n} \cdot \boldsymbol{v} = 0$. This yields smooth eigenmodes which have been regularised by viscosity (see, for example, Hollerbach & Kerswell, 1995; Rieutord *et al.*, 2001; Rieutord & Valdettaro, 1997; Tilgner, 1999).

The EVPs need to be solved numerically and depend on the Ekman number E, which renders the computation of eigenmode spectra a tedious task. The alternative is to focus only on the geometrical structure of the eigenmodes but to drop all phase and amplitude information. This is possible since solutions take the form of characteristics when equation (2.37) is hyperbolic for $0 < \sigma < 2$ (e.g. Bronstein *et al.*, 2005, p. 541). There are two families of functions that form the *webs of characteristics* $c_\pm = \text{const}$ (Maas & Lam, 1995), namely

$$c_\pm = z \pm r \sqrt{\frac{4}{\sigma^2} - 1}. \tag{2.39}$$

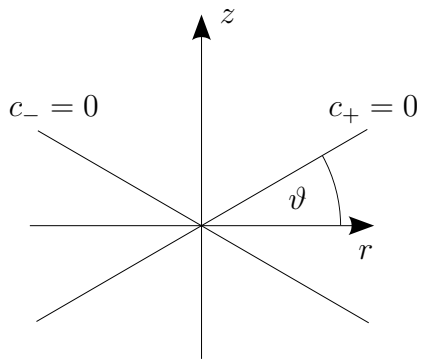

Figure 2.3: Reduction of the double cone (figure 2.1) to the 'St. Andrew's cross' for characteristics of inertial wave solutions. Characteristics $c_\pm$ are parallel to the group velocity $\boldsymbol{c}_\mathrm{g}$ so that ϑ gives the inclination angle with respect to the radius r.

Substitution of the dispersion relation (2.24) into equation (2.39) yields

$$c_\pm = z \pm r \tan\vartheta. \tag{2.40}$$

This equation gives a purely geometrical view and is related to inertial waves by $\vartheta = \vartheta(\sigma)$, which means the inclination of the characteristics is a function of the wave frequency σ only. In a radial-axial plane, the double cone (see figure 2.1(a)) reduces to the 'St. Andrew's cross' shown in figure 2.3. Wave energy propagates along the webs $c_\pm$ parallel to $(\cos\vartheta\,\boldsymbol{e}_r \pm \sin\vartheta\,\boldsymbol{e}_z)$. At $t = 0$, one can mark a point and follow its path onwards. As time progresses, the marker traces out an *(inertial wave) ray*. Hence, *ray tracing* addresses the method of following such rays from one reflection point to another.

Note that the procedure outlined is exact in a 2-D Cartesian space but only an approximation in the radial-axial plane of the annulus due to the neglect of radial terms. However, since no wave ray will ever come near the axis the approximation can be expected to be good for large radii and a small gap.

Reflection law and the effect of focusing explained for the rhomboidal wave attractor

The rays corresponding to characteristics of inertial waves reflect at a wall by conserving the angle ϑ. The reason is energy conservation, which requires that incident and reflected wave have the same frequency and the characteristics the same inclination (see figure 2.3). The conservation of momentum and the fixed wall orientation (fixed surface normal $\boldsymbol{n}$) select in which of the four directions of the 'St. Andrews cross' the reflected wave or ray propagates (for a detailed discussion see Phillips, 1963). Inertial wave reflection is, thus, fundamentally different from specular reflection (e.g. light waves, sound waves, or billiard balls).

This difference is illustrated in figure 2.4 for a radial-axial section of the annular confinement (figure 1.3). Two rays in figure 2.4 are launched in the same direction and with the same initial inclination ϑ. The launch points are different so that the rays reflect in P_1 and P_2 respectively. In figure 2.4(a) the outer cylinder wall is approached. It is parallel to the rotation axis $\boldsymbol{e}_z$ so that specular reflection occurs also for the inertial wave ray and there is no difference compared

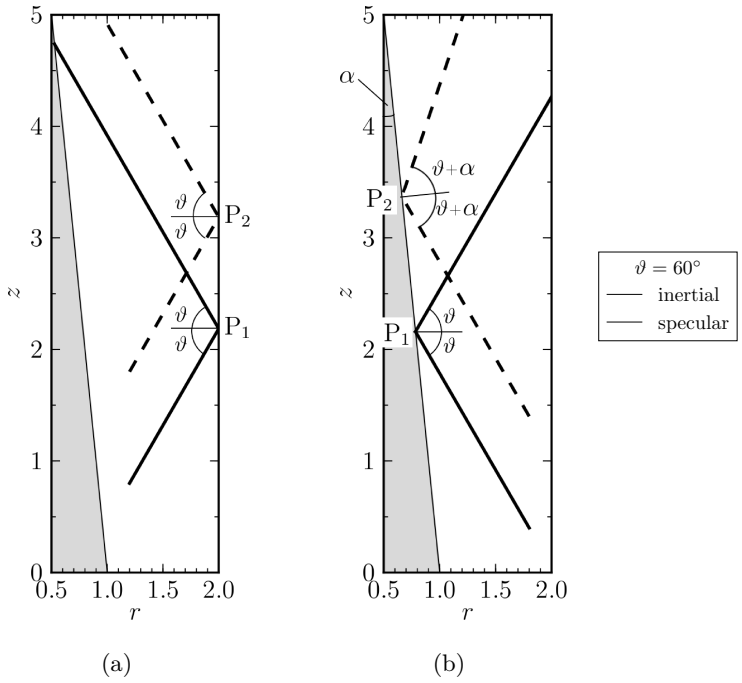

Figure 2.4: Wave rays are launched in the bottom half of the flow domain and propagate to the upper left (a) or upper right (b) respectively. Panel (a) shows the specular reflection at the outer cylinder wall. Panel (b) shows the difference between specular and anomalous reflection at the oblique frustum wall. The initial ray inclination is $\vartheta = 60°$ (corresponding to $\sigma = 1$ for the inertial wave ray). The angle $\alpha = 5.71°$ denotes the inclination of the frustum with respect to the z-axis.

to a billiard ball. (This is similar at the lids, which are perpendicular to $\boldsymbol{e}_z$.) By contrast, the frustum is approached by the rays in figure 2.4(b) and the inertial wave ray reflects anomalously from the oblique frustum wall. So, even if we would have chosen the same launch point for both rays, the ray paths would diverge as soon as a reflection at an oblique wall is encountered.

Note that the divergence of ray paths would still be different when the wave rays would not propagate precisely in the axial-radial plane. Such 3-D effects are beyond the present study but have been addressed recently by Rabitti & Maas (2013, 2014).

From here on, only inertial waves will be considered. The anisotropic dispersion relation (2.24) exhibits a degeneration with respect to the wavelength $\lambda = 2\pi k^{-1}$. That is, waves of different wavelength ($\lambda_1 > \lambda_2$) have the same frequency ($\sigma_1 = \sigma_2$) when their wave vectors are parallel ($\boldsymbol{k}_1 \parallel \boldsymbol{k}_2$). Launching two inertial wave rays, for example, allows to interpret them as neighbouring wave crests in a small wave packet.

In figure 2.5(a) a dashed and a dotted ray are launched in the bottom half of the domain and propagate toward the upper right. The ray inclination is $\vartheta = 76.4°$, which corresponds to wave frequency $\sigma = 0.47$. Tracing the rays and applying the reflection law shows that the rays propagate in anti-clockwise direction around the confinement as indicated by the large arrow. At the frustum wall, inertial waves undergo an anomalous reflection. Interestingly, the wave rays do not retrace themselves but come closer to each other and pass between the launch points. Viewing the rays as crest in a wave packet again means that the wavelength λ has

decreased by reflecting at the frustum and the reflection is said to be *focusing* (Maas & Lam, 1995).

The effect of focusing is illustrated by small arrows in figure 2.5(a). Focusing continues to occur whenever the rays return to the frustum such that the distance between both rays tends to zero. To be more precise, the rays are focused on a lower-dimensional object, a so-called *wave attractor* (e.g. Harlander, 2008; Harlander & Maas, 2006; Maas, 2005; Maas *et al.*, 1997; Maas & Lam, 1995). The wave attractor in figure 2.5(a) is a rhomboid plotted with a solid black line. This rhomboid is approached by all wave rays in the limit of a very large number of reflections. The wave rays approaching the wave attractor implies that the corresponding wave energy will be focused into a tiny fraction of the fluid volume. As λ decreases, the wave number $k \equiv |\boldsymbol{k}|$ increases so that phase and group velocities tend to zero, as can be seen from equation (2.25). The result is only qualitative at this stage since we have not solved the equations of motion by a neglect of phase and amplitude of the wave. Nevertheless, it is remarkable that a simple application of the reflection law can provide such insight into the fluid dynamical system.

Note that if we would let the ray propagate in opposite direction, the anomalous reflection at the frustum wall would become defocusing by the wave attractor becoming repellent. In the long run, however, the ray will switch direction and approach the wave attractor again. This is far from obvious but can be understood better by the aid of a Poincaré section, which we will discuss in the following.

Consider a ray that has been traced for several reflections so that the sequence (P_n) of reflection points has been generated (n is the index counting the reflections). The ray path is visualised by connecting the points P_n with lines following the characteristics (see figure 2.5(a)). Omitting the connecting lines means we only look into the sequence (P_n), which has been obtained by a *Poincaré section* along the domain boundary ∂V (e.g. Bronstein *et al.*, 2005, p. 834). The boundary of the radial-axial section in the annulus is formed by four segments, namely $\partial V = \overline{\mathrm{AB}} \cup \overline{\mathrm{BC}} \cup \overline{\mathrm{CD}} \cup \overline{\mathrm{DA}}$ as shown in figure 2.5(a).

Let s denote the arc length measuring the relative distance from corner A that increases in clockwise direction along ∂V, that is,

$$s : \partial V \mapsto [0, 1) \qquad \text{with} \quad s(\mathrm{A}) = 0, \tag{2.41}$$

where s is periodic on $[0, 1)$. The sequence of reflection points (P_n) has an equivalent representation by the sequence of arc lengths (s_n). The reflection law provides the rule how to construct P_{n+1} from P_n and P_{n-1}, so that the next value s_{n+1} can be computed.

Figure 2.5(b) shows a 2-D embedding on the basis of a Poincaré section using delay coordinates, here the iterated arc s_{n+1} is plotted against its ancestor s_n (for details on delay coordinates see, for example, Ott, 1993, pp. 19). Line styles and arrows in figure 2.5(b) have been selected in close correspondence to figure 2.5(a). Big arrows give the direction of the ray propagation (figure 2.5(a)) and the iteration through the arcs s_n respectively (figure 2.5(b)). Small arrows indicate the convergence toward the wave attractor due to the focusing reflection at the frustum. The arc lengths corresponding to points A–D are indicated by dash-dotted lines and labels along the abscissa and ordinate in figure 2.5(b). The dashed and dotted rays from figure 2.5(a) are traced another round trip so that each of them provides eight points $(+, \times)$ in figure 2.5(b). The rhomboidal wave attractor has collapsed to four points indicated by the black dots. The grey lines (dashed, dotted, solid) running horizontally and vertically are only auxiliary by connecting subsequent points (s_n, s_{n+1}) in order to guide the eye.

It seems that there is an underlying structure in the embedding which is worth to be explained in more detail. Together with the diagonal line from $(0, 0)$ to $(1, 1)$ we can transform the

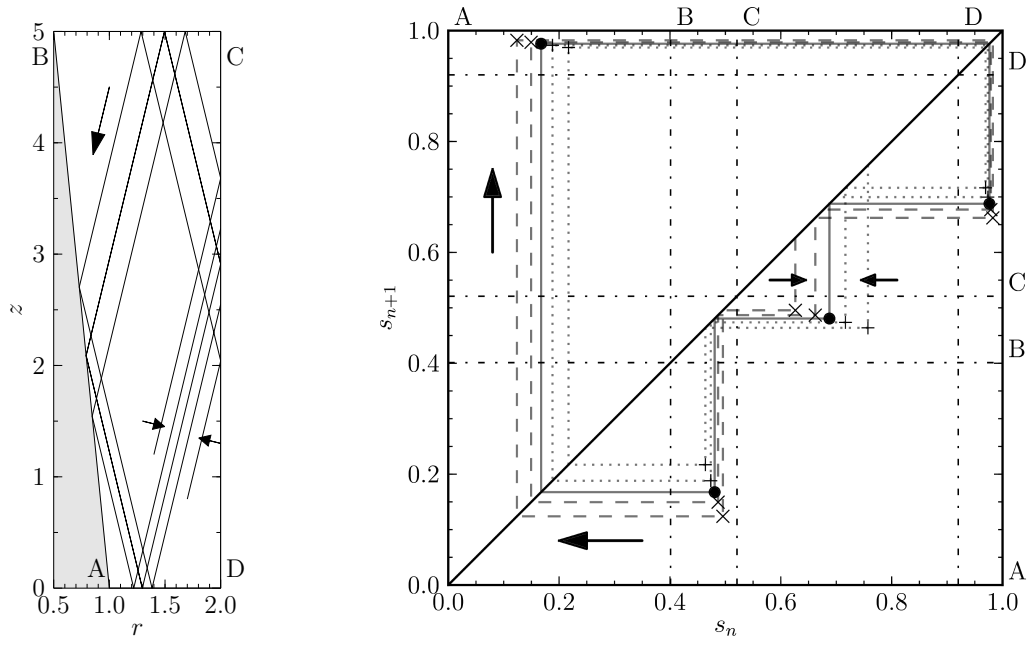

(a) radial-axial section

(b) Poincaré section along the boundary

Figure 2.5: Formation of the rhomboidal wave attractor in a radial-axial section of the annular confinement (a) and in a corresponding Poincaré section taken along the whole boundary (b). Ray tracing has been performed for the frequency parameter $\sigma = 0.47$. Panel (a) shows the focusing of two rays traced for a single round trip (− −, ⋯). The resulting wave attractor is shown by a solid line (—), having omitted only the first $n \leqslant 400$ reflections. Panel (b) shows a 2-D embedding (s_n, s_{n+1}) for subsequent reflections n and $n+1$ using a Poincaré section along the domain boundary with the normalised arc length s measured from point A. The wave attractor reduces to four points, a period 4 orbit (•). The two rays of panel (a) are traced for another round trip in panel (b) to show the convergence toward the fixed points. Grey lines are auxiliary and highlight the connectivity between the iterated values s_n. See the text for details.

evaluation of the reflection law into an evaluation of a map, that is, a recurrence relation $s_{n+1} = f(s_n)$. Starting from an arbitrary tuple (s_{n-1}, s_n), e.g. the black dot close to $(0.7, 0.5)$, the next iterate (s_n, s_{n+1}) is obtained by moving first horizontally to the bisectrix (diagonal auxiliary line), which yields an intersection at around $(0.5, 0.5)$. Second, one moves vertically to the graph of $f(s)$. The problem here and in general is that $f(s)$ is only known implicitly, but can be obtained by the aid of a geometrical construction that involves the reflection law, i.e. by performing the ray tracing from one wall reflection point to the next. In that way one obtains the iterate $f(0.5) \approx 0.15$, which is the black dot at around $(0.5, 0.15)$. From there the procedure can start afresh. Note, however, that with a point between B and C, one follows down, reflects between A and B, and changes (on the bisectrix) from a decreasing s to a larger s located between A and D.

All the points shown (crosses × and as pluses +) have been obtained by the procedure outlined above. It is interesting that these points seem to converge toward the black dots along lines that form the graph of $f(s)$. Plotting $f(s)$ into figure 2.5(b) would allow us to evaluate the map *explicitly*. This enables to analyse $f(s)$ in terms of an explicitly known function in order to gain a deeper understanding of the wave attractor. However, an explicit expression for

$f(s)$ can be obtained analytically only in very special cases (e.g. Maas & Lam, 1995), which is not given here. Instead, we will make use of the ray tracing algorithm to reconstruct the graph of $f(s)$ by letting many more rays reflect at the boundary. This will be discussed further in the next paragraph.

Before starting with the reconstruction of $f(s)$, it is important to realise that ray tracing uses information of the ancestors P_n and P_{n-1} in order yield a unique reflection point P_{n+1}. If we lack the information of P_{n-1}, it is possible to reach *two* points, $\mathrm{P}_{n+1}^{\pm}$, or corresponding arcs, $s_{n+1}^{\pm}$, by following characteristics of the web c_+ or c_-. This circumstance is reflected by the *bi-modal map* (see Maas & Lam, 1995)

$$s_{n+1}^{\pm} = f_{\pm}\left(s_n\right). \tag{2.42}$$

Let f_+ (f_-) be defined such that the arc s_{n+1}^{+} $\left(s_{n+1}^{-}\right)$ is larger (smaller) than s_n. Application of f_+ (f_-) corresponds to a clockwise (anti-clockwise) shift of P_n along the domain boundary. Let us take the rhomboidal wave attractor shown in figure 2.5(a) as an example. Focusing occurs for anti-clockwise ray propagation, which means f_- exhibits focusing and f_+ defocusing. First, the graph $f_-(s)$ is reconstructed numerically by tracing one reflection of a large number of rays (about 24000). Rays were launched from all along the domain boundary with the launch point density taking into account both the slope of the characteristics and the inclination of the wall. For the rhomboidal wave attractor it is $\sigma = 0.47$ or $\vartheta = 76.4°$, which is relatively steep so that launch points are more densely distributed along the lids than they are along the frustum or the outer cylinder. Second, the graph $f_+(s)$ is reconstructed by selecting the other characteristic passing through each of the launch points.

Figure 2.6 shows the result of the reconstruction of the graphs $f_-(s)$ and $f_+(s)$ by thick solid and dashed lines respectively for $\sigma = 0.47$. Abscissa and ordinate labels are the same as in figure 2.5(b) since we have evaluated the recurrence relation (2.42) once for a large number of points. The crosses and pluses shown in figure 2.5(b) are now part of the thick black solid line of f_-. The black dots and their connecting line, which correspond to the rhomboidal wave attractor, are repeated in figure 2.6. The dots mark the four *fixed points* of the bi-modal map $f_{\pm}$. Focusing occurs only for f_-, for which the fixed points form a stable period 4 orbit (e.g. Ott, 1993, p. 36) and yield the *attracting set*. Changing from f_- to f_+ makes the period 4 orbit unstable and the formerly attracting set becomes repelling.

An iteration of f_+ cannot go on indefinitely since $s_{n+1} = f_+\left(s_n\right)$ is multivalued, as can be seen, for example, for $0.43 < s_{n+1} < 0.50$ and $0.52 < s_{n+1} < 0.59$ in figure 2.6. The ray tracing solution, though, is unique, which means the evaluation of the reflection law yields the correct value of s_{n+1}. It turns out that an inconsistency due to multiple solutions to the map f_+ is resolved by an application of the reflection law (implicit evaluation of the map), which resolves the problem by switching to the single-valued map f_-. Consequently, any ray ends up on the wave attractor (provided that a wave attractor consists not only of a single point; as noted by Klein *et al.*, 2014). With the numerical reconstruction of the graphs $f_{\pm}(s)$ in figure 2.6 it is now possible to evaluate the iteration *explicitly*. In accord with figure 2.5(b), we could take the initial arc $s_0 = 0.75$ corresponding to the plus (+) below the rightmost small arrow and select the map f_- since it exhibits focusing. Back in figure 2.6, we mark $s_0 = 0.75$ on the s_n-axis and move in vertical direction to the intersection with f_-, which yields $f_-(s_0) \approx 0.46$. After that we proceed by moving horizontally to the intersection with the diagonal helper line and obtain the iterated arc $s_1 = f_-(s_0)$. Then we move vertically again in order to feed back the argument in accord with the recurrence relation (2.42) and obtain the second iterate $s_2 = f_-(s_1) \approx 0.22$ etc. The focusing reflection occurs at the frustum, segment $\overline{\mathrm{AB}}$, so that the first round trip

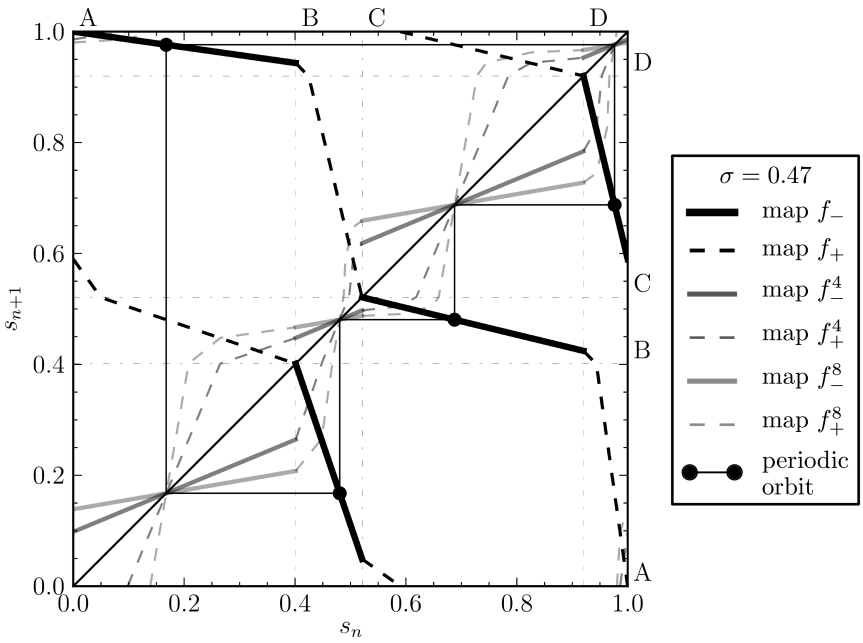

Figure 2.6: The bi-modal map $f_\pm$ (thick solid and dashed black lines) reconstructed by ray tracing for the rhomboidal wave attractor case at frequency parameter $\sigma = 0.47$ (compare to figure 2.5). Black dots (•) indicate the four fixed points of $f_\pm$. The pluses and crosses in figure 2.5(b) converge to the fixed points along the graph of f_- given by the thick black line. The fixed points of the bi-modal map $f_\pm$ are decoupled and projected on the diagonal by the moments $f_\pm^{4l}$ (here $l = 1, 2$; solid and dashed grey lines). The index $4l$ denotes an increased delay between piercings of the Poincaré section to multiples of 4 providing a more appropriate embedding.

yields $(s_4, s_5) \approx (0.71, 0.47)$. The latter corresponds to the plus (+) closer to the fixed point below the rightmost small arrow in figure 2.5(b).

Looking at the reconstruction of the bi-modal map in figure 2.6 it is far from obvious that the black dots form a stable orbit and it is very hard if not impossible to infer the fixed points from the graphs of $f_\pm$ alone. We can only see that the bi-modal map $f_\pm$ is piecewise linear and that f_+ is multivalued (as noted earlier). The latter implies that f_+ and f_- themselves are not measure-preserving (in a sense of a probability measure for the distribution of reflection points; see Ott, 1993, pp. 51–56). This is easiest to see in figure 2.6 by the thick black lines of f_- covering only a fraction of the interval $\overline{\mathrm{AB}}$, $\overline{\mathrm{BC}}$, $\overline{\mathrm{CD}}$, or $\overline{\mathrm{DA}}$ along the ordinate. Ray tracing, however, has provided us information about the existence and the period of a stable orbit, here a period 4 orbit corresponding to the rhomboidal wave attractor.

Presence of a period 4 orbit means that there is a recurrence of the ray or the reflection point every fourth iteration of the map, which suggests to look into moments $f_\pm^{4l}$ $(l = 1, 2, \ldots)$. We take the recurrence relation (2.42) and replace $f_\pm$ by $f_\pm^{4l}$. Evaluation and reconstruction of $f_\pm^{4l}$ is thus straightforward and follows the procedure outlined for $f_\pm$. The moments $f_\pm^4$ and $f_\pm^8$ $(l = 1, 2)$) are shown in figure 2.6 by grey lines that fade away with increasing l. The graphs of $f_\pm^4$ and $f_\pm^8$ intersect the diagonal helper line in four points (s_i', s_i') with $i = 1, 2, 3, 4$. The points obviously correspond to the four fixed points of $f_\pm$, which have been decoupled to four period 1 orbits by considering a more appropriate embedding using a delay of $4l$ reflections (compare to Ott, 1993, pp. 24–26).

It is interesting that the slope of f_-^{4l} is smaller than unity in s_i', while that of f_+^{4l} is larger. Following Ott (1993, p. 35), this yields the fixed point stability property

$$\frac{\mathrm{d}f_-^{4l}}{\mathrm{d}s}(s_i') < 1 \quad \text{(stable)}, \qquad \frac{\mathrm{d}f_+^{4l}}{\mathrm{d}s}(s_i') > 1 \quad \text{(unstable)}. \tag{2.43}$$

Considering the moments, we do not only get the fixed point coordinates s_i' but also their stability properties. As can be seen in figure 2.6, all fixed points of f_-^{4l} are stable, whereas all fixed points of f_+^{4l} are unstable. Hence, a wave attractor has as many reflection points as the bi-modal map $f_\pm$ has fixed points and a wave attractor can only exist when all fixed points are stable, that is, attracting (for further discussion see, for example, Maas, 2005; Maas & Lam, 1995; Rieutord *et al.*, 2001). Note that the moments in figure 2.6 have a tendency to become piecewise constant as l increases, except for a few singular points. For f_-^{4l}, an increase of the delay, $4l \to \infty$, is equivalent to the number of reflections becoming arbitrarily large, $n \to \infty$. A single iteration of the map f_-^{∞}, thus, yields the fixed points immediately. Singular points occur only at the corners A–D, where the function jumps and the slope is not defined anyway. For f_+^{4l}, the fixed points s_i' become singular and the slope of f_+^{4l} tends to infinity for increasing l. The fixed points are repelling in this case and an increase of the delay l means the iterated point has moved further away. However, as the sequence (s_n^+) is repelled by one fixed point, it necessarily approaches another one which is also repelling. A combination suggests that the vicinities of the s_i' are cleared more rapidly as l increases so that reflection points are more frequently encountered between the fixed points. Indeed, the slope of f_+^{4l} tends to zero between the fixed points for increasing l.

It is worth noting that in the language of dynamical systems (compare to Ott, 1993, pp. 6–14), a ray path corresponds to an *orbit* and the wave attractor to a *limit cycle*. Both must not be confused with the attractor and the orbit of the fluid dynamical system.

Structural stability of the rhomboidal wave attractor and the bifurcation diagram

We have discussed the emergence of the rhomboidal wave attractor in the previous paragraphs in detail and linked it to the properties of a one-dimensional map—the bi-modal map $f_\pm$ (see figure 2.6). For that discussion, the frequency parameter σ and the inclination ϑ of inertial wave rays was kept constant ($\sigma = 0.47$, which corresponds to $\vartheta = 76.4°$). It would be interesting to know: What happens to the rhomboidal wave attractor in figure 2.5(a) when the frequency is varied?

To answer this question let us start from the rhomboidal wave attractor, from which we will start varying the frequency σ gradually. We are primarily interested in the wave attractor, which means the fixed points of the bi-modal map $f_\pm$. Instead of reconstructing $f_\pm$ for the various frequencies, it is sufficient to apply the numerical ray tracing algorithm and reflect a one ray $O(10^4)$ times. A transient phase of a few thousand reflections is skipped so that reasonable convergence is assured to yield wave attractors with up to about 100 reflection points (up to period 100 orbit).

In the case of the rhomboidal wave attractor (period 4 orbit) only a few hundred reflections are needed for convergence to machine precision. The result of this procedure is shown in figure 2.7, which shows the structural stability of the rhomboidal wave attractor by decreasing the frequency from $\sigma = 0.47$ in figure 2.7(d) down to 0.43 (c), 0.393 (b), and 0.39 (a). The frequency is then increased to $\sigma = 0.5$ (e), 0.53 (f), 0.574 (g), and 0.58 (h). The rhomboid is deformed as the frequency is varied due to the change of inclination of the characteristics but it

remains structurally intact for in figures 2.7(b–g), which means the rhomboidal wave attractor or simply exists for $0.393 \leqslant \sigma \leqslant 0.574$. More precisely one would say the rhomboidal wave attractor is structurally stable in $0.393 \leqslant \sigma \leqslant 0.574$. The rhomboid degenerates into a line at a bounding frequency, that is, slightly below $\sigma = 0.393$ or slightly above $\sigma = 0.574$. The degenerated wave attractor connects the lower left and upper right corner (see figure 2.7(b)) or the lower right and upper left corner (see figure 2.7(g)) respectively. For an even smaller frequency $\sigma = 0.39$ (a) or an even larger frequency $\sigma = 0.58$ (f), the rhomboidal wave attractor ceases to exist and is replaced by a much more complicated geometrical object of much longer periodicity if any at all. The reason is a *bifurcation* of the bi-modal map $f_\pm$ (e.g. Borcia & Harlander, 2012; Maas, 2005; Maas & Lam, 1995).

A bifurcation occurs because $f_\pm$ changes in shape slightly when σ is varied. Structural stability of the wave attractor is hence a property of the bi-modal map. The fixed points shown in figure 2.6 can move along the stable manifold described by f_- (thick solid line) for $0.393 \leqslant \sigma \leqslant 0.574$. But when the frequency has decreased to $\sigma = 0.39$ or increased to $\sigma = 0.58$, the fixed points collide with the unstable manifold described by f_+ (thick dashed lines) and the map undergoes a tangent bifurcation (compare to Ott, 1993, pp. 44–47). In order to make this clear, a reconstruction of $f_\pm$ has been performed similar to the one shown in figure 2.6, but for the frequency value $\sigma = 0.58$ just *after* bifurcation which is shown in figure 2.8(a). The reconstructions in figures 2.6 and 2.8(a) look quite similar, but the difference is in the details. The map f_- in figure 2.8(a) maps the whole intervals $\overline{\mathrm{AB}}$ to $\overline{\mathrm{DA}}$ and $\overline{\mathrm{CD}}$ to $\overline{\mathrm{BC}}$. It also connects with the f_+ branch in these corners. This means that wave rays are no longer 'trapped' in the f_- branch. Instead, f_+ and f_- are switched at times due to the implicit evaluation using the ray reflection law. (One might want to define $f_\pm$ more carefully which would yield a map with more fragmented co-domains as, for example, in Rieutord *et al.*, 2001, but this is not a problem here.)

The important point here is that there is no longer a period 4 orbit for the bi-modal map at $\sigma = 0.58$. The critical period 4 orbit at $\sigma = 0.574$ (open circles) is plotted only for orientation. In addition to $f_\pm$, the moments $f_\pm^4$ and $f_\pm^8$ are shown in figure 2.8(a) for comparison to figure 2.6. With the disappearance of the period 4 orbit, however, the embedding to multiples of 4 has lost its meaning. Nevertheless, the moments $f_\pm^4$ and $f_\pm^8$ in figure 2.8(a) run from the bottom left to the upper right corner and come close to the diagonal in the vicinity of the fixed points of the critical period 4 orbit. This indicates a remaining prevalence in the recurrence to iterations with multiples of 4. Because of focusing, the rays still return to the vicinities of the critical fixed points. This is visible by the levelling of $f_\pm^{4l}$ in $\overline{\mathrm{AB}}$ and $\overline{\mathrm{CD}}$ for increasing l, or alternatively by the 'seemingly periodic' ray path shown in figure 2.7(h).

It must be emphasized that there is *no exact* recurrence within the numerical precision in the sequence (s_n) up to $l = 250$, that is, up to a delay of $\Delta n = 1000$ iterations. Hence, reflection points cluster in the vicinity of the upper left and lower right corners in figure 2.7(h) without the ray retracing itself. Put another way, there is a high probability to find a ray in the vicinity of the degenerated wave attractor of figure 2.7(g) or a reflection point near the critical period 4 orbit, but not *on* them.

Figure 2.8(b) zooms the area around lower left fixed point $(0.4, 0.4)$ of the critical period for 4 orbit. It is obvious that the diagonal helper line is no longer intersected by the moments $f_\pm^4$ and $f_\pm^8$, which again indicates presence of a tangent bifurcation of the bi-modal map. We can no longer discuss stability properties of the fixed points as we did under equation (2.43) for $\sigma = 0.47$ since we do not know the fixed points for $\sigma = 0.58$ neither if there are any. I conjecture that there are ergodic orbits bounding the rhomboidal wave attractor frequency band or, to be more general, any other wave attractor frequency band. Ergodicity does not

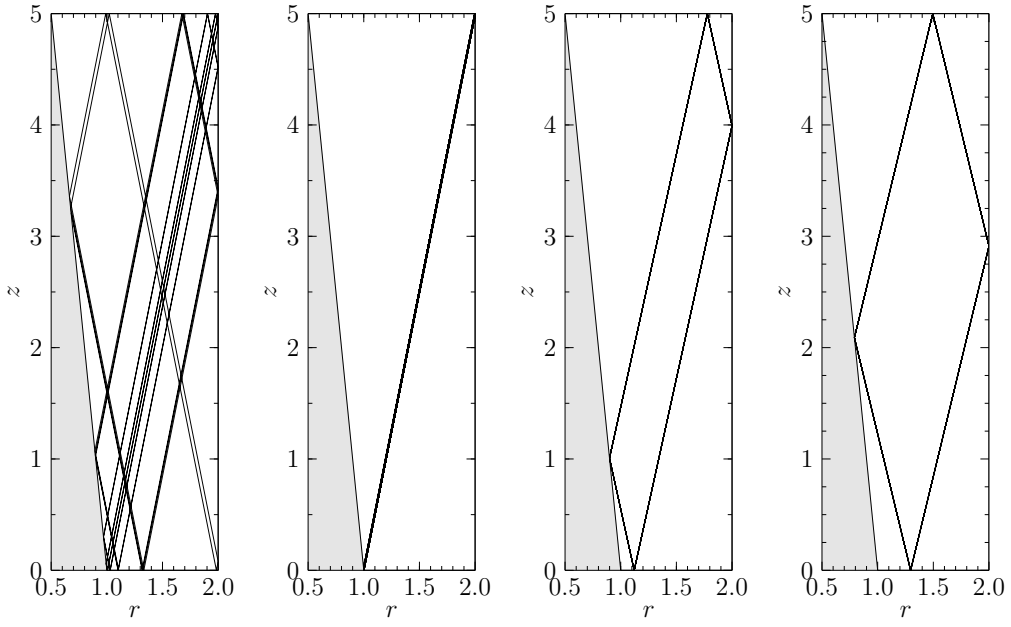

(a) $\sigma = 0.390$ (b) $\sigma = 0.393$ (c) $\sigma = 0.430$ (d) $\sigma = 0.470$

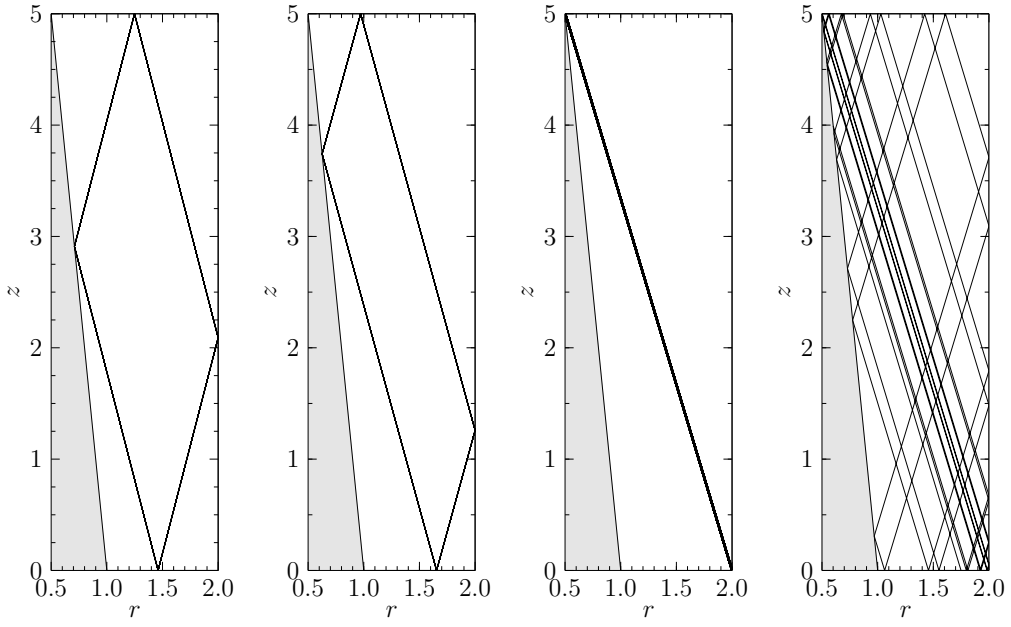

(e) $\sigma = 0.500$ (f) $\sigma = 0.530$ (g) $\sigma = 0.574$ (h) $\sigma = 0.580$

Figure 2.7: Structural stability of the rhomboidal wave attractor due to variation of the frequency σ. The rhomboidal structure is stable within $0.393 \leqslant \sigma \leqslant 0.574$ (b–g) but breaks up due to a bifurcation of the bi-modal map for lower (a) or larger (h) values of σ respectively.

make any statement about the probability density of the reflection points along the boundary except that there is zero probability to find a periodic orbit. The proof or falsification of the conjecture has to be given elsewhere.

An immediate question arising is which bifurcations of the bi-modal map of the annulus occur at the remaining frequencies of the inertial wave band, $0 < \sigma < 2$? The difficulty is that there is no theory available that could predict the number of fixed points at a particular frequency. Hence, one has to step through the frequency range numerically in order to get an overview of the various bifurcations. Borcia & Harlander (2012) studied wave attractors by ray tracing in an annulus similar to that in figure 1.3 for various inclinations of the frustum. One of the configurations investigated by them corresponds precisely to the annulus of this study (Borcia, 2013, personal communication) so that we can directly refer to these results in order to get an overview of the various bifurcations of the bi-modal map.

Figure 2.9 shows the latter ray-tracing results in terms of the *bifurcation diagram* to be discussed further in the following. Borcia & Harlander (2012) pointed out that it is sufficient to consider only a reduced Poincaré section that consists of the top lid and the outer cylinder, say $\overline{\mathrm{BC}}$ and $\overline{\mathrm{CD}}$ respectively as shown in figure 2.5. They proceeded with recording $n_{\max} = 20000$ reflections of a single ray launched from an arbitrary point. A transient stage of the first $n \leqslant 5000$ reflections has been removed from the sequence of reflection points for the analysis. The coordinates $r_{n'} \in \overline{\mathrm{BC}}$ and $z_{n''} \in \overline{\mathrm{CD}}$ (with the reflection indices $n' + n'' < n$, where $n' \neq n''$ in general) have been computed numerically for various frequencies $0 < \sigma < 2$ with an increment of $\Delta\sigma = 0.001$.

Figure 2.9(a) shows the reflection point coordinates $r_{n'}$ at the lid in dependence on the frequency σ, whereas figure 2.9(b) shows the coordinate $z_{n''}$ at the outer cylinder. Every reflection in the respective intervals are marked by a small black dot over the corresponding value of σ. The frequency interval $0.393 \leqslant \sigma \leqslant 0.574$, for example, exhibits the rhomboidal wave attractor, which has only one reflection point at all walls (see figure 2.5). The ray has practically converged to the wave attractor within the transient stage and only the fixed points are repeatedly visited, that is, the single dot in figures 2.9(a, b). The position of the dot changes monotonically across the frequency band of the rhomboidal wave attractor, which simply reflects the structural stability corresponding to figures 2.7(b–g). The number of black dots over σ increases suddenly just outside the frequency band of the rhomboidal wave attractor, say for $\sigma = 0.39$ and $\sigma = 0.58$. The reason is a bifurcation of the bi-modal map (see equation (2.42)) due to which the rhomboidal wave attractor vanishes and is replaced by a long orbit (compare to figures 2.7(a, h)), hence the name 'bifurcation diagram'.

The dots along r and z in figures 2.9(a, b) yield the number of reflections which means they are an indicator of the length of a wave attractor. White patches ('windows') in figure 2.9 correspond to low-order wave attractors, which are separated by black regions. An interesting aspect is that the 'windows' differ in width but are otherwise always finite. The width of a 'window' is a measure for the structural stability of a wave attractor (compare to figure 2.7) against variation of the frequency σ, which determines the inclination of the characteristics (see figure 2.3). Note that the 'windows' are distributed over the whole frequency range and they seem to form a Cantor set (compare, for example, with Ott, 1993, p. 40), where a larger number of reflections yields a smaller 'window' and a structurally less stable wave attractor. Note also that the black regions become denser for as the frequency increases ($\sigma \to 2$). On finer scales, the black regions exhibit a substructure of smaller 'windows' (not shown here, but similar to Maas, 2005). Completely black vertical lines, though, correspond to *ergodic orbits* for which the ray will fill out the entire domain and never actually retraces itself (Manders & Maas, 2003).

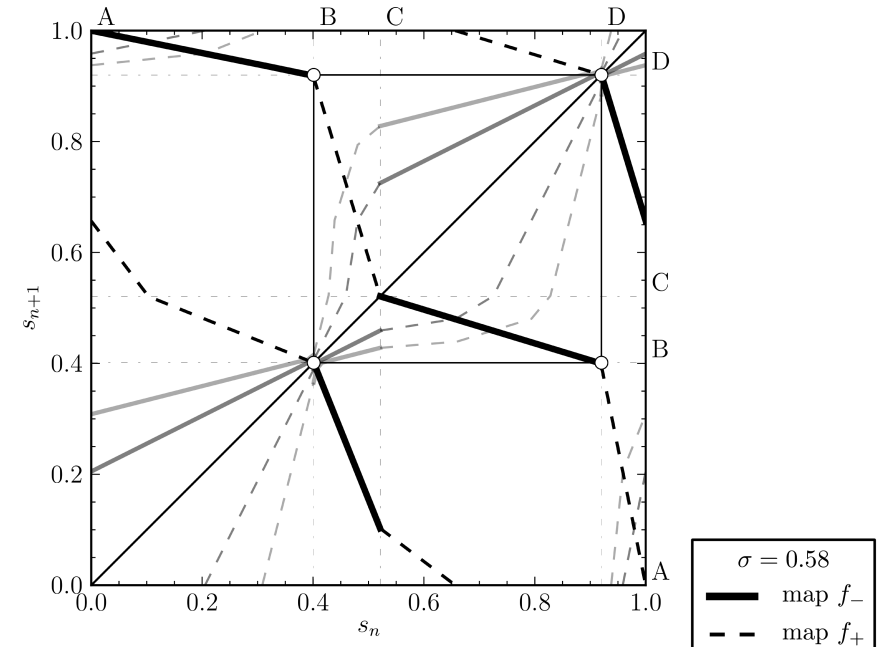

(a) Bi-modal map over the whole boundary.

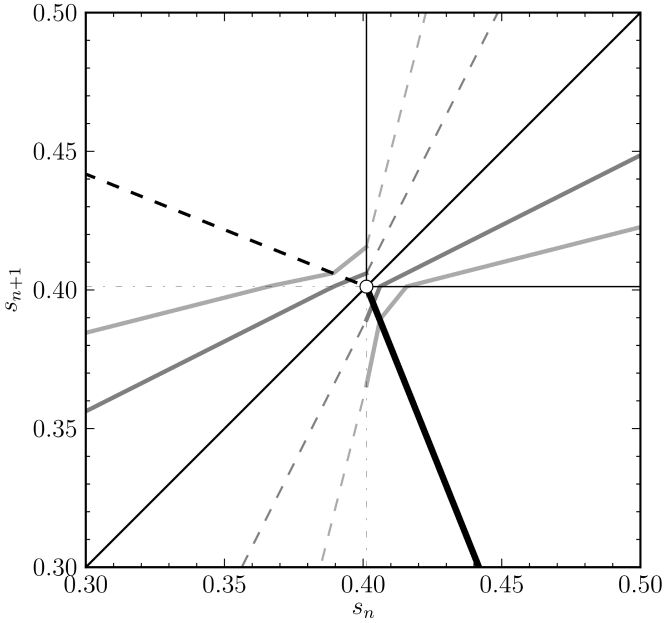

(b) Close-up at $(s_n, s_{n+1}) = (0.4, 0.4)$.

Figure 2.8: Panel (a) shows the bi-modal map $f_\pm$ reconstructed by ray tracing at $\sigma = 0.58$ after a bifurcation occurred. Otherwise, the figure labels and content is analogous to figure 2.6. For comparison, the critical period 4 orbit at slightly lower frequency ($\sigma = 0.574$) is given by open circles ($\circ$). Panel (b) zooms the area around the point $(0.4, 0.4)$, one of the fixed points forming the critical period 4 orbit. The moments $f_\pm^4$, $f_\pm^8$ avoid an intersection with the diagonal helper line indicating a tangent bifurcation of the bi-modal map. See the text for details.

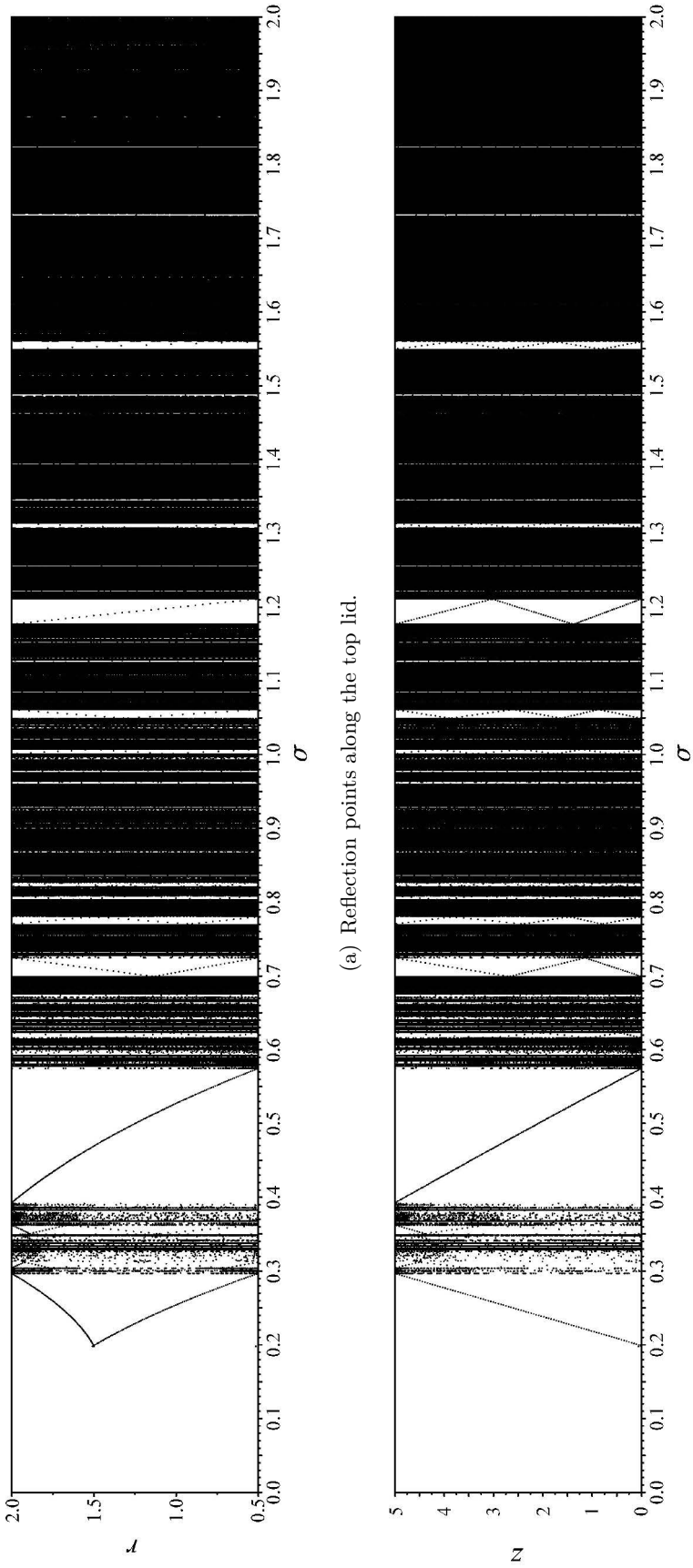

(a) Reflection points along the top lid.

(b) Reflection points along the outer cylinder.

Figure 2.9: The bifurcation diagram due to variation of the frequency parameter σ computed by ray tracing for the annular confinement in figure 1.3 with a frustum inclination of $\alpha = 5.71°$ to the axis. Panel (a) shows the radial coordinate r of ray reflections along the top lid, whereas panel (b) shows the vertical coordinate z of ray reflections along the outer cylinder. One ray has been launched and traced for 20000 reflections, but a transient stage of the first 5000 reflections has been omitted in the plot. The white regions ('windows') correspond to low-order wave attractors (LOWAs), black regions to very long orbits such as high-order wave attractors or even ergodic orbits. The diagram serves as reference spectrum for chapter 6. (Courtesy of I. D. Borcia (2013), BTU Cottbus - Senftenberg.)

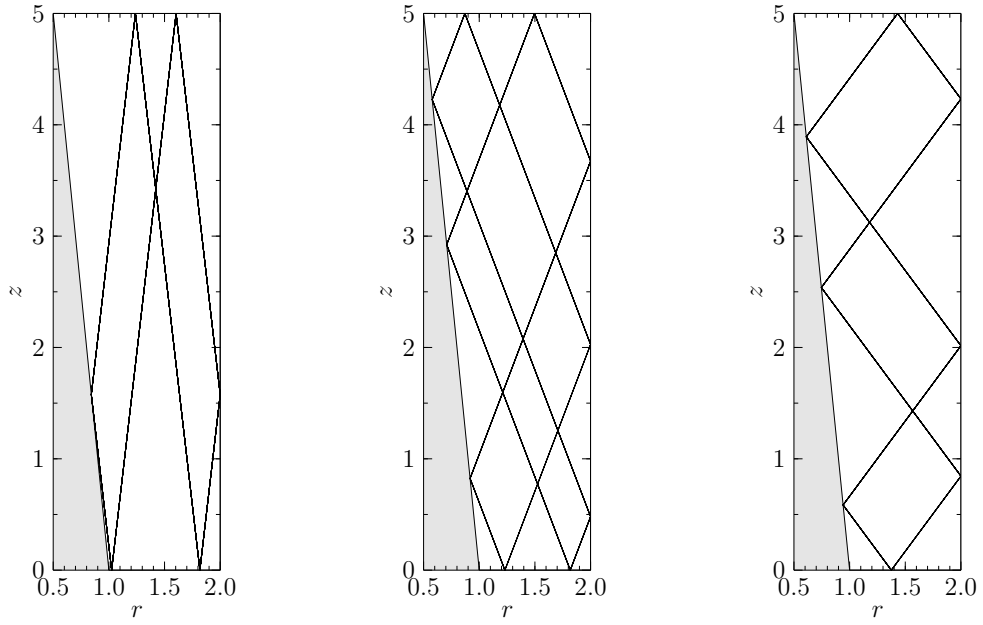

(a) $\sigma = 0.23$ (b) $\sigma = 0.71$ (c) $\sigma = 1.19$

Figure 2.10: Realisations of three low-order wave attractors (LOWAs). Panel (a) shows the $(2, 1)$ wave attractor, panel (b) the $(2, 3)$ wave attractor, and panel (c) the $(1, 3)$ wave attractor. The wave ray converges to the corresponding wave attractor within a few hundred reflections from any launch point in the radial-axial section.

At low frequencies ($0 < \sigma \leqslant 0.2$), however, the bifurcation diagram (figure 2.9) does not show any substructure. This is because at $\sigma = 0.2$ one web of characteristics is parallel to the frustum wall (critical slope case; see Manders & Maas, 2003). The bi-modal map bifurcates and gives rise to a point attractor that lies in the top inner corner of the radial-axial section (denoted B in figure 2.5). The physical reason is to be seen in the characteristics being steeper than the frustum wall, which yields the wedge problem for $0 < \sigma < 0.2$ (e.g. Maas, 2005, figure 8).

Classification of ray orbits in the annulus

Let us recall that the inertial wave rays are characteristics of the Poincaré equation (2.37) when $0 < \sigma < 2$. Corresponding inclinations of the characteristics are $\pi/2 > \vartheta > 0$ (see figure 2.3). We found that an inertial wave reflects neutrally at vertical and horizontal walls, or that it is either focused or defocused at an oblique wall. A confinement requires wave rays to return to the wall repeatedly, which yielded a wave attractor when there is net focusing. In other words, the number of focusing reflections needs to outweigh the defocusing reflections in one round trip. With respect to the annulus (figure 1.3) we have studied in detail only the rhomboidal wave attractor, which we found to exist in $0.393 \leqslant \sigma \leqslant 0.574$ (see figure 2.7). Bifurcations of the bi-modal map (see figures 2.6 and 2.8) led to a replacement of the rhomboidal wave attractor by much longer ray orbits, which are not necessarily wave attractors. The 'spectrum' of ray orbits in the annulus has been given in terms of the bifurcation diagram (see figure 2.9) and we can now proceed by classifying these ray orbits.

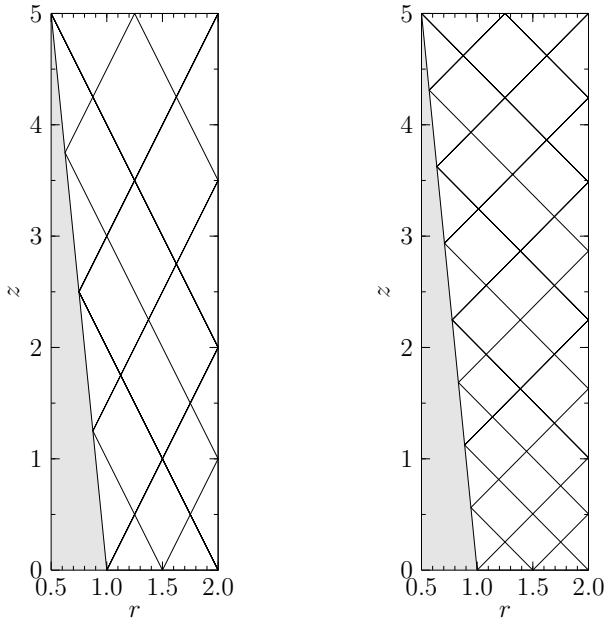

(a) $\sigma \approx 0.8944$ (b) $\sigma \approx 1.4070$

Figure 2.11: Three realisations for both of the two simplest low-order neutral orbit (LONOs). Panel (a) shows the $(1, 2)$ neutral orbit, panel (b) the $(1, 4)$ neutral orbit. The rays retrace themselves after one round trip due to the absence of net focusing so that the structures emerging depend entirely on the initial condition (launch point and direction).

Following Borcia & Harlander (2012), we denote wave attractors by the tuple (m, n) with $m = 1, 2, \ldots$ the number of reflections along the top lid (radius r) and $n = 1, 2, \ldots$ those along the outer cylinder (vertical coordinate z). In this terminology, the rhomboidal wave attractor shown in figures 2.7(b–g) is a $(1, 1)$ wave attractor. The $(1, 1)$ wave attractor is the simplest-possible attractor which is not just a point. (The point attractor in the top inner corner would be a $(0, 0)$ wave attractor.) Low values of m and n, say $m, n < 10$, yield *low-order wave attractors (LOWAs)*. LOWAs have a simple geometrical structure, thus, a short path length, and occur here for odd n only. This is relevant with respect to applications, since a wave (packet) propagating along the characteristics would be subject to viscous damping so that losses are minimised when the path length is short and reflections are few. A few more LOWAs are shown in figure 2.10 corresponding to the widest 'windows' in the bifurcation diagram (figure 2.9). Figure 2.10(a) shows the $(2, 1)$ LOWA at $\sigma = 0.23$, figure 2.10(b) the $(2, 3)$ LOWA at $\sigma = 0.71$, and figure 2.10(c) the $(1, 3)$ LOWA at $\sigma = 1.19$. The tuples (m, n) can be obtained either by counting the reflections manually or by looking into the bifurcation diagram by counting the black dots over the selected frequency.

An interesting property of the annulus (figure 1.3) is that some ray orbits do not exhibit net focusing (see Borcia & Harlander, 2012), which we may denote by $(\tilde{m}, \tilde{n})$. What are these other orbits?

In short, these orbits are characterised by even n ($\tilde{n}$) and occur when focusing and defocusing reflections balance exactly in one round trip of the ray. We will refer to these orbits as *neutral orbits* from here on and use $\tilde{m}$, $\tilde{n}$) to differentiate them from wave attractors. Following the wave attractor classification, neutral orbits with values of $\tilde{m}, \tilde{n} < 10$ are called *low-order neutral*

orbits (LONOs). Finding the neutral orbits is a bit difficult since their frequency 'windows' have collapsed to a single point and one has no chance to find them numerically in the bifurcation diagram (figure 2.9). Moreover, it can be shown that the ray patterns emerging depend entirely on the initial condition so that every point in the annulus belongs to one realisation of a neutral orbit that co-exist at the same frequency (e.g. Manders & Maas, 2003). Borcia & Harlander (2012) have shown how to obtain the neutral orbits in the annulus by a geometrical construction. We look for two ray paths connecting two different corners of the domain to the same tuple of reflections $(\tilde{m}, \tilde{n})$. The corresponding value of the frequency σ is then computed from the inclination of the characteristics by the aid of equation (2.24). The construction reveals that neutral orbits in the annulus need to have $\tilde{m}$ *odd* and $\tilde{n}$ *even* (see Borcia & Harlander, 2012).

Realisations of the two simplest neutral orbits exhibited by the annulus with an inner frustum are shown in figure 2.11. Figure 2.11(a) shows the $(1, 2)$ LONO at $\sigma \approx 0.8944$, figure 2.11(b) the $(1, 4)$ LONO at $\sigma \approx 1.4070$. Three different initial conditions have been used to yield three different realisations for each frequency. This is in contrast to wave attractors, which yield a single orbit per frequency (compare to figure 2.10). Moreover, we can safely drop the tilde from $\tilde{m}$ and $\tilde{n}$ since the wave attractors (m, n) and the neutral orbits $(\tilde{m}, \tilde{n})$ are unique, which means a periodic orbit is either a wave attractor or a neutral orbit and yields finite values for m, $\tilde{m}$, n, $\tilde{n}$ as shown, for example, in figures 2.10 and 2.11. The only difference is that wave attractors occupy a finite frequency band, whereas a neutral orbit exists only at one particular frequency.

The 'spectrum' of ray orbits thus consists of wave attractors, neutral orbits, but also ergodic orbits supposedly just at the boundaries of wave attractor windows as, for example, in figure 2.7(a). The relevance of all these idealised (inertial wave) ray orbits for the Navier–Stokes flow will be discussed further in chapters 4 and 6, but it is worth to note here already that a neutral orbit corresponds to a normal mode solution to equation (2.37). The collapse of the frequency 'window' of the neutral orbit to a single frequency may be seen as an indicator since also a normal mode exists only at a single frequency (eigenvalue). Borcia & Harlander (2012) showed that the neutral orbits in the annulus correspond to 'surviving' normal modes of the straight annulus. This is a strong statement that allows to link the present configuration to more idealised ones that do not possess wave attractors at all (see, e.g., Boisson *et al.*, 2012; Borcia *et al.*, 2014; Lopez & Marques, 2014; Sauret *et al.*, 2012). Interestingly, also the opposite is possible. In the parabolic basin no normal modes or neutral orbits can be found but wave attractors and supposedly ergodic orbits (Maas & Lam, 1995).

In summary, the annulus shown in figure 1.3 exhibits wave attractors and neutral orbits (or 'surviving' normal modes for that matter), which make it an interesting object for fundamental research. It needs to emphasized at this point that we have discussed only axisymmetric solutions by restricting our attention to a radial-axial section, but ray tracing can also be done in a 3-D domain. Studies for a prism (Manders & Maas, 2004) and a spherical shell (Rabitti & Maas, 2013, 2014), however, show that a wave attractor exhibits zonal trapping. This implies that the wave attractors of the 2-D problem correspond to wave attractors of the 3-D problem.

The relevance of the LOWAs and LONOs obtained by ray tracing in a radial-axial section will be discussed further in chapters 4 and 6 by comparing the ray tracing results to direct numerical simulations for waves excited by libration of the annulus. Before moving on to the numerical results, chapter 3 discusses the details of the numerical flow solver.

3 Navier–Stokes solver for axisymmetric confinements with wall topography

The equations of motion with respect to the co-rotating frame of reference have been introduced and discussed in chapter 2. They take into account viscous forces (for finite Ekman number) and momentum advection (for finite Rossby number). By restricting our attention to the linear inviscid limit, we have discussed inertial waves in an unbounded domain and inertial wave attractors in the annular confinement. The task at hand is a clarification of the relevance of inertial waves and wave attractors in the librating annulus. Direct numerical simulations (DNS) will serve as reference, which means we need to make sure that the numerical solver yields accurate approximate solutions to the Navier–Stokes equations before starting to work on the scientific questions. Hence, the aim of this chapter is to give a comprehensive overview of the scientific solver used in this study. The reader who is familiar with numerical solvers in terrain-following coordinates or who is not interested in the technical details may safely skip this chapter and continue with the results in chapter 4.

The numerical solver HYBRID-NEW uses terrain-following coordinates and implements the contravariant Navier–Stokes equations. The approach allows to incorporate the frustum accurately and efficiently but requires to work out the coordinate transformations manually. Familiarisation with curvilinear coordinates is essential for development and customisation of the solver (e.g. by the implementation of the Coriolis force as part of this work). In the following, first, the mapping will be introduced and the contravariant form of the Navier–Stokes equations will be derived. Second, the discretisation of the contravariant equations and their numerical solution will be discussed. HYBRID-NEW has a 30 year history (see appendix A.1), which means the discretisation methods of semi-implicit time advancement and finite-differencing in space are all state-of-the-art. Nevertheless, one is faced with many details once the implementation of the dynamical core needs to be modified (e.g. for parallelisation). A code documentation exists but not all aspects are equally well covered; some remarks can be found in the source code, while others are scattered over various publications. Therefore, this chapter also aims to give a brief but complete overview on how the dynamical core works and to collect the relevant publications. It is beyond the scope of this work to discuss the convergence properties. We will proof the point only for implementation of curl added recently.

3.1 Contravariant Navier–Stokes equations in flux form

The usage of terrain-following coordinates for the treatment of irregular boundaries is a well-known concept (Gal-Chen & Somerville, 1975a,b). A coordinate transformation is performed semi-analytically such that the irregular domain is mapped to a box. This aids accuracy since the domain boundaries will coincide with coordinate surfaces. An efficient implementation is obtained by a discretisation with finite differences. A time-dependent coordinate transformation of such kind has been used for various incompressible flow problems (see, for example, Luo & Bewley, 2004).

It is worth to emphasize that it has been a key to perform direct numerical simulations of time-dependent mean flow induced by gravity waves by allowing to model precisely the forcing used in the laboratory experiment (see Plumb & McEwan, 1978; Wedi & Smolarkiewicz, 2004, 2006). Luo & Bewley (2004) used a fully contravariant formulation, which means also the velocities are transformed such that the components are parallel or perpendicular to the domain boundary in order to make the implementation of boundary conditions as simple as possible. The type of terrain-following coordinates used for this study are time-*in*dependent generalised coordinates. Instead of the velocity volume fluxes are used as dynamical variable in order to aid mass conservation in curvilinear stretched grids (e.g. Choi, 1993; Rosenfeld *et al.*, 1991) and to remove the singularity at the axis in a full cylinder or pipe flow configuration (e.g. Kaltenbach & Hauschild, 2004).

Generalised coordinates and transformation matrices

Generalised coordinates are used to bring the Navier–Stokes equations in contravariant form before implementation. An introduction to generalised coordinates can be found in various books, where the material collected here has been compiled largely from Kuttler (2011); Schade (1997); Thompson *et al.* (1985), as well as the code documentation of the HYBRID-NEW solver (Kaltenbach & Hauschild, 2004; Kaltenbach *et al.*, 2014). The notation has been streamlined and is given here once again for the sake of completeness. The purpose is to provide the reader with all the informations necessary to follow the derivation of the contravariant form of the Navier–Stokes equations implemented without the need to consult external references.

Basis vectors of an orthonormal basis are denoted $\boldsymbol{e}_i$, where the symbol '$\boldsymbol{e}$' indicates a basis vector of unit length and the Latin index ($i = 1, 2, 3$) that it is Cartesian. Generalised basis vectors are denoted $\boldsymbol{a}_\mu$ or $\boldsymbol{a}^\mu$ respectively, where $\boldsymbol{a}_\mu$ is the covariant basis vectors and $\boldsymbol{a}^\mu$ the contravariant one. The symbol '$\boldsymbol{a}$' indicates that co- and contravariant basis vectors are in general not of unit length. The Greek index ($\mu = 1, 2, 3$) indicates generalised components. Positioning of indices is crucial only for the Greek indices (generalised coordinates), but unimportant for the Cartesian components. The bases $\{\boldsymbol{a}_\mu\}$ and $\{\boldsymbol{a}^\mu\}$ form the *holonomic dual basis* (Schade, 1997, pp. 197–202, 294). The holonomic dual basis is orthogonal and reciprocal in the sense that

$$\boldsymbol{a}_\mu \cdot \boldsymbol{a}^\nu = \delta_\mu^\nu, \tag{3.1}$$

where δ_μ^ν denotes the Kronecker symbol (e.g. Bronstein *et al.*, 2005, p. 273).

Einstein's summation convention is implied when an index appears twice in one product, for example, $A^\mu \boldsymbol{a}_\mu$ or $B^i \boldsymbol{e}_i$, unless mentioned otherwise. A vector $\boldsymbol{A}$ has the Cartesian and generalised decompositions

$$\boldsymbol{A} = A^i \boldsymbol{e}_i \qquad \text{and} \qquad \boldsymbol{A} = A_\mu \boldsymbol{a}^\mu = A^\nu \boldsymbol{a}_\nu, \tag{3.2}$$

and, hence, the projections read $A^\mu = \boldsymbol{A} \cdot \boldsymbol{a}^\mu$ and so on.

Figure 3.1 illustrates the definition of the coordinates and corresponding basis vectors. The projections of the position vector $\boldsymbol{r}$ are denoted

$$x^i = x_i = \boldsymbol{r} \cdot \boldsymbol{e}_i \qquad \text{for the Cartesian components,} \tag{3.3}$$

$$\xi^\mu = \boldsymbol{r} \cdot \boldsymbol{a}^\mu \qquad \text{for the generalised components,} \tag{3.4}$$

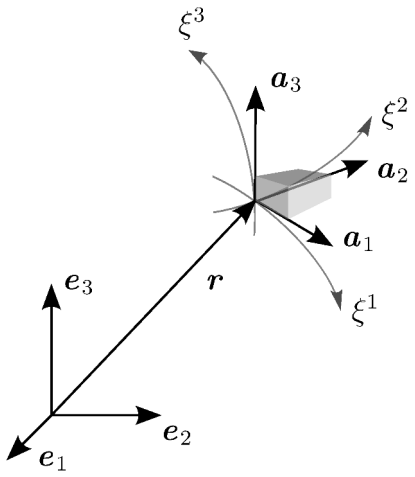

Figure 3.1: Definition of the generalised coordinates with respect to an underlying Cartesian basis.. Contravariant coordinate lines are denoted ξ^1, ξ^2, ξ^3 with the corresponding covariant basis reads $\{\boldsymbol{a}_\mu | \mu = 1, 2, 3\}$. For comparison, the Cartesian coordinates are denoted x^1, x^2, x^3 and have the orthonormal basis $\{\boldsymbol{e}_i | i = 1, 2, 3\}$. The position vector $\boldsymbol{r}$ has the decompositions $\boldsymbol{r} = \xi^\mu \boldsymbol{a}_\mu$ with respect to the generalised coordinates and $\boldsymbol{r} = x^i \boldsymbol{e}_i$ with respect to the Cartesian coordinates (Einstein's summation convention implied).

in order to avoid confusion when indices are specified explicitly. The Cartesian coordinates x^i and the generalised coordinates ξ^ν are connected by the transformations

$$x^i = F^i(\xi^1, \xi^2, \xi^3), \qquad \xi^\nu = G^\nu(x^1, x^2, x^3). \tag{3.5}$$

F^i and G^ν denote the coordinate functions, which have to be at least two times continuously differentiable. Hence, the forward transformation F^i has the Jacobi matrix (see Bronstein *et al.*, 2005, p. 653)

$$(c^i_{\ \mu}) := \frac{\mathrm{D}(F^1, F^2, F^3)}{\mathrm{D}(\xi^1, \xi^2, \xi^3)} \begin{pmatrix} \partial F^1/\partial \xi^1 & \partial F^1/\partial \xi^2 & \partial F^1/\partial \xi^3 \\ \partial F^2/\partial \xi^1 & \partial F^2/\partial \xi^2 & \partial F^2/\partial \xi^3 \\ \partial F^3/\partial \xi^1 & \partial F^3/\partial \xi^2 & \partial F^3/\partial \xi^3 \end{pmatrix} = (\boldsymbol{a}_1, \boldsymbol{a}_2, \boldsymbol{a}_3)\,, \tag{3.6}$$

where the columns of the Jacobi matrix $(c^i_{\ \mu})$ store the covariant basis vectors expressed with respect to an underlying Cartesian basis. The determinant of equation (3.6) yields the Jacobian of the transformation, namely

$$J = \det(c^i_{\ \mu}) = \boldsymbol{a}_1 \cdot (\boldsymbol{a}_2 \times \boldsymbol{a}_3)\,, \tag{3.7}$$

where the triple product reflects that the Jacobian is a measure for the local volume distortion exhibited by the new coordinates (ξ^1, ξ^2, ξ^3).

Linear independence of the basis vectors $\boldsymbol{a}_\mu$ yields $J \neq 0$ and ensures the existence of the inverse transformation G^ν. For practical reasons, let

$$(\gamma^\nu{}_j) := J(c^i{}_\mu)^{-1} = J\left(\boldsymbol{a}^1, \boldsymbol{a}^2, \boldsymbol{a}^3\right)^{\mathrm{T}}, \tag{3.8}$$

in which the rows of $(\gamma^\nu{}_j)$ store the contravariant basis vectors but scaled with the Jacobian J.

The components of the contravariant basis vectors are also given with respect to the underlying Cartesian basis. Assuming right-handed bases means $J > 0$ and orthogonality yields the contravariant basis vectors given by the covariant ones, namely

$$\boldsymbol{a}^\mu = \left.\frac{\boldsymbol{a}_\kappa \times \boldsymbol{a}_\lambda}{J}\right|_{(\kappa\lambda\mu)=(123)}, \tag{3.9}$$

where $(\kappa\lambda\mu) = (123)$ denotes any of the cyclic permutations of $\kappa = 1$, $\lambda = 2$, $\mu = 3$.

The generalised basis provides us the metric (tensor). The covariant (contravariant) components of the metric $g_{\mu\nu}$ ($g^{\mu\nu}$) are needed to lower or raise an index respectively. Lowering and raising is done by the contractions (see Schade, 1997, pp. 213, 224)

$$A_\mu = g_{\mu\nu}A^\nu \qquad \text{and} \qquad A^\kappa = g^{\kappa\lambda}A_\lambda. \tag{3.10}$$

The co- and contravariant components are given by (compare to Kaltenbach *et al.*, 2014)

$$g_{\mu\nu} := \boldsymbol{a}_\mu \cdot \boldsymbol{a}_\nu, = c^i{}_\mu c^i{}_\nu \qquad \text{and} \qquad g^{\kappa\lambda} := \boldsymbol{a}^\kappa \cdot \boldsymbol{a}^\lambda = \frac{1}{J^2}\gamma^\kappa{}_j\gamma^\lambda{}_j, \tag{3.11}$$

wherefore the co- and contravariant components can be transformed into each other very efficiently when the dual basis is orthogonal. According to Kaltenbach *et al.* (2014), the contravariant metric can be obtained from

$$g^{\kappa\nu} = \frac{1}{J^2}\left(g_{\lambda\rho}g_{\mu\sigma} - g_{\lambda\sigma}g_{\mu\rho}\right) \qquad \text{with} \quad (\kappa\lambda\mu) = (123), \quad (\nu\rho\sigma) = (123). \tag{3.12}$$

Hence, both matrices $(g_{\mu\nu})$ and $(g^{\mu\nu})$ can be computed straightforwardly once the Jacobi matrix $(c^i{}_\mu)$ is known. For practical reasons, let

$$\Lambda^{\mu\nu} := Jg^{\mu\nu}. \tag{3.13}$$

It remains to compute $(\gamma^\mu{}_i)$ in order to close the set of transformation matrices. More efficient than an inversion of the Jacobi matrix $(c^i{}_\mu)$ is an index-raising operation, which yields (remember that the Latin index is not fixed in position; compare to Kaltenbach *et al.*, 2014)

$$\gamma^\mu{}_i = \Lambda^{\mu\nu}c^i{}_\nu. \tag{3.14}$$

Equation (3.14) suggests that only $(c^i{}_\mu)$ and $(\Lambda^{\mu\nu})$ need to be stored in a numerical implementation. From these two, all other transformation matrices can be constructed efficiently. In fact, we will assume availability of $(c^i{}_\mu)$ and $(\Lambda^{\mu\nu})$, for the formulation of the equations of motion implemented in the solver HYBRID-NEW. Before deriving the equations, let us simplify the general transformation matrices in order to treat the annular confinement more efficiently.

Transformation matrices for axisymmetric configurations

Axisymmetry of the annular confinement (see figure 1.3) can be exploited by letting the coordinate functions F^i and G^ν (see equation (3.5)) be composed of a poloidal-toroidal transformation. The details have been worked out by Kaltenbach & Hauschild (2004) (alternatively, see the updated documentation Kaltenbach *et al.*, 2014) as an extension of the 2-D generalised framework of Choi (1993).

The starting point for Kaltenbach & Hauschild (2004) has been the split forward transformation F^i, namely

$$\left.\begin{aligned} x^1 &= F^1(\xi^1,\xi^2,\xi^3) = r(\xi^1,\xi^2)\,\cos\xi^3(\varphi), \\ x^2 &= F^2(\xi^1,\xi^2,\xi^3) = r(\xi^1,\xi^2)\,\sin\xi^3(\varphi), \\ x^3 &= F^3(\xi^1,\xi^2,\xi^3) = z(\xi^1,\xi^2), \end{aligned}\right\} \tag{3.15}$$

which means the backward transformation G^μ is given by

$$\left.\begin{aligned} G^1(x^1,x^2,x^3) &= \xi^1(r,z), \\ G^2(x^1,x^2,x^3) &= \xi^2(r,z), \\ G^3(x^1,x^2,x^3) &= \xi^3(\varphi) = \arctan\left(x^2/x^1\right). \end{aligned}\right\} \tag{3.16}$$

In equations (3.15) and (3.16), $r = \sqrt{(x^1)^2+(x^2)^2}$ is the polar radius, $\varphi \in [0, 2\pi)$ the azimuthal angle, and $z = x^3$ is the vertical coordinate of the underlying cylindrical coordinate system (r, φ, z). The functions $r\,(\xi^1,\xi^2)$ and $z\,(\xi^1,\xi^2)$ form the poloidal part of the decomposition, whereas $\varphi = \xi^3$ the toroidal part. We need to remember the constraints on the coordinate functions F^i and G^μ mentioned under equation (3.5). In an axisymmetric configuration smoothness of $r(\xi^1,\xi^2)$ and $z(\xi^1,\xi^2)$ is required, which means the domain cannot be arbitrary.

In the annulus of figure 1.3, for example, the inner frustum cannot be just a linear function since it would not be perpendicular to the lids at the edges. I have resolved this by smoothing the frustum boundary towards the lids. Details of the procedure are not of interest here but given in appendix A.2. Another option might have been to use curved lids in favour of a straight frustum wall by using a second cylindrical coordinate system for the poloidal components (in the axial-radial plane) with the origin centred at the intersection of the elongated frustum wall and the outer cylinder. This would result in an annular cut of a spherical container, but was discouraged by a stronger deviation from the experimental configuration described in chapter 1.

Let us continue with the computation of the axisymmetric transformation matrices. The latter are needed for an efficient implementation by carrying out analytically as many mapping steps as possible. Equation (3.15) has the Jacobi matrix (see Kaltenbach *et al.*, 2014)

$$(c^i_{\ \mu}) = \begin{pmatrix} \tilde{c}_1^{1/2}\cos\varphi & \tilde{c}_2^{1/2}\cos\varphi & -\tilde{c}_3^{1/2}\sin\varphi \\ \tilde{c}_1^{1/2}\sin\varphi & \tilde{c}_2^{1/2}\sin\varphi & \tilde{c}_3^{1/2}\cos\varphi \\ c_1^3 & c_2^3 & 0 \end{pmatrix}, \tag{3.17}$$

in which the reduced set of coefficients are given by

$$\tilde{c}_1^{1/2} \equiv \frac{\partial r}{\partial \xi^1}, \quad \tilde{c}_2^{1/2} \equiv \frac{\partial r}{\partial \xi^2}, \quad \tilde{c}_3^{1/2} \equiv r, \quad c_1^3 \equiv \frac{\partial z}{\partial \xi^1}, \quad c_2^3 \equiv \frac{\partial z}{\partial \xi^2}. \tag{3.18}$$

Equation (3.17), thus, has the Jacobian

$$J = \det(c^i_{\ \mu}) = \tilde{c}_3^{1/2}\left(\tilde{c}_2^{1/2}c_1^3 - \tilde{c}_1^{1/2}c_2^3\right), \tag{3.19}$$

which precisely exhibits two mapping steps. First, the mapping from Cartesian to cylindrical coordinates resulting in the factor $\tilde{c}_3^{1/2} = r$. Second, the mapping from cylindrical components (r, z) to the generalised components (ξ^1, ξ^2) giving the bracketed terms.

The covariant components of the metric are straightforwardly computed from equation (3.11) which yields (Kaltenbach *et al.*, 2014)

$$(g_{\mu\nu}) = \begin{pmatrix} \tilde{c}_1^{1/2}\tilde{c}_1^{1/2} + c_1^3c_1^3 & \tilde{c}_1^{1/2}\tilde{c}_2^{1/2} + c_1^3c_2^3 & 0 \\ \tilde{c}_1^{1/2}\tilde{c}_2^{1/2} + c_1^3c_2^3 & \tilde{c}_2^{1/2}\tilde{c}_2^{1/2} + c_2^3c_2^3 & 0 \\ 0 & 0 & \tilde{c}_3^{1/2}\tilde{c}_3^{1/2} \end{pmatrix}. \tag{3.20}$$

With the aid of equations (3.12) and (3.13), the contravariant components $\Lambda^{\mu\nu}$ read (see Kaltenbach *et al.*, 2014)

$$\begin{aligned}(\Lambda^{\mu\nu}) = (Jg^{\mu\nu}) &= \frac{1}{J}\begin{pmatrix} g_{22}g_{33} & -g_{21}g_{33} & 0 \\ -g_{12}g_{33} & g_{11}g_{33} & 0 \\ 0 & 0 & J^2/g_{33} \end{pmatrix} \\ &= \frac{1}{J}\begin{pmatrix} \tilde{c}_3^{1/2}\tilde{c}_3^{1/2}\left[c_2^3c_2^3 + \tilde{c}_2^{1/2}\tilde{c}_2^{1/2}\right] & -\tilde{c}_3^{1/2}\tilde{c}_3^{1/2}\left[c_1^3c_2^3 + \tilde{c}_1^{1/2}\tilde{c}_2^{1/2}\right] & 0 \\ -\tilde{c}_3^{1/2}\tilde{c}_3^{1/2}\left[c_1^3c_2^3 + \tilde{c}_1^{1/2}\tilde{c}_2^{1/2}\right] & \tilde{c}_3^{1/2}\tilde{c}_3^{1/2}\left[c_1^3c_1^3 + \tilde{c}_1^{1/2}\tilde{c}_1^{1/2}\right] & 0 \\ 0 & 0 & J^2\left[\tilde{c}_3^{1/2}\tilde{c}_3^{1/2}\right]^{-1} \end{pmatrix}.\end{aligned} \tag{3.21}$$

Note that raising both indices of the metric is equivalent to a matrix inversion. First, by expressing the contravariant elements $g^{\mu\nu}$ in terms of covariant ones $g_{\mu\nu}$, it happens that g_{11} and g_{22} appear 'swapped' in the J-scaled metric $(\Lambda^{\mu\nu})$. Second, off-diagonal elements ($\Lambda^{\mu\nu}$ with $\mu \neq \nu$) have negative sign and exhibit a transposition of the constituting covariant indices.

Finally, we obtain the J-scaled inverse Jacobi matrix $(\gamma^\mu_{\ i})$ from equation (3.14), namely

$$(\gamma^\mu_{\ i}) = \begin{pmatrix} -\tilde{c}_3^{1/2}c_2^3\cos\varphi & -\tilde{c}_3^{1/2}c_2^3\sin\varphi & \tilde{c}_3^{1/2}\tilde{c}_2^{1/2} \\ \tilde{c}_3^{1/2}c_1^3\cos\varphi & \tilde{c}_3^{1/2}c_1^3\sin\varphi & -\tilde{c}_3^{1/2}\tilde{c}_1^{1/2} \\ -\left[J/\tilde{c}_3^{1/2}\right]\sin\varphi & \left[J/\tilde{c}_3^{1/2}\right]\cos\varphi & 0 \end{pmatrix}. \tag{3.22}$$

In the latter equation, the matrix elements $\gamma^\mu_{\ i}$ have been expressed in terms of the Jacobi matrix elements $c^j_{\ \nu}$. It is worth to note the transposition of the indices in the elements of $(\gamma^\mu_{\ i})$ compared to $(c^i_{\ \mu})$.

The axisymmetric transformation given by equations (3.15) and (3.16) yields a collapse of the metrical factors in the transformation matrices. A numerical implementation of the axisymmetric version is, hence, much more efficient than an implementation of the matrices for the general 3-D case. On the one hand, because of a reduction of the storage requirements since the transformation matrices need to be stored only for the radial-axial section. On the other hand, because fewer terms have to be computed which reduces the number of operations.

We will come back to the transformation matrices at a later stage when the grid quality of the spatial discretisation scheme is tested. But let us continue further with an application of the transformation to the velocity field and the equations of motion.

Velocities, volume fluxes, and the transformed equations of motion

An application of equation (3.2) to the velocity vector $\boldsymbol{v}$ yields the Cartesian velocity components v^i $(i = 1, 2, 3)$ and the contravariant velocity components $u^\mu = \boldsymbol{v} \cdot \boldsymbol{a}^\mu$ $(\mu = 1, 2, 3)$ (similar notation to Luo & Bewley, 2004). The symbol 'v' denoted projections of the velocity vector on an orthonormal basis, whereas the symbol 'u' denotes those on the generalised basis. Time-independent coordinates imply $\mathrm{d}\boldsymbol{a}^\mu/\mathrm{d}t \equiv 0$, which yields the mapping between the Cartesian and contravariant velocities as (see Kaltenbach *et al.*, 2014)

$$v^i = \left(\partial_\mu x^i\right) \frac{\mathrm{d}\xi^\mu}{\mathrm{d}t} = c^i_{\ \mu} u^\mu, \qquad u^\mu = (\partial_i \xi^\mu) \frac{\mathrm{d}x^i}{\mathrm{d}t} = \frac{1}{J} \gamma^\mu_{\ i} v^i. \tag{3.23}$$

Equation (3.23) is used to transform between the u^μ and the v^i, which is needed for the initialisation of the model, to incorporate time-dependent boundary conditions, or when model output is written. In the first and second case, the components v^i are mapped to the u^μ, whereas in the third case it is the other way around. The Cartesian velocity components are easier to interpret or it is easier to formulate the boundary conditions for them than it is for the contravariant ones. Moreover, Cartesian velocities are often required when secondary software is used, e.g. for visualisation purposes. Transformations from one set of velocities to the other take time and the operation is subject to numerical errors. Hence, the dynamical core should operate only in transformed variables so that a mapping into Cartesian components is performed only if it is necessary.

We will see later (see sections 3.4 and 3.5) that the divergence of the velocity field needs to computed frequently in a numerical algorithm that solves the incompressible Navier–Stokes equations. The numerical efficiency of the solver can be improved by replacing contravariant velocities u^μ with contravariant volume fluxes q^μ, that is,

$$q^\mu := J u^\mu. \tag{3.24}$$

The transformations between contravariant volume fluxes and the Cartesian velocities reads

$$\left.\begin{aligned} q^1 &= \tilde{c}_3^{1/2}\Big(- c_2^3 \left[v^1 \cos\varphi + v^2 \sin\varphi\right] + \tilde{c}_2^{1/2} v^3\Big), \\ q^2 &= \tilde{c}_3^{1/2}\Big(+ c_1^3 \left[v^1 \cos\varphi + v^2 \sin\varphi\right] - \tilde{c}_1^{1/2} v^3\Big), \\ q^3 &= \frac{J}{\tilde{c}_3^{1/2}}\Big(- v^1 \sin\varphi + v^2 \cos\varphi\Big), \end{aligned}\right\} \tag{3.25}$$

and

$$\left.\begin{aligned} v^1 &= \frac{1}{J}\Big(\cos\varphi \left[\tilde{c}_1^{1/2} q^1 + \tilde{c}_2^{1/2} q^2\right] - \sin\varphi\, \tilde{c}_3^{1/2} q^3\Big), \\ v^2 &= \frac{1}{J}\Big(\sin\varphi \left[\tilde{c}_1^{1/2} q^1 + \tilde{c}_2^{1/2} q^2\right] + \cos\varphi\, \tilde{c}_3^{1/2} q^3\Big), \\ v^3 &= \frac{1}{J}\left(c_1^3 q^1 + c_2^3 q^2\right) \end{aligned}\right\} \tag{3.26}$$

in terms of the Jacobi matrix elements $c^i_{\ \mu}$, which are given in equations (3.17) and (3.18).

A focus on axisymmetric configurations suggests to compute cylindrical velocities (v_r, v_φ, v_z) to aid interpretation of the results. The cylindrical velocities can be obtained from the Cartesian velocities or—more efficiently—directly from the volume fluxes, that is,

$$\left.\begin{aligned} v_r &= v^1 \cos\varphi + v^2 \sin\varphi = \frac{1}{J}\left(\tilde{c}_1^{1/2} q^1 + \tilde{c}_2^{1/2} q^2\right), \\ v_\varphi &= v^2 \cos\varphi - v^1 \sin\varphi = \frac{1}{J}\tilde{c}_3^{1/2} q^3, \\ v_z &= v^3 = \frac{1}{J}\left(c_1^3 q^1 + c_2^3 q^2\right). \end{aligned}\right\} \tag{3.27}$$

Note that configurations like a full cylinder or a pipe have a polar coordinate singularity at the axis, that is, $J|_{\text{axis}} = 0$. The usage of volume fluxes regularises the problem by $q^\mu\big|_{\text{axis}} \equiv 0$, but the velocity vector cannot be recovered on the axis.

The volume fluxes contain the Jacobian J of the coordinate transformation, which means the volume fluxed keep track of the change of the control volume. Speaking of the control volume hints at mass conservation properties, which is addressed by looking into the transformation of the continuity equation (2.7). The continuity equation is transformed by an application of the conservative derivative (Thompson *et al.*, 1985, p. 112), which yields the so-called strong conservation form of the continuity equation (e.g. Vinokur, 1974)

$$0 = \boldsymbol{\nabla} \cdot \boldsymbol{v} = \frac{1}{J}\partial_\mu \left(J u^\mu\right). \tag{3.28}$$

A substitution of the volume flux definition (3.24) into equation (3.28) and using $J \neq 0$ allows to collapse the continuity equation to

$$0 = \partial_\mu q^\mu. \tag{3.29}$$

Equation (3.29) does not contain any metrical factors. This aids mass conservation and numerical efficiency in the discrete approximation (e.g. Rosenfeld *et al.*, 1991). It is worth emphasizing that equation (3.29) only uses the 'new' variables given by the volume fluxes q^μ and the generalised coordinates ξ^ν.

The last step consists in the transformation of the momentum equation (2.6) so that only volume fluxes q^μ and generalised coordinates ξ^ν appear. (The scalars given by the excess pressure ϕ and time t remain unchanged.) We follow Choi (1993) and Kaltenbach & Hauschild (2004) by mapping the Cartesian projections of the momentum equation (see equation (2.10)) via the chain rule. The results for axisymmetric configurations have been given for the non-rotating frame of reference by Kaltenbach & Hauschild (2004). I have added the Coriolis force into the framework and implemented it into the solver (see the extension of the code documentation; Klein, 2014a).

The left hand side of equations (2.10) is transformed straightforwardly by a transformation of the velocities (see equations (3.23) and (3.24)). One has for the momentum equation

$$\gamma^\mu_{\ i}\left(\partial_t v^i\right) = \partial_t q^\mu = -\mathcal{G}^\mu - \mathcal{N}^\mu + \mathcal{L}^\mu - \mathcal{C}^\mu. \tag{3.30}$$

Expressions on the right hand side of equation (3.30) are not yet known, but they consist of the transformed excess pressure gradient term $\mathcal{G}^\mu$, the transformed momentum advection term $\mathcal{N}^\mu$, the transformed viscous term $\mathcal{L}^\mu$, and the transformed Coriolis force term $\mathcal{C}^\mu$. In the following,

the expansions of the different terms with respect to generalised coordinates will be discussed briefly.

The conservative form of the *non-linear advection term* reads $-R\boldsymbol{\nabla}\cdot(\boldsymbol{v}\circ\boldsymbol{v})$. A contraction of the Cartesian projections with $\gamma^\mu_{\ i}$ and the substitution of $v^i = J^{-1}c^i_{\ \nu}q^\nu$ due to equations (3.23) and (3.24) yields

$$-\mathcal{N}^\mu = -R\gamma^\mu_{\ i}\frac{\partial\left(v^j v^i\right)}{\partial x^j} = -R\frac{1}{J}\gamma^\mu_{\ i}\frac{\partial}{\partial\xi^\nu}\left(\frac{1}{J}c^i_{\ \lambda}q^\lambda q^\nu\right). \tag{3.31}$$

The latter equation states that Cartesian components $v^i = J^{-1}c^i_{\ \nu}q^\nu$ are advected by the contravariant volume fluxes q^λ in the direction of the generalised coordinates. Metrical factors are present on the right hand side and two contractions need to be carried out, which makes computation of the momentum advection terms quite expensive. The only simplification is due to restricting the attention to axisymmetric geometry which collapses some of the contractions. The implemented terms read (see Kaltenbach *et al.*, 2014)

$$\begin{aligned}
-\mathcal{N}^1 =& -\frac{\tilde{c}_3^{1/2}}{J}\left(\tilde{c}_2^{1/2}\frac{\partial}{\partial\xi^1}\frac{1}{J}\left[c_1^3q^1q^1+c_2^3q^2q^1\right]-c_2^3\frac{\partial}{\partial\xi^1}\frac{1}{J}\left[\tilde{c}_1^{1/2}q^1q^1+\tilde{c}_2^{1/2}q^2q^1\right]\right)\\
&-\frac{\tilde{c}_3^{1/2}}{J}\left(\tilde{c}_2^{1/2}\frac{\partial}{\partial\xi^2}\frac{1}{J}\left[c_1^3q^1q^2+c_2^3q^2q^2\right]-c_2^3\frac{\partial}{\partial\xi^2}\frac{1}{J}\left[\tilde{c}_1^{1/2}q^1q^2+\tilde{c}_2^{1/2}q^2q^2\right]\right)\\
&-c_2^3\left(\frac{\tilde{c}_3^{1/2}}{J}q^3\right)^2-\frac{1}{J}\frac{\partial}{\partial\xi^3}\left(q^1q^3\right),\\
-\mathcal{N}^2 =& -\frac{\tilde{c}_3^{1/2}}{J}\left(-\tilde{c}_1^{1/2}\frac{\partial}{\partial\xi^1}\frac{1}{J}\left[c_1^3q^1q^1+c_2^3q^2q^1\right]+c_1^3\frac{\partial}{\partial\xi^1}\frac{1}{J}\left[\tilde{c}_1^{1/2}q^1q^1+\tilde{c}_2^{1/2}q^2q^1\right]\right)\\
&-\frac{\tilde{c}_3^{1/2}}{J}\left(-\tilde{c}_1^{1/2}\frac{\partial}{\partial\xi^2}\frac{1}{J}\left[c_1^3q^1q^2+c_2^3q^2q^2\right]+c_1^3\frac{\partial}{\partial\xi^2}\frac{1}{J}\left[\tilde{c}_1^{1/2}q^1q^2+\tilde{c}_2^{1/2}q^2q^2\right]\right)\\
&+c_1^3\left(\frac{\tilde{c}_3^{1/2}}{J}q^3\right)^2-\frac{1}{J}\frac{\partial}{\partial\xi^3}\left(q^2q^3\right),\\
-\mathcal{N}^3 =& -\frac{1}{\tilde{c}_3^{1/2}}\frac{\partial}{\partial\xi^1}\left(\frac{\tilde{c}_3^{1/2}}{J}q^3q^1\right)-\frac{1}{\tilde{c}_3^{1/2}}\frac{\partial}{\partial\xi^2}\left(\frac{\tilde{c}_3^{1/2}}{J}q^3q^2\right)\\
&-\frac{1}{\tilde{c}_3^{1/2}J}\left(\tilde{c}_1^{1/2}q^1q^3+\tilde{c}_2^{1/2}q^2q^3\right)-\frac{1}{J}\frac{\partial}{\partial\xi^3}\left(q^3q^3\right).
\end{aligned}$$

For the *viscous term* Choi (1993) and Kaltenbach & Hauschild (2004) started from the divergence form, $\boldsymbol{\nabla}\cdot(E\boldsymbol{\nabla}\circ\boldsymbol{v})$, for which the contraction with $\gamma^\mu_{\ i}$ yields

$$\mathcal{L}^\mu = \gamma^\mu_{\ i}\frac{\partial}{\partial x^j}\left(E\frac{\partial v^i}{\partial x^j}\right) = \frac{1}{J}\gamma^\mu_{\ i}\frac{\partial}{\partial\xi^\kappa}\left(E\Lambda^{\kappa\lambda}\frac{\partial}{\partial\xi^\lambda}\left[\frac{1}{J}c^i_{\ \nu}q^\nu\right]\right), \tag{3.32}$$

where the divergence form has been used to avoid implementation of the generalised double-curl. Keeping the off-diagonal terms $\Lambda^{\mu\nu}\big|_{\mu\neq\nu}$ (in contrast to the Laplacian in orthogonal coordinates Bronstein *et al.*, 2005, p. 679) and putting E behind the first derivative allows an accurate representation of the viscosity, which aids to include a sub-grid scale turbulence model by an

eddy viscosity (e.g. Kaltenbach *et al.*, 1999, but the extension to axisymmetric configurations has not yet been done). At the moment no turbulence model is used.

The structure of equation (3.32) is such that Cartesian velocity components, $v^i = J^{-1}c^i_\nu q^\nu$, are diffused along the generalised coordinates. The implemented expressions are rather lengthy and read (summation over Greek indices is suppressed; see Kaltenbach *et al.*, 2014)

$$\begin{aligned}
\mathcal{L}^1 = {}& \frac{\tilde{c}_3^{1/2}}{J}\left[\tilde{c}_2^{1/2}\left(\frac{\partial}{\partial\xi^\mu}E\Lambda^{\mu\mu}\frac{\partial}{\partial\xi^\mu}\right)\Big|_{\mu\in\{1,2\}}\frac{c_1^3q^1}{J} - c_2^3\left(\frac{\partial}{\partial\xi^\nu}E\Lambda^{\nu\nu}\frac{\partial}{\partial\xi^\nu}\right)\Big|_{\nu\in\{1,2\}}\frac{\tilde{c}_1^{1/2}q^1}{J}\right]\\
&+\frac{\tilde{c}_3^{1/2}}{J}\left[\tilde{c}_2^{1/2}\left(\frac{\partial}{\partial\xi^\kappa}E\Lambda^{\kappa\kappa}\frac{\partial}{\partial\xi^\kappa}\right)\Big|_{\kappa\in\{1,2\}}\frac{c_2^3q^2}{J} - c_2^3\left(\frac{\partial}{\partial\xi^\sigma}E\Lambda^{\sigma\sigma}\frac{\partial}{\partial\xi^\sigma}\right)\Big|_{\sigma\in\{1,2\}}\frac{\tilde{c}_2^{1/2}q^2}{J}\right]\\
&+\frac{\tilde{c}_3^{1/2}}{J}\left[\tilde{c}_2^{1/2}\left(\frac{\partial}{\partial\xi^\mu}E\Lambda^{\mu\nu}\frac{\partial}{\partial\xi^\nu}\right)\Big|^{\mu\neq\nu}_{\mu,\nu\in\{1,2\}}\frac{c_1^3q^1}{J} - c_2^3\left(\frac{\partial}{\partial\xi^\kappa}E\Lambda^{\kappa\sigma}\frac{\partial}{\partial\xi^\sigma}\right)\Big|^{\kappa\neq\sigma}_{\kappa,\sigma\in\{1,2\}}\frac{\tilde{c}_1^{1/2}q^1}{J}\right]\\
&+\frac{\tilde{c}_3^{1/2}}{J}\left[\tilde{c}_2^{1/2}\left(\frac{\partial}{\partial\xi^\mu}E\Lambda^{\mu\nu}\frac{\partial}{\partial\xi^\nu}\right)\Big|^{\mu\neq\nu}_{\mu,\nu\in\{1,2\}}\frac{c_2^3q^2}{J} - c_2^3\left(\frac{\partial}{\partial\xi^\kappa}E\Lambda^{\kappa\sigma}\frac{\partial}{\partial\xi^\sigma}\right)\Big|^{\kappa\neq\sigma}_{\kappa,\sigma\in\{1,2\}}\frac{\tilde{c}_2^{1/2}q^2}{J}\right]\\
&+\frac{c_2^3}{\tilde{c}_3^{1/2}J}E\Big(\tilde{c}_1^{1/2}q^1+\tilde{c}_2^{1/2}q^2\Big)+\frac{c_2^3}{\tilde{c}_3^{2/3}}\left(E\frac{\partial}{\partial\xi^3}+\frac{\partial}{\partial\xi^3}E\right)\frac{\tilde{c}_3^{1/2}q^3}{J}+\frac{1}{J}\left(\frac{\partial}{\partial\xi^3}E\Lambda^{33}\frac{\partial}{\partial\xi^3}\right)q^1,
\end{aligned}$$

$$\begin{aligned}
\mathcal{L}^2 = {}& \frac{\tilde{c}_3^{1/2}}{J}\left[-\tilde{c}_1^{1/2}\left(\frac{\partial}{\partial\xi^\mu}E\Lambda^{\mu\mu}\frac{\partial}{\partial\xi^\mu}\right)\Big|_{\mu\in\{1,2\}}\frac{c_1^3q^1}{J} + c_1^1\left(\frac{\partial}{\partial\xi^\nu}E\Lambda^{\nu\nu}\frac{\partial}{\partial\xi^\nu}\right)\Big|_{\nu\in\{1,2\}}\frac{\tilde{c}_1^{1/2}q^1}{J}\right]\\
&+\frac{\tilde{c}_3^{1/2}}{J}\left[-\tilde{c}_1^{1/2}\left(\frac{\partial}{\partial\xi^\kappa}E\Lambda^{\kappa\kappa}\frac{\partial}{\partial\xi^\kappa}\right)\Big|_{\kappa\in\{1,2\}}\frac{c_2^3q^2}{J} + c_1^3\left(\frac{\partial}{\partial\xi^\sigma}E\Lambda^{\sigma\sigma}\frac{\partial}{\partial\xi^\sigma}\right)\Big|_{\sigma\in\{1,2\}}\frac{\tilde{c}_2^{1/2}q^2}{J}\right]\\
&+\frac{\tilde{c}_3^{1/2}}{J}\left[-\tilde{c}_1^{1/2}\left(\frac{\partial}{\partial\xi^\mu}E\Lambda^{\mu\nu}\frac{\partial}{\partial\xi^\nu}\right)\Big|^{\mu\neq\nu}_{\mu,\nu\in\{1,2\}}\frac{c_1^3q^1}{J} + c_1^3\left(\frac{\partial}{\partial\xi^\kappa\sigma}E\Lambda^{\kappa\sigma}\frac{\partial}{\partial\xi^\sigma}\right)\Big|^{\kappa\neq\sigma}_{\kappa,\sigma\in\{1,2\}}\frac{\tilde{c}_1^{1/2}q^1}{J}\right]\\
&+\frac{\tilde{c}_3^{1/2}}{J}\left[-\tilde{c}_1^{1/2}\left(\frac{\partial}{\partial\xi^\mu}E\Lambda^{\mu\nu}\frac{\partial}{\partial\xi^\nu}\right)\Big|^{\mu\neq\nu}_{\mu,\nu\in\{1,2\}}\frac{c_2^3q^2}{J} + c_1^3\left(\frac{\partial}{\partial\xi^\kappa}E\Lambda^{\kappa\sigma}\frac{\partial}{\partial\xi^\sigma}\right)\Big|^{\kappa\neq\sigma}_{\kappa,\sigma\in\{1,2\}}\frac{\tilde{c}_2^{1/2}q^2}{J}\right]\\
&-\frac{c_1^3}{\tilde{c}_3^{1/2}J}E\Big(\tilde{c}_1^{1/2}q^1+\tilde{c}_2^{1/2}q^2\Big)-\frac{c_1^3}{\tilde{c}_3^{1/2}}\left(E\frac{\partial}{\partial\xi^3}+\frac{\partial}{\partial\xi^3}E\right)\frac{\tilde{c}_3^{1/2}q^3}{J}+\frac{1}{J}\left(\frac{\partial}{\partial\xi^3}E\Lambda^{33}\frac{\partial}{\partial\xi^3}\right)q^2,
\end{aligned}$$

$$\begin{aligned}
\mathcal{L}^3 = {}& \frac{1}{\tilde{c}_3^{1/2}}\left(\frac{\partial}{\partial\xi^\mu}E\Lambda^{\mu\mu}\frac{\partial}{\partial\xi^\mu}\right)\Big|_{\mu\in\{1,2\}}\frac{\tilde{c}_3^{1/2}q^3}{J}+\frac{1}{\tilde{c}_3^{1/2}}\left(\frac{\partial}{\partial\xi^\kappa}E\Lambda^{\kappa\sigma}\frac{\partial}{\partial\xi^\sigma}\right)\Big|^{\kappa\neq\sigma}_{\kappa,\sigma\in\{1,2\}}\frac{\tilde{c}_3^{1/2}q^3}{J}\\
&+\frac{\tilde{c}_1^{1/2}}{\tilde{c}_3^{1/2}J}\left(E\Lambda^{33}\frac{\partial}{\partial\xi^3}+\frac{\partial}{\partial\xi^3}E\Lambda^{33}\right)q^1+\frac{\tilde{c}_2^{1/2}}{\tilde{c}_3^{1/2}J}\left(E\Lambda^{33}\frac{\partial}{\partial\xi^3}+\frac{\partial}{\partial\xi^3}E\Lambda^{33}\right)q^2\\
&+\frac{1}{J}\left(\frac{\partial}{\partial\xi^3}E\Lambda^{33}\frac{\partial}{\partial\xi^3}-E\Lambda^{33}\right)q^3.
\end{aligned}$$

The contravariant form of the *excess pressure gradient* results from a straightforward transformation of the gradient operator. Using the non-conservative derivative (see Thompson *et al.*, 1985, pp. 112–116), one has

$$-\mathcal{G}^\mu = -\gamma^\mu_{\ i}\left(\partial^i\phi\right) = -\Lambda^{\mu\nu}\left(\partial_\nu\phi\right) = \begin{cases} -\Lambda^{11}\dfrac{\partial\phi}{\partial\xi^1} - \Lambda^{12}\dfrac{\partial\phi}{\partial\xi^2} & \text{for} \quad \mu = 1, \\ -\Lambda^{21}\dfrac{\partial\phi}{\partial\xi^1} - \Lambda^{22}\dfrac{\partial\phi}{\partial\xi^2} & \text{for} \quad \mu = 2, \\ -\Lambda^{33}\dfrac{\partial\phi}{\partial\xi^3} & \text{for} \quad \mu = 3, \end{cases} \tag{3.33}$$

in which $(\Lambda^{\mu\nu})$ is given by equation (3.21). The local orthogonality of the dual basis ensures that the conservative and the non-conservative derivative are equivalent, which is a consequence of the geometric conservation law (see Thompson *et al.*, 1985, p. 104, or the upcoming equations (3.61) and (3.62) for the application to axisymmetric configurations).

The *Coriolis force*, $-2\boldsymbol{e}_z \times \boldsymbol{v}$, is transformed by expanding the cross product in Cartesian components followed by a projection on the generalised basis. It is a 'by-product' of the generalised curl and cross-products (e.g. Klein, 2014a). Application of the chain rule and a substitution of the transformation matrices $(c^i_{\ \mu})$ and $(\Lambda^{\mu\nu})$ yields

$$\begin{aligned} -\mathcal{C}^\mu = -2\gamma^\mu_{\ i}\varepsilon_{i3k}v^k &= -\frac{2}{J}\left(\gamma^\mu_{\ 2}c^1_{\ \nu} - \gamma^\mu_{\ 1}c^2_{\ \nu}\right)q^\nu \\ &= \begin{cases} -2\dfrac{\tilde{c}_3^{1/2}\tilde{c}_3^{1/2}}{J}c^3_{\ 2}q^3 = -2\dfrac{c^3_{\ 2}q^3}{\Lambda^{33}} & \text{for} \quad \mu = 1, \\ +2\dfrac{\tilde{c}_3^{1/2}\tilde{c}_3^{1/2}}{J}c^3_{\ 1}q^3 = +2\dfrac{c^3_{\ 1}q^3}{\Lambda^{33}} & \text{for} \quad \mu = 2, \\ -\dfrac{2}{\tilde{c}_3^{1/2}}\left(\tilde{c}_1^{1/2}q^1 + \tilde{c}_2^{1/2}q^2\right) & \text{for} \quad \mu = 3, \end{cases} \end{aligned} \tag{3.34}$$

where ε_{ijk} denotes the Levi-Civita tensor (e.g. Bronstein *et al.*, 2005, p. 273). Here, one has $\boldsymbol{e}_z \equiv \boldsymbol{e}_3$ which aids to the compact expressions in equation (3.34). Interestingly, many of the metrical terms have collapsed under the cross product, which is a direct consequence of the generalised cross product in an orthogonal dual basis,

$$\boldsymbol{A} \times \boldsymbol{B} = \boldsymbol{a}_\lambda \epsilon^{\lambda\mu\nu} g_{\mu\kappa} g_{\nu\sigma} A^\kappa B^\sigma, \tag{3.35}$$

and $\epsilon^{\lambda\mu\nu} = J^{-1}\varepsilon_{\lambda\mu\nu}$ the contravariant Levi-Civita tensor (e.g. Kuttler, 2011). The governing equations (3.29) and (3.30) in the co-rotating frame of reference have been expressed with respect to the new variables contravariant volume fluxes q^μ and generalised coordinates ξ^ν. Explicit forms of all right hand side terms have been given and can be implemented straightforwardly. The explicit expressions assume the dual basis to be locally orthogonal and the generalised coordinates to be axisymmetric, which facilitates the usage for solving the Navier–Stokes equations in axisymmetric confinements, like annuli, cylinders, or pipes. Coriolis force has been added recently for the case that the axis of the system rotation is aligned with the symmetry axis of the coordinate transformation. Comparing the generalised momentum equations (3.30) to those in cylindrical coordinates (see equations (2.12)) shows that the generalised coordinate framework requires substantial overhead in order to study the flow in an annulus

with an inner frustum (see figure 1.3), for example. The benefit is that the boundary conditions can be treated straightforwardly and accurately.

Finally, we are left with the formulation of the *boundary conditions* for the volume fluxes. The boundary conditions for the librating annulus have been given in terms of cylindrical velocity components in equations (2.15), (2.16) and (2.17). An application of equation (3.25) to the wall velocity yields

$$q^1 = q^2 = 0, \qquad q^3 = \frac{J}{\tilde{c}_3^{1/2}} v_\varphi \qquad \text{at} \quad \xi^1 = 0, 1 \quad \text{and} \quad \xi^2 = 0, 1. \tag{3.36}$$

Only the volume flux component q^3 is non-zero at a librating wall similar to the azimuthal velocity v_φ. The periodic Dirichlet conditions in azimuthal direction $(\varphi = \xi^3)$ apply also for the fluxes q^μ.

All the ingredients necessary for the implementation have been worked out analytically as far as possible. In the following section we will continue with a description of the discretisation scheme and the numerical algorithm.

3.2 Spatial discretisation

We aim to compute approximate solutions to the contravariant Navier–Stokes equations (3.29) and (3.30) numerically subject to the boundary forcing due to equations (3.36). Different aspects have been regarded important for a numerical investigation of inertial waves and wave attractors in a librating confinement:

- the concentration of wave energy near on a wave attractor is accompanied by strong velocity gradients in the vicinity of the wave attractor and requires high resolutions in the whole fluid domain (compare to figure 2.10);
- the inertial waves exhibit focusing reflections at the oblique walls and slow down as the wavelength decreases (see equation (2.25)) which means simulated times need to be long enough to develop a wave attractor which calls for an efficient numerical scheme;
- the wave excitation mechanism due to libration of the wall needs to be resolved in order to stay as close as possible to a corresponding laboratory experiment (Seelig, 2014) which also means that we do not want to make any assumptions beyond the incompressible Navier–Stokes equations.

Both numerical efficiency and accuracy are addressed by direct numerical simulations (DNS; for a review see Moin & Mahesh, 1998) by resolving all scales of the flow directly. Long time simulations demand a numerical scheme that has negligible numerical diffusion of the kinetic energy and that is able to guarantee mass conservation. The scheme used for the present study fulfils all these requirements. It is implemented in the HYBRID-NEW solver using finite-differences for the wall-bounded directions, but the spectral derivative for the azimuthal direction. Both methods are state-of-the-art and comprehensive convergence or performance analyses are omitted here. The latest solver version has been evaluated by Ghasemi V. (2016) with respect to Taylor–Couette flow by a comparison of HYBRID-NEW's solutions to published DNS data.

In the following, we will first discuss the spatial discretisation used in the HYBRID-NEW solver. After that, we will look into the numerical accuracy for the grids used to simulate the

flow in the librating annulus (figure 1.3) and discuss also the dimensionless parameters (Rossby and Ekman numbers) that can be reached by the numerical grids used.

Finite-difference approximation for the wall-bounded directions

Spatial discretisation of equations (3.29) and (3.30) is based on an equipartition of the box $[0,1] \times [0,1] \times [0,2\pi]$ for the generalised coordinates (ξ^1, ξ^2, ξ^3), which yields the grid cell dimensions in the transformed domain as

$$\Delta\xi^1 = \frac{1}{N_1}, \quad \Delta\xi^2 = \frac{1}{N_2}, \quad \Delta\xi^3 = \frac{2\pi}{N_3}, \tag{3.37}$$

where N_μ ($\mu = 1, 2, 3$) denotes the number of grid boxes in each of the corresponding directions ξ^μ.

Figure 3.2 illustrates the arrangement of the variables, where small arrows mark the respective volume flux components. Filled markers at the arrow bases give the position in the grid. The volume flux boundary condition is indicated by unfilled markers. The excess pressure ϕ is needed only inside the flow domain since the boundary condition (3.36) does not contain the excess pressure. Black lines in figure 3.2 show the edges of the grid cells corresponding to the indices

$$1 \leqslant i \leqslant N_1 + 1, \quad 1 \leqslant j \leqslant N_2 + 1, \quad 1 \leqslant k \leqslant N_3 + 1, \tag{3.38}$$

which count the nodes along ξ^1, ξ^2, ξ^3 respectively.

HYBRID-NEW employs the second-order central-difference approximation (see, e.g., Orlandi, 2000; Roache, 1998) for the wall-bounded directions, which yields volume flux components q^1 and q^2 staggered on a 2-D Arakawa C-grid (Arakawa & Lamb, 1977), sometimes also called marker-and-cell grid (or MAC grid; see Harlow & Welch, 1965). The azimuthal volume flux component q^3 is collocated with the excess pressure ϕ at grid cell centres (see figure 3.2). The grid cell centres are located at shifted positions $\left(i + \frac{1}{2}, j + \frac{1}{2}, k + \frac{1}{2}\right)$.

As an example, let $\phi_{i+1/2,j+1/2,k+1/2}$ denote the value of the excess pressure ϕ at the position $\boldsymbol{r}_{i+1/2,j+1/2,k+1/2}$. The extension to the volume fluxes q^μ is straightforward and given in table 3.1. The small boxes in figure 3.2 traced out by dotted lines illustrate the storage scheme of the variables by taking the 'floor' values (i, j, k) of each node. The grid is specified by the coordinates of the grid box corners, $\boldsymbol{r}_{i,j,k}$. Axisymmetry can be exploited so that only a 2-D grid has to be constructed carefully in order to specify the geometry of the radial-axial section (r, z). The azimuthal coordinate of the nodes can be constructed easily, for instance during the start of the solver, but will be specified further down when we discuss the spectral derivative.

The staggered grid requires both differencing and interpolation operators in order to formulate a numerical scheme for equations (3.29) and (3.30). Let ψ denote a scalar field (e.g. ϕ) or a vector component (e.g. q^μ). Using finite-difference approximations means one expands the solution locally (around $\xi^\mu = \xi_0^\mu$) with respect to the polynomial basis (Taylor expansion)

$$\psi(\xi^\mu) = \psi(\xi_0^\mu) + \frac{1}{1!}(\partial_\mu\psi)\Big|_{\xi_0^\mu}(\xi^\mu - \xi_0^\mu) + \frac{1}{2!}\left(\partial_\mu^2\psi\right)\Big|_{\xi_0^\mu}(\xi^\mu - \xi_0^\mu)^2 + \dots . \tag{3.39}$$

The partial derivative $\partial_\mu\psi$ can be approximated by the *central difference* (Bronstein *et al.*, 2005, p. 408) given by the two-point stencil (e.g. for $\mu = 1$)

$$\left.\frac{\partial\psi}{\partial\xi^1}\right|_i = \frac{\psi_{i+1/2} - \psi_{i-1/2}}{\Delta\xi^1} + O\left(\left[\Delta\xi^1\right]^2\right), \tag{3.40}$$

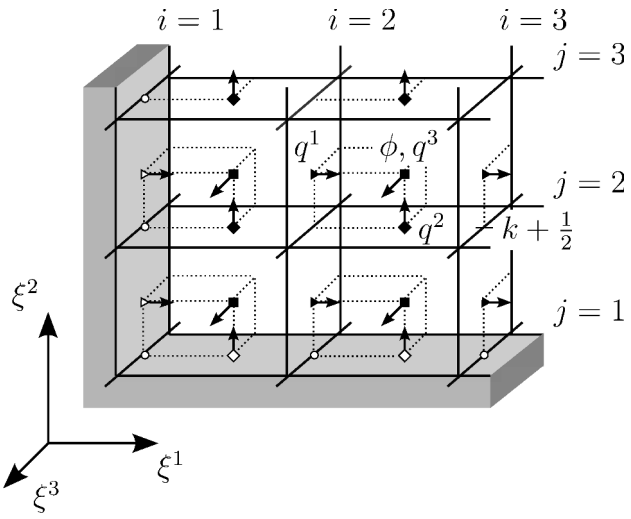

Figure 3.2: Staggering of the volume fluxes q^μ ($\mu = 1, 2, 3$) and the excess pressure ϕ in the numerical Navier–Stokes solver HYBRID-NEW. Filled markers give the positions of interior nodes for the respective volume flux components indicated by small arrows. Unfilled markers show the nodes at which Dirichlet boundary conditions are specified for the q^μ, where the walls are illustrated by a grey shading. Coordinate lines ξ^μ are marked by black lines and mark the grid box edges. Small boxes with a dotted line indicate the storage scheme to indices (i, j, k) for coordinates $\left(\xi^1, \xi^2, \xi^3\right)$ respectively.

Table 3.1: Position indices used in HYBRID-NEW for the staggered volume fluxes q^μ ($\mu = 1, 2, 3$), the excess pressure ϕ, and the vertex coordinates (r, z). The listing is supplementary to figure 3.2.

Variable	Interior position	ξ^1-boundary	ξ^2-boundary
$r,\ z$	$(i, j)\ \forall k$	$(i, j)\ \forall k$	$(i, j)\ \forall k$
ϕ	$\left(i + \frac{1}{2}, j + \frac{1}{2}, k + \frac{1}{2}\right)$	—	—
q^1	$\left(i, j + \frac{1}{2}, k + \frac{1}{2}\right)$	$\left(i, j + \frac{1}{2}, k + \frac{1}{2}\right)$	$\left(i, j, k + \frac{1}{2}\right)$
q^2	$\left(i + \frac{1}{2}, j, k + \frac{1}{2}\right)$	$\left(i, j, k + \frac{1}{2}\right)$	$\left(i + \frac{1}{2}, j, k + \frac{1}{2}\right)$
q^3	$\left(i + \frac{1}{2}, j + \frac{1}{2}, k + \frac{1}{2}\right)$	$\left(i, j + \frac{1}{2}, k + \frac{1}{2}\right)$	$\left(i + \frac{1}{2}, j, k + \frac{1}{2}\right)$

where $\psi_{i+1/2}$ denotes a node centred in ξ^1-direction, as it is the case for ϕ, q^2 and q^3 in figure 3.2. The 'passive' indices j and k have been omitted and may take integer or non-integer values. The gradient along ξ^1 is computed for the cell boundary, that is, located at an integer index i, where it is second-order accurate.

Equation (3.40) applies in the same way to the ξ^2-direction and is straightforwardly extended to the remaining staggered positions. The corresponding interpolation operator $\overline{(\cdot)}^{\mu}$ is a two-point average that is second-order accurate. For $\mu = 1$, for example, one has

$$\overline{\psi}^1\Big|_i = \frac{\psi_{i-1/2} + \psi_{i+1/2}}{2} = \psi_i + O\left(\left[\Delta\xi^1\right]^2\right). \tag{3.41}$$

Both differentiation, equation (3.40), and interpolation, equation (3.41), are consistent with respect to their approximation order.

The central-difference approximations for *higher-order derivatives* $\left(\partial_\mu^n\psi = \partial_\mu \cdots \partial_\mu\psi\right)$ are obtained by applying the discrete operator in equation (3.40) n times by working from the outside to the inside. Presence of metrical factors requires some care. The generalised Laplacian—or the viscous term in equation (3.32) for that matter—have uni-directional derivatives of the form (e.g. in ξ^1-direction)

$$\begin{aligned}\partial_1\left(\Lambda^{11}\partial_1\psi\right)\Big|_{i+1/2} &\approx \frac{\Lambda^{11}\left(\partial_1\psi\right)}{\Delta\xi^1}\bigg|_{i+1} - \frac{\Lambda^{11}\left(\partial_1\psi\right)}{\Delta\xi^1}\bigg|_{i} \\ &\approx \frac{\Lambda^{11}_{i+1}\left(\psi_{i+3/2} - \psi_{i+1/2}\right) - \Lambda^{11}_{i}\left(\psi_{i+1/2} - \psi_{i-1/2}\right)}{\left(\Delta\xi^1\right)^2}.\end{aligned} \tag{3.42}$$

Directions ξ^2 and ξ^3 are treated analogously. The cross-derivative terms are obtained similarly, for example, when differentiating first in ξ^1- and then in ξ^2-direction, one has

$$\begin{aligned}\partial_2\left(\Lambda^{21}\partial_1\psi\right)\Big|_{i+1/2,j+1/2} &\approx \frac{\Lambda^{21}\left(\partial_1\psi\right)}{\Delta\xi^2}\bigg|_{i+1/2,j+1} - \frac{\Lambda^{21}\left(\partial_1\psi\right)}{\Delta\xi^2}\bigg|_{i+1/2,j} \\ &\approx \frac{\Lambda^{21}_{i+1/2,j+1}\left(\psi_{i+1,j+1} - \psi_{i,j+1}\right) - \Lambda^{21}_{i+1/2,j}\left(\psi_{i+1,j} - \psi_{i,j}\right)}{\Delta\xi^1\Delta\xi^2}.\end{aligned} \tag{3.43}$$

A complication arises due to unknown values of ψ at integer indices ($\psi_{i,j}$, $\psi_{i+1,j}$ etc.). This is remedied by substituting interpolations $\overline{\psi}^{\mu}$. Equation (3.41) yields the four-point stencil

$$\psi_{i,j} \approx \overline{\psi}^{1,2}\Big|_{i,j} = \frac{\psi_{i+1/2,j+1/2} + \psi_{i-1/2,j+1/2} + \psi_{i+1/2,j-1/2} + \psi_{i-1/2,j-1/2}}{4}, \tag{3.44}$$

which is second-order accurate. The ξ^2-direction is treated analogously, which yields a nine-point stencil for 2-D generalised Laplacian in the (ξ^1, ξ^2)-plane (compare to LeVeque, 2007, pp. 64) or the viscous terms $\mathcal{L}^\mu$ of equation (3.32) respectively.

Note that the interpolations affect the order of convergence. According to Morinishi *et al.* (1998), interpolations should be of the same order of accuracy as the differencing scheme. This is fulfilled here but can be difficult when higher-order accurate schemes are used (e.g. Vasilyev, 2000).

One-sided difference approximation for the volume flux boundary condition

Dirichlet conditions are prescribed at the wall which makes them incompatible with the staggered wall-tangential volume fluxes (see the filled and unfilled nodes in figure 3.2). There are different options how to resolve this discrepancy but the simplest and most efficient solution is the *one-sided difference approximation* (LeVeque, 2007, pp. 210). Consider the gradient $\partial_1 q^2$, for example, for which the central-difference approximation of equation (3.40) yields the gradient located at $i = 5/4$, that is, a quarter grid cell from the domain boundary. For simplicity, let us take the gradient at $i = 5/4$ as an approximation for the gradient at the wall ($i = 1$), namely

$$\left.\frac{\partial q^2}{\partial \xi^1}\right|_{1,j} = \frac{q^2_{3/2,j} - q^2_{\mathrm{w},j}}{\Delta\xi^1/2} + O\left(\Delta\xi^1\right), \tag{3.45}$$

where $q^2_{\mathrm{w},j} = q^2_{1,j}$ denotes the volume flux boundary condition prescribed at the wall. The volume fluxes at the wall can be computed for any node at the boundary due to equation (3.36).

Note that staggering resolves the discontinuity of the boundary conditions at the edges of the annulus (see figure 1.3, as well as equations (2.16) and (2.16)) and no additional regularisation has been used in this study. Nevertheless, it might be worth to consider such regularisation in a future investigation to limit the maximum velocity shear and to make the boundary condition independent of the resolution Czarny *et al.* (for instance similar to 2003).

The differencing scheme suffers from a reduction to first-order accuracy in the vicinity of the boundaries. This can be seen by substituting the Taylor expansion (3.39) into equation (3.45). Second-order accuracy, though, can be recovered by an extension of the two-point stencil, which would reduce numerical efficiency given the large number of terms implemented (see equations (3.33)–(3.32)).

It is worth noting that the reduction to first-order accuracy near the wall implies that application of the curl operator can be problematic. Implementing the viscous forces by the double-curl (see equation (2.6)), for example, yields an $O(1)$ error near the wall due to which the solution would become unphysical or even unstable (not shown explicitly here). This has been avoided by implementing the divergence form of the viscous term, equation (3.32), for which Dirichlet boundary conditions pose no problem by working them in similarly to the Laplacian (e.g. LeVeque, 2007). In HYBRID-NEW, the curl operator is only used for the computation of diagnostic quantities, for example, the vorticity (see section 3.3).

Before evaluating the numerical scheme, however, let us complete the spatial discretisation by looking at the treatment of the azimuthal direction.

Spectral derivative for the azimuthal direction

Axisymmetry is exploited in the discretisation by centring all variables along the ξ^3-direction at $k + 1/2$ (see figure 3.2). The azimuthal coordinate has the values

$$\xi^3_{i,j,k+1/2} = \varphi_{i,j,k+1/2} = \frac{2\pi}{N_3}\left(k - \frac{1}{2}\right) \quad \text{for} \quad k \in \{1, 2, \ldots, N_3\} \quad \forall i, j\,. \tag{3.46}$$

Let $\psi(\xi^1, \xi^2, \xi^3, t)$ denote a scalar field or vector component and $\hat{\psi}(\xi^1, \xi^2, \kappa_3, t)$ the corresponding complex amplitude in κ_3-space. The fields ψ and $\hat{\psi}$ are connected by the Fourier transformation (Bronstein *et al.*, 2005, pp. 438–441, 748)

$$\begin{aligned} \psi(\xi^3) = \mathcal{F}_3^{-1}\left(\hat{\psi}\right) &= \sum_{\kappa_3=-\infty}^{+\infty} \hat{\psi}(\kappa_3)\, \exp\left(+\mathrm{i}\kappa_3\xi^3\right) \\ &\approx \sum_{\kappa_3=-N_3/2}^{N_3/2-1} \hat{\psi}(\kappa_3)\, \exp\left(+\mathrm{i}\kappa_3\xi^3\right), \end{aligned} \tag{3.47}$$

and

$$\begin{aligned} \hat{\psi}(\kappa_3) = \mathcal{F}_3(\psi) &= \frac{1}{2\pi}\int_0^{2\pi} \mathrm{d}\xi^3\, \psi(\xi^3)\, \exp\left(-\mathrm{i}\kappa_3\xi^3\right) \\ &\approx \frac{1}{N_3}\sum_{k=1}^{N_3} \psi(\xi^3_{k+1/2})\, \exp\left(-\mathrm{i}\kappa_3\xi^3_{k+1/2}\right). \end{aligned} \tag{3.48}$$

The discretised expressions result from a truncation of the number of Fourier modes, equation (3.47), and the evaluation at the finite set of quadrature points $\xi^3_{k+1/2}$, equation (3.48). The truncation error collects high-wavenumber content and yields exponential convergence when the solution is smooth and sufficiently resolved.

Truncated or not, the *spectral derivative* for first and nth order derivatives along the azimuth reads (compare to Canuto *et al.*, 2006, pp. 52)

$$\partial_3\psi = \mathcal{F}_3^{-1}\left(-\mathrm{i}\kappa_3\hat{\psi}\right), \qquad \partial_3^n\psi = \mathcal{F}_3^{-1}\left(\left[-\mathrm{i}\kappa_3\right]^n\hat{\psi}\right). \tag{3.49}$$

Truncation and periodicity, however, constrain the spectrum of the wavenumbers κ_3. The wavenumbers are equispaced according to

$$0 = 2\pi\kappa_3 \mod 2\pi \qquad \Rightarrow \qquad \Delta\kappa_3 = \Delta k = 1, \tag{3.50}$$

where

$$\kappa_3 = \begin{cases} k-1 & \text{for} \quad 1 \leqslant k \leqslant N_3/2, \\ -(N_3+1-k) & \text{for} \quad N_3/2 < k \leqslant N_3. \end{cases} \tag{3.51}$$

The implementation of equations (3.49) uses external routines which implement Fast Fourier Transformations (FFT). The latest version of HYBRID-NEW links against the FFTW library (Frigo & Johnson, 1997, 2005). An existing alternative is the somewhat slower JMFFT library (Teuler, 1998), which is shipped with the source code to aid portability.

De-aliasing

The Navier–Stokes equations possess a quadratic non-linearity that leads to a mixing of wave numbers, which would quickly lead to non-linear instability if aliasing is would be left unconsidered.

Let us start with the ξ^μ-space that has been discretised according to equations (3.37) and, thus, yields wave numbers κ_3 by applying equation (3.51), which works out analogous for the

components denoted by $\mu = 1, 2$ in the transformed space. For equispaced grid boxes the Nyquist (critical) wave numbers read

$$\kappa_{\mathrm{c},\mu} = \frac{1}{2\Delta\xi^\mu} \propto \frac{N_\mu}{2}. \tag{3.52}$$

The *sampling theorem* (see Press *et al.*, 1992, pp. 494–498) renders aliasing a modulo operation

$$\kappa^*_\mu = \Big([\tilde{\kappa}_\mu + \kappa_{\mathrm{c},\mu}] \mod 2\kappa_{\mathrm{c},\mu} \Big) - \kappa_{\mathrm{c},\mu}, \tag{3.53}$$

which means any wave number $|\tilde{\kappa}_\mu| > \kappa_{\mathrm{c},\mu}$ is projected back into the interval $(-\kappa_{\mathrm{c},\mu}, \kappa_{\mathrm{c},\mu})$ and finds an alias κ^*_μ there.

First, let us look at the *periodic azimuthal direction* ξ^3, for which aliasing is most problematic. The Nyquist wave number reads $\kappa_{\mathrm{c},3} = N_3/2$. Orszag (1971) realised that an additional truncation by 2/3 can be used to remove the aliasing error completely. For ψ, χ scalar fields and $\hat{\psi}$, $\hat{\chi}$ their complex amplitudes 2/3-truncation yields (integer division implied)

$$\psi(\xi^3)\chi(\xi^3) = \sum_{\kappa_3,\kappa'_3=-N_3/3}^{N_3/3-1} \hat{\psi}(\kappa_3)\hat{\chi}(\kappa'_3) \exp\Big(\mathrm{i}\left[\kappa_3 + \kappa'_3\right]\xi^3\Big), \tag{3.54}$$

in which the mixed wave numbers $\kappa_3 + \kappa'_3$ exceed the 2/3-truncated interval. However, all aliased wave numbers $(\kappa_3 + \kappa'_3)^*$ lie outside the truncation since

$$-\frac{2N_3}{3} \leqslant (\kappa_3 + \kappa'_3) < \frac{2N_3}{3} - 2 \qquad \Rightarrow \qquad \frac{N_3}{3} \leqslant \Big|(\kappa_3 + \kappa'_3)^*\Big| \leqslant \frac{N_3}{2}. \tag{3.55}$$

All the aliased wave numbers according to equation (3.55) can be removed by setting $\hat{\psi}, \hat{\chi} = 0$ for $|\kappa_3| \geqslant N_3/3$ before transforming back into ξ^3-space. This is known as 2/3-*rule*. The corresponding filter is a window in κ_3-space (dotted vertical line in figure 3.3). The 2/3-rule is the default in the HYBRID-NEW solver and is implemented with an FFT. The wavenumber truncation is performed before and after the evaluation of the non-linear terms.

As alternative, the *grid shift method* can be used in HYBRID-NEW. Grid shifting has been suggested by Orszag & Patterson, Jr. (1972), but requires explicit time-stepping to be used for the non-linear term (see also Canuto *et al.*, 2006; Rogallo, 1981, and section 3.4). In a nutshell: aliased wave numbers receive a randomised phase error so that the aliasing-error vanishes in a temporal average. Grid shifting has been known as more efficient than the 2/3-rule when there are multiple periodic directions and/or when no implicitly-padded FFT algorithms are available (e.g. Roberts & Bowman, 2011).

For the present study, the grid shift has been used only in a few instances without notable difference in the results and even the run time of the model has been comparable in the cases studied. The reason is due to the treatment of the azimuthal direction only, which requires several 1-D FFTs, which can be computed efficiently with little memory overhead.

For the *wall-bounded directions* ξ^1 and ξ^2 aliasing turns out to be lesser a problem. The following discussion applies similarly to both directions and we can limit our attention to the ξ^1-direction to aid clarity. The Fourier transformations given by equations (3.47) and (3.48) are applied to ξ^1 and yield the wave number κ_1 in the transformed space, which is limited by the corresponding Nyquist wave number $\kappa_{\mathrm{c},1} = \pi/\Delta\xi^1$. In the discretised momentum equation (3.30), interpolations of the volume flux components, for example q^1, are required,

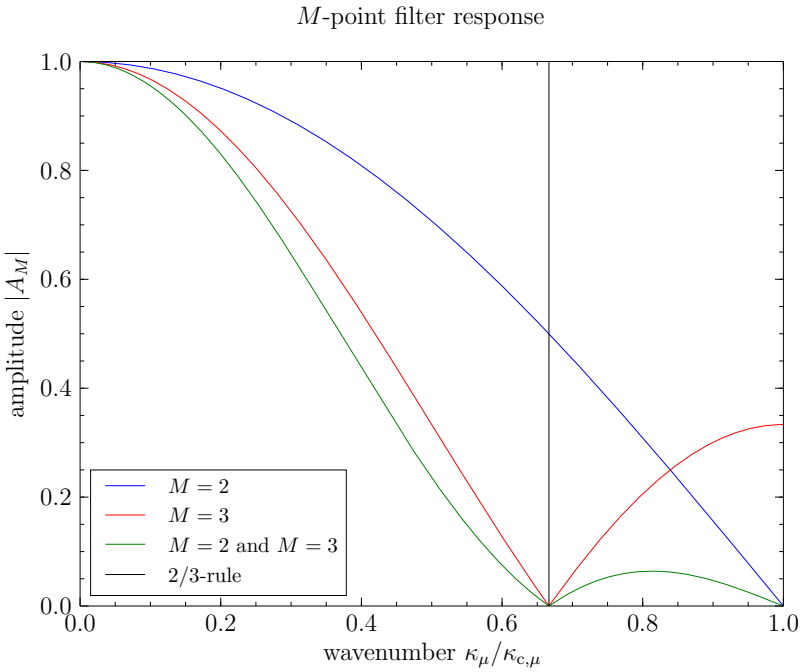

Figure 3.3: Comparison of different de-aliasing filters used in HYBRID-NEW assuming an equidistant grid for the generalised coordinate ξ^μ ($\mu = 1, 2, 3$). The Nyquist critical wave number is denoted $\kappa_{c,\mu}$. The 2/3-rule (dotted vertical line) is used for the periodic azimuthal direction ξ^3. Filtering along wall-bounded directions ξ^1 and ξ^2 is due to two-point interpolations ($M = 2$, solid line) and performed implicitly by interpolations in the discretised momentum advection term. An explicit three-point average ($M = 3$, dashed line) is optional in HYBRID-NEW. Combination of the two-point interpolations and three-point average ($M = 2$ and $M = 3$, dash-dotted line) yields 2/3-like behaviour and removes aliased wave numbers efficiently. The additional three-point average has *not* been used for the present study (reasons are discussed in the text).

that is, $\overline{q^1}^1\big|_{i+1/2}$. The volume flux q^1 is located at cell face centres at integer index i (see figure 3.2). Hence, the Fourier transformation of the interpolated volume flux component yields

$$\mathcal{F}_1\left(\overline{q^1}^1\big|_{i+1/2}\right) = \hat{q}^1(\kappa_1)\, A_2(\kappa_1)\,, \tag{3.56}$$

in which $A_2(\kappa_1)$ is the (real-valued) filter response function of the two-point average.

Equation (3.56) exhibits an amplitude error for $A_2(\kappa_1) \neq 1$, where the interpolation is the reason for a modification of the complex amplitudes $\hat{q}^1(\kappa_1)$. An extension of the two-point average to M-point averages ($M \geqslant 2$) is straightforward. By the aid of a few trigonometric identities (e.g. Bronstein *et al.*, 2005, pp. 80–82) one obtains

$$\begin{aligned} A_M(\kappa_1) &= \frac{1}{M}\sum_m \exp\left(\mathrm{i}m\kappa_1\Delta\xi^1\right) \qquad \text{with} \quad m = -\frac{M}{2}, -\frac{M}{2}+1, \ldots, \frac{M}{2} \\ &= \frac{1}{M}\frac{\sin\left(M\frac{\pi}{2}\kappa_1/\kappa_{\mathrm{c},1}\right)}{\sin\left(\frac{\pi}{2}\kappa_1/\kappa_{\mathrm{c},1}\right)}. \end{aligned} \tag{3.57}$$

Figure 3.3 shows different filter response functions $A_M(\kappa_\mu)$ for $M = 2, 3$ (solid and dashed lines) in comparison to a mixed filter (dash-dotted line) and the 2/3-truncation (dotted line), which has been discussed above. The component index μ in figure 3.3 may take any of the values $\mu = 1, 2, 3$. All interpolations have $A_M \leqslant 1$ due to the smoothing action, which tends to stabilise the solution by an additional (spurious numerical) damping. The filter response functions have roots at $\kappa_{\mu,m} = \pm 2\kappa_{\mathrm{c},\mu} m/M$ ($m = 2, 3, \ldots$), which implies that the corresponding wave numbers are removed from the spectrum entirely. This can be exploited in the construction of a '2/3-like' filter that removes aliased wave numbers by combining a two-point and a three-point average. The corresponding filter response function is denoted $A_{2,3}(\kappa_\mu) = A_3(\kappa_\mu)\, A_2(\kappa_\mu)$ and shown in figure 3.3 by a dash-dotted line.

The two-point interpolations are implied in the discretised momentum equation, which means one only needs to perform an additional three-point moving average in order to replace the 2/3-rule (which requires Fourier transformations) to remove aliased wave numbers in an equispaced grid. Curvature and grid stretching are hidden in the coordinate transformations, but both imply an uneven sampling of the solution with respect to the Cartesian or cylindrical basis. Following the arguments put forward by Press *et al.* (1992, pp. 569–572), uneven sampling removes misinterpretation of the phase and aliasing is effectively suppressed and the Nyquist wave number $\kappa_{\mathrm{c},\mu}$ (see equation (3.52)) with respect to the generalised basis is no longer a strict limit.

For the annular confinement shown in figure 1.3, the numerical grids used exhibit stretching towards the wall so that aliasing is largely removed in the wall-bounded directions. However, stretching is weak so that aliasing is not removed completely. The corresponding amplitudes can be damped to the accuracy limit by using sufficiently high resolutions, which means the physically relevant wave numbers need to fulfil $|\kappa_\mu| \ll \kappa_{\mathrm{c},\mu}$. The latter ensures that the amplitude error is small and that the κ_μ-space is large enough to damp down high wave numbers before aliasing spoils the solution. Damping is, on the one hand, due to the action of viscosity, but it is sped up, on the other hand, for the high wave numbers by numerical damping of the interpolation filters (compare to figure 3.3).

3.3 Accuracy of the spatial discretisation scheme and the limit of DNS

We have already discussed the coordinate transformations, the transformed equations of motion and the spatial discretisation. The aim of this section is to evaluate the numerical accuracy of HYBRID-NEW for the grids used to simulate the flow in the annulus (see figure 1.3) and to estimate threshold values of the dimensionless parameters for which direct numerical simulations (DNS) are still possible. First, we look at the numerical grids themselves by defining and comparing various measures for the grid quality. Second, we move on to the discrete transformation matrices and discuss the effects of the grid quality. Third, the accuracy of the implementation in HYBRID-NEW is tested briefly for the newly-added curl operator by looking into the vorticity. Because of axisymmetry the attention is restricted to a radial-axial section (r, z), or the generalised coordinates ξ^1 and ξ^2 respectively. At last, the Ekman and Rossby numbers accessible by DNS are discussed for the numerical resolutions feasible with the current implementation of HYBRID-NEW on the available computing machinery.

Grid stretching, grid quality, and numerical accuracy in the annulus

We consider a radial-axial section of the annulus in figure 1.3. The coordinate lines $\xi^1(r, z)$ and $\xi^2(r, z)$ are approximated by a list of tuples $(r_{i,j}, z_{i,j})$. The tuples specify the coordinates of the grid cell corners.

Smoothing and grid stretching. The flow in the annulus will be excited by wall motions. Even without knowing any details of the solution yet, it seems reasonable to refine the grid locally at the wall since we expect strong shear there; either due to wall libration (oscillation) or when a bulk flow is brought to rest over a non-librating wall. The grid generator shipped with HYBRID-NEW uses tanh-stretching for local grid refinement (e.g. Thompson *et al.*, 1985; Vinokur, 1980, 1983). The grid remains fixed throughout a simulation and is not adaptively refined.

Let us look into the tanh-stretching by considering only a 1-D problem first, which consists of the generalised coordinate $\xi \in [0, 1]$ and the vertical coordinate $z \in [0, h]$. The vertical coordinate is subject to symmetric stretching so that grid points cluster near the top and bottom. Only a single stretching parameter is needed and denoted $s \in (0, 1)$, where $s \to 0$ means no stretching and $s \to 1$ strong stretching. For practical reasons, the auxiliary stretching parameter reads

$$s' := \frac{1}{2} \ln\left(\frac{1+s}{1-s}\right). \tag{3.58}$$

Hence, the grid points z_i $(i = 1, 2, \ldots)$ are obtained from the equispaced vertices $\xi_i = i\Delta\xi$ by computing

$$z_i = \frac{h}{2} \frac{1 + \tanh\left(s'\left[\xi_i - 1/2\right]\right)}{\tanh\left(s'/2\right)}. \tag{3.59}$$

The stretching functions in a 2-D grid are similar to equation (3.59) but instead of h, the arc length for each of the coordinate lines is required. I have fixed the stretching parameters for the axial and radial direction of the annular grid at $s_1 = 0.99$ and $s_2 = 0.96$ due to the aspect ratio of the annulus (see figure 3.4). Here, s_1 denotes stretching in axial direction or, more precisely, of the coordinate lines ξ^1 ($j = \text{const.}$), whereas s_2 addresses the stretching in radial direction, that is, coordinate lines ξ^2 ($i = \text{const.}$). For the construction of various grids,

the number of grid boxes, N_1 and N_2, has been optimised such that grid cells near the corners and in the centre of the radial-axial section have aspect ratios close to unity, $\Delta r/\Delta z \approx 1$, as can be seen in figure 3.4.

A side-effect of grid stretching is that the grid points in the (r, z)-plane cluster at the wall when N_1 and N_2 is increased and the solution is resolved disproportionally better. This can potentially compensate a reduction of the convergence order exhibited by the usage of the one-sided difference approximation at the wall (see equation (3.45)).

Stretching does not destroy local orthogonality in a straight annulus or cylinder but the frustum does. The dual basis, however, has to be locally orthogonal, which means the coordinate lines corresponding to fixed i and j have to be perpendicular. Smoothing of the frustum wall is required in order to meet this constraint near the lids. Slope transitions of height $\Delta z = 0.2$ have been added to the frustum near the lids. (For details of the slope transitions and the frustum shape function are given in appendix A.2.)

Figure 3.4 shows the standard grid, which exhibits stretching in wall-normal directions and slope transitions as can be seen by the close-ups in figures 3.4(b, c). The coordinates of the corners A–D remained fixed compared to a fully linear frustum shape so that the inclination α of the frustum with respect to the vertical (see figure 1.3) has increased from $\alpha_{\text{lin}} = 5.71°$ to $\alpha_{\text{max}} = 5.93°$ in figure 3.4(a).

The slightly larger slope of the frustum implies a modification of the geometry by $O\left(10^{-3}\right)$ and is part of the discretisation error. We can considered it lesser a problem here, because the simulation of inertial waves and wave attractors is intended. Let us recall from section 2.4 that inertial waves reflect by preserving the angle to the rotation axis. Due to the structural stability of low-order wave attractors, we expect only a slight shift of their frequency 'windows' (see the bifurcation diagram in figure 2.9).

Grid quality. Various grid have been constructed in that way for different resolutions (N_1, N_2). We can now proceed with an assessment of the *grid quality*. Starting from the standard grid (see figure 3.4) with $N_1 \times N_2 = 640 \times 192$ the resolution has been increased and reduced and different measures of the grid quality have been computed.

Table 3.2 collects the measures of grid quality regarded as important. We shall discuss them briefly in the following.

The first two columns of table 3.2 give the minimum and the maximum inscribed cell-circle diameters, d_{min} and d_{max} respectively. It is not surprising that the values reduce with increasing values of N_1 and N_2. However, the in-cell diameters are saturate when the aspect ratios of grid cells are not close to unity in the corners and the centre of the radial-axial section. No convergence is observed even if N_1 or N_2 are increased as can be seen in table 3.2. Nevertheless, the maximal and minimal in-cell diameters are valuable measures. Their difference, for example, is an indicator for the non-uniformity of the grid cells. The in-cell diameters themselves are important for estimating the Courant number of the temporal integration scheme (the Courant number will be discussed in section 3.4).

The third column in table 3.2 gives the maximum norm of

$$\Delta\beta_{i,j} = \beta_{i,j} - 90°, \tag{3.60}$$

which denotes the deviation of the intersecting angle $\beta_{i,j}$ from 90°. The intersecting angle is measured between the grid lines j = const. and i = const., which intersect at the node $(r_{i,j}, z_{i,j})$. The intersecting angle is computed for interior nodes only from linear interpolations between the neighbouring nodes with indices $i \pm 1$ (for j = const.) and $j \pm 1$ (for i = const.).

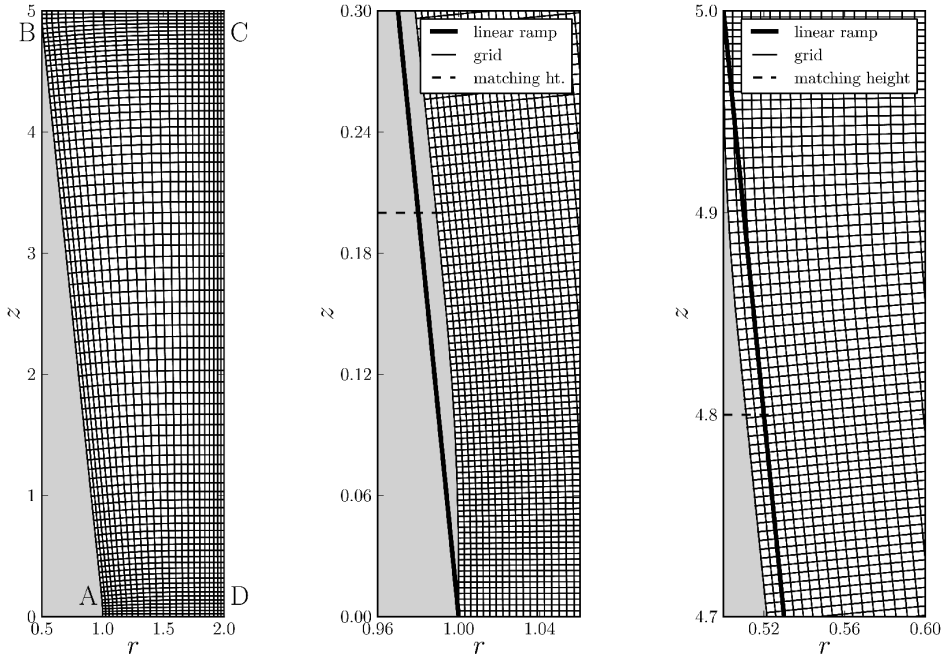

(a) Whole domain (b) Close-up at A (c) Close-up at B

Figure 3.4: The standard grid in an radial-axial section used for simulating the flow in the annular confinement with a resolution of $N_z \times N_r = N_1 \times N_2 = 640 \times 192$ grid boxes and stretching parameters $s_1 = 0.99$ and $s_2 = 0.96$. The trapezoid ABCD follows the definition of figure 1.3. To aid visibility, only every eighth grid line is shown in (a). Panels (b) and (c) zoom the corners A and B respectively by showing every grid line. Polynomial slope transitions of height $\Delta z = 0.2$ replace the part below or above the matching height. The central part of the frustum wall $\overline{\mathrm{AB}}$ is linear (see the text and appendix A.2 for details). (From M. Klein *et al.* (2014). 'Inertial wave excitation and focusing in a liquid bounded by a frustum and a cylinder'. *J. Fluid Mech.*, **751**, p. 263, figure 3, reproduced with permission. Numbers have changed because a different reference length is used here.)

The deviation $\Delta\beta_{i,j}$ is a measure for the discrete non-orthogonality exhibited by the grid. It can serve as an estimate for the error exhibited by the transformation matrices and, thus, the violation of conservation properties due to non-orthogonality in the discrete sense. Interestingly, $|\Delta\beta_{i,j}|_{\max}$ remains of the same order of magnitude ($\sim 0.01°$) for all grids in table 3.2, which can hint at a shortcoming of the measure.

Evaluation of local orthogonality by $\Delta\beta_{i,j}$ might overestimate the numerical error by to not taking into account the scheme used for the computation of the transformation matrices. This is remedied by evaluating numerically the geometric conservation law (Thompson *et al.*,

1985, p. 104) with the same scheme the transformation matrices are computed. The geometric conservation law in axisymmetric configurations reads (see Kaltenbach *et al.*, 2014)

$$0 = \frac{\partial}{\partial \xi^1}\left(\tilde{c}_3^{1/2}\tilde{c}_2^{1/2}\right) - \frac{\partial}{\partial \xi^2}\left(\tilde{c}_3^{1/2}\tilde{c}_1^{1/2}\right) = \frac{\partial}{\partial \xi^1}\left(r\frac{\partial r}{\partial \xi^2}\right) - \frac{\partial}{\partial \xi^2}\left(r\frac{\partial r}{\partial \xi^1}\right), \tag{3.61}$$

$$0 = -\frac{\partial}{\partial \xi^1}\left(\tilde{c}_3^{1/2}c_2^3\right) + \frac{\partial}{\partial \xi^2}\left(\tilde{c}_3^{1/2}c_1^3\right) - \frac{J}{\tilde{c}_3^{1/2}} = -\frac{\partial}{\partial \xi^1}\left(r\frac{\partial z}{\partial \xi^2}\right) + \frac{\partial}{\partial \xi^2}\left(r\frac{\partial z}{\partial \xi^1}\right) - \frac{J}{r}. \tag{3.62}$$

The latter two equations are computed in the solver HYBRID-NEW during initialisation together with the transformation matrix elements using a central-difference approximation. The geometric conservation law is computed at different locations of the staggered grid as the transformation matrices: cell corners (i, j), cell centres $(i + 1/2, j + 1/2)$, but also the cell faces $(i, j + 1/2)$ and $(i + 1/2, j)$. The last four columns of table 3.2 give the maximum norms of $|\Delta_{\mathrm{GC}}|^{\mathrm{c}}$ and $|\Delta_{\mathrm{GC}}|^{\mathrm{m}}$ due to evaluation of equation (3.61) and (3.62) at cell corners and cell centres ('m' for mass points) respectively. Interpolations are required when the geometric conservation law is evaluated at the cell corners, but not when it evaluated at cell centres (remember that the grid is provided by a list of cell corner nodes). This is clearly visible in table 3.2 when comparing the magnitude of the discrete non-orthogonality error in the last two column pairs, that is, 10^{-4} *versus* 10^{-12}.

The non-orthogonality error saturates for the cell centre positions at $O\left(10^{-11}\right)$, which is the accuracy of the algebraic grid generator. By contrast, the non-orthogonality is five orders of magnitude larger at the cell corners. The reason is a linear interpolation in the curvilinear grid, for example $r_{i+1/2,j} \approx \left(r_{i,j} + r_{i+1,j}\right)/2$, which dominates the non-orthogonality and is comparable to the residual of the intersecting angle $\Delta\beta_{i,j}$. The non-orthogonality error for the cell faces is also governed by the interpolations in the curvilinear grid and the corresponding order of magnitude of the error is comparable to $|\Delta_{\mathrm{GC}}|^{\mathrm{c}} \lesssim 10^{-4}$ (not shown explicitly here).

Remarks on the magnitude of the discretisation error. Let us close the discussion of the grid quality with a few remarks on accuracy. Discretisation of equations (3.61) and (3.62) is performed with the same differencing scheme that has been used for the computation of the transformation matrices. This circumstance suggests that the transformation matrices possess discrete non-orthogonality errors, which are of similar order as the residual of the geometrical conservation law. The error is negligible $\left(\sim 10^{-11}\right)$ only for the matrix components computed at cell centres but much larger $\left(\sim 10^{-4}\right)$ for those at cell corners and cell faces. This is the case for any of the grids listed in table 3.2. Mapping of a non-zero initial condition in terms of Cartesian or cylindrical velocity components to staggered volume fluxes (see equations (3.25)) introduces an $O\left(10^{-4}\right)$ error. This is avoided by starting from a homogeneous initial condition or by performing model restarts from the staggered volume fluxes directly. Interpolations of the volume fluxes do not suffer from this kind of interpolation error so that the continuity equation (3.29) can be computed accurately at all times.

Cartesian or cylindrical velocity components can be obtained from the volume fluxes with minimal error after an interpolated of the volume fluxes so that equations (3.26) are evaluated at cell centres only. By contrast, the discretised momentum equation (3.30) requires the transformation matrices at different positions, which prevents the non-orthogonality error to be lower than $O\left(10^{-4}\right)$. Hence, we cannot expect the numerical errors more than 10^4 times smaller than the forcing.

Table 3.2: Different measures of the grid quality computed for axisymmetric grids in the radial-axial section at various resolutions. N_1 denotes the number of grid boxes in axial direction, N_2 those in radial direction. The minimum (maximum) inscribed cell-circle diameter is denoted $d_{\min}$ ($d_{\max}$). Violation of local orthogonality is measured (i) by the maximum deviation $|\Delta\beta|_{\max}$ from an intersecting angle of 90°, and (ii) by the maximum residuals $|\Delta_{\mathrm{GC}}|^{\mathrm{c}}_{\max}$, $|\Delta_{\mathrm{GC}}|^{\mathrm{m}}_{\max}$ of the geometric conservation law evaluated at grid cell corners ('c') and centres ('m') respectively. The standard grid of figure 3.4 is marked with an asterisk (∗).

	N_1	N_2	$d_{\min}$ $\times 10^{-2}$	$d_{\max}$ $\times 10^{-2}$	$\lvert\Delta\beta\rvert_{\max}$ $\times 10^{-2}$ [°]	$\lvert\Delta_{\mathrm{GC}}\rvert^{\mathrm{c}}_{\max}$ $\times 10^{-4}$		$\lvert\Delta_{\mathrm{GC}}\rvert^{\mathrm{m}}_{\max}$ $\times 10^{-12}$	
	512	64	0.335	1.490	9.55	5.93	12.8	0.464	1.03
	512	128	0.335	1.491	4.69	1.48	3.26	0.453	1.04
	512	192	0.298	1.155	3.08	0.650	1.47	0.465	1.10
	640	128	0.268	1.192	4.74	1.48	3.25	0.576	1.29
∗	640	192	0.268	1.155	3.13	0.653	1.46	0.579	1.36
	640	256	0.223	0.867	2.32	0.365	0.83	0.576	1.37
	768	128	0.223	0.993	4.77	1.48	3.25	0.671	1.55
	768	192	0.223	0.993	3.16	0.656	1.46	0.715	1.61
	768	256	0.223	0.867	2.35	0.367	0.83	0.700	1.71

It is worth to note that the central-difference scheme used to compute the transformation matrices could be modified such that the non-orthogonality error is reduced at cell corners and cell faces. The error level might be reduced, but the convergence order of the central-difference scheme remains the same.

Validation of the convergence order exemplified for the vorticity

The error level due to grid quality (i.e. local orthogonality) and the convergence order of the differencing scheme have been discussed above and in the preceding section 3.2. A thorough check of the implementation has been performed by Choi (1993) for the 2-D generalised coordinates in planar geometry. Kaltenbach and colleagues have checked the conservation and convergence properties also for the axisymmetric geometry (Will, 2011, personal communication). Similar analyses are beyond the scope of this work and not strictly necessary since the dynamical core has only been extended by the Coriolis force (see section 3.1). HYBRID-NEW did neither contain an implementation of the curl operator nor of the vorticity when I started working with it in 2011. In rotating flow, however, vorticity and related variables such has helicity or enstrophy are valuable diagnostic quantities that are, in particular, of interest for the study of inertial waves (compare to section 2.3). Therefore, an important contribution to the solver has been the implementation of the generalised curl operator, which we discuss briefly in the following for the vorticity.

The coordinate-independent form of the vorticity reads $\boldsymbol{\zeta} \equiv \boldsymbol{\nabla} \times \boldsymbol{v}$. In order to obtain vorticity and, hence, an expression for the curl operator in generalised coordinates one has to

take into account the change of the basis (e.g. Kuttler, 2011). Evaluating the cross product in Cartesian coordinates and an application of the chain rule yields (see Klein, 2014a)

$$\zeta^\lambda \boldsymbol{a}_\lambda = \boldsymbol{\nabla} \times \left(u_\nu \boldsymbol{a}^\nu\right) = \boldsymbol{a}_\lambda \varepsilon_{lmn} \frac{\partial \xi^\lambda}{\partial x^l} \frac{\partial \xi^\mu}{\partial x^m} \frac{\partial \xi^\nu}{\partial x^n} \left(\frac{\partial u_\nu}{\partial \xi^\mu} - u_\kappa \Gamma^\kappa_{\nu\mu}\right), \tag{3.63}$$

where ε_{lmn} denotes (the Cartesian components of) the Levi-Civita tensor (e.g. Bronstein *et al.*, 2005, p. 273), and $\Gamma^\kappa_{\mu\nu}$ denotes the Christoffel symbols of the second kind (e.g. Kuttler, 2011). For an orthogonal dual basis, the Christoffel symbols of the second kind are given by

$$\Gamma^\kappa_{\nu\mu} := \boldsymbol{a}^\kappa \cdot \frac{\partial \boldsymbol{a}_\mu}{\partial \xi^\nu} = -\boldsymbol{a}_\mu \cdot \frac{\partial \boldsymbol{a}^\kappa}{\partial \xi^\nu}, \tag{3.64}$$

and they are symmetric with respect to the lower indices $\left(\Gamma^\kappa_{\mu\nu} = \Gamma^\kappa_{\nu\mu}\right)$, which is a consequence of commutating second derivatives and the geometric conservation law (Thompson *et al.*, 1985, p. 104). (This can be proven by expressing $\boldsymbol{a}^\mu$ and $\boldsymbol{a}_\nu$ in terms of the transformation matrices (c^n_ν) and $(\gamma^\mu{}_m)$ given in equation (3.6) and (3.8).) We proceed with a simplification of equation (3.63).

First, we introduce the generalised Levi-Civita tensor

$$\epsilon^{\lambda\mu\nu} := \frac{1}{J} \varepsilon^{\lambda\mu\nu} = \varepsilon_{lmn} \frac{\partial \xi^\lambda}{\partial x^l} \frac{\partial \xi^\mu}{\partial x^m} \frac{\partial \xi^\nu}{\partial x^n}, \tag{3.65}$$

which results from an application of determinant properties. Here, $\varepsilon^{\lambda\mu\nu}$ is just the usual Levi-Civita tensor but with compliant, contravariant indices. Both $\varepsilon^{\lambda\mu\nu}$ and $\epsilon^{\lambda\mu\nu}$ are antisymmetric in all indices.

Second, the generalised Levi-Civita tensor is substituted into the contravariant vorticity given by equation (3.63). Symmetry of the Christoffel symbols of the second kind with respect to the lower indices and antisymmetry of the generalised Levi-Civita tensor yield (e.g. Klein, 2014a; Kuttler, 2011)

$$\zeta^\lambda = \epsilon^{\lambda\mu\nu} \frac{\partial u_\nu}{\partial \xi^\mu}, \tag{3.66}$$

which has the same structure as the Cartesian representation of the curl operator, but with carefully positioned indices and the Jacobian included in the generalised Levi-Civita tensor. That is, by equation (3.66) one computes contravariant vorticity components ζ^λ from covariant velocity components u_ν. Since only contravariant volume fluxes $q^\mu = Ju^\mu$ are available in the numerical solver, lowering of the velocity or the volume flux index is required. Equation (3.66) may be applied in the same way to any other vector variable, which means equation (3.66) yields the curl operator with respect to generalised coordinates (in short, the contravariant or generalised curl operator).

An implementation of the generalised curl operator is a straightforward task using the discretisation outlined in section 3.2. For the analysis of the rotational part, here the vorticity, one is typically interested in the Cartesian or cylindrical projections rather than the generalised components ζ^λ themselves.

Here we are primarily concerned with an axisymmetric configuration (i.e. the annulus of figure 1.3) so that we can limit our attention to the computation of the cylindrical projections $(\zeta_r, \zeta_\varphi, \zeta_z)$ from the volume fluxes q^μ. Three operations are necessary to succeed: (i) mapping of contravariant velocities u^μ into volume fluxes q^μ, (ii) lowering of the volume flux index, and

(iii) a projection of the vorticity vector on the cylindrical basis $\{\boldsymbol{e}_r, \boldsymbol{e}_\varphi, \boldsymbol{e}_z\}$. Carrying out these operations yields (cf. Klein, 2014a)

$$\left.\begin{aligned}
\zeta_r &= + \frac{\tilde{c}_3^{1/2}}{J}\left[\frac{\partial}{\partial\xi^2}\left(\frac{g_{33}q^3}{J}\right) - \frac{\partial}{\partial\xi^3}\left(\frac{g_{21}q^1 + g_{22}q^2}{J}\right)\right] \\
&\quad - \frac{\tilde{c}_2^{1/2}}{J}\left[\frac{\partial}{\partial\xi^1}\left(\frac{g_{33}q^3}{J}\right) - \frac{\partial}{\partial\xi^3}\left(\frac{g_{11}q^1 + g_{12}q^2}{J}\right)\right], \\
\zeta_\varphi &= \frac{\tilde{c}_3^{1/2}}{J}\left[\frac{\partial}{\partial\xi^1}\left(\frac{g_{21}q^1 + g_{22}q^2}{J}\right) - \frac{\tilde{c}_3^{1/2}}{J}\frac{\partial}{\partial\xi^2}\left(\frac{g_{11}q^1 + g_{12}q^2}{J}\right)\right], \\
\zeta_z &= + \frac{c_1^3}{J}\left[\frac{\partial}{\partial\xi^2}\left(\frac{g_{33}q^3}{J}\right) - \frac{\partial}{\partial\xi^3}\left(\frac{g_{21}q^1 + g_{22}q^2}{J}\right)\right] \\
&\quad - \frac{c_2^3}{J}\left[\frac{\partial}{\partial\xi^1}\left(\frac{g_{33}q^3}{J}\right) - \frac{\partial}{\partial\xi^3}\left(\frac{g_{11}q^1 + g_{12}q^2}{J}\right)\right].
\end{aligned}\right\} \tag{3.67}$$

Note that it is due to the generalised curl (equation (3.66)) that the covariant metric components $g_{\mu\nu}$ are needed in equation (3.67). These, however, have the side effect that the computation of the vorticity reduces the efficiency of the numerical solver by demanding the computation or storage of the metric ($g_{\mu\nu}$) in addition to the Jacobi matrix (c_μ^m) and the scaled metric ($\Lambda^{\mu\nu}$). However, equations (3.67) are the only ones allowing a consistent discretisation and implementation of the generalised curl operator. This is not limited to the computation of the vorticity, wherefore it is relevant for future investigations extending the scope, for example, to magnetohydrodynamics (MHD).

Note further that simplifications are possible for the problem at hand, i.e. for the cylindrical vorticity components to be computed from volume flux components. One can make use of commutating second derivatives in equations (3.67) after an expansion of the metric components into Jacobi matrix elements. Details of the procedure are not of concern here and have been given in detail in Klein (2014a).

Equations (3.67) are implemented using the central-difference approximation outlined earlier. The vorticity is a purely diagnostic variable in the HYBRID-NEW solver and it suffices to compute it only at the cell centre positions (see figure 3.2). It was noted in the discussion of the one-sided difference approximation that the discrete curl suffers from a reduction to first-order accuracy, which means the vorticity error can reach $O(1)$ at the wall. This is remedied in the implementation by computing the vorticity values of the outermost grid cell layer by a straight-forward linear extrapolation from the nearest interior nodes. The single crucial assumption is that the flow is well-resolved near the wall. The approach was proven to be robust and first order accurate at the boundaries using the test cases of rigid body rotation, Poiseuille flow, as well as some libration-induced flows (the boundary layer flows discussed in more detail in section 5.2).

For the rest of this section, let us look into the rigid body rotation test case to assure ourselves of the correctness of the discretised equations (3.67). Some of the grids given in table 3.2 are used, which are all similar to the one shown in figure 3.4. Curvature due to the frustum wall and tanh-stretching at the boundary render this test non-trivial already.

Let us assume the fluid in a state of rigid body super-rotation and revolving around the symmetry axis. For simplicity, let the velocity profile be given by $\boldsymbol{v}_{\mathrm{rb}} = \boldsymbol{e}_z \times \boldsymbol{r}$, which is

prescribed as initial condition and mapped to the volume fluxes q^μ. The corresponding vorticity is $\boldsymbol{\zeta}_{\mathrm{rb}} = 2\boldsymbol{e}_z$ and serves as reference.

The vorticity components are computed numerically from the discretised equations (3.67), which is sensitive to the gradients and interpolations in the directions of ξ^1 and ξ^2 for the terms containing q^3 since only $q^3 \neq 0$.

Figure 3.5 shows the absolute errors $|\Delta\zeta_z| = |\zeta_2 - 2|$ and $|\Delta\zeta_r| = |\zeta_r|$ plotted against the number of grid boxes N_2 in radial direction (compare to figure 3.4). Two error norms are shown: the cell volume-weighted average L^1 and the maximum norm L^∞, given by

$$L^1(\psi) = \frac{1}{V}\,\Delta\xi^1\,\Delta\xi^2\,\Delta\xi^3 \sum_{i,j,k} J_{i+1/2,j+1/2}\;\psi_{i+1/2,j+1/2,k+1/2}, \tag{3.68}$$

$$L^\infty(\psi) = \max_{i,j,k}\;\psi_{i+1/2,j+1/2,k+1/2}, \tag{3.69}$$

with V the domain volume, $\Delta\xi^\mu$ the cell dimensions in the transformed space, and ψ a place holder for the error of a vorticity component.

We expect second-order accuracy in the interior, where the errors $|\Delta\zeta_z|$ and $|\Delta\zeta_r|$ should be proportional to $\left(\Delta\xi^2\right)^2 \propto N_2^{-2}$. This is clearly exhibited by the L^1 norm shown in figure 3.5(a). By contrast, L^∞ shown in figure 3.5(b) puts the emphasize on the values near the boundary and exhibits a degeneration to first-order accuracy, with the error proportional to $L^\infty \propto \Delta\xi^2 \propto N_2^{-1}$. The reduction is expected on the basis of the one-sided difference approximation used in the discretisation (see section 3.2). However, first-order accuracy is a bit surprising here since uniformity of the vorticity, $\boldsymbol{\zeta}_{\mathrm{rb}} = 2\boldsymbol{e}_z$, suggests that the extrapolations in the vorticity implementation remove the first-order errors at the outermost grid cell layer. What we see is, in fact, the error of the linear extrapolation due to the tanh-stretching of the grid (see equation (3.59) and figure 3.4). The linear extrapolation is not able to capture the non-linear grid refinement properly. In generic cases, however, the extrapolation approach was found to ensure a convergence of the vorticity and the viscous term in rotational form ($-E\boldsymbol{\nabla}\times[\boldsymbol{\nabla}\times\boldsymbol{v}]$) by avoiding a degeneration of the errors to $O(1)$ at the boundaries.

At last, it is worth to note that the vorticity component ζ_φ remained identically zero and has not been addressed by the current rigid body rotation test case. This can be remedied by a tilt of the axis of rotation against the symmetry axis of the confinement, but has not been done here. Instead, Hagen–Poiseuille flow (e.g. Landau & Lifshitz, 1987, pp. 51–53) has been investigated in a similar way and reveals that the ζ_φ-implementation converges as well (not shown here).

Ekman and Rossby numbers accessible by DNS

The standard grid (see figure 3.4) has a resolution in the radial-axial section of $N_z \times N_r = N_1 \times N_2 = 640 \times 192$ grid cells. Measures of the minimum and maximum grid cell dimensions are given in table 3.2 by the minimum and maximum inscribed cell-circle diameters $d_{\min}$ and $d_{\max}$. On the basis of these quantities we can proceed and check for the accessible parameters by looking into the viscous boundary layer and the free stream solution. The free stream solution is either considered laminar containing internal shear layers (propagating inertial waves), or considered turbulent.

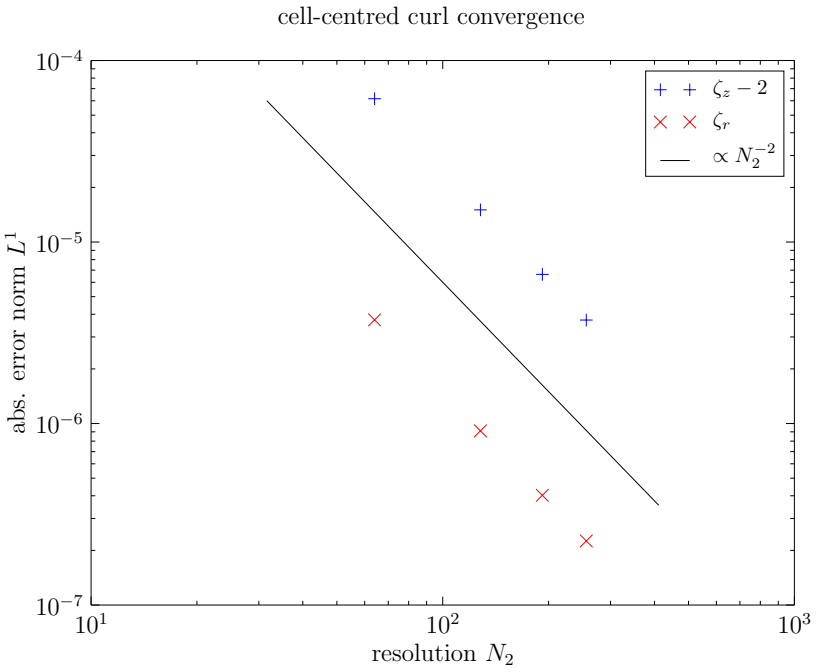

(a)

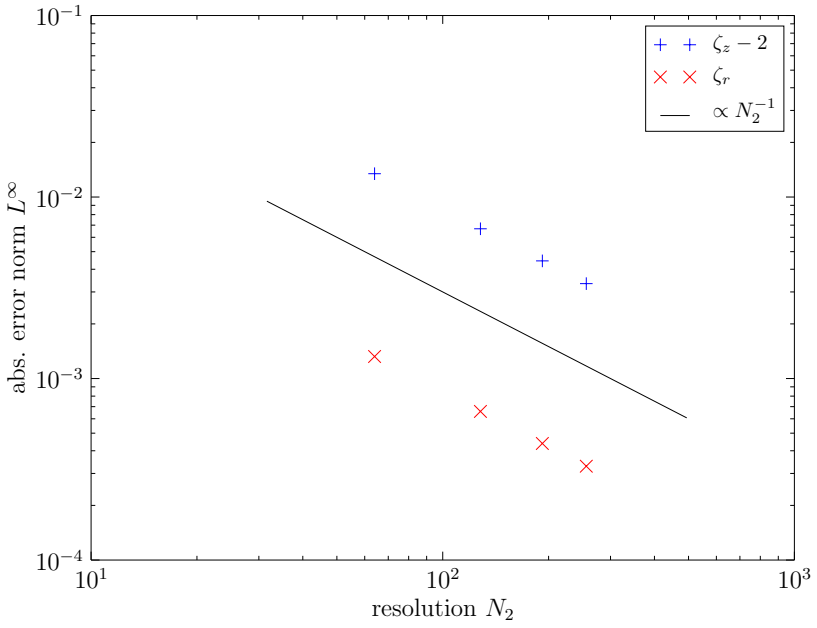

(b)

Figure 3.5: Convergence of the radial and axial vorticity components for prescribed rigid body super-rotation. In HYBRID-NEW, the curl is computed at grid cell centres and the outermost values are obtained by an extrapolation from the interior. Correctness of the implementation is exemplified for the cylindrical vorticity components ζ_r and ζ_z in the case of a prescribed rigid body super-rotation in the annular confinement with an inner frustum. The reference vorticity components are $\zeta_{\mathrm{rb},z} = 2$ and $\zeta_{\mathrm{rb},r} = 0$. The grids used are similar to the one in figure 3.4.

Estimation I: oscillating boundary layer. The viscous boundary layer over a librating wall can be approximated by an oscillatory (Stokes) boundary layer for which the thickness δ_S reads (Batchelor, 1967, p. 354)

$$\delta_S \propto E^{1/2}\omega^{-1/2}. \tag{3.70}$$

The libration frequency lies in the inertial wave band, which means $\omega \sim 1$ can be used to compute an estimate for the lowest accessible Ekman number. (The same result is obtained by looking at the Ekman layer; e.g. Greenspan, 1969, p. 32.) Ekman numbers for geophysical problems are of the order $E \lesssim 10^{-12}$ (e.g. Noir *et al.*, 2009), for which equation (3.70) yields a boundary layer thickness of the order $\delta_S \sim 10^{-6}$ and smaller. The boundary layer in Earth's liquid outer core, for example, is only a few meters thick while the radius of the core radius is of the order ~ 1000 km.

Coming back to the annular confinement of figure 1.3, a minimum grid cell diameter of the order 10^{-6} is required, which yields numerical resolutions to the order $N_r \times N_z \sim 10^5 \times 10^5 = 10^{10}$ (for stretched grids) or even higher, which is far beyond what can be realised. Table 3.2 yields the minimum inscribed cell-circle diameter of the order $d_{\min} \sim 10^{-3}$ and resolutions $N_r \times N_z \lesssim 200 \times 1000 = 2 \times 10^5$. Hence, $\delta_S \gtrsim d_{\min}$ yields a minimum Ekman number of the order $E \sim 10^{-6}$. Following the argumentation of Rieutord *et al.* (2001); Rieutord & Valdettaro (1997), an Ekman number as large as 10^{-6} suggests that only the simulated wave attractors of lowest order will correspond to the wave attractors found by ray tracing. (A discussion of the maximum value of the Ekman number that still yields wave attractor solutions will be done in section 4.5.)

Estimation II: oscillating internal shear layers. Kerswell (1995) investigated the scaling properties of oscillatory internal shear layers or propagating inertial waves. For $E \ll 1$, the width of the thinnest shear layer scales like

$$\delta_K \propto E^{1/3} \qquad \text{for} \quad E^{1/3} \ll 1. \tag{3.71}$$

The numerical grids used in this work have a maximum inscribed cell-circle diameter of the order $d_{\max} \sim 10^{-2}$ reached in the centre of the flow domain (see table 3.2). Requiring that $\delta_K \gtrsim d_{\max}$ also yields a minimum Ekman number of the order $E \sim 10^{-6}$. This is consistent with the previous estimate and permits the usage of stretched grids.

Estimation III: Kolmogorov micro-scale in the case of turbulent flow. Let us assume that the free stream solution is strongly turbulent such that the strain induced by non-linear advection dominates over Coriolis force. In this scenario, we may assume presence of a turbulent cascade according to Kolmogorov (1941). We can make use of Kolmogorov's theory to obtain an estimate for the upper limit of the Reynolds number *Re* defined in equation (2.9). The turbulent cascade implies power input at large scale is dissipated only at the Kolmogorov micro-scale. The latter is given by

$$\eta := \left(\frac{\nu^3}{\bar{\epsilon}}\right)^{1/4}, \tag{3.72}$$

where ν denotes the fluid's kinematic viscosity and $\bar{\epsilon}$ is the specific time-mean energy dissipation rate for stationary statistics, where the bar $\overline{(\cdot)}$ denotes a temporal average.

Dissipation has been addressed briefly in section 2.1 but without quantification, hence, the task at hand is to estimate $\bar{\epsilon}$ for the librating annulus. Following, for example, Batchelor (1967,

pp. 151–153), one obtains the (dimensional) dissipation function Φ of an incompressible flow as

$$\Phi = 2\nu\,(\boldsymbol{\tau}\cdot\cdot\,\boldsymbol{\tau}) \qquad \text{with} \quad \boldsymbol{\tau} = \frac{1}{2}(\boldsymbol{\nabla}\circ\boldsymbol{v}) + \frac{1}{2}(\boldsymbol{\nabla}\circ\boldsymbol{v})^{\mathrm{T}}, \tag{3.73}$$

which denotes the (dimensional) rate of strain tensor. The dissipation function Φ measures the local energy dissipation per time intervall and unit mass. By the aid of Φ, the specific energy dissipation rate follows from the spatial average

$$\bar{\epsilon} = \frac{1}{V}\int_V \bar{\Phi}\,\mathrm{d}V, \tag{3.74}$$

where V denotes the whole volume of the annular confinement. At this point additional assumptions are necessary.

A simplified scenario consists in a straight annulus of infinite height that is bounded by two concentric cylinders. Libration of the inner cylinder yields rotation rates of $\Omega_2 = \Omega_0$ and, for example, $\Omega_1 = \Omega_0\,(1+\varepsilon)$ at the peak prograde libration phase $\omega t = \pi/2$ (see equation (1.2)). In the limit of very small libration frequencies, let us approximate the large scale solution a circular Couette flow, which given by azimuthal velocity profile (in the non-rotating frame of reference; see Landau & Lifshitz, 1987, p. 60)

$$v_\varphi^{\mathrm{C}}(r) = \Omega_0 r + \varepsilon\Omega_0 \left(\frac{r_2^2}{r_1^2} - 1\right)^{-1} \left(\frac{r_2^2}{r} - r\right). \tag{3.75}$$

In our simple scenario, the velocity shear in equation (3.75) provides the power input to the turbulent cascade. We proceed by computing the rate of strain tensor and the dissipation function according to equation (3.73) for the circular Couette flow. The rate of strain tensor is symmetric which implies that rotary motions in the form of rigid body rotation ($v_\varphi \propto r$) do not contribute to the energy dissipation. In cylindrical coordinates, only $\tau_{r\varphi}$ and $\tau_{\varphi r}$ are non-zero, that is,

$$\tau_{r\varphi} = \tau_{\varphi r} = \frac{1}{2}\Big[\frac{1}{r}\underbrace{\frac{\partial v_r}{\partial\varphi}}_{0} + r\frac{\partial}{\partial r}\left(\frac{v_\varphi}{r}\right)\Big] = -\frac{\varepsilon\Omega_0}{r^2}\frac{r_1^2 r_2^2}{r_2^2 - r_1^2}. \tag{3.76}$$

Substituting $\Phi = 4\nu\tau_{r\varphi}^2$ in equation (3.74), we obtain an estimate for the specific dissipation rate

$$\bar{\epsilon} = \frac{8\nu}{r_2^2 - r_1^2}\int_{r_1}^{r_2} \tau_{r\varphi}^2\, r\,\mathrm{d}r = 4\nu\varepsilon^2\Omega_0^2 \frac{r_2^2 r_1^2}{\left(r_2^2 - r_1^2\right)^2}, \tag{3.77}$$

which yields the Kolmogorov micro-scale as

$$\eta = \sqrt{\frac{\nu}{\varepsilon\Omega_0}}\sqrt{\frac{r_2^2 - r_1^2}{2r_1 r_2}}. \tag{3.78}$$

The second square root in equation (3.78) is a geometry factor which is of $O(1)$ for radius ratios in the interval $0.02 < r_1/r_2 < 0.8$. The annular confinement with an inner frustum (see figure 1.3) has radius ratios $0.25 < r_1/r_2 < 0.5$ so that the geometry factor can be neglected

for an estimation of the power input in the case of a Couette-like solution. Thus, we arrive at the *dimensionless* estimate for the Kolmogorov micro-scale

$$\eta^* = \frac{\eta}{L} \approx Re^{-1/2} = E^{1/2} R^{-1/2}. \tag{3.79}$$

Equation (3.79) provides the basis for comparison to the two situations discussed above, where we aim to estimate the resolution requirements to resolve turbulent flow for reasonable Rossby and Ekman numbers. Presence of a turbulent cascade means that inertial forces are larger than the Coriolis force. At the very least, the order of magnitude of non-linear advection and Coriolis force should be comparable, that is, a Rossby number $R \sim 1$. We can insert the minimum Ekman number $E \sim 10^{-6}$ from the previous estimations, which yields a dimensionless Kolmogorov micro-scale of $\eta^* \sim 10^{-3}$ that must not be smaller than the grid spacing. The latter is fulfilled for the grids listed in table 3.2 at least for the minimum inscribed cell-circle diameters since $\eta^* \sim d_{\min} \sim 10^{-3}$.

In conclusion, the numerical grids used in this study resolve all turbulence scales, but the resolutions are at the edge of DNS. However, turbulence DNS is not a crucial point here since we are primarily interested in the study of inertial waves and wave attractors with the flow generally stable. Nevertheless, a collapse of the stable flow to turbulence can be captured by the resolutions proposed. From previous studies, the critical Rossby number is known to depend on Ekman number and the libration frequency (e.g. Sauret *et al.*, 2012), from which we estimate that the flow in the librating annulus is stable for $R \lesssim 10^{-1}$ for $E \gtrsim 10^{-6}$ and $\omega \sim 1$. Hence, based on the Couette flow estimate there is an additional order of magnitude the Rossby number can be increased to. The argumentation applies also to the azimuthal direction. Typically about 128–256 grid boxes are needed for an acceptable representation of the statistics when the flow is turbulent (for a detailed analysis see Ghasemi V., 2016). At best, the Rossby number (libration amplitude) is so small that the flow remains axisymmetric and only 2-D simulations need to be performed. Speaking of numerical simulations, we still lack the details of the time integration scheme used in HYBRID-NEW, which is the subject of the next section.

3.4 Semi-implicit time integration and the fractional-step method

HYBRID-NEW uses a semi-implicit time advancement composed of the Crank–Nicolson and a Runge–Kutta scheme. The current implementation differs a bit from those described in the classical references, which makes it worth to collect the details of the approach used for the present study.

In the following, we begin with the temporal discretisation and leads us to the fractional-step method, which is the standard tool to simulate incompressible flows. After that, we continue with an outline of the semi-implicit scheme and how it is combined with the fractional-step method. The section is closed by a discussion of the time step and the Courant number for inertial waves in the annular confinement and the flow induced by libration.

Temporal discretisation and the fractional-step method

The fractional-step method is the standard tool for a temporal integration of the incompressible Navier–Stokes equations. It was first proposed by Chorin (1968), but several variants of the original scheme have been developed over the past decades. A review of the most common variants has been given Brown *et al.* (2001), which still is up-to-date. The fractional-step

method aims to guarantee incompressibility of the velocity field ($\boldsymbol{\nabla}\cdot\boldsymbol{v}=0$) for all times by keeping the acceleration field solenoidal, that is, $\boldsymbol{\nabla}\cdot(\partial_t\boldsymbol{v})=0$. Knowledge of the solenoidal accelerations allows to approximate the velocity field at time $t=t^{n+1}$ from the previous state at $t=t^n$. (The upper Latin index n denotes the discrete time levels; spatial indices are suppressed.)

The fractional-step method used in HYBRID-NEW is based on the scheme of Kim & Moin (1985), which employs the 'pressure-free' acceleration field $\boldsymbol{A}(\boldsymbol{v})$ as auxiliary variable. In analogy to the central-difference approximation for the partial derivatives in space also the time rate of change should be centred. The momentum equation (2.6) is evaluated at intermediate time levels $n+1/2$, which yields

$$\left(\partial_t\boldsymbol{v}+\boldsymbol{\nabla}\phi\right)\big|^{n+1/2}=\boldsymbol{A}\left(\boldsymbol{v}\right)\big|^{n+1/2} \tag{3.80}$$

in the form of Kim & Moin (1985).

The central-difference approximation analogue to equation (3.40) yields

$$\partial_t\boldsymbol{v}\big|^{n+1/2}=\frac{\boldsymbol{v}^{n+1}-\boldsymbol{v}^n}{\Delta t}+O\big(\,[\Delta t]^2\,\big), \tag{3.81}$$

which is substituted into equation (3.80). Dropping the higher-order terms yields the update equation

$$\boldsymbol{v}^{n+1}+\Delta t\boldsymbol{\nabla}\phi^{n+1/2}=\boldsymbol{v}^n+\Delta t\boldsymbol{A}\left(\boldsymbol{v}\right)\big|^{n+1/2}, \tag{3.82}$$

in which the unknown or 'new' values of the dynamical variables are located on the left hand side.

Temporal staggering yields the velocity vector $\boldsymbol{v}$ at integer time levels t^n, but the scalar excess pressure ϕ at intermediate ones $t^{n+1/2}$. The pressure-free accelerations $\boldsymbol{A}(\boldsymbol{v})$ need to be projected on a solenoidal state. This is realised by a Helmholtz–Hodge decomposition (compare to the discussion of the excess pressure in section 2.1), which requires the solution to the Poisson equation

$$\nabla^2\phi^{n+1/2}=\boldsymbol{\nabla}\cdot\boldsymbol{A}\left(\boldsymbol{v}\right)\big|^{n+1/2}. \tag{3.83}$$

Obviously, the sources for the excess pressure ϕ are due to the divergence of the pressure-free accelerations $\boldsymbol{A}(\boldsymbol{v})$. The question of how the Poisson equation (3.83) is solved numerically is decoupled from the time integration scheme and addressed separately in section 3.5).

In summary, the *fractional-step* is formed by solving equation (3.83) in order to obtain the new excess pressure $\phi^{n+1/2}$, which is then substituted into equation (3.82) in order to obtain the updated velocity field $\boldsymbol{v}^{n+1}$. Hence, the time integration scheme results from an alternating solution to equations (3.82) and (3.83). The evolution of $\boldsymbol{v}(\boldsymbol{r},t)$ and $\phi(\boldsymbol{r},t)$ is approximated by time-stepping through the sequences $(\boldsymbol{v}^0,\boldsymbol{v}^1,\ldots,\boldsymbol{v}^n,\ldots)$ and $\left(\phi^{1/2},\phi^{3/2},\ldots,\phi^{n+1/2},\ldots\right)$ respectively. Only the gradient $\boldsymbol{\nabla}\phi$ is needed in the equations of motion, which allows to re-define the excess pressure by an arbitrary scalar function $\phi_0(t)$. This can be exploited in the numerical implementation, in which $\phi_0(t)$ remains unknown so that the pressure time series cannot be interpreted. (A discussion of the reasons why is beyond the scope of this section and we will come back to this aspect in section 3.5.)

Note that the fractional-step applies straightforwardly also to the volume fluxes $\boldsymbol{q}=q^\mu\boldsymbol{a}_\mu$. We are asked to consider equations (3.29) and (3.30) instead of equations (2.6) and (2.7). In addition, the accelerations $\boldsymbol{A}(\boldsymbol{v})$ are formally replaced by $\mathcal{A}(\boldsymbol{q})$.

For the completion of the time integration scheme, though, the question remains how to obtain a proper estimate of the pressure-free accelerations $\boldsymbol{A}(\boldsymbol{v})$ or $\mathcal{A}(\boldsymbol{q})$ at the future time level $n+1/2$? This will be addressed in the following.

Semi-implicit time advancement by a mixed Crank–Nicolson / Runge–Kutta algorithm

The fractional-step method ensures solenoidality and, thus, conservation of mass for the numerical solution to the Navier–Stokes equations. The missing ingredient to the fractional-step method is how to approximate the pressure-free accelerations $\boldsymbol{A}(\boldsymbol{v})$ at the future time level $n+1/2$. Looking into the momentum equation (2.6) tells us that we need to find a way to estimate it from the velocities $\boldsymbol{v}^n$ and the excess pressure $\phi^{n-1/2}$. In HYBRID-NEW, a semi-implicit scheme is used for this purpose to address numerical accuracy and computational efficiency. The semi-implicit scheme treats the various forces of the momentum equation differently, either explicitly or implicitly. On the one hand, the action of Coriolis force, momentum advection terms, viscous cross and the azimuthal derivative terms, but also the Dirichlet boundary conditions are explicitly integrated to the future time level $n+1/2$ by a third-order Runge–Kutta scheme (RK3). On the other hand, uni-directional viscous terms in wall-normal directions are treated implicitly by Crank–Nicolson scheme (CN2) to resolve viscous time-step limitations in the locally refined grids. In the following, we will first discuss the CN2 scheme and then the RK3 scheme.

The *Crank–Nicolson scheme* (CN2) implemented at present differs from the one used originally. When HYBRID-NEW was developed, all uni-directional viscous terms were treated implicitly (which required factoring; see Choi, 1993; Choi *et al.*, 1993). For the diffuser flow studies, though, only the wall-normal ξ^2-direction has been treated implicitly (no more factoring; see Kaltenbach & Hauschild, 2004). In the annular confinement, an intermediate approach is used by treating implicitly the uni-directional viscous terms in the wall-bounded directions ξ^1 and ξ^2 (see Kaltenbach *et al.*, 2014). The latest version of HYBRID-NEW supports both implicit and explicit treatment of uni-directional viscous terms in ξ^1-direction, which is selected in dependence on the boundary conditions specified.

For the present study only the scheme with an implicit treatment of the uni-directional viscous terms in ξ^1- and ξ^2-direction has been used. The momentum equation (3.30) allows to split the pressure-free accelerations into

$$\mathcal{A}(\boldsymbol{q}) = -\mathcal{N}(\boldsymbol{q}) - \mathcal{C}(\boldsymbol{q}) + \mathcal{L}_1(\boldsymbol{q}) + \mathcal{L}_2(\boldsymbol{q}) + \mathcal{L}'(\boldsymbol{q}), \tag{3.84}$$

where we have used vector notation to avoid confusion with component indices. The linear operators $\mathcal{L}_1$ and $\mathcal{L}_2$ represent the viscous uni-directional derivatives $\partial_1\left[E\Lambda^{11}\partial_1(\cdot)\right]$ and $\partial_2\left[E\Lambda^{22}\partial_2(\cdot)\right]$ respectively. Correspondingly, $\mathcal{L}'$ denotes the remaining viscous cross and azimuthal derivative terms, $-\mathcal{N}(\boldsymbol{q})$ is non-linear in $\boldsymbol{q}$ and collects the momentum advection terms, $-\mathcal{C}(\boldsymbol{q})$ is linear in $\boldsymbol{q}$ and denotes the Coriolis force. We may interpret the calligraphic symbols also as operator matrices due to the spatial discretisation, which means $\boldsymbol{q}$ denotes the

'big' column vector of all the volume fluxes. With $\mathcal{G}(\phi)$ denoting the discrete excess pressure gradient, equation (3.80) takes the form

$$\frac{\boldsymbol{q}^{n+1}-\boldsymbol{q}^{n}}{\Delta t} = -\mathcal{G}(\phi^{n+1/2}) + \big[\,-\mathcal{N}(\boldsymbol{q}) - \mathcal{C}(\boldsymbol{q}) + \mathcal{L}'(\boldsymbol{q})\,\big]\Big|_{\text{expl.}}^{n+1/2} + \underbrace{\frac{1}{2}\big[\mathcal{L}_1\left(\boldsymbol{q}^{n+1}\right) + \mathcal{L}_1(\boldsymbol{q}^{n})\,\big] + \frac{1}{2}\big[\mathcal{L}_2\left(\boldsymbol{q}^{n+1}\right) + \mathcal{L}_2(\boldsymbol{q}^{n})\,\big]}_{\text{CN2}}. \quad (3.85)$$

A rearrangement of equation (3.85) yields the update equation

$$\left[\mathbf{1} - \frac{\Delta t}{2}\mathcal{L}_1 - \frac{\Delta t}{2}\mathcal{L}_2\right]\boldsymbol{q}^{n+1} + \Delta t\mathcal{G}(\phi^{n+1/2}) = \left[\mathbf{1} + \frac{\Delta t}{2}\mathcal{L}_1 + \frac{\Delta t}{2}\mathcal{L}_2\right]\boldsymbol{q}^{n} + \Delta t\big[\,-\mathcal{N}(\boldsymbol{q}) - \mathcal{C}(\boldsymbol{q}) + \mathcal{L}'(\boldsymbol{q})\,\big]\Big|_{\text{expl.}}^{n+1/2}, \quad (3.86)$$

where $\mathbf{1}$ is the identity operator having the matrix representation $\mathbf{1} = \operatorname{diag}(1, 1, \ldots, 1)$. Forces at time level $n + 1/2$ are unknown but will be approximated explicitly from $\boldsymbol{q}^n$.

The Crank–Nicolson treatment complicates the numerical solution since it requires an operator inversion. At this point we diverge a bit from the scheme of Kim & Moin (1985) and adopt the pressure-correction approach of van Kan (1986). This means that ϕ approximates the excess pressure and does not represent the pseudo-pressure of Kim & Moin (1985). Linearity of the viscous operators can be exploited such that the left-hand side operator inversion is performed for volume flux update $\Delta\boldsymbol{q} = \boldsymbol{q}^{n+1} - \boldsymbol{q}^{n}$. The volume flux update $\Delta\boldsymbol{q}$ is *approximately* solenoidal by an incorporation of the previous pressure gradient $\mathcal{G}(\phi^{n-1/2})$. With aid of equation (3.86) one has the update algorithm

$$\left[\mathbf{1} - \frac{\Delta t}{2}\mathcal{L}_1 - \frac{\Delta t}{2}\mathcal{L}_2\right]\Delta\boldsymbol{q} = [\mathbf{1} + \Delta t\mathcal{L}_1 + \Delta t\mathcal{L}_2]\boldsymbol{q}^{n} - \Delta t\mathcal{G}(\phi^{n-1/2}) + \Delta t\big[\,-\mathcal{N}(\boldsymbol{q}) - \mathcal{C}(\boldsymbol{q}) + \mathcal{L}'(\boldsymbol{q})\,\big]\Big|_{\text{expl.}}^{n+1/2}, \quad (3.87)$$

$$\boldsymbol{q}' = \boldsymbol{q}^{n} + \Delta\boldsymbol{q} + \Delta t\mathcal{G}(\phi^{n-1/2}), \quad (3.88)$$

$$\boldsymbol{q}^{n+1} = \boldsymbol{q}' - \Delta t\mathcal{G}(\phi^{n+1/2}), \quad (3.89)$$

which uses two time levels of the pressure gradient and the auxiliary volume flux $\boldsymbol{q}'$ that corresponds to the 'intermediate velocity boundary condition' in the scheme of Kim & Moin (1985).

Note that equations (3.87)–(3.89) show that the volume fluxes are second-order accurate since

$$\mathcal{G}(\phi^{n+1/2}) - \mathcal{G}(\phi^{n-1/2}) = O(\Delta t). \quad (3.90)$$

An inversion of the sparse matrix on the left hand side of equation (3.87) is a costly numerical operation. The uni-directional operators $\mathcal{L}_1$ and $\mathcal{L}_2$, however, possess three-point stencils for which the individual operator matrices can be brought in tridiagonal form when the one-sided

difference approximation is used (see section 3.2). This is already exploited in HYBRID-NEW to increase computational efficiency by a *factorisation* of the left hand side operator, namely

$$\left[\mathbf{1} - \frac{\Delta t}{2}\mathcal{L}_1\right]\left[\mathbf{1} - \frac{\Delta t}{2}\mathcal{L}_2\right] = \left[\mathbf{1} - \frac{\Delta t}{2}\mathcal{L}_1 - \frac{\Delta t}{2}\mathcal{L}_2\right] + O\left([\Delta t]^2\right). \tag{3.91}$$

The factors $[\mathbf{1} - (\Delta t/2)\mathcal{L}_1]$ and $[\mathbf{1} - (\Delta t/2)\mathcal{L}_2]$ in equation (3.91) are diagonally dominant for small time steps $\Delta t \ll 1$. This means that the inversions are numerically stable and can be done efficiently with standard algorithms for tridiagonal matrices like the Thomas algorithm (see Press *et al.*, 1992, 1996). Matrix factorisation, however, comes at the expense of limiting the accuracy of the time integration scheme to second-order as indicated by $O\left([\Delta t]^2\right)$ in equation (3.91). This is not a problem here, since the volume fluxes have been second-order accurate only due to the CN2 scheme. The restriction of the order of accuracy due to factoring needs to be kept in mind if an extension to a higher-order accuracy of the time integration scheme is envisioned.

The update scheme given by equations (3.87)–(3.89) is not complete since it lacks the fractional-step, that is, the Poisson equation (3.83). Conceptually, the new excess pressure is computed at the intermediate time levels $n + 1/2$, which means we need to compute it from the intermediate and divergent volume fluxes $\boldsymbol{q}'$. This can be viewed as a correction of the predictor $\boldsymbol{q}'$ so that $\boldsymbol{q}^{n+1}$ is solenoidal. With $\mathcal{D}$ denoting the discrete divergence operator, the Poisson equation of scheme given by equations (3.87)–(3.89) reads

$$\mathcal{D}\mathcal{G}\left(\phi^{n+1/2}\right) = \frac{1}{\Delta t}\mathcal{D}\left(\boldsymbol{q}'\right). \tag{3.92}$$

Scaling of the right hand side of equation (3.92) with $(\Delta t)^{-1}$ shows that the excess pressure is restricted to first-order accuracy (see also Perot, 1993). Due to $\phi^{n+1} = \phi^{n+1/2} + O(\Delta t)$ we might as well interpret ϕ as collocated with $\boldsymbol{q}$ at integer time levels n (as suggested by Kim & Moin, 1985). Temporal staggering, however, shows that the excess pressure is secondary in incompressible flow in the sense that it is a reaction to the velocity or volume flux field specified. This is most prominent with respect to the initial condition ($n = 0$), which shows that only $\boldsymbol{q}^0$ (or $\boldsymbol{v}^0$ for that matter) needs to specified but not ϕ^0. Instead, $\phi^{1/2}$ is computed from $\boldsymbol{q}^0$ and $\phi^{-1/2} \equiv 0$. As discussed by Brown *et al.* (2001), the computation of second-order accurate excess pressure collocated at integer time levels introduces difficulties. Otherwise the pressure should be skipped in the analyses of the numerical solutions.

We have outlined the fractional-step method and the implicit CN2 used for the viscous terms. It remains to look into the explicit third-order *Runge–Kutta scheme* (RK3) for the approximation of the pressure-free accelerations. The RK3 scheme is implemented as low-storage scheme and works on a predictor-corrector basis in three sub-steps. Using the nomenclature of Le &

Moin (1991), an explicit three-step scheme for the governing equations (3.29) and (3.30) can be cast into the form

$$\begin{aligned}\frac{\boldsymbol{q}^m - \boldsymbol{q}^{m-1}}{\Delta t} = &-\zeta_m\Big[\mathcal{N}\left(\boldsymbol{q}^{m-2}\right) + \mathcal{C}\left(\boldsymbol{q}^{m-2}\right) - \mathcal{L}\left(\boldsymbol{q}^{m-2}\right)\Big](1-\delta_{m1}) \\ &- \gamma_m\Big[\mathcal{N}\left(\boldsymbol{q}^{m-1}\right) + \mathcal{C}\left(\boldsymbol{q}^{m-1}\right) - \mathcal{L}\left(\boldsymbol{q}^{m-1}\right)\Big] \\ &+ \alpha_m\Big[\mathcal{L}_1\left(\boldsymbol{q}^{m-1}\right) + \mathcal{L}_2\left(\boldsymbol{q}^{m-1}\right)\Big] + \beta_m\Big[\mathcal{L}_1\left(\boldsymbol{q}^{m}\right) + \mathcal{L}_2\left(\boldsymbol{q}^{m}\right)\Big] \\ &- (\alpha_m + \beta_m)\,\mathcal{G}(\phi^{m-1/2}), \end{aligned} \tag{3.93}$$

$$\mathcal{D}\left(\boldsymbol{q}^m\right) = 0, \tag{3.94}$$

in which $m = 1, 2, 3$ denotes the sub-time index. The sub-time volume flux boundary conditions are $\boldsymbol{q}^m\big|_{m=0} = \boldsymbol{q}^n$ and $\boldsymbol{q}^m\big|_{m=3} = \boldsymbol{q}^{n+1}$. Terms with indices $m-2$ are skipped for $m = 1$ as indicated by the term with the Kronecker symbol δ_{lm} (e.g. Bronstein *et al.*, 2005, p. 261). At present, HYBRID-NEW performs a fractional-step in each sub-step. Slight modifications to the scheme outlined above arise from the integration weights α_m, β_m, γ_m, ζ_m. The time-dependent boundary conditions, for example equation (3.36), are evaluated together with the excess pressure gradient with a sub-time increment $\Delta t^m = (\alpha_m + \beta_m)\,\Delta t$.

The scheme given by equations (3.93) and (3.94) is very similar to those outlined by Le & Moin (1991); Rai & Moin (1991), or Orlandi (2000, pp. 22–23), but the integration weights differ. In fact, the weights are not unique since they only need to fulfil

$$\sum_{m=1}^{3}(\alpha_m + \beta_m) = \sum_{m=1}^{3}(\gamma_m + \zeta_m) = 1. \tag{3.95}$$

For the present study I have used

$$\left.\begin{aligned} &\gamma_1 = \frac{1}{\sqrt{3}}, && \gamma_2 = \frac{1}{2\sqrt{3}}, && \gamma_3 = 1, \\ &\zeta_1 = 0, && \zeta_2 = \frac{1}{2} - \frac{1}{\sqrt{3}}, && \zeta_3 = -\frac{1}{2} - \frac{1}{2\sqrt{3}}, \\ &&& \alpha_m = \beta_m = \frac{\gamma_m + \zeta_m}{2}, \end{aligned}\right\} \tag{3.96}$$

as suggested in the source code comments. The reason according to Kaltenbach and colleagues is that the weights given by equations (3.96) yield an improvement of the temporal de-aliasing when the grid shift method is used (see section 3.2). Nevertheless, different sets of weights have been implemented in the past. A brief check (not shown here) led to the conclusion that none of the sets of weights is superior to another with respect to the libration-induced flow in the annulus of figure 1.3. On the one hand, this can be attributed to usage of 2/3-rule de-aliasing for the azimuthal direction. On the other hand, the error of the RK3 scheme is of the order $O([\Delta t]^3)$ and most likely overshadowed here by the factoring and pressure correction errors, which are of the order $O([\Delta t]^2)$. Hence, the overall accuracy of the time integration scheme is limited here by the implicit viscous terms.

Stability, Courant number, and time step selection

Both spatial and temporal discretisation strategies implemented in the HYBRID-NEW solver have been discussed. Spatial discretisation uses a grid which provides the details of a specific annular geometry to the solver (see, for example, figure 3.4). The grid cell sizes in three dimensions can be computed once the resolution for the azimuthal direction has been set. Let d denote the minimum inscribed cell-sphere diameter of all the grid boxes (compare to table 3.2, but now account also for the azimuthal direction). We are asked to fix the last remaining parameters, the time step Δt.

Selection of the time step is a matter of numerical stability, accuracy and computational efficiency. Stability limitations are coupled strongly to the spatio-temporal discretisation strategy and addressed by the Courant number C (or CFL number; see Courant *et al.*, 1928). For the numerical scheme to be stable, the speed of the numerical integration, $U_{\mathrm{num}} = C\Delta t/d$, needs to be faster than any physical transport of corresponding velocity U_{tra}. The numerical integration speed depends on the time step Δt, the grid spacing d, and the Courant number C. In a rotating incompressible fluid, U_{tra} is the maximum of the advective transport ($R\boldsymbol{v}$), the phase and group velocities of inertial waves ($\boldsymbol{c}_{\mathrm{p}}$, $\boldsymbol{c}_{\mathrm{g}}$ due to the action of the Coriolis force) and the diffusive viscous transport (which dominates in the boundary layer). The Rossby number R occurs in front of the advection velocity because the governing equations (2.6) and (2.7) are with respect to the co-rotating frame of reference and have been scaled.

Diffusive limitations arise typically near the boundaries when wall-normal viscous terms become large. The wall-normal viscous terms are treated implicitly by the CN2 scheme, which is stable for any Δt. Hence, only the inertial terms need to be of concern with respect to stability since they are treated explicitly by the RK3 scheme. We demand that

$$\frac{U_{\mathrm{tra}}\Delta t}{d} \leqslant C \qquad \text{with} \quad U_{\mathrm{tra}} = \max\left(R|\boldsymbol{v}|,\ |\boldsymbol{c}_{\mathrm{p}}|,\ |\boldsymbol{c}_{\mathrm{g}}|\right) \tag{3.97}$$

is fulfilled throughout the simulation in the whole flow domain.

According to Orlandi (2000, p. 23), the hybrid scheme CN2/RK3 is limited by $C \leqslant \sqrt{3} \approx 1.7$. For fixed discretisation parameters Δt and d, one can either estimate U_{tra} in parallel to the numerical simulation or by *ad hoc* assumptions. Both variants are used but in a slightly different way by computing and monitoring an advective Courant number, C_{adv}, during the simulation, whereas a Courant number of the inertial waves, C_{wave}, is estimated before the simulation.

The wave Courant number C_{wave} is not easily computed from the numerical solution so, instead, an estimate for C_{wave} is used to fix Δt for the simulation. Such an estimation is necessarily specific and requires to take into account the geometry (see figure 1.3), as well as the phase and group velocities of the inertial waves (see section 2.3). For simplicity, consider a plane inertial wave with wave vector $\boldsymbol{k}$ and wavelength $\lambda = 2\pi|\boldsymbol{k}|^{-1}$. A generic wave vector is oblique so that phase and group velocities are of similar order, namely $|\boldsymbol{c}_{\mathrm{p}}| \sim |\boldsymbol{c}_{\mathrm{g}}| \sim 2\lambda$ (compare to equations (2.25)). The fastest wave has maximum wavelength which cannot be larger than the basin scale, that is, $\lambda_{\max} \sim 1$ in accord with the dimensionless grid in figure 3.4. The resolution in azimuthal direction used for the annular confinement is relatively coarse in the sense that the minimum inscribed cell-sphere diameters are limited by the resolution in a radial-axial section. We may therefore take the inscribed cell-circle diameters $d_{\min}$ and $d_{\max}$ (see table 3.2) as measures for the grid cell sizes. Selecting the standard grid (see figure 3.4) and $C_{\mathrm{wave}} = C \approx 1.7$, a pessimistic estimate for the time step lies in the range

$$0.5 \times 10^{-2} \lesssim \Delta t \lesssim 3.5 \times 10^{-2} \qquad \text{with the default at} \quad \Delta t = \frac{2\pi}{400} \approx 1.571 \times 10^{-2}, \tag{3.98}$$

Table 3.3: Advective Courant numbers C_{adv} of 4 representative numerical solutions obtained with HYBRID-NEW for the librating annulus with (i) the frustum in libration, and (ii) the lids plus outer cylinder in libration. The minimum and maximum Courant numbers were computed in the statistically stationary state over one libration period (time span $2\pi/\omega$). The Ekman number was fixed at $E = 3.19 \times 10^{-5}$ (a discussion follows in chapter 4). The standard grid (figure 3.4) was used but the azimuthal resolution N_3 was changed in accord with the Rossby number R depending on whether the flow remained axisymmetric or not.

BC	ω	R	N_3	Δt $\times 10^{-2}$	$C_{\mathrm{adv}}^{\mathrm{min}}$	$C_{\mathrm{adv}}^{\mathrm{max}}$
(i)	0.47	0.2	1	1.571	0.0402	0.243
		0.4	128	1.047	0.0818	0.587
(ii)	1.40	0.2	1	1.571	0.0843	0.300
		0.4	128	1.047	0.1687	0.383

where the default value corresponds to 400 time steps per revolution of the vessel. Similar estimations have been done also for other grids used for this work. For the grids listed in table 3.2, nominal time steps are in the range given by equation (3.98).

Any time step selected in that way is kept fixed throughout a simulation. By construction, the scheme operates close to the theoretical Courant limit of the inertial waves ($C_{\mathrm{wave}} \approx C \approx 1.7$), but this does not mean that it is close to being unstable. That is, the fastest wave has the longest wavelength, but in the annular confinement (see figure 1.3) inertial waves are focused on the wave attractor (see section 2.4). This means spatial compression due to which λ decreases and the waves slow down. Waves in the vicinity of a wave attractor therefore yield much smaller wave Courant numbers than the unfocused wave. Nevertheless, propagation of the basin-scale wavelength needs to be resolved since we do not know yet how waves are excited and if the transient stage exhibits defocusing before the waves are focused on the wave attractor. The estimation is pessimistic in the sense that the value of Δt is rather too small.

Numerical instability can result from the non-linear advection terms in the case of turbulent flow. Monitoring the advective Courant number therefore ensures that the scheme is stable ($C_{\mathrm{adv}} < C$). The advective Courant number is given by the maximum norm

$$\begin{aligned} C_{\mathrm{adv}} &= \max_{i,j,k} \left(R \frac{|\boldsymbol{v}| \Delta t}{d} \bigg|_{i+1/2,j+1/2,k+1/2} \right) \\ &\approx \max_{i,j,k} \left(R \frac{|q^\mu| \, \Delta t}{J \Delta \xi^\mu} \bigg|_{i+1/2,j+1/2,k+1/2} \right), \end{aligned} \tag{3.99}$$

where Einstein's summation convention is implied for the index μ and the indices $i + 1/2$, $j + 1/2$, $k + 1/2$ show that C_{adv} is computed at grid cell centres.

Table 3.3 shows typical values obtained by an evaluation of equation (3.99) for a DNS obtained by typical values of the Rossby number R, Ekman number E and the dimensionless libration frequency ω (the flow at these parameters will be discussed in chapter 4). Numerical results are compared to each other for two different Rossby numbers, and the two configurations (i) frustum in libration and (ii) lids plus outer cylinder in libration. Two different azimuthal resolutions N_3 were used to account for the break of axisymmetry when the flow exhibits developing centrifugal instability, where $N_3 > 1$ means 3-D simulation and $N_3 = 1$ quasi-2-D

axisymmetric simulation. The Courant numbers $C_{\mathrm{adv}}^{\mathrm{min}}$ and $C_{\mathrm{adv}}^{\mathrm{max}}$ denote the minimum and maximum values in the time series $C_{\mathrm{adv}}(t)$ recorded in the statistically stationary state over one libration period with a duration of $2\pi/\omega$.

The main message of table 3.3 is that, for the representative parameters, advection velocities are typically much smaller than the maximum wave speed due to $C_{\mathrm{adv}} \ll C_{\mathrm{wave}} \lesssim 1$. Nevertheless, as both Rossby number and the azimuthal resolution increase it might be that C_{adv} becomes more restrictive than C_{wave} but non-linear instability has not been encountered here. Even a modification of the time step by factors 2–4 did not change the results notably since $C_{\mathrm{adv}} < C \approx 1.7$. This brings us back to the wave Courant number by indicating that the pessimistically estimated time step is indeed sufficiently small.

Note that inaccuracies of the implicit terms are sufficiently small as well. For the standard grid and representative parameters, this is assured by the viscous frictional time scale being of similar order as the pessimistic time step estimate (Ghasemi V., 2013, personal communication).

Note further that an adaptive time step could be used in order to remove the need of estimation but would require to develop an algorithm testing the Courant number of the inertial waves. This problem has not yet been solved in the implementation of HYBRID-NEW. In fact, I am not aware of any such numerical test. It might well be that inertial waves are one of the reason why geophysical flow solvers need to run at very low advective Courant numbers in order to be stable and reasonably accurate. Extending the mathematical model to stratified or compressible fluids means Courant numbers of gravity waves and sound waves need to be considered as well. Both of the latter contribute to the time step limitations of the explicit numerical scheme and complicate the time step selection.

3.5 Numerical solution to the Poisson equation

We have seen in the discussion of the fractional-step method (see section 3.4) that the solution to the Poisson equation arises because of the incompressibility constraint. The Poisson equation (3.83) or (3.92) respectively needs to be solved in order to obtain the new excess pressure $\phi^{n+1/2}$. The excess pressure gradient is then used to perform an irrotational-solenoidal decomposition (Helmholtz–Hodge decomposition; see, for example, Arfken & Weber, 2005, pp. 97) of the intermediate volume fluxes to yield the new volume fluxes $\boldsymbol{q}^{n+1}$.

The Poisson equation is an elliptic PDE, which means it is non-local in the sense that it needs to be solved in the whole domain at once. Different numerical solution methods have been developed encompassing iterative, direct and transform methods (for an overview see Press *et al.*, 1992, ch. 19).

We begin with the transformed Poisson equation, its boundary conditions, and how it has been discretised in the curvilinear framework. After that, we proceed with an overview of the numerical algorithm and a few remarks regarding the implementation.

The transformed Poisson equation

Two different solution methods are available in HYBRID-NEW. The first is a multigrid algorithm that employs successive over-relaxation along the wall-normal ξ^2-coordinates (line-SOR) which dates back to Choi (1993) and is still supported. The second algorithm implements a hybrid approach consisting of a Fourier transformation in azimuthal direction ξ^3 and a direct solution in the (ξ^1, ξ^2)-plane, which is based on the central-differencing scheme. The hybrid solver has been developed by Kaltenbach and colleagues (Kaltenbach & Hauschild, 2004). Surprisingly, test simulations for representative parameters and the standard configuration (see

figure 3.4) showed that the hybrid solver is faster than the multigrid algorithm. We can therefore limit our attention to the hybrid solver.

The Poisson solver operates at a particular time level so that we can drop the superscript from $\phi^{n+1/2}$ to aid readability. The complex amplitude of the excess pressure is due to a Fourier transformation along the azimuth (see equation (3.48)) and denoted $\hat{\phi} = \mathcal{F}_3(\phi)$. By the aid of the Fourier transformation, the 3-D Poisson equation (3.92) is split into $N_3/2$ 2-D Poisson equations for each of the discrete wave numbers κ_3.

Applying the Fourier transformation to the right hand side of equation (3.92) and yields $\widehat{\mathcal{D}}$, the transformed divergence operator, and $\hat{\boldsymbol{q}}'$, the transformed volume fluxes at an intermediate time level. The contravariant components of $\hat{\boldsymbol{q}}'$ are still staggered with respect to the indices i and j (see figure 3.2). An application of the central-difference approximation yields

$$\begin{aligned}\frac{1}{\Delta t}\widehat{\mathcal{D}}\left(\hat{\boldsymbol{q}}'\right)\Big|_{i+1/2,j+1/2} &\\ \approx \frac{1}{\Delta t}\frac{1}{J}\left(\frac{\hat{q}'^{1}_{i+1,j+1/2}-\hat{q}'^{1}_{i,j+1/2}}{\Delta\xi^1}+\frac{\hat{q}'^{2}_{i+1/2,j+1}-\hat{q}'^{2}_{i+1/2,j}}{\Delta\xi^2}-\mathrm{i}\kappa_3\hat{q}'^{3}_{i+1/2,j+1/2}\right)&\\ \text{for}\quad \kappa_3=0,1,\ldots,\frac{N_3}{2}-1,\end{aligned}\tag{3.100}$$

which denotes the sources of $\hat{\phi}(\kappa_3)$ at grid cell centre positions $(i+1/2, j+1/2)$.

The left hand side of equation (3.92) is obtained likewise by an application of $\mathcal{F}_3(\cdot)$, which yields transformed Laplace operator

$$\begin{aligned}\widehat{\mathcal{DG}}(\hat{\phi}) = \frac{1}{J}\Big[\partial_1\Lambda^{11}\partial_1+\partial_2\Lambda^{22}\partial_2+\partial_1\Lambda^{12}\partial_2+\partial_2\Lambda^{21}\partial_1-\kappa_3^2\Lambda^{33}\Big]\hat{\phi}&\\ \text{for}\quad \kappa_3=0,1,\ldots,\frac{N_3}{2}-1\end{aligned}\tag{3.101}$$

The discretisation of $\widehat{\mathcal{DG}}$ is performed with the central-difference approximation for the ξ^1- and ξ^2-direction (see section 3.2). The uni-directional derivatives are obtained from equation (3.42) and the cross-derivative terms from equation (3.43). Both $\hat{\phi}$ and $\widehat{\mathcal{DG}}(\hat{\phi})$ are located at 2-D grid cell centres $(i+1/2, j+1/2)$, which yields the nine-point stencil. The corresponding operator matrix has nine non-zero bands, up to the boundary conditions to be discussed shortly.

Note that contributions at negative wave numbers, $\hat{\phi}(-\kappa_3)$, are obtained by a complex conjugation since the excess pressure ϕ needs to be real-valued (compare to Bronstein *et al.*, 2005, pp. 439–440) Note further that de-aliasing by 2/3-truncation reduces the maximum wave number also for the excess pressure from $N_3/2$ to $N_3/3$.

Boundary conditions

It remains to specify boundary conditions for the direct solver in the non-periodic directions ξ^1 and ξ^2. The volume flux boundary conditions have been given in equation (3.36) from which the excess pressure boundary conditions are to be obtained. Analytically, the momentum equation (3.30) yields Neumann boundary conditions for the excess pressure. Numerically, this works out a bit different.

We have formulated a three-level fractional-step method with the intermediate volume fluxes $\boldsymbol{q}'$, which corresponds precisely to the scheme of Kim & Moin (1985). Staggering of the variables

(see figure 3.2) yields that the excess pressure and the second-order derivatives are located at grid cell centres so that no pressure value is needed on the domain boundary. This implies that the volume flux boundary condition comes into play via the divergence on the right hand side, equation (3.100). The boundary values of the transformed intermediate volume fluxes $\hat{q}'^1$ and $\hat{q}'^2$ receive the transformed but otherwise *unmodified* Dirichlet boundary conditions $\hat{q}^1_\mathrm{w}$ and $\hat{q}^2_\mathrm{w}$, that is,

$$\left.\begin{aligned} \hat{q}'^1_{i,j+1/2} &= \hat{q}^1_{\mathrm{w},i} \qquad \text{for} \quad i = 1, N_1+1, \\ \hat{q}'^2_{i+1/2,j} &= \hat{q}^2_{\mathrm{w},j} \qquad \text{for} \quad j = 1, N_2+1. \end{aligned}\right\} \tag{3.102}$$

The physical interpretation is that the wall velocities prescribed must not be modified by the excess pressure gradient. Consequently, the operator $\widehat{\mathcal{DG}}$ on the left hand side, equation (3.101), must obtain *homogeneous* Neumann boundary conditions

$$\left.\begin{aligned} \left.\frac{\partial\hat{\phi}}{\partial\xi^1}\right|_{i,j+1/2} &= 0 \qquad \text{for} \quad i = 1, N_1+1, \\ \left.\frac{\partial\hat{\phi}}{\partial\xi^2}\right|_{i+1/2,j} &= 0 \qquad \text{for} \quad j = 1, N_2+1. \end{aligned}\right\} \tag{3.103}$$

Note that equations (3.102) and (3.103) always have to be applied together, which is sometimes referred to as 'the Poisson equation contains its own boundary conditions' or 'the Poisson equation does not need boundary conditions' (e.g. Brown *et al.*, 2001). The physical reason has been mentioned, but on the level of the discretised Poisson equation one could also say that the boundary condition has been put on the right hand side so that the discretised Laplacian $\widehat{\mathcal{DG}}$ has a nine-band matrix that acts only on the interior values of $\hat{\phi}_{i+1/2,j+1/2}$. It needs to be stressed at this point that the homogeneous Neumann condition used for implementation does not necessarily mean that the excess pressure approaches a zero gradient at the wall. Replacement of the intermediate volume fluxes at the boundary yields an increased divergence near the walls, which means a large curvature of the excess pressure.

Note further that the Dirichlet condition q^μ_w needs to be compatible with mass conservation (e.g. Gresho & Sani, 1987), which is obviously the case for equations (3.102) and (3.103). Therefore, any change in the intermediate volume flux Dirichlet condition demands a compensating change of the Neumann boundary conditions for the excess pressure. One is free to use other but consistent combinations of excess pressure and intermediate volume flux boundary conditions, but the one outlined above yields the simplest and, therefore, the most accurate and efficient implementation.

Solution method for the transformed Poisson equation

Regularisation of the Poisson problem with Neumann boundary conditions. The operator matrices of $\widehat{\mathcal{DG}}$ corresponding to equation (3.101) are diagonally dominant for all $\kappa_3 \neq 0$ and, hence, non-singular and invertible. This does not apply to operator matrix for $\kappa_3 = 0$, which is singular because of the Neumann conditions. Instead of prescribing Dirichlet conditions along the boundary, let us exploit the gauge freedom $\phi + \phi_0(t)$ by pinning the pressure value at some point $\boldsymbol{r}_\mathrm{pin}$, namely

$$\phi\left(\boldsymbol{r}_\mathrm{pin}, t\right) = 0 \quad \forall t. \tag{3.104}$$

In the operator matrix of $\widehat{\mathcal{DG}}$ for $\kappa_3 = 0$, the row corresponding to the pinning point $\boldsymbol{r}_\mathrm{pin}$ is replaced by a homogeneous Dirichlet boundary condition. The latter is formally identical to

the addition of a Dirac δ-source at $\boldsymbol{r}_{\mathrm{pin}}$ (e.g. Bronstein *et al.*, 2005, p. 740). One obtains for the transformed variables

$$\widehat{\mathcal{DG}}(\hat{\chi}) = -A\delta\left(\xi^1 - \xi^1_{\mathrm{pin}}\right)\delta\left(\xi^2 - \xi^2_{\mathrm{pin}}\right)\delta\left(\kappa_3\right) \qquad \text{with} \quad \hat{\chi} = \hat{\phi} - \hat{\phi}', \tag{3.105}$$

where $\hat{\chi}$ denotes the error caused by the newly-introduced Dirichlet condition, $\hat{\phi}$ denotes the transformed excess pressure computed with the present numerical scheme, and $\hat{\phi}'$ denotes be the correct transformed excess pressure unavailable to us. Equation (3.105) yields $\hat{\chi}$ a Green's function of the operator $\widehat{\mathcal{DG}}$ (e.g. Bronstein *et al.*, 2005, pp. 550–553, 687–692).

The Green's function can be viewed as spurious mode with an amplitude A proportional to the discrete violation of mass conservation at the grid box at the pinning point, that is, $A \propto \mathcal{D}\left(\boldsymbol{q}'\right)$ at $\boldsymbol{r} = \boldsymbol{r}_{\mathrm{pin}}$. In first place, $\hat{\chi} \neq 0$ is not necessarily a problem if one is interested only in the volume flux solution. However, a non-zero gradient, $\mathcal{G}\left(\chi\right) \neq 0$, is problematic since it enters the momentum equation (3.93) and, thus, leads to an erroneous flow solution by affecting the volume flux updates. Unfortunately, $\hat{\chi} \neq 0$ means $A \neq 0$ and, thus, yields $\mathcal{G}\left(\chi\right) \neq 0$.

The strategy for error reduction consists in a minimisation of the sources in the vicinity of the pinning point, which means a local minimisation of the divergence of the intermediate volume fluxes. That is,

$$\widehat{\mathcal{DG}}(\hat{\chi}) \to 0, \qquad \hat{\chi} \to 0 \qquad \text{for} \quad \mathcal{D}\left(\boldsymbol{q}'\right)\big|_{\boldsymbol{r}=\boldsymbol{r}_{\mathrm{pin}}} \to 0. \tag{3.106}$$

Note that pinning should be done next to a (non-librating) wall or next to an edge of the annulus. We expect flow amplitudes and the divergence to be small there thanks to the presence of a viscous boundary layer (e.g. Batchelor, 1967, pp. 302–314, 353–355). Nevertheless, the mean excess pressure level keeps floating since the gauge function $\phi_0(t)$ remains unknown. Pinning of the excess pressure in one point yields an efficient scheme at the expense that the excess pressure time series cannot be interpreted.

We have relied heavily on the scheme of Kim & Moin (1985) which demands a remark regarding the excess pressure and the pseudo-pressure. In principle, the semi-implicit time-integration scheme used for this study yields a pseudo-pressure solution and not directly the excess pressure and is an effect of the implicit treatment. Here, the viscous terms have been split into implicit (CN2) wall-normal directions and explicit (RK3) remaining terms so that the correction proposed by Kim & Moin (1985) cannot be used directly. It turns out that the correction is not as simple for the present time-integration scheme. However, the distinction between the excess pressure and the pseudo-pressure is only necessary if large time steps are used and the excess pressure is needed as diagnostic variable. The time series of the excess pressure cannot be interpreted at present due to pressure pinning, which means we simply skip any processing of the pseudo-pressure and leaf the question to a future investigation.

Remarks on the direct solver implementation. Let us close this section with a few remarks on the direct solver implementation in HYBRID-NEW. The grids used in this study share the property $N_2 \lesssim N_1$ (see table 3.2) so that storage is most efficient by arranging N_1^2 blocks of rank N_2 in a square matrix. The band width is $2N_2 + 1$ and only $N_1 N_2(2N_2 + 1)$ floating point numbers have to be stored for each wave number (instead of $N_1^2 N_2^2$ in the full square matrix). Coordinates are fixed in time so that initialisation is done only once.

The direct solution to N_3 transformed real-valued Poisson equations (or $2N_3/3$ equations in the case of 2/3-truncation) is done sequentially. Each 2-D problem is solved by a Gauß–Seidel elimination by calling LAPACK routines for LU-factorisation and matrix inversion (Anderson

et al., 1999). Computational efficiency is improved by solving a 2-D Poisson equation only if a corresponding p-norm, L^p, of the right hand side (RHS) is of the order of the discretisation error. For RHS given by equation (3.100), the Poisson solver is only invoked if

$$L^p\left(|\mathrm{RHS}|\right) \gtrsim C^p \qquad \text{with} \quad C^p \approx L^p\left(|\Delta_{\mathrm{GC}}|^{\mathrm{c}}\right). \tag{3.107}$$

The threshold C^p in equation (3.107) is set manually but estimated on the basis of the orthogonality error $|\Delta_{\mathrm{GC}}|^{\mathrm{c}}$ (see table 3.2). In HYBRID-NEW only the norms for $p = 1$ and $p = \infty$ are tested. I have used $C^p \equiv 10^{-5}$, which is smaller than the maximum deviation from local orthogonality (see table 3.2). The reason is that orthogonality errors are small inside the flow domain but the flow amplitude and divergence of the intermediate volume fluxes is large. The situation appears to be reversed at a non-librating wall where the right hand side errors might be smaller than expected. It depends on the flow if the selected threshold values for C^p can be optimised but this has not been investigated here.

In the hybrid algorithm, only the forward transformation (from ξ^3- to κ_3-space) of the sources of the Poisson equation and the backward transformation of the excess pressure is required whenever the Poisson solver is invoked (here every sub-time step). The transformations are simply 1-D, which means very efficient by using external FFT routines (Frigo & Johnson, 1997; Teuler, 1998).

This concludes the discussion of the numerical solver. In the next chapters, the simulation results obtained with the numerical solver outlined above will be discussed in detail and will validate the methodological approach by a comparison to laboratory experiments.

4 Inertial wave attractors and modes excited by frustum libration and lids plus outer cylinder libration

The wave attractors discussed in chapter 2 tell us which spatial structures of the flow in the annular confinement are related to inertial waves. Wave attractors have been obtained by strong idealisations: only the inviscid linearised Navier–Stokes equations (Ekman number $E = 0$, Rossby number $R = 0$) have been considered, and amplitude and phase information have been removed from the flow variables of the 3-D flow[1]. The purpose of this chapter is to fill all these deficiencies by performing direct numerical simulations (DNS) of the flow in the rotating annulus in which libration is used to excite inertial waves.

In contrast to the computation of linear eigenmodes ($R = 0$, $E \ll 1$; e.g. Rieutord *et al.*, 2001; Rieutord & Valdettaro, 1997; Tilgner, 1999), the strength of DNS is that it allows to decide *which* flow structures can be excited by a given forcing mechanism and it can clarify directly if the flow is unstable or not. DNS have been performed with HYBRID-NEW, the Navier–Stokes solver described in detail in chapter 3. The numerical solutions presented in the following focus on small but finite Rossby and Ekman numbers ($R \ll 1$, $E \ll 1$) in order to have a good chance to observe wave-dominated flow, whose spatial structure can be compared to the wave attractors obtained by ray tracing (RT). Nevertheless, we are interested in a sensible but small non-linearity in order to see to which point ray tracing is a good approximation. Technical limitations restrict the numerical resolution and, thus, the dimensionless parameters when we require that the viscous boundary layer and the Kolmogorov micro-scale are resolved. In effect, the minimum and maximum values of the dimensionless parameters for true DNS of the non-linear Navier–Stokes equations.

In the following, the flow structures excited by wall libration are discussed, all of which have been obtained by direct numerical solution of the incompressible Navier–Stokes equations. First, we look into simple spatial structures corresponding to the rhomboidal $(1, 1)$ wave attractor (figure 2.7) for the frustum libration boundary condition. The rhomboidal wave attractor serves as an example to discuss the numerical solution. We will look into the time dependency, compare the spatial structures to corresponding laboratory experiments of Seelig (2014). After that, non-linear effects are discussed by filtering the full numerical solution at the harmonics 2ω and 3ω of the libration frequency. Second, for the lids and outer cylinder libration boundary condition the $(1, 4)$ neutral orbit (figure 2.11(b)) is representative and is discussed in analogy to the rhomboidal wave attractor, but the focus is a bit different: the annulus with a frustum exhibits 'surviving' normal modes of the straight annulus (Borcia & Harlander, 2012) and we will therefore look exemplary for the axisymmetric $(1, 4, 0)$ mode corresponding to the $(1, 4)$ LONO. Third, we compare the weakly non-linear numerical solutions to the linear theory of ray tracing for both libration boundary conditions. Fourth and fifth, we look at the response

[1] In 2-D flow, the complex partial pressure can compensate for that by means that it is an invariant for the web of characteristics outside the boundary layer. For a detailed explanation and the method of 'dressing the characteristics' see Maas (2005); Maas & Lam (1995)

of the numerical solution to variations of the Rossby R and the Ekman number E respectively. In addition to spatial structures local frequency spectra are discussed to elucidate the onset of instability and turbulence.

The annulus is axisymmetric and aligned with axis of rotation so that cylindrical coordinates (r, φ, z) and cylindrical velocity components (v_r, v_φ, v_z) are used in the following. All variables are taken in non-dimensional form consistently with the mathematical model given by equations (2.13) and (2.12). The corresponding non-dimensional grid dimensions can be seen in figure 3.4). Axisymmetric (quasi-2-D) and full 3-D simulations have been performed depending on whether the flow is centrifugally stable or unstable. The flow visualisation, however, will be restricted to a radial-axial section of the annular confinement only.

4.1 The rhomboidal wave attractor excited by frustum libration

The rhomboidal $(1, 1)$ wave attractor exists in the frequency band $0.393 \leqslant \sigma \leqslant 0.574$. In particular, the wave attractor at frequency $\sigma = 0.47$ has been in the focus of the theoretical investigations in section 2.4. Therefore, we focus on the rhomboidal wave attractor case first by selecting the dimensionless libration frequency to $\omega = 0.47$.

Stable flows are required to allow for a comparison of DNS results to geometric ray tracing. The dimensionless parameters $E = 3.19 \times 10^{-5}$ and $R = 0.2$ yield stable flow and have been selected in correspondence to the laboratory experiment of Seelig (2014). Wave excitation by libration demands a Rossby number large enough so that the momentum advection exceeds the discretisation error. The relative discretisation error notable in the velocities is of the order 10^{-4} for the numerical grids used in this work (see section 3.3). Therefore, $R \sim 10^{-2}$ is the minimum Rossby number to ensure that non-linearity is resolved to a percent, say $|\boldsymbol{\nabla} \cdot (\boldsymbol{v} \circ \boldsymbol{v})| \sim 10^{-2}$.

For a better comparison with the measurements of Seelig (2014), dimensional parameters are given in table 4.1 corresponding to the table-top experiment of figure 1.3. Default values are marked by an asterisk $(*)$. One can see that the default Ekman number corresponds to a rotation rate of $\Omega_0 = 30$ rpm and that the default Rossby number corresponds to a libration velocity of $U = 63\ \mathrm{mm\,s^{-1}}$ at the outer cylinder measured in the co-rotating frame of reference.

Time dependency

Figure 4.1 shows the radial velocity v_r in a radial-axial section of the annulus at different libration phases ($\omega t = \mathrm{const}$) for the flow excited by frustum libration with libration frequency $\omega = 0.47$. Red colours correspond to radially outward flow to the right, whereas blue colours correspond to radially inward flow to the left. The time slices (a–h) are shown in order to give an impression of the flow evolution. Here, only the prograde half of the libration period is shown ($0 \leqslant \omega t < \pi$, in accord with equation (1.2)) with an increment of $\Delta(\omega t) = \pi/8$. A transient stage of 56 libration periods or roughly 750 non-dimensional time units passed before the time slices were recorded. The flow is stationary and the time series repeats—to visual accuracy—with reversed sign in the retrograde libration phase ($\pi \leqslant \omega t < 2\pi$, not shown here). A rhomboidal structure can be discerned in all the panels (a–h) and corresponds well to the wave attractor pattern obtained by ray tracing (see figure 2.7(a) or 4.3(a)). Presence of the rhomboid suggests that the flow excited by libration, indeed, exhibits inertial waves and, moreover, the waves excited are focused on the wave attractor. In fact, a similar wave attractor has been found in a librating prism (Maas, 2001).

In figure 4.1, there is no instability or turbulent motion sensible which indicates that most of the kinetic energy on the wave attractor is simply dissipated. Focusing and dissipation result

Table 4.1: Values of the dimensionless parameters used in this study and the corresponding dimensional parameters and scaling factors for the laboratory experiment of Seelig (2014). The default parameters are marked by an asterisk (∗). Dimensional values are obtained from the librational forcing (see equation (1.2)) and the annulus geometry (outer cylinder radius $r_2 = 200$ mm and a length scale of $L = 100$ mm). From the Ekman number E and the Rossby number R, equation (2.8) yield the mean rotation rate Ω_0 and the velocity scale U, where we assume water as working fluid (kinematic viscosity $\nu = 1.0018\ \mathrm{mm^2\,s^{-1}}$; see Grigull *et al.*, 1990). The velocity scale U is given only for $\Omega_0 = 30$ rpm.

	E	Ω_0 [rpm]	Ω_0 [$\mathrm{rad\,s^{-1}}$]		R	U @ 30 rpm [$\mathrm{mm\,s^{-1}}$]
	3.19×10^{-3}	0.3	0.0314		0.02	6.3
	9.57×10^{-4}	1.0	0.1047		0.10	31
	3.19×10^{-4}	3.0	0.3142	∗	0.20	63
	9.57×10^{-5}	10	1.047		0.26	82
∗	3.19×10^{-5}	30	3.142		0.30	94
	9.57×10^{-6}	100	10.47		0.40	126

in a *wave beam* of finite width that propagates along the rhomboid. As discussed by ray tracing (see section 2.4), the wave beam propagates in anti-clockwise direction as indicated by the arrows in figure 4.1(a). The wave beam undergoes spatial compression when it reflects at the frustum and the velocity amplitude increases. Viscous broadening (see chapter 2.3) competes with focusing and limits the minimum beam width of the wave attractor (for a detailed analysis see Hazewinkel *et al.*, 2008). The wave beams here correspond to internal oscillatory shear layers (e.g. Kerswell, 1995), which are three-dimensional but axisymmetric structures. Even though a wave beam rather refers to a two-dimensional object, we shall use the term in the following for the sake of brevity.

With the aid of figure 4.1 it is possible to show that the flow is composed of inertial waves. Selecting, for example, the lower right arm of the wave attractor that connects the bottom lid and the outer cylinder, yields the direction of the phase velocity $\boldsymbol{c}_\mathrm{p}$ by noting how the phase of the velocity changes over time. For the lower right arm, the $\boldsymbol{c}_\mathrm{p}$ points in negative radial and positive vertical direction. The dispersion relation (see figure 2.1) suggests that the group velocity $\boldsymbol{c}_\mathrm{g}$ points in positive radial and vertical direction such that it is perpendicular to $\boldsymbol{c}_\mathrm{p}$, which is in very good agreement with the numerical solution as indicated by the arrows in figure 4.1(a).

The wave beam propagating along the rhomboidal wave attractor is composed of waves with different wavelengths. In order to reflect the dependence of the phase and group velocity on the wavelength (see equation (2.25)), the local mean phase and group velocities are denoted by $\boldsymbol{c}_\mathrm{p}$, $\boldsymbol{c}'_\mathrm{p}$ and $\boldsymbol{c}_\mathrm{g}$, $\boldsymbol{c}'_\mathrm{g}$ respectively. The length of the arrows, however, has no meaning here and, moreover, there is no azimuthal vector component since the numerical solution is axisymmetric (quasi-2-D). Nevertheless, the wave beam is wider at the primed variables which means $\boldsymbol{c}_\mathrm{p} < \boldsymbol{c}'_\mathrm{p}$ and $\boldsymbol{c}_\mathrm{g} < \boldsymbol{c}'_\mathrm{g}$. This suggests that the solution near the wave attractor is self-similar (see also Maas, 2009) since the phase propagates across the wider beam equally fast as it does across the thinner beam.

Energy, though, needs to propagate around the rhomboid with a single velocity once the solution is stationary (otherwise it would become inhomogeneous). Therefore, an imbalance is counteracted by an increased energy dissipation at smaller spatial scales, that is, after the

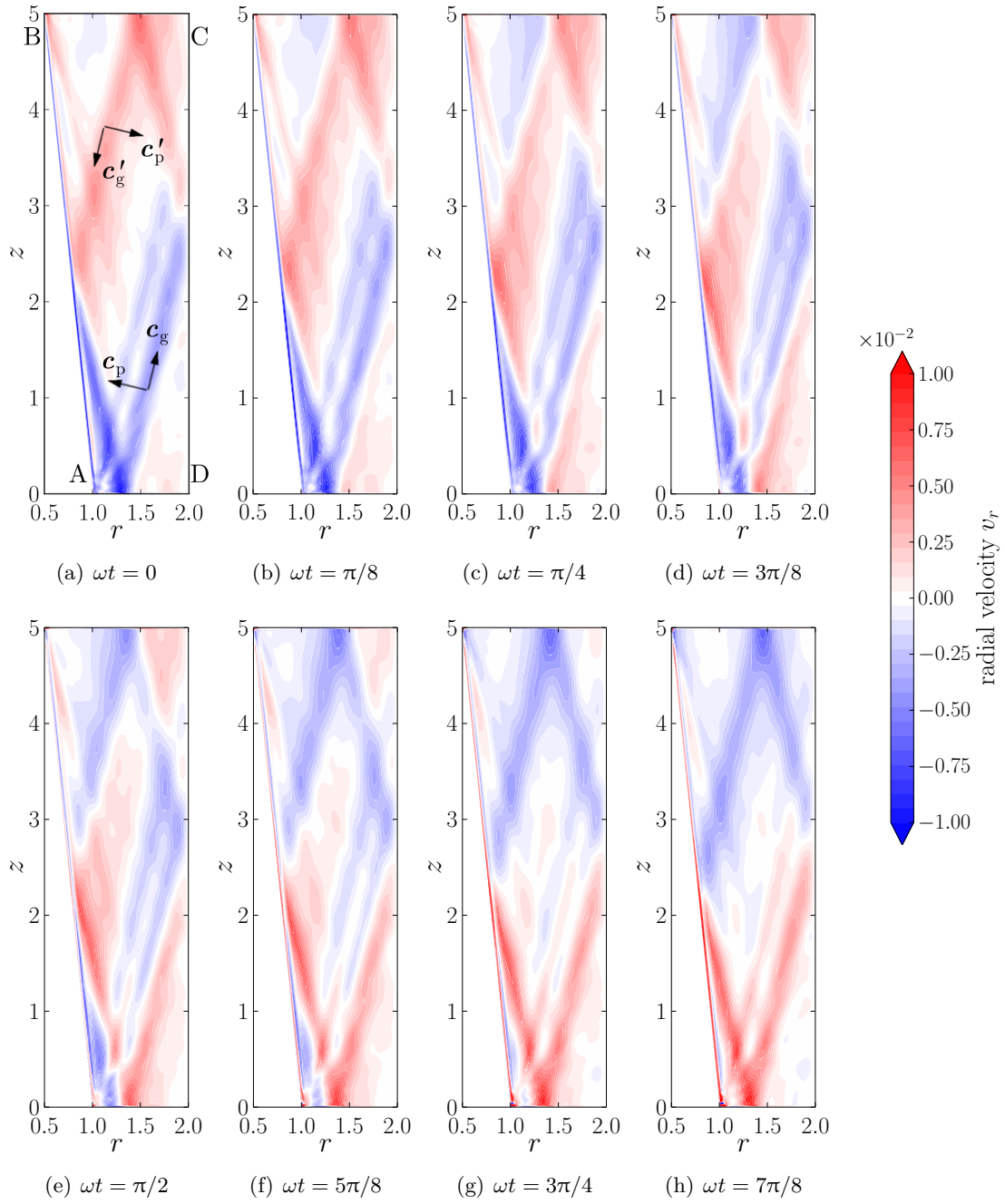

(a) $\omega t = 0$ (b) $\omega t = \pi/8$ (c) $\omega t = \pi/4$ (d) $\omega t = 3\pi/8$

(e) $\omega t = \pi/2$ (f) $\omega t = 5\pi/8$ (g) $\omega t = 3\pi/4$ (h) $\omega t = 7\pi/8$

Figure 4.1: Contours of the radial velocity v_r in a radial-axial section at different libration phases ωt in the prograde half of a libration period ($0 \leqslant \omega t < \pi$) after a transient stage of 56 libration periods has been passed. The flow is excited by frustum libration at $\omega = 0.47$ for the default values of the dimensionless parameters $R = 0.2$ and $E = 3.19 \times 10^{-5}$. Red (blue) corresponds to radially outward (inward) flow. The highest velocities are observed near the corner A, where the radial velocity exceeds the scale used by a factor 4. The flow is stable and axisymmetric, which means non-linearity is weak so that the time evolution repeats itself almost identically with reversed sign in the retrograde phase. The rhomboidal $(1, 1)$ wave attractor is clearly visible and compares well with ray tracing (cf. figure 2.7(d)).

focusing reflection (energy dissipation is discussed shortly for the filtered fields, but the argumentation is analogous to Hazewinkel *et al.*, 2008).

Figure 4.1 exhibits the highest velocity amplitudes in the vicinity of the librating frustum $\overline{\mathrm{AB}}$ and, in particular, near the corners A and B. The waves emitted from the corners can be discerned as individual wave beams, so-called *corner beams*. Corner beams have been reported earlier (e.g. Beardsley, 1970; McEwan, 1970; Sauret *et al.*, 2012; Swart *et al.*, 2010) and they contribute significantly to the transport of kinetic energy from the boundary layer into the bulk of fluid. Their generation will be discussed in chapter 5.

Let us concentrate on the corner beam originating from the corner A of the radial-axial section. The corner beam has the same frequency and the same phase as the wave attractor as can be inferred from the time series in figure 4.1(a–h). Same wave frequency implies that the corner beam propagates parallel to the wave attractor. The corner beam undergoes focusing when it reflects at the frustum wall, which is very similar to the dashed line shown in figure 2.5(a). After just one or two focusing reflections of the corner beam from A, the wave energy is practically concentrated on the wave attractor.

The discussion is essentially similar for the second corner beam that originates from B, but the latter appears to be damped in the focusing stage because several reflections at the frustum are needed until it reaches the wave attractor. The corner beam from B is weaker because of the r-dependent libration velocities, namely $v_{\mathrm{w},\varphi} \propto r$ and $r_\mathrm{B}/r_\mathrm{A} = 1/2$. The corner beam from A dominates the energy input to the wave attractor. The latter means that we are virtually faced with a single point source for the waves. The phase of the source though depends on the libration phase as we shall see in chapter 5. The corner beam thus has a unique phase, and as it is getting focused on the wave attractor constructive interference is needed to build up the flow amplitudes. This seems to explain why the corner beam from A and the wave attractor are oscillating in phase.

Helicity density and the propagation of wave energy

The time series of the radial velocity component allowed to confirm the direction of the phase velocity. By the aid of the dispersion relation of inertial waves (see figure 2.1), we have been able to construct the direction of the group velocity, which we found to agree well with the weakly non-linear viscous solution (see figure 4.1). A more compact way to assure ourselves of the presence and dominance of inertial waves, we can build on the theoretical aspects discussed earlier (see section 2.3). That is, inertial waves have positive (negative) helicity when they propagate in (against) the direction of the mean rotation rate, here $\boldsymbol{e}_z$ (see equation (2.30) and Davidson, 2013, p. 54). The helicity density is given by $\boldsymbol{v} \cdot \boldsymbol{\zeta}$, where $\boldsymbol{v}$ is the local velocity vector and $\boldsymbol{\zeta} \equiv \boldsymbol{\nabla} \times \boldsymbol{v}$ the local vorticity vector. In the case of the rhomboidal wave attractor we can, indeed, find two branches of upward and downward propagating inertial waves which becomes clearer when looking into the helicity density.

Figure 4.2 shows contours of the helicity density $\boldsymbol{v} \cdot \boldsymbol{\zeta}$ in a radial-axial section at different libration phases ($\omega t = \mathrm{const}$) for the flow excited by frustum libration with libration frequency $\omega = 0.47$ at default dimensionless parameters $R = 0.2$, $E = 3.19 \times 10^{-5}$ Reddish colours (solid contours) correspond to positive helicity, say right-handed spiral structures in the velocity field; bluish colours (dashed contours) correspond to negative helicity or left-left handed spiral structures in the velocity field (e.g. Kurgansky, 2002; Moffatt, 1969). Equation (2.30) yields that positive (negative) helicity corresponds to wave energy propagating downward (upward). The rhomboidal wave attractor shown in figure 4.2(a–d) exhibits the expected behaviour with wave energy propagating upward along the outer two diagonals, but downward along the inner

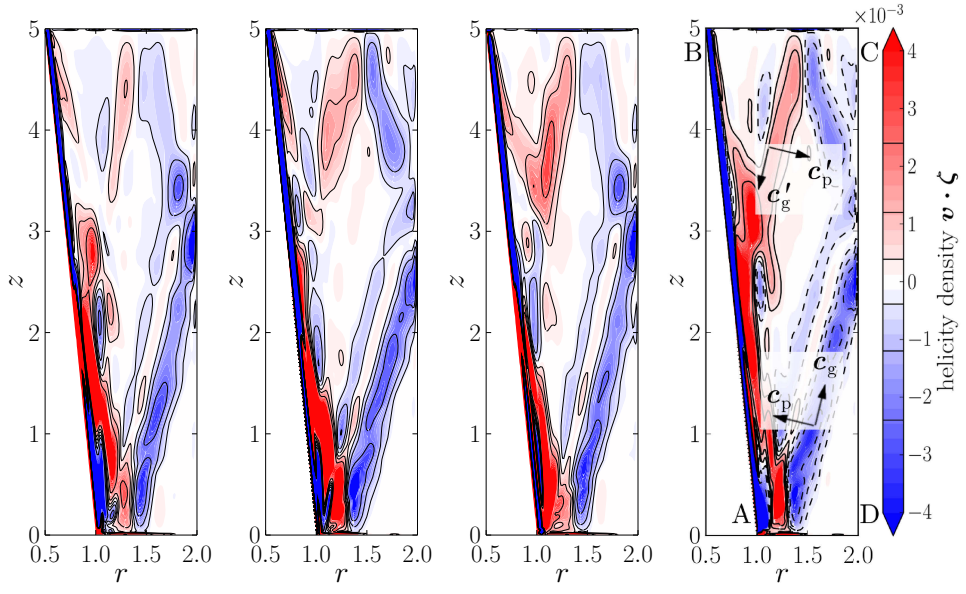

(a) $\omega t = 0$ (b) $\omega t = \pi/2$ (c) $\omega t = \pi$ (d) $\omega t = 3\pi/2$

Figure 4.2: Contours of the helicity density $\boldsymbol{v}\cdot\boldsymbol{\zeta}$ in a radial-axial section at different libration phases ωt in one libration period ($0 \leqslant \omega t < 2\pi$). The flow is excited by frustum libration at $\omega = 0.47$ for the default values of the dimensionless parameters. The rhomboidal wave attractor is clearly visible. Wave energy propagates upward on the outer two diagonals (blue), but downward along the inner two diagonals (red) according to equation (2.30). Schematic phase velocities $\boldsymbol{c}_\mathrm{p}$, $\boldsymbol{c}_\mathrm{p}'$ and group velocities $\boldsymbol{c}_\mathrm{g}$, $\boldsymbol{c}_\mathrm{g}'$ in panel (d) have been repeated from figure 4.1(a). The time evolution of the helicity is modified in the pro- (a, b) and retrograde (c, d) half-periods because of interference of the corner beams from corner B with that from corner A and the wave attractor respectively.

two diagonals. In the stationary state the sign and magnitude of the helicity density are also almost constant in time since the fluctuations of the flow are dominated by a single frequency, i.e., the imposed libration frequency.

The rational behind the described flow organisation is the focusing reflection at the frustum wall, due to which only anti-clockwise propagating waves are focused on the wave attractor. So, while the time series of the radial velocity component (see figure 4.1) yields the direction of the phase velocity $\boldsymbol{c}_\mathrm{p}$, a single snapshot of the helicity density, for example figure 4.2(d), provides information about the group velocity $\boldsymbol{c}_\mathrm{g}$, since $\boldsymbol{e}_z \cdot \boldsymbol{c}_\mathrm{g} \propto -\boldsymbol{v}\cdot\boldsymbol{\zeta}$. The wave beams and the wave attractor simulated are, thus, in qualitative agreement with the linear wave theory, as visualised by figure 2.1.

Furthermore, the focusing reflection leads to spatial compression and a significant increase of the helicity density along the line connecting $(r, z) = (0.8, 2.4)$ and $(1.2, 0.0)$, along which helicity density is about 10 times larger than the scale used in figure 4.2. However, the largest helicity densities are reached in the oscillating boundary layer over the librating frustum, where $|\boldsymbol{v}\cdot\boldsymbol{\zeta}| \sim 10^1$ or about 1000 times larger helicity density than in the fluid bulk. The helicity density remains localised near the wall and leaves the near-wall region mainly in the form of the corner beams emitted from the top and bottom corners (the boundary layer structure and corner beam excitation will be discussed further in chapter 5). At the focusing reflection, though, the oscillating boundary layer is obviously modified by the wave beam reflecting at the

wall, as can be seen by the helicity density having positive sign at $(r, z) = (0.9, 2.0)$, whereas it is negative towards the lids.

Note that the time slices in figure 4.2 have been selected throughout the libration period, which means only figures 4.1(a, e) correspond to figures 4.2(a, b) respectively. The evolution of helicity density is not fully symmetric with respect to the pro- and retrograde libration half-periods. The wave attractor itself stays approximately the same for all libration phases, but the superposition and interference of the wave attractor with the corner beam from corner B, the presence of other frequencies and spin-up/spin-down effects destroy the perfect symmetry between the two libration half-periods.

Comparison between DNS results and laboratory measurements

Figure 4.3 compares the flow structures of the numerical solution to those measured in a corresponding laboratory experiment (see Seelig, 2014, pp. 56, 60–61). For the numerical solution shown in figure 4.3(a), the flow is visualised in terms of the radial velocity v_r repeating the previous figure 4.1(a). In figure 4.3(b), the flow in the laboratory experiment is visualised in terms of a light intensity I measured in arbitrary units (a.u.), which is sufficient for the comparison of spatial structures. The light intensity was obtained by illuminating a radial-axial section with a laser light-sheet and recording the light reflected from immersed particles (small platelets).

A time series of the backscattered light has been recorded covering several libration periods. The image sequence was then processed further. The snapshot shown in figure 4.3(b) is the result of a reconstruction using the filtered time series (for details see Klein *et al.*, 2014; Seelig, 2014, pp. 43–48, 55–57). The configuration, forcing mechanism and the dimensionless parameters are precisely the same in the numerical simulations and in the laboratory experiment, which allows direct comparisons of the results.

The wave beam inclinations ($\vartheta \approx 76°$) are in very good agreement between DNS and laboratory measurements. They are identical within the confidence interval of the laboratory experiment ($\Delta\vartheta \approx 1°$). Also the wave beam widths are in agreement and cover about equally large fractions of the radial-axial section. However, one can only discern parts of the rhomboidal wave attractor and the corner beams in figure 4.3(b). The optical measurements cannot resolve the flow near the boundaries due to parasitic reflections at the wall and because of total reflection inside the outer glass cylinder. The latter, in particular, renders the annulus volume $r \geqslant 1.8$ inaccessible to measurements and the masked part has been replaced by wave rays (as mentioned by Klein *et al.*, 2014; Seelig, 2014, p. 56).

Besides those errors, the visual appearance of the flow differs a bit between the laboratory experiment and the simulated radial velocity with respect to the colours (phase) along the wave attractor. On the one hand, the phase ωt is not known in the laboratory measurement which complicates the direct comparison. On the other hand, the measuring technique uses small platelets, which are oriented coherently by the velocity shear. The velocity amplitude itself is of secondary importance. Hence, also the phase information is affected in the sense that the phase relation between two points on the wave attractor is different for the radial velocity and the light intensity.

Note further that figures 4.3(a, b) not only exhibit a qualitative agreement with respect to the spatial structures, but also a quantitative agreement with respect to the fluid velocity. The particle imaging velocity (PIV) measurements reported by Seelig (2014, pp. 60–61) yield velocity magnitudes $|\boldsymbol{v}_{\mathrm{lab}}| \sim 1\,\mathrm{mm\,s^{-1}}$. In figure 4.3(a) the non-dimensional velocities on the wave attractor are of the order $v_r \sim 10^{-2}$ and a multiplication with the velocity scale

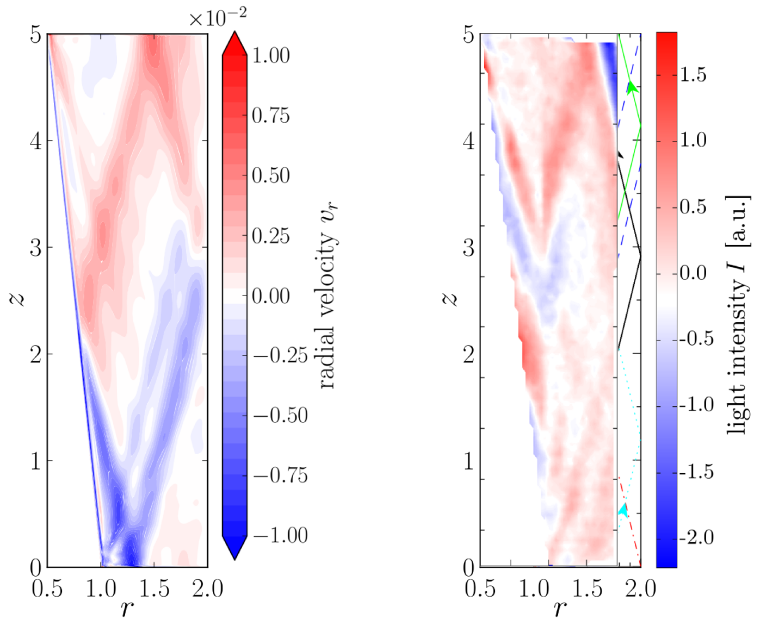

(a) DNS at $\omega t = 0$

(b) laboratory measurement at $\omega t = \text{const}$

Figure 4.3: Comparison of DNS and laboratory measurement regarding the spatial patterns for the flow excited by frustum libration with libration frequency $\omega = 0.47$ in the frequency band of the rhomboidal wave attractor. The same dimensionless parameters have been used in both cases: $R = 0.2$ and $E = 3.19 \times 10^{-5}$. Panel (a) shows the radial velocity v_r obtained by DNS at libration phase $\omega t = 0$ repeated from figure 4.1(a). Panel (b) shows a snapshot of the measured flow in terms of a reflected light intensity I (from M. Klein *et al.* (2014). 'Inertial wave excitation and focusing in a liquid bounded by a frustum and a cylinder'. *J. Fluid Mech.*, **751**, p. 267, figure 6(b), reproduced with permission). DNS and measurement agree with respect to the spatial patterns, the wave beam inclinations and widths, as well as the dimensional velocity scale of $\sim 1\ \mathrm{mm\,s^{-1}}$ (see table 4.1 and Seelig, 2014, pp. 60–61).

$U = 63\ \mathrm{mm\,s^{-1}}$ (see table 4.1) yields radial velocities of $|v_r U| \sim 0.6\ \mathrm{mm\,s^{-1}}$. Accounting for the projection on the radial direction only yields velocities simulated in agreement with the velocities measured up to the confidence interval of $\Delta v \sim 0.1\ \mathrm{mm\,s^{-1}}$ (see Seelig, 2014, pp. 59).

Altogether, the direct numerical solution matches the measured data available in all respects for precisely the same flow parameters. This is remarkable and validates the applicability of the idealised mathematical model, equations (2.6) and (2.7), and the numerical solution procedure outlined in chapter 3. DNS gives access to all dynamical variables of the flow which will allow us to uncover the wave excitation mechanism (see in chapters 5 and 6).

Up to this point, the flow remained stable and the libration frequency ω has provided the dominating frequency in the system as we have seen by comparison to the inclination of characteristics obtained by linear theory (see sections 2.3 and 2.4). Nevertheless, figures 4.3(a, b) give a somewhat 'noisy' impression. In the laboratory measurement, panel (b), the noise is due to the various errors and do not allow any interpretation. The numerical accuracy of the DNS in panel (a), however, is good enough to yield the 'noise' additional frequency content originating

from the non-linearity of the Navier–Stokes equations. We will therefore look at the linear and weakly non-linear aspects of the numerical solution in the following section.

Frequency-filtered radial velocity component

In order to investigate the additional frequency content, the time series computed numerically needs to be decomposed by a frequency filter, but which frequencies to choose? We know that non-linearity is weak ($R = 0.2$) and that the dominating frequency is given by the forcing frequency. The librational forcing (see equation (1.2)) injects a single frequency $\sigma = \omega$, that is, it has a δ-spectrum. The non-linearity of the momentum equation (2.6) exhibits to frequency mixing. Self-interaction of the components oscillating with the forcing frequency gives rise to the mixed frequency 2ω. The latter component can interact again with the forcing frequency or also with itself so that contributions at 3ω and 4ω emerge and so on and so forth. In that way a *harmonic sequence* is established with respect to $\sigma_l = l\omega$ ($l = 1, 2, \ldots$), which explains the variability of the flow[2].

The solution shown in figure 4.1 is stable, which suggests to apply the Fourier filter outlined in appendix A.3 for the harmonics σ_l. Amplitudes and phases are obtained via equation (A.8) and the radial velocity component v_r, for example, has the decomposition

$$v_r(\boldsymbol{r}, t) \quad \longrightarrow \quad v_{r,l\omega}(\boldsymbol{r}), \quad \theta_{r,l\omega}(\boldsymbol{r}), \tag{4.1}$$

where $v_{r,l\omega}$ denotes the real-valued amplitude of the lth harmonic and $\theta_{r,l\omega}$ denotes the corresponding phase difference to the reference phase $l\omega t$, which is an integer multiple of the libration phase ωt. All flow features related to linear inertial waves need to have frequencies in the inertial wave band, that is, $0 < \sigma_l < 2$. For the rhomboidal wave attractor excited by $\omega = 0.47$, we can expect the wave field composed of four linear inertial wave frequencies. Small Rossby numbers imply that the velocity amplitudes of higher harmonics decrease rapidly like $|\boldsymbol{v}_l| \propto R^{l-1}$ (mind the scaling of the dimensionless velocities) so that we will restrict our attention to the forcing frequency $l = 1$ and its harmonics $l = 2$ and $l = 3$ with $l\omega$ in the inertial wave band ($l\omega < 2$). The validity range of the filtering at the harmonics will be discussed later in sections 4.4 and 4.5.

Note that $l = 0$ corresponds to the mean flow which is not investigated here. (For a detailed study of the mean flow in annular configurations the reader is referred to Ghasemi V. (2016) and Seelig (2014).)

Figure 4.4 shows the Fourier decomposition of the radial velocity v_r for the simulated rhomboidal wave attractor shown in figure 4.1, which has been excited by frustum libration with $\omega = 0.47$ at default parameters $R = 0.2$, $E = 3.19 \times 10^{-5}$. Following equation (4.1), figures 4.4(a–c) show the amplitudes $v_{r,l\omega}$ of the radial velocity for the first three frequencies ($l = 1, 2, 3$), whereas figures 4.4(d–f) show the corresponding phases $\theta_{r,l\omega}$. Comparing the orders of magnitude of the radial velocity amplitudes, panels (a–c), reveals that the forcing frequency contains the majority of the variability. In the bulk, the amplitudes of the radial velocities reach 10^{-2} in panel (a), 2×10^{-3} in panel (b), and 4×10^{-4} in panel (c). The velocity amplitudes of the harmonics are smaller by factors $v_{r,2\omega}/v_{r,1\omega} \sim 0.2 = R$ and $v_{r,3\omega}/v_{r,1\omega} \sim 0.04 = R^2$ respectively. As expected from a weak quadratic non-linearity, velocity amplitudes are proportional to R^{l-1} modulo a wave excitation efficiency factor of $O\left(10^{-2}\right)$ (the wave excitation efficiency will be discussed separately in chapter 6). Near the librating frustum and, in particular near

[2]The variability of the flow can only be explained by a harmonic sequence for as long as there is no turbulence and no developing instability. The flow dominated by inertial waves is therefore non-linear but highly organised.

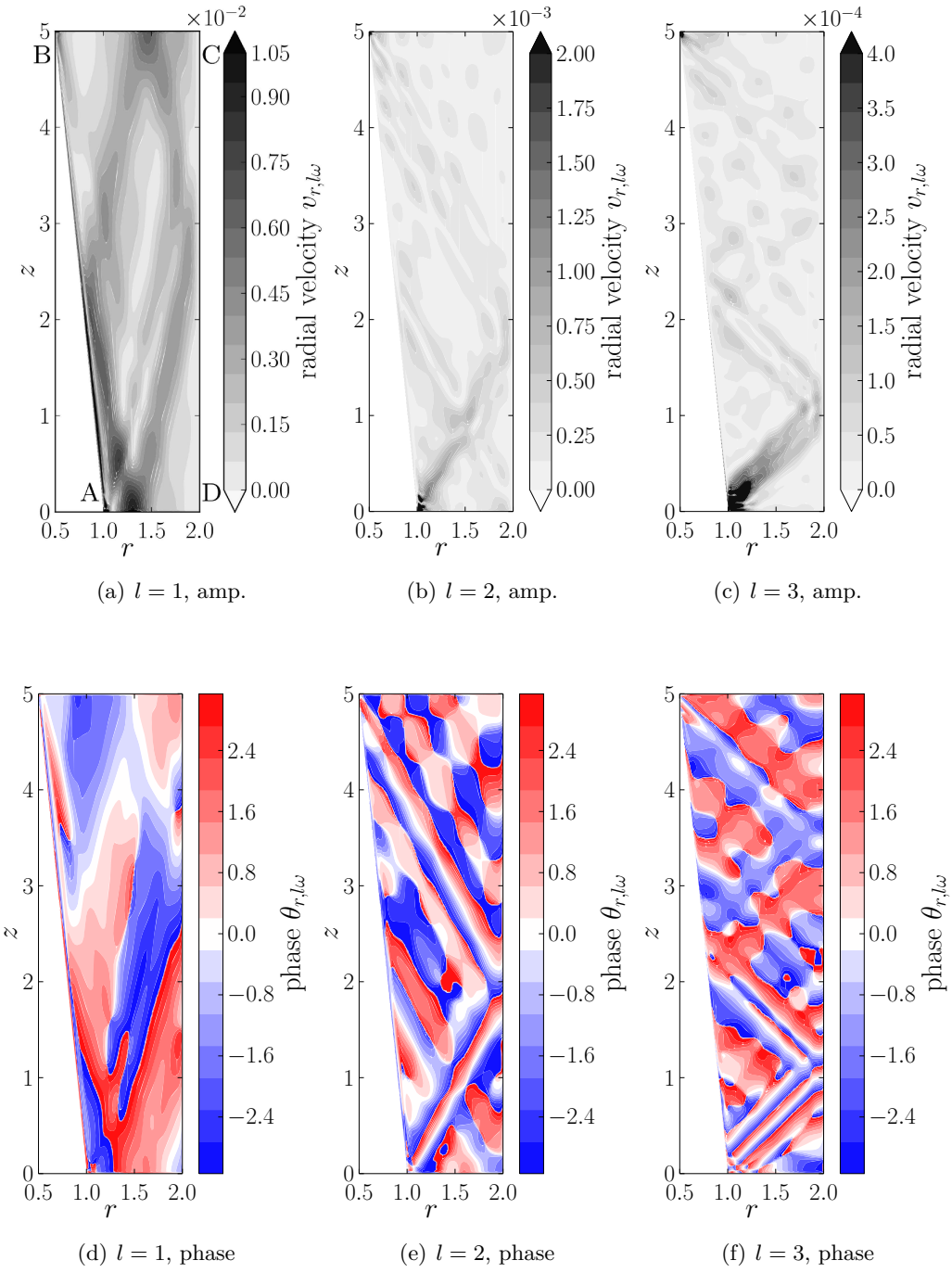

(a) $l = 1$, amp. (b) $l = 2$, amp. (c) $l = 3$, amp.

(d) $l = 1$, phase (e) $l = 2$, phase (f) $l = 3$, phase

Figure 4.4: Contours of the frequency-filtered radial velocity for the rhomboidal wave attractor excited by frustum libration with libration frequency $\omega = 0.47$ at default dimensionless parameters $R = 0.2$, $E = 3.19 \times 10^{-5}$. Radial velocity amplitude $v_{r,l\omega}$ (a–c) and phase $\theta_{r,l\omega}$ (d–f) are shown in a radial-axial section for the forcing frequency ω ($l = 1$) and its two lowest harmonics $l\omega$ ($l = 2, 3$). The phase has values in $[-\pi, \pi)$, where red (blue) corresponds to the stationary oscillation being ahead (behind) the reference phase $l\omega t$. The rhomboidal wave attractor can only be seen at the forcing frequency (a, d). Both harmonics are 'free modes' and exhibit independent spatial structures (b, c, e, f). Kinetic energy is redistributed by inertial waves for all the filter frequencies shown.

the corner A, the scaling breaks down so that the velocity amplitudes at the harmonics have comparable radial velocity amplitudes of the order 10^{-2} (not shown explicitly; the boundary layer and the corner flow will be discussed separately in chapter 5).

At the *forcing frequency*, the radial velocity amplitude $v_{r,1\omega}$ shown in figure 4.4(a) clearly exhibits the rhomboidal wave attractor. The wave attractor and the corner beams have smooth (Gaussian) wave beam profiles. No more noise is visible in comparison to one of the snapshots in figure 4.1. The prevailing characteristic inclination is about $\vartheta = 76^\circ$ and agrees well with linear wave theory (see section 2.3). The same inclination is exhibited by the corresponding phase $\theta_{r,1\omega}$, which is shown in figure 4.4(d). There are just a few exceptions, though, which result from a superposition of wave beams, boundary layer, and discretisation errors. We will discuss all three briefly in the following.

First, at around $(r, z) = (1.0, 3.5)$ the corner beam from corner B is superposed with the wave attractor which obtains its phase from the corner beam from corner A (see the discussion of figure 4.1). The simulated velocity amplitudes of the wave attractor and of the corner beam have comparable order of magnitude, but they have different phase. The superposition of the wave attractor and the corner beam leads to a distortion of the phase contours which are otherwise parallel to the characteristic discussed in section 2.4. Second, towards the wall, especially towards the frustum, one can see that the phase contours turn wall-parallel, which indicates the presence of a viscous boundary layer and breakdown of the linear wave theory there. The boundary layer effectively modifies the size of the flow domain seen by the waves (see Borcia *et al.*, 2014). The effect is relevant here since it will shift the wave attractor frequencies by $O\left(E^{1/2}\right)$ (compare to figure 2.9), which is lesser a problem in geophysical flows thanks to their tiny Ekman numbers. Third, in the centre of the flow domain at around $(r, z) = (1.5, 3.0)$ the radial velocity amplitude becomes very small so that the phase is corrupted there by numerical errors and deviates from the characteristics. A last interesting aspect regarding the phase in figure 4.4(d) is that there is no unique phase on the wave attractor. Following the wave beam in anti-clockwise direction shows that the phase jumps roughly by π when the wave beam reflects at the frustum or the outer cylinder.

For the focusing reflection of the wave attractor, the wave beam propagating from $(r, z) = (1.5, 5.0)$ to $(1.0, 2.5)$ has negative phase and positive phase after reflecting at the frustum when it propagates from $(r, z) = (1.0, 2.5)$ to $(1.3, 0.0)$. This is in agreement with the reflection law of inertial waves (see Phillips, 1963).

Amplitude and phase of the *harmonics* $l = 2, 3$ are shown in figures 4.4(b, c) and 4.4(e, f) respectively. The harmonic frequencies $2\omega = 0.94$ and $3\omega = 1.41$ are close to $\sigma = 0.8944$ and 1.4070, for which we have found the $(1, 2)$ and $(1, 4)$ LONOs (see figure 2.11). The $(1, 2)$ LONO connects corners A and B by a tilted-V pattern, whereas the $(1, 4)$ LONO connects the corners by a tilted-W pattern.

Neither the $(1, 2)$ LONO nor the $(1, 4)$ LONO is realised at the harmonics of the forcing frequency, but the harmonic wave beams emitted from the corners almost resemble the respective ray patterns, which is seen in the amplitude and the phase. The reason is viscous damping plus the focusing and defocusing reflections at the frustum wall which in combination allow to trace the corner beams only for a few reflections before they have been damped down. Viscosity is stronger after the focusing reflection and accelerates the damping. This effect destroys the theoretically exact compensation of focusing and defocusing reflections. The numerical solution therefore does not exhibit as much complexity as one might expect from the long ray orbits (that is, black vertical lines at the harmonic frequencies in figure 2.9). Since the harmonic frequencies 2ω and 3ω lie in the inertial wave band, the corresponding spatial structures ex-

cited are sometimes called 'free modes'. From the spatial structure of the velocity amplitudes in figures 4.4(b, c), we can discern the locations of higher harmonic generation: the corner A, in particular, but also B and the focusing reflection of the wave attractor at the frustum wall. The frustum libration causes large shear at corner A so that it is not surprising that we find intense dynamics there. The width of the corner beams can be used to draw conclusions about the fluid-internal source located in the corner (see Cortet *et al.*, 2010; Machicoane *et al.*, 2015), which is beyond the scope of this work though.

Spatial distribution of the kinetic energy dissipation rate

We have looked into the radial velocity component in order to study the spatial structures in the numerical solution to the rhomboidal wave attractor excited by frustum libration. We found that focusing of wave beams can explain the pattern formation. The wave attractor remains of finite width, though, due to the action of viscous forces. In the stationary but forced solution to the Navier–Stokes equations (see figure 4.1), a balance between focusing and viscous broadening is realised (Hazewinkel *et al.*, 2008). It is worth to look into the structure of energy dissipation in order to assure that the model of Hazewinkel *et al.* (2008) obtained for the librating prism applies also to the librating annulus here.

The local energy dissipation rate is given by the dissipation function $\Phi(\boldsymbol{r}, t)$ defined in equation (3.73). In the latter, scaling of the variables yields the non-dimensional dissipation function

$$\Phi = 2E\,(\boldsymbol{\tau} \cdot\cdot\, \boldsymbol{\tau}) \qquad \text{with} \quad \boldsymbol{\tau} = \frac{1}{2}(\boldsymbol{\nabla} \circ \boldsymbol{v}) + \frac{1}{2}(\boldsymbol{\nabla} \circ \boldsymbol{v})^{\mathrm{T}} \tag{4.2}$$

denoting the rate of strain tensor with respect to the scaled velocities in the co-rotating frame of reference. The dissipation function is a quadratic quantity with respect to the velocity shear. Hence, the time-averaged contributions to the energy dissipation at the harmonics $l\omega$ ($l = 1, 2, \ldots$) of the libration frequency ω is obtained by the aid equation (A.11), which yields real-valued and positive definite fields $\Phi_{l\omega}(\boldsymbol{r})$ as

$$\Phi_{l\omega} = E\left(\hat{\boldsymbol{\tau}}_{l\omega}^{\dagger} \cdot\cdot\, \hat{\boldsymbol{\tau}}_{l\omega}\right) \tag{4.3}$$

with $\hat{\boldsymbol{\tau}}_{l\omega}(\boldsymbol{r})$ the complex amplitude of the filtered rate of strain tensor obtained by applying equations (A.7)–(A.9) to $\boldsymbol{\tau}(\boldsymbol{r}, t)$.

Figure 4.5 shows the frequency-filtered time-averaged contributions $\Phi_{l\omega}/E$ to the dissipation function for the non-linear viscous solution to the rhomboidal wave attractor excited by frustum libration with $\omega = 0.47$ and default values of the Ekman and Rossby numbers. $\Phi_{l\omega}/E$ denotes the contributions to the dissipation function rescaled with the Ekman number so that it corresponds to a quadratic norm of the strain rate tensor, say $\Phi_{l\omega}/E = ||\hat{\boldsymbol{\tau}}_{l\omega}||^2$. The contours in figure 4.5 are plotted in a radial-axial section of the annulus; they are shown for the forcing frequency ω ($l = 1$) and the two lowest harmonics $l\omega$ ($l = 2, 3$) in analogy to figures 4.4(a–c).

At the *libration frequency* ($l = 1$), figure 4.5(a), one observes that energy dissipation is indeed localised at the wave beams and the rhomboidal wave attractor is clearly visible. Though, it is almost impossible to discern the corner beam originating from corner A; only the local maximum at around $(r, z) = (1.5, 2.8)$ hints at the existence of that corner beam. By contrast, the corner beam originating from corner B is clearly visible in the dissipation function. Hence, the situation appears reversed compared to the radial velocity amplitude (see figure 4.4(a)). The reason seems to be the phase, for example $\theta_{r,1\omega}$ as shown in figure 4.4(d).

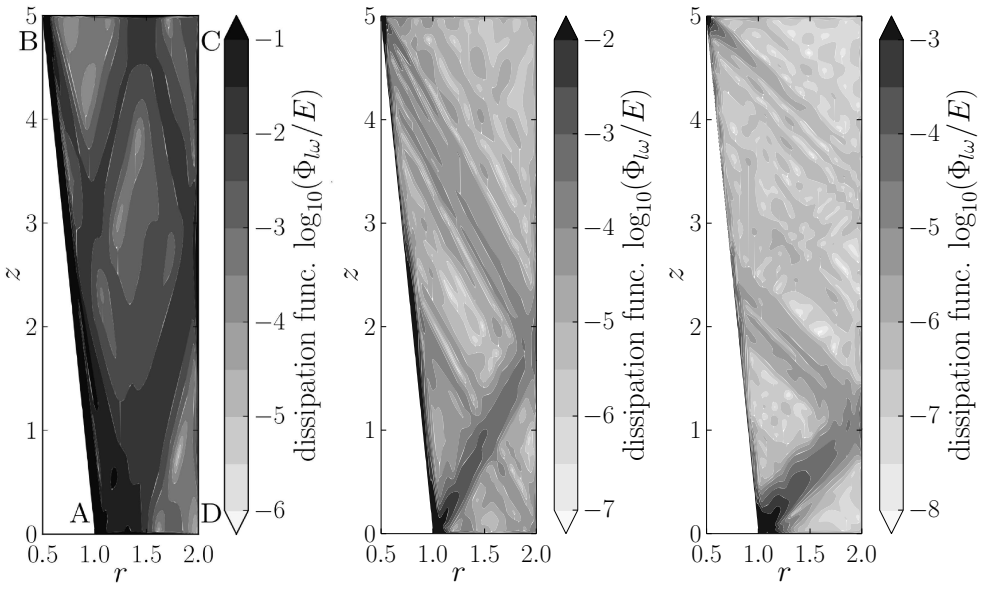

(a) $l = 1$ (b) $l = 2$ (c) $l = 3$

Figure 4.5: Contours of the frequency-filtered time-averaged dissipation function for the rhomboidal wave attractor excited by frustum libration with libration frequency $\omega = 0.47$ at default dimensionless parameters $R = 0.2$, $E = 3.19 \times 10^{-5}$. The contributions $\Phi_{l\omega}$ ($l = 1, 2, 3$) are shown in logarithmic scale in a radial-axial section for the forcing frequency ω (a) and the two lowest harmonics 2ω (b) and 3ω (c). The energy dissipation is localised at the wave beams and the wave attractor where velocity shear is large (compare to figure 4.4). The rhomboidal wave attractor can only be discerned at the forcing frequency.

Indeed, comparing the phase in figure 4.4(d) to the dissipation function contribution $\Phi_{1\omega}$ in figure 4.5(a) yields comparable spatial structures with respect to the visibility of the corner beams. The implication is that energy is mainly injected at corner A in the form of a corner beam. The corner beam propagates in the bulk of fluid, where it is subject to focusing reflections and approaches the wave attractor. On the wave attractor, the concentrated kinetic energy is dissipated by the action of viscosity which suggests a strongly localised heat source inside the fluid. However, the focusing reflections at the frustum are weak so that the waves approach the wave attractor gradually.

Due to viscous broadening, several wave beams of similar phase are superposed (since they originate mainly from corner A) and lead to a smooth phase variation and a relatively smooth distribution of the energy dissipation in the bottom right part of the rhomboidal wave attractor. Nevertheless, spatial compression due to the focusing reflection at the frustum wall results in an increase of the energy dissipation as can be seen by $\Phi_{1\omega}/E \sim 10^{-1}$ at $(r, z) = (1.0, 1.5)$, whereas $\Phi_{1\omega}/E \sim 10^{-2}$ at $(r, z) = (1.0, 2.8)$. The spatial structure of the dissipation function in the interior are visually in agreement with the results reported by Hazewinkel *et al.* (2008).

Moreover, the dissipation rate reaches its maximum values $(\Phi_{1\omega}/E \sim E^{-1} \approx 3 \times 10^4)$ near the librating frustum, which is due to the presence of a viscous oscillatory boundary layer (to be discussed further in chapter 5).

The contributions to the dissipation function at the *harmonics* $l = 2, 3$ are shown in figures 4.5(b, c), but their scales are different. The scale reduces in steps of one order of magnitude from figure 4.5(a) to 4.5(c). The spatial patterns observed in figures 4.5(b, c) exhibit wave beams of harmonic frequencies $2\omega = 0.94$ and $3\omega = 1.41$ that originate from the corners (see the discussion of figure 4.4). Energy dissipation at the harmonics of the forcing frequency is localised at the corners A and B, which is due to significant non-linearity in the oscillating boundary layer. At the harmonic 2ω, figure 4.5(b), energy dissipation is also localised along the librating frustum, hinting at non-linear self-interaction of the oscillating boundary layer flow with itself.

Furthermore, it seems as if the boundary layer exhibits small-scale eddies around the focusing reflection at $(r, z) = (0.8, 2.2)$, which is not the case for the harmonic 3ω in panel (c). This hints at an onset of instability of the boundary layer flow at around the harmonic 2ω triggered by the wave beam (corner beam) returning to the librating wall. Non-linear interaction happens between three partners, the oscillating boundary layer due to libration, the incident and the reflected wave beam of larger wave vector due to focusing. A thorough analysis of this instability is beyond the scope of this work, but an analysis of the stability properties would certainly be interesting and would serve to find the stability boundaries of recent analytical works (e.g. Gerkema, 2006; Peacock & Tabaei, 2005; Tabaei *et al.*, 2005).

4.2 Neutral orbit and mode excited by lids plus outer cylinder libration

Neutral orbits in the annulus have frequency eigenvalues in the range[3] $0.9 \lesssim \sigma < 2$. All but the $(1, 2)$ LONO (see figure 2.11(a)) have frequency eigenvalues in the range $1 < \sigma < 2$ due to which harmonics $\sigma_l = l\omega$ $(l = 2, 3, \ldots)$ are outside the inertial wave band and cannot propagate freely. This is in contrast to the rhomboidal wave attractor case discussed in section 4.1. Moreover, the density of LONO frequencies increases toward $\sigma = 2$ and the excitation of LONO was found to be much more efficient in the case of lids and outer cylinder libration than in the case of frustum libration[4].

A simple but representative example for neutral orbits is the $(1, 4)$ LONO with a frequency eigenvalue of $\sigma = 1.4070$ (see figure 2.11(b)) As was discussed in section 2.4, presence of a neutral orbit hints at a corresponding normal mode solution. For the selected example this would be the 'surviving' $(1, 4, 0)$ mode of the straight annulus with (m, n, k) denoting the radial, axial and azimuthal wave numbers respectively. The frequency eigenvalues of modes and neutral orbits are sharp and in contrast to the wave attractor frequency bands. In order to excite a LONO and/or a mode in the DNS, the libration frequency ω was varied around the frequency eigenvalue σ, which was obtained by geometric ray tracing in the first place.

In the following, we proceed in analogy to the wave attractor case of section 4.1 by discussing first the time dependency, the flow structures in comparison to laboratory measurements and ray tracing, as well as the frequency-filtered velocity field for the LONO. After that, the libration frequency is modified in order to excite the $(1, 4, 0)$ mode. Finally the mode excited is discussed in detail.

[3] One might expect more LONOs at smaller frequencies with multiple reflections along the lids. This seems impossible to achieve in the annular confinement with the conical inner wall since no balance between focusing and defocusing can be achieved in that case (see also Borcia & Harlander, 2012).

[4] Efficiency aspects of wave excitation will be discussed in more detail in chapters 5 and 6.

Time dependency

Neutral orbit. Figure 4.6 shows the radial velocity v_r in a radial-axial section of the annulus at different libration phases ($\omega t = \text{const}$) for the flow excited by lids plus outer cylinder libration at libration frequency $\omega = 1.4$. Red colours correspond to radially outward flow to the right, whereas blue colours correspond to radially inward flow to the left. The time slices, panels (a–h), are shown to give the reader an idea of the flow evolution. Here, only the potentially unstable retrograde half of the libration period is shown ($\pi \leqslant \omega t < 2\pi$, in accord with equation (1.2)) with time slices recorded at an increment of $\Delta(\omega t) = \pi/8$. A transient stage of 76 libration periods or roughly 340 non-dimensional time units has been skipped before the time slices were recorded. The flow is stationary and the time series repeats up to the level of visual accuracy with reversed sign in the prograde libration phase ($0 \leqslant \omega t < \pi$, not shown here). There are two dominating structures in figure 4.6: a basin-scale oscillation pattern reminiscent of an eigenmode (to be discussed shortly) and corner beams.

The corner beams are excited at all four corners A–D, but in particular at C and D. The reason is related to the radial dependency of the wall velocity, $v_{\mathrm{w},\varphi} \propto r$, where $r_\mathrm{C} = r_\mathrm{D} = 2$ and $r_\mathrm{A}/r_\mathrm{C} = 0.5$, $r_\mathrm{B}/r_\mathrm{C} = 0.25$. By the aid of the time slices, figures 4.6(a–h), it is easy to confirm that phase velocity $\mathrm{c_p}$ is oriented such that wave energy propagates with group velocity $\mathrm{c_g}$ from the corners into the bulk (compare to figure 2.1). In figure 4.6(a), only the phase velocities $\mathrm{c_p}$, $\mathrm{c_p'}$ and group velocities $\mathrm{c_g}$, $\mathrm{c_g'}$ corresponding to the corner beams from corners D and C are shown. The velocity magnitudes and the widths of these corner beams is comparable. The phase relation is such that their superposition leads to destructive interference, that is, a white tilted-W pattern in figures 4.6(a–h).

Interestingly, the $(1, 4)$ LONO given by the dashed line in figure 2.11(b) is realised as a nodal line in the radial velocity field of figure 4.6 and seems to give rise to the excitation of a smooth basin-scale oscillation pattern that 'fills' the tilted-W pattern in figures 4.6(d–g). The destructive interference along the tilted-W, though, seems rather coincidental here and is due to the forcing (librating lids).

Normal mode. At the moment, we cannot decide if the basin-scale oscillation in figure 4.6 is a normal mode since we do not know the spectrum eigenmodes for the annulus with an inner frustum (besides, perhaps, the two modes computed by Henderson & Aldridge, 1992). However, resonance as seen by the velocity amplitudes is weak and the presence of some smaller patchy structures in figures 4.6(a, b, g, h) indicate that the 'surviving' $(1, 4, 0)$ mode of the straight annulus is not notably excited. The corner beams do not retrace themselves accurately so that reflected wave beams are diverging from the tilted-W pattern that is supposed to connect the corners C and D (dashed line in figure 2.11(b)). In effect, the superposition of the various wave beams yields a complicated interference pattern. The reason for the corner beams diverging from the tilted-W pattern has been given already and is due to the presence of a viscous boundary layer that slightly modifies the annulus geometry sensed by the inertial waves (Borcia *et al.*, 2014).

In contrast to wave attractors, neutral orbits are not structurally stable and we need to find the correct libration frequency in order to excite the $(1, 4, 0)$ mode resonantly. The frequency of the viscous eigenmode is expected to shift proportional to $E^{1/2}$, but the amplitude of the drift and its sign are unknown. Therefore, several simulations have been performed changing the libration frequency in steps of $\Delta\omega = \pm 0.005$ from $\omega = 1.4$. Other flow parameters are kept constant.

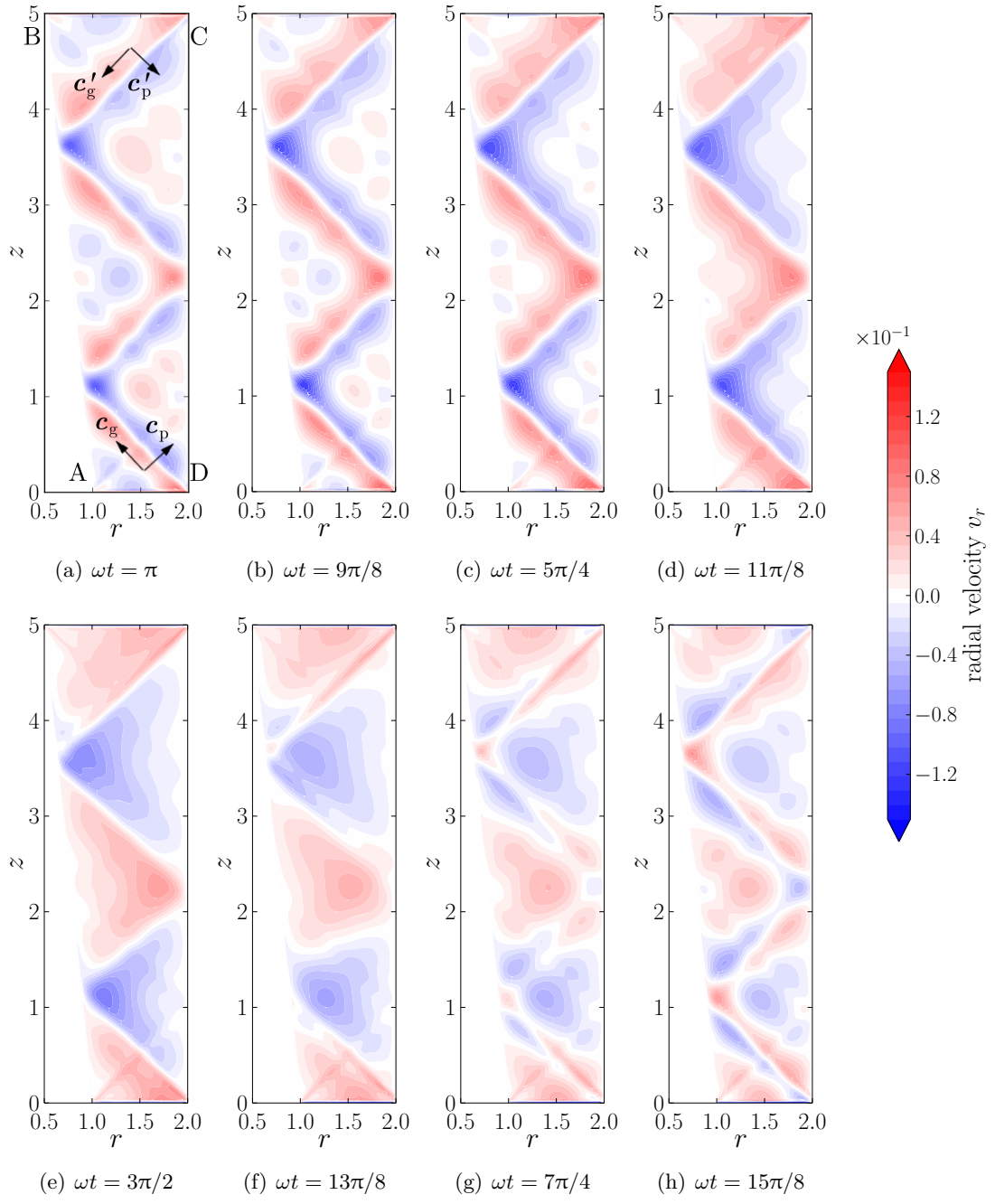

(a) $\omega t = \pi$ (b) $\omega t = 9\pi/8$ (c) $\omega t = 5\pi/4$ (d) $\omega t = 11\pi/8$

(e) $\omega t = 3\pi/2$ (f) $\omega t = 13\pi/8$ (g) $\omega t = 7\pi/4$ (h) $\omega t = 15\pi/8$

Figure 4.6: Contours of the radial velocity v_r in a radial-axial section at different libration phases ωt in the retrograde half of a libration period ($\pi \leqslant \omega t < 2\pi$) after a transient stage of 76 libration periods has been passed. The flow is excited by lids plus outer cylinder libration at $\omega = 1.4$ for the default values of the dimensionless parameters $R = 0.2$ and $E = 3.19 \times 10^{-5}$. Red (blue) corresponds to radially outward (inward) flow. Panels (b,c,d) exhibit the largest velocities over the librating lids in the vicinity of the corners C and D, where the radial velocity exceeds the scale used by a factor 3. The flow is stable and axisymmetric, which means non-linearity is weak and the time evolution repeats itself with reversed sign in the prograde phase. The tilted-W pattern of the $(1, 4)$ LONO can be discerned as white nodal line connecting the outer corners; the spatial pattern compares well with the planar prediction obtained by ray tracing.

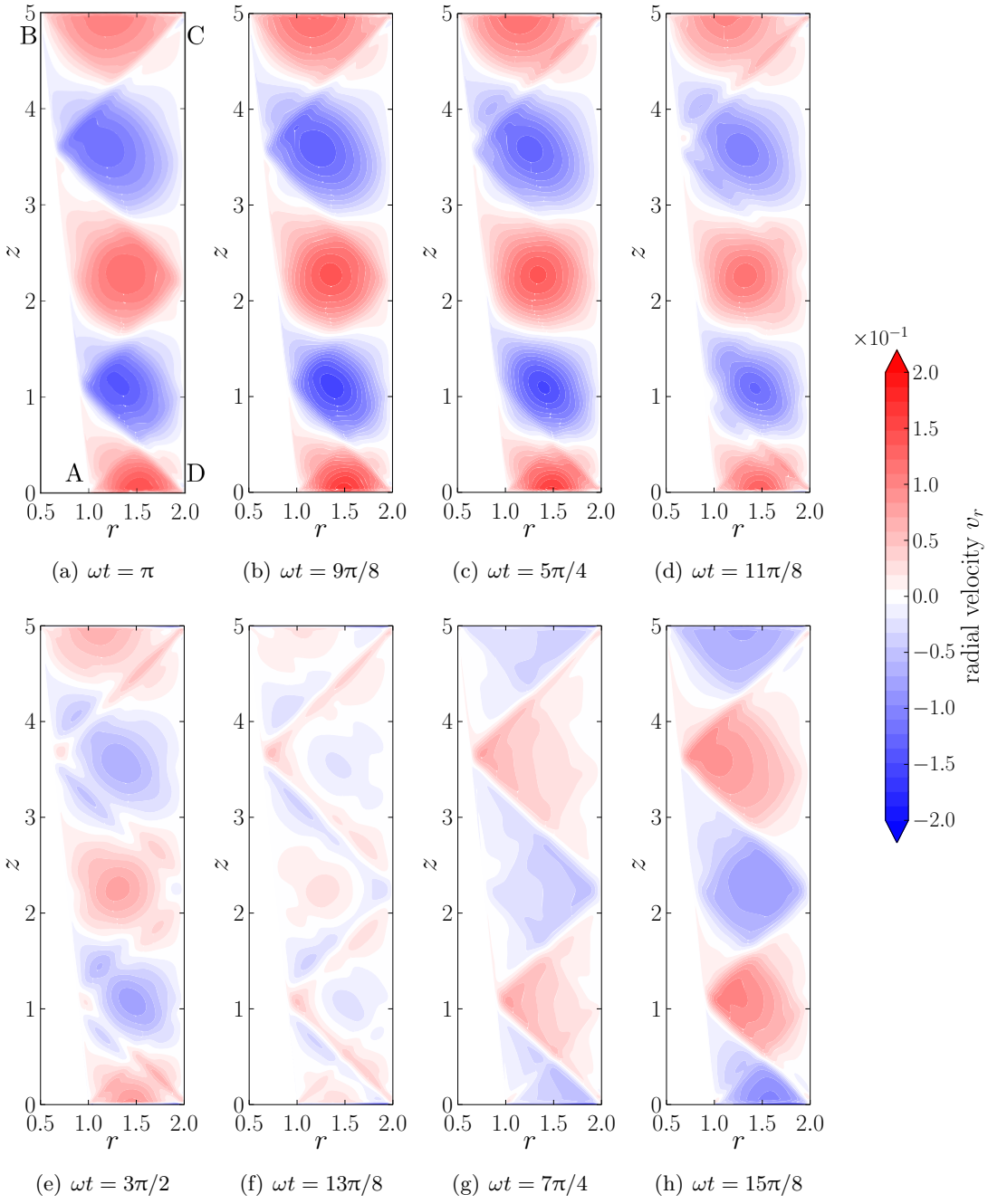

(a) $\omega t = \pi$ (b) $\omega t = 9\pi/8$ (c) $\omega t = 5\pi/4$ (d) $\omega t = 11\pi/8$

(e) $\omega t = 3\pi/2$ (f) $\omega t = 13\pi/8$ (g) $\omega t = 7\pi/4$ (h) $\omega t = 15\pi/8$

Figure 4.7: Contours of the radial velocity v_r in a radial-axial section at different libration phases ωt in the retrograde half of a libration period ($\pi \leqslant \omega t < 2\pi$) after a transient stage of 76 libration periods has passed. The flow is excited by lids plus outer cylinder libration at $\omega = 1.38$ for the default values of the dimensionless parameters $R = 0.2$ and $E = 3.19 \times 10^{-5}$. Red (blue) corresponds to radially outward (inward) flow. The flow exhibits a strong eigenmode resonance: the 'surviving' $(1, 4, 0)$ mode of the straight annulus excited which was expected at $\omega = 1.4$ (see figure 4.6). The tilted-W pattern connecting the two outer corners C and D is much more localised here than it is in figure 4.6, which indicates a frequency shift of the LONO frequency induced by the presence of a viscous boundary layer.

Figure 4.7 shows the radial velocity v_r in a radial-axial section of the annulus at different libration phases ($\omega t = \text{const}$) for the flow excited by lids plus outer cylinder libration at the *resonant* libration frequency $\omega = 1.38$. (As we will discuss further in chapter 6, such resonant excitation of a normal mode yields a significant increase of the kinetic energy stored in the system.) The resonance is observed at a smaller libration frequency than expected from ray tracing, which hints at a reduction of the aspect ratio of the domain volume due to the presence of a boundary layer which is inaccessible to the waves.

In figures 4.7(a–d, h), a smooth basin-scale pattern is clearly dominant and reminiscent of a normal mode of the straight annulus. The normal mode excited here consists of 4 antinodes in axial direction and 1 antinode in radial direction. The flow is axisymmetric, which means the $(1, 4, 0)$ has indeed been excited by libration of the lids together with the outer cylinder. Moreover, a tilted-W pattern is also visible and appears to be more localised than in figure 4.7. This is another indicator for the effective annulus geometry being modified by viscosity such that the frequency of the $(1, 4)$ LONO is shifted to $\sigma \approx 1.38$. The $(1, 4)$ LONO of modified frequency is directly visible by a tilted-W pattern that connect the two outer corners C and D and is formed by the corner beams.

Corner beams result from the librational forcing applied to the annulus, whereas the normal mode exists independently of the forcing due to the confinement geometry. It would be interesting to know if the normal mode itself is excited by the corner beams as suggested by Boisson *et al.* (2012), or if it is excited by the boundary condition plus boundary layer flow (Lopez & Marques, 2011), or by corner beams and boundary condition together (Lopez & Marques, 2014). The problem is complicated but of fundamental relevance since one asks if the corner beams can be represented by series expansion into eigenmodes of the confinement. At present, it seems that the corner beams can be interpreted as a sort of detached boundary layer. One might therefore speculate that a normal mode is driven by the interference pattern of velocity shear, which results from the (quasi-linear) superposition of the corner beams excited.

A definite answer to the question raised is beyond the scope of this work, but the interested reader is referred to the PhD thesis of Ghasemi V. (2016), who discusses the problem in more detail and addresses also the relevance of curvature terms (radii of the cylinders), which has not been in the focus of this work.

Helicity density and the propagation of wave energy

We follow the structure of section 4.1 and look into time slices of the helicity density for the LONO frequency $\omega = 1.40$ and the resonant excitation of the 'surviving' normal mode at $\omega = 1.38$ for the time series shown in figures 4.6 and 4.7 respectively.

Figure 4.8 shows contours of the helicity density $\boldsymbol{v} \cdot \boldsymbol{\zeta}$ in a radial-axial section at different libration phases ($\omega t = \text{const}$) for the flow excited by lids plus outer cylinder libration for default dimensionless parameters $R = 0.2$, $E = 3.19 \times 10^{-5}$. Red colour (solid contours) correspond to positive helicity (right-handed spiral structures in the velocity field); blue colour (dashed contours) correspond to negative helicity (left-left handed spiral structures in the velocity field). Equation (2.30) yields that positive (negative) helicity corresponds to wave energy propagating downward (upward). Unlike the wave attractor case shown in figure 4.2, the helicity evolution is almost symmetric in the prograde and retrograde libration half-period so that only the phases $\omega t = \pi$, $3\pi/2$ are shown in figures 4.8(a, b) and 4.8(c, d), but for two different libration frequencies $\omega = 1.40$ and $\omega = 1.38$ respectively. The temporal symmetry in the helicity evolution seems to be due to the excitation of a standing wave pattern, say a (normal) mode.

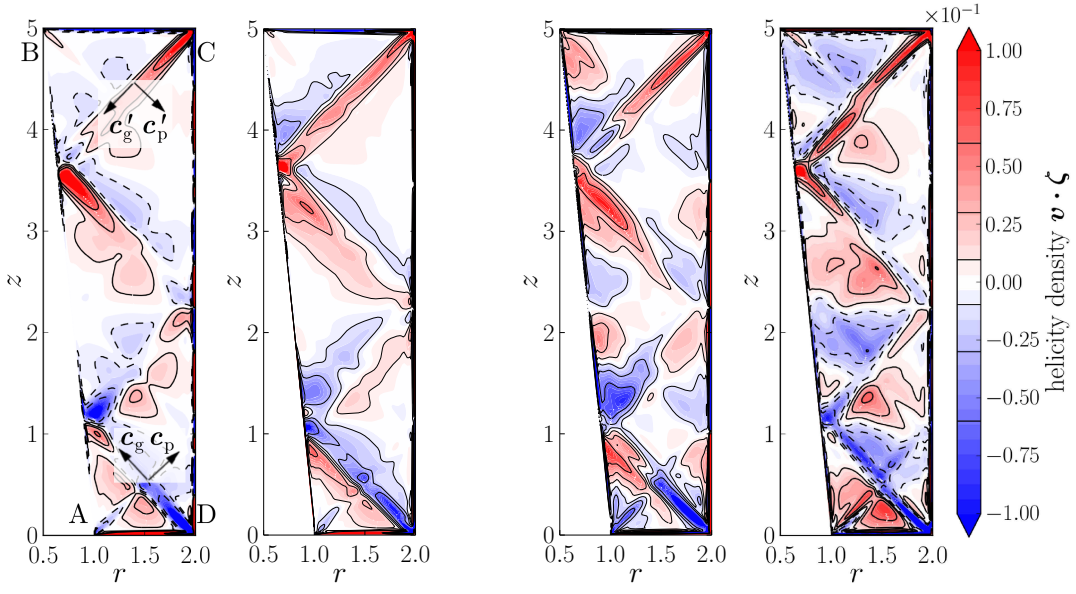

(a) $\omega t = \pi$ (b) $\omega t = 3\pi/2$ (c) $\omega t = \pi$ (d) $\omega t = 3\pi/2$

Figure 4.8: Contours of the helicity density $\boldsymbol{v}\cdot\boldsymbol{\zeta}$ in a radial-axial section at different libration phases ωt in the retrograde libration half-period ($\pi \leqslant \omega t < 2\pi$). The flow is excited by lids plus outer cylinder libration at $\omega = 1.40$ (a, b) and $\omega = 1.38$ (c, d) for the default values of the dimensionless parameters. The tilted-W pattern corresponding to the $(1, 4)$ LONO can be discerned in (a–d) due to the corner beams. Wave energy propagates upward from the bottom corners (negative helicity) and downward from the upper corners (positive helicity). Schematic phase velocities $\boldsymbol{c}_\mathrm{p}$, $\boldsymbol{c}_\mathrm{p}'$ and group velocities $\boldsymbol{c}_\mathrm{g}$, $\boldsymbol{c}_\mathrm{g}'$ in panel (a) have been repeated from figure 4.6(a). A smooth oscillation pattern of the $(1, 4, 0)$ mode can be discerned in panels (c, d).

Figures 4.8(a, b) show the helicity density at the libration frequency $\omega = 1.40$, which corresponds to the $(1, 4)$ LONO predicted by ray tracing (see figure 2.11(b)). The corner beams from corners C and D are dominating the helicity density, especially in figures 4.8(b), so that a tilted-W pattern can be discerned connecting these corners. Wave energy propagates upward from corners A and D (blue), but downward from corners B and C (red), which is in agreement with linear wave theory (remember that $\boldsymbol{e}_z \cdot \boldsymbol{c}_\mathrm{g} \propto -\boldsymbol{v}\cdot\boldsymbol{\zeta}$ as noted in section 4.1). The snapshots of the helicity density have been taken for the statistically stationary state in which several wave beams are superposed. The helicity density of the resulting interference pattern is time-dependent as can be seen by comparing figures 4.8(a, b) at around $(r, z) \approx (1.5, 1.5)$, which is due to interference of the corner beams.

Figures 4.8(c, d) show the helicity density at the libration frequency $\omega = 1.38$, which corresponds to the $(1, 4, 0)$ mode resonantly excited by libration. The wave beams above the frustum reflections are only visible during part of the libration period and there is a complex oscillation pattern visible between the tilted-W-like corner beams. The oscillation pattern owes its existence to the normal mode excited by means that approximate mirror planes are visible at $z \approx 1.2$, 2.4, 3.5. In addition there is a superposition with the corner beams which are always present (similar to Ghasemi V., 2016). The discussion with respect to the corner beams works out similar to the previous paragraph, but the interesting point is related to the helicity density of the normal mode.

A comparison of figures 4.8(c, d) to 4.8(a, b) reveals the additional features that result from an excitation of the normal mode. The most prominent new features are the helicity 'dipoles'[5] in figures 4.8(d) located at around $z \approx 1.1$, 2.3, 3.6 and $r \approx 1.5$, that is, located inside the small rhomboids formed by the two tilted-W patterns that connect the corners C, D and A, B (compare to figure 2.11(b)). The helicity 'dipoles' correspond to the velocity anti-nodes (see figure 4.7). The fourth helicity 'dipole', though, is cut in half; one half is next to the upper lid and the other half with opposite sign next to the bottom lid. Helicity can be associated with spiral structures in the velocity field (e.g. Kurgansky, 2002, pp. 26, 29), hence, the helicity 'dipoles' hint at a complicated 3-D flow structure related to the $(1, 4, 0)$ mode but the flow is still axisymmetric.

Note that the helicity density in the fluid bulk in figure 4.8 is of the order $|\boldsymbol{v}\cdot\boldsymbol{\zeta}| \sim 10^{-1}$, that is, approximately eight times larger than for the rhomboidal wave attractor (see figure 4.2). In the oscillating boundary layers over the librating wall segments, however, helicity magnitudes are comparable and can be as large as $O\left(10^{1}\right)$. The normal mode excited modifies the oscillating boundary layers as can be seen, for example, at the outer cylinder. Comparing figure 4.8(c) to 4.8(a) shows that the helicity density exhibits four elongated pieces along $\overline{\mathrm{CD}}$, for which sign alternates $(+1, -1, +1, -1)$ when the normal mode is excited. One can hypothesize that the oscillating boundary layer over the lids is also modified so that the emission of corner beams, which leads to the enhancement observed in figure 4.8(c) with respect to the tilted-W pattern connecting corners A andB. It needs to be emphasized that the corner beams are related to the forcing and not part of the 'surviving' $(1, 4, 0)$ normal mode of the straight annulus (compare to Borcia *et al.*, 2014; Borcia & Harlander, 2012).

Comparison between DNS results and laboratory measurements

Let us close this section with a comparison of the flow patterns obtained by DNS to those observed in the laboratory measurements analogously to the wave attractor case. Unfortunately, no fine-grained scan of the libration frequency has been performed in the laboratory and only the measurement at $\omega = 1.4$ within ± 0.1 (see Klein *et al.*, 2014; Seelig, 2014, p. 68). Moreover, the laboratory measurement has been performed for $R = 0.4$, which is beyond the centrifugal stability threshold of the boundary layer (see Sauret *et al.*, 2012) due to which near-wall turbulence has to be expected (e.g. Ghasemi V. *et al.*, 2016). It is not the objective here to discuss the unstable flow so that the numerical simulations are performed for the standard Rossby number $R = 0.2$.

Figure 4.9 compares the flow structures of the numerical solution to those measured in a corresponding laboratory experiment (see Seelig, 2014, pp. 54, 58). Similar to the rhomboidal wave attractor (figure 4.3), the numerical solution shown in figure 4.9(a) visualises the flow by contours of the radial velocity v_r, repeating figure 4.6(a), whereas the flow in the laboratory experiment shown in figure 4.9(b) is visualised by the reflected light intensity I. Figures 4.9(a, b) exhibit similarities and differences. Two tilted-W patterns can be discerned that connect the outer two corners or the inner two corners respectively. The tilted-W patterns are realisation of the $(1, 4)$ LONO and correspond to the dashed and dotted lines in figure 2.11(b). The origin of the tilted-W pattern is the excitation of corner beams as discussed above. The width of the wave beams in the numerical simulations and the measurements is also comparable.

[5] A helicity 'dipole' can be thought of as an oscillatory circulation cell with the velocity but not the helicity changing sign periodically (conceptually. the flow structure of a helicity 'dipole' is similar to the steady Taylor vortices shown, for example, by Marcus, 1984, figure 20).

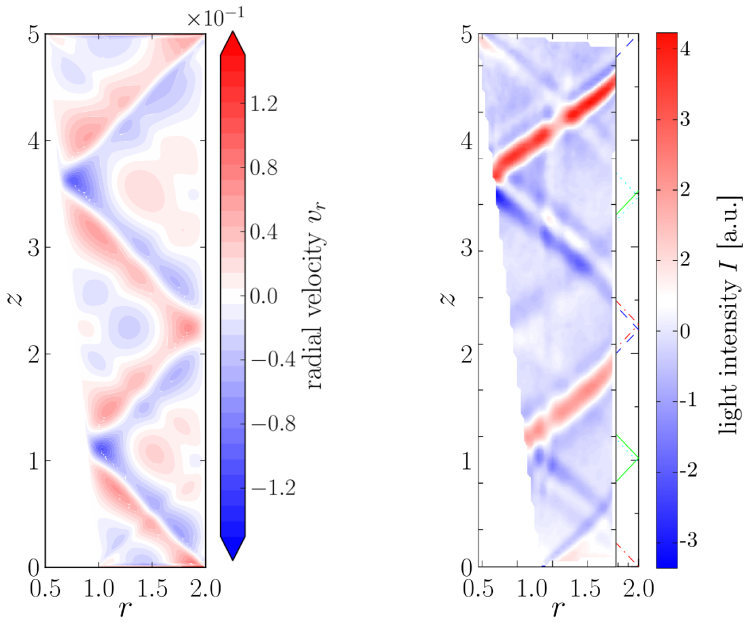

(a) DNS at $\omega t = 0$

(b) laboratory measurement at $\omega t = \text{const}$

Figure 4.9: Comparison of DNS and laboratory measurement regarding the spatial patterns for the flow excited by lids and outer cylinder libration with libration frequency $\omega = 1.4$ at Ekman number $E = 3.19 \times 10^{-5}$, but for different Rossby numbers R. Panel (a) shows the radial velocity v_r at libration phase $\omega t = \pi$ ($R = 0.2$; repeated from figure 4.6(a)). Panel (b) shows a snapshot of the reflected light intensity I for the flow in the laboratory experiment (from M. Klein *et al.* (2014). 'Inertial wave excitation and focusing in a liquid bounded by a frustum and a cylinder'. *J. Fluid Mech.*, **751**, p. 270, figure 9(b), reproduced with permission). The inclinations and widths of the wave beams in the simulated and measured fields are in very good agreement. The measurement technique used immersed platelets and is more sensitive to shear than it is to the velocity magnitude.

Altogether, the visual impression of the velocity field simulated and the light intensity measured is slightly different because the optical measurement procedure. The discussion of the rhomboidal wave attractor measurements applies here identically, which means different colours along the wave beam in figure 4.9(a) than in (b) are related to the sensitivity of the measurements to the shear rather than the velocity amplitude. The inclinations of the wave beams is $\vartheta \approx 46°$ in the numerical simulations and the laboratory measurements, which is in good agreement with linear theory (see equation (2.24)). However, the measurements exhibit a tilted-W pattern which is increasingly distorted towards the outer cylinder. This indicates that the confidence interval of the slope, $\Delta\vartheta \approx 1°$, cannot be fulfilled for $r > 1.5$. The reason is the lens effect due to curvature of the outer glass cylinder, sensed much stronger here than for the rhomboidal wave attractor, for which we noted that total reflection does not allow optical measurements for $r > 1.8$. Similar to the wave attractor case, the masked part in figure 4.9(b) has been replaced by wave rays (see Klein *et al.*, 2014; Seelig, 2014, p. 59).

Note that the inaccuracy of the wave beam inclination of $\Delta\vartheta \approx 1°$ yields an inaccuracy of the (forcing) frequency of $\Delta\omega \approx \Delta\sigma \approx 0.03$ (see equation (2.24)). Hence, it might well be that the $(1, 4, 0)$ normal (see figure 4.7) is excited in the laboratory experiment by a nominal libration

frequency of $\omega = 1.4$, but it is simply not visible in figure 4.9(b) because of the insensitivity to the velocity amplitude (compare to Borcia *et al.*, 2014).

Unfortunately, a clarification is not possible here since no velocity measurements are available for the lids and outer cylinder libration case. On the basis of the numerical simulations performed for $E = 3.19 \times 10^{-5}$, $R = 0.2$ with $\omega = 1.4$ (figures 4.6) and $\omega = 1.38$ (figure 4.7), as well as the scaling factors listed in table 4.1, the velocities in the bulk may reach 10 mm s^{-1} or even 25 mm s^{-1} when the mode is excited. Simulations for $R = 0.4$ (not shown here) yield fluid velocities in the bulk as large as 30–40 mm s^{-1}, which is supposedly the case in the measurements shown in figure 4.9(b).

Frequency-filtered radial velocity component

Normal mode excitation yields large kinetic energy in the system (to be discussed in chapter 6), which means the $(1, 4, 0)$ mode is a candidate to exhibit non-linear effects. In worst case, this could result in a turbulent collapse (e.g. Kerswell, 1999; McEwan, 1970). Of course, the numerical solution shown in figure 4.7 is far from such a scenario since it remained axisymmetric and stable up to 160 libration periods (the longest simulation time used in this study) without turbulent degeneration. In the following, the time series of the radial velocity v_r is projected on the harmonic frequencies $\sigma_l = l\omega$ in order to obtain velocity amplitudes $v_{r,l\omega}$ and phases $\theta_{r,l\omega}$ analogously to the rhomboidal wave attractor studied earlier (see equation (4.1) and appendix A.3). As before, weak non-linearity permits to restrict the attention to $l = 1, 2, 3$.

Figure 4.10 shows the Fourier decomposition of the radial velocity v_r for the $(1, 4, 0)$ mode excited by lids and outer cylinder libration corresponding to the snapshots shown in figure 4.7. The flow has been excited with the reduced libration frequency $\omega = 1.38$, but is otherwise obtained for the default parameters $R = 0.2$, $E = 3.19 \times 10^{-5}$. Following equation (4.1), figures 4.10(a–c) show the amplitudes $v_{r,l\omega}$ for the forcing frequency ($l = 1$) and its two harmonics ($l = 2, 3$), whereas figures 4.10(d–f) show the corresponding phases $\theta_{r,l\omega}$. Comparing the orders of magnitude of the radial velocity amplitudes, panels (a–c), tells us that the majority of the variability is concentrated at the forcing frequency. In the bulk, the amplitudes of the radial velocities reach 2×10^{-1} in panel (a), 5×10^{-3} in panel (b), and 10^{-3} in panel (c). At the forcing frequency, the velocities excited do not reach $O(1)$ of the wall libration which hints at a small wave excitation efficiency of the librational forcing (to be discussed in chapter 6). The velocity amplitudes of the harmonics are smaller by factors $v_{r,2\omega}/v_{r,1\omega} \sim 2 \times 10^{-2} \ll R$, but $v_{r,3\omega}/v_{r,2\omega} \sim 0.2 = R$. The R^{l-1}-scaling is violated at the forcing frequency, whereas the higher harmonics differ by the expected factor of R. The violation of the scaling at the forcing frequency is interesting as it hints at the dominance of linear dynamics when a normal mode is resonantly excited even under the full non-linear Navier–Stokes equations.

At the *forcing frequency*, the radial velocity amplitude $v_{r,1\omega}$ in figure 4.10(a) exhibits the 4 antinodes of the normal mode, which seem to appear as circulation cells reminiscent of Taylor vortices (Andereck *et al.*, 1986). These circulation cells, however, are oscillatory here. Besides the mode, also the tilted-W pattern connecting the corners C and D can be discerned, which owes its existence to the corner beams excited by the librational forcing (see the paragraphs on the time dependency). The impression of the flow in figure 4.10(a) supports the speculation from above that the mode is excited by the interference pattern of the superposed corner beams, which means the normal mode is excited such that the shear is minimised. This hypothesis is supported by the phase $\theta_{r.1\omega}$ shown figure 4.10(d), in which the corner beams only yield small local deformation of the phase contours, but there are no phase rotations on short distance. The phase of the mode can adjust freely and develops in such a way that it matches the phase

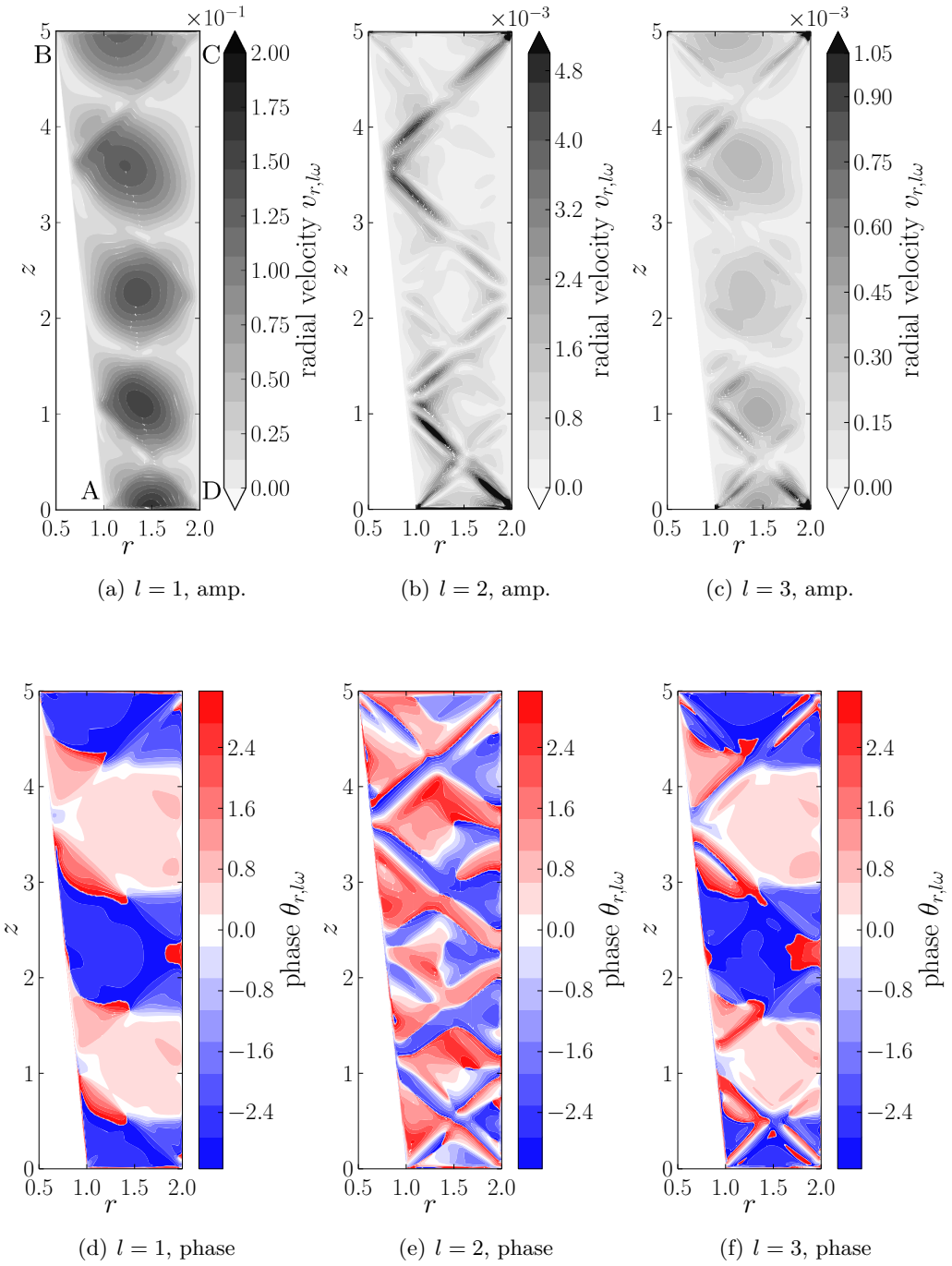

(a) $l = 1$, amp. (b) $l = 2$, amp. (c) $l = 3$, amp.

(d) $l = 1$, phase (e) $l = 2$, phase (f) $l = 3$, phase

Figure 4.10: Contours of the frequency-filtered radial velocity for the $(1, 4, 0)$ normal mode excited by lids plus outer cylinder libration with libration frequency $\omega = 1.38$ at default dimensionless parameters. Radial velocity amplitude $v_{r,l\omega}$ (a–c) and phase $\theta_{r,l\omega}$ (d–f) are shown in a radial-axial section for the forcing frequency ω ($l = 1$) and its harmonics $l\omega$ ($l = 2, 3$). The phase has values in $[-\pi, \pi)$, where red (blue) corresponds to the stationary oscillation being ahead (behind) the reference phase $l\omega t$. The normal mode pattern is visible in (a, d), but also in (c, f). The harmonic 2ω is a 'bound mode' for which the mode pattern is not visible (b, e). The harmonic 3ω is also a 'bound mode' which exhibits the spatial structures of the source frequencies 1ω and 2ω (c, f).

of the interference pattern imposed by the tilted-W pattern (for an in-depth discussion see Ghasemi V., 2016).

The important point here is that amplitude and phase, figures 4.10(a, d), are dominated by basin-scale structures which yields small gradients and, in particular, small velocity shear $|\partial v^i/\partial x^j| \ll 1$. This implies small non-linear modifications since the momentum advection, $-Rv^j\,(\partial v^i/\partial x^j)$ as given by equation (2.6), is proportional to the velocity shear. Consequently, the non-linear forcing of harmonic frequencies is much weaker than expected from the velocity amplitudes alone.

Amplitude and phase of the *harmonics* $l = 2, 3$ are shown in figures 4.10(b, c) and 4.10(e, f) respectively. The harmonic frequencies $2\omega = 2.76$ and $3\omega = 3.14$ are well beyond the linear inertial wave band and sometimes called 'bound modes' since the corresponding kinetic energy can only be redistributed by molecular diffusion or by non-linear advection, but not in the form of inertial waves. This circumstance is clearly visible by the harmonics exhibiting the same characteristic inclination $\vartheta \approx 46°$ and the tilted-W patterns as the $(1, 4)$ LONO associated with the driving flow at the forcing frequency $\omega = 1.38$.

Interestingly, the first harmonic ($l = 2$) shown in figures 4.10(b, e) does not exhibit the normal mode pattern, but there is structure on smaller spatial scales visible in the solution. Velocity shear and non-linearity are localised at the edges of the corner beams due to which less intense wave beams arise on each side and parallel to the tilted-W patterns (see the dashed and dotted lines in figure 2.11). Hence, the 2ω 'bound mode' results from a self-interaction of the driving flow oscillating with the libration frequency ω (see Lam & Maas, 2008; Tilgner, 2007, but here applied to the 2ω harmonic instead of the mean flow).

Strikingly, the second harmonic ($l = 3$) shown in figures 4.10(c, f) exhibits the normal mode pattern again in contrast to the first harmonic. The spatial pattern of the amplitude appear as composite of the source frequencies ω and 2ω, that is,

$$v_{r,3\omega} \approx v_{r,1\omega}\, v_{r,2\omega} \qquad \text{and} \qquad \theta_{r,3\omega} \approx \theta_{r,1\omega} + \theta_{r,2\omega}. \tag{4.4}$$

The latter equations reflect the mixing of complex amplitudes in the non-linear momentum advection, but they are only approximately valid since we have neglected to compute the gradient and to consider the other velocity components. Hence, the antinodes of the normal mode are properly visible also in the centre of the domain at $(r, z) = (1.4, 2.2)$ even though $v_{r,2\omega}$ vanishes there.

Spatial distribution of the kinetic energy dissipation rate

The linear and non-linear properties of the numerical solution to the $(1, 4, 0)$ mode excited have been discussed also with respect to the velocity shear $\boldsymbol{\nabla} \circ \boldsymbol{v}$ which has not been shown explicitly though. Since the velocity shear is closely related to the dissipation of kinetic energy, let us continue with the dissipation function (see equation (4.2)). We proceed analogously to the rhomboidal wave attractor case (see section 4.1) and compute the frequency-filtered time-averaged contributions $\Phi_{l\omega}$ for $l = 1, 2, 3$ according to equation (4.3). In the following, the dissipation properties of the mode will be outlined and compared to the rhomboidal wave attractor.

Figure 4.11 shows the frequency-filtered time-averaged contributions $\Phi_{l\omega}/E$ to the dissipation function for the non-linear viscous solution to the $(1, 4, 0)$ mode excited by lids plus outer cylinder libration with $\omega = 1.38$ and default values of the Ekman and Rossby numbers. $\Phi_{l\omega}/E$ denotes the contributions to the dissipation function rescaled with the Ekman number and

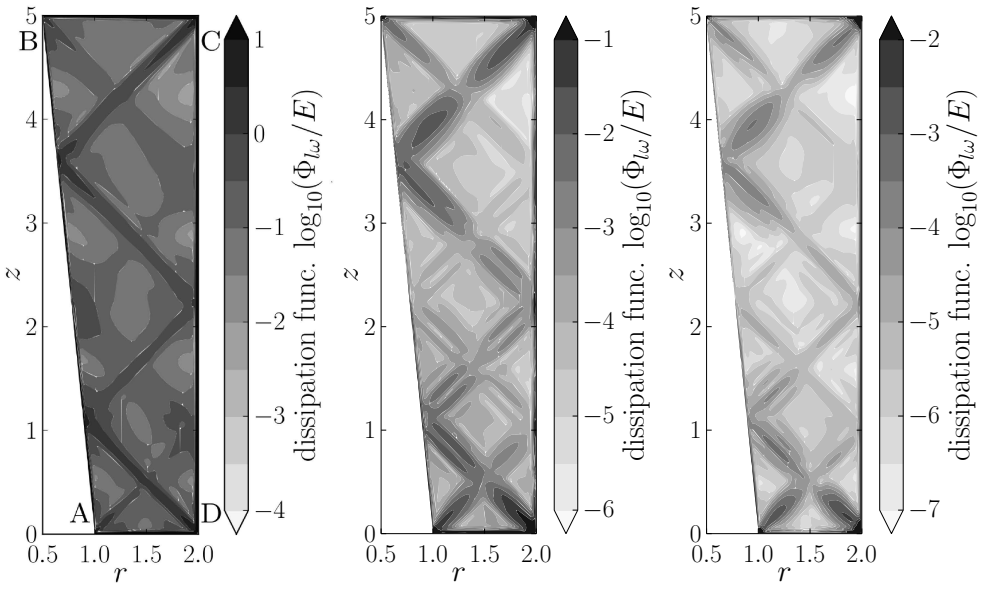

(a) $l = 1$ (b) $l = 2$ (c) $l = 3$

Figure 4.11: Contours of the frequency-filtered time-averaged dissipation function for the $(1, 4, 0)$ mode excited by lids plus outer cylinder libration with libration frequency $\omega = 1.38$ at default dimensionless parameters $R = 0.2$, $E = 3.19 \times 10^{-5}$. The contributions $\Phi_{l\omega}$ $(l = 1, 2, 3)$ are shown in logarithmic scale in a radial-axial section for the forcing frequency ω (a) and the two lowest harmonics 2ω (b) and 3ω (c). The energy dissipation at the forcing frequency is localised at the wave beams, here the tilted-W patterns of the $(1, 4)$ LONO (a). The harmonics are 'bound modes' and dissipation is localised at the edges of the corner beams where non-linear forcing by the non-linear term in the Navier–Stokes equations is largest (b, c). The $(1, 4, 0)$ mode pattern (see figure 4.10(a)) is not visible here, which suggests that the normal mode is only weakly damped.

corresponds to a norm of the strain rate tensor. The contours in figure 4.11 are plotted in a radial-axial section of the annulus for the forcing frequency ω $(l = 1)$ and the two lowest harmonics $l\omega$ $(l = 2, 3)$ in analogy to figures 4.10(a–c).

At the *libration frequency* $(l = 1)$, figure 4.11(a), shows that the energy dissipation is strongly localised. First, energy dissipation is localised in the boundary layer over the librating lids and outer cylinder with $\Phi_{1\omega}/E$ as large as $O\left(E^{-1}\right)$ similar to the librating frustum wall (see section 4.1). Second, energy dissipation is localised at the two tilted-W patterns that connect the corners C, D and A, B, respectively, due to the excitation of corner beams. The contribution $\Phi_{1\omega}$ to the dissipation function does not exhibit the $(1, 4, 0)$ normal mode pattern, which is in strict contrast to the radial velocity amplitude $v_{r,1\omega}$ (see figure 4.10(a)), which agrees well with a recent study on the straight annulus (Borcia *et al.*, 2014) and even a box (Boisson *et al.*, 2012). Hence, the selection of the quantity used for flow visualisation can be more crucial for normal modes than for the wave attractors. The rhomboidal wave attractor could be discerned in the velocity field and the dissipation function, whereas a normal mode excited by libration cannot be visualised with the dissipation function, say velocity gradients in general.

It is worth noting that the scale used in figure 4.11(a) is two orders of magnitude larger than for the wave attractor case (compare to figure 4.5(a)), which reflects the larger fluid velocities

induced in the lids plus outer cylinder libration case whereas the corner beams propagating along the tilted-W patterns are also narrower than the simulated wave attractor. Contrary to intuition, the reason is absence of focusing, which means the corner beams here are fed directly on the tilted-W pattern and do not leave the latter while subject to damping. By contrast, the corner beams in the case of the wave attractor are focused gradually to the wave attractor which leads to a smooth distribution of energy and energy dissipation in parts of the domain in the continuously forced solution (as discussed for figure 4.5(a)).

Furthermore, the reflections of the corner beams in figure 4.11(a), especially at the frustum, yield a local increase of the energy dissipation rate and hints at an additional energy loss of the wave beam when it reflects at the wall.

The contributions to the dissipation function at the *harmonics* $l = 2, 3$ are shown in figures 4.11(b, c) but possess different scales. The scale reduces in steps of one order of magnitude from figure 4.11(a) to 4.11(c). A synopsis of the radial velocity amplitudes (see figures 4.10(b, c)) and the energy dissipation filtered at the forcing frequency (see figure 4.11(a)) yields the expectation that the dissipation at the harmonic 'bound modes' $2\omega = 2.76$ and $3\omega = 4.14$ should be localised along the tilted-W patterns of the corner beams. This expectation is precisely fulfilled in figures 4.11(b, c). Dissipation is observed along the edges of the corner beams where shear and non-linear forcing is large. Since the kinetic energy cannot be redistributed by inertial waves, the contributions $\Phi_{2\omega}$ and $\Phi_{3\omega}$ exhibit the same slopes as $\Phi_{1\omega}$.

The only visual difference between figures 4.11(b, c) concerns the strength of the shading, which is an artefact of the contour levels used. The implication is that basin-scale gradients do not notably contribute to the dissipation of kinetic energy at any of the frequencies $\sigma_l = l\omega$ that contain the variability of the flow. Hence, the non-linear modes excited are able to store large kinetic energy. It is likely that an increase of the Rossby number (stronger non-linearity) or an optimal perturbation yields a collapse of the normal mode by releasing the energy stored in the basin-scale fluid oscillation to turbulence (see McEwan, 1970, hypothesizing that the sliced cylinder exhibits neutral orbits and 'surviving' normal modes). However, such a collapse has *not* been observed for the parameters used in this study. It is important to note that an intense accumulation of kinetic energy is only possible for normal modes since there is no net focusing of inertial waves. This is different for wave attractors, which always exhibit spatially compression in one direction due to the action of focussing. It is therefore interesting to study in which sense the fluid behaves differently when a wave attractor is excited compared to when a normal mode is excited (we will address the question of resonance later in chapter 6).

In summary, we have gained a detailed understanding of the linear and non-linear properties of the weakly non-linear solutions to the Navier–Stokes equations that are dominated by inertial waves. We have investigated the radial velocity, the frequency-filtered radial velocity, as well as the energy dissipation. Weakly non-linear solutions require Rossby numbers $R \ll 1$ and velocity amplitudes $|\boldsymbol{v}| \lesssim 1$, so that the flow is stable and its variability given by the frequency ω and its lowest harmonics $l\omega$ $(l = 2, 3)$ (plus the mean flow; see Ghasemi V., 2016; Seelig, 2014). For the present study, the frequency filter has been optimised for numerical efficiency by studying the flow only at the harmonics $l\omega$. This procedure, though, only makes sense when the flow is stable and dominated by the harmonics of the forcing frequency. Filtering is useful for data compression when only a few frequencies are of interest, like here the forcing frequency ω and it s harmonics.

In the next section we will use the filtered velocity in order to perform a fair comparison between ray tracing and DNS. After that, the validity of filtering at harmonics will be discussed for Rossby number variations.

4.3 Comparison of ray orbits to frequency-filtered numerical solutions

The flow structures obtained by DNS have been discussed in the previous sections and have already been linked to ray tracing (RT). Two cases have been considered, the rhomboidal $(1,1)$ wave attractor excited by frustum libration (see section 4.1) and the $(1,4,)$ neutral orbit excited by lids plus outer cylinder libration (see section 4.2). The important result of both cases studied so far has been that the non-linear viscous solution to the Navier–Stokes equations is dominated by linear inertial waves by virtue that ray patterns obtained for wave frequencies $\sigma = 0.47$, 1.4 correspond to the spatial patterns excited by a libration frequencies $\omega = 0.47$, 1.4 respectively. However, the cases selected are very particular. As we know from the bifurcation diagram (see figure 2.9), complicated spatial structures are possible related to inertial waves and it is certainly worth to explore this by DNS for a few more frequencies. We continue to restrict our attention to low-order structures (LOWAs and LONOs) due to the comparably large Ekman numbers in the DNS.

In the following, a comparison of the wave patterns will be done separately for the case of frustum libration and the case of lids plus outer cylinder libration using the default dimensionless parameters $R = 0.2$ and $E = 3.19 \times 10^{-5}$, but varying the libration frequency ω. For a fair comparison of ray tracing and weakly-nonlinear DNS, frequency-filtered velocities are used, which are given by the complex amplitudes $\hat{\boldsymbol{v}}_{l\omega}$ ($l = 0, 1, 2, \ldots$; see appendix A.3). The velocity field of inertial waves has a 3-D structure, which suggests to give all velocity components equal weight, for example by computing the kinetic energy density $v^2/2$ (with $v \equiv |\boldsymbol{v}|$ for brevity). The kinetic energy density is positive definite but oscillates in time due to the librational forcing so that it has a non-zero mean. We restrict our attention to the dominating structures oscillating with the forcing frequency ω. The temporal average of the kinetic energy associated with the oscillation pattern observed at the forcing frequency is denoted $v_{1\omega}^2(\boldsymbol{r})/2$, which is obtained by the aid of equation (A.11), namely

$$\frac{v_{l\omega}^2}{2} = \frac{1}{4}\left(\hat{\boldsymbol{v}}_{l\omega}^{\dagger} \cdot \hat{\boldsymbol{v}}_{l\omega}\right). \tag{4.5}$$

Waves excited by frustum libration

Figure 4.12 shows the time-mean kinetic energy density $v_{1\omega}^2/2$ related to velocity components oscillating with the libration frequency ω together with ray orbits obtained by ray tracing (see section 2.4). Numerical simulations have been performed with the frustum in libration and for default dimensionless parameters (see table 4.1). The libration frequency increases from figure 4.12(a) to (f). The complexity of the spatial structures changes dramatically with the frequency parameter, which is in qualitative agreement with the bifurcation diagram (see figure 2.9). The energy density contours in figures 4.12(a–c) are scaled logarithmically, where each shade corresponds to a half an order of magnitude. The kinetic energy densities in figures 4.12(a–c) are two orders of magnitude larger than in figures 4.12(d–f), which hints at the excitation of inertial waves by frustum libration being more efficient at low frequencies than it is at higher frequencies (this will be discussed in more detail in chapter 6).

Furthermore, DNS and ray tracing (RT) have been performed for precisely the same geometry, that is, for the smoothed frustum as in the numerical grid (see figure 3.4). The dashed and dotted lines in figure 4.12 trace the first three reflections of the corner beams emitted from the lower and upper inner corners adjacent to the librating frustum. The solid line in figures 4.12(a–

c) and (e, f) gives the spatial structure of the corresponding low-order wave attractor (LOWA), whereas in figure 4.12(d) it is just a particular realisation of the low-order neutral orbit (LONO).

Figure 4.12(b) shows the rhomboidal $(1,1)$ wave attractor, where libration frequency ω and ray tracing frequency σ are identical ($\omega = \sigma = 0.47$). Indeed, the spatial pattern obtained by ray tracing are in very good agreement with those obtained by DNS. That is, the rays shown correspond very well to the maxima of the kinetic energy density.

By overlaying kinetic energy density with the rays, the effect of viscous broadening is visualised. The logarithmic scale exaggerates the smooth spatial distribution of the kinetic energy in the DNS somewhat. (In linear scaling, the localisation would be more prominent with an impression closer to the radial velocity as shown in figure 4.4(a).) Nevertheless, it is remarkable how well the flow patterns are captured by ray tracing here. A violation can only be observed along the librating frustum due to the presence of an oscillating boundary layer. Kinetic energy densities in the frustum boundary layer are of the order $v_{1\omega}^2/2 \sim 10^{-1}$, but this kinetic energy remains confined to the boundary layer. The boundary layer is visible in all panels of figure 4.12.

Figure 4.12(d) shows the $(1,2)$ LONO excited with $\omega = 0.9$ and the ray pattern obtained at a slightly lower frequency $\sigma = 0.8944$, because the ray pattern would diverge notably already since it is periodic only for a very specific frequency. The spatial pattern exhibits a tilted-V pattern (compare to figure 2.11(a)) and is generally much simpler than the $(1,1)$ wave attractor, but the kinetic energy densities are almost two orders of magnitude smaller. The corner beams emitted from the two inner corners are superposed along the tilted-V pattern and exhibit destructive interference so that the kinetic energy density is small at the dashed line that connects the inner two corners (the other tilted-V pattern). The solid ray orbit is a particular realisation of the $(1,2)$ LONO and approximately traces the kinetic energy maxima located next to but not on the tilted-V pattern due to imperfect destructive interference of the corner beams.

Imperfect interference of the corner beams has two main reasons. First, the variable radius of the frustum due to which libration velocities at the top inner corner are lower than at the bottom inner corner. Second, viscosity and the presence of a boundary layer modifies the effective confinement geometry due to which the LONO pattern and the corresponding frequency eigenvalue are modified. The frequency shift is confirmed by DNS since the $(1,2,0)$ mode[6] can be excited with the libration frequency $\omega = 0.88$ rather than $\omega = 0.90$, which agrees with the viscous frequency shift of $\Delta\sigma \approx -0.02$ noted earlier (compare to Borcia *et al.*, 2014).

Figures 4.12(a, c, f) show the $(2,1)$ LOWA, the $(2,3)$ LOWA, and the $(1,3)$ LOWA excited by libration frequency of (a) $\omega = 0.22$, (c) $\omega = 0.70$, and (f) $\omega = 1.18$ respectively. The ray orbits shown correspond to the frequency parameter (a) $\sigma = 0.22$, (c) $\sigma = 0.705$, which is slightly larger than the libration frequency, and (f) $\sigma = 1.18$. The visual correspondence is similar to the rhomboidal wave attractor: the slopes and the spatial patterns themselves are in good agreement, but the wave attractor (solid line) is more complex and possesses more reflection points. More reflections make the wave attractors more sensitive to modifications of the geometry or frequency drift, both induced by viscosity. So, in contrast to the rhomboidal wave attractor (see figure 4.12(b)), the rays do no longer correspond to the maximum of the kinetic energy density. In contrast to the rhomboidal $(1,1)$ wave attractor, the $(2,3)$ and $(1,3)$ LOWAs shown in figures 4.12(c, f) occupy theoretical frequency bands that are smaller than the viscosity-induced shift of the frequency that yields a DNS pattern corresponding to the ray pattern.

[6]Details of the resonance will be discussed further in chapter 6.

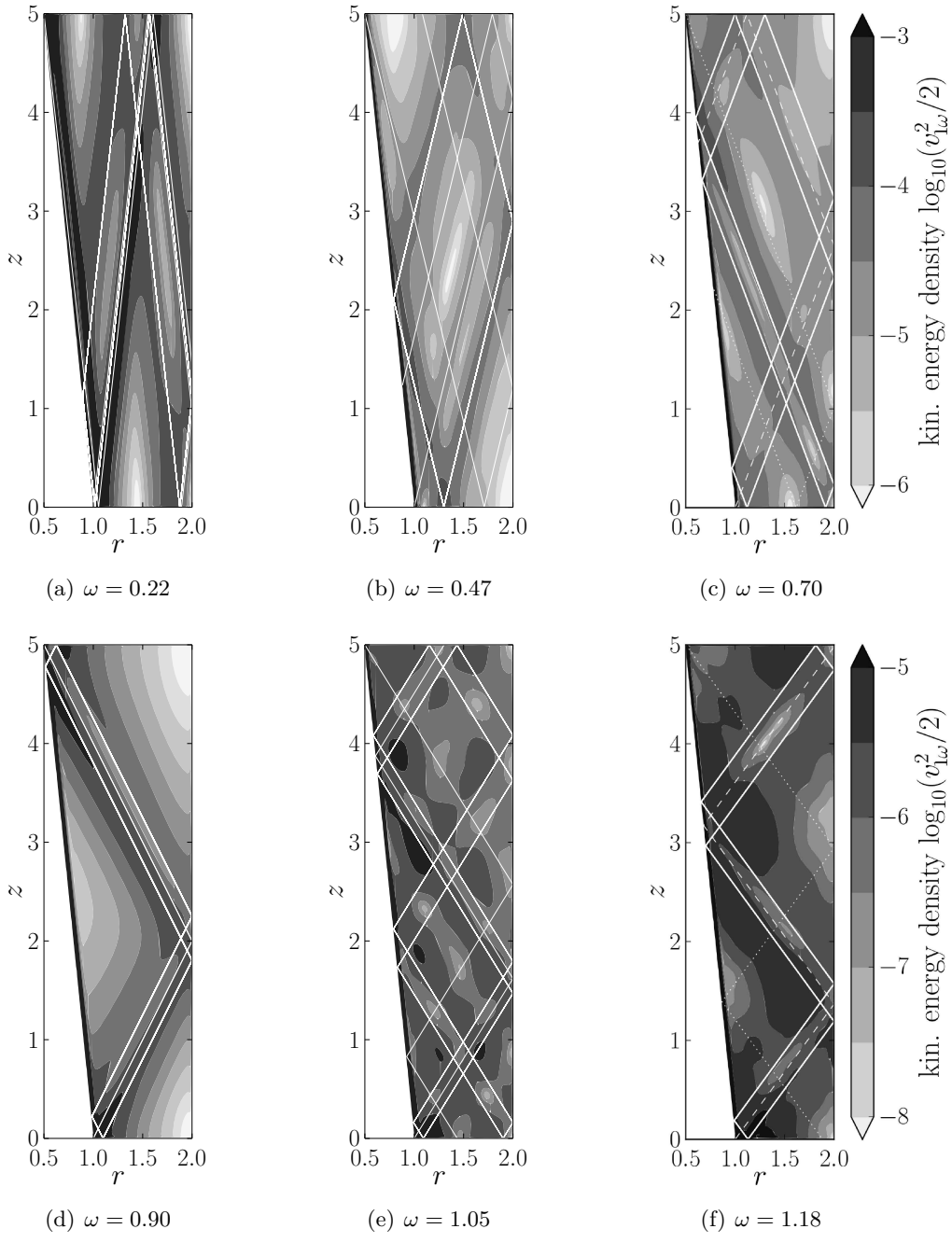

(a) $\omega = 0.22$ (b) $\omega = 0.47$ (c) $\omega = 0.70$

(d) $\omega = 0.90$ (e) $\omega = 1.05$ (f) $\omega = 1.18$

panel	(a)	(b)	(c)	(d)	(e)	(f)
ω	0.22	0.47	0.70	0.90	1.05	1.18
σ	0.2200	0.4700	0.7050	0.8944	1.0510	1.1800

Figure 4.12: Contours of the filtered kinetic energy density $v_{1\omega}^2/2$ in the case of the flow is excited by frustum libration for various libration frequencies ω. Corresponding wave rays are plotted on top with frequency σ (see the table). The solid line shows the LOWA or LONO; dashed and dotted lines show the corner beams up to the third reflection. The correspondence between DNS and RT is best for the $(1, 1)$ LOWA in (a), but worsens with an increasing number of ray reflections. See the text for details.

In effect, ray tracing should be performed for an effective geometry that takes the presence of the boundary layer into account (see Borcia *et al.*, 2014), though, this requires knowledge of the boundary layer structure. The latter will be addressed in more detail in chapter 5.

Figures 4.12(e, f) show the $(2,5)$ LOWA and the $(1,3)$ LOWA, which have been excited by libration frequency $\omega = 1.05$ and 1.18 respectively. The ray orbits shown correspond to the frequency parameter (e) $\sigma = 1.051$ and (f) $\sigma = 1.18$, which is slightly larger than the libration frequency. The visual correspondence is not as good as it was in the other examples shown. The slopes of the spatial patterns is represented correctly, but the localisation of the kinetic energy along the ray patterns tends to vanish. For the $(2,5)$ LOWA (see figures 4.12(e)), the frequency band of the wave attractor has decreased to $\Delta\sigma \approx 0.01$ (see figure 2.9 for $\sigma \approx 1.05$) and has been shifted entirely to lower frequencies due to viscosity. The numerical solution is reminiscent of an interference pattern, which seems to result from a superposition of the corner beam originating from the lower inner corner with its reflections.

Waves excited by lids plus outer cylinder libration

Figure 4.13 shows the time-mean kinetic energy density $v_{1\omega}^2/2$ related to velocity components oscillating with the libration frequency ω together with ray orbits obtained by ray tracing. The results are presented analogously to the frustum libration case discussed above (see figure 4.12). For later reference, the libration frequencies and the order of the ray orbits selected are partly different from those presented above; only $\omega = 0.90$ and $\omega = 1.18$ in figures 4.13(c, e) can be compared directly to figures 4.12(d, f). The numerical simulations have been performed with the lids and outer cylinder in libration for default dimensionless parameters $R = 0.2$, $E = 3.19 \times 10^{-5}$. As before, the libration frequency increases from figure 4.12(a) to (f) and the kinetic energy is plotted in logarithmic scale to emphasise the bulk flow. The energy scale is the same for all the panels in figure 4.13, which hints at the excitation of inertial waves by lids plus outer cylinder libration being much more efficient at higher libration frequencies ($\omega \gtrsim 1$) than for the frustum in libration (this will become clearer in chapter 6).

Moreover, the oscillating boundary layers over the librating outer cylinder and lids, in particular, are barely visible in figure 4.13. The boundary layer over the outer cylinder is frequency dependent (see equation (3.70)), but the lid boundary layer is very thin in general (we will explore this in more detail in chapter 5). Nevertheless, kinetic energy densities reach $v_{1\omega}^2/2 \sim 10^{-1}$ in the vicinity of the librating wall and yields strong shear near the librating walls.

As in figure 4.12, the dashed and dotted lines in figure 4.13 trace the first three reflections of the corner beams emitted from the outer and inner corners adjacent to the librating lids. The solid line in figures 4.13(a, b) and (d, e) gives the spatial structure of the corresponding low-order wave attractor (LOWA), whereas in figure 4.13(c, f) the solid lines give two realisations of the low-order neutral orbit (LONO).

Figures 4.13(c, f) show the $(1,2)$ LONO and the $(1,4)$ LONO, respectively. The libration frequency ω and the theoretical LONO frequency σ (see figure 2.11) differ only slightly by $|\omega - \sigma| \approx 0.006$, which corresponds to an uncertainty of the characteristic inclination ϑ (see equation (2.24) and figure 2.3) of $\Delta\vartheta \approx 0.5°$. The latter is too small to be visible by the naked eye given the smooth distribution of the localisation of kinetic energy density and the low-order ray patterns are in very good agreement. The spatial patterns are dominated by the corner beams emitted from the outer corners (dashed lines). In contrast to the frustum libration, the corner beams from the outer corners have similar amplitudes. The weaker corner beams emitted from the inner two corners (dotted lines) can be discerned as well by a deformation of the contours of the kinetic energy density, for example in figure 4.13(c) at around $(r, z) = (1.0, 4.0)$

and $(1.3, 0.3)$. More precisely, not the corner beams themselves are visible but the energy maxima surrounding the tilted-V pattern, figure 4.13(c), or tilted-W patterns, figure 4.13(f), which result from an imperfect destructive interference of the corner beams. The ray orbits shown by solid lines trace these maxima approximately.

It is remarkable that the LONOs can be discerned that well even though they do not possess the structural stability property as the wave attractors do (see section 2.4). The reason is related to the forcing mechanism, due to which wave energy is mainly injected by corner beams. Hence, the wave energy stays in the vicinity of the tilted-V pattern, figure 4.13(c), or the tilted-W pattern, figure 4.13(f). The viscous diffusion (Ekman number) is too large here that a higher-order spatial pattern could be excited. The visual impression is thus dominated by the corner beams in a finite frequency band around the LONO frequency that has been shifted due to viscosity. The resonant excitation of a normal mode, though, tells us where the LONO frequency has been shifted to (compare to section 4.2).

Figure 4.13(a) shows the almost degenerated $(1, 1)$ wave attractor (see figure 2.7(g)). The libration frequency ω and the frequency parameter of ray tracing are identical and read $\omega = \sigma = 0.57$, which has been selected for comparison since it exhibits larger kinetic energy densities than the rhomboidal wave attractor excited by $\sigma = 0.57$ (to be discussed in chapter 6). The $(1, 1)$ wave attractor has only 4 reflections for each frequency which renders it structurally stable against viscosity-induced frequency shifts. In fact, the spatial patterns shown in figure 4.13(a) are in excellent agreement. The maxima in the kinetic energy density can be identified properly and belong not only to the wave attractor (solid line), but also the corner beams and their reflections, which is most prominent for the dashed lines tracing the more intense corner beams that originate from the outer corners.

Figure 4.13(b) shows the flow pattern corresponding to the $(3, 4)$ LOWA for closely corresponding libration and wave ray frequencies ($\sigma \approx \omega = 0.65$). The spatial structures correspond to a very small frequency band (see figure 2.9), but exhibits comparably large kinetic energy values (to be discussed in chapter 6). The spatial structures agree only for the corner beams but not so much with respect to the wave attractor. The impression is that some wave energy approaches the wave attractor but viscosity damps the corner beams while they are focused to the wave attractor. See in this respect the kinetic energy maximum between the corner beam and the wave attractor originating from the focusing reflection near $(r, z) = (0.9, 3.2)$, from where it extends to the lower right at about $(r, z) = (1.6, 0.8)$.

Figure 4.13(e) shows the $(1, 3)$ LOWA excited with the same frequency $\omega = 1.18$ and ray frequency parameter $\sigma = 1.18$ as in figure 4.12(f), but here the lids and outer cylinder are in libration instead of the frustum. The appearance differs notably from the frustum libration case. First, the excitation and superposition of four corner beams leads to a different interference pattern which is more homogeneous here than for the frustum libration case. This can be attributed to the focusing of the wave energy towards the wave attractor (solid line). The focusing seems to require too many reflections for the corner beams from the bottom right and top left corner, which means they are damped while distributing the energy in the flow domain. In that way lids plus outer cylinder libration yields a two orders of magnitude larger energy level then the frustum libration case. Second, the kinetic energy density is localised mainly along the corner beams (dashed and dotted lines), which can be traced for a couple of reflections. The focusing reflection at $(r, z) = (0.9, 1.4)$ yields one of the largest values of the kinetic energy, but is not on the wave attractor. Surprisingly, the wave attractor (solid line) is rather difficult to discern. Even the focusing reflections at around $(r, z) = (0.7, 3.2)$ gives the impression that it belongs to the corner beam originating from the upper right corner. Third, the ray pattern together with the patches of local kinetic energy maxima near the reflection

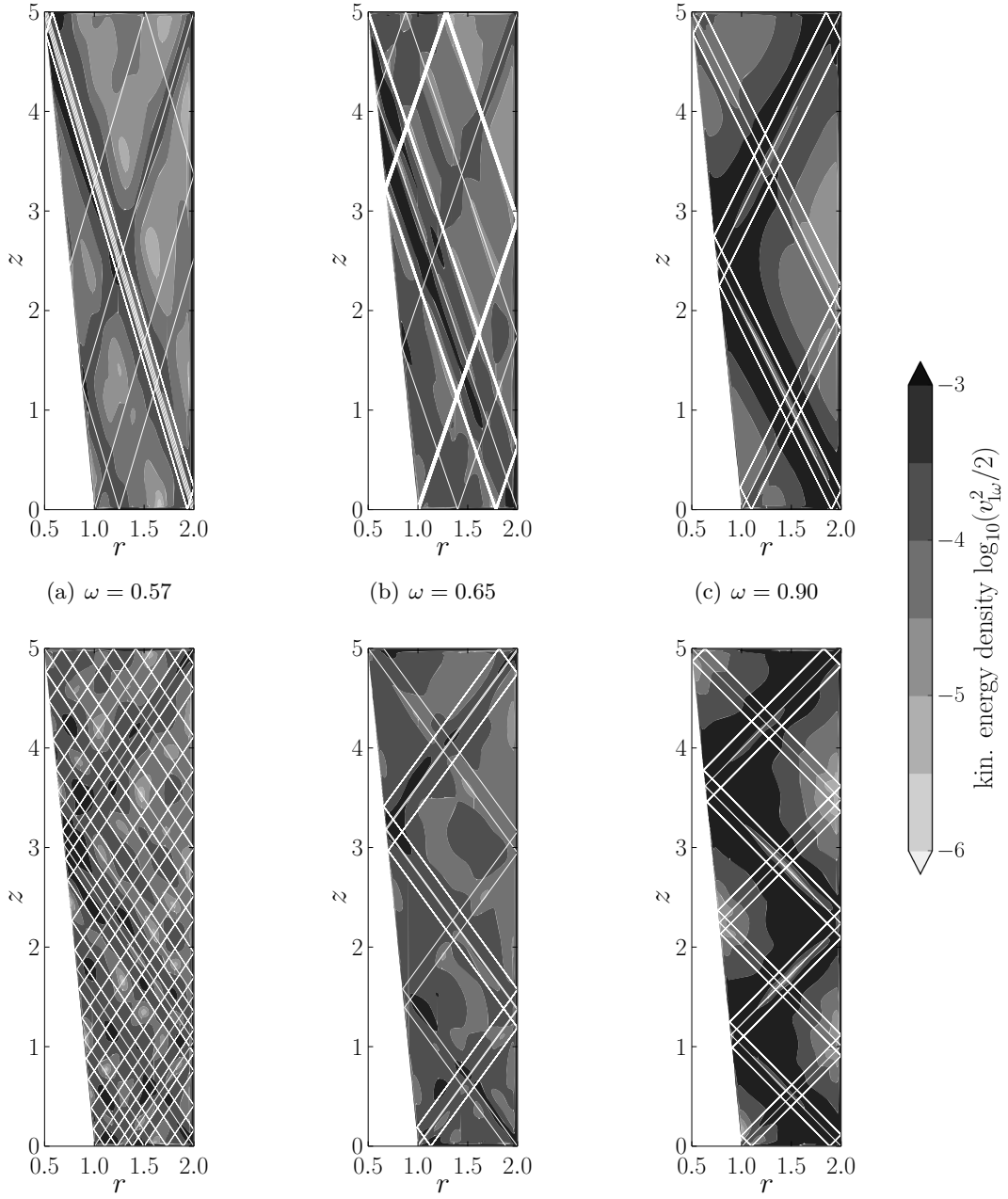

(a) $\omega = 0.57$ (b) $\omega = 0.65$ (c) $\omega = 0.90$

(d) $\omega = 1.10$ (e) $\omega = 1.18$ (f) $\omega = 1.40$

panel	(a)	(b)	(c)	(d)	(e)	(f)
ω	0.57	0.65	0.90	1.10	1.18	1.40
σ	0.5700	0.6496	0.8944	1.1032	1.1800	1.4066

Figure 4.13: Contours of the filtered kinetic energy density $v_{1\omega}^2/2$ in the case of the flow is excited by lids plus outer cylinder libration for various libration frequencies ω. Corresponding wave rays are plotted on top with frequency σ (see the table). The solid line shows the LOWA or LONO; dashed and dotted lines show the corner beams up to the third reflection. The correspondence between DNS and RT is best for the $(1, 2)$ and $(1, 4)$ LONOs in (c, f). See the text for details.

points is reminiscent of a normal mode. However, there is no LONO nearby and it would be interesting to compute the linear eigenmodes in the vicinity of $\sigma = 1.18$, a task beyond the scope of this work.

Figure 4.13(d) shows and the $(6, 16)$ higher-order wave attractor for later reference. The density of rays makes an in-depth comparison difficult, but the overall impression is similar to what we found above. That is, corner beams can be traced accurately and one is able to follow them 1–2 reflections. The interference pattern is rather complicated and exhibits energy localised at patches. It is not clear at present if the patchy structure is related to the excitation of a nearby higher-order normal mode or just a visual impression due to the interference of the corner beams.

This concludes the comparison of ray tracing and the numerical simulations. We move on by investigating the applicability of the frequency filter by discussing the effects of Rossby number variations in the next section.

4.4 Effects of Rossby number variations

The Rossby number R measures the strength of non-linear advection in comparison to Coriolis force and has been defined in equation (2.8). It enters the momentum equation (2.6), which shows that R controls the strength of the non-linearity. Hence, R is the key parameter that controls if a flow is linear, weakly non-linear, or turbulent. Up until now only the default parameters $R = 0.2$, $E = 3.19 \times 10^{-5}$ have been studied (see table 4.1) and we have based previous analyses on the assumption that the variability of the flow can be explained by a few harmonics $l\omega$ ($l = 1, 2, \ldots$) of the libration frequency ω. The purpose of this section is to assure ourselves of the validity range of the weak non-linearity assumption, which permits to restrict frequency-filtering to a few harmonics of the forcing frequency.

The dependency on the Rossby number is investigated by radial-axial sections of the radial velocity v_r and the filtered kinetic energy density $v_{1\omega}^2/2$ computed from the velocity components oscillating with the libration frequency ω, but also highly-resolved local frequency spectra. The local spectra provide additional information about the frequency content of the numerical solution. Otherwise, time slices of the radial velocity (or any other velocity component) are useful to visualise how organised or how chaotic the non-linear numerical solution looks like when other frequencies than the forcing frequency are also excited. This is important for an evaluation of the critical Rossby number up to which linear wave theory (here ray tracing; see section 2.4) can capture the dominating flow patterns of the non-linear solution, which was explicitly avoided in section 4.3. The filtered kinetic energy density, though, allows to evaluate how non-linearity modifies the flow patterns oscillating with the forcing frequency.

In the following, two representative cases are studied, first, the rhomboidal $(1, 1)$ wave attractor excited by frustum libration at $\omega = 0.47$; second, the $(1, 4)$ LONO and the $(1, 4, 0)$ normal mode excited by lids plus outer cylinder libration at $\omega = 1.4$ and $\omega = 1.38$ respectively. It is shown exemplary how the libration-induced flow changes when it becomes unstable and non-axisymmetric due to an instability of the oscillating boundary layer (properties of the instability are *not* discussed here; for details, the reader is referred to Ghasemi V. *et al.*, 2016; Lopez & Marques, 2011; Sauret *et al.*, 2012). According to Sauret *et al.* (2012), the stability threshold is a function $R_c(E, \omega)$, which means it depends on the Ekman number and the libration frequency but the transition is generic and we can restrict our attention using only the Ekman number of $E = 3.19 \times 10^{-5}$.

The rhomboidal wave attractor excited by frustum libration for various Rossby numbers

Figure 4.14 shows the variability of the rhomboidal wave attractor with respect to the Rossby number R for a time slice of the radial velocity v_r (a–d), and in terms of the filtered kinetic energy density $v_{1\omega}^2/2$ (e–h). The flow is excited by frustum libration with $\omega = 0.47$ at default Ekman number $E = 3.19\times10^{-5}$. The Rossby number increases from the left to the right in both rows; velocity scales corresponding to the Rossby numbers selected are collected in table 4.1 for the parameters of the corresponding laboratory experiment of Seelig (2014). Let us recall that the velocity and kinetic energy are taken relative to the co-rotating frame of reference and scaled with the libration amplitude ε (see equation (1.2)). The Rossby number $R \propto \varepsilon$ (see equation (2.8)) controls the strength of the non-linear term in the momentum equation (2.6), which means the flow changes qualitatively, but the magnitude of the *dimensionless* velocities and kinetic energy density remain of the same order for the various Rossby numbers. This is obviously the case in figure 4.14, where panels (a–d) yield $v_r \sim 10^{-2}$ in the bulk and $\sim 10^{-1}$ in the vicinity of the frustum. Correspondingly, figures 4.14(e–h) yield $v_{1\omega}^2/2 \sim 10^{-3}$ in the bulk and $\sim 10^{-1}$ at the wall.

Figures 4.14(b, f) show the radial velocity and filtered kinetic energy density for the default parameters. Figure 4.14(b) has been taken from the time series shown in figure 4.1, whereas figure 4.14(f) is repeated from figure 4.12(b) but without the ray orbits. We shall discuss the spatial structures of the other figures in a bit more detail in comparison to this reference case.

Figures 4.14(a, e) show the radial velocity and filtered kinetic energy density for a very small Rossby number $R = 0.02$, which is only one tenth of the default value. The visual accuracy allows to discern deviations down to about 10%, which means $R = 0.02$ is small enough to approximate the flow in the linear limit $R \to 0$. The gross of the flow structures in figures 4.14(a, e) are in agreement with the reference in figures 4.14(b, f). That is, one can clearly discern the rhomboidal wave attractor and the two corner beams originating from corners A and B. The latter is remarkable since it hints at the corner beams being part of the linear solution rather than a localised non-linearity. Moreover, the radial velocity field in figure 4.14(a) looks less noisy than the reference in panel (b), which can be seen, for example, when comparing the fluid velocities around $(r, z) = (1.5, 3.5)$. The less noisy impression is an indicator for the presence of additional frequencies in the non-linear solution. The corresponding velocity perturbations need to scale with the Rossby number like $|\hat{\boldsymbol{v}}_\sigma| \propto R^a$ for $\sigma \neq \omega$, where $R < 1$ and $a \gtrsim 1$. In fact, we have seen already that weak non-linearity yields $a = l - 1$ at the harmonics $\sigma = l\omega$, that is, $|\hat{\boldsymbol{v}}_{2\omega}| \propto R$ (see the discussion of figure 4.4). We will come back to this shortly when we look at the local spectra.

Figures 4.14(c, g) show the radial velocity and filtered kinetic energy density for a slightly super-critical Rossby number $R = 0.3$. The rhomboidal wave attractor and the corner beams from corners A and B are still dominating the flow in both panels. In figure 4.14(g), though, the corner beam emitted from corner A appears weaker than in figures 4.14(e, f), as can be seen at around $(r, z) = (1.2, 4.0)$.

Figure 4.14(c) also exhibits corner beams of harmonic frequencies as can be seen from the second wave beams emitted from corner B, for example, with an inclination corresponding to 2ω waves (compare to figure 4.4(b)). Furthermore, figure 4.14(c) shows that two thirds of the oscillating boundary layer ($z < 3.3$) over the librating frustum has undergone transition by breaking up into Görtler vortices (compare to Sauret *et al.*, 2012, who considered a straight cylinder). The boundary layer instability develops only when the boundary layer flow is centrifugally unstable. For the frustum libration, instability occurs in the prograde libration

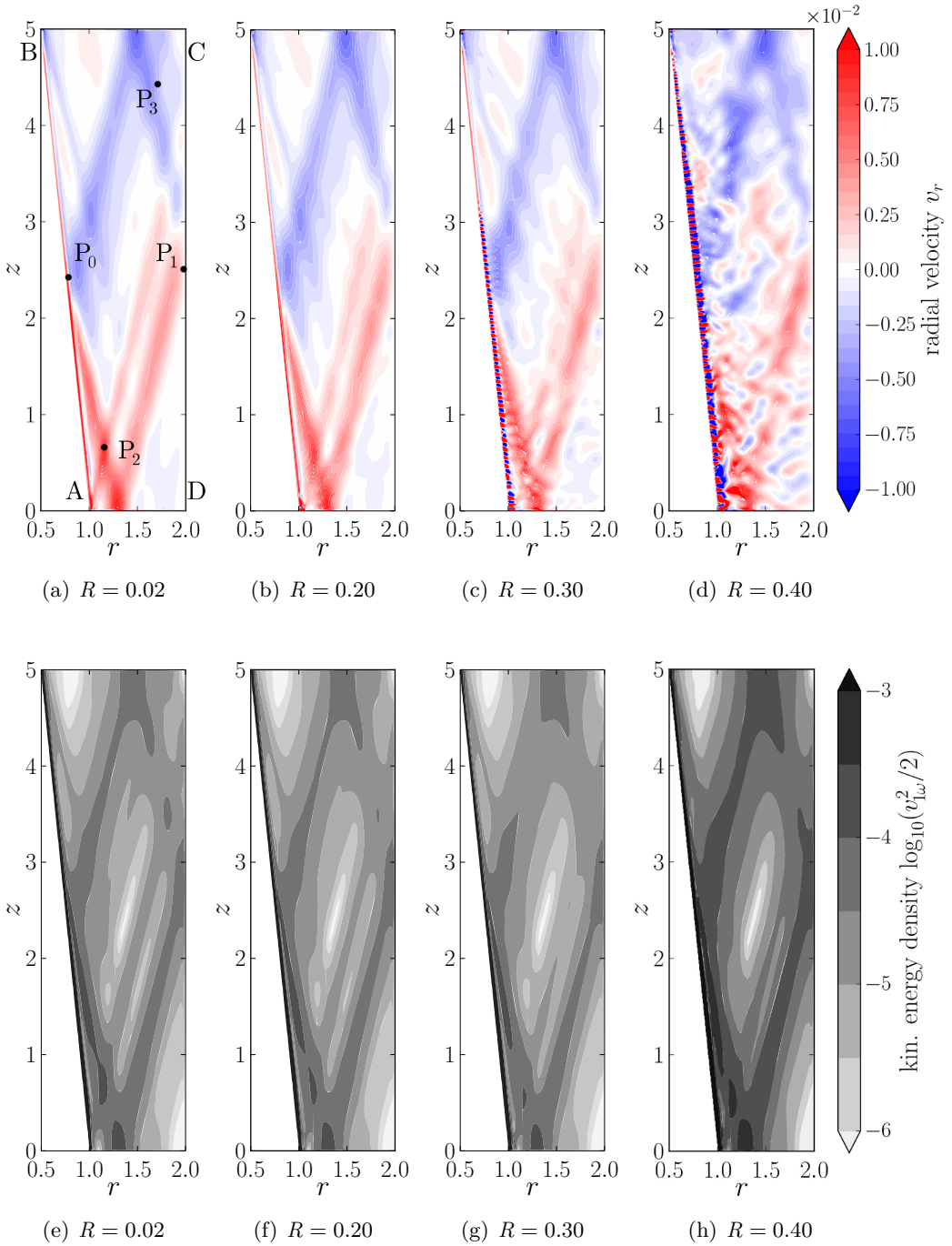

(a) $R = 0.02$ (b) $R = 0.20$ (c) $R = 0.30$ (d) $R = 0.40$

(e) $R = 0.02$ (f) $R = 0.20$ (g) $R = 0.30$ (h) $R = 0.40$

Figure 4.14: The rhomboidal wave attractor excited by frustum libration with forcing frequency $\omega = 0.47$ at Ekman number $E = 3.19 \times 10^{-5}$ for various Rossby numbers R. Panels (a–d) show the dimensionless radial velocity v_r in a radial-axial section at the end of the prograde libration phase ($\omega t = \pi$); panels (e–h) show the corresponding time-mean kinetic energy density $v_{1\omega}^2/2$ filtered at the forcing frequency. Panels (a, e) approximate the linear limit. Panels (b, f) correspond to figures 4.1 and 4.12(b). Panels (c, g) show the onset of centrifugal instability of the frustum boundary layer. Panels (d, h) exhibit spontaneously emitted inertial waves due to the unstable frustum boundary layer. The points P_0–P_3 mark the positions for which local spectra have been computed.

half-period $0 \leqslant \omega t < \pi$, where the libration phase $\omega t = \pi/2$ is centrifugally most unstable due to maximum wall velocity (see equation (2.16)). The boundary layer is centrifugally stable in the retrograde libration half-period $\pi \leqslant \omega t < 2\pi$, which gives the Görtler vortices time to decay before another 'burst' of the instability is triggered (not shown explicitly). A detailed discussion of the instability is beyond the scope of this work and the reader is referred to recent studies on the matter (e.g. Ghasemi V. *et al.*, 2016; Lopez & Marques, 2011; Noir *et al.*, 2010; Sauret *et al.*, 2012).

Figures 4.14(d, h) show the radial velocity and filtered kinetic energy density for the super-critical Rossby number $R = 0.4$. Figure 4.14(d) reveals that the oscillatory frustum boundary layer turned centrifugally unstable so that Görtler vortices could develop along the whole frustum. The flow is qualitatively different here since it is no longer axisymmetric[7] (not shown explicitly here; but see Ghasemi V. *et al.*, 2016; Lopez & Marques, 2011; Noir *et al.*, 2010). The corner beams can no longer be discerned in figure 4.14(d). Instead, the unstable boundary layer, or more precisely the Görtler vortices, emit inertial waves spontaneously at various frequencies (compare to Sauret *et al.*, 2013, but we will come back to this aspect shortly).

It is very interesting that the wave attractor has the largest velocity amplitudes and the largest filtered kinetic energy densities among all the panels shown in figures 4.14(a–d) and 4.14(e–h). At the same time, the filtered kinetic energy density field is the smoothest in figure 4.14(h), which suggests that the wave energy at frequency ω is focussed on the wave attractor from all along the frustum by superposition of waves with different phase. The effect of smoothing of the wave attractor by non-linearity is agreement with a recent study by (see Jouve & Ogilvie, 2014, who investigated a 2-D rhomboidal wave attractor).

In conclusion, there are a few important points worth to be emphasized. First, numerical results suggest that corner beams emitted at the forcing frequency are features of the linear dynamics. The corner beams are relatively reduced in amplitude due to non-linearity since part of the available kinetic energy of the boundary layer flow can be emitted also at harmonic frequencies $l\omega$ ($l = 2, 3, \ldots$) in the form of additional corner beams. The Rossby number needs to be sub-critical (centrifugally stable). Second, the linear dynamics dominate the flow organisation up to the largest Rossby number used ($R = 0.4$). That is, the boundary layer may become unstable so that a broad spectrum of wave frequencies is excited at various points along the wall. The bulk flow remains stable because it is of much smaller amplitude with velocities of the order $|\boldsymbol{v}| \sim 10^{-2}$ than the forcing with wall velocities $|\boldsymbol{v}_\mathrm{w}| \leqslant 1$. Hence, kinetic energy is redistributed by inertial waves but separately for each frequency component so that the bulk flow becomes a complex interference pattern resulting from an almost linear superposition of all these waves at various frequencies. Yet, the flow is dominated by the imposed libration frequency, that is, the rhomboidal wave attractor. At super-critical Rossby numbers (here $R > 0.3$), frequency filtering is necessary to separate the wave attractors excited from each other and from turbulent motions.

Neutral orbit and normal mode excited by lids plus outer cylinder libration for various Rossby numbers

Figures 4.15(a, b) and 4.15(c, d) show the dependency on the Rossby number R for the $(1, 4)$ LONO and the $(1, 4, 0)$ normal mode excited by lids plus outer cylinder libration with forcing

[7] The 3-D simulation has been performed for the standard grid (see table 3.2) and 84 effective Fourier modes in azimuthal direction *after* truncation. The transient stage was minimised by initialising the flow with the statistically stationary and axisymmetric solution obtained for $R = 0.2$, which has been perturbed randomly in azimuthal direction with a perturbation velocity amplitude of $|\Delta\boldsymbol{v}| = 10^{-3}$.

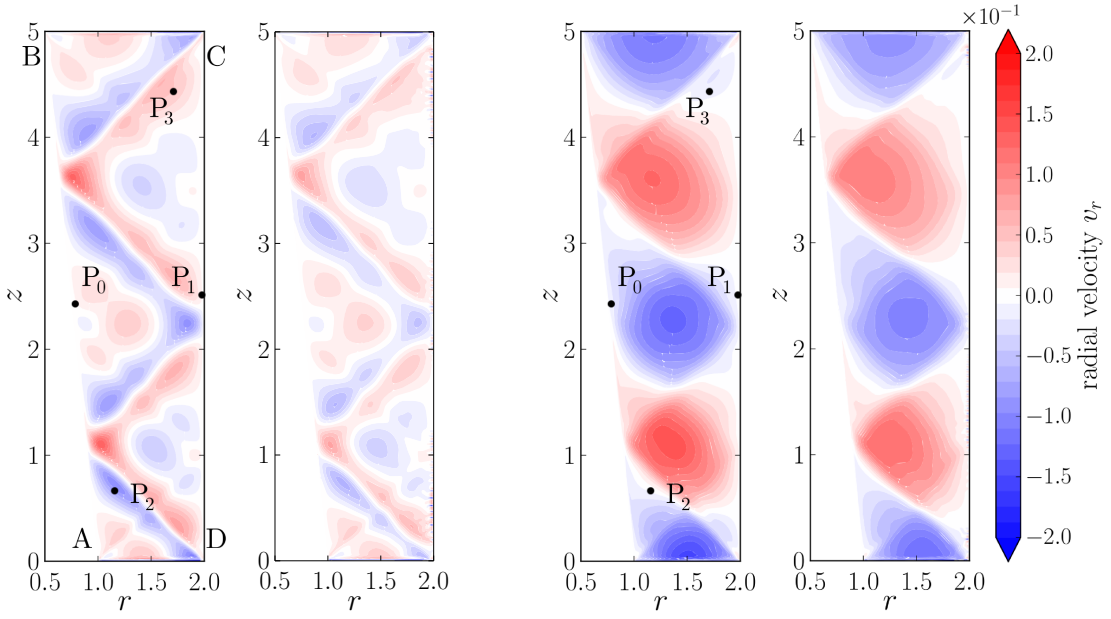

(a) $R = 0.02$ (b) $R = 0.40$ (c) $R = 0.02$ (d) $R = 0.40$

Figure 4.15: The $(1, 4)$ LONO (a, b) and the $(1, 4, 0)$ normal mode (c, d) excited by lids plus outer cylinder libration with forcing frequency $\omega = 1.40$ and 1.38, respectively, at Ekman number $E = 3.19 \times 10^{-5}$ for two different Rossby numbers R. The dimensionless radial velocity v_r in a radial-axial section is shown at the beginning of the prograde libration phase ($\omega t = 0$). Panels (a, c) approximate the linear limit. Panels (b, d) exhibit spontaneously emitted inertial waves from the unstable Stokes layer over the outer cylinder. The points P_0–P_3 mark the positions for which local spectra have been computed.
The $(1, 4)$ LONO excited by lids plus outer cylinder libration with forcing frequency $\omega = 1.4$ (a, b) and the $(1, 4, 0)$ normal mode excited with $\omega = 1.4$ (c, d) in terms of the radial velocity v_r at the end to the retrograde libration half-period ($\omega t = 0$). The flow is shown for two different Rossby numbers R at default Ekman number $E = 3.19 \times 10^{-5}$. Panels (a, c) approximate the linear limit $R \to 0$. Panels (b, d) show the flow for the oscillating boundary layer over the outer cylinder being centrifugally unstable. The points P_0–P_3 mark the positions for which high-resolution frequency spectra have been computed.

frequency $\omega = 1.40$ and $\omega = 1.38$ respectively. In contrast to figure 4.14, the flow is visualised only by the radial velocity v_r for the smallest and largest Rossby numbers used in this study (see table 4.1). The time slice $\omega t = 0$ in figure 4.15 has been selected in analogy to figure 4.14 such that it corresponds to the end of the libration half-period for which the oscillating boundary layer flow can become centrifugally unstable. The instability occurs first for the boundary layer over the outer cylinder which turns unstable in the retrograde half-period $\pi \leqslant \omega t < 2\pi$ (this is comparable to the configuration studied by Sauret *et al.*, 2012).

In general, figures 4.15(a, b) and 4.15(c, d) look strikingly similar to figures 4.6 and 4.7, respectively, lacking any notable change of the flow patterns. This is remarkable since the velocity amplitudes are much larger than it has been the case for the rhomboidal wave attractor (see figures 4.14(a–d)), but the flow is dominated by quasi-linear dynamics. The reason lies in the viscous stability of the oscillating boundary layer (Sauret *et al.*, 2012) due to which the boundary layer flow does not turn fully unstable for the forcing frequencies $\omega \approx 1.4$ here. It is very difficult to discern the few small 'wiggles' near $z = 0.2$, 4.8, 2.3 at the outer cylinder

$\overline{\mathrm{CD}}$ in figures 4.15(b, d). The stability of the flow pattern with respect to the Rossby number also explains why the tilted-W pattern could be visualised so properly in the corresponding laboratory experiment (see figure 4.3(b), which corresponds to $R = 0.4$).

Another notable difference between figure 4.15(a) and 4.15(b), or figure 4.15(c) and 4.15(d), is a non-linear scaling of the velocity amplitudes with the Rossby number. The velocity field has been scaled linearly with the libration amplitude ε (see section 2.1), hence, the less intense shading of the dominating wave patterns at $R = 0.4$ (b, d) compared to $R = 0.02$ (a, c) indicates that the amplitude of the waves excited increases slower than linear, say $U|\boldsymbol{v}| \propto \varepsilon^a$ with $0 < a < 1$ in the bulk (in terms of dimensional velocities; see table 4.1 for the scale velocities U). The interpretation works out similar to the wave attractor case discussed above: non-linearity decreases the efficiency of the corner beam excitation due to which less energy is injected into the fluid bulk at the forcing frequency ω. When $\omega < 1$, corner beams at harmonic frequencies $l\omega$ ($l \geqslant 2$) can transport kinetic energy form the boundary layer into the bulk (see figure 4.14(c)). Here, it is $\omega > 1$ such that all harmonic frequencies are outside the inertial wave band. The question arises, which non-linear flow features are driven by the non-linearity? To address this question, a more detailed knowledge of the frequency content of the numerical solution is required, which is the subject of the following paragraphs.

Local frequency spectra of the azimuthal velocity component

The objective of this section is to assure ourselves of the frequency content in the non-linear direct numerical solution and how it depends on the strength of the non-linear term, that is, the Rossby number. Four positions have been selected in the annular confinement for the computation of local spectra. The extraction points are denoted P_0–P_3. P_0 and P_1 are located at about mid-height $z = 2.5$ at the librating frustum or the librating outer cylinder respectively. P_2 and P_3 are located in the lower left and upper right of a radial-axial section of the annular confinement (see figure 4.14 and 4.15). Time series of the velocity vector $\boldsymbol{v}\,(\mathrm{P}_i, t)$ ($i = 1, 2, 3, 4$) have been recorded over 20–50 (integer) libration periods in the statistically stationary state with full temporal resolution. The time series have been transformed by the aid of equations (A.7)–(A.9) computing all possible frequencies of the discrete Fourier transform.

In the following, the frequency spectra are shown in terms of the power spectral density (PSD), for example $|\hat{v}_\varphi(\sigma)|^2$ for the azimuthal velocity. The azimuthal velocity component v_φ has been selected to have fluid velocities normalised to 1 near the librating wall. The PSD is computed from the complex velocity amplitude $\hat{v}_\varphi$ and its complex conjugate $\hat{v}_\varphi^\dagger$, namely

$$|\hat{v}_\varphi(\sigma)|^2 = \hat{v}_\varphi^\dagger(\sigma)\,\hat{v}_\varphi(\sigma). \tag{4.6}$$

We begin the discussion of the PSD with the rhomboidal wave attractor. After that, we move on to the $(1, 4)$ neutral orbit and the $(1, 4, 0)$ normal mode.

Local frequency spectra in the case of the rhomboidal wave attractor. Figure 4.16 shows the PSD according to equation (4.6) for the $(1, 1)$ wave attractor excited by frustum libration. The spectra shown in figure 4.16 correspond precisely to the numerical solutions shown earlier (see figure 4.14). The harmonics $l\omega$ ($l = 1, 2, \ldots$) of the forcing frequency ω are given for orientation along the horizontal axis by vertical bars whose lengths decrease with l; the inertial wave band limit $\sigma = 2$ is shown by a grey vertical line. The solid blue and red lines have been extracted at P_2 and P_3 in the fluid bulk, the dashed black line has been obtained at P_0 in the oscillating boundary layer near the frustum, and the dotted line gives the filter response. The

filter response has been obtained by sampling the prescribed wall velocity $v_{\mathrm{w},\varphi} \propto \sin(\omega t)$ at the finite time levels of the time integration scheme (see section 3.4). The time step has been kept constant in the simulations but it is generally *not* an integer fraction of the libration period $2\pi/\omega$ due to which the librational δ-forcing 'leaks' into neighbouring frequencies (compare to Press *et al.*, 1992, figure 13.4.2, p. 548). Hence, there are two errors contributing to the filter response: leakage and truncation of the time series. Both are not limited to the forcing frequency, but broaden any spectral peak. Let us look at the different spectra individually.

Figures 4.16(a, b) show the spectra for the Rossby numbers $R = 0.02$ and 0.2 for which the flow is stable. The variability of the flow is dominated by the components oscillating with the forcing frequency $\omega = 0.47$, where a sharp peak can be discerned. At P_0, the PSD is of the order $|\hat{v}_\varphi|^2 \sim 10^{-1}$, which is slightly less than the reference due to leakage in the Fourier filter. Otherwise, the PSD of the oscillating boundary layer is similar to the filter response, which is due to the dominance of the linear viscous dynamics near the wall. At P_2 and P_3 in the bulk, velocity amplitudes are no larger than $|\boldsymbol{v}| \sim 10^{-2}$ (compare to figure 4.1), which yields $|\hat{v}_\varphi|^2 \sim 10^{-4}$. The PSD decays rapidly to $|\hat{v}_\varphi|^2 \lesssim 10^{-10}$ to the left and right of the forcing frequency and yields the error level $|\Delta\boldsymbol{v}| \sim 10^{-5}$ (which is even smaller than the estimate in section 3.3).

Considering only those frequencies with $|\hat{v}_\varphi|^2 \geqslant 10^{-10}$ in figures 4.16(a, b) shows that the variability of the rhomboidal wave attractor case is indeed given by a few harmonics $l\omega$. For $R = 0.02$, figure 4.16(a), only the harmonic $2\omega = 0.94$ is definitely larger than the error level, but the PSD is also about 5 orders of magnitude smaller than it is at the forcing frequency. For $R = 0.2$, figure 4.16(b), the harmonics $2\omega = 0.94$, $3\omega = 1.41$ and $4\omega = 1.88$ yield freely propagating waves (see figure 4.4) and have a PSD above the error level. More importantly, the PSD shown are 2–4 orders of magnitude larger than those at the neighbouring frequencies. Interestingly, at P_2 (blue line), the PSD is also larger than the error level for $\sigma \leqslant 0.3$. An additional harmonic can also be discerned at $5\sigma = 2.35$. P_2 is located at the intersection of the corner beam from the bottom inner corner A (see figure 4.14(a)), which suggests locally enhanced non-linearity.

Considering that there is notable low-frequency content in the spectra, one can conclude that the numerical solution is still evolving on long time scales spanning several libration periods. This may not be just a transient effect since 30 initial libration periods have already been skipped before the analysis took place. Hence, in order to obtain more robust results regarding the low-frequency variability of the wave-dominated flow, very long integration times of several hundred libration periods may be necessary as noted, for example, by Ghasemi V. (2016); Mason & Kerswell (1999). With the present numerical implementation such an undertaking was not feasible so that this point needs to be addressed in a future study.

Figures 4.16(c) shows the local spectra for the case of $R = 0.3$, at which the oscillating frustum boundary layer has just turned centrifugally unstable. The flow is still dominated by the forcing frequency as can be seen easily by the sharp peak at $\sigma = 0.47$, but the dominance of the harmonics $l\omega$ is no longer the case everywhere in the flow domain. Instability of the boundary layer leads to a broad spectrum of frequencies excited, as can be seen for P_0 (dashed black line). Except for the forcing frequency, the PSD has values between $10^{-8} \leqslant |\hat{v}_\varphi|^2 \leqslant 10^{-6}$ for $\sigma \leqslant 4$ beyond the inertial wave band. The PSD fluctuates notably, but it is above the estimated error level ($\sim 10^{-8}$) and above the filter response (approached only by frequencies $\sigma > 5$). At P_2 (blue line) in the bulk, shape of the PSD in the inertial wave band is largely similar to the PSD of the boundary layer, that is, a dominance by the forcing frequency together with a broad spectrum of frequencies. Only the 2ω peak at $\sigma 0 = 0.94$ stands out and is readily expected from a weak non-linearity. However, due to the instability more frequencies are available for

mixing due to which the 2ω peak has a somewhat smaller amplitude in figure 4.16(c) than it has in figure 4.16(b). Most of the kinetic energy reaching P_2 are inertial waves, as can be seen by the steep drop of the PSD at around $\sigma = 2$. The point P_3 (red line) yields a similar behaviour of the spectrum, but the drop is much steeper. The reason is that P_3 is relatively far away from the instability in the lower part of the frustum boundary layer. Due to geometry and viscous damping, only those inertial waves can contribute to the spectrum which are focused in the vicinity of P_3 within a few reflections before they are damped by viscosity. Here, mainly the harmonics $2\omega = 0.94$ and $3\omega = 1.41$ can be discerned.

Figure 4.16(d) shows the local spectra for $R = 0.4$ for which the oscillating frustum boundary layer has become centrifugally unstable. The forcing frequency $\sigma = \omega = 0.47$ is dominant in all the spectra with a PSD of the same order as at the smaller Rossby numbers (see figures 4.16(a–c)). For the frequencies $\sigma < 2$ in figure 4.16(d), the PSD is larger than 10^{-8}, which means well above the estimated error level. At P_0 in the oscillating boundary layer, the PSD lies between $10^{-5} \leqslant |\hat{v}_\varphi|^2 \leqslant 10^{-4}$ for $\sigma < 2$ in the inertial wave band (excluding the forcing frequency), which means it is only 3–4 orders of magnitude smaller than it is at the forcing frequency. A broad range of frequencies is therefore excited due to the developing instability of the boundary layer.

Nevertheless, there are peaks notable at the harmonics 2ω, 3ω and 4ω, suggesting that non-linearity is weak. For frequencies $2 < \sigma < 4$ outside the inertial wave band, the spectrum falls off like $|\hat{v}_\varphi|^2 \propto \sigma^{-4}$. Here, $\sigma = 4$ corresponds roughly to the resolution limit of the second-order numerical scheme and the steeper fall-off observed for $\sigma > 4$ exhibits the dispersion relation of the second-order numerical scheme (e.g. Durran, 2010, pp. 153). At P_2 and P_3 in the bulk, the PSD is distributed over the whole inertial wave band, followed by a notable fall-off at $\sigma = 2$ onwards. This shows that the bulk flow is dominated by inertial waves, which have been emitted spontaneously at various frequencies from the unstable boundary layer (for details, see Sauret *et al.*, 2013). Interestingly, only the peak at the forcing frequency remains in the spectra obtained at P_2 and P_3, whereas the harmonics $l\omega$ ($l \geqslant 2$) are just as strongly excited as the other frequencies. This indicates breakdown of the weak non-linearity. Unexpectedly, the linear dynamics of the flow is emphasized by letting the forcing frequency become dominant again, whereas the other frequencies are indistinguishable by forming a 'noisy background'.

In summary, weak non-linearity has been validated for the case of the rhomboidal wave attractor excited by frustum libration for $R \leqslant 0.2$ at $E = 3.19 \times 10^{-5}$ and $\omega = 0.47$. The local spectra revealed that the flow is dominated by the forcing frequency and a few harmonics as long as the oscillating boundary layer is stable. For $R \geqslant 0.3$, instability of the oscillating boundary layer has been observed leading to a broader spectrum of frequencies excited and weak non-linearity breaks down in the sense that the variability is spread over a broad range of frequencies. The flow is still weakly non-linear in the sense that most of the frequencies observed in the bulk are related to inertial waves ($0 < \sigma < 2$). Interaction of the waves and instability of the basic flow competes with the formation of harmonics of the forcing frequency. The harmonics of the forcing frequency cannot gain energy compared to the broad spectrum of frequencies excited.

By contrast to intuition, the latter results in a dominance of the (linear) flow structures oscillating with the forcing frequency even though the flow is more non-linear and ray tracing is still useful to capture the dominating spatial structures. One reason for the dominance of the forcing frequency is likely related to the boundary layer instability, which occurs periodically due to libration. The instability develops as 'burst' once in every libration period, here in the prograde half-period, but the flow stabilises again in the retrograde half-period before a new 'burst' occurs (see Ghasemi V. *et al.*, 2016; Sauret *et al.*, 2012). The results suggest that

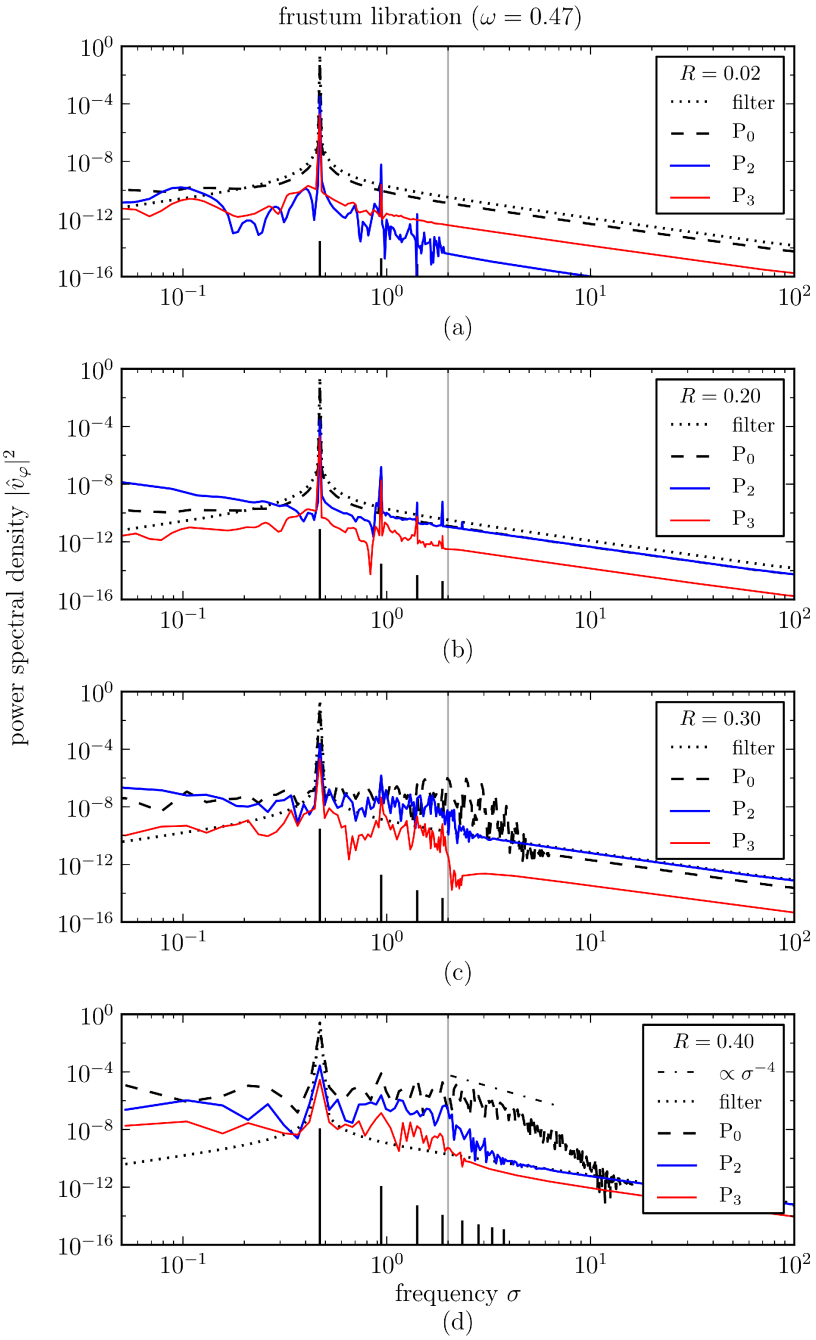

Figure 4.16: Power spectral density $|\hat{v}_\varphi(\sigma)|^2$ at three points for various Rossby numbers R for the case of the rhomboidal wave attractor excited by frustum libration (see figure 4.14). Fixed parameters are $\omega = 0.47$, $E = 3.19 \times 10^{-5}$. The Rossby number increases from (a) to (d). In each panel, the solid blue and red lines have been obtained in the fluid bulk, whereas the dashed black line has been obtained in the oscillating boundary layer over the frustum. The dotted spectrum gives the filter response, which is dominated by leakage due to truncation of the time series and the finite time step. The dash-dotted line yields the observed spectral decay outside the inertial wave band for the resolved frequencies. The vertical solid grey line denotes the inertial wave band limit ($\sigma = 2$). Small vertical solid lines give the harmonic frequencies $l\omega$ ($l = 1, 2 \ldots$).

the periodic bursting ensures the strong presence of the forcing frequency in the response, but modulates the broadband spectrum. This is different from other forcing types like differential rotation, where no periodicity is imposed at all (see e.g. Rieutord *et al.*, 2012). As discussed earlier, the simulations performed resolve the instability and the turbulent structures (see section 3), which is sufficient for this work in which we concentrate on stable in the following chapters. A detailed analysis of the instability, though, requires much higher resolutions which is beyond the scope of this work, but discussed by Ghasemi V. (2016); Ghasemi V. *et al.* (2016).

Local frequency spectra in the case of the LONO and normal mode. Figures 4.17 and 4.18 show the local spectra according to equation (4.6) for the $(1, 4)$ neutral orbit and the $(1, 4, 0)$ mode, respectively, excited by lids plus outer cylinder libration. The spectra have been computed for the same points, P_0–P_3, but we restrict our attention to P_1 in the oscillating boundary layer at the outer cylinder and P_2 in the bulk (see figure 4.15). As before, results for Rossby numbers $R = 0.02$, 0.2, 0.3, 0.4 are shown. In the inertial wave band ($\sigma < 2$), the PSD is larger than the estimated numerical errors which means the filter response function is always dominating the spectral error.

Figures 4.17(a–c) show the local spectra for $R = 0.02$, 0.2, 0.3 for the $(1, 4)$ LONO excited with libration frequency $\omega = 1.4$, whose spatial pattern is shown in figure 4.15(a). The forcing frequency dominates the spectra. The boundary layer flow measured at P_1 agrees well with the filter response, which shows that the flow is stable and dominated by linear viscous dynamics near the wall. By contrast, the bulk flow, exhibits notable non-linear features. At P_2, the spectrum of the PSD exhibits only the harmonic $2\omega = 2.8$ (only a very small kink is present at $3\omega = 4.2$ in figure 4.17(c)). The harmonic 2ω increases in magnitude with the Rossby number, a R^2-dependency as can be seen, for example, by the factor $(0.02/0.2)^2 = 100$ for the peak at $\sigma = 2.8$ in figure 4.17(a) and 4.17(b). The frequency is outside the inertial wave band, which means kinetic energy cannot be redistributed by inertial waves.

Frequency mixing seems to be inhibited in figures 4.17(a–c) but, interestingly, an anharmonic frequency has occurred at $\sigma = 0.87$ (the left dotted vertical line). The frequency $\sigma = 0.87$ coincides with that of the $(1, 2, 0)$ mode or the $(1, 2)$ LONO, whose frequency has been shifted due to viscosity. The DNS results suggests that a form of 'spatial coupling' may be one mechanism for the generation of anharmonic frequencies, which is a surprising and unexpected observation. A clarification of the internal mechanism causing this behaviour, however, is beyond the scope of this work and has to be addressed elsewhere in the future.

Besides the frequency $\sigma = 0.87$ in figures 4.17(a–c) a small but broad peak at its harmonic $\sigma = 1.74$ can be discerned (central dotted vertical line), as well as another anharmonic frequency at around $\sigma = 1.9$. The origin of these frequencies can only be explained by an instability of the basic flow (e.g. Duguet *et al.*, 2006; Kerswell, 1999, 2002). The effect, however, is small since the anharmonic frequencies have a PSD of the order $|\hat{v}_\varphi|^2 \sim 10^{-7}$, which is just large enough to be resolved properly by the numerics.

Figure 4.17(d) shows the local spectra for $R = 0.4$ after the boundary layer has become unstable in some places (see figure 4.15(b)). The boundary layer has turned unstable at P_1, which is easily seen by the local spectrum which is composed of many frequencies $\sigma < 10$. The time step has been reduced for this simulation to account for the faster libration. This has doubled the numerical resolution of $\sigma \approx 8$, after which the second-order dispersion becomes notable (see the discussion for the rhomboidal wave attractor). The frequency content of the boundary layer is largely homogeneous in the inertial wave band (excluding the forcing frequency) and decreases like $|\hat{v}_\varphi|^2 \sim \sigma^{-4}$ for the resolved frequencies outside the inertial wave

band ($2 < \sigma < 8$). Furthermore, the spectrum obtained at P_2 is interesting with respect to the anharmonic frequency peaks which have disappeared. Hence, the bulk flow is dominated by the forcing frequency ω and its harmonic 2ω. The PSD of all other frequencies in the inertial wave band has increased from $|\hat{v}_\varphi|^2 \lesssim 10^{-8}$ to about 10^{-7} and is distributed very homogeneously for $\sigma < \omega = 1.4$; there is also no steep fall-off of the PSD at $\sigma = 2$. It appears that the additional frequency content helps to spread the kinetic energy more homogeneously over the inertial wave band so that the linear solution remains dominant in the bulk even though the bulk flow itself is weakly non-linear. It needs to be emphasized, though, that the flow for $R = 0.4$ is non-axisymmetric, whereas it is axisymmetric for $R \leqslant 0.3$. Hence, the azimuthal wave numbers appear to be essential for the interaction of inertial waves and the excitation of a broad frequency spectrum (e.g. Albrecht *et al.*, 2015; Kerswell, 1999, and references therein), but does not imply turbulent collapse of the flow state.

Figures 4.18(a–c) show the local spectra for $R = 0.02$, 0.2, 0.3 for the $(1, 4, 0)$ mode excited with libration frequency $\omega = 1.38$, whose spatial pattern is shown in figure 4.15(c). The local spectra obtained for the normal mode are generally very similar to those obtained for the LONO (see figure 4.17), which is in particular the case for the spectra of the boundary layer computed at P_1. In the bulk, at point P_2, non-linearity effects have increased due to larger fluid velocities by resonant excitation of the normal mode. The PSD at $2\omega = 2.76$ reaches almost two orders of magnitude larger values over the base line of the filter response than the corresponding peak in figures 4.17(a–c). In addition, also the harmonic $3\omega = 4.14$ has been excited in figures 4.18(b, c) but not in 4.17(b, c). The anharmonic frequency content at $\sigma = 0.87$, 1.74, $\sigma = 1.9$ in figures 4.18(a–c) is comparable to that in figures 4.17(a–c), but figure 4.18(c) exhibits another peak at $\sigma = 3.3$. One can speculate that more frequencies will appear when non-linearity increases, for example, when more energy can be pumped into the normal mode without letting the boundary layer turn unstable (compare to Duguet *et al.*, 2006; Ghasemi V., 2016).

Figure 4.18(d) shows the local spectra for $R = 0.4$, for which the spatial structure of the flow is shown in figure 4.15(d). The local spectrum in the oscillating boundary layer looks odd which is due to the boundary layer not becoming turbulent at the point P_1. The PSD is concentrated at the frequencies $\sigma = 3.2$, 4.6, 6.0, 7.4 outside the inertial wave band, which are not harmonics of the forcing frequency. Strikingly, the latter frequencies are offset by $\Delta\sigma = 1.4$, which is approximately the forcing frequency $\omega = 1.38$ but might be just by chance. There are also two additional low-frequency maxima at $\sigma = 0.87$ and 0.45 in figure 4.18(d) compared to figure 4.17(d). A clarification of the origin of the various frequencies is beyond the scope of this work, but the 3-D simulation assures that the system behaviour is not spurious. In the bulk, the spectrum at (P_2) is dominated by peaks at the forcing frequency ω and at the two harmonics 2ω, 3ω, whereas anharmonic frequency peaks have weakened ($\sigma = 0.87$ and 1.74) or have vanished compared to the solutions obtained at smaller Rossby numbers.

In conclusion, the normal mode excited delays the development of the boundary layer instability to larger Rossby numbers compared to a nearby libration frequency for which no low-order mode is excited. Contrary to intuition, weakly non-linear properties of the solution (harmonic frequencies) are more notable in a non-axisymmetric solution *after* the oscillating boundary layer has become unstable. A broad spectrum of wave frequencies and azimuthal wave numbers is present but of small amplitude so that kinetic energy can be distributed over the flow domain and over the inertial wave band. Hence, anharmonic frequency peaks notable for the axisymmetric solution at $R \leqslant 0.3$ have weakened or even vanished compared to neighbouring frequencies in the more non-linear and non-axisymmetric solution at $R = 0.4$.

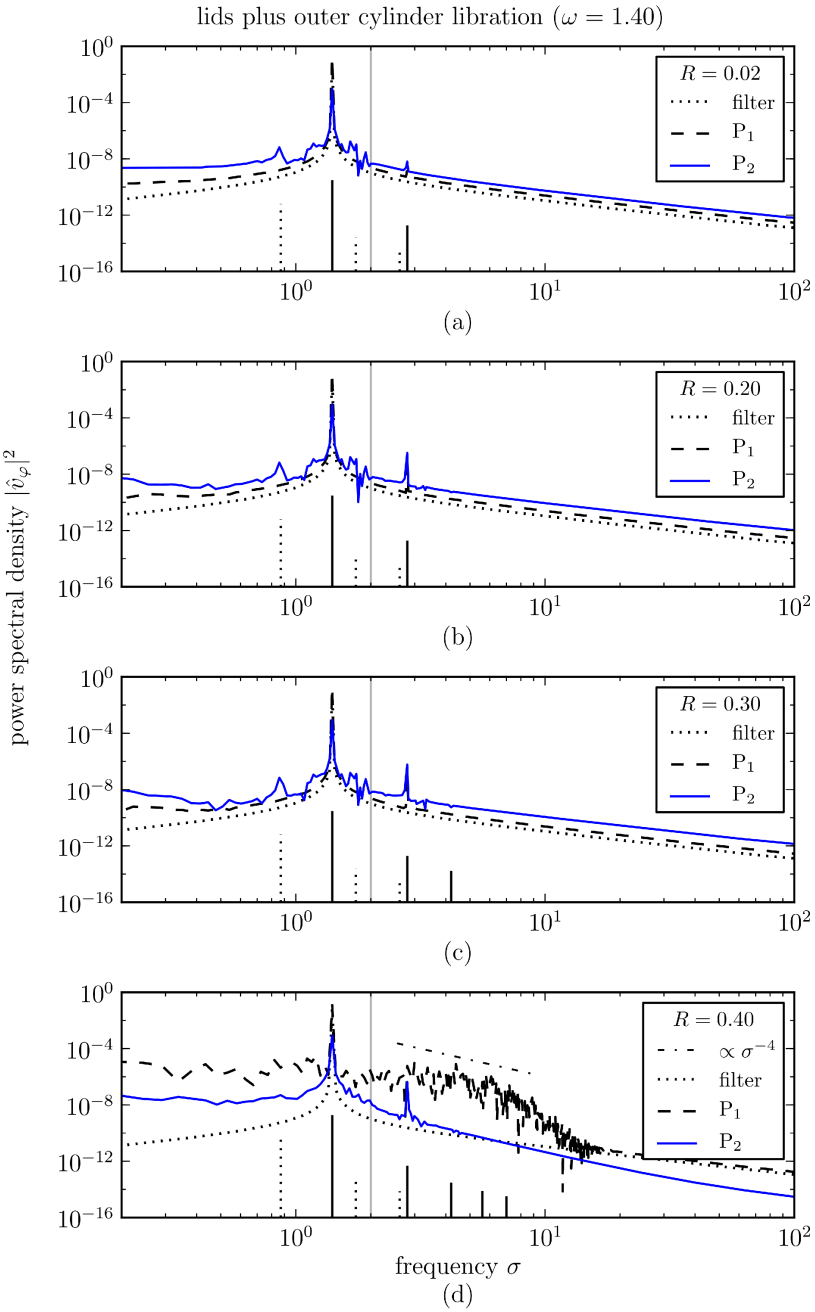

Figure 4.17: Power spectral density $|\hat{v}_\varphi(\sigma)|^2$ at two points for various Rossby numbers R for the case of the $(1, 4)$ LONO excited by lids plus outer cylinder libration (see figures 4.15(a, b)). Fixed parameters are $\omega = 1.40$, $E = 3.19 \times 10^{-5}$. The Rossby number increases from (a) to (d). The solid blue line has been obtained in the bulk, whereas the dashed black line has been obtained in the vicinity of the outer cylinder. The dotted spectrum gives the filter response due to truncation of the time series and a finite time step. The vertical solid grey line denotes the inertial wave band limit ($\sigma = 2$). The dash-dotted line yields the observed spectral decay outside the inertial wave band for the resolved frequencies. Vertical solid lines mark the harmonic frequencies $l\omega$ ($l = 1, 2 \ldots$); dotted lines mark the harmonics of the anharmonic frequency $\sigma = 0.87$.

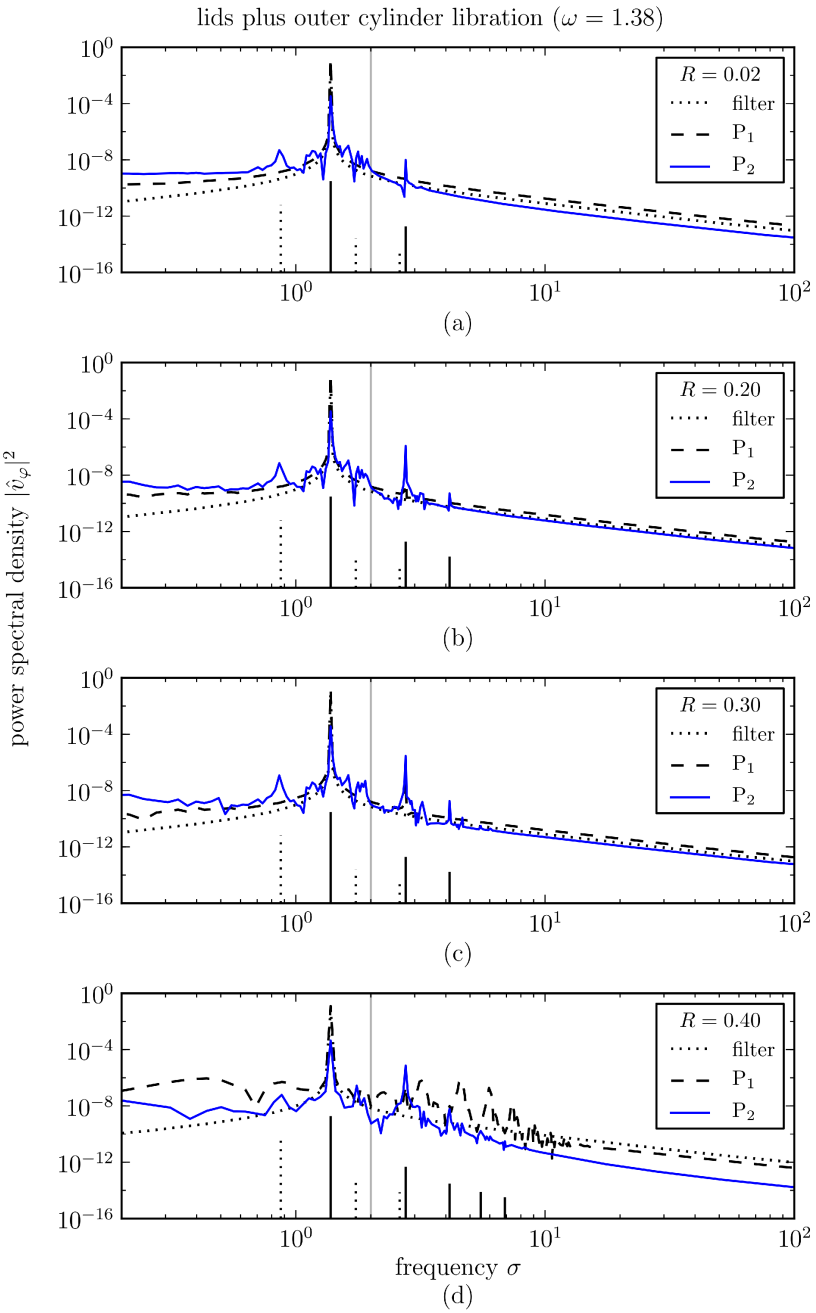

Figure 4.18: Power spectral density $|\hat{v}_\varphi(\sigma)|^2$ at two points for various Rossby numbers R for the case of the $(1, 4, 0)$ mode excited by lids plus outer cylinder libration (see figures 4.15(c, d)). Fixed parameters are $\omega = 1.38$, $E = 3.19 \times 10^{-5}$. The Rossby number increases from (a) to (d). In each panel, the solid blue line has been obtained in the fluid bulk and the dashed black line in the oscillating boundary layer over the outer cylinder. The dotted spectrum gives the filter response, which is dominated by leakage due to truncation of the time series and the finite time step. The vertical solid grey line denotes the inertial wave band limit ($\sigma = 2$). Vertical solid lines mark the harmonic frequencies $l\omega$ ($l = 1, 2 \ldots$); dotted lines mark the harmonics of the anharmonic frequency $\sigma = 0.87$.

In that respect, it is worth to note also that the role of triads in the generation of harmonic and anharmonic frequencies is not yet clear for the case of wave attractors. The difficulty is that the wave length observed on the wave attractor is not fixed but only bounded from below by viscosity. Hence, there are various wave vectors present in the superposition of (plane) waves that form the wave field and the wave beams respectively. To address triads and wave attractors in a future study, it seems promising to investigate first the interaction of azimuthal wavenumbers in addition to the temporal frequency content for a flow regime that is no longer axisymmetric without altering the present flow configuration (e.g. $R > 0.3$).

4.5 Effects of Ekman number variations

The Ekman number E has been defined in equation (2.8), where we have discussed that E measures the strength of viscous forces in comparison to the Coriolis force. The Ekman number also controls the potential power uptake of the fluid but also the damping. An increase of the Ekman number yields an increase of both power uptake and damping. Increased damping, however, also decreases the wave number which can be excited in the system which can destroy the power uptake condition, for example, when inertial waves can not be excited any longer in the annular confinement. The purpose of this section is to show exemplary the situation of a too large Ekman number for which excitation of a wave attractor or a normal mode is inhibited and to demonstrate what small scale features occur when the Ekman number is reduced. The dependency on the Ekman number is investigated by radial-axial sections of the filtered kinetic energy density $v_{l\omega}^2/2$ for the forcing frequency ($l = 1$) and its first harmonic ($l = 2$) according to equation (4.5).

In the following, two representative cases are studied, first, the rhomboidal $(1, 1)$ wave attractor excited by frustum libration at $\omega = 0.47$; second, the $(1, 4, 0)$ normal mode excited by lids plus outer cylinder libration at $\omega = 1.38$. The Rossby number is kept fixed here at its default value $R = 0.2$. It is shown exemplary how the libration-induced flow changes when the Ekman number is varied over roughly two orders of magnitude for values in the range $9.57 \times 10^{-6} \leqslant E \leqslant 3.19 \times 10^{-3}$. The smallest Ekman number used is larger than the threshold value 10^{-6}, which has been estimated in section 3.3 for typical numerical resolutions used in this work. Table 4.1 lists the rotation rates of the laboratory experiment (Seelig, 2014) corresponding to the Ekman numbers selected here.

The rhomboidal wave attractor excited by frustum libration for various Ekman numbers

Figure 4.19 shows the kinetic energy density for the flow excited by the libration frequency $\omega = 0.47$ for various Ekman numbers. Figures 4.19(a–d) in the upper row show the spatial pattern oscillating with the forcing frequency ω, whereas figures 4.19(e–h) in the lower row show the spatial patterns oscillating with the harmonic of the forcing frequency 2ω. The contour levels are plotted in logarithmic scale every half an order of magnitude, using the same scale for each row. The Ekman number increases from the left to the right.

Figures 4.19(c, g) correspond to the case of default dimensionless parameters with Ekman number $E = 3.19 \times 10^{-5}$. Figure 4.19(c), is repeated from the comparison to ray tracing (see figure 4.12(b)). The flow structures related to the forcing frequency have been discussed thoroughly in section 4.1. Let us just recall that the numerical solution exhibits the rhomboidal wave attractor and corner beams emerging from the top and bottom inner corners A and B. Similarly, figure 4.19(g) exhibits a tilted-V pattern due to the emission of harmonic corner

beams at corners A and B with a frequency of $2\omega = 0.94$ which is close to the $(1, 2)$ LONO (see figure 2.11(a)). Two other wave beams at 2ω were found to originate from the focusing reflection at around $(r, z) = (0.9, 2.4)$, propagating towards the corners D and C away from the frustum.

Figures 4.19(d, h) show the filtered kinetic energy densities for the Ekman number $E = 9.57 \times 10^{-6}$, which is 3.33 times smaller than in figures 4.19(c, g). The spatial patterns in figure 4.19(c) and 4.19(d), as well as in figure 4.19(g) and 4.19(h) are generally similar but more fine structure can be discerned in the solution obtained at the smaller Ekman number. In figure 4.19(d), for example, one can clearly see the corner beams emerging from the two inner corners A and B. The corner beam from corner A can be traced by the naked eye by three reflections, that is, from point A at $(r, z) = (1.0, 0.0)$, over $(2.0, 4.0)$ and $(1.8, 5.0)$, to $(0.9, 1.5)$ at the frustum. At the frustum, the wave beam undergoes a focusing reflection, due to which it practically reaches the rhomboidal wave attractor given the finite wave beam widths. Similarly, one can trace the weaker corner beam originating from corner B at $(r, z) = (0.5, 5.0)$ for four reflections, $(1.7, 0.0)$, $(2.0, 1.4)$, $(1.2, 5.0)$, $(0.7, 3.2)$ at the frustum, where it is also focused toward the wave attractor (compare to figure 2.5).

The rhomboidal wave attractor appears more pronounced than for the default Ekman number in figures 4.19(d) even though the kinetic energy density has decreased by half an order of magnitude (about one shade). This drop in magnitude is interesting as it shows that wave energy is injected less efficiently when the Ekman number decreases or, in other words, the power uptake has decreased with the Ekman number. This overall energy loss is partly compensated by reduced damping which results in a more localised kinetic energy density along the rhomboid. The observation here agrees well with a recent numerical study of Jouve & Ogilvie (2014), who performed 2-D DNS of a rhomboidal wave attractor in a tilted box for similar Ekman numbers. The limit of very small Ekman numbers, $10^{-12} \lesssim E \lesssim 10^{-6}$, has been investigated for the spherical shell, either by an analysis of viscous eigenmodes (e.g. Rieutord *et al.*, 2001; Rieutord & Valdettaro, 1997, 2010) or by numerical simulations (e.g. Ogilvie & Lin, 2004; Tilgner, 1999). The spherical shell exhibits wave attractors just like the annulus with an inner frustum and similar behaviour of the solution is expected here. That is, the numerical solution will become more localised at the wave attractor obtained by ray tracing (see figure 2.5) when the Ekman number decreases.

Interestingly, the oscillation pattern at the harmonic 2ω shown in figure 4.19(h) exhibits *larger* magnitudes than in figure 4.19(g). In fact, the Reynolds number of the flow ($Re = R/E$, see equation (2.9)) has increased by 3.33 from $Re = 6270$ in figure 4.19(g) to about $Re = 20900$ in figure 4.19(h). Hence, non-linearity has a stronger effect on the flow evolution, which means that part of the energy injected at the forcing frequency excites additional frequencies. In particular, looking closely at the frustum wall between $(r, z) = (1.0, 0.0)$ and $(0.7, 3.0)$ exhibits two interesting properties. First, the harmonic wave beams originating from the focusing reflection of the rhomboidal wave attractor at $(r, z) = (0.8, 2.4)$ have larger amplitude due to an interaction of the wave oscillating with ω interacting non-linearly with the oscillating boundary layer or the reflected wave. Second, oscillations with 2ω of high energy are located irregularly in the vicinity of the bottom half of the frustum. This indicates onset of instability of the oscillating frustum boundary layer similar to what has been shown in figures 4.14(c, g). The reason is the viscous stability criterion (see Sauret *et al.*, 2012), which yields a reduction of the critical Rossby number when the Ekman number reduces.

Figures 4.19(a, e) and 4.19(b, f) show the kinetic energy densities for the Ekman numbers $E = 3.19 \times 10^{-3}$ and 3.19×10^{-4} respectively. The rhomboidal wave attractor (upper row) and the harmonic corner beams (lower row) can only be discerned up to the Ekman number

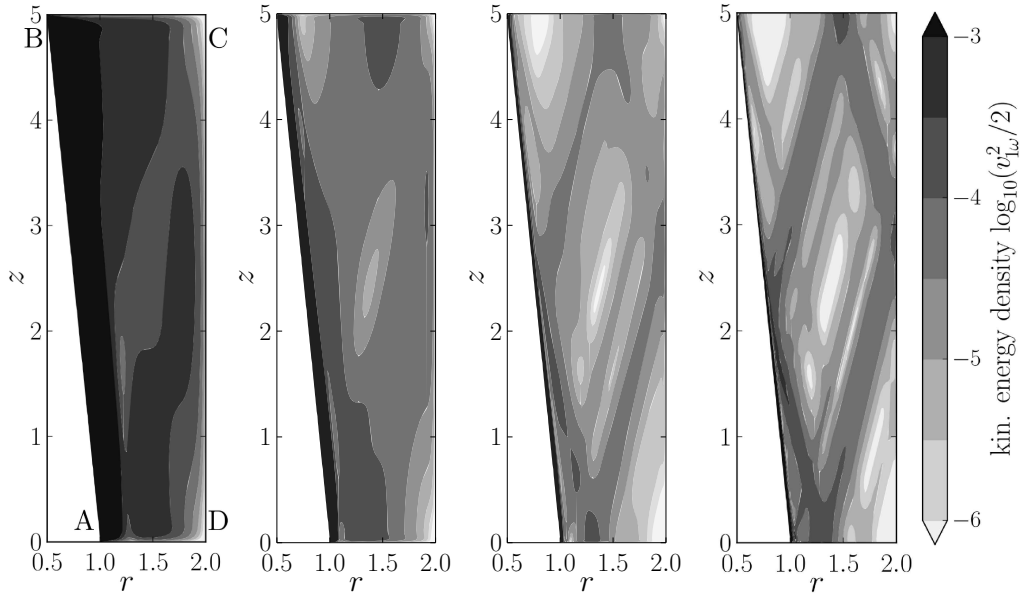

(a) $E = 3.19 \times 10^{-3}$ (b) $E = 3.19 \times 10^{-4}$ (c) $E = 3.19 \times 10^{-5}$ (d) $E = 9.57 \times 10^{-6}$

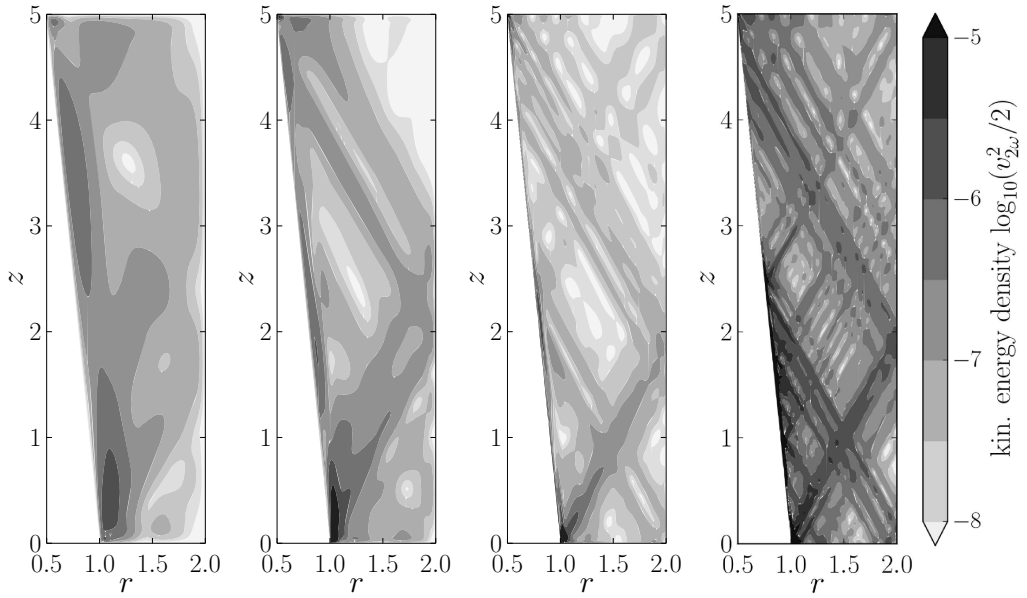

(e) $E = 3.19 \times 10^{-3}$ (f) $E = 3.19 \times 10^{-4}$ (g) $E = 3.19 \times 10^{-5}$ (h) $E = 9.57 \times 10^{-6}$

Figure 4.19: The rhomboidal wave attractor excited by frustum libration with forcing frequency $\omega = 0.47$ for various Ekman numbers E visualised by contours of the filtered kinetic energy density $v_{l\omega}^2/2$. Panels (a–d) show the dominating flow pattern oscillating at the forcing frequency ($l = 1$), where panel (c) corresponds to figure 4.12(b) but without the ray orbit. Panels (e–h) show the flow patterns oscillating at the first harmonic ($l = 2$). The harmonic is shown in order to keep track of non-linear features like harmonic corner beams or instability.

$E = 3.19 \times 10^{-4}$, figures 4.19(b, f), which corresponds to a Reynolds number of $Re = 630$ or a mean rotation rate of the laboratory experiment of $\Omega_0 = 3$ rpm (see table 4.1). The upper limit of the Ekman number for which inertial wave beams can be discerned agrees with the observations of Hollerbach & Kerswell (1995), who simulated inertial wave attractors in a spherical shell.

For even larger Ekman numbers, figures 4.19(a, e) corresponding to a Reynolds number $Re = 63$, the flow patterns are strongly smoothed and qualitatively different, that is, inertial wave beams can no longer be observed. The magnitude of the kinetic energy increases with the Ekman number, which indicates a larger power uptake by the system. Interestingly, the magnitude of the 2ω oscillations in figures 4.19(e, f) remained of the same order as in the case of the default Ekman number shown in figure 4.19(g). The corner beams and the harmonic corner beams are present in all cases that exhibit inertial waves, say figures 4.19(b–d) and 4.19(f–h) respectively.

Normal mode excited by lids plus outer cylinder libration for various Ekman numbers

Figure 4.20 shows the kinetic energy density for the flow excited by libration frequency $\omega = 1.38$ for various Ekman numbers. Figures 4.20(a–d) in the upper row show the spatial pattern oscillating with the forcing frequency ω, whereas figures 4.20(e–h) in the lower row show the spatial patterns oscillating with the harmonic of the forcing frequency 2ω. The contour levels are plotted in logarithmic scale every half an order of magnitude, using the same scale for each row. The Ekman number decreases from the left to the right.

Figures 4.20(c, g) correspond to the case of default dimensionless parameters with Ekman number $E = 3.19 \times 10^{-5}$. The flow structures related to the forcing frequency have been discussed thoroughly in section 4.2. Let us just recall that the numerical solution exhibits the axisymmetric $(1, 4, 0)$ mode and corner beams emerging from all four corners, but mainly from the top and bottom outer corners C and D such that a tilted-W pattern is formed (see figure 2.11(b)). The corner beams are not visible in the present scaling in the kinetic energy density of the flow patterns oscillating with ω, figure 4.20(c), but the corner beams are exhibited by the flow patterns oscillating with the harmonic 2ω, figure 4.20(g). The frequency $2\omega = 2.76$ is outside the inertial wave band so that the kinetic energy remains localised at the sources where it is excited non-linearly and also damped due to viscosity.

Figures 4.20(d, h) show the filtered kinetic energy densities for an Ekman number $E = 9.57 \times 10^{-6}$, which is 3.33 times smaller than the default. The spatial patterns in figure 4.20(c) and 4.20(d), as well as figure 4.20(g) and 4.20(h) are generally similar. The kinetic energy density of the mode pattern shown in figure 4.20(d) has decreased by about half an order of magnitude compared to figure 4.20(c), which can be seen best for the antinode at $(r, z) = (1.4, 3.7)$. The reduction of the kinetic energy density due to a reduced Ekman number is comparable to the wave attractor case discussed above. The mode can only be excited resonantly at a particular frequency, which suggests that the reduction of the energy of the mode is largely related to detuning rather than non-linearity.

As discussed in section 4.2, non-linearity has only little effect on the structure of a low-order eigenmode. This is backed by the flow structures oscillating with 2ω shown in figure 4.20(h), for which the kinetic energy level has in general decreased by half an order of magnitude compared to figure 4.20(g), which can be seen by completely white areas in the upper right part of the flow domain.

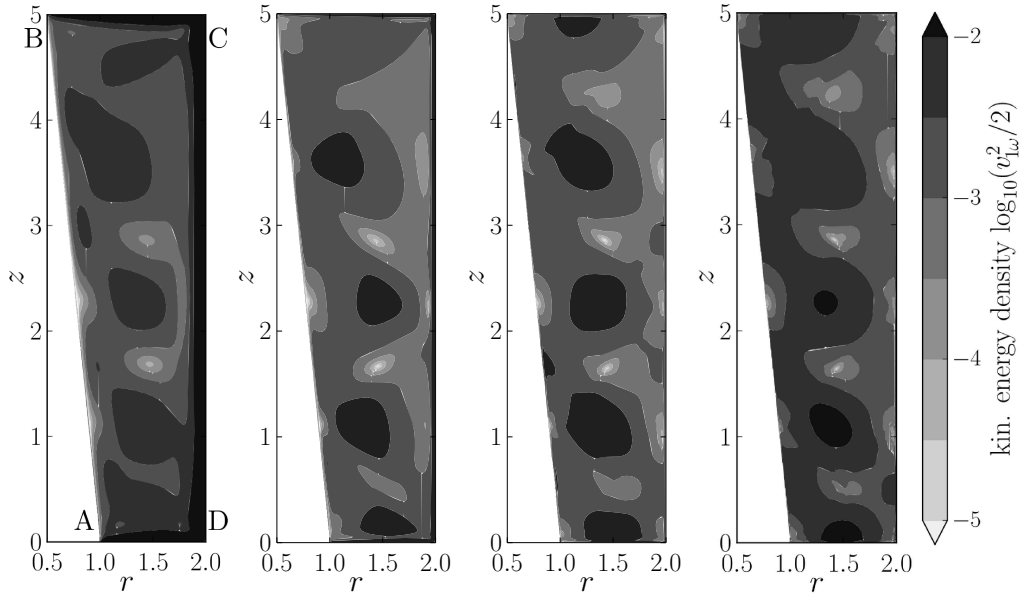

(a) $E = 3.19 \times 10^{-3}$ (b) $E = 3.19 \times 10^{-4}$ (c) $E = 3.19 \times 10^{-5}$ (d) $E = 9.57 \times 10^{-6}$

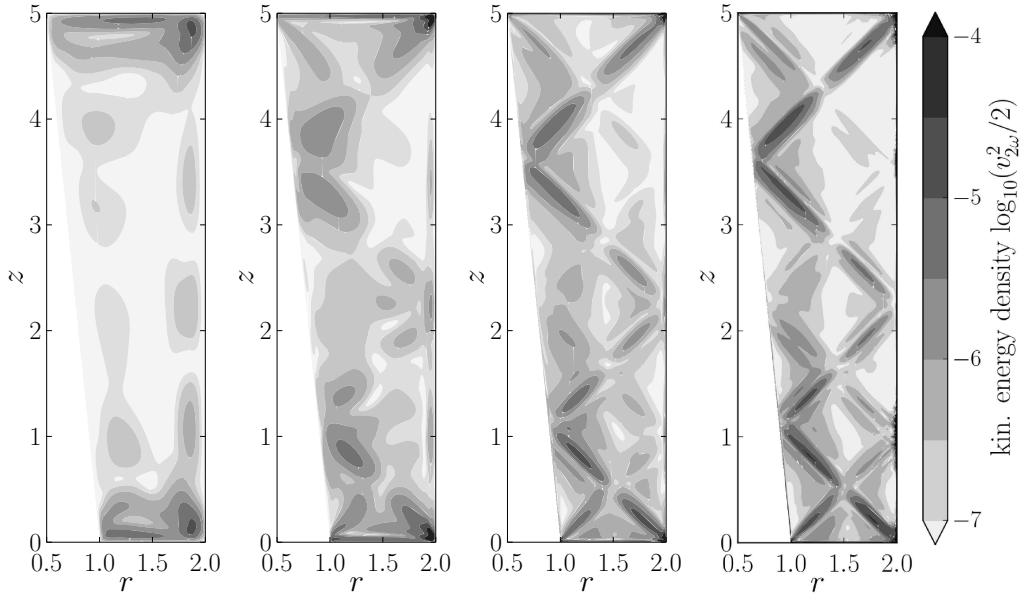

(e) $E = 3.19 \times 10^{-3}$ (f) $E = 3.19 \times 10^{-4}$ (g) $E = 3.19 \times 10^{-5}$ (h) $E = 9.57 \times 10^{-6}$

Figure 4.20: The $(1, 4, 0)$ mode excited by lids plus outer cylinder libration with forcing frequency $\omega = 1.38$ for various Ekman numbers E visualised by contours of the filtered kinetic energy density $v_{l\omega}^2/2$. Panels (a–d) show the dominating flow pattern oscillating at the forcing frequency ($l = 1$). Panels (e–h) show the flow patterns oscillating at the first harmonic ($l = 2$). The harmonic is shown in order to keep track of non-linear features like harmonic corner beams or instability.

Interestingly, the tilted-W pattern does not exhibit a reduction of the kinetic energy density $v_{2\omega}^2/2$ when the Ekman number is reduced, but the kinetic energy density is more concentrated along the tilted-W pattern. Moreover, there is additional fine structure visible along in the vicinity of the tilted-W patterns for the smaller Ekman number analogue to the wave attractor case. Here, one can discern maxima surrounding the tilted-W pattern, for instance at $(r, z) = (1.7, 2.5)$. This is not an effect of resolving more fine structure by a reduction of the Ekman number, instead, it is another indicator for viscous detuning. That is, the neutral ray orbit is not structurally stable against frequency variations or modifications of the flow domain due to a reduction of boundary layer thickness (see Borcia *et al.*, 2014). Hence, corner beams are not fed on the LONO but on a much longer ray orbit (see section 2.4). Due to the relatively large Ekman number here, only the first couple of reflections can be followed for which the corner beams or wave rays stay in the vicinity of the tilted-W pattern.

We can speculate that the LONO and the mode can be excited resonantly again by increasing the libration frequency from $\omega = 1.38$ gradually towards 1.4066, the frequency of the LONO obtained by ray tracing (see figure 2.11(b)). A numerical investigation is beyond the scope of this work. Nevertheless, more details on the normal mode excitation in the annular confinement are discussed by Ghasemi V. (2016).

Figures 4.20(a, e) and 4.20(b, f) show the kinetic energy densities for the Ekman numbers $E = 3.19 \times 10^{-3}$ and 3.19×10^{-4} respectively. The normal mode pattern (upper row) and the tilted-W pattern of the corner beams (lower row) can only be discerned up to the Ekman number $E = 3.19 \times 10^{-4}$. The normal mode pattern, though, exhibits antinodes at radially shifted locations, for example, the maximum at $(r, z) = (1.4, 3.7)$ in figure 4.20(c) is shifted to $r = 1.2$ in figure 4.20(b), which is closer to the tilted-W pattern connecting the outer corners C and D. This is another indicator of detuning, which means the normal mode has shifted to a resonance frequency $\sigma < 1.38$ here. As a reminder, we have attributed detuning mostly to viscosity here, that is, to the presence of a boundary layer that modifies the confinement geometry sensed by the waves. Another aspect is the generation of an azimuthal mean flow due to non-linearity which slightly modifies the underlying mean rotation rate (for a discussion see Ghasemi V., 2016).

The magnitude of the kinetic energy density, though, has not decreased which suggests that the off-resonant excitation is compensated by a larger power uptake of the fluid. The tilted-W pattern shown in figure 4.20(f) is notably smoothed and the kinetic energy density of the patterns oscillating with 2ω appears generally less localised. However, the maxima along the tilted-W pattern, for instance at $(r, z) = (1.0, 4.0)$, have reduced by about half an order of magnitude (one shade). The reasons are increased damping but also an effective decrease of the non-linearity due to smaller velocity gradients in a smoother solution. At $E = 3.19 \times 10^{-3}$, figure 4.20(a), it is interesting that 'traces' of the normal mode pattern can still be discerned. This is the case for the two antinodes at $(r, z) = (1.4, 1.0)$ and $(1.4, 2.3)$, but the kinetic energy density has decreased by half an order of magnitude compared to figure 4.20(b). The tilted-W pattern, though, is no longer visible in figure 4.20(e) which indicates that corner beams are no longer excited. Instead, the bulk flow seems to be an oscillatory circulation driven directly by the oscillating boundary layers. The oscillating boundary layer over the librating outer cylinder and the lids is now thick enough to be visible by completely black regions in figure 4.20(a).

In conclusion, the maximum Ekman number up to which inertial waves can be identified has been obtained by investigating two representative cases, the rhomboidal wave attractor excited by frustum libration and the $(1, 4, 0)$ mode excited by lids plus outer cylinder libration. The maximum Ekman number is of the order $E \sim 10^{-4}$. For larger Ekman numbers, the flow excited by libration is a basin-scale circulation which is driven by the oscillating boundary

layer. For smaller Ekman numbers, here as small as $E = 9.57 \times 10^{-6}$, the numerical solution exhibits the wave attractor and neutral orbit patterns similar to those obtained by ray tracing (see section 2.4).

The trend seen for Ekman numbers in the range $3.19 \times 10^{-4} \leqslant E \leqslant 9.57 \times 10^{-6}$ hints at a convergence of the wave beams in the fluid bulk to the patterns predicted by ray tracing. This is straightforward for the wave attractor and the corner beams, whose widths reduce together with the Ekman number (for the scaling laws, see Kerswell, 1995). For a neutral orbit or a corresponding normal mode, the correspondence is observed with respect to a convergence of the viscously shifted resonance frequency towards the frequency predicted by linear inviscid theory. The main reason for viscous frequency shifts is the presence of a boundary layer, which yields a modification of the domain geometry (e.g. Borcia *et al.*, 2014). Reduction of the Ekman number reduces the boundary layer thickness, which means the full domain can be occupied by inertial waves only in the linear inviscid limit ($R \to 0,\ E \to 0$). The latter is unrealistic since $R = 0$ would imply that the libration amplitude is zero and $E = 0$ would mean that viscosity is zero.

Extrapolating the results obtained so far yields ray tracing a useful method to predict the flow patterns of the full wave-dominated solution, where the forcing frequency in the inertial wave band gives the dominating frequency. The caveat is that a finite Ekman number shifts the frequencies of the structures obtained by ray tracing. Hence, the linear inviscid approximation cannot predict the flow patterns correctly even for the stable flow for wave attractor frequency bands (the white parts in figure 2.9) are of the same order or smaller than the viscous frequency shift. Moreover, also the frequencies of neutral orbits or the corresponding normal modes can never be predicted correctly since their frequency band has collapsed to a single frequency which will always be shifted by viscosity.

Finally, it remains to clarify the origin of the corner beams in order to complete the understanding of the energy injection into the fluid bulk. As we have seen with respect to the wave attractor, the corner beams serve to transport the majority of the kinetic energy from the oscillating boundary layer into the bulk. We will address the excitation of corner beams by wall libration in the next chapter (chapter 5) by investigating the local solution.

5 Corner flow due to libration and the localisation of inertial wave excitation

The purpose of this section is to clarify the excitation mechanism of the corner beams emitted from the corners adjacent to a librating wall. Corner beams are inertial waves emitted from the corners adjacent to a librating wall and they are localised in the direction perpendicular to the energy propagation (see chapter 4). Kinetic energy can leave the boundary layer region notably only in the form of corner beams, which makes the latter essential for the redistribution of kinetic energy in the fluid system and the energy injection into the fluid bulk. Corner beams are known for half a century (e.g. Beardsley, 1970; McEwan, 1970), but their excitation mechanism has remained unclear. Moreover, Kerswell (1995) and Swart *et al.* (2010) discuss how inertial wave beams (oscillatory internal shear layers) are emitted due to an 'eruption' of the oscillating boundary layer. Boisson *et al.* (2012) observed the corner beams in a recent laboratory experiment and commented on the role of the boundary layer flow. Unfortunately, the measurements could not access the near wall region and the local dynamics could still not be clarified. Therefore, DNS have been performed here that resolve the corner regions of the annular confinement (figure 1.3). The numerical solution serves as reference, but boundary layer theory will be applied to the librating annulus in order to develop a simple analytical model that will provide scaling laws with respect to the dimensionless parameters R, E, ω.

In the following, we begin with a study of the corner flow obtained by DNS in order to elucidate the local flow supposed to be responsible for wave excitation. The numerical solution to the corner flow serves as guide for the simplification of the problem so that an analytical model can be build by combining and extending the work of Swart *et al.* (2010) and Boisson *et al.* (2012). The analytical model will be local and accounts only for the unperturbed viscous boundary layer. The analytical solution will therefore be checked against the direct numerical solution in order to assess the validity in the librating annulus when non-linearity and inertial waves are present. At the end, the analytical solution will be used to formulate the model for the corner beam excitation, which will provide us the scaling laws for the kinetic energy injection by the corner beams. The scaling law for the libration frequency will be derived in the following and will serve as reference for the response spectra to be discussed further in chapter 6.

5.1 Corner flow in the librating annulus

The results shown in chapter 4 suggest that only a fraction of the kinetic energy localised in the oscillating boundary layer is actually converted into wave energy. Velocity amplitudes in the bulk and related to inertial waves are of the order $|\boldsymbol{v}| \sim 10^{-2}$, which is 100 times smaller than the libration velocity measured at the wall. (As before, scaled velocities are used taken relative to the co-rotating frame of reference; see table 4.1 for the scaling factors.)

No theory for the excitation of corner beams exists which renders direct numerical simulations (DNS) a valuable tool. The strength of DNS lies in the resolution of all the dynamical features of the flow without additional assumptions beyond the mathematical model given by

the incompressible Navier–Stokes equations (2.6), the continuity equation (2.7), and boundary conditions. This enables to study the local flow responsible for wave excitation, which is not possible or at least still very difficult in state of the art laboratory experiments (e.g. Boisson *et al.*, 2012; Borcia *et al.*, 2014; Seelig, 2014; Swart *et al.*, 2010).

In the following, the corner flow of the two configurations studied will be discussed in more detail. First, the corner flow near the bottom inner corner when the frustum is librating; second, the corner flow near the bottom outer corner when the lids together with the outer cylinder are librating. The first case addresses the more artificial situation when a librating wall is adjacent to a non-librating wall, which means the corner exhibits a jump of the wall velocity. The second case addresses the situation when both walls adjacent to the corner are librating together so that there is only a jump in the wall slope.

Frustum libration and the flow induced near the bottom inner corner

Figure 5.1 shows a snapshot of the radial velocity component v_r for the case of the rhomboidal wave attractor excited by frustum libration at forcing frequency $\omega = 0.47$ and default Ekman number $E = 3.19 \times 10^{-5}$. The Rossby number of $R = 0.02$ has been selected to minimise non-linear flow features. The snapshot shown corresponds to the end of the prograde libration half-period ($\omega t = \pi$). Figure 5.1(a) shows the bulk flow and is repeated from figure 4.14(a) to remind the reader of the flow patterns, which have been discussed earlier (see chapter 4). Most prominent is the rhomboidal wave attractor and the dominating corner beam emitted from the bottom inner corner A. One should also note the localisation of the largest velocity amplitudes along the librating frustum wall $\overline{\mathrm{AB}}$. The libration frequency $\omega = 0.47$ has been selected on purpose since the rhomboidal wave attractor ensures that no wave beam returns to the wave-emitting corner. The rhomboid also restricts the feedback of the bulk flow on the oscillating frustum boundary layer to a small volume at $r = 0.75$, $2.0 \leqslant z \leqslant 3.0$ where the focusing reflection occurs. In any case, the flow in figure 5.1(a) suggests that only a tiny volume around the two inner corners is responsible wave emission.

Figure 5.1(b) shows the close-up of the flow in the lower left part of the domain as indicated by the black rectangle in figure 5.1(a). The dominating flow structures are given by the lower part of the rhomboidal wave attractor with a reflection at $(r, z) = (1.3, 0.0)$, as well as the corner beam emitted from a small volume near corner A. Also visible is the boundary layer. On the one hand, the oscillating boundary layer over the frustum wall by positive (outward) radial velocity just over the wall, which is followed by a thin layer of negative (inward) radial velocity; see the blue patch with the centre at $(r, z) = (1.0, 0.5)$. On the other hand, a thin (Ekman) boundary layer over the lid can be discerned due to the deformation of the radial velocity contours just above the lid at $z = 0.0$. Near corner A the radial velocity exhibits the largest amplitudes but the dynamics responsible for wave emission are not yet visible in the magnification used so that a second close-up is required.

Corner flow in the case of a small Rossby number. Figure 5.2 shows the corner flow in a volume corresponding to the black rectangle marked in figure 5.1(b) for a small Rossby number $R = 0.02$. In order to reveal the flow dynamics, velocity pivots (v_r, v_z) are plotted together with contours of the helicity density (contours). The helicity density is a measure for screw-like structures in the velocity field (e.g. Kurgansky, 2002; Moffatt, 1969) and is given by the product $\boldsymbol{v} \cdot \boldsymbol{\zeta}$, where $\boldsymbol{\zeta} \equiv \boldsymbol{\nabla} \times \boldsymbol{v}$ the vorticity vector. The time series is shown for one libration period, the prograde libration half-period $0 \leqslant \omega t < \pi$ is shown in figures 5.2(a–d), the retrograde half-period $\pi \leqslant \omega t < 2\pi$ is shown in figures 5.2(e–h). There are two dominating helical structures:

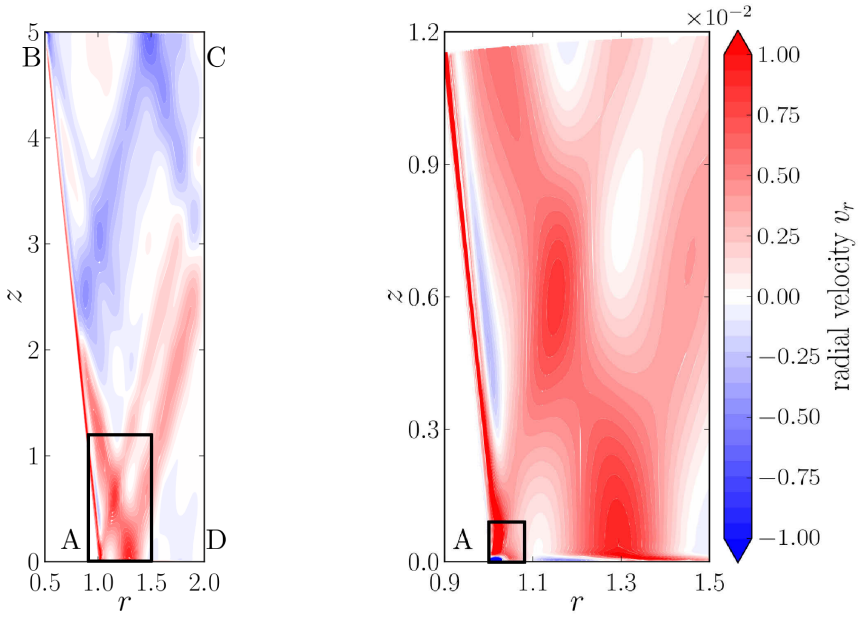

(a) Whole domain (b) Close-up at A

Figure 5.1: Full-domain view (a) and a first magnification (b) showing radial velocity contours at the end of the prograde libration half-period at $\omega t = \pi$ using the same colour scale in both panels. The flow is excited by frustum libration with $\omega = 0.47$ and exhibits the rhomboidal wave attractor due to which wave beams cannot return to the wave-emitting corner. Panel (a) is repeated from figure 4.14(a) and illustrates the magnification shown in panel (b) by a black rectangle. Panel (b) shows that the primary wave beam (corner beam) originates from a tiny volume near the corner A. Kinetic energy propagates from the lower left to the upper right. The boundary layers over the frustum and the lid can be discerned but the corner flow itself requires a higher magnification still as indicated by the black rectangle in panel (b). The dimensionless parameters are $R = 0.02$, $E = 3.19 \times 10^{-5}$.

first, the (oscillating) corner vortex in the volume $1.00 < r < 1.02$, $0.00 < z < 0.03$; second, the (oscillating) frustum boundary layer in $1.00 < r < 1.02$, $z > 0.03$. Both corner vortex and frustum boundary layer exhibit a reversal of the sign of the velocity and the vorticity (not shown) in the two libration half-phases such that the helicity density has a fixed sign (positive next to the lower inner corner). This can be clearly seen by comparing, for instance, figures 5.2(a) and 5.2(e).

In the corner vortex, the fluid spirals in anti-clockwise direction in figure 5.2(a) but in clockwise direction in figure 5.2(e) as indicated by the solid curved arrows. The azimuthal unit vector points into the drawing plane, which means the azimuthal vorticity ζ_φ at $(r, z) = (1.01, 0.01)$ is negative in figure 5.2(a) but positive in figure 5.2(e). The helicity density is positive in both images which implies that the azimuthal velocity v_φ is negative and directed out of the drawing plane at $(r, z) = (1.01, 0.01)$ in figure 5.2(a) but positive and directed into the drawing plane in figure 5.2(e). In figures 5.2(b, f) the corner vortex has vanished temporarily but is building up again in figures 5.2(c, g) and 5.2(d, h). Interestingly, there is a thin negative patch of helicity between the corner vortex and the frustum wall visible in figures 5.2(c, g) and 5.2(d, h), which indicates rather complex flow dynamics near the corner induced by libration.

Note that at the upper corner B the dynamics are basically similar to those shown in figure 5.2, but helicity has negative sign there because of the phase shift $\Delta(\omega t) = \pi$ with respect to the wall-tangential boundary layer current being directed to or from the corner B compared to A (not shown explicitly).

In conclusion, the corner beams are not visible in figure 5.2 because their helicity density is about 100 times smaller than that of the boundary layer flow. In figures 5.2(a, e), a dashed arrow is used to illustrate the corner beam propagation for orientation. The waves emitted from the bottom corner need to have negative helicity (compare to sections 2.4 and figure 4.2) while the corner vortex has positive helicity. Hence, wave emission is not strictly related to the corner vortex, but both, wave emission and corner vortex, are observed together.

Looking into the time dependency of the numerical solution (figure 5.2) suggests the following simplified picture of the dynamics. Libration of the frustum drives a wall-tangential boundary layer current, which is first directed along the frustum in azimuthal direction due to the viscous drag but changes gradually into vertical direction (still parallel to the wall) due to the action of the Coriolis force. The net effect is an oscillating flow directed vertically along the frustum as illustrated by the thick solid arrows at the top of figures 5.2(a, e) as will be discussed in more detail further down in this chapter.

The vertical velocity at $(r, z) = (1.00, 0.09)$, for example, is directed upwards in figures 5.2(a–d) but downwards in figures 5.2(e–h). The corresponding boundary layer current is deflected in radial direction in the vicinity of the corners due to geometrical constraints as indicated by another solid black arrow around $(r, z) = (1.01, 0.04)$. Since the flow has reversed sign at the upper corner B, a basin-scale circulation is induced which requires the induction of a compensating flow due to the conservation of angular momentum: the corner vortices at corners A and B. The boundary layer current constitutes a mass flux. The deflected mass flux is inert and keeps on moving radially while being affected by the Coriolis force such that the radial mass flux is turned gradually in azimuthal direction. The Coriolis force hence acts as restoring force such that the perturbation remains localised. Since the boundary layer current and deflected mass flux oscillate with the libration frequency $\omega < 2$, inertial waves can be excited due to the perturbation, which yields the corner beams.

It is worth noting that I am unaware of an analytical solution to the libration-induced corner flow. Wang (1970), for example, explicitly skipped the discussion of the corner flow and no subsequent publication followed that would have closed this lack of understanding. Nevertheless, numerical solutions reveal a certain similarity of the corner flow in a radial-axial section to 2-D corner flow without rotation (compare to Moffatt, 1964). Here, wall libration induces a boundary layer current towards the corner in a radial-axial section. However, the flow here has an azimuthal component so that it is three-dimensional which complicates the analytical treatment. It would be interesting to see if an analytical corner vortex could be constructed following Moffatt (1964) and Wang (1970) and if this solution yields inertial wave emission. This task, however, is way beyond the scope of this work and has to be addressed in future studies.

Corner flow in the case of a moderate Rossby number. Figure 5.3 shows the corner flow in a volume corresponding to the black rectangle marked in figure 5.1(b). The default Rossby number $R = 0.20$ has been selected in order to complement figure 4.2. Figure 5.3 uses the same visualisation as figure 5.2: velocity pivots (v_r, v_z) are plotted together with contours of the helicity density (contours); the same scales are used to allow a direct comparison. In

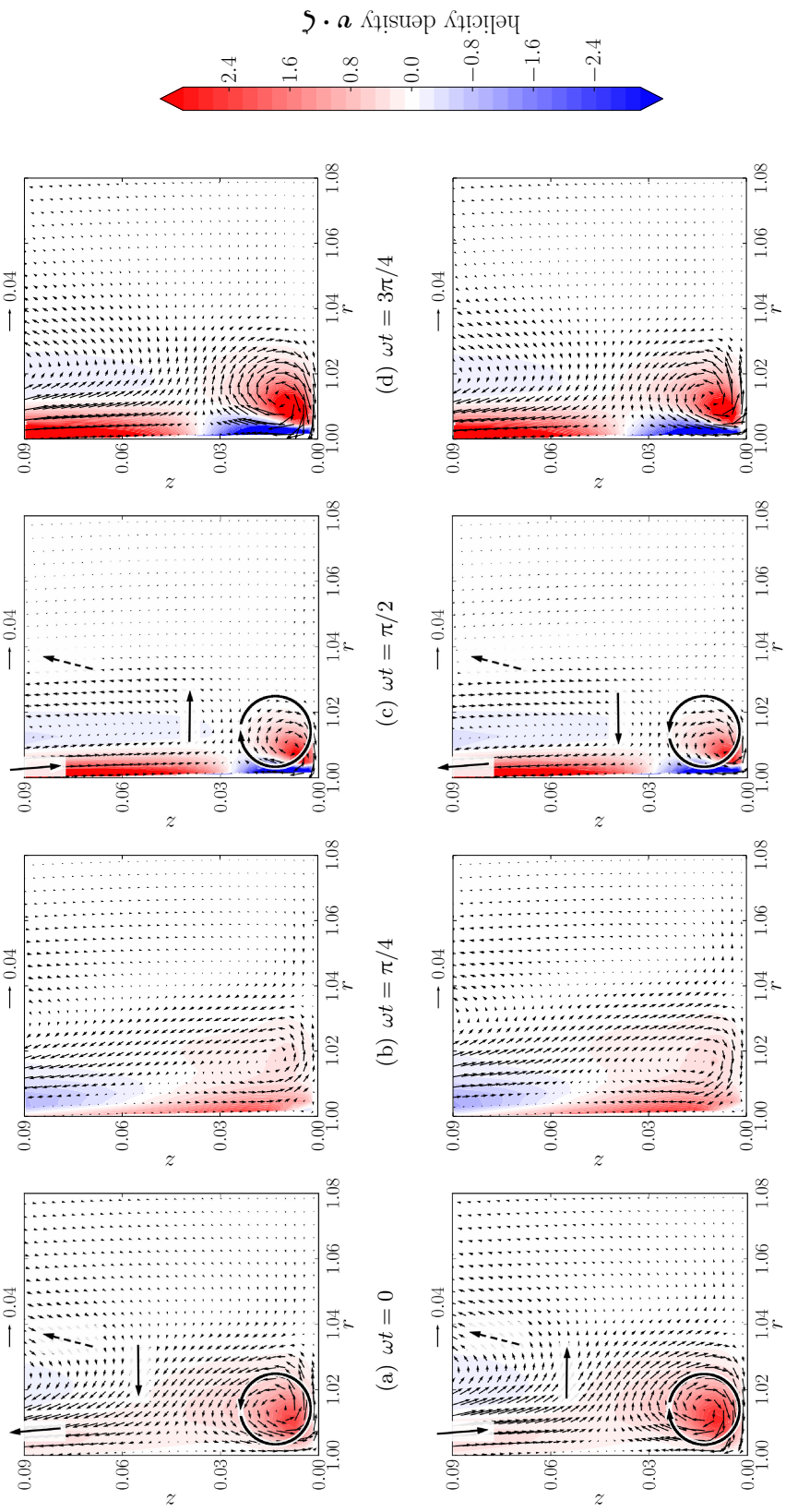

(a) $\omega t = 0$ (b) $\omega t = \pi/4$ (c) $\omega t = \pi/2$ (d) $\omega t = 3\pi/4$

(e) $\omega t = \pi$ (f) $\omega t = 5\pi/4$ (g) $\omega t = 3\pi/2$ (h) $\omega t = 7\pi/4$

Figure 5.2: Magnification of the corner flow near the bottom inner corner according to the rectangle in figure 5.1. The flow is excited by frustum libration with forcing frequency $\omega = 0.47$ and dimensionless parameters $R = 0.02$, $E = 3.19 \times 10^{-5}$. The flow is visualised by contours of the helicity density $\boldsymbol{v} \cdot \boldsymbol{\zeta}$ and velocity pivots (v_r, v_z). Panels (a–d) correspond to the prograde libration half-period, panels (e–h) to the retrograde libration half-period. The solid black arrows indicate the dominating flow: (i) flow along the wall induced by libration, (ii) radially directed velocity near the corner due to deflection of the wall-tangential flow, (iii) corner vortex. The corner beam has about 100 times smaller helicity magnitude than the corner flow and is not visible in the present scaling, but the propagation is illustrated by a dashed arrow.

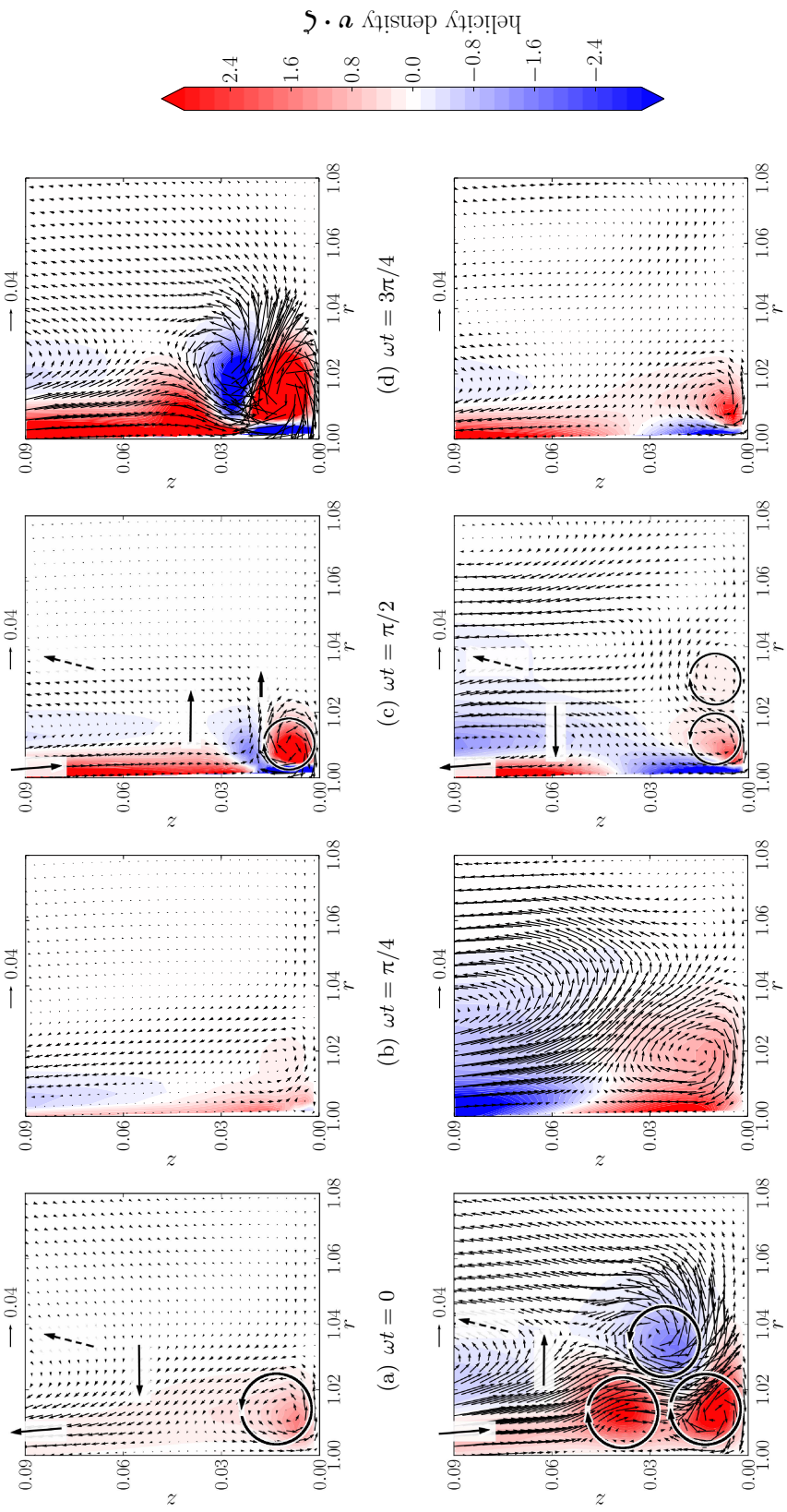

Figure 5.3: Magnification of the corner flow near the bottom inner corner according to the rectangle in figure 5.1. The flow is excited by frustum libration with forcing frequency $\omega = 0.47$ and dimensionless parameters $R = 0.20$, $E = 3.19 \times 10^{-5}$ (larger Rossby number compared to figure 5.2). The flow is visualised by contours of the helicity density $\boldsymbol{v} \cdot \boldsymbol{\zeta}$ and velocity pivots (v_r, v_z). Panels (a–d) correspond to the prograde libration half-period, panels (e–h) to the retrograde libration half-period. The solid black arrows indicate the dominating flow: (i) flow along the wall induced by libration, (ii) radially directed velocity due to deflection of the wall-tangential flow, (iii) vortices induced by the deflecting boundary layer current and the instability of the corner vortex. The corner beam has about 100 times smaller helicity magnitude than the corner flow and is not visible in the present scaling, but the propagation is illustrated by a dashed arrow.

general, the velocity amplitudes and the helicity density have increased in figure 5.3 compared to figure 5.2, which can be attributed to non-linearity.

Moreover, the corner vortex becomes unstable for $R = 0.20$ during the prograde libration half-period. The onset of the instability is roughly at $\omega t = \pi/2$, figure 5.3(c), where the wall velocity $v_{\mathrm{w},\varphi}$ reaches its maximum. Compared to figure 5.2(c), the positive helicity exceeds the colour scale at the centre of the corner vortex $(r, z) = (1.01, 0.01)$ and there is a small but strong radial jet forming at $(r, z) = (1.01, 0.02)$ just on top of the corner vortex. The radial jet is accompanied by a patch of negative helicity at $(r, z) = (1.01, 0.025)$. As time progresses, the instability grows but remains localised.

In figure 5.3(d) an intense patch of negative helicity has formed at $(r, z) = (0.028, 1.01)$ between two patches of positive helicity. The strong radial jet has grown and is now located at $(r, z) = (1.03, 0.02)$ but is still directed outward. In figure 5.3(e) the instability has started to decay and the radial jet is no longer visible as such. Instead, a relatively big counter-clockwise rotating vortex has formed at $(r, z) = (1.03, 0.02)$ which possesses negative helicity. This vortex is 'shielded' from the frustum wall by the two patches of positive helicity (two clockwise rotating vortices). In figure 5.3(f) then the vortex of negative helicity has vanished and the two vortices of positive helicity have merged so that only a single (corner) vortex can be discerned at $(r, z) = (1.02, 0.015)$. The decay of this (corner) vortex continues and there is no more sign of instability in figure 5.3(h) so that the cycle can start again in the next libration period.

In conclusion, the instability remains localised in the boundary layer near the inner corner A at $(r, z) = (1.0, 0.0)$. The evolution of the instability is closely correlated with the wall-libration and the oscillating boundary layer current driven along the frustum wall. The instability leads to a strong but localised radially outward directed jet near the corner during $\pi/2 < \omega t < \pi$. This radial jet is synchronised with the instability and the instability depends on the wall libration. Hence, there is a coherent radial outflow near the corner which can potentially increase the excitation of corner beams. The non-linear increase of wave excitation, however, only works for small Rossby numbers. For Rossby numbers large enough to have the flow become locally turbulent means that inertial waves are rather emitted spontaneously and incoherently with a broad spectrum of frequencies (see Sauret *et al.*, 2013) so that corner beams oscillating with the forcing frequency would weaken. This scenario is in qualitative agreement with the observations made in figure 4.14, where we have seen a decrease of wave beam amplitudes with increasing Rossby number.

Consequently, it is not quite clear yet if the corner vortex is a solution to the linearised equations of motion ($R = 0$) or a solution to the weakly non-linear ones ($R \ll 1$). The latter would mean that non-linearity is necessary but just not strong enough to cause instability. Since for $R = 0.20$ the flow is already unstable locally, it would be interesting to investigate the statistics of the unstable corner flow, perhaps analogous to the instability of the oscillating boundary layer (see Ghasemi V. *et al.*, 2016). It remains to look into the complementary configuration with the corner adjacent to two librating walls, which is the subject of the next section.

Lids plus outer cylinder libration and the flow induced near the bottom outer corner

Figure 5.4 shows a snapshot of the radial velocity component v_r for the case of lids plus outer cylinder libration but otherwise same parameters as in figure 5.1, that is, libration frequency $\omega = 0.47$, Rossby number $R = 0.02$ and Ekman number $E = 3.19 \times 10^{-5}$. The snapshot

has been taken at $\omega t = 0$, that is, at the end of the potentially unstable retrograde libration half-period. As before, the libration frequency has been selected such that no corner beam is reflected back into a corner (which is obviously fulfilled) and the Rossby number has been chosen small to avoid instability of the flow.

In contrast to the frustum libration case shown in figure 5.1(a), the rhomboidal wave attractor cannot be discerned in figure 5.4(a). There seem to be two reasons for this behaviour. First, focusing of the dominating corner beams from the outer corners C and D takes too many reflections to reach the wave attractor. Hence, the waves have been damped down before they have actually reached the rhomboidal wave attractor. Second, it seems that the waves excited at all four corners A–D annihilate by destructive interference, which is seemingly reflected by the vertical line of zero radial velocity located at $r \approx 1.4$. In other words, the symmetry of the forcing does not permit the excitation of the wave attractor when both lids are librating synchronously (for a discussion of the symmetry of the forcing but with respect to normal modes see e.g. Lopez & Marques, 2011).

Furthermore, it is worth to note that the largest radial velocities occur over the librating lids ($\overline{\mathrm{AD}}$ and $\overline{\mathrm{BC}}$), which indicates again that an understanding of the boundary layer flow is crucial for the clarification of inertial wave excitation by libration.

Figure 5.4(b) magnifies the volume near the bottom outer corner D as indicated by the black rectangle in figure 5.4(a). In figure 5.4(b) one can discern the corner beam emitted from corner D and its reflection, which returns to the lid at $(r, z) = (1.7, 0.0)$. Strong corner beam excitation is not trivial here since the outer cylinder is also librating and there is no singularity in the wall velocity across the corner unlike in the frustum libration case discussed above.

Moreover, it is known that the boundary layer over the lids is of Ekman type so that it exhibits strong Ekman pumping or suction (e.g. Busse *et al.*, 2007) and raises the question why inertial waves are not excited from the whole lid? The radial velocity hints at an explanation: a strong radial current is induced over the librating lid which has only vertical but no azimuthal vorticity. The radial flow along the lid has to be deflected when it reaches the outer corner D (or C at the upper lid) which induces azimuthal vorticity locally as discussed for the frustum libration case already. The local dynamics, however, are not yet resolved in the first magnification and we proceed by zooming in further by magnifying the volume illustrated by the rectangle in figure 5.4(b).

Figure 5.5 shows the corner flow in a volume corresponding to the black rectangle marked in figure 5.4(b) for a small Rossby number $R = 0.02$ analogous to the frustum libration case (see figure 5.2). Velocity pivots (v_r, v_z) are plotted together with contours of the helicity density $\boldsymbol{v} \cdot \boldsymbol{\zeta}$ (contours). Corner beams are emitted in the direction of the dashed arrow but they are not visible here since they have about 50 times smaller values of the helicity density than the boundary layer flow. The prograde libration half-period $0 \leqslant \omega t < \pi$ is shown by figures 5.5(a–d), the retrograde half-period $\pi \leqslant \omega t < 2\pi$ by figures 5.5(e–h). The snapshots reveal that the oscillating boundary layer is dominated by positive helicity, which is roughly symmetric in the pro- and retrograde libration half-periods.

Interestingly, a corner vortex is only visible in figures 5.5(a) and 5.5(e) with velocity pivots pointing along a circle in anti-clockwise and clockwise direction respectively with the centre at $(r, z) = (1.99, 0.01)$. The corner vortex is driven by the deflection of the radial boundary layer current, which is driven by the lid libration (solid arrow on the left) as we will see shortly (see section 5.2).

By contrast, figures 5.5(c, d) and 5.5(g, h) exhibit a small patch of negative helicity located at $(r, z) = (1.98, 0.01)$ and embedded in a boundary layer flow of positive helicity. This negative patch of helicity results from an overlap of two different types of oscillating boundary layers:

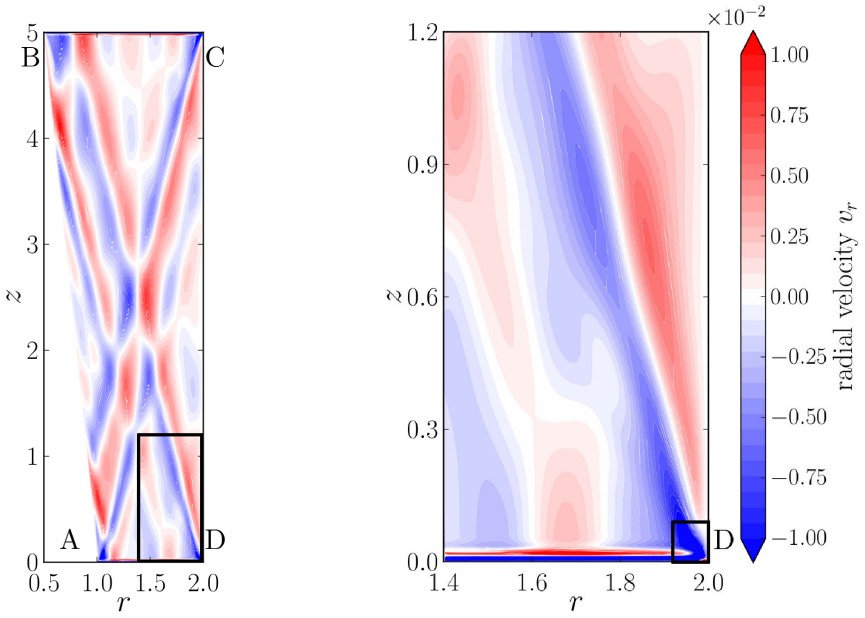

(a) Whole domain (b) Close-up at D

Figure 5.4: Full-domain view (a) and a first magnification (b) showing radial velocity contours at the end of the retrograde libration half-period at $\omega t = 0$ using the same colour scale in both panels. The flow is excited by lids plus outer cylinder libration with $\omega = 0.47$, $R = 0.02$, $E = 3.19 \times 10^{-5}$, but it does not exhibit the rhomboidal wave attractor because the corner beams are damped in the focusing stage. Panel (a) illustrates the magnification shown in panel (b) by a black rectangle. Panel (b) shows that one of the corner beams originates from a tiny volume near the corner D. The boundary layer over the lid can be discerned, but not over the outer cylinder, because the radial velocity is wall-normal and must vanish at the outer cylinder. The corner flow itself requires a higher magnification as indicated by the small black rectangle in panel (b).

an oscillating Stokes–Stewartson[1] boundary layer over the outer cylinder and an oscillating Ekman layer over the lid. In general, both differ strongly in their thickness and the boundary layer currents induced so that the local dynamics can be quite complex where two types of boundary layers overlap (here $1.97 < r < 2.00$, $0.00 < z < 0.02$). Nevertheless, negative helicity corresponds to an anti-clockwise motion in figures 5.5(c, d) and a clockwise motion in figures 5.5(g, h) as indicated by the curved arrow. This suggests that an oscillating corner vortex is part of the local solution but much weaker than the boundary layer currents.

It is worth noting that the corner flow does barely change when the Rossby number is increased to $R = 0.20$. Therefore, the corresponding figure is skipped here. The major difference is that the corner flow becomes unstable by generating a second vortex in radial direction on top of the already existing one. This is generally similar to the frustum libration case (see figure 5.3), but much less intense and phase shifted by $\Delta(\omega t) = \pi$ since the frustum libration is centrifugally unstable (velocity decreasing for increasing radii) in the prograde libration half-period, but the outer wall in the retrograde half-period.

[1]Here, the various boundary layers are generally very thin compared to the radius of the outer cylinder. Curvature is therefore neglected. Also neglected are non-linear effects such as mean flows. Therefore, the boundary layer over the librating outer cylinder will be addressed as *Stokes layer* in the following sections.

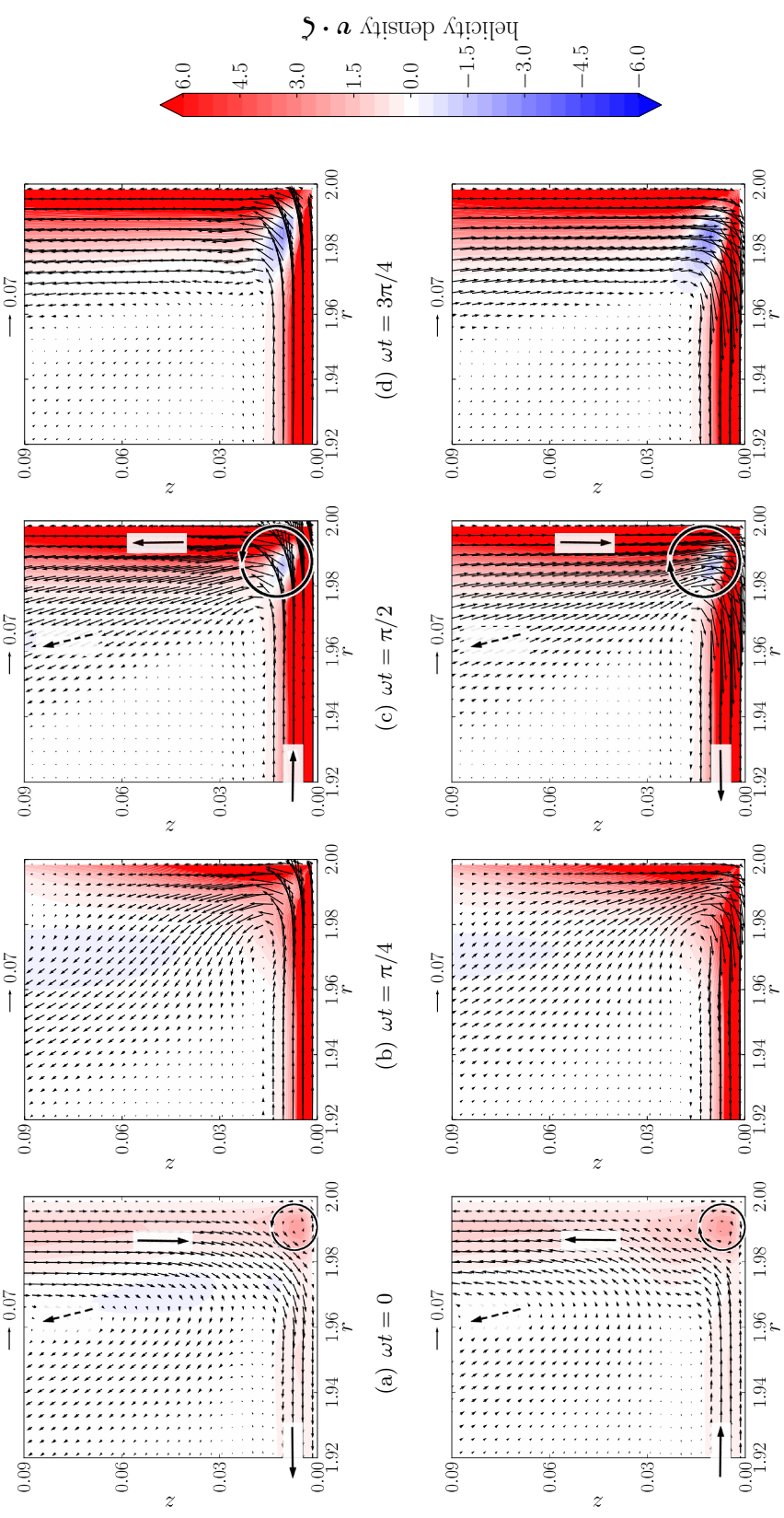

Figure 5.5: Magnification of the corner flow near the bottom outer corner according to the rectangle in figure 5.4. The flow is excited by lids plus outer cylinder libration with forcing frequency $\omega = 0.47$ and dimensionless parameters $R = 0.02$, $E = 3.19 \times 10^{-5}$. The flow is visualised by contours of the helicity density $\boldsymbol{v} \cdot \boldsymbol{\zeta}$ and velocity pivots (v_r, v_z). Panels (a–d) correspond to the prograde libration half-period, panels (e–h) to the retrograde libration half-period. The solid black arrows indicate the dominating flow: (i) flow along the wall induced by libration, (ii) radially directed velocity due to deflection of the wall-tangential flow, (iii) the corner vortex. The corner beam has about 50 times smaller helicity magnitude than the corner flow and is not visible in the present scaling, but the propagation is illustrated by a dashed arrow.

In conclusion, in the lids plus outer cylinder libration the results suggest that the corner beam excitation is also related to a deflection of a boundary layer current driven by the Ekman pumping mechanism over the librating lid (see figure 5.4(b)). Geometrical constraints only allow a deflection into axial direction and a large part of the current creeps along the outer cylinder wall for some distance before it detaches. Only a small fraction of the current induced by the librating lid therefore recirculates locally in the form of a corner vortex (see figure 5.5). Nevertheless, deflection of the outflow—be there a corner vortex or not—is in sync with wall libration. Fluid parcels are periodically displaced locally in radial direction. A small recirculation of the deflected flow appears to be just the necessary ingredient to yield not only an oscillating velocity, but also oscillating vorticity and helicity near the corner such that inertial waves can be excited locally.

In the following, we continue with the quantification of wave excitation by building a simple analytical model with the aid of boundary layer theory. Let us first repeat and extend state-of-the-art boundary layer theory (section 5.2) before continuing with the formulation of the model for the corner beam excitation (section 5.3).

5.2 Boundary layers in the annular confinement

In the previous section, the local structure of the numerical solution has been investigated using two magnifications of the corner regions in a radial-axial section of the annular confinement (figure 1.3). We concluded that the corner flow and the corner beams are a consequence of the boundary layer currents, which may 'pump' fluid to a corner or 'suck' fluid from a corner respectively. The hypothesis is that the strength of the pumping/suction governs the strength of the corner vortex, of the radially deflected mass flux and, thus, the corner beam excitation. In order to study the boundary layer currents and mass fluxes, idealised boundary layers are investigated which are relevant in the librating annulus. The time dependency due to a librating wall enters only parametrically, which means existing steady theory Pedlosky & Greenspan (1967); Greenspan (1969, pp. 85–91, 118–124); Busse *et al.* (2007, pp. 126) can be modified in analogy to Wang (1970) and Swart *et al.* (2010).

In the following, we concentrate on the near-wall structure of the flow, which is governed by viscosity and Coriolis force far away from any of the corners and we will consider only laterally infinite domains. The boundary layer thickness is typically much thinner than the annular gap (see chapter 4) and since the annular configuration excludes the axis, we can restrict our attention to a local Cartesian approximation. Moreover, the oscillating boundary layer over a librating wall has 1–2 orders of magnitude larger velocity amplitudes than the bulk flow (see chapter 4) so that the feedback from the free-stream solution will be neglected in the local analysis. Below, we will first derive the linearised local equations of motion. Second, the Stokes and Ekman layer will be given in streamlined notation. Third, the oscillating Ekman layer will be discussed in more detail since it is essential for the excitation of corner beams and not so well covered in existing literature.

Local axes and the boundary layer equations on the f-plane

The starting point is given by the scaled equations (2.6) and (2.7) in the co-rotating frame of reference together with the libration boundary conditions of equations (2.15)–(2.17) of the

annular confinement (see figure 1.3). The boundary layer thickness $\delta_{\mathrm{BL}} \sim E^{1/2}$ (compare to equation (3.70)) must be significantly smaller than the basin scale, that is,

$$\delta_{\mathrm{BL}} \ll 1 \qquad \text{and} \qquad r_1, r_2, h \sim 1 \tag{5.1}$$

for r_1, r_2 denoting the annulus radii and h the annulus height.

We consider only the viscous boundary layer for which non-linear terms are smaller than viscous forces and the Coriolis force. Viscosity must not vanish, but non-linearity can be arbitrary small. Here, we linearise the momentum equation (2.6) by assuming $R \ll E^{1/2}$. Hence, the dimensionless parameters in equation (2.6) read

$$E^{1/2} \ll 1, \qquad R = 0. \tag{5.2}$$

Note that vanishing Rossby number implies $R \not\propto \varepsilon$ since libration would have zero amplitude. Nevertheless, in the linearised equations we consider the fluid velocity $\boldsymbol{v}$ scaled with the local libration amplitude $U = \varepsilon f r/2$, where r is the local radius of the librating wall and $f = 2\Omega_0$ the Coriolis parameter.

The inequality in equation (5.1) allows to make use of a local Cartesian approximation. The local axes are illustrated in figure 5.6. The coordinates (x', y', z') denote the Cartesian coordinates of the local axes. We require that x' points locally in the azimuthal (zonal) direction $\boldsymbol{e}_\varphi$ and that z' points into the fluid in local wall-normal direction (anti-parallel to the surface normal $\boldsymbol{n}$). The right-handedness of the local axes yields y' to be wall-tangential in a radial-axial section and to point into the direction $\boldsymbol{e}_\varphi \times \boldsymbol{n}$. Cylindrical velocities (v_r, v_φ, v_z) are mapped to local Cartesian velocities (u', v', w'), where u' denotes the zonal velocity, v' the wall-tangential velocity in the radial-axial section, and w' the wall-normal velocity. On the lids, the tangential axes are parallel to an underlying Cartesian axes due to which unprimed notation is used (see figure 5.6). This will be useful later on to distinguish between the librating frustum and the librating bottom lid at a later point. The transformation from the bottom lid coordinates into the frustum basis reads

$$\boldsymbol{e}'_x = \boldsymbol{e}_x, \qquad \boldsymbol{e}'_y = \boldsymbol{e}_y \sin\alpha + \boldsymbol{e}_z \cos\alpha, \qquad \boldsymbol{e}'_z = \boldsymbol{e}_z \sin\alpha - \boldsymbol{e}_y \cos\alpha. \tag{5.3}$$

We are faced with an axisymmetric confinement and axisymmetric forcing due to libration. Hence, the laminar local solutions are expected to be axisymmetric has well. In the local Cartesian approximation, axisymmetry corresponds to zonal invariance, that is, $\partial(\cdot)/\partial x' \equiv 0$ for any of the flow variables. Therefore, we continue with the stream function formulation.

Let ψ denote the poloidal (radial-axial) stream function such that the local velocity components v' and w' are given by

$$v' = -\frac{\partial \psi}{\partial z'}, \qquad w' = \frac{\partial \psi}{\partial y'}. \tag{5.4}$$

This stream function formulation automatically ensures solenoidality for any x'-invariant solution since $\boldsymbol{\nabla} \cdot \boldsymbol{v} = \partial v'/\partial y' + \partial w'/\partial z' \equiv 0$. The momentum equations for v' and w' (compare to equation (2.10) using primed variables) can be combined in a single PDE for ψ by cross-differentiation and subtraction in such a way that the excess pressure terms cancel. The inequality (5.1) can be stressed a little bit further since the boundary layer flow is approximately invariant in the wall-tangential direction for points close enough to the wall (e.g. $z' \lesssim \delta_{\mathrm{BL}}$), hence

$$\left|\frac{\partial}{\partial y'}(\cdot)\right| \ll \left|\frac{\partial}{\partial z'}(\cdot)\right|. \tag{5.5}$$

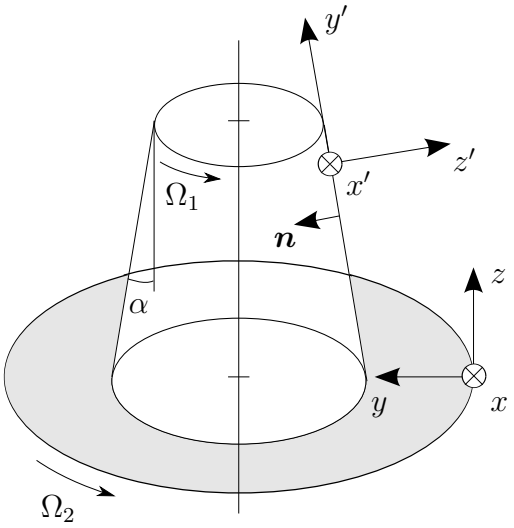

Figure 5.6: Definition of the local right-handed axes (x', y', z'). The local axes are oriented such that x' points in the local azimuthal direction and z' points in wall-normal direction into the fluid (anti-parallel to the surface normal $\boldsymbol{n}$). Unprimed coordinates are used for the local axes associated with the bottom lid since it is parallel to the underlying Cartesian coordinates. The inner wall (frustum) is inclined towards the central axis with the cone half-angle α, here $\alpha = 5.71°$ if not mentioned otherwise. Rotation rates Ω_1 and Ω_2 refer to the two different libration boundary conditions and indicate which parts in the clipped geometry can rotate independently. (From M. Klein *et al.* (2014). 'Inertial wave excitation and focusing in a liquid bounded by a frustum and a cylinder'. *J. Fluid Mech.*, **751**, p. 258, figure 1(b), reproduced with permission.)

Finally, one obtains two PDEs for the poloidal stream function ψ and the zonal velocity u' forming the *boundary layer equations on the f-plane equations* (or simply *f-plane equations*)

$$\frac{\partial}{\partial t}\frac{\partial^2\psi}{\partial z'^2} = f_*\frac{\partial u'}{\partial z'} + E\frac{\partial^4\psi}{\partial z'^4}, \qquad \frac{\partial u'}{\partial t} = -f_*\frac{\partial \psi}{\partial z'} + E\frac{\partial^2 u'}{\partial z'^2}, \tag{5.6}$$

in which f_* denotes the *effective* Coriolis parameter

$$f_* \equiv f\sin\alpha. \tag{5.7}$$

In the present scaling, the dimensionless conventional Coriolis parameter is given by $f = 2$. The local wall inclination is denoted α and measured with respect to the z-axis (axis of rotation; see figure 5.6). On the bottom lid, one has $\alpha = \pi/2$ and $f_* = f$. On the top lid, $\alpha = -\pi/2$ and $f_* = -f$. On the frustum, one has $\alpha = 5.71°$ (5.93° in the numerical grid; see figure 3.4) so that $f_* = 0.2$. The flow at the outer cylinder is of different quality since $\alpha = \pi$ and $f_* = 0$, which means the Coriolis force does not affect the local dynamics of the outer cylinder boundary layer. Hence, the f-plane equations (5.6) suggest that the boundary layer flow is in a first approximation sensitive only to the wall-tangential component of the Coriolis force. This leaves us to solve a quasi-2-D problem for the 3-D axisymmetric velocity field, which is sometimes called a '2.5-D model'.

Equation (5.6) is completed by a no-slip boundary condition at the wall and regularity at large distance from the wall, namely

$$\left.\begin{aligned} \psi = \boldsymbol{n}\cdot\boldsymbol{\nabla}\psi = 0, \qquad u' = U'\sin(\omega t) \qquad &\text{for} \quad z' = 0, \\ \psi \to 0, \qquad u' \to u_{\text{bulk}} \qquad &\text{for} \quad z' \to +\infty, \end{aligned}\right\} \tag{5.8}$$

where U' denotes the local libration velocity relative to the co-rotating frame of reference and u_{bulk} denotes the steady (or only weakly time-dependent) free-stream solution.

In the following, two idealised configurations are relevant with respect to the flow in the annular confinement. First, $U' \neq 0$ and $u_{\text{bulk}} = 0$ in the case of the wall under consideration is librating and the bulk flow vanishes approximately. This will be used for the oscillating boundary layers, given by the Stokes layer and the oscillating Ekman layer. Second, $U' = 0$ and $u_{\text{bulk}} \neq 0$ in the case of the wall is not librating but the bulk flow looses energy by skin friction, which will be used for the Ekman layer.

Stokes layer over the librating outer cylinder

The boundary layer flow due to an oscillatory wall in a non-rotating environment is well-known and constitutes the so-called Second Problem of (Stokes, 1851) (see Batchelor, 1967, pp. 353–355). The corresponding configuration in the annulus corresponds to the outer cylinder in libration since $f_* = 0$, which means no sensible effect of the Coriolis force and the f-plane equations (5.6) decouple. The boundary conditions given by equations (5.8) yield $\psi \equiv 0$ and, correspondingly, $v' = w' = 0$. The librating outer cylinder induces only the purely zonal flow

$$\frac{\partial u'}{\partial t} = E\frac{\partial^2 u'}{\partial z'^2} \qquad \text{with} \quad u'\big|_{z'=0} = U'\sin(\omega t) \tag{5.9}$$

and $z' = r_2 - r$ measuring the distance from the outer cylinder. Separation of variables (see Bronstein *et al.*, 2005, p. 543) and matching of the boundary condition yields the *Stokes layer solution*

$$u' = U' \sin\left(\omega t - \frac{z'}{\delta_\mathrm{S}}\right) \exp\left(-\frac{z'}{\delta_\mathrm{S}}\right) \qquad \text{with} \quad \delta_\mathrm{S} \equiv \sqrt{\frac{2E}{\omega}}, \tag{5.10}$$

in which δ_S denotes the Stokes layer thickness that depends on the forcing frequency and viscosity, here given by the Ekman number (compare to equation (3.70) and see figure 5.9 below for the ω-dependency). The oscillatory perturbation imposed by libration diffuses into the domain and prevents the system from reaching equilibrium. Dissipation and cancellation of the oscillating perturbation, though, limits the affected fluid volume to a thin layer.

Figure 5.7 shows the laminar Stokes layer profile according to equation (5.10) in comparison to the boundary layer profile extracted from the weakly non-linear DNS for two different libration phases $\omega t = 0$, $\pi/2$ in the statistically stationary state. The variability of the Stokes layer profile is illustrated by a shaded area, which corresponds to the analytical solution. The Stokes layer thickness δ_S is marked by a by dotted vertical line.

The DNS has been performed for $\omega = 0.91$, $R = 0.2$, $E = 3.19 \times 10^{-5}$ and provides the reference in terms of the azimuthal velocity ($u' = v_\varphi$), which has been extracted by an interpolation to the radial coordinate at height $z = 4.0$ (see figure 4.13(c)). The libration frequency $\omega = 0.91$ has been selected to ensure that the corner beams emitted due to the lids and outer cylinder libration are fed almost on a tilted-V pattern that connects the top and bottom outer or inner corners respectively (see figure 2.11(a)). Hence, the corner beams reflect a couple of times in the vicinity of the corners and at around mid height $z = 2.5$ before they are damped. The selected libration frequency also ensures that the excitation of the $(1, 2, 0)$ mode is avoided so that figure 5.7 yields a fair comparison.

In general, figure 5.7 exhibits very good agreement with respect to amplitude and phase between weakly non-linear DNS and the boundary layer solution. This is remarkable, given the strong assumptions made for the computation of the analytical solution, but it indicates that the boundary layer approximations are generally valid in the annulus as long as there is only a weak bulk flow over the librating outer cylinder.

Note in this respect that the profiles of v' and w' in the DNS fulfil $|v'| \sim |w'| \ll |u'|$, where maximum absolute values of v' and w' are at least one order of magnitude smaller than the maximum amplitude of u' for the near-wall region $z'/\delta_\mathrm{S} \leqslant 3$ (not shown explicitly).

Note further that the excess pressure ϕ does *not* vanish even though it does not enter the f-plane equations (5.6). The Poisson equation for the f-plane equations reads

$$\frac{\partial^2 \phi}{\partial z'^2} = f \frac{\partial u'}{\partial z'} \qquad \Rightarrow \qquad \frac{\partial \phi}{\partial z'} = f u', \tag{5.11}$$

which means the Stokes layer flow is in geostrophic balance and the excess pressure ϕ follows the Stokes layer profile given by equation (5.10). Hence, instead of saying *'the (excess) pressure is constant across the boundary layer'*, a more general statement would be *'the (excess) pressure is balanced in the boundary layer'*. This hints at the possibility that the excess pressure could be unbalanced in some situation, for example in a non-axisymmetric state, such that the success of the boundary layer approximations is generally case dependent (for an elaboration see e.g. Batchelor, 1967, pp. 302–308).

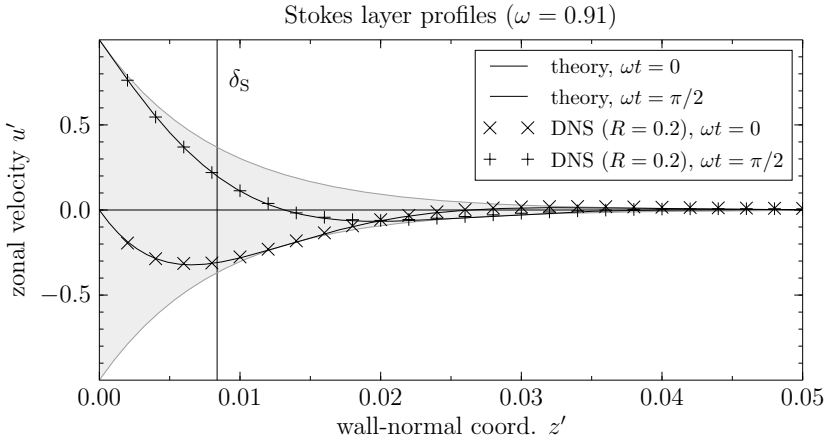

Figure 5.7: Stokes layer profiles at the librating outer cylinder for two libration phases $\omega t = 0$, $\pi/2$ comparing the analytical solution to the boundary layer equations to the weakly non-linear numerical solution obtained for lids plus outer cylinder libration. The DNS has been performed for the dimensionless parameters $R = 0.2$, $E = 3.19 \times 10^{-5}$ and libration frequency $\omega = 0.91$ to ensure that inertial waves are not excited resonantly and corner beams located around two tilted-V patterns (compare to figure 4.13(c)). The azimuthal velocity ($u' = v_\varphi$) has been obtained by interpolating to the radial coordinate at height $z = 4.0$. The local coordinate is given by $z' = r_2 - r$ and is shown for $z'/\delta_S \leqslant 6$, where the Stokes layer thickness δ_S is given by a dotted vertical line. The variability of the analytical solution is illustrated by a shaded area.

Ekman layer over non-librating lid and frustum due to a steady bulk flow

The Ekman boundary layer is well-known (Ekman, 1905) and usually discussed in terms of a geostrophically balanced bulk flow over a horizontal wall that is kept fixed in the co-rotating frame of reference (e.g. Greenspan, 1969, pp. 30–34). The essential differences to the Stokes boundary layer is that Coriolis force affects the flow due to which the f-plane equations (5.6) do *not* decouple. Therefore, the boundary layer is of Ekman layer type as soon as the wall is notably inclined to the vertical so that $f_* \neq 0$ (or $\alpha \neq 0$, see figure 5.6). The dynamics are a little more complex than those of the Stokes layer wherefore we consider first the classical steady situation here before moving on to a librating wall. The solution obtained is approximately valid for weakly time-dependent bulk flows, which means the classical Ekman problem to be discussed shortly can serve to estimate the energy dissipation rates by non-librating lids or frustum.

In the local Cartesian approximation, the starting point is an axisymmetric swirl flow given by the (locally uniform) zonal bulk flow $u_{\text{bulk}} = 1$. The bulk flow is in geostrophic balance, that is,

$$\boldsymbol{\nabla}\phi = -f u_{\text{bulk}} \boldsymbol{e}_z \times \boldsymbol{e}'_x \qquad \Leftrightarrow \qquad \frac{\partial \phi}{\partial y'} = -f_* u_{\text{bulk}}, \qquad \frac{\partial \phi}{\partial z'} = (f \cos\alpha)\, u_{\text{bulk}}. \tag{5.12}$$

This uniformity of the bulk flow yields zero vorticity with respect to the local Cartesian axis, which means there will be no wall-normal transport, say $w' = 0$. This is an over-simplification and is only approximately valid (for the axisymmetric case with a vortical bulk flow see Greenspan, 1969, pp. 30–34). Nevertheless, the analytical treatment is simpler in the Cartesian coordinates and will capture the main features.

We continue analogous to Busse *et al.* (2007, pp. 126–129) and use the linearised Navier–Stokes equations (2.10) for $R = 0$ and primed variables. This turns out more efficient than the stream function formulation since the excess pressure gradients can be removed by substituting the geostrophic balance, equation (5.12), and an exploit of the zonal invariance, $\partial(\cdot)/\partial x' \equiv 0$. Moreover, the inequality (5.5) yields $u'(z')$ and $v'(z')$, which are both functions of the wall-normal coordinate z' only. The velocity field is laminar and the continuity equation (2.11) is fulfilled automatically. Combining u' and v' in one complex variable $\hat{\chi} := (1 - u') + \mathrm{i}v'$ yields a single ordinary differential equation (ODE) for the steady state, namely

$$\frac{\mathrm{d}^2\hat{\chi}}{\mathrm{d}z'^2} = -\mathrm{i}\frac{f_*}{E}\hat{\chi} \qquad \text{with} \quad \hat{\chi}(0) = 1, \quad \hat{\chi}(z') \xrightarrow{z'\to+\infty} 0. \tag{5.13}$$

Equation (5.13) has an exponential solution. Matching of the boundary conditions yields the (classical) *Ekman layer solution*

$$\left.\begin{aligned} u' = 1 - \cos\left(\frac{z'}{\delta'_{\mathrm{E}}}\right)\exp\left(-\frac{z'}{\delta'_{\mathrm{E}}}\right), \qquad v' = \operatorname{sgn}(f_*)\sin\left(\frac{z'}{\delta'_{\mathrm{E}}}\right)\exp\left(-\frac{z'}{\delta'_{\mathrm{E}}}\right) \\ \text{with} \quad \delta'_{\mathrm{E}} \equiv \sqrt{\frac{2E}{|f_*|}}, \end{aligned}\right\} \tag{5.14}$$

in which δ'_{E} denotes the Ekman layer thickness over a surface inclined with an angle $\alpha = \arcsin(f_*/f)$ towards the rotation axis. As usual, the unprimed Ekman layer thickness δ_{E} is obtained over the lids, where $|f_*| = f$. The Ekman layer thickness obeys $\delta'_{\mathrm{E}} \geqslant \delta_{\mathrm{E}}$ and becomes minimal over the lids. The classical Ekman layer solution given by equations (5.14) is strictly valid only for steady flow. However, the thicknesses δ'_{E} over the frustum ($f_* = 0.2$) and δ_{E} over the lid ($f = 2$) are plotted over the entire frequency range in figure 5.9 (see below) to aid comparison with the oscillating boundary layers.

Figure 5.8 shows the *Ekman spiral* for the velocity components given by equation (5.14) for two situations, a geostrophically balanced bulk flow over a horizontal surface (bottom lid; solid line) and the bulk flow over an inclined surface (frustum; dashed line). The Ekman spiral is described by the tip of the tangential velocity vector $(u', v')^{\mathrm{T}}$ (e.g. Greenspan, 1969, p. 33) and is the same for both cases studied. In wall-normal direction (out of the drawing plane), however, the spiral is stretched in accord with the boundary layer thicknesses δ'_{E} and δ_{E} since the Ekman layer solution is self-similar to the stretched coordinates z'/δ'_{E} and z'/δ_{E}. Unfortunately, there is no corresponding DNS to which the analytical solution could be compared to directly.

Note that it is due to the construction that the excess pressure ϕ exhibits the geostrophic balance in the bulk and the boundary layer. The Poisson equation for the excess pressure on the f-plane reads

$$\frac{\partial^2\phi}{\partial z'^2} = (f\cos\alpha)\frac{\partial u'}{\partial z'} \qquad \Rightarrow \qquad \frac{\partial\phi}{\partial z'} = (f\cos\alpha)\,u', \tag{5.15}$$

in which the latter equation just expresses the momentum balance (equation (5.12)) in the limit of a small wall-tangential gradient, $|\partial\phi/\partial y'| \ll 1$. Hence, only the zonal velocity component u' contributes to the geostrophic balance on the f-plane, which is in fact similar to the Stokes layer solution at the outer cylinder (see equation (5.11)).

Note further that there are net energy and momentum fluxes from the bulk into the boundary layer due to the friction exerted by the wall. The viscous surface stress is given by $E\boldsymbol{\tau}\cdot\boldsymbol{n}$ at

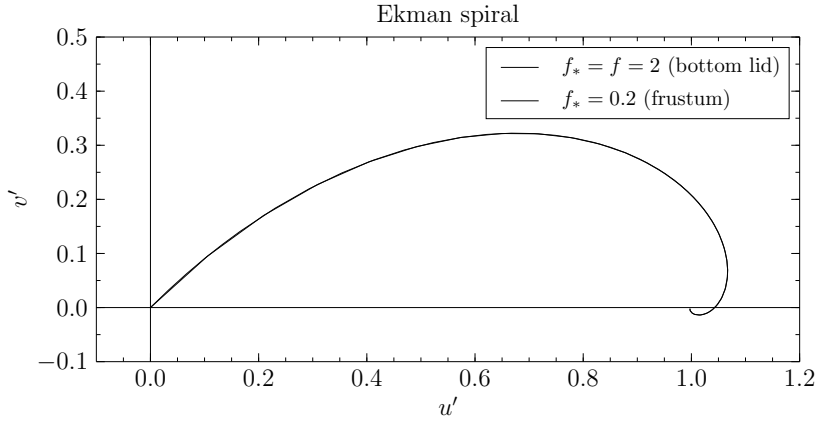

Figure 5.8: Velocity hodograph (Ekman spiral) of the analytical solution to the Ekman layer equations obtained for a uniform bulk flow of amplitude $u_{\mathrm{bulk}} = 1$. The Ekman spiral traces the tip of the velocity vector $(u', v')^{\mathrm{T}}$. The velocity vector vanishes at the wall ($z' = 0$), but approach $(u', v')^{\mathrm{T}} = (1.0, 0.0)^{\mathrm{T}}$ for $z' \to +\infty$. The Ekman spiral is the same for the bulk flow over the frustum ($f_* = 0.2$) and over the bottom lid ($f_* = f = 2$) because the analytical solution is similar with respect to the boundary layer coordinate z'/δ'_{E} and z'/δ_{E} respectively.

$z' = 0$, where $\boldsymbol{n} = -\boldsymbol{e}'_z$ and the rate of strain tensor $\boldsymbol{\tau}$ (compare with equation (3.73)). The shear stress exerted *on* the wall reads

$$-E\boldsymbol{\tau}\cdot\boldsymbol{n}\Big|_{z'=0} = E\left(\frac{\partial u'}{\partial z'} + \frac{\partial v'}{\partial z'}\right)\Big|_{z'=0} = \sqrt{\frac{Ef_*}{2}}\,\frac{u_{\mathrm{bulk}}}{2}\left[\boldsymbol{e}'_x + \operatorname{sgn}(f_*)\,\boldsymbol{e}'_y\right] \tag{5.16}$$

and exhibits the well-known $\pi/4$-tilt compared to the direction of the bulk flow. The shear stress acts on the circumference of the frustum or a lid and, thus, exerts torque on the annular boundary. Both shear stress and torque exhibit a proportionality to $E^{1/2}$ and $|f_*|^{1/2}$.

Dimensional arguments suggest that the total energy dissipation rate D is proportional to the total kinetic energy K of the flow divided by an appropriate time scale $|f_*|^{-1}$ of the Ekman layer dynamics. The energy dissipation rate across the boundary layer is of the order $Eu_{\mathrm{bulk}}^2/\delta_{\mathrm{E}}'^2$ per unit volume, which follows from an evaluation of the dissipation function Φ (see equation (3.73)). Since $K \propto u_{\mathrm{bulk}}^2$, one obtains the proportionality

$$D \propto |f_*|K. \tag{5.17}$$

Equation (5.17) states that the energy dissipation rate of a (steady) bulk flow is proportional to the kinetic energy of the bulk flow and the wall inclination towards the rotation axis, $\alpha = \arcsin(f_*/f)$. For a weakly time-dependent flow in geostrophic balance excited in the annulus one can estimate that the majority of the kinetic energy is dissipated by friction with the top and bottom lids and not the frustum. In fact, since $f_*/f = 0.1$, the energy dissipation rate in

the Ekman boundary layer over the lid is about an order of magnitude larger than over the frustum[2].

Oscillating Ekman layer over the librating lid and frustum

In the librating annulus, an *oscillating Ekman layer* (also known as *rotary Ekman layer*) addresses the boundary layer that forms over a non-vertical librating wall ($\alpha \neq 0,\ f_* \neq 0$). The time-dependent f-plane equations (5.6) are rarely discussed in literature so that the solution is discussed in a bit more detail below by following Swart *et al.* (2010, appendix A), but without stratification. Hence, we are faced with an 'inverse' configuration compared to the oceanographic problem of a tidally driven flow over a rigid surface that has been used to explain the structure of tidal currents over the continental shelf or in estuaries (e.g. Prandle, 1982; Thorade, 1928).

A librating surface yields periodically changing spin-up and spin-down conditions near the wall. Neglecting the time dependency and looking only at the maximum prograde and retrograde libration amplitudes at libration phase $\omega t = \pi/2$ and $3\pi/2$ (see equation (1.2)) yields positive and negative vorticity generation by the frustum and the bottom lid (compare to Greenspan, 1969, pp. 30–34). The vorticity generation is due to the rigidity of the librating wall which induces a radial dependency of the azimuthal wall velocity, say $v_{\mathrm{w},\varphi} \propto r$. The alternating generation of positive and negative vorticity by a librating wall is the most general property and not limited to the annular geometry. The vorticity generation has been exploited by Kurgansky (2011, personal communication), who considered the low-frequency limit $\omega \ll 1$ first and set the outline of how to obtain the wall-normal structure of the oscillating boundary layer. As part of this work, I have extended Kurgansky's approach by relaxing the low-frequency condition and computed also the velocity solution, which we shall discuss in more detail in the following paragraphs.

Vorticity-divergence form of the f-plane equations and its solution. We make use of the local Cartesian formulation but do *not* yet imply zonal invariance. Hence, the wall-normal vorticity ζ' and the wall-tangential divergence D' read

$$\zeta' := \boldsymbol{e}'_z \cdot \left(\boldsymbol{\nabla}_\parallel \times \boldsymbol{v}\right) = \frac{\partial v'}{\partial x'} - \frac{\partial u'}{\partial y'}, \qquad D' := \boldsymbol{\nabla}_\parallel \cdot \boldsymbol{v} = \frac{\partial u'}{\partial x'} + \frac{\partial v'}{\partial y'}. \tag{5.18}$$

Taking the time rate of change of equations (5.18), followed by a cross-differentiation and substitution of the f-plane equations (5.6) yields the vorticity-divergence form of the f-plane equations

$$\frac{\partial \zeta'}{\partial t} + f_* D' = E\frac{\partial^2 \zeta'}{\partial z'^2}, \qquad \frac{\partial D'}{\partial t} - f_* \zeta' = E\frac{\partial^2 D'}{\partial z'^2}. \tag{5.19}$$

Equations (5.19) are closed by the boundary conditions for the local tangential surface

$$\left.\begin{array}{lll} \zeta' = \varepsilon f_* \sin(\omega t), & D' = 0 & \text{for} \quad z' = 0, \\ \zeta' \to 0, & D' \to 0 & \text{for} \quad z' \to +\infty. \end{array}\right\} \tag{5.20}$$

[2]The surface area of the frustum is 7.5π, whereas that of the top and bottom lid together is 6.75π for the annulus of height $h = 5$, frustum radius $0.5 \leqslant r_1 \leqslant 1$ and outer cylinder radius $r_2 = 2$. Top and bottom lid together cover 90% of the surface area of the frustum and the contributions to the energy dissipation can, hence, be compared approximately without additional weighting.

Note that the boundary conditions (5.20) are always non-divergent at a rigid wall but the vorticity is non-zero. This means that the boundary conditions are 'rotary' and so will be the induced boundary layer flow; hence the name 'rotary Ekman layer'.

We seek stationary time-harmonic solutions to equations (5.19) of the form

$$\zeta' = X_1 \sin(\omega t) + X_2 \cos(\omega t), \qquad D' = Y_1 \sin(\omega t) + Y_2 \cos(\omega t), \tag{5.21}$$

where $X_{1,2}(z')$, $Y_{1,2}(z')$ denote real-valued amplitudes that vary only in wall-normal direction z'. For practical reasons, $X_{1,2}$ and $Y_{1,2}$ are collected in the complex amplitudes

$$\hat{Z}_1 := X_1 + \mathrm{i}Y_1, \qquad \hat{Z}_2 := X_2 + \mathrm{i}Y_2. \tag{5.22}$$

A straightforward calculation yields

$$\mathcal{L}\hat{Z}_1 = -\omega \hat{Z}_2, \qquad \mathcal{L}\hat{Z}_2 = \omega \hat{Z}_1 \qquad \Rightarrow \qquad \mathcal{L}^2 \hat{Z}_{1,2} = -\omega^2 \hat{Z}_{1,2}, \tag{5.23}$$

where

$$\mathcal{L} \equiv \left[E \frac{\partial^2}{\partial z'^2} + \mathrm{i} f_* \right]. \tag{5.24}$$

The general solution to equations (5.23) is obtained by solving first for $\hat{Z}_1$ and then for $\hat{Z}_2$, where regularity means $|\hat{Z}_{1,2}| < +\infty$. Hence

$$\left.\begin{aligned} \hat{Z}_1 &= \hat{A} \exp\left([\mathrm{i}s - 1] \frac{z'}{\delta'_-} \right) + \hat{B} \exp\left([\mathrm{i} - 1] \frac{z'}{\delta'_+} \right), \\ \hat{Z}_2 &= -\mathrm{i}\hat{A} \exp\left([\mathrm{i}s - 1] \frac{z'}{\delta'_-} \right) + \mathrm{i}\hat{B} \exp\left([\mathrm{i} - 1] \frac{z'}{\delta'_+} \right), \end{aligned}\right\} \tag{5.25}$$

in which

$$s \equiv \mathrm{sgn}\,(f_* - \omega) \qquad \text{and} \qquad \delta'_\pm \equiv \sqrt{\frac{2E}{|f_* \pm \omega|}}. \tag{5.26}$$

The sign s is positive $(+1)$ for libration frequencies $\omega < f_*$, whereas it is negative (-1) for libration frequencies $\omega > f_*$. The two nested thicknesses of the oscillating Ekman layer are given by $\delta'_\pm$, where equations (5.25) suggests that the oscillating Ekman layer consists of two nested layers of different thickness (to be discussed in more detail shortly).

We are left with fixing the constants in order to obtain the boundary layer solution in terms of the wall-normal vorticity and the tangential divergence. Equations (5.25) need to fulfil the

boundary conditions given by equations (5.20), which yields real-valued $\hat{A} = \hat{B} = \varepsilon f_*/2$. Hence, with s and $\delta_\pm$ according to equation (5.26), one obtains

$$\left.\begin{aligned}
\zeta' &= \frac{\varepsilon f_*}{2}\sin(\omega t)\left[\exp\left(-\frac{z'}{\delta'_-}\right)\cos\left(\frac{z'}{\delta'_-}\right)+\exp\left(-\frac{z'}{\delta'_+}\right)\cos\left(\frac{z'}{\delta'_+}\right)\right] \\
&\quad+\frac{\varepsilon f_*}{2}\cos(\omega t)\left[s\,\exp\left(-\frac{z'}{\delta'_-}\right)\sin\left(\frac{z'}{\delta'_-}\right)-\exp\left(-\frac{z'}{\delta'_+}\right)\sin\left(\frac{z'}{\delta'_+}\right)\right], \\
D' &= \frac{\varepsilon f_*}{2}\sin(\omega t)\left[s\,\exp\left(-\frac{z'}{\delta'_-}\right)\sin\left(\frac{z'}{\delta'_-}\right)+\exp\left(-\frac{z'}{\delta'_+}\right)\sin\left(\frac{z'}{\delta'_+}\right)\right] \\
&\quad-\frac{\varepsilon f_*}{2}\cos(\omega t)\left[\exp\left(-\frac{z'}{\delta'_-}\right)\cos\left(\frac{z'}{\delta'_-}\right)-\exp\left(-\frac{z'}{\delta'_+}\right)\cos\left(\frac{z'}{\delta'_+}\right)\right].
\end{aligned}\right\} \tag{5.27}$$

Equation (5.27) states the local solution for the oscillating Ekman layer to the f-plane equations in terms of the wall-normal vorticity and the tangential divergence, which already exhibits the wall-normal structure of the boundary layer. If one is interested only in the wall-normal extent of the oscillating Ekman layer there is no need to compute the velocity solution.

Figure 5.9 shows the theoretical thickness of the oscillating Ekman layer ($\delta'_\pm,\ \delta_\pm$) and of the Stokes layer (δ_S), which vary with the libration frequency ω. Also shown are the thicknesses in comparison to the classical Ekman layer thickness over the constantly rotating frustum (δ'_E) or lid (δ_E) respectively. The primed notation is used for the boundary layer over the librating frustum ($f_* = 0.2$), unprimed notation $\delta_\pm$ is used for the librating bottom lid ($f_* = f = 2$).

The oscillating Ekman layer thickness δ'_- erupts at $\omega = 0.2$ but δ_- at $\omega = 2$. At the lids, the inclination $\alpha = \pm\pi/2$ is maximised, which means $\omega = |f_*| = 2$ is the largest eruption frequency possible. For the oscillating Ekman layer it is $\delta'_- \geqslant \delta'_+$, $\delta_- \geqslant \delta_+$. Both cases have in common that the value of the corresponding classical Ekman layer is approached for low frequencies $\omega \to 0$. Note also that the Stokes layer thickness δ_S erupts for $\omega \to 0$, that is, in the limit of steady flow. The boundary layer thicknesses shown in figure 5.9 have been scaled with the minimum gap width $\Delta r = r_2 - r_1(0)$ of the confinement and the mean rotation rate Ω_0 of the system so that the Ekman number is in place of the kinematic viscosity. The default Ekman number $E = 3.19 \times 10^{-5}$ and libration frequencies $0 < \omega < 2$ from within the inertial wave band and cutting out the eruptions ($|f_* - \omega| \leqslant 0.1$) yields a typical boundary layer thickness in the range of $4 \times 10^{-3} < \delta_\mathrm{BL} < 4 \times 10^{-2}$. That is, the theoretical boundary layer thickness spans only 1/25th to 1/250th of the minimum annular gap width and only 1/125th to 1/1250th of the annulus height. This is one of the reasons why DNS of the librating annulus are computationally demanding when the Ekman number is small (see the discussion in section 3.3).

Velocity solution to the oscillating Ekman layer. Our ultimate aim is to clarify the corner beam excitation by wall libration, for which we need the complete velocity solution. In the following, the analytical solution to the boundary layer equations in terms of the velocity is computed first. After that, all three vector components are checked against the weakly nonlinear solution obtained by DNS of the annulus with a librating frustum or with librating lids and outer cylinder. For the DNS, default parameters $R = 0.2$, $E = 3.19 \times 10^{-5}$ will be used, but the libration frequency is selected in such a way that the feedback from the bulk flow is minimal at the location where the boundary layer profiles are extracted. In order to simplify the notation, let $\alpha > 0$ and $f_* > 0$ unless mentioned otherwise.

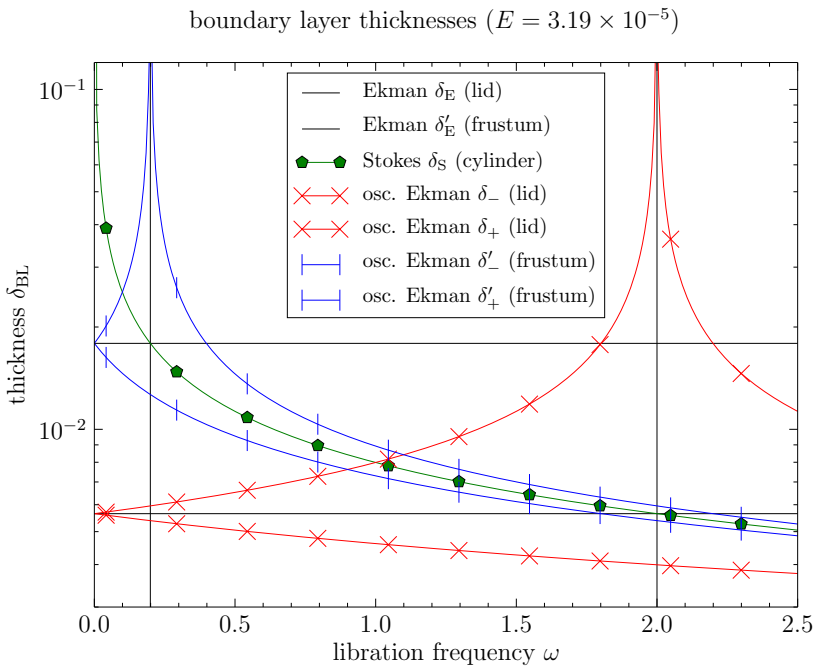

Figure 5.9: Comparison of the theoretical boundary layer thicknesses for the boundary layer types in the annular confinement. Plots are shown for the default Ekman number $\left(E = 3.19 \times 10^{-5}\right)$ and various libration frequencies ω. Primed Ekman layer thicknesses δ'_E, $\delta'_\pm$ correspond to the frustum with an effective Coriolis parameter $f_* = 0.2$; unprimed Ekman layer thicknesses δ_E, $\delta_\pm$ correspond to the bottom lid with $f_* = f = 2$. The Stokes layer thickness δ_S and the oscillating Ekman layer thickness δ'_- or δ_- 'erupt' when the libration frequency matches the corresponding effective Coriolis parameter (vertical dotted lines at $\omega = 0.0,\ 0.2,\ 2.0$). The classical Ekman layer thickness δ_E or δ'_E (solid and dashed horizontal lines) are given for orientation, but they are strictly valid only for a time-independent flow (differential rotation). (From M. Klein *et al.* (2014). 'Inertial wave excitation and focusing in a liquid bounded by a frustum and a cylinder'. *J. Fluid Mech.*, **751**, p. 274, figure 10, reproduced with permission. Numbers have been changed to acknowledge the length scale used in the present study.)

Let us begin with the wall-normal velocity w'. The wall-tangential divergence D' given in equation (5.27) is generally non-zero in wall-normal direction, which requires the flow to have a non-zero wall-normal component due to the continuity equation (2.11) in primed variables. The wall-normal velocity is obtained by an integration of

$$\frac{\partial w'}{\partial z'} = -D' \qquad \text{with} \quad w'\big|_{z'=0} = 0, \tag{5.28}$$

in which the boundary condition is due to impermeability of the wall. The wall-normal integration along z' can be performed straightforwardly. Using the stretched coordinate $\xi = z'/\delta_{BL}$, where δ_{BL} denotes the boundary layer thickness, allows to write

$$\int (\cdot)\, \mathrm{d}z' = \delta_{BL} \int (\cdot)\, \mathrm{d}\xi. \tag{5.29}$$

The boundary layer thickness δ_{BL} enters parametrically and needs to be replaced in accord with the stretched coordinate used. One would replace, for example, δ_{BL} by δ'_- or δ'_+ for the

nested layers in equation (5.27). This yields two stretched coordinates $\xi_\pm = z'/\delta'_\pm$ along which the integrations are performed. The wall-normal integration of equation (5.27) is completed by substituting the two standard integrals (see Bronstein *et al.*, 2005, p. 1082, no. 459 and 460)

$$\left.\begin{aligned} I_{\cos}(\xi) &= \int \mathrm{e}^{-\xi}\cos\xi\,\mathrm{d}\xi = -\frac{\mathrm{e}^{-\xi}}{2}(\cos\xi - \sin\xi)\,, \\ I_{\sin}(\xi) &= \int \mathrm{e}^{-\xi}\sin\xi\,\mathrm{d}\xi = -\frac{\mathrm{e}^{-\xi}}{2}(\cos\xi + \sin\xi)\,, \end{aligned}\right\} \tag{5.30}$$

due to which one obtains the *wall-normal velocity* of the oscillating Ekman layer as

$$\begin{aligned} w' = &-\frac{f_*}{2fr}\sin(\omega t)\left[s\delta'_-\Big(1+2I_{\sin}\left(z'/\delta'_-\right)\Big)+\delta'_+\Big(1+2I_{\sin}\left(z'/\delta'_+\right)\Big)\right] \\ &+\frac{f_*}{2fr}\cos(\omega t)\left[\delta'_-\Big(1+2I_{\cos}\left(z'/\delta'_-\right)\Big)-\delta'_+\Big(1+2I_{\cos}\left(z'/\delta'_+\right)\Big)\right]. \end{aligned} \tag{5.31}$$

Equation (5.31) is normalised with the local libration velocity $\varepsilon fr/2$ relative to the co-rotating frame of reference. The prefactor expands into $f_*/(2fr) = \sin\alpha/(2r)$, which indicates that the magnitude of the wall-normal velocity depends on geometry, more precisely, on the wall inclination α.

Note that the analytical solution given by equation (5.31) is singular at the libration frequency $\omega = f_*$, which is a consequence of the boundary layer eruption. The singularity is discussed by Maas & van Haren (1987), who show that a z'^2-profile will be established for the velocity. In practice, we can expect that the z'^2-profile will be present for a small frequency band around $\omega \approx f_*$ but will be subject to regularisation due to non-linearity and the 3-D viscous terms of the full Navier–Stokes equations.

The zonal velocity u' and the wall-tangential velocity v' are coupled by the Coriolis force, which suggests to compute the solution for both of them together. The no-slip boundary condition for both velocity components in the co-rotating frame of reference reads

$$u' = \frac{\varepsilon fr}{2}\sin(\omega t)\,, \qquad v' = 0 \qquad \text{at} \quad z' = 0. \tag{5.32}$$

This boundary condition requires the origin of the tangential axes to be located at the apex of the cone that describes the frustum or in the centre of the ring that forms the lid, hence

$$y' = -\frac{r}{\sin\alpha} \qquad \text{for} \quad \alpha \neq 0. \tag{5.33}$$

Substituting equation (5.33) in equation (5.32), however, yields a violation of the y'-invariance (see equation (5.5)) since u' changes sign when y' changes sign. This inconsistency compared to the boundary layer approximation, equation (5.5), is due to curvature: the librating frustum or lid possesses non-zero vorticity, whereas the velocity boundary condition does not possess vorticity in the local Cartesian approximation. One might prefer to use a consistent formulation, for instance, by extending the steady solution in Greenspan (1969, pp. 30–34) to librational forcing, but the mathematical treatment is much simpler in the local Cartesian formulation. Fortunately, the inconsistency is weak and so that the inconsistency can be corrected manually.

In order to correct the vorticity, consider a Cartesian *patch* on the librating frustum or lid (see figure 5.6). Axisymmetry means that the Cartesian patch has periodic boundary conditions in x'-direction. For the origin fixed on the rotational axis, one has $|y'| \gg \delta'_\pm$ for the frustum and

the lid. Fluid can reside only in the volume $z' > 0$, $y' < 0$ (more precisely, $y' < -r_1(h)/\sin\alpha$, where $r_1(h)$ is the minimum frustum radius). Extending the tangential plane to $y' > 0$ implies recirculation to take place there. Hence, in the Cartesian patch at $y' < 0$, only half of the circulation around the z'-axis is captured. This suggests to reduce the tangential vorticity ζ' in equation (5.27) *manually* by multiplication with 1/2. The tangential divergence D' in equation (5.27) has been computed together with ζ', which suggests to reduce it by the same factor for the computation of the velocities u' and v'. Hence, ζ' and D' have the corrections

$$\zeta'' = \frac{\zeta'}{2}, \qquad D'' = \frac{D'}{2}, \tag{5.34}$$

and the velocity components u' and v' are obtained by integrating ζ'' and D'' along y', which yields

$$u' = -y'\zeta'', \qquad v' = y'D''. \tag{5.35}$$

Substituting ζ'' and D'', as well as $y' = -r/\sin\alpha$ and $f = 2$ into equations (5.35) yields the *zonal and tangential velocity components* as

$$\begin{aligned} u' = {} & \frac{1}{2}\sin(\omega t)\left[\exp\left(-\frac{z'}{\delta'_-}\right)\cos\left(\frac{z'}{\delta'_-}\right) + \exp\left(-\frac{z'}{\delta'_+}\right)\cos\left(\frac{z'}{\delta'_+}\right)\right] \\ & + \frac{1}{2}\cos(\omega t)\left[s\,\exp\left(-\frac{z'}{\delta'_-}\right)\sin\left(\frac{z'}{\delta'_-}\right) - \exp\left(-\frac{z'}{\delta'_+}\right)\sin\left(\frac{z'}{\delta'_+}\right)\right], \end{aligned} \tag{5.36}$$

$$\begin{aligned} v' = {} & \frac{1}{2}\sin(\omega t)\left[-s\,\exp\left(-\frac{z'}{\delta'_-}\right)\sin\left(\frac{z'}{\delta'_-}\right) - \exp\left(-\frac{z'}{\delta'_+}\right)\sin\left(\frac{z'}{\delta'_+}\right)\right] \\ & + \frac{1}{2}\cos(\omega t)\left[\exp\left(-\frac{z'}{\delta'_-}\right)\cos\left(\frac{z'}{\delta'_-}\right) - \exp\left(-\frac{z'}{\delta'_+}\right)\cos\left(\frac{z'}{\delta'_+}\right)\right]. \end{aligned} \tag{5.37}$$

Equations (5.36) and (5.37) have been rescaled with the local libration velocity $\varepsilon f r/2$ in the co-rotating frame so that u', v', w' (see equation (5.31)) are scaled in the same way. The wall-normal velocity w' is by a geometrical factor $(f_*\delta_{\mathrm{BL}})/(fr)$ smaller in magnitude than the zonal and tangential velocity components u' and v'.

Note in this respect that the Stokes layer is approached in the limit of large curvature radii ($r \gg 1$) or small wall inclinations towards the rotation axis ($|f_*| \ll 1$) by the wall-normal velocity w' and the tangential velocity v' tending to zero (the oscillating Ekman layer is therefore also known as Stokes–Ekman layer; see, e.g., Salon & Armenio, 2011).

Note further that the boundary layer solution exhibits a phase lag with respect to the reference phase ωt as can be seen by the presence of sine and cosine functions. The phase lag depends on the distance z' from the wall but also on the libration frequency ω since $\delta'_\pm(\omega)$ is a function of the libration frequency.

Note in addition that ζ'' and D'' given by equations (5.34) have been used for the computation of u' and v' to correct for the surface curvature, whereas the wall-normal velocity w' has been obtained from D' given by equation (5.27). This slight inconsistency in using D'' for one variable and D' for another is a bit unsettling and may give the impression that the analytical solution is improperly constructed. In order asses the validity of the laminar boundary layer solution in the librating annulus we will compare the analytical solution to the direct numerical solution below.

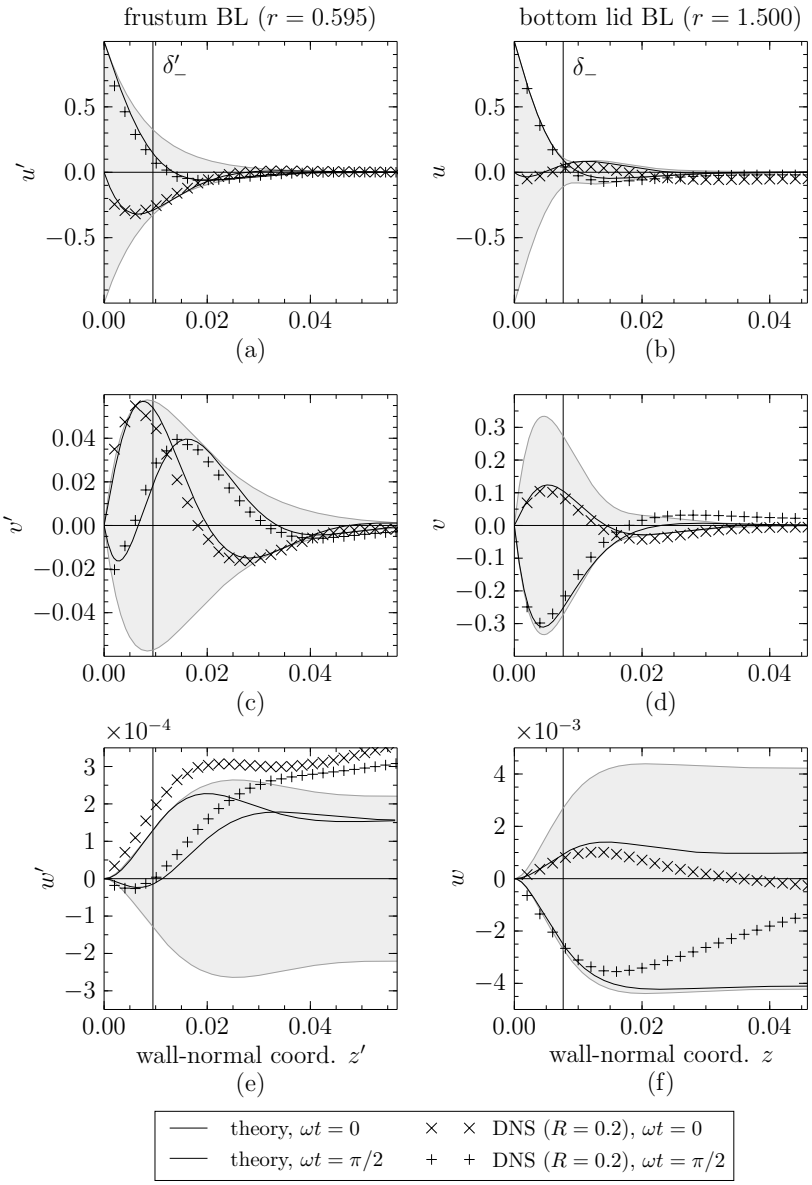

Figure 5.10: Oscillating Ekman layer profiles over the librating frustum and lid for two different libration phases $\omega t = 0$, $\pi/2$. The analytical solution given by equations (5.36), (5.37), and (5.31) is compared to the DNS of the frustum libration case (a, c, e), and the lids plus outer cylinder libration case (b, d, f). The DNS has been performed for the dimensionless parameters $R = 0.2$, $E = 3.19 \times 10^{-5}$ and libration frequency $\omega = 0.91$ to ensure that inertial waves are located around two tilted-V patterns (see figure 4.12(d) and 4.13(c)). Panels (a, c, e) show the frustum boundary layer profiles for $\omega > f_* = 0.2$. The origin of the wall-normal coordinate $z' = 0$ corresponds to the point $(r, z) = (0.595, 4.0)$. Panels (b, d, f) show the bottom lid boundary layer profiles for $\omega < f_* = f = 2$. The origin of the wall-normal coordinate $z' = 0$ corresponds to the point $(r, z) = (1.5, 0.0)$. Each numerical velocity component has been rescaled with the local wall velocity amplitude as seen from the co-rotating frame of reference. Ekman layer thicknesses δ'_- (a, c, e) and δ_- (b, d, f) are shown by dotted vertical line and the variability of the analytical solution is illustrated by a shaded area

Figure 5.10 shows the wall-normal profiles of all three velocity components (u', v', w') across the oscillating Ekman layer for the analytical solution and the DNS using default dimensionless parameters $R = 0.2$ (only DNS), $E = 3.19 \times 10^{-5}$. The velocity profiles are shown for the libration phases $\omega t = 0$ and $\pi/2$. The variability is illustrated by a shading of the area between the minimum and maximum analytical profiles. The numerical solution has been interpolated to a wall-normal coordinate and has been rescaled with the local libration velocity of the wall for comparison to the analytical solution. The libration frequency $\omega = 0.91$ is the same as for the Stokes layer profiles (see figure 5.7) in order to ensure that corner beams form a simple spatial structure by remaining close to the tilted-V pattern (see figures 4.12(d) and 4.13(c)) and that resonant excitation of the $(1, 2, 0)$ mode is avoided to yield a fair comparison between DNS and boundary layer theory.

Figures 5.10(a, c, e) show the profiles of u', v', w' over the librating frustum (case $\omega > f_*$) for the wall-normal coordinate originating from $(r, z) = (0.595, 4.0)$, which is far from the top inner corner. The theoretical boundary layer thickness $\delta'_- = 9.5 \times 10^{-3}$ is given for orientation by a dotted vertical line. It is quite remarkable how well the analytical solution corresponds to the DNS for both libration phases shown. Surprisingly, it is in particular the manually corrected analytical solution for u' and v' in figures 5.10(a, c) for which the best correspondence to the numerical solution can be observed.

As a reminder, the manual correction was necessary to account correctly for wall curvature and vorticity in an otherwise locally planar (Cartesian) approximation. The results obtained justify the manual correction *a posteriori*. Note that only the wall-normal Ekman pumping velocity w' (see figure 5.10(e)) has been computed from the uncorrected local divergence D'. The agreement is best close to the wall within $0 < z' < 2\delta'_- \approx 0.02$. Otherwise, the analytical and numerical profiles are in qualitative agreement and of the same order of magnitude for the near-wall region shown. The difference between the idealised analytical solution and the numerical solution becomes unacceptable for $z' \geqslant 0.03$.

Figures 5.10(b, d, f) show the profiles of u', v', w' over the librating bottom lid (case $\omega < f_*$) for the flow excited by lids and outer cylinder in libration. The wall-normal coordinate originates from $(r, z) = (1.5, 0.0)$ in the middle of the bottom lid. The theoretical boundary layer thickness $\delta_- = 7.7 \times 10^{-3}$ is given for orientation by a dotted vertical line. In contrast to the frustum libration case, it is $\omega < f_*$ here due to which the velocity gradients are steeper close to the wall which leads to the impression that the lid boundary layer is thinner than the frustum boundary layer (compare to the left column in figure 5.10) even though δ_- is only 20% smaller than δ'_-. However, the velocity amplitudes of v' and w' are larger over the lid by the factor $f/f_* = 10$, that is, an increased effect of the Coriolis force and, thus, an increased tangential divergence that drives the wall-normal flow. Nevertheless, the agreement between analytical and numerical solution is comparable to the frustum libration case and the analytical solution. The analytical solution fails to capture the wall-normal velocity correctly for $z' > 2\delta_- \approx 0.015$, which is most probably due to the non-zero bulk flow in the annulus. The wall-normal velocity w' is affected the most by a non-zero bulk flow due to its small amplitude.

Note that the boundary layer in the numerical solution is not better resolved than indicated by the markers. That is, the mesh size near the wall corresponds roughly to the marker spacing and resolves δ'_- over the frustum and δ_- over the lid with about 4 grid boxes, but only with 2 grid boxes at $z' = 0.04$. Hence, the DNS performed here resolves the oscillating boundary layer just well enough to capture its structure but the resolution is otherwise far from that used, for instance, by Salon & Armenio (2011). An as highly-resolved DNS here would have rendered the numerical solution for the whole annulus impossible. The level of agreement between the analytical solution and DNS is otherwise comparable to the solutions for the librating cylinder

shown by Lopez & Marques (2011), which gives us confidence that the near-wall dynamics are sufficiently resolved in the numerical model.

This concludes the assessment of the analytical solution and we can proceed by computing Ekman pumping and Ekman flux as an intermediate step to explain the excitation of the corner beams.

Ekman pumping and Ekman flux. It is well-known from the study of differentially rotating discs that a localised vortical flow drives a tangential (radial) mass flux, the *Ekman flux*, which is compensated by the wall-normal *Ekman pumping (suction)*; see, for example, Greenspan (1969, p. 32) or Busse *et al.* (2007, pp. 128). For brevity, we will skip the term 'suction' and refer only to the Ekman pumping which may be of positive or negative sign. The Ekman flux is a result of boundary layer currents driven by libration and is just the right ingredient for localised wave excitation since it provides a net mass flux to or from a corner of the annular cavity (compare to the numerical simulations discussed in section 5.1). In order to decide whether the Ekman flux is relevant for inertial wave excitation we need to clarify the direction of the Ekman flux, its time dependency, its frequency dependency, and its dependency on the Rossby and Ekman numbers. The points are addressed by the aid of the velocity solution. As before, we use $\alpha > 0$ and $f_* > 0$ unless mentioned otherwise.

The *Ekman pumping velocity* w'_{E} is given by the wall-normal velocity component at the top of the oscillating boundary layer. Taking the limit $\xi_\pm \to +\infty$ of equation (5.31) yields

$$\begin{aligned} w'_{\mathrm{E}} &= -\frac{f_*}{2fr}\left(s\delta'_- + \delta'_+\right)\sin\left(\omega t\right) + \frac{f_*}{2fr}\left(\delta'_- - \delta'_+\right)\cos\left(\omega t\right) \\ &= A'_z \sin\left(\omega t + \theta'_z\right). \end{aligned} \tag{5.38}$$

The Ekman pumping velocity oscillates around zero (compare to figures 5.10(e, f)), which is a direct consequence of the tangential divergence and the periodically generated positive and negative vorticity due to wall libration. In the lower line of equation (5.38), A'_z and θ'_z denote amplitude and phase of the Ekman pumping velocity, which are given by (e.g. Bronstein *et al.*, 2005, pp. 83)

(i) for $\omega < f_*$ $\quad (s = +1)$:

$$A'_z = \sqrt{2E}\,\frac{f_*}{fr}\sqrt{\frac{f_*}{f_*^2 - \omega^2}}, \qquad \tan\theta'_z = \frac{\sqrt{f_*+\omega} - \sqrt{f_*-\omega}}{-\sqrt{f_*+\omega} - \sqrt{f_*-\omega}}, \tag{5.39}$$

(ii) for $\omega > f_*$ $\quad (s = -1)$:

$$A'_z = \sqrt{2E}\,\frac{f_*}{fr}\sqrt{\frac{\omega - \sqrt{\omega^2 - f_*^2}}{\omega^2 - f_*^2}}, \qquad \tan\theta'_z = 1. \tag{5.40}$$

Note that the latter definition of the phase differs slightly from that used by Klein *et al.* (2014). The reason is that the phase can now be computed unambiguously by the aid of the arctan2 function.

Figure 5.11 shows the amplitude A'_z and phase θ'_z of the Ekman pumping velocity w'_{E} for various libration frequencies $0 < \omega < 2.5$ below and above the effective Coriolis parameter f_*. As before, the default Ekman number of $E = 3.19 \times 10^{-5}$ has been used. Amplitude and phase

of the Ekman pumping velocity are shown over the librating lid ($f_* = f = 2$, solid line) and over the librating frustum ($f_* = 0.2$, dashed line).

Figure 5.11(a) shows the amplitude A'_z, which exhibits a singularity at $\omega = f_*$, approaches a plateau for $\omega \ll f_*$, and vanishes for $\omega \gg f_*$. The dependency of the amplitude on the libration frequency ω is qualitatively similar to the boundary layer thicknesses δ_- and δ'_- shown in figure 5.9 (thick solid lines). This indicates that, the fluid volume affected by wall libration increases with the boundary layer thickness and so does the Ekman pumping. The energy uptake of the fluid increases accordingly and can be expected to reach a maximum at $\omega = f_*$ due to the boundary layer eruption.

Comparing the lid and frustum libration case shows that not the absolute boundary layer thickness is important for the magnitude of the Ekman pumping velocity but the tangential divergence. That is, for $\omega \leqslant 0.1$, A'_z for the frustum is about half an order of magnitude smaller than A_z for the lid. For $0.3 \leqslant \omega \leqslant 2.5$ the difference is 1–2 order of magnitude due to the different effective Coriolis parameters. Hence, the thin oscillating Ekman layer over the librating lid yields a much larger Ekman pumping amplitude for frequencies in the inertial wave band than the thicker oscillating Ekman layer over the librating frustum. The only exception occurs at $\omega \approx 0.2$, where the frustum boundary layer erupts. This supports qualitatively the laboratory measurements reported by Seelig (2014, figure 7.4.1, p. 68), for which lid plus outer cylinder libration yields generally larger wave amplitudes then the frustum libration does. This will be discussed in more detail in chapter 6.

Figure 5.11(b) shows the phase θ'_z of the Ekman pumping velocity for various libration frequencies ω. The phase is π ahead of the libration for $\omega \ll f_*$, but reduces gradually to $3\pi/4$ when ω increases to f_*. Close to f_*, the phase drops rapidly from $3\pi/4$ to $\pi/4$, where it remains fixed when the libration frequency increases further. Qualitatively, the phase rotation by $\pi/2$ across the eruption frequency is a resonance-like behaviour which is different though than for the (damped) driven harmonic oscillator, which exhibits a phase drop from 0 to $-\pi$ (e.g. Jaworski & Detlaf, 1972, p. 121). The phase of the Ekman pumping is relevant in the sense that it yields a shift of the fluid being pumped out of and into the boundary layer compared to the libration reference phase ωt. For low-frequency forcing ($\omega \ll f_*$), the Ekman pumping is virtually in phase with libration, but has simply opposite sign, which means prograde (retrograde) frustum or lid libration corresponds to vertical inflow (outflow) of the boundary layer. For high-frequency forcing ($\omega \gg f_*$), the Ekman pumping is only a bit out of phase with libration, which means during 3/4 of the prograde (retrograde) libration half-period the oscillating boundary layer exhibits vertical outflow (inflow).

The *Ekman flux* $\boldsymbol{Q}_\parallel$ of the oscillating Ekman layer is obtained by a vertical integration of the velocities u' and v' given by equations (5.36) and (5.37) in analogy to the flux deficit in the steady problem as discussed by Busse *et al.* (2007, p. 126). One obtains the Ekman flux vector by the aid of the local axes (see figure 5.6) as

$$\boldsymbol{Q}_\parallel = Q'_x \boldsymbol{e}'_x + Q'_y \boldsymbol{e}'_y = \int_0^{z'/\delta_{\mathrm{BL}} \to +\infty} \left(u' \boldsymbol{e}'_x + v' \boldsymbol{e}'_y \right) \mathrm{d}z'. \tag{5.41}$$

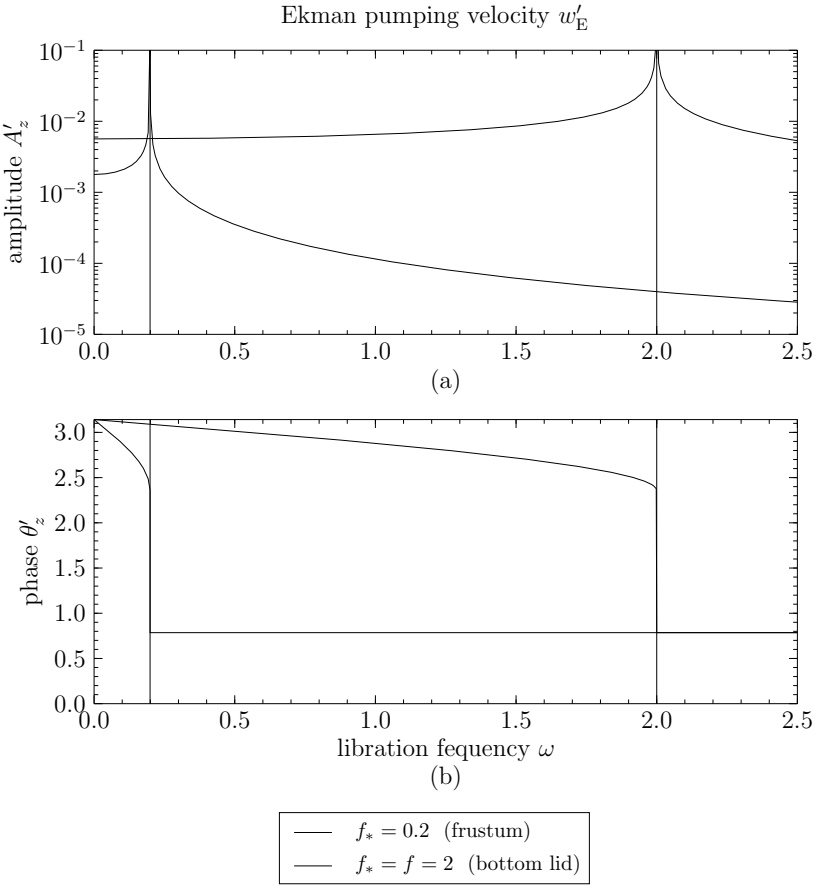

Figure 5.11: Idealised Ekman pumping over the librating frustum (dashed line) and the librating bottom lid (solid line). Amplitude (a) and phase (b) of the Ekman pumping velocity w'_{E} according to equations (5.39) and (5.40) are shown for various libration frequencies ω. The Ekman number $E = 3.19 \times 10^{-5}$ has been used and velocity component has been scaled with the local libration velocity in the co-rotating frame of reference.

The substitution of equations (5.29), (5.30), (5.36) and (5.36) yields the zonal and wall-tangential flux components, namely

$$\left.\begin{aligned} Q'_x &= +\frac{\delta'_- + \delta'_+}{4}\sin(\omega t) + \frac{\delta'_- - s\delta'_+}{4s}\cos(\omega t) = A'_x \sin\left(\omega t + \theta'_x\right), \\ Q'_y &= -\frac{\delta'_- + s\delta'_+}{4s}\sin(\omega t) + \frac{\delta'_- - \delta'_+}{4}\cos(\omega t) = A'_y \sin\left(\omega t + \theta'_y\right). \end{aligned}\right\} \tag{5.42}$$

Figure 5.12 shows hodographs of the Ekman flux vector $\boldsymbol{Q}_{\parallel}$, where figure 5.12(a) corresponds to the librating frustum with $f_* = 0.2$ and figure 5.12(b) to the librating bottom lid with $f_* = f = 2$. The hodographs shown have been obtained by tracing the tip of the Ekman flux vector over 98% of a libration period, $0 \leqslant \omega t \leqslant 1.96\pi$, in order to show the direction of the traverse. The libration phase $\omega t = 0$ is marked by a line to the origin. All hodographs have been obtained for the default Ekman number $E = 3.19 \times 10^{-5}$, but for different libration frequencies ω. The tip of the Ekman flux vector describes an ellipse, which is due to the Coriolis force that deflects the zonal velocity perturbation imposed by libration in the second wall-tangential direction. The velocity components u' and v' are correlated so that a net deflection of the mass flux results (compare to the $\pi/4$-tilt in the steady Ekman layer; e.g. Busse *et al.*, 2007, pp. 160). In both figures 5.12(a, b), the shapes of the ellipses depend strongly on the libration frequency ω and the Coriolis parameter f_*.

For $\omega < f_*$, the principal axis of the ellipses in figure 5.12 is tilted by $-\pi/4$ so that Q'_y and Q'_x reach the same amplitude almost together. The axial ratio of the ellipses diverges in the low-frequency limit $\omega \ll f_*$, where the ellipse finally degenerates into a diagonal line segment of negative slope. This indicates that a quasi-steady Ekman layer is approached, that is, both Ekman flux components oscillate together with the libration ωt and with identical amplitude so that the Ekman flux vector is tilted by $-\pi/4$ ($+\pi/4$) to the zonal libration velocity in the prograde (retrograde) libration half-period.

For $\omega > f_*$, the principal axis of the ellipses in figure 5.12 is parallel to the zonal direction. In the high-frequency limit $\omega \gg f_*$, the phase shift between Q'_x and the libration velocity approaches $-\pi$. The ellipses degenerate to a horizontal line segment by $Q'_y \to 0$. This means the Stokes layer limit is approached since the induced mass flux becomes anti-parallel to the zonal libration velocity. At very high libration frequency, also Q'_x will finally tend to zero. It is straightforward to confirm this limiting case by a vertical integration of the Stokes layer profile (see equation (5.10)). Hence, the mass flux driven in the direction of the corners vanishes almost completely $\left(|Q'_y| \ll |Q'_x|\right)$.

For $\omega \to f_*$, the ellipses in figure 5.12 turn into circles, which means that the Ekman flux vector no longer exhibits an oscillation in amplitude but simply rotates around the wall-normal direction. The two nested layer thicknesses fulfil $\delta'_- \gg \delta'_+$ so that the boundary layer structure has changed qualitatively to a single periodically oscillating Ekman layer.

Note that the elliptical hodographs shown in figure 5.12 are reminiscent to those found in the ocean (see, e.g., Maas & van Haren, 1987; Thorade, 1928). Here the ellipses are traversed in clockwise direction, whereas in the ocean of the corresponding northern hemisphere the ellipses are traversed in anti-clockwise direction since the boundary is fixed. The reason is simply the opposite sign of the effective Coriolis parameter over the librating frustum or bottom lid in the annulus compared to the oscillatory flow over the sea bottom in which the 'wall' (ocean floor) is fixed and the flow is oscillating due to tidal forcing.

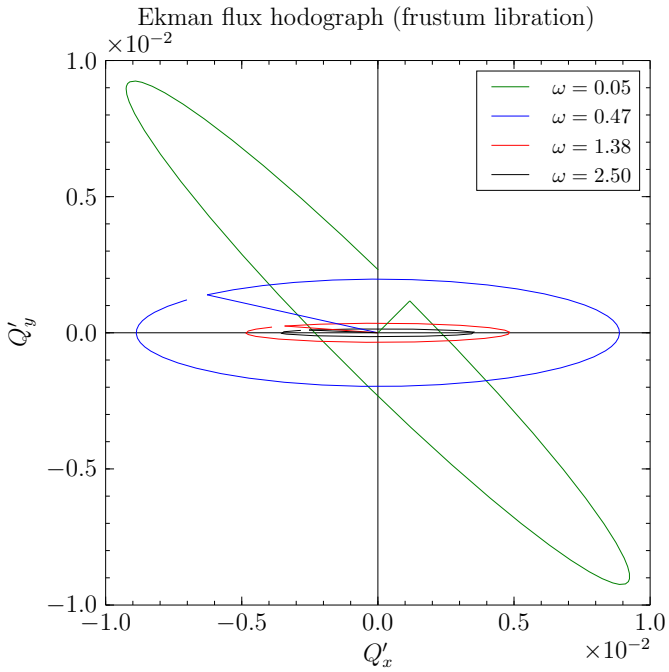

(a) $f_* = 0.2$

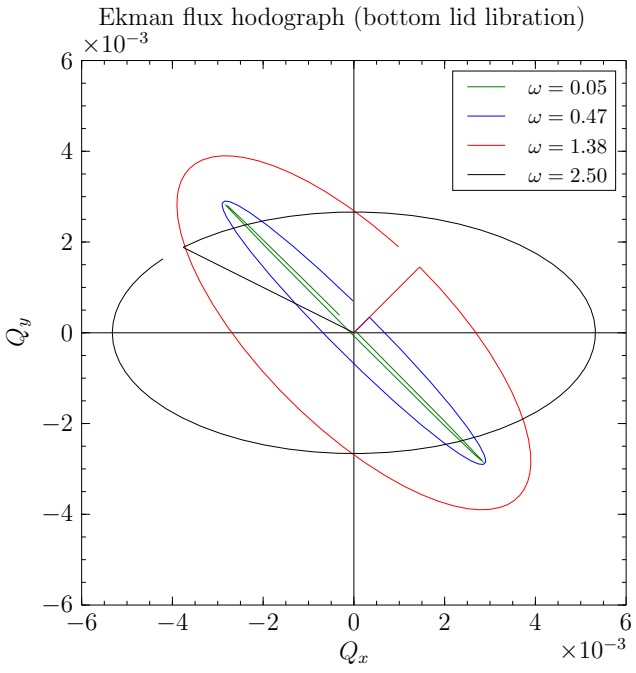

(b) $f_* = f = 2$

Figure 5.12: Hodographs of the Ekman flux vector $\boldsymbol{Q}_\parallel = Q'_x \boldsymbol{e}'_x + Q'_y \boldsymbol{e}'_y$ over the librating frustum (a) and the librating lid (b). The hodographs form ellipses and have been obtained by boundary layer theory for various libration frequencies ω and the default Ekman number 3.19×10^{-5}. The ellipses are plotted for 98% of a libration period in the range $0 \leqslant \omega t \leqslant 1.96\pi$, where $\omega t = 0$ is indicated by a radial line to the origin. The frustum boundary layer is thicker than that of the lid for $\omega < 1.0$ (see figure 5.9) and exhibits larger Ekman flux amplitudes.

For a more compact formulation of equations (5.42), a decomposition of the Ekman flux components into amplitude and phase can be performed. The decomposition works analogous to the Ekman pumping velocity and yields

(i) for $\omega < f_*$ $(s = +1)$:

$$A'_x = A'_y = \sqrt{\frac{E}{2}}\sqrt{\frac{f_*}{f_*^2 - \omega^2}}, \qquad \tan\theta'_x = (-1)\tan\theta'_y = \frac{\sqrt{f_* + \omega} - \sqrt{f_* - \omega}}{\sqrt{f_* + \omega} + \sqrt{f_* - \omega}}, \tag{5.43}$$

(ii) for $\omega > f_*$ $(s = -1)$:

$$A'_{x/y} = \sqrt{\frac{E}{2}}\sqrt{\frac{\omega \pm \sqrt{\omega^2 - f_*^2}}{\omega^2 - f_*^2}}, \qquad \tan\theta'_x = \frac{\tan\theta'_y}{-1} = \frac{-1}{1}. \tag{5.44}$$

In the latter equations, A'_x receives the positive sign in front of the inner square root, whereas A'_y receives the negative sign. Interestingly, both amplitude A'_y and phase θ'_y of the wall-tangential Ekman flux component are proportional or even identical to the Ekman pumping amplitude A'_z and phase θ'_z (see figure 5.11). Since the wall-tangential Ekman flux component Q'_y is directed to or from a corner of the annular confinement there is a potential correlation between the strength of the Ekman pumping, Ekman flux and the excitation of corner beams which we shall discuss in more detail below.

Note that the phases θ'_x and θ'_y are given in such a way that a unique value in $[-\pi, \pi)$ is obtained by an evaluation with the arctan2 function. In contrast to θ'_y, the phase θ'_x increases from 0 at $\omega = 0$ to $\pi/4$ for $\omega \to f_*^-$. However, the phase θ'_x drops sharply to $-\pi/4$ for $\omega > f_*$ (not shown explicitly), which corresponds to a phase rotation of $-\pi/2$ as exhibited by the hodographs in figure 5.12. The phases, however, do not depend on the Ekman number since the structure of the velocity field is modified only when the ratio δ'_+/δ'_- of the two nested layers changes. This can happen only when the libration frequency ω or the effective Coriolis parameter f_* (the wall inclination) are modified.

Note also the proportionality $A'_x, A'_y \propto E^{1/2}$, which reflects that the Ekman flux is restricted to the boundary layer of thickness $\delta'_\pm \propto E^{1/2}$. As the Ekman number increases, the boundary layer encompasses a larger fluid volume and, hence, a larger fluid mass. The Ekman flux is therefore a measure for the mass flux in the oscillating boundary layer, where a larger flux amplitude means a larger fluid mass is in motion but not that the fluid velocities have increased. In fact, the Ekman number enters the velocity solution only via the boundary layer thicknesses, equations (5.36) and (5.37), which means the velocity profiles are only stretched in wall-normal direction when the Ekman number increases so that the velocity amplitudes are still the same.

In conclusion, the key properties of the oscillating Ekman layer are as follows: first, the wall-tangential flux component $\left(Q'_y\right)$ is non-zero due to which fluid is driven to a corner of the librating frustum or lid in the annular confinement. This is in qualitative agreement with the numerical results discussed in section 5.1 and suggests that the Ekman flux induced by libration is the primary flow. Second, it turns out from boundary layer theory that the flux component Q'_y and the Ekman pumping velocity (w'_E) are correlated. Induction of the Ekman pumping implies the induction of a compensating, wall-tangential mass flux component which has the same phase lag. The amplitudes of the wall-tangential Ekman flux and the wall.normal Ekman pumping velocity possess the same dependencies on the libration frequency, the libration amplitude and the Ekman number. This raises the question to which degree the Ekman pumping mechanism

and the corner beams are actually correlated. This will be discussed further in the next section and will yield a model for the wave excitation by libration.

5.3 Model for the corner beam excitation

In the previous section we have assured ourselves of the correctness of the analytical oscillating boundary layer solution in the vicinity of the wall. We have seen that the boundary layer structure is relatively complex by the oscillating Ekman layer consisting of two nested layers that scale differently with the libration frequency (see figure 5.9). The idealised boundary layer flow in terms of the analytical solution to the velocity field was found to approximate the numerical solution accurately up to two times the boundary layer thickness even when inertial waves have been excited in the bulk.

We also know already that inertial waves are excited in the form of corner beams in the corners adjacent to a librating wall (see chapter 4), which has been attributed to an intricate corner flow (see section 5.1). The purpose of this section is to simplify the local solution further in order to develop a model for the corner beam excitation that circumvents solving the corner flow problem analytically. The analytical solutions to the boundary layer equations will prove useful since it will provide us with analytical expressions on how the corner beam amplitude depends on the libration frequency, on the configuration (wall inclination to the rotation axis), and on the dimensionless numbers.

In the following, we will discuss the implications of the (wall-tangential) Ekman flux induced by the librating frustum and lid of the annular confinement. First, the boundary layer solution is used to compute the wall-tangential flux divergence and how it is related to the Ekman pumping velocity. This will show us that the whole boundary layer over the frustum or lid 'erupt' at specific frequencies corresponding to the critical slope. Second, the flux difference across the corners is investigated. This will lead us to an interpretation that the boundary layer exhibits also a 'local eruption' in the vicinity of the corner. A detailed analysis will yield a model for the corner beam excitation which is based on a local flux difference. Third, the hypothesis of a local flux difference at the corners is assessed by weakly non-linear DNS for the case of frustum libration and the case of lids plus outer cylinder libration for a fixed libration frequency in order to guide us toward a model for the wave energy emitted in the form of corner beams. (Further details of the wave excitation model are given separately in chapter 6.)

Flux difference, flux divergence, and the localised boundary layer eruption

It has been mentioned in the previous section that the wall-tangential flux component Q'_y in a radial-axial section (see figure 5.6) and the wall-normal Ekman pumping velocity w'_E exhibit similar analytical expressions for their amplitude and phase. This strong correlation between the wall-normal and wall-tangential flow components provides the guideline for quantification of the corner beam excitation due to a mass flux converging to a corner. Thinking of fluxes suggests to integrate over the whole boundary layer thickness. Therefore, the flux *deficit* formulation (see Busse *et al.*, 2007, pp. 126) is applied to the oscillating Ekman layer. A wall-normal integration of the continuity equation (5.28) and the application of the zonal invariance, $\partial(\cdot)/\partial x' \equiv 0$, yields the mass flux balance in the form

$$w'_\mathrm{E} = -\int_0^{+\infty} D' \,\mathrm{d}z' = -\boldsymbol{\nabla}\cdot\boldsymbol{Q}_\parallel \qquad \text{with} \quad \boldsymbol{\nabla}\cdot\boldsymbol{Q}_\parallel = \frac{\partial Q'_y}{\partial y'}. \tag{5.45}$$

Equation (5.45) shows that the Ekman pumping velocity w'_{E} is coupled to the wall-parallel divergence of the Ekman flux, $\boldsymbol{\nabla}_{\parallel} \cdot \boldsymbol{Q}_{\parallel}$, where the zonal invariance renders only the wall-tangential component Q'_y relevant for the balance. The component Q'_y results from the action of Coriolis force on the viscously diffusing zonal perturbation imposed by libration.

A word of caution regarding equation (5.45) is in order before we continue. The slight inconsistency of the local Cartesian formulation of the velocity solution (see section 5.2) requires to compute w'_{E} from the wall-tangential divergence D', equation (5.27). However, Q'_x and Q'_y given by equations (5.42) have been obtained from the velocity components u' and v', which have been computed from the curvature-corrected divergence D'' (equation (5.34)) as explained earlier. Hence, Q'_y (and Q'_x) needs to be multiplied by 2 and the y'-dependency has to be considered when Q'_y of the f-plane model is substituted.

Hypothesis of the corner beam excitation mechanism. Consider, for example, the librating frustum and two points in the boundary layer to the right and left hand side of the bottom inner corner A (compare to figure 5.1). Following the wall tangential coordinate y' in clockwise direction in a radial-axial section (see figure 5.6) yields the local coordinates $y'_1 < y'_{\mathrm{A}}$ for the point to the right and $y'_2 > y'_{\mathrm{A}}$ to the left of the corner A. Hence, the flux divergence at each of the two locations reads $\left(\partial Q'_y/\partial y'\right)|_1$ and $\left(\partial Q'_y/\partial y'\right)|_2$. The boundary condition and the wall-inclination change with y' across the corner, which means that also the boundary layer structure has to change. The boundary layer adjusts smoothly and one can expect that the boundary layer structure changes across an interval $\Delta y'$ at the corner A in which the boundary layers of the librating frustum and the non-librating lid overlap. Here, the interval is of the order of the boundary layer thickness, say $\Delta y' = O\left(\delta_{\mathrm{BL}}\right)$, where δ_{BL} denotes the maximum thickness of all the boundary layer types involved (compare to figure 5.9).

The adjustment of the boundary layer structure across the corner requires the flux divergence to change as well. Hence, equation (5.45) yields an *excess* Ekman pumping velocity $\Delta w'_{\mathrm{E}}$ localised near the bottom inner corner A, which is given by

$$\Delta w'_{\mathrm{E}}\Big|_{\mathrm{A}} \approx -\frac{1}{\Delta y'}\left(\left.\frac{\partial Q'_y}{\partial y'}\right|_2 - \left.\frac{\partial Q'_y}{\partial y'}\right|_1\right). \tag{5.46}$$

Equivalently, one can say that equation (5.46) yields that a mismatch in the flux divergence causes a *local boundary layer eruption*.

The boundary layer solution developed in section 5.2 has an exponential dependency on the wall-normal coordinate z' and a linear dependency on the wall-tangential coordinate y'. This holds for any small patch on the librating frustum. Hence, the wall-tangential flux divergence $\partial Q'_y/\partial y'$ has to be proportional to the wall-tangential flux Q'_y itself modulo a parametric dependency of the amplitude on y', the distance from the rotation axis. Over the librating frustum (or lid) near the bottom inner corner A, for example, one has

$$\frac{\partial Q'_y}{\partial y'} \propto \frac{Q'_y}{y'} \approx \frac{Q'_y}{y'_{\mathrm{A}}}. \tag{5.47}$$

As a consequence, the excess Ekman pumping velocity $\Delta w'_{\mathrm{E}}$ is induced also when the wall-tangential fluxes $Q'_y|_1$ and $Q'_y|_2$ to the right and left of the corner A differ. That is, $y'_1 \approx y'_{\mathrm{A}}$

and $y_2' \approx y_\mathrm{A}'$, so that $Q_y'\big|_1 \neq Q_y'\big|_2$ is required. Substituting equation (5.47) into equation (5.46) yields

$$\Delta w_\mathrm{E}'\Big|_\mathrm{A} \approx A' \left(Q_y'\Big|_2 - Q_y'\Big|_1 \right), \tag{5.48}$$

which renders the excess Ekman pumping velocity $\Delta w_\mathrm{E}'$ a consequence of the *flux difference* $Q_y'\big|_2 - Q_y'\big|_1$ taken across the corner adjacent to a librating wall of the annulus (here corner A; see figure 5.13(a) which is discussed below). The factor A' is unknown at present and accounts for geometry, for example, curvature and the amplitude of the local libration velocity. A' can be obtained by fitting the amplitude of the flux Q_y' obtained analytically to that in a numerical solution obtained by DNS.

Figure 5.13(a) shows a schematic of the corner beam excitation due to mass flux difference. The excess Ekman pumping velocity $\Delta w_\mathrm{E}'$ is localised near the bottom inner corner A. The outflow occurs from a small volume of overlapping frustum and lid boundary layers, a patch of the order $O\left(\delta_\mathrm{BL}^2\right)$ in the radial-axial section of the annulus. The outflow is jet-like and has to be directed roughly along the bisectrix of the corner in the first place due to geometric constraints. Hence the jet has a radial component which leads to a radial acceleration of fluid parcels on the top of the boundary layer near the bottom inner corner A (see figures 5.1 and 5.2), but due to Coriolis force, the fluid parcels outside the boundary layer are forced on a circular path in the radial-azimuthal section in the vicinity of the bottom inner corner. The fluid parcels outside the boundary layer are only weakly affected by viscous forces so that kinetic energy can leave the boundary layer in the form of inertial waves. Librational forcing implies that the flux difference and the excess Ekman pumping change sign periodically. Hence, libration frequencies from within the inertial wave band ($0 < \omega < 2$) permit that the kinetic energy of the deflected fluid parcels can propagate away from its source near corner A in the form of inertial waves.

Figure 5.13(b) shows a schematic of the Ekman flux deflection near the bottom outer corner D due to librating lids and outer cylinder. The Ekman flux is induced here by the librating bottom lid and deflected at the corner D when it reaches the outer cylinder. The whole argumentation of the frustum libration case from above applies analogously to the lids plus outer cylinder libration case here because the Stokes layer over the librating outer cylinder, as given by equation (5.10), does not drive a wall-tangential flux to or from a corner. Therefore, it does not contribute to corner beam excitation.

It is worth to note, however, that the deflected Ekman flux, which is now directed vertically along the outer cylinder, decreases only gradually with increasing distance from the lid (see figures 5.4 and 5.5). On the one hand, this gradual decrease of the vertical boundary layer current over the outer cylinder is surprising but, on the other hand, it is in qualitative agreement with the analytical solution given by Wang (1970). He showed that the boundary layer equations can be linearised to the orders $E^{1/2}$ and E when the Ekman number and libration amplitude (Rossby number R) are small. A primary and a secondary circulation is driven by the mass flux deflection in the corner as solutions to the linearised Navier–Stokes equations Wang (1970, figure 1). A more detailed comparison to the analytical solution, however, is not the objective here.

Before we continue, note that the most important requirement for the excitation of corner beams is a rapid change of the boundary condition. This can be narrowed down to a localised change of the vorticity boundary condition. In applications it is not the libration velocity that changes rapidly, but rather the wall slope as in the case of the outer cylinder and lids in libration. Hence, one can expect the excitation of inertial wave beams wherever the inclination

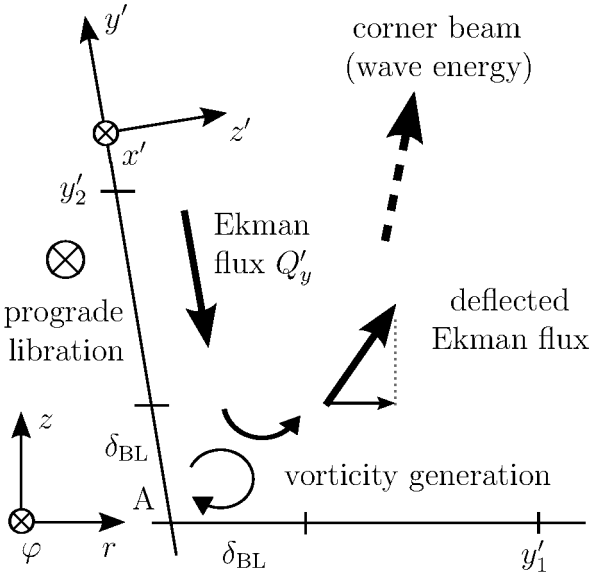

(a) Frustum libration, lower inner corner

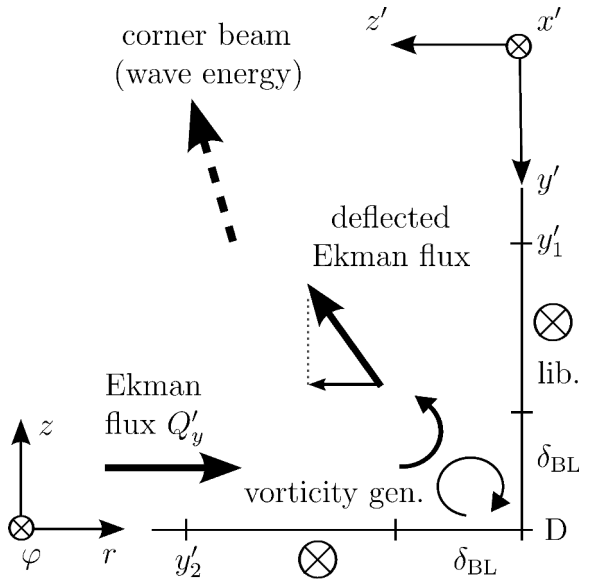

(b) Lids and outer cylinder libration, lower outer corner

Figure 5.13: Schematic of the excitation mechanism of the corner beams due to a deflection of the Ekman flux component Q_y'. Panel (a) shows the bottom inner corner A adjacent to the librating frustum and non-librating lid. Panel (b) shows the bottom outer corner D for the lid and the outer cylinder in libration. Thick black solid arrows indicate the mass flux in the prograde libration phase ($0 < \omega t < \pi$). The deflected Ekman flux (thick bent arrow) leaves the boundary layer of thickness δ_{BL}. The radial component of the deflected Ekman flux just outside the boundary layer (thin projection) will be affected by the Coriolis force and is thus the key candidate for localised inertial wave excitation by libration. The corner flow is complicated and given here only in heavily simplified form by a thin circular arrow for orientation.

of the librating domain boundary changes on short distances. This can happen, for example, at continental shelves in the ocean or in otherwise irregularly shaped domains. A special case is the near-equator region in the librating sphere or spherical shell for which the theory developed suggests the presence of mass fluxes driven synchronously to or from the equator in the Ekman layer of the northern and southern hemisphere. Where the currents collide, mass conservation requires an oscillating outflow from the boundary layer at the equator directed in radial direction. This jet-like outflow in radial direction might be a precursor for wave emission and early turbulent collapse of the equatorial boundary layer (for a discussion of the near-equator turbulence and localisation of wave emission see e.g. Koch *et al.*, 2013; Sauret *et al.*, 2013).

It remains to evaluate the flux difference hypothesis in the corners of the annular domain which will be done in the following by comparing the analytical estimate to DNS results of the weakly non-linear flow. Both configurations, frustum libration and lids plus outer cylinder in libration, will be discussed separately.

Assessment of the flux difference in the annulus. Part I: frustum libration. Figure 5.14 shows the integrated wall-tangential fluxes $2\pi r Q'_y\big|_2$ over the frustum (thick blue line; thin dashed and dotted line) and $2\pi r Q'_y\big|_1$ over the lid (thick dashed line) comparing the numerical and the analytical solution. Notice that the analytical solution has been multiplied with the wall radius r to yield approximately the same velocity scale as imposed locally in the DNS by the libration boundary condition. The positions y'_1 and y'_2 are illustrated in figure 5.13(a). The integration of the wall-tangential velocity has been carried out in azimuthal direction and in wall-normal direction across a few boundary layer thicknesses, which yielded the factor $2\pi r$ (r is the mean distance from the rotation axis; here approximately the wall radius at the bottom inner corner so that $r \approx r_1(0) = 1$). The analytical solution to the fluxes have been obtained from the idealised boundary layers due to which we expect *in the case of frustum libration*

$$\left.\begin{aligned} 2\pi r Q'_y\Big|_1 &= 0 \qquad \text{over the lid,} \\ 2\pi r Q'_y\Big|_2 &\neq 0 \qquad \text{over the frustum.} \end{aligned}\right\} \tag{5.49}$$

The analytical and the numerical solutions have been computed for the Ekman number $E = 3.19 \times 10^{-5}$ and libration frequency $\omega = 0.47$, which corresponds to the default case of the rhomboidal wave attractor (see section 4.1). The DNS has been performed for two different Rossby numbers, a small one $R = 0.02$ to minimise non-linear effects and the default one at $R = 0.2$. Both solutions are plotted for three libration periods T_{lib}, which is defined as

$$T_{\mathrm{lib}} := 2\pi/\omega. \tag{5.50}$$

Figure 5.14(a) shows the fluxes to the left and right of the bottom inner corner A (compare to figure 5.13(a)) for a small Rossby number $R = 0.02$. In general, the simple theory is in good qualitative agreement with the numerical reference solution. Especially the order of magnitude is acceptable, but lesser the phase. The thick lines correspond to the numerical solution obtained by integrating in wall-normal direction over $0 \leqslant z' \leqslant 3\delta'_-$ (over the frustum) and $0 \leqslant z' \leqslant 3\delta_{\mathrm{E}}$ (over the non-librating lid). The fluxes are computed far from the corner A by setting $|y'_1 - y'_{\mathrm{A}}| = 10\delta'_-$ and $|y'_2 - y'_{\mathrm{A}}| = 10\delta_{\mathrm{E}}$ correspondingly. The numerical solution provides the reference within a confidence interval provided by the shading, which has been

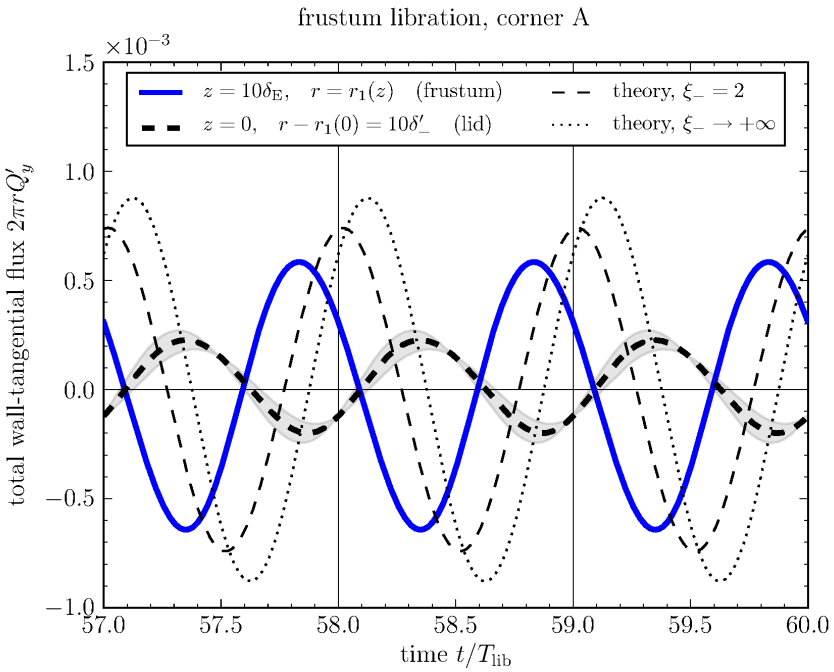

(a) $R = 0.02$

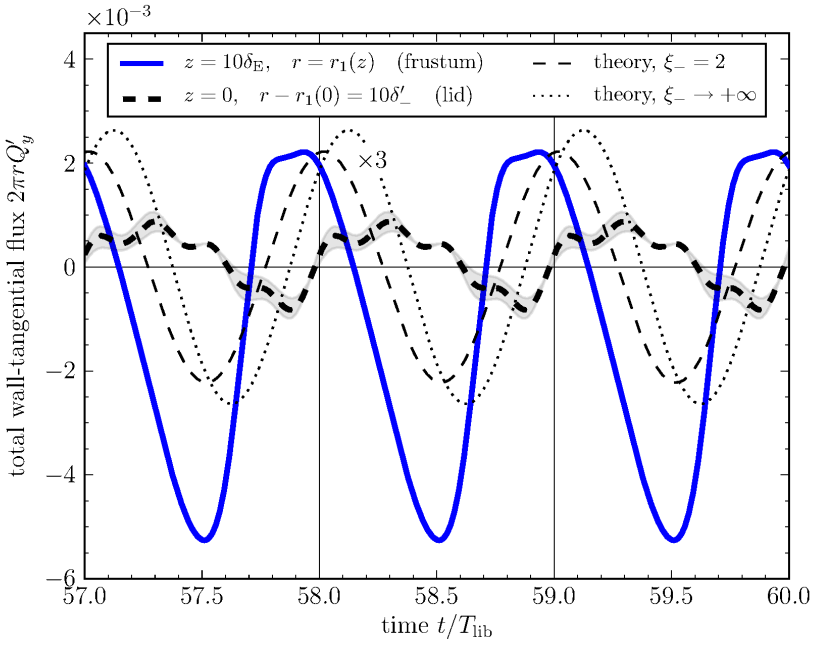

(b) $R = 0.20$

Figure 5.14: Time series over three libration periods T_{lib} of the azimuthally integrated wall-tangential mass flux $2\pi r Q'_y$ in the boundary layer near the bottom inner corner A adjacent to the librating frustum (see figure 5.13(a)). Panel (a) shows the fluxes obtained at Rossby number $R = 0.02$ and panel (b) those at $R = 0.2$ for fixed Ekman number $E = 3.19 \times 10^{-5}$ and libration frequency $\omega = 0.47$ obtained numerically compared to those obtained by boundary layer theory. The fluxes have been computed at $z = 10\delta_{\mathrm{E}} \approx 0.06$ over the frustum and at $r = r_1(0) + 10\delta'_- \approx 1.12$ over the lid. (Panel (b) from M. Klein *et al.* (2014). 'Inertial wave excitation and focusing in a liquid bounded by a frustum and a cylinder'. *J. Fluid Mech.*, **751**, p. 278, figure 11(a), reproduced with permission.)

estimated by varying the upper bound of the wall-normal integration by one boundary layer thickness (for the boundary layer thicknesses see figure 5.9).

The wall-tangential fluxes obtained by DNS become sinusoidal and indicate that the boundary layer obeys linear dynamics. The mass flux over the lid does not vanish in the numerical solution and is phase-shifted by π against the Ekman flux over the librating frustum. This can be attributed to an oscillatory circulation in the confinement (similar to Wang, 1970), but also to inertial waves and the rhomboidal wave attractor in the bulk (see section 4.1), which feed back on the boundary layer structure. Nevertheless, the mass flux over the non-librating lid is substantially smaller than that over the frustum. This supports the flux difference hypothesis outlined even if not the whole Ekman flux contributes to corner beam excitation and a fraction remains as 'creeping flow' over the lid.

The analytical solution shown in figure 5.14(a) has been obtained by an idealised integration of $0 \leqslant \xi_- < +\infty$ (thin dotted line) and a truncated integration of $0 \leqslant \xi_- \leqslant 2$ (thin dashed line; compare to figure 5.10), where $\xi_- \equiv z'/\delta'_-$ denoted the appropriate stretched coordinate over the frustum boundary layer. Amplitudes have been multiplied by $\sin\alpha'/\sin\alpha$ to account for the slope transitions, where $\alpha' \approx 0.4°$ is the effective wall inclination at vertical height $z = 10\delta_\mathrm{E} \approx 0.06$ above the bottom lid (see figure 3.4(b)).

The most striking discrepancy between the numerical and the analytical solutions shown in figure 5.14(a) concerns the phase. Analytical values are $\Delta(\omega t) \approx 0.6\pi$ ahead of the simulated ones (thin dotted *versus* thick solid line). That is, the oscillating Ekman flux in the DNS is closer to the reference phase ωt than expected from simple linear f-plane theory. The discrepancy is only partially due to a truncation of the vertical integration, since only a small shift can be seen between the thin dotted *versus* thin dashed line. Therefore, we suspect the corner flow to affect the flux computed at height $z \approx 0.06$. As can be seen in figure 5.2, the extraction height corresponds to the height where most of the wall-tangential flux is deflected. However, fluxes computed at larger distances z from the bottom lid are increasingly affected by inertial waves and the rhomboidal wave attractor, since the wave beam after the focusing reflection remains relatively close to the frustum wall (see figures 5.2 and 4.1). For the scope of this work, we can accept the discrepancy of the phase since in a temporal average only the approximately correct amplitude is of importance.

Figure 5.14(b) shows the fluxes to the left and right of the bottom inner corner A for the default Rossby number $R = 0.2$. The figure is arranged similarly to that of the case of $R = 0.02$ so that we can focus on the differences when the Rossby number increases. Obviously, the fluxes computed numerically exhibit a significant non-linear *increase* of the Ekman flux between the frustum and bottom lid boundary layer by an increase of the amplitude by about a factor 3 and higher.

Idealised boundary layer theory underestimates the flux amplitude by this factor 3. The analytical solution has been magnified manually as indicated by the label '$\times 3$' in figure 5.14(b). The potentially unstable retrograde libration half-period, $0.5\,(t/T_\mathrm{lib} \mod 1) < 1.0$, exhibits the largest anharmonic gain due to the 'bursts' of the boundary layer instability in the corner region (see figure 5.3). Interestingly, the Ekman flux is increased by the instability of the corner flow (see figure 5.3), which yields an increased flux difference and an increase of the excess Ekman pumping velocity due to equation (5.48). However, wave excitation does not necessarily increase in the same way since the temporal evolution of the wall-tangential flux is no longer sinusoidal. Hence, broader frequency content in the local solution excites inertial waves of different frequencies instead (see figure 4.16). Interestingly, the mismatch of the phase has reduced, which might be by chance due to the phase lag of the instability (see figure 5.3).

Assessment of the flux difference in the annulus. Part II: lids plus outer cylinder libration. Figure 5.15 shows the integrated wall-tangential fluxes $2\pi r Q'_y\big|_2$ over the bottom lid (thick red line; thin dotted line) and $2\pi r Q'_y\big|_1$ over the outer cylinder (thick dashed line) comparing the numerical and the analytical solution. The figure arrangement is similar to figure 5.14 (see previous paragraphs), but now the integrated wall-tangential fluxes near the bottom outer corner D are compared over the positions y'_1 and y'_2 as illustrated in figure 5.13(b). The analytical solution yields a Stokes layer over the outer cylinder and an oscillating Ekman layer over the bottom lid, hence one expects *in the case of lids plus outer cylinder libration*

$$\left.\begin{aligned} 2\pi r Q'_y\Big|_1 &= 0 \qquad \text{over the outer cylinder,} \\ 2\pi r Q'_y\Big|_2 &\neq 0 \qquad \text{over the bottom lid.} \end{aligned}\right\} \tag{5.51}$$

In the following, the analytical velocity components have been multiplied with the local wall radius where the wall-normal integration has been carried out numerically ($r \approx r_2$) in order to match the local velocity magnitude of the numerical solution.

Figure 5.15(a) shows the numerical and analytical fluxes near the bottom outer corner D for a small Rossby number $R = 0.02$. The flow is excited by libration frequency $\omega = 0.47$ to ensure wave beams approach the rhomboidal wave attractor (see section 4.1) and do not return to the wave-emitting corner. All fluxes shown in figure 5.15(a) have a sinusoidal time dependence, which suggests a dominance of the linear dynamics by the induced mass flux following the libration. In fact, the Ekman flux over the lid is predicted correctly in amplitude *and* phase as can be seen by the numerical solution (thick solid red line) and the analytical solution (dotted line) being virtually identical. This is in contrast to the frustum libration case shown above. The Ekman flux obtained numerically has been computed at the radial position $r = r_2 - 10\delta_S \approx 1.9$ over the bottom lid (compare to figure 5.9) and again $3(\pm 1)$ boundary layer thicknesses have been used for the wall-normal integration to estimate the confidence interval. The uncertainty associated with a truncation of the numerical integration, however, is again negligible since the red shading is indistinguishable from the solid red line itself.

The corner flow (see figures 5.4, 5.5) and the analytical solution to Wang (1970, figure 1) corresponding to the fluxes in figure 5.15(a) exhibit a mass flux in vertical direction along the outer cylinder that detaches only gradually with increasing distance from the lid. Hence, it is not surprising that the wall-tangential flux over the outer cylinder (thick dashed black line in figure 5.15(a)) does not vanish in a radial integral across the boundary layer at $z = 10\delta_- \approx\approx 0.15$. Nevertheless, the amplitude of the deflected and vertically-directed flux is smaller than that of the Ekman flux over the lid even within the confidence interval (grey shading). Hence, there is a flux difference across the corner D, which in turn corresponds to a localised excess Ekman pumping velocity according to equation (5.48). The small flux difference is thus supposed to be responsible for corner beam excitation in accord with the schematic shown in figure 5.13(b).

Figure 5.14(b) shows the fluxes to the left and right of the bottom outer corner D for the default moderate value of the Rossby number $R = 0.2$. The figure is arranged similarly to the case of $R = 0.02$ so that we focus on possible differences due to an increased Rossby number. Most important is that the Ekman flux does *not* show any sign of non-linear increase here. This means that the Ekman flux obtained by the DNS scales linearly[3] with the libration amplitude

[3]Remember that the linear dependency on the libration amplitude has already been removed by adopting the dimensionless formulation so that the Ekman flux according to equation (5.42) is expected to obey $\boldsymbol{Q}' = O(\varepsilon^0)$ in case the analytical, laminar solution is a good approximation.

at least up to a libration amplitude (Rossby number) of the order 0.2. In fact, it is quite remarkable how unaffected the thick solid line is even in the factor 10 stronger non-linearity here compared to the frustum libration case (see figure 5.14(b)). Laminar boundary layer theory is thus able to predict the Ekman flux over the librating lid very accurately for the range of Rossby numbers investigated.

In contrast to the linear dependency of the Ekman flux amplitude on the libration frequency it is worth to point out that the mass flux difference exhibits a non-linear increase, here by about a factor 3 after removing the linear contribution[4]. The latter reduction of the mass flux difference is accompanied by a reduction of the amplitude of the vertically-directed mass flux over the outer cylinder, say $Q'_y\big|_1$. This is surprising and suggests that an increased non-linearity leads to an instability of the corner flow (or corner vortex; see figures 5.5 and 5.13(b)). The instability can develop during the unstable retrograde half-phase of libration but remains localised to the corner, where it seems to enhance the Ekman flux deflection.

As a consequence, the Ekman pumping velocity is increased locally and so is the wave excitation efficiency. This non-linear increase of the Ekman pumping also explains why corner beams are strongly excited in the case of lids plus outer cylinder libration compared to the case of frustum libration, which is especially notable in the laboratory experiments of Seelig (2014) (repeated here in figures 4.9 and 4.3, respectively). It can be summarised, that the corner vortex is another example of vortex generation due to instability, here in the Ekman boundary layer, that stabilises the system locally.

Note that the mass fluxes near corner A, which is now adjacent to the librating bottom lid and the uniformly rotating frustum, turn out very similar to corner D (see Klein *et al.*, 2014, their figure 11). It turns out that the Ekman flux has the same phase, but its amplitude is reduced by a factor 1/2 due to the radius ratio ($r_1(0)/r_2 = 1/2$) of the frustum.

Intermediate summary. The excitation mechanism of corner beams emerging from corners or velocity jumps in the libration boundary condition can be attributed to a kind of 'localised boundary layer eruption'. Boundary layer theory suggests the presence of an oscillatory excess Ekman pumping velocity in the corner, while numerical results reveal a complex helical flow structure that is supposed to be responsible for inertial wave excitation. However, simplifying the problem as much as possible leads to the conclusion that the radial component of excess Ekman pumping velocity might govern inertial wave excitation by libration—be there a corner vortex or not. The radial velocity component of the excess Ekman pumping velocity displaces fluid parcels more vigorously near the corner. The radial flow induced is affected by the Coriolis force due to which fluid parcels are forced on a circular path in a radial-azimuthal section of the annulus (see figure 5.13). In that way vorticity is generated near the corner. The proposed mechanism is qualitatively in line with numerical simulations and laboratory measurements (Seelig, 2014), which exhibit distinct inertial wave patterns for forcing frequencies from within the inertial wave band $0 < \omega < 2$.

Regarding the proposed mass flux difference in the corner, in fact, good qualitative and quantitative agreement has been obtained between DNS and boundary layer theory for the lids plus outer cylinder libration case for Rossby numbers $R \leqslant 0.2$. Surprisingly, the agreement is a bit worse in the frustum libration case. Even when the Rossby number is as small as $R = 0.02$ a phase shift between DNS and boundary layer theory can be seen which may be attributed to a stronger corner vortex in the frustum libration case compared to the lids plus outer cylinder

[4]The non-liner increase is from $\max\left(2\pi Q'_y\big|_2 - 2\pi Q'_y\big|_1\right) = 0.07 - 0.06 = 0.01$ in figure 5.15(a) at $R = 0.02$ to $\max\left(2\pi Q'_y\big|_2 - 2\pi Q'_y\big|_1\right) = 0.07 - 0.04 = 0.03$ in figure 5.15(b) at $R = 0.2$.

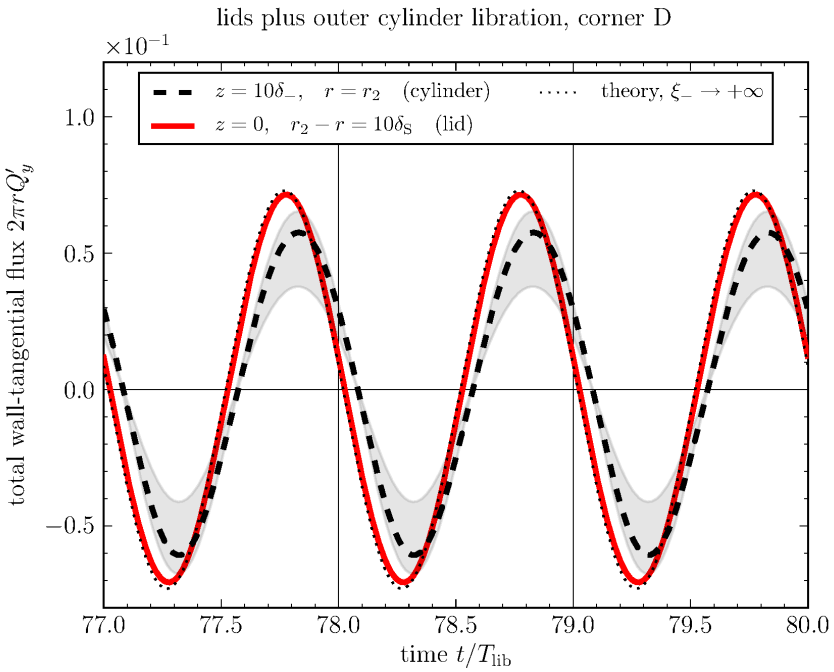

(a) $R = 0.02$

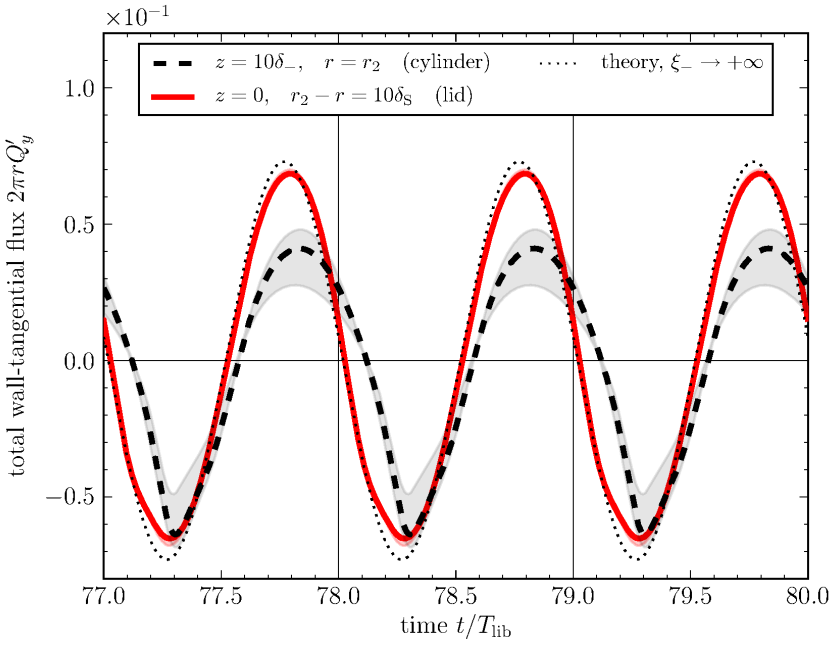

(b) $R = 0.20$

Figure 5.15: Time series over three libration periods T_{lib} of the azimuthally integrated wall-tangential mass flux $2\pi r Q'_y$ in the boundary layer near the bottom outer corner D adjacent to two librating wall pieces (see figure 5.13(b)). Panel (a) shows the fluxes obtained at Rossby number $R = 0.02$ and panel (b) those at $R = 0.2$ for fixed Ekman number $E = 3.19 \times 10^{-5}$ and libration frequency $\omega = 0.47$ obtained numerically compared to those obtained by boundary layer theory. The fluxes have been computed at $z = 10\delta_- \approx 0.07$ over the outer cylinder and at $r = r_2 - 10\delta'_- \approx 1.89$ over the lid. (Panel (b) from M. Klein *et al.* (2014). 'Inertial wave excitation and focusing in a liquid bounded by a frustum and a cylinder'. *J. Fluid Mech.*, **751**, p. 278, figure 11(b), reproduced with permission.)

libration case. At $R = 0.2$ the corner flow in the frustum libration case exhibits instability due to which the flux difference has increased. In general, the frustum boundary layer is less stable than the lid boundary layer because of an effectively smaller Coriolis force, that is, the Coriolis parameter is $f_* = 0.2$ which is a factor 10 smaller than over the lid.

Formulation of the wave excitation model as an extract of the boundary layer analysis. We are now in the position to formulate a linear model for wave excitation by wall libration. The total kinetic energy K_{wave} of the inertial waves excited by wall libration in the form of corner beams must be proportional to the square of the *excess* Ekman pumping velocity $(\Delta w'_{\mathrm{E}})^2$. This excess Ekman pumping velocity can in turn be expressed by an Ekman flux difference across the corner (discontinuity of the boundary condition). For the corners in the librating annulus, equations (5.49) and (5.51) enforce conditions on the Ekman flux, which is then more conveniently written in terms of the local Ekman pumping velocity by the aid of equations (5.42) and (5.47). Altogether, the *linear model for the excitation of inertial waves by wall libration* is given by

$$K_{\mathrm{wave}}(\omega) = A\, w'^2_{\mathrm{E}}(\omega) \qquad \text{for} \quad \omega \in (0,2), \tag{5.52}$$

where K_{wave} is the total kinetic energy of the inertial wave field, w'_{E} is the local Ekman pumping velocity over the wall segment adjacent to the discontinuity of the boundary condition (here the Ekman pumping velocity over the librating frustum or lid), ω is the dimensionless libration frequency, and A is a proportionality factor that accounts for the geometry and the efficiency of kinetic energy conversion from the boundary layer flow into wave energy in the fluid bulk.

The value of A depends on the case and can be obtained by a fit to DNS data or laboratory measurements. In the next section, we will thus consider A a fitting parameter and study the frequency dependency $K_{\mathrm{wave}}(\omega)$ in the librating annular confinement for two different forcing configurations.

6 Dependency of the inertial waves excited on the libration frequency

The objective of this chapter is to study the effects of inertial waves excited and the implications for the flow on the system scale by looking at integral quantities at various libration frequencies ω. The focus is on the response of the fluid in the annular confinement to libration frequencies from within the inertial wave band, $0 < \omega < 2$. The objective of this chapter is to clarify the following three aspects.

- First, it is intended to clarify if the corner beams excited by a local boundary layer eruption (see chapter 5) are the dominating source of wave energy and for which configuration wave energy injection is optimal. The problem is addressed by computing response spectra by DNS and analytically for the case of frustum libration and the case of lids plus outer cylinder libration. The spectra obtained are compared qualitatively to recent laboratory measurements by Seelig (2014).

- Second, it is intended to clarify which spatial patterns can be excited resonantly by libration and if there is a difference between wave attractors and normal modes, but also if there is a difference between frustum and lids plus outer cylinder libration. According to section 2.4, the spatial patterns under considerations are low-order ray orbits, low-order wave attractors (LOWAs) and low-order neutral orbits (LONOs) that correspond to normal mode solutions (e.g. Borcia & Harlander, 2012).

- Third, it is intended to clarify non-linear wave excitation and when it is optimised in an overall linear flow. It was shown in section 4.4 that non-linearity is weak for the default parameters $R = 0.2$, $E = 3.19 \times 10^{-5}$ by means that the bulk flow is stable and highly organised. However, there are additional frequencies besides the libration frequency present in the non-linear solution which have been found to belong to non-linear inertial waves. Such additional frequency content has been suspected relevant for an instability of the wave-dominated flow provided it is non-axisymmetric (e.g. Kerswell, 1999; Mason & Kerswell, 1999; McEwan, 1970). For the configurations and parameters investigated in this work, though, librational forcing is unable to break axisymmetry of the flow. The additional frequencies are weak and mainly localised at harmonics $l\omega$ ($l = 2, 3, \ldots$) of the forcing frequency ω. In order to understand better the transition to a non-axisymmetric or even turbulent flow it seems worth to study the system response at the harmonics 2ω and 3ω separately from the forcing frequency ω in order to check for an optimum non-linear wave excitation. The effect of 'spatial coupling' of wave attractors, which is potentially related to triads and the anharmonic frequency content, is not considered here.

In the following, the system response to wall libration is studied for different integral quantities. In order to be able to generalise the results, two configurations are considered, the case of frustum libration and the case of lids plus outer cylinder libration.

First, the kinetic energy filtered at the forcing frequency ω is studied by a decomposition of the flow domain into bulk and boundary layer. The domain decomposition is applied to separate the scaling of the boundary layer from that of the bulk flow so that a comparison to the analytical solution can be performed by assuming wave energy is injected by corner beams. The ratio of bulk to boundary layer kinetic energy is used as a measure for wave excitation efficiency.

Second, the kinetic energy response at the harmonics 2ω and 3ω of the forcing frequency is studied also using the domain decomposition. No theory exists for the system response at harmonics of the libration frequency. Hence, with the aid of the system response at the libration frequency, possible interaction mechanisms are suggested on the basis of frequency mixing.

Third, in addition to kinetic energy the dissipation rate has been computed in more recent simulations. This allowed to compute the quality factor (or just Q factor; it is the ratio of the total kinetic energy and the energy dissipated in a reference time interval) of the annulus, which avoids any ambiguity introduced by the domain decomposition. The system response in terms of the Q factor is discussed for a temporal average and filtered at the frequencies $l\omega$ with $l = 1, 2, 3$ in order to compare linear and non-linear effects.

Fourth and last, resonance conditions of inertial waves are investigated in terms of the total kinetic energy, dissipation rate, Q factor and helicity for a few selected cases. The temporal average and individual contributions of the frequencies $l\omega$ with $l = 1, 2, 3$ are considered.

6.1 Kinetic energy and wave excitation efficiency at the forcing frequency

In chapter 5, a mechanism for the corner beam excitation has been proposed that relates the velocity amplitude of the corner beam to the mass flux difference across the corner. The wave energy injected scales with the Ekman number E and the libration frequency ω as the Ekman pumping velocity w'_{E} due to equation (5.52). The dependency of the wave energy density on the Ekman number reads $|\boldsymbol{v}|^2 \propto E$, which simply reminds us that kinetic energy provided by libration is injected by viscous forces and may leave the boundary layer region in a second step. More difficult and not so well understood is the dependency of the wave energy on the libration frequency (see for example Seelig, 2014, pp. 67–70), which will be studied in detail in the following.

The total wave energy in the bulk K^{bulk} and the total kinetic energy of the boundary layer over a librating wall K^{BL} differ in their frequency dependencies since

$$K^{\mathrm{bulk}} \propto \overline{w'^2_{\mathrm{E}}}, \qquad K^{\mathrm{BL}} \propto \overline{\boldsymbol{Q}'^2_{\parallel}} = \overline{\left(Q'^2_x + Q'^2_y\right)}. \tag{6.1}$$

The bulk flow is dominated by waves, wherefore we expect equation (5.52) to apply for K^{bulk}. In the boundary layer, the wall-parallel azimuthal mass flux dominates the kinetic energy, but there is an additional effect of the Coriolis force that induces also a radial flow (Ekman pumping). The latter appears as secondary, wall-tangential flow and is perpendicular to the azimuthal flow. As discussed in section 5.2, the wall-normal and wall-tangential flows are correlated and obey the same frequency dependency. Thus, it is sufficient to investigate only the wall-tangential flow, more precisely, the wall-tangential Ekman flux $\boldsymbol{Q}'_{\parallel} = \boldsymbol{e}_x Q'_x + \boldsymbol{e}_y Q'_y$, where $\boldsymbol{e}_x$ is the local azimuthal direction and $\boldsymbol{e}_y$ perpendicular to $\boldsymbol{e}_x$ but also wall-tangential. The unknown proportionality factors account for the efficiency of the transformation of kinetic energy trapped in the boundary layer into wave energy in the bulk. However, the proportionality

factors also account for the volume of the bulk and the boundary layer, respectively. We omit a theoretical estimation of the proportionality factors in the annulus here and simply make them free parameters that need to be obtained from the DNS data.

Before continuing with the analysis, let us briefly discuss the domain decomposition method used to separate the boundary layer from the bulk.

Domain decomposition

According to the results shown in chapter 5, the boundary layer region in the numerical solutions obtained extends up to about 2–3 theoretical boundary layer thicknesses, which is in agreement with recent studies that have used also much higher resolutions of the boundary layer (e.g. Lopez & Marques, 2011; Salon & Armenio, 2011). A robust computation of the actual boundary layer thickness from the numerical solution itself is rather difficult, which means one is practically forced to use an estimation based on the theoretical thicknesses (see figure 5.9). An implementation of this estimate would be straightforward but has been considered impractical for at least two reasons. First, the theoretical estimate fails for libration frequencies close to the boundary layer eruption, $|\omega - f_*| \ll 1$ with $f_* = f \sin\alpha$ the effective Coriolis parameter, so that some kind of limiter would be needed that introduces some ambiguity. Second, the theoretical boundary layer thickness depends strongly on the libration frequency and effective Coriolis parameter (see figure 5.9). Thus, the volumetric ratio $V^{\mathrm{BL}}/V^{\mathrm{bulk}}$ of the boundary layer and bulk varies with the parameters ω and E. Even worse, $V^{\mathrm{BL}}/V^{\mathrm{bulk}} \not\ll 1$ for the Ekman numbers accessible (see table 4.1) which would yield a substantial bias in the corresponding kinetic energy ratio $K^{\mathrm{BL}}/K^{\mathrm{bulk}}$.

In order to avoid these difficulties and ambiguity, the numerical grid (see figure 3.4) and the domain decomposition (see figure 6.1; details follow shortly) were kept constant throughout this study even though at the eruption frequency the boundary layer will theoretically span the whole flow domain. It was tested that this does not affect the domain decomposition results for the majority of libration frequencies since the boundary layer thickness quickly decreases (compare to figure 5.9) below the maximum value introduced by the domain decomposition. However, we accept a slight systematic error for libration frequencies very close to the eruption frequency. For this eruption frequency, this simple approach cannot be applied.

Figure 6.1 shows the domain decomposition used for all libration frequencies investigated[1]. Five subdomains have been defined, which exclude the corner regions in order to avoid that the corner flow affects the scaling properties. The thickness of the boundary layer regions has been selected such that the bulk (subdomain $i = 5$) does not contain the boundary layer flow for libration frequencies $|\omega - f_*| \geqslant 0.05$.

Note that 2–3 theoretical boundary layer thicknesses are actually considered here as boundary layer based on the DNS results discussed in section 5.2.

Note further that a too large boundary layer domain only results in a small error since the kinetic energy density in the boundary layer ($|\boldsymbol{v}|^2 \sim 1$) is much larger than in the bulk ($|\boldsymbol{v}|^2 \lesssim 10^{-2}$; compare to chapter 4). In other words, the kinetic energy of the boundary layer K^{BL} may be overestimated when ω is far from the eruption frequency f_*, but the error is only of the order of a percent and typically even smaller. It depends on the distribution of the kinetic

[1]Over the outer cylinder (Stokes–Stewartson layer) we require $\omega \gg E^{1/2}$ to avoid spin-up. In addition, ω should be large enough to fulfil the viscous stability criterion to keep the boundary layer flow centrifugally stable (Sauret *et al.*, 2012). For the parameters selected, $\omega \leqslant 0.05$ yields unstable conditions over the frustum. The boundary layer flow is stable (except for the corners) for $\omega \geqslant 0.1$, which is the frequency range in the focus of this study.

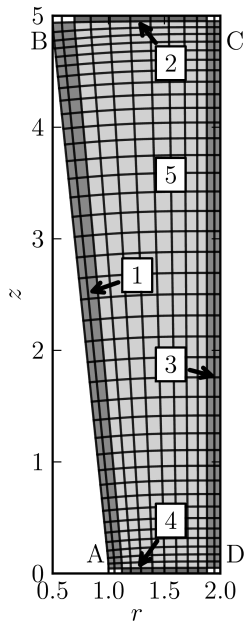

Figure 6.1: The domain decomposition used for computation of the response spectra of the kinetic energy and the wave excitation efficiency. The subdomains bulk ($i = 5$) and boundary layer ($i = 1, 2, 3, 4$) are fixed in size (grey shaded areas). Areas with overlapping subdomains (white) adjacent to corners A–D are excluded from the considerations. Every 16th grid line of the standard grid (see figure 3.4) has been plotted for orientation.

energy in the bulk how much K^{bulk} is underestimated. Typical situations in the focus of this study exhibit inertial wave beams crossing the domain volume (see section 2.4 and chapter 4) so that a large part of their energy will be captured by K^{bulk}.

We use that $K^{\mathrm{bulk}} \equiv K^{(5)}$ (compare to figure 6.1), whereas K^{BL} denotes the sum over all subdomains corresponding to *oscillating* boundary layers without corners. The corner regions have been removed since the role of the corner vortices seems passive with respect to wave emission as discussed in sections 5.1 and 5.3.

The time-averaged total kinetic energies $\bar{K}^{(i)}$ and the frequency-filtered total kinetic energies $K_{l\omega}^{(i)}$ ($l = 1, 2, \ldots$) in the subdomain i are given by

$$\bar{K}^{(i)} = \frac{1}{T} \int_T \mathrm{d}t \int_{V_i} \frac{|\boldsymbol{v}|^2}{2} \,\mathrm{d}V, \qquad K_{l\omega}^{(i)} = \int_{V_i} \frac{|\hat{\boldsymbol{v}}_{l\omega}|^2}{2} \,\mathrm{d}V \tag{6.2}$$

The first equation applies to the real-valued velocity field $\boldsymbol{v}$, where the bar $\overline{(\cdot)}$ denotes a temporal average over some integer libration periods, for example $T = MT_{\mathrm{lib}}$ with $M \gtrsim 10$ and $T_{\mathrm{lib}} = 2\pi/\omega$. The second equation applies to a (complex) filtered velocity field (see appendix A.3). In both equations V_i denotes the volume of the subdomain i and the upper index i is suppressed when the spatial integral encompasses the whole fluid volume V.

The numerical integration is performed in the curvilinear grid using the weighted sum

$$\int_{V_i} \frac{|\boldsymbol{v}|^2}{2} \,\mathrm{d}V \approx \frac{\Delta\xi^1 \,\Delta\xi^2 \,\Delta\xi^3}{2} \sum_{i',j',k'} J_{i'+1/2,j'+1/2,k'+1/2} \left|\boldsymbol{v}_{i'+1/2,j'+1/2,k'+1/2}\right|^2, \tag{6.3}$$

where i', j', k' are the grid box indices, J is the local Jacobian of the coordinate transformation, and $\Delta\xi^\mu$ ($\mu = 1, 2, 3$) are the grid box dimensions with respect to the generalised coordinates ξ^μ (see chapter 3 for details on the generalised coordinate framework). Here, $|\boldsymbol{v}|^2$ has been computed from the cylindrical velocity components (v_r, v_φ, v_z).

This concludes the interlude on the domain decomposition and we continue with an assessment of the kinetic energy response spectra for the bulk and the boundary layer. We will first discuss the case of frustum libration and then the case of lids plus outer cylinder libration. After that, we will bring both together by addressing the wave excitation efficiency.

Energy response spectra for the case of frustum libration

The objective of this section is to clarify the frequency dependency of the flow by computing the kinetic energy of the flow in the boundary layer and the bulk. This will allow us to draw conclusions about whether or not the wave excitation mechanism proposed in chapter 5 can explain the frequency dependency. A weakly non-linear flow is studied here using the default parameters $R = 0.2$ and $E = 3.19 \times 10^{-5}$, which corresponds precisely to the parameters of the laboratory experiments of Seelig (2014). All cases shown in the following exhibit weakly non-linear flow in the sense that the majority of the kinetic energy is located at the libration frequency ω. Hence, we restrict our attention to the frequency-filtered kinetic energy $K_{1\omega}^{(i)}$ (for the filtering method see appendix A.3). The filtering approach is, in fact, very similar to the data processing used for the laboratory measurements (compare to Seelig, 2014, pp. 43–48). In the following, the discussion of section 4.3 is extended to many more libration frequencies. Libration frequencies are primarily selected from within the inertial wave band and slightly above, namely $0 < \omega < 2.5$.

Figure 6.2 shows the system response in terms of the filtered kinetic energy of the bulk, $K_{1\omega}^{(5)}$ (filled blue circles) and the oscillating frustum boundary layer, $K_{1\omega}^{(1)}$ (unfilled blue circles), as functions of the forcing frequency ω. Also shown are laboratory measurements of Seelig (2014, p. 68), which have been plotted by unfilled black diamonds; given in terms of an optical backscattering signal proportional to the light intensity I, but in arbitrary units (a.u.). The dashed lines correspond to equation (6.1) and show the expected frequency dependency of the kinetic energy in the bulk in the case of corner beam excitation (see section 5.3). The proportionality to the Ekman pumping velocity $w'_{\mathrm{E}}(\omega)$ is given for each quantity separately and will be discussed in more detail shortly. The dash-dotted line shows the frequency dependency of an ideal oscillating boundary layer (see equation (6.1)). A black dotted vertical line indicates the eruption frequency $\omega = f_* = 0.2$ of the frustum boundary layer, whereas a black solid vertical line shows the inertial wave band limit $\omega = f = 2$.

The shaded areas in figure 6.2 show the frequency bands of relevant low-order wave attractors (LOWAs), which correspond to the broad white areas in the bifurcation diagram (figure 2.9), but excluding the $(0, 0)$ point attractor in $\omega < 0.2$. Grey dashed vertical lines show the frequencies of low-order neutral orbits (LONOs) obtained by ray tracing (e.g. figure 2.11), which are not visible in the bifurcation diagram. Six short black lines along the upper ω-axis correspond to the spatial patterns shown in figure 4.12, in which the ray orbits are compared to numerical solutions.

Assessment of the wave excitation mechanism. Figure 6.2 allows to compare the theoretical prediction to the simulated spectra $K_{1\omega}^{(1)}(\omega)$ and $K_{1\omega}^{(5)}(\omega)$, but also to the measured spectrum

$I_{1\omega}^{(5)}(\omega)$. Theoretical spectra (dashed and dash-dotted lines) have been obtained on the basis of equations (6.1), but an adjustment was necessary with respect to the laboratory measurements.

It has been argued by Klein *et al.* (2014) and Seelig (2014) that the optical measurements with immersed platelets are sensitive to the local velocity shear $||\boldsymbol{\tau}||$ (see equation (3.73)) rather than the local velocity magnitude and a modification of the theoretical frequency dependency is necessary for the measurements. Following the corner beam excitation hypothesis, kinetic energy is localised along wave beams, which are of a given width that depends only on the Ekman number (see the discussion of viscous broadening in section 2.3). Hence, the shear is proportional to the velocity amplitude of the corner beam and so is the backscattered light intensity, namely $I \propto ||\boldsymbol{\tau}|| \propto |\boldsymbol{v}_{\text{wave}}|$ (compare to Klein *et al.*, 2014). This yields

$$K_{1\omega}^{(1)} = A_1 \overline{\boldsymbol{Q}_{\parallel}'^2}, \qquad K_{1\omega}^{(5)} = A_5 \overline{w_{\text{E}}'^2}, \qquad I_{1\omega}^{(5)} = A_{\text{lab}} \left[\overline{w_{\text{E}}'^2}\right]^{1/2}, \tag{6.4}$$

where the prefactors A_1, A_5 and A_{lab} are proportionality constants to be obtained by fitting to the simulated or measured data.

As it turns out, the simulated spectra and the fitted theoretical estimate, but also the measured spectra and the fitted theoretical estimate shown in figure 6.2 are in very good agreement with respect to the global properties. That is, a global maximum can be discerned at the boundary layer eruption frequency $\omega = 0.2$ in all spectra and the spectral decay predicted on the grounds of boundary layer theory matches the baseline of the data points very well. The baselines of the simulated and measured spectra correspond approximately to non-resonantly excited waves for which the shape of the confinement is unimportant. The only purpose of the confinement is to provide a discontinuity of the libration boundary condition. This implies that a fair comparison between the corner beam excitation model (see chapter 5) and the full numerical solution is only realised for the non-resonant cases, in which wave energy follows the boundary layer theory. Moreover, the spectral shapes are in qualitative agreement with the boundary layer thickness (see figure 5.9), which implies that a decreasing boundary layer thickness corresponds to a reduction of the Ekman flux that is at heart of the corner beam excitation.

Note that the kinetic energy of the bulk exhibits a distinct drop at the inertial wave band limit $\omega = 2$, which indicates that the kinetic energy of the bulk is indeed dominated by inertial waves. The residual circulation has kinetic energy of the order $\sim 10^{-7}$, which corresponds to the truncation error estimate (see chapter 4).

Note further that the response spectrum of the oscillating boundary layer has generally much larger values than the bulk, that is, $K_{1\omega}^{(1)}(\omega) \gg K_{1\omega}^{(5)}(\omega)$. This indicates that only a fraction of kinetic energy absorbed by the fluid is actually transformed into wave energy. The majority of the kinetic energy is 'trapped' in the boundary layer and dissipated there. The conversion into wave energy is most efficient when the boundary layer erupts because of the non-linear dependency of the wall-tangential mass flux Q_y' on the libration frequency ω (see equation (5.42)). The boundary layer scaling has been modified compared to Klein *et al.* (2014), that is, the Ekman flux is now used for comparison to the simulated kinetic energy spectra and not just the Ekman pumping velocity plus an *ad hoc* offset for the zonal wall libration. The present extension generalises the frequency dependency of the boundary layer to all libration frequencies.

Non-monotonic properties of the response spectra. Figure 6.2 exhibits the interesting property that the kinetic energy response spectrum $K_{1\omega}^{(5)}(\omega)$ is strongly non-monotonic. This is far

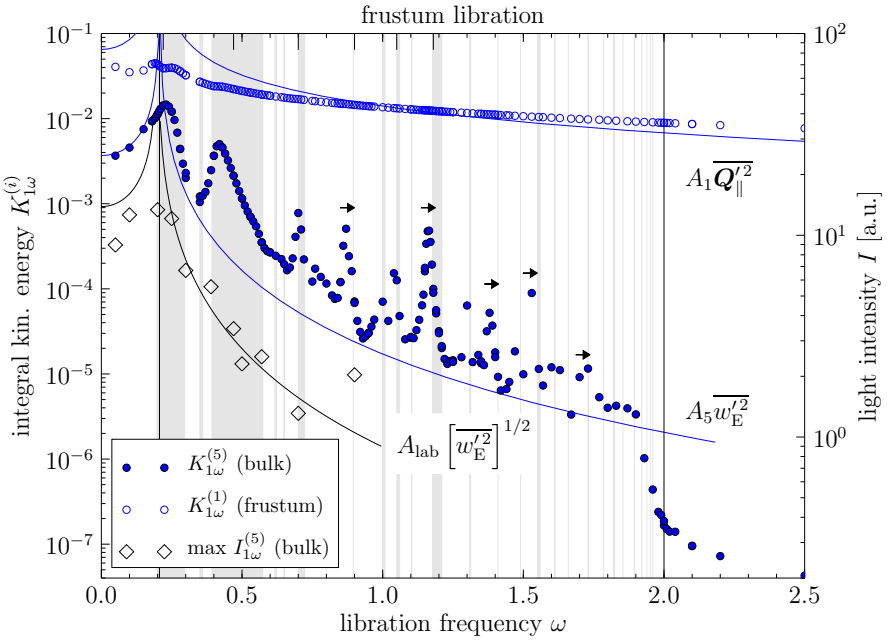

Figure 6.2: Response spectra for $R = 0.2$ and $E = 3.19 \times 10^{-5}$ with the frustum in libration. Filtered kinetic energies $K_{1\omega}^{(i)}$ are shown for the subdomains $i = 5$ (bulk) and $i = 1$ (frustum boundary layer) in comparison to laboratory measurements of Seelig (2014) for the backscattered light intensity $I_{1\omega}^{(5)}$ (arbitrary units). Shaded areas show a few low-order wave attractor frequency bands and the dashed grey lines some low-order neutral orbit frequencies obtained by ray tracing. Small solid lines on the upper ω-axis show the frequencies used in figure 4.12. Fitted proportionality constants read $A_1 \approx 842$, $A_5 \approx 2230$, $A_{\mathrm{lab}} \approx 11000$. (From M. Klein *et al.* (2014). 'Inertial wave excitation and focusing in a liquid bounded by a frustum and a cylinder'. *J. Fluid Mech.*, **751**, p. 280, figure 12, reproduced with permission. A different scaling and an increased number of numerical data points is used here.)

beyond the corner beam excitation model and related to resonant excitation of inertial waves. Interestingly, not only the 'classical' resonances occur which are related to the normal modes (or LONOs respectively) but also to wave attractors (for a discussion of resonant excitation of inertial waves see, for example, Greenspan, 1969, p. 67). One objective of this chapter is to elucidate the resonance mechanism for inertial wave attractors. We will come back to this point later and accept for the moment that resonance conditions are possible for both LOWAs and LONOs.

Note that the measured spectrum shown in figure 6.2, $I_{1\omega}^{(5)}(\omega)$, suffers from insensitivity to velocity magnitudes and sparseness of available data. Moreover, it is discussed by Borcia *et al.* (2014) and Ghasemi V. (2016) that corner beams dominate the shear and since they are also largely unaffected even when inertial waves are excited resonantly, the measurements are inadequate to detect the resonance. Therefore, we will concentrate on the simulated energy spectra.

Resonant wave excitation manifests itself by a sharp increase of the kinetic energy in the bulk. That is, kinetic energy increases by an order of magnitude or more when the libration frequency is varied slightly. Notable resonances correspond to the LOWA frequency bands marked by the shading, that is, around $\omega = 0.25$, 0.35, 0.70, 1.05, 1.18, 1.30 and 1.55. Only

the peaks at $\omega = 0.87$ and 1.38 are very close to LONO frequencies, which suggests excitation of a 'surviving' normal mode of the straight annulus (as discussed in section 4.2). The average frequency resolution that could be realised by the DNS performed in this work is $\Delta\omega = 0.03$, but has been reduced down to $\Delta\omega = 0.01$ across the narrower wave attractor bands and around LONO frequencies (grey dashed lines) for $0.2 \leqslant \omega \leqslant 1.4$. The system response is thus resolved better by factors 2 (globally) to 5 (locally) compared to the spectra of Klein *et al.* (2014, figure 12), but are otherwise similar.

Figure 6.2 reveals the substructure of the broadest resonance peaks that correspond to the wave attractors of lowest order (compare to Beardsley, 1970; Thompson, 1979). The complexity of the response spectrum is remarkable given the relatively large Ekman number of $E \sim 10^{-5}$ used here. It is apparent that the frequency resolution of $\Delta\omega = 0.03$ is still not sufficient since a few resonances are sampled only by a single data point, for example, those at $\omega = 1.3$ and 1.55. Note in this respect that the latter resonance at $\omega = 1.55$ was not captured by the less-well resolved response spectra shown by Klein *et al.* (2014, figure 12). Based on the asymptotic study of Rieutord & Valdettaro (1997) for the spherical shell, one can expect that the situation gets worse since the response spectra are likely to become more complex and heavily non-monotonic by the excitation of higher-order wave attractors or normal modes when the Ekman number reduces.

Small arrows over the simulated resonance peaks in figure 6.2 indicate that the numerical solution exhibits the spatial pattern of a nearby LOWA or LONO, whose frequency (band) does not overlap with the simulated resonance peak. The corresponding LOWA or LONO frequency is located at the tip of the arrow, which means ray orbits have frequencies *right-shifted* compared to the resonance frequency obtained by DNS. However, the bifurcation diagram (figure 2.9) forms the reference spectrum for small Ekman numbers ($E \to 0$), which is an idealisation but closer to the situation in actual geophysical flows with $E \lesssim 10^{-14}$. Hence, it is preferable to say that resonance frequencies exhibit a *left-shift* of the frequency induced by viscosity. Such a left-shift has been observed recently by Borcia *et al.* (2014) for a librating straight annulus and by Lopez & Marques (2014) for a librating cylinder. Both groups argue that the aspect ratio of the flow domain accessible by inertial waves is reduced due to the presence of boundary layers. Here, the presence of a boundary layer means that a larger percentage of the radial gap, $\Delta r(z) = r_2 - r_1(z)$, is affected than of the height and the effective aspect ratio is therefore *smaller* than $\Delta r(0)/h = 1/5$.

In summary, various response spectra have been shown in figure 6.2 for the frustum libration case. The spectra obtained for the bulk and oscillating boundary layer support the model for corner beam excitation and confirm that the energy of the wave field follows the boundary layer in the case of waves being excited non-resonantly in the form of corner beams as hypothesized in section 5.3. The response spectra of the bulk confirm that the kinetic energy is dominated by inertial waves and generally much smaller than the kinetic energy trapped in the boundary layer, except in the case of boundary layer eruption, where wave excitation is most efficient. Inertial waves can also be excited resonantly so that total kinetic energy can sharply increase by an order of magnitude or more. The energy of the bulk flow excited, though, is too small to have a notable effect on the boundary layer which, in hindsight, justifies the strong assumptions made in chapter 5.

We move on to the case of lids plus outer cylinder libration and address the similarities and differences with respect to the wave excitation by corner beams and non-monotonic properties of the response spectra.

Energy response spectra for the case of lids and outer cylinder libration

Figure 6.3 shows the system response in terms of the filtered kinetic energy of the bulk $K_{1\omega}^{(5)}$ (filled red circles), the oscillating bottom lid boundary layer $K_{1\omega}^{(4)}$ (unfilled red circles) and the oscillating Stokes boundary layer, $K_{1\omega}^{(3)}$ (unfilled green diamonds) as functions of the forcing frequency ω. Also shown are laboratory measurements of Seelig (2014, p. 68) which have been plotted by unfilled black diamonds for an optical backscattering signal proportional to the light intensity I. All shaded frequency bands and grey dashed vertical lines are the same as in figure 6.2. The boundary layer resonance at $f_* = 0.2$ is no longer present here and the corresponding dotted vertical line has been removed in figure 6.3. The six short black lines along the upper ω-axis have been adjusted as well to indicate the spatial patterns shown in figure 4.13, in which the ray orbits are compared to numerical solutions. The dashed and dash-dotted scaling laws are based on the boundary layer theory and corner beam excitation, equations (6.1) and (6.4), but for different effective Coriolis parameters over the librating lid ($f_* = f = 2$) and librating outer cylinder ($f_* = 0$).

Assessment of the wave excitation mechanism. Figure 6.3 reveals that kinetic energy is mainly localised in the Stokes layer (thin green diamonds) for almost all frequencies in the inertial wave band, $0 < \omega < 2$. The velocities in the Stokes layer are of $O(1)$ over the librating outer cylinder, which means very large velocity amplitudes over $\approx 58\%$ of the annulus surface[2]. Integration and temporal averaging of the squared equation (5.10) yields

$$K_{1\omega}^{(3)}(\omega) \propto \delta_\mathrm{S} \int_0^{+\infty} \frac{\mathrm{e}^{-2\xi}}{2} \overline{\sin^2(\omega t - \xi)}\, \mathrm{d}\xi = \frac{\delta_\mathrm{S}}{8} \qquad \Rightarrow \qquad K_{1\omega}^{(3)}(\omega) = B_3 \delta_\mathrm{S}(\omega), \tag{6.5}$$

where the prefactor B_3 is obtained by a fit to DNS data. The frequency dependency according to equation (6.5) is in excellent agreement with the numerical solution down to libration frequencies of $\omega = 0.05$, but except for two strong resonances at $\omega = 0.87$ and 1.38 (to be discussed shortly). This indicates that the Stokes layer approximates the local dynamics very accurately, even when inertial waves are present and even when centrifugal instability occurs at low libration frequencies (for the viscous stability criterion of the Stokes layer see Sauret *et al.*, 2012). The most important point is that the spectral shape corresponding to the Stokes layer—an eruption at $\omega \to 0$—cannot be discerned in the bulk. This is in agreement with the corner beam excitation hypothesis (see section 5.3), that is, the Stokes layer lacks a wall-tangential mass flux directed to or from a corner. Hence, the kinetic energy spectra show that it is important *how* the fluid is perturbed if inertial waves shall be excited. In other words, it is not sufficient to prescribe just some sort of wall motion to force inertial waves.

We proceed by looking into the remaining spectra for the bulk and the (bottom) lid boundary layer. Using unprimed variables to distinguish the case of lids plus outer cylinder libration from the case of frustum libration (see chapter 5), one obtains the theoretical predictions for the other response spectra as

$$K_{1\omega}^{(4)} = B_4 \overline{\boldsymbol{Q}_\parallel^2}, \qquad K_{1\omega}^{(5)} = B_5 \overline{w_\mathrm{E}^2}, \qquad I_{1\omega}^{(5)} = B_\mathrm{lab} \left[\overline{w_\mathrm{E}^2}\right]^{1/2}, \tag{6.6}$$

[2]The annular confinement has a total surface area of $A_\mathrm{tot} = 107.7$ using the (scaled) dimensions of figure 3.4. Individual contributions amount to $A_1 = 23.7$ (frustum), $A_2 = 11.8$ (top lid), $A_3 = 62.8$ (outer cylinder), and $A_4 = 9.4$ (bottom lid).

where B_4, B_5 and B_{lab} are proportionality constants to be obtained by a fit to the simulated or measured data. The baselines of all spectra shown in figure 6.3 exhibit qualitative agreement with the boundary layer theory and corner beam excitation hypothesis. The argumentation is analogous to the frustum libration case above. The difference is that the libration frequencies in the inertial wave band are all smaller than the eruption frequency ($\omega = f = 2$). It follows from the discussion of the Ekman flux (see chapter 5) that there is always a wall-tangential mass flux component driven to or from a corner of the radial-axial section of the annulus. This explains why the kinetic energy in the bulk, $K_{1\omega}^{(5)}(\omega)$, has a qualitatively similar trend as the kinetic energy in the boundary layer over the lids, $K_{1\omega}^{(4)}(\omega)$. It is much clearer in figure 6.3 than it is in figure 6.2 that a constant value is approached for $\omega \to 0$. The frequency scaling laws (broken lines) reach a maximum at $\omega = f = 2$ due to the Ekman layer eruption over the librating lids.

It is interesting that the eruption frequency $\omega = 2$ does not correspond to a *global* maximum of the bulk kinetic energy as in the frustum libration case. This can be attributed to damping of higher order modes but also to geometry and deficiencies of the domain decomposition. That is, corner beams are emitted almost vertically for $\omega \to 2$, which means they are 'masked' from the bulk. Hence, the spectral drop of $K_{1\omega}^{(5)}$ occurs already at $\omega \approx 1.95$ rather than $\omega = 2$ precisely. Nevertheless, we can clearly see that the kinetic energy in the bulk is dominated by inertial waves since $K_{1\omega}^{(5)}$ drops to $\approx 5 \times 10^{-5}$ at $\omega = 2.5$ (not visible in the scaling of figure 6.3), say by a factor of 10^3. This is in fact similar to the frustum libration case discussed above.

It is worth to note that the measurements of Seelig (2014, p. 68) also exhibit the global trend predicted by boundary layer theory, but the data fluctuates heavily. Limitations of the measuring technique have been discussed already by Klein *et al.* (2014), who suggest to exclude the data points at $\omega = 1.0$, 0.5, 0.25 marked by short dotted lines from the upper axis. The reason is a breakdown of the filtering technique for the measurements performed from the laboratory frame of reference. That is, it is very likely that all sorts of spurious reflections are sampled so that they spoil the measurements in an unpredictable way. Also excluded from a fit is the measurement at $\omega = 2$ on the edge of the inertial wave band. Excluding these four measurements for good reasons leaves us with a very good but qualitative agreement between the measurements and the model for wave energy injection by corner beams.

It is quite remarkable that the very different system response in the lids plus outer cylinder libration case compared to the frustum libration case can be explained by the same wave excitation mechanism. Building a model for wave excitation from DNS alone would have been very difficult if not impossible. This shows the synergy effect in fundamental research obtained by a combination of DNS, laboratory experiments and theory. Equations (6.4) and (6.6) give the scaling laws of the flow dominated by inertial waves excited non-resonantly by wall libration. The prefactors A_i and B_i have been fitted here but could be estimated in principle if one would take into account the annulus geometry and an unknown coefficient for inertial wave excitation. This is not pursued further here, since the coefficients can be obtained directly from the volume-corrected A_i and B_i if one assumes that inertial wave excitation is universal. Instead, let us focus on the resonance conditions related to inertial waves in the remaining part of this thesis.

Non-monotonic properties of the response spectra. Figure 6.3 shows non-monotonic behaviour of the response spectra. This is most notable in the kinetic energy spectra $K_{1\omega}^{(i)}(\omega)$ rather than the measured backscattered light intensity $I_{1\omega}^{(5)}(\omega)$ and, in particular, for the normal mode resonances at $\omega = 0.87$ and 1.38. As noted for frustum libration case, laboratory measurements are sensitive to shear and emphasize the corner beams rather than the smooth

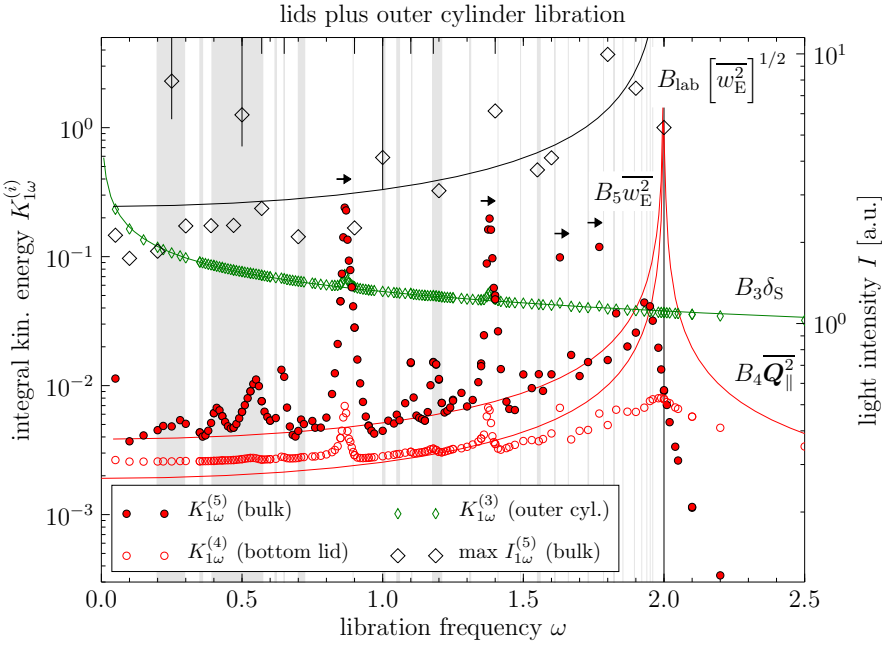

Figure 6.3: Response spectra for $R = 0.2$ and $E = 3.19\times10^{-5}$ with the lids and outer cylinder in libration. Filtered kinetic energies $K_{1\omega}^{(i)}$ are shown for the subdomains $i = 5$ (bulk), $i = 4$ (bottom lid boundary layer) and $i = 3$ (outer cylinder boundary layer) in comparison to laboratory measurements of Seelig (2014) for the backscattered light intensity $I_{1\omega}^{(5)}$ in arbitrary units. Shaded areas show a few low-order wave attractor frequency bands and the dashed grey lines some low-order neutral orbit frequencies obtained by ray tracing. Small solid lines on the upper ω-axis show the frequencies used in figure 4.12. Fitted proportionality constants read $B_3 \approx 6.7$, $B_4 \approx 240$, $B_5 \approx 242$, $B_{\mathrm{lab}} \approx 680$. (From M. Klein *et al.* (2014). 'Inertial wave excitation and focusing in a liquid bounded by a frustum and a cylinder'. *J. Fluid Mech.*, **751**, p. 283, figure 13, reproduced with permission. A different scaling and more of numerical data points are shown here.)

basin-scale oscillation patterns associated with normal modes (compare to Borcia *et al.*, 2014; Ghasemi V., 2016). Hence, normal mode resonances are not visible in the measurements. In the following, we will therefore limit our attention to the simulated kinetic energy spectra in the bulk, $K_{1\omega}^{(5)}(\omega)$, and over the bottom lid, $K_{1\omega}^{(4)}(\omega)$.

The baseline of the kinetic energy response spectrum $K_{1\omega}^{(5)}(\omega)$ in figure 6.3 varies over an order of magnitude across the inertial wave band, whereas it varies over three orders of magnitude in the frustum libration case (see figure 6.2). This leads to the impression that the resonances are stronger in the case of lids plus outer cylinder libration compared to the case of frustum libration, but this is not true. Looking at the strongest resonances in each configuration yields a relative increase of the kinetic energy in the bulk over the theoretical baseline by about 1–1.5 orders of magnitude, which means, factors 10–50. The baselines of the energy spectra correspond to the non-resonant response, which is related to the primary corner beams. In fact, the baselines predicted by the simple boundary layer theory describes the global frequency dependency quite well by connecting almost all local minima of the simulated kinetic energy spectrum $K_{1\omega}^{(5)}(\omega)$ for both configurations investigated.

It is interesting that in the case of lids plus outer cylinder libration normal mode resonances are dominant in $K_{1\omega}^{(5)}(\omega)$ (see figure 6.3), whereas in the case of frustum libration the LOWAs are dominant (see figure 6.2). In figure 6.3, normal mode resonance peaks are slightly shifted to the left from corresponding LONO frequencies (dashed vertical line at the tip of each small black arrow). The resonance frequencies obtained by DNS are $\omega \approx 0.87$, 1.38, 1.63 and 1.77 for an average frequency resolution of $\Delta\omega = 0.03$ comparable to the frustum libration case. The resolution has been reduced to $\Delta\omega = 0.01$ around notable resonance peaks at $\omega \approx 0.87$ and 1.38. The kinetic energy spectra shown in figure 6.3 are thus better resolved than those of Klein *et al.* (2014, figure 13) by factors 2–10. (Note that precisely the same parameters have been used here but that a different reference length has been selected, which affects the numerical values plotted.)

An immediate consequence of the refined frequency resolution is that the resonances at $\omega = 0.87$ and 1.38 are much better visible now. They are resolved by about 10–15 points here instead of 2–3 in Klein *et al.* (2014, figure 13). Also the resonances at $\omega = 1.63$ and 1.77 appear much stronger due to better overall resolution in figure 6.3, but they are not yet sufficiently resolved (only $\Delta\omega = 0.03$ has been realised until now).

We can see that all of the strong resonance peaks simulated are consistently left-shifted compared to ray tracing (as discussed above). Hence, we can conclude that Klein *et al.* (2014) used an insufficient frequency resolution that lead to the impression that resonance peaks where right-shifted with respect to the ray tracing prediction. This suggests that all normal mode resonances have similar properties, that is, (i) a normal mode resonance is narrow and (ii) wave energy can increase by an order of magnitude or more at resonance.

Wave attractors are also excited resonantly in the case of lids plus outer cylinder libration as can be seen in the $K_{1\omega}^{(5)}$ spectrum in figure 6.3. The corresponding peaks are located at $\omega \approx 0.41$, 0.56 0.65, 1.05 and 1.18. Strikingly though the resonances of the case of frustum libration at $\omega \approx 0.25$ and $\omega \approx 0.43$ have disappeared. Looking at the frequency band of the rhomboidal wave attractor, $0.39 \leqslant \sigma \leqslant 0.57$, an interesting substructure can be observed, which is qualitatively different from that in the case of frustum libration (see figure 6.2). In the case of lids plus outer cylinder libration corner beams are excited mainly at the two outer corners of a radial-axial section. This is the reason for the presence of two resonance peaks in the $(1, 1)$ wave attractor band. The two $(1, 1)$ wave attractor resonances correspond almost to the two limiting ray orbits. The flow patterns correspond approximately to the ray orbits shown figures 2.7(c, f). This means that the localisation of the corner beam excitation in combination with interference of the corner beams (see chapter 4) is responsible for the differences in the system response.

Note also the peak at $\omega = 0.05$ in the $K_{1\omega}^{(5)}$ spectrum in figure 6.3 which is not a resonance. The boundary layer flow has become centrifugally unstable and inertial waves are excited spontaneously by a non-linear mechanism (see Sauret *et al.*, 2013, 2012). It is the Stokes layer over the librating outer cylinder which has turned unstable. The developing instability is accompanied by spontaneous wave emission, which means kinetic energy conversion from the Stokes layer 'reservoir' into wave energy is enhanced by near-wall turbulence (for a detailed discussion of the local flow see Ghasemi V. *et al.*, 2016).

The kinetic energy spectra of the oscillating boundary layer over the lids, here in terms of $K_{1\omega}^{(4)}$ shown in figure 6.3, is described qualitatively by the idealised boundary layer theory (see equation (6.6)). DNS and theory are in good agreement, which is comparable to the frustum libration case (see figure 6.2). Even though the agreement between theoretical prediction and simulation seems worse compared to Klein *et al.* (2014, figure 13), the benefit of the present

theory is that it extends to all libration frequencies by fitting only the magnitude and not an additional offset for the low frequencies $0 < \omega < 2.5$. In both configurations studied, the kinetic energy of the Ekman flux is overestimated near the boundary layer eruption frequency so that a stronger spectral decay is expected than observed in the DNS. This hints at a deficiency of the idealised boundary layer theory, which indicates that details of the confinement and curvature need to be taken into account if improvement is envisioned. To which extend this is feasible analytically has to be left open to a future investigation. In the full non-linear Navier–Stokes equations, the boundary layer eruption will be regularised in any case, either by wall-tangential viscous or non-linear terms.

This concludes the study of the kinetic energy response spectra for the two configurations frustum libration and lids plus outer cylinder libration. In the next section we will compare both configurations more closely by looking into the wave excitation efficiency.

Wave excitation efficiency

The kinetic energy spectra discussed of the two configurations frustum libration and lids plus outer cylinder libration cannot be compared directly to each other. The difficulty arises from differences in the kinetic energy stored in the system and is an effect of the forcing mechanism rather than resonance. The objective is to correct for the different frequency dependencies of the boundary layer types contributing to wave excitation. A coefficient can be defined by the aid of the domain decomposition (see figure 6.1). The idea is to correct the wave energy in the bulk by the 'reservoir' at a particular libration frequency ω.

Here, wall-libration is prescribed, which means it serves as an infinite power source. The amount of energy the fluid-dynamical system can draw from the source over some time span is limited only by its internal dynamics. The forcing is bound to the wall motion, which means the boundary layer flow is responsible for the power uptake of the system. The kinetic energy in the boundary layer is therefore limited and can be considered as the actual 'reservoir' of kinetic energy that may or may not be converted into kinetic energy in the bulk[3].

Following Klein *et al.* (2014), we define the *wave excitation efficiency* as the ratio of the kinetic energy in the bulk, $K_{1\omega}^{\mathrm{bulk}}$, to the kinetic energy of the oscillating boundary layer, $K_{1\omega}^{\mathrm{BL}}$, namely

$$\frac{K_{1\omega}^{\mathrm{bulk}}}{K_{1\omega}^{\mathrm{BL}}} = K_{1\omega}^{(5)} \Bigg/ \sum_{i:\,\mathrm{osc.\ BL}} K_{1\omega}^{(i)} \,. \tag{6.7}$$

Frequency-filtering at the forcing frequency (index 1ω) ensures that only the dominating contributions with the time scale $2\pi/\omega$ are taken into account. An unavoidable systematic error is due to imperfections and non-uniqueness of the domain decomposition used. The wave excitation efficiency defined by equation (6.7) is levelled but not precisely normalised. Values larger than one are possible and depend on the dimensionless parameters R and E, the system properties like the power uptake or the dissipation in the boundary layer and the bulk, but also on the domain decomposition used. The systematic error introduced by the domain decomposition, however, affects both configurations in a similar way. At the very least we have obtained a quantity that allows us to compare objectively the frequency dependency of the wave field excited in different configurations.

Figure 6.4 shows the wave excitation efficiency $K_{1\omega}^{\mathrm{bulk}}/K_{1\omega}^{\mathrm{BL}}$ as function of the libration frequency ω comparing the case of frustum libration to the case of lids plus outer cylinder libration.

[3]The kinetic energy in the bulk is not limited to waves since, for example, mean flows can be driven also by a non-linear boundary layer flow (e.g. Busse, 2010).

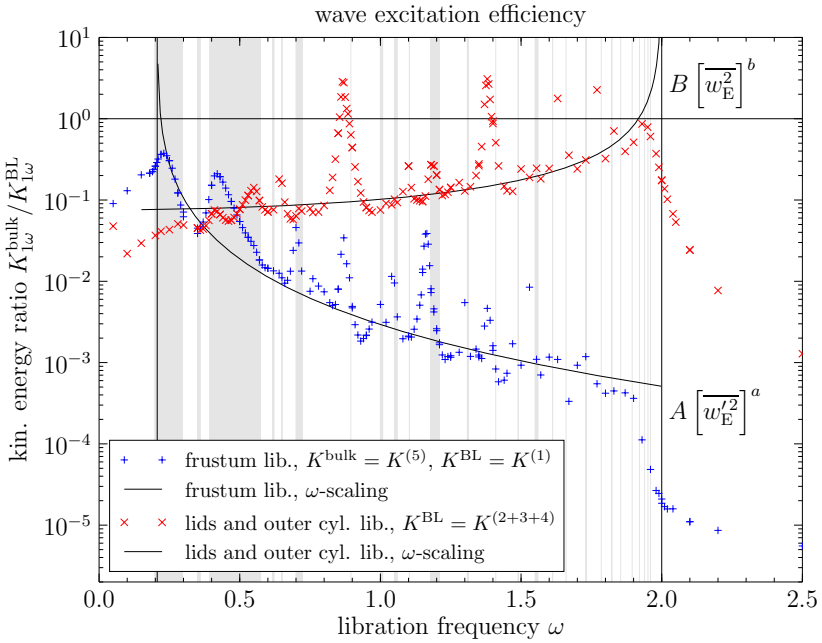

Figure 6.4: The wave excitation efficiency defined as the ratio of kinetic energies in the bulk and the oscillating boundary layer over librating wall segments, $K_{1\omega}^{\mathrm{bulk}}/K_{1\omega}^{\mathrm{BL}}$, for the two configurations investigated. The wave excitation efficiency has been computed from the kinetic energy spectra shown in figures 6.2 and 6.3. Scaling exponents (see table 6.1) have been obtained by a least-squares fit to the amplitude of the Ekman pumping velocities $w_{\mathrm{E}}'(\omega)$ and $w_{\mathrm{E}}(\omega)$ excluding notable resonance peaks. (From M. Klein *et al.* (2014). 'Inertial wave excitation and focusing in a liquid bounded by a frustum and a cylinder'. *J. Fluid Mech.*, **751**, p. 284, figure 14, reproduced with permission. The number of numerical data points has been extended.)

Table 6.1: Fit parameters for the wave excitation efficiency $K_{1\omega}^{\mathrm{bulk}}/K_{1\omega}^{\mathrm{BL}}$ shown in figure 6.4, but using different domain decompositions to show the robustness of the results. The domain decompositions are labelled by the tuple $(\Delta N_r, \Delta N_z)$, the number of grid cells trimmed from the bulk in radial and axial direction respectively. Notable resonance peaks have been excluded from the fit. The asterisk $(*)$ marks the domain decomposition used in figures 6.2–6.4.

	$(\Delta N_r, \Delta N_z)$	A $\times 10^3$	a	B $\times 10^3$	b
	$(12, 6)$	60.4	0.88	4.14	0.91
	$(24, 12)$	25.6	0.84	5.28	0.98
$*$	$(32, 16)$	16.0	0.82	6.20	1.03
	$(48, 24)$	5.60	0.79	7.22	1.11
	$(56, 48)$	3.04	0.77	4.84	1.12

The wave excitation efficiency shown has been computed from the kinetic energy spectra discussed in the previous sections (see figures 6.2 and 6.3). Frequencies of low-order neutral orbits (normal modes) and frequency bands of low-order wave attractors are given for orientation by grey dashed vertical lines and grey patches respectively. The black dotted vertical line at $\omega = 0.2$ marks the eruption frequency of the oscillating Ekman layer over the frustum, whereas the solid black line at $\omega = 2$ marks the eruption frequency of the oscillating Ekman layer over the lids and the wave band limit. A dotted horizontal line marks the value of $K_{1\omega}^{\mathrm{bulk}}/K_{1\omega}^{\mathrm{BL}} = 1$.

It is interesting that the non-resonant properties of the kinetic energy spectra are still visible in the excitation efficiency shown in figure 6.4. However, this is understandable from the corner beam excitation mechanism, that is, the wall-tangential mass flux in the radial-axial plane. That is, any oscillating Ekman layer has roughly constant kinetic energy far from its eruption frequency (see unfilled markers in figures 6.2 and 6.3). This suggests to fit $K_{1\omega}^{\mathrm{bulk}}/K_{1\omega}^{\mathrm{BL}}$ to the squared Ekman pumping velocity, say $A\big[\overline{w_{\mathrm{E}}'^2}\big]^a$ or $B\big[\overline{w_{\mathrm{E}}^2}\big]^b$ respectively. The parameters a and A apply to the case of frustum libration; the parameters b and B to the case of lids plus outer cylinder libration. Due to geometrical restrictions of the domain decomposition (see figure 6.1), the DNS data is fitted only over the interval $0.24 \leqslant \omega \leqslant 1.95$ excluding resonance peaks.

Table 6.1 collects the parameters obtained by a least-squares fit for different domain decompositions and both configurations, where the spectra shown in figures 6.2–6.4 correspond to the line marked with an asterisk ($*$). The prefactors A and B are not so important here because of the normalisation, though they are given here for the sake of completeness. The exponents a and b are more important here since they contain information about the relative change of the bulk and boundary layer kinetic energies. On the one hand, a scaling exponent larger than or close to one ($a, b \gtrsim 1$) would mean that the bulk kinetic energy scales differently than the boundary layer. In the case of librational forcing, for example, this would be the case when there is notable kinetic energy trapped in the boundary layer that cannot be converted into wave energy. On the other hand, a scaling exponent much smaller than one ($a, b \ll 1$) would mean that the bulk and boundary layer kinetic energies are strongly correlated and a constant fraction of the kinetic energy available would be converted into wave energy.

The exponents a and b are both close to one, as one would expect from the linear theory developed in section 5.3 and resonances neglected. However, on average $a \approx 0.82 < 1$, whereas $b \approx 1.03$. It is interesting that a falls with an increasing boundary layer extent while b increases, which indicates that the scaling exponents depend on the domain decomposition. The essential difference between the case of frustum libration (exponent a) and the case of lids plus outer cylinder libration (exponent b) is that a has been obtained for frequencies $\omega > f_* = 0.2$ and b for frequencies $\omega < f_* = 2$. The increasing trend of b in table 6.1 is probably related to the Stokes layer and its entirely different frequency dependency compared to the bulk.

The observation $a < 1 \leqslant b$ suggests that kinetic energy of the boundary layer is converted into wave energy a bit more efficiently in the case of frustum libration than in the case of lids plus outer cylinder libration. However, the kinetic energy has generally larger magnitudes in the lids plus outer cylinder libration case which overshadows any such small modification of the scaling exponents. So, if we would have selected an outer sloping wall and a straight inner wall we would see the dominance of the lid libration in the waves excited. Supposedly, additional resonance peak might appear due to a modification of the boundary layer currents that surge the corner flow. At the very least one additional peak can be expected in this hypothetical scenario which is due to the boundary layer eruption when the critical slope is met.

A remark on the domain decompositions (see figure 6.1) seems to be in order. Inspection of the kinetic energy spectra for different decompositions (not shown here) suggests that only

domain decompositions $(\Delta N_r, \Delta N_z) = (32, 16)$–$(52, 28)$ are acceptable. Decompositions with a larger boundary layer domain suffer from a too small bulk portion (bad wave capture by the bulk), whereas a smaller boundary layer domain attributes boundary layer flow to the bulk (wave energy notably spoiled by the boundary layer kinetic energy). It is in particular the value of the kinetic energy in the bulk $K^{\text{bulk}} = K^{(5)}$ that is affected the most by a change of the domain decomposition and so is the ratio $K_{1\omega}^{\text{bulk}}/K_{1\omega}^{\text{BL}}$. In principle, error bars could be computed (as in Sauret *et al.*, 2012, figure 17) but figure 6.4 would become very difficult to read. Since only the qualitative properties and the scaling exponents have been of interest in this section, there is no harm in omitting the error bars given the robustness according to table 6.1.

In summary, the following general observations regarding the wave excitation efficiency can be made. First, non-resonant wave excitation by libration is most efficient when the libration frequency is smaller than the effective Coriolis parameter ($\omega < f_*$), because the boundary layer current has a strong component directed toward the corner. This is because Coriolis force has enough time to establish an Ekman boundary layer structure (see section 5.2). Second, non-resonant wave excitation by libration reaches its maximum at the boundary layer eruption frequency which is identical to the effective Coriolis parameter ($\omega \approx f_*$). Third, libration frequencies $\omega > f_*$ in the inertial wave band yield a slightly larger energy conversion efficiency than libration frequencies $\omega < f_*$, but kinetic energy magnitudes suffer from the strong spectral decay that overshadows any gain in the conversion efficiency. The decrease of the kinetic energy is due to the primary flow in the oscillating boundary layer. The latter approaches a Stokes layer in the limit of $\omega \gg f_*$ since the Coriolis force has no time to affect the flow, which is dragged along the wall and damped down by viscosity. Hence, the boundary layer current in the direction of the corners decreases with the libration frequency (see section 5.2) and so does wave excitation efficiency. Fourth, resonance leads to a sharp increase of the wave excitation efficiency, typically between 0.5–1.5 orders of magnitude.

The fundamental difference between a wave attractor resonance and a normal mode (standing wave) resonance is the phase relation. That is, in the case of a standing wave resonance, two propagating waves interfere constructively with each other by propagating along the same axis in *opposite* directions. In the case of a wave attractor resonance, two waves still appear to interfere constructively only but they propagate in the *same* direction. It is due to focusing that one wave propagates slower than the other and due to viscous broadening that finally a stationary propagation speed is reached on the wave attractor.

The common ground between a wave attractor resonance and a standing wave resonance is that a constructive interference mechanism is at work which requires a fixed phase relation. It is interesting that the properties of inertial waves actually allow both types of resonance, the 'classical' standing wave resonance and the 'propagating wave' resonance in the case of wave attractors where it is the confinement geometry and the forcing mechanism decide which of them is more efficient. The implication is, that inertial waves provide a resonance mechanism not only in regularly shaped confinements but also in very irregular confinement geometries. Here, in the librating annulus, both modes and wave attractors exist, and the librational forcing imposes a frequency and a symmetry. As it turns out, the frustum libration has more pronounced wave attractor resonances than normal mode resonances, whereas lids plus outer cylinder libration exhibits more pronounced normal mode resonances. This is only because wave attractors cannot be excited as efficiently as in the frustum libration case.

In the next section we will extend the investigation of kinetic energy response spectra to the contributions at the harmonics of the forcing frequency. This will provide us with insight to the frequency dependency of non-linear inertial waves.

6.2 Kinetic energy at harmonics of the forcing frequency

The harmonics 2ω and 3ω have been discussed in section 4.4 for a few selected libration frequencies. The excitation due to non-linearity has been addressed and we concluded that non-linear inertial waves are always driven by libration because the Rossby number R must be larger than zero. The local spectra shown in section 4.4 confirmed that the non-dimensional parameters $R = 0.2$ and $E = 3.19 \times 10^{-5}$ yield a weakly non-linear flow, whose variability is dominated by the libration frequency ω and the low-order harmonics 2ω and 3ω.

The objective of this section is to complete the discussion with respect to the leading-order non-linear waves with frequencies 2ω and 3ω. In the previous sections of this chapter the linear system response has been studied by computing spectra $K^{(i)}_{1\omega}(\omega)$ in the subdomains i. The same method is used in the following by computing the spectra $K^{(i)}_{2\omega}(\omega)$ and $K^{(i)}_{3\omega}(\omega)$ according to equation (6.2). To the best of my knowledge, there is no theory that could describe the weakly non-linear system response for wave attractors inertial waves in general. Therefore, the DNS and the linear theory will be brought together in order to check for possible interactions responsible for non-linear wave excitation.

Energy response spectra for the case of frustum libration

Figures 6.5(a, b) show the kinetic energy response spectra $K^{(i)}_{2\omega}(\omega)$ and $K^{(i)}_{3\omega}(\omega)$ over the libration frequency ω. Both figures supplement the $K^{(i)}_{1\omega}(\omega)$ spectrum (see figure 6.2), which means the same configuration has been used: wave excitation by frustum libration, Rossby number $R = 0.2$, Ekman number $E = 3.19 \times 10^{-5}$, and unchanged domain decomposition.

The bifurcation diagram (figure 2.9) has been included again in figures 6.5(a, b) giving the low-order wave attractor (LOWA) frequency bands by grey patches and low-order neutral orbit (LONO) frequencies by dashed grey lines. This serves to remind us of resonances of the primary flow at frequency ω. The Ekman layer eruption frequency $f_* = 0.2$ is marked by a dotted black vertical line. There are three essential differences in figures 6.5(a, b) compared to the spectra shown in figure 6.2.

First, the kinetic energies have been scaled with $R^{-2(l-1)}$ to correct for the amplitude according to weakly non-linear theory so that $\max K^{(i)}_{l\omega}$ will be approximately of the order one.

Second, the effective wave band limit $\sigma_{\mathrm{c},l}$ is given by a dash-dotted vertical line and reads

$$\sigma_{\mathrm{c},l} = \frac{2}{l} \qquad \text{since} \quad 0 < l\omega < f = 2. \tag{6.8}$$

The steep drops at $\omega = 1$ in figure 6.5(a) and $\omega = 0.67$ in figure 6.5(b) for the bulk kinetic energies $K^{(5)}_{2\omega}$ and $K^{(5)}_{3\omega}$ respectively indicate that the bulk kinetic energy is dominated by inertial waves as well.

Third, the frequency dependencies of non-resonantly excited waves are shown by thick solid lines for the bulk and thick dashed lines for the boundary layer are motivated on qualitative arguments and have been fitted to the simulated energy spectra. These will be discussed further in the following after an interlude on the interaction mechanisms.

Weakly non-linear theory suggests that the primary flow at the frequency ω needs to interact with itself in order to generate harmonics 2ω, 3ω and higher. The boundary layer flow possesses the largest velocity amplitudes and reaches order one. The primary wave field, which is oscillating with the forcing frequency ω, has at least a factor 10 smaller velocity amplitudes (see chapter 4). Hence, a hierarchy of velocity amplitudes is established for the flow compon-

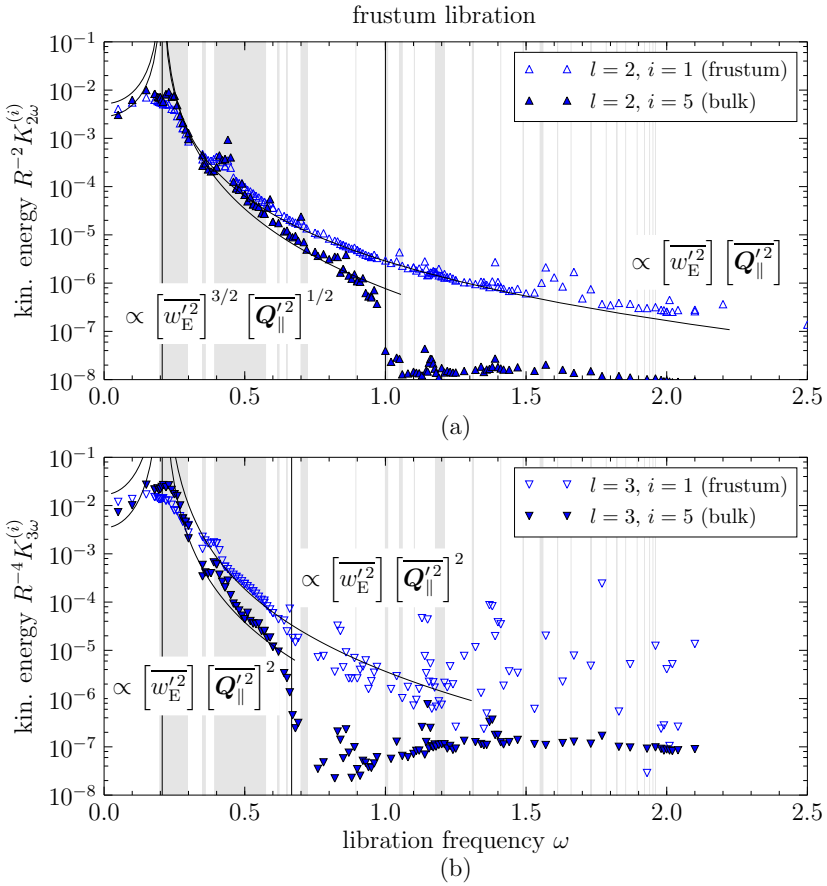

Figure 6.5: Kinetic energy response spectra at the harmonics 2ω and 3ω of the forcing frequency ω for the case of frustum libration supplementing figure 6.2 ($R = 0.2$, $E = 3.19 \times 10^{-5}$). Panel (a) shows the response spectra $K^{(i)}_{2\omega}$, whereas panel (b) shows the response spectra $K^{(i)}_{3\omega}$. The simplified bifurcation diagram at frequency ω is given for orientation by grey lines and patches. A dotted vertical line marks the boundary layer eruption frequency. A dash-dotted vertical line marks the wave band limit for each harmonic.

ents oscillating with harmonics frequencies $l\omega$ in which each frequency $l\omega$ has a dominating contribution due to the interaction of two flow features at lower frequencies $l'\omega$ and $l''\omega$, where $l = l' + l''$ and $l', l'' < l$.

The open question is, which interaction mechanisms are possible for an inertial wave field and an oscillating boundary layer? The conservation of kinetic energy is ensured by the frequency condition $l = l' + l''$ so that the momentum equation (Navier–Stokes equations) will decide which interactions of inertial waves and boundary layer are possible. Unfortunately, non-linear inertial waves are not yet very well understood. Instead, some recent work has been done with respect to internal gravity waves (e.g. Gerkema, 2006; Gostiaux *et al.*, 2006; Ogilvie, 2005; Tabaei *et al.*, 2005). For the moment, let us assume that inertial waves exhibit equivalent interactions as internal gravity waves[4]. The frequency dependencies postulated in that way are then to be checked against DNS results.

Table 6.2 collects potential interaction mechanisms that might excite the 2ω- and 3ω-harmonics. The mechanisms are ordered in such a way that the kinetic energy decreases for the case of a strong boundary layer flow and a weaker wave field in the bulk. The results of chapter 4 suggest that (i) higher harmonic wave beams can be excited directly by an instability of the corner flow (see sections 4.4 and 5.1) and (ii) inertial waves can return to the oscillating boundary layer, where large velocity amplitudes and gradients might allow non-linear interactions (e.g. Gerkema, 2006; Gostiaux *et al.*, 2006; Peacock & Tabaei, 2005; Tabaei *et al.*, 2005). Other options for higher-harmonic generation might be (iii) wave-wave interactions, either due to a crossing wave beams (e.g. analogous to Tabaei *et al.*, 2005) or (iv) a self-interaction of inertial waves (as counterpart to mean flow excitation, see Ghasemi V., 2016; Tilgner, 2007).

Note with respect to (i) that the corner flow causes a non-linearity in the boundary layer by a correlation of wall-normal and wall-parallel velocity components (Reynolds stresses). The details of the dynamics, though, are intricate (see section 5.1). The correlations are taken into account schematically by considering products of the amplitudes of the Ekman pumping velocity w'_{E} (wall-normal) and the Ekman flux $\boldsymbol{Q}'_{\parallel}$ (wall-parallel). For the harmonic 3ω it is difficult to confirm or reject a particular interaction mechanism at the present state. However, making use of the hierarchy with respect to velocity magnitudes the guess has been to take the correlation of the 2ω flow and the Ekman flux $\boldsymbol{Q}'_{\parallel}$, which corresponds to the largest velocity magnitudes.

Note further that the argumentation can be extended to the oscillating Ekman layer, where the correlation of wall-parallel (zonal) and wall-normal (radial) velocity components yields non-zero correlations (compare to Ghasemi V. *et al.*, 2016). The difference is that kinetic energy will in general remain trapped in the boundary layer.

Let us come back to the energy spectra shown in figures 6.5(a, b). The boundary layer energy shown in figure 6.5(b) suffers from noise at libration frequencies $\omega \gtrsim 0.8$ and forbids further interpretation. This is less dramatic in figure 6.5(a), but frequencies $\omega > 1.5$ are also subject to non-monotonic behaviour. We are primarily interested in inertial waves, so that we restrict our attention to the (effective) inertial wave band, $\omega < \sigma_{\mathrm{c},l}$. All kinetic energy spectra shown decay to the left and right of the boundary layer eruption frequency $\omega = f_* = 0.2$. They encompass seven orders of magnitude instead of six in figure 6.2. The spectra shown in figures 6.5(a, b) are also much smoother in the effective inertial wave band than those of the primary flow (see figure 6.2) which suggests that resonances have little effect on the harmonics.

[4]This is an *ad hoc* assumption, but roots in the fact that the wave equations of internal gravity waves and inertial waves are very similar. This has been used recently by Seelig (2014, pp. 73) to treat the interaction of an inertial wave and a mean flow analogous to the case of internal gravity waves.

Table 6.2: Possible interaction mechanisms responsible for the non-linear system response in the kinetic energy spectra $K_{l\omega}^{\mathrm{bulk}}(\omega)$ and $K_{l\omega}^{\mathrm{BL}}(\omega)$ for the harmonics $l = 2, 3$. It is assumed that the primary flow is composed of boundary layer and wave beams (corner beams). The primary flow oscillates with the forcing frequency ω. Weakly non-linear theory yields harmonics $l\omega$ to have kinetic energy of the order $R^{2(l-1)}$ times an unknown frequency dependency. The superscripts $\perp$ and $\parallel$ address the wall-parallel and wall-normal velocity components of the boundary layer flow (BL), whereas $(\perp, \parallel)$ denotes a geometric average of wall-normal and wall-parallel velocity components. An asterisk $(*)$ is used when there are several possibilities and a dash (—) when the candidate mechanism does not apply at the present location.

harm.	mechanism	location	scaling $K_{l\omega}^{\mathrm{bulk}}(\omega)$	scaling $K_{l\omega}^{\mathrm{BL}}(\omega)$
$l=2$	$\mathrm{BL}_{1\omega}^{\perp}$-$\mathrm{BL}_{1\omega}^{\parallel}$	osc. Ekman BL	$*$	$\left[\overline{w_{\mathrm{E}}'^2}\right]\left[\overline{\boldsymbol{Q}_{\parallel}'^2}\right]$
	$\mathrm{BL}_{1\omega}^{\perp}$-$\mathrm{BL}_{1\omega}^{(\perp,\parallel)}$	corner flow	$\left[\overline{w_{\mathrm{E}}'^2}\right]^{3/2}\left[\overline{\boldsymbol{Q}_{\parallel}'^2}\right]^{1/2}$	$\left[\overline{w_{\mathrm{E}}'^2}\right]^{3/2}\left[\overline{\boldsymbol{Q}_{\parallel}'^2}\right]^{1/2}$
	$\mathrm{wave}_{1\omega}$-$\mathrm{BL}_{1\omega}^{(\perp,\parallel)}$	reflection	$\left[\overline{w_{\mathrm{E}}'^2}\right]^{3/2}\left[\overline{\boldsymbol{Q}_{\parallel}'^2}\right]^{1/2}$	$*$
	$\mathrm{wave}_{1\omega}$-$\mathrm{wave}_{1\omega}$	bulk	$\left[\overline{w_{\mathrm{E}}'^2}\right]^{2}$	—
$l=3$	$\mathrm{BL}_{1\omega}^{\perp}$-$\mathrm{BL}_{1\omega}^{\parallel}$-$\mathrm{BL}_{1\omega}^{\parallel}$	osc. Ekman BL	$*$	$\left[\overline{w_{\mathrm{E}}'^2}\right]\left[\overline{\boldsymbol{Q}_{\parallel}'^2}\right]^{2}$
	$\mathrm{BL}_{1\omega}^{\parallel}$-$\mathrm{BL}_{1\omega}^{(\perp,\parallel)}$-$\mathrm{BL}_{1\omega}^{(\perp,\parallel)}$	corner flow	$\left[\overline{w_{\mathrm{E}}'^2}\right]\left[\overline{\boldsymbol{Q}_{\parallel}'^2}\right]^{2}$	$\left[\overline{w_{\mathrm{E}}'^2}\right]\left[\overline{\boldsymbol{Q}_{\parallel}'^2}\right]^{2}$
	$\mathrm{wave}_{1\omega}$-$\mathrm{BL}_{1\omega}^{?}$-$\mathrm{BL}_{1\omega}^{?}$	reflection	$*$	$*$
	$\mathrm{wave}_{1\omega}$-$\mathrm{BL}_{2\omega}$	reflection	$\left[\overline{w_{\mathrm{E}}'^2}\right]^{2}\left[\overline{\boldsymbol{Q}_{\parallel}'^2}\right]$	$*$
	$\mathrm{wave}_{2\omega}$-$\mathrm{BL}_{1\omega}^{(\perp,\parallel)}$	reflection	$\left[\overline{w_{\mathrm{E}}'^2}\right]^{5/2}\left[\overline{\boldsymbol{Q}_{\parallel}'^2}\right]^{1/2}$	$*$
	$\mathrm{wave}_{1\omega}$-$\mathrm{wave}_{1\omega}$-$\mathrm{wave}_{1\omega}$	bulk	$\left[\overline{w_{\mathrm{E}}'^2}\right]^{3}$	—
	$\mathrm{wave}_{2\omega}$-$\mathrm{wave}_{1\omega}$	bulk	$\left[\overline{w_{\mathrm{E}}'^2}\right]^{3}$	—

An exception to this is the $(1,1)$ wave attractor band, which exhibits a small but distinct peak at $\omega = 0.44$ in figure 6.5(a) and another one at shifted frequency $\omega = 0.42$ in figure 6.5(b). These peaks correspond to $2\omega \approx 0.88$ (a) and $3\omega = 1.26$ (b) respectively. This suggests excitation of the $(1,2,0)$ mode for $2\omega = 0.88$ and excitation of the $(2,7)$ wave attractor for $3\omega = 1.26 \approx 1.3$. So, it seems that the interaction frequency is able to express itself when it coincides with another LOWA or LONO (normal mode), which is what we called 'spatial coupling' earlier.

Regarding the global frequency dependencies of $K_{l\omega}^{(5)}(\omega)$ and $K_{l\omega}^{(1)}(\omega)$ in figures 6.5(a, b), it is remarkable how well the spectra are actually described by the rudimentary weakly non-linear theory outlined above. Thick solid and dashed lines show the frequency dependencies corresponding to the best fit among the possible scaling laws listed in table 6.2.

One observes that $K_{l\omega}^{(1)}$ in the oscillating Ekman layer seems to be governed by an interaction of wall-parallel and wall-normal velocity components. The latter is denoted $\mathrm{BL}_{1\omega}^{\perp}$-$\mathrm{BL}_{1\omega}^{\parallel}$ and $\mathrm{BL}_{1\omega}^{\perp}$-$\mathrm{BL}_{1\omega}^{\parallel}$-$\mathrm{BL}_{1\omega}^{\parallel}$ in table 6.2.

On the basis of the DNS results discussed in sections 4.4 and 5.1, the kinetic energy spectra $K_{l\omega}^{(5)}$ in the bulk should be dominated by higher harmonics originating from the corner flow. The corner flow, as we have discussed already, is slightly unstable for the parameters selected and implies mixing of momentum. Mixing can be taken into account qualitatively by computing a velocity scale $U_{(\perp,\parallel)}$ by the geometric average

$$U_{(\perp,\parallel)} := \delta_{\mathrm{BL}}^{-1/2} \sqrt{\left[\overline{w_{\mathrm{E}}'^2}\right]^{1/2} \left[\overline{\boldsymbol{Q}_{\parallel}'^2}\right]^{1/2}} \tag{6.9}$$

of the squared amplitudes of the wall-normal Ekman pumping velocity w_{E}' and the wall-parallel Ekman flux $\boldsymbol{Q}_{\parallel}'$ corrected by the boundary layer thickness δ_{BL}. In the kinetic energy spectra, only powers of $U_{(\perp,\parallel)}^2$ can appear. Assuming that the turbulent patch has approximately constant size and is larger than the viscous boundary layer thickness (see section 5.1), one has the simpler form

$$U_{(\perp,\parallel)}^2 \propto \left[\overline{w_{\mathrm{E}}'^2}\right]^{1/2} \left[\overline{\boldsymbol{Q}_{\parallel}'^2}\right]^{1/2}. \tag{6.10}$$

Thus, the superscript $(\perp,\parallel)$ used in table 6.2 indicates when the geometric average has been used, e.g., in terms of equation (6.10).

The frequency dependency induced by the corner flow has now been expressed in terms of the primary flow given by the oscillating Ekman layer. Even if a wave–boundary-layer interaction would yield a similar frequency dependency (see table 6.2), the boundary layer flow would dominate the kinetic energy spectra due to its larger amplitudes. Figures 6.5(a, b) show that the higher harmonic energy spectra $K_{l\omega}^{(5)}$ of the bulk are indeed described by the frequency dependencies corresponding to the proposed corner flow mechanisms denoted $\mathrm{BL}_{1\omega}^{\perp}$-$\mathrm{BL}_{1\omega}^{(\perp,\parallel)}$ and $\mathrm{BL}_{1\omega}^{\parallel}$-$\mathrm{BL}_{1\omega}^{(\perp,\parallel)}$-$\mathrm{BL}_{1\omega}^{(\perp,\parallel)}$ $\parallel$ according to table 6.2.

In summary, it needs to be emphasized that the qualitative arguments might give the correct frequency dependencies for the wrong reasons since a solid physical basis is still missing. At the very least, though, we have obtained a parametrisation of the higher-harmonic system response for the non-resonantly excited inertial waves. The system response is governed by non-linearity in the boundary layer, which excites non-linear inertial waves. The proposed parametrisation therefore relates the frequency dependency of the non-linear waves to the primary flow given by an oscillating Ekman layer over the librating wall. This is a substantial reduction of complexity.

It is beyond the scope of this work to develop the weakly non-linear theory further with respect to inertial waves. Instead, we proceed by evaluating the validity of the proposed frequency dependencies in the lids plus outer cylinder libration case.

Energy response spectra for the case of lids and outer cylinder libration

Figures 6.6(a, b) show the kinetic energy response spectra $K_{2\omega}^{(i)}(\omega)$ and $K_{3\omega}^{(i)}(\omega)$ for the case of lids plus outer cylinder libration. The subdomains selected correspond to the bulk ($i = 5$), the oscillating Ekman layer over the bottom lid ($i = 4$), and the Stokes layer over the outer cylinder ($i = 3$). The dimensionless parameters were fixed at $R = 0.2$ and $E = 3.19 \times 10^{-5}$, and the standard domain decomposition was used (figure 6.1). The higher-harmonic energy spectra supplement the system response at the forcing frequency ω (see figure 6.3) and have been corrected to orders $R^{2(l-1)}$ ($l = 2, 3$) of the Rossby number R. Otherwise, the layout of figures 6.6(a, b) is similar to the frustum libration case (see figures 6.5(a, b)). The grey shaded areas and dashed grey vertical lines mark the LOWA frequency bands and LONO frequencies obtained by ray tracing giving the reference spectrum of the primary flow for orientation. A dotted vertical line marks the Ekman layer eruption frequency $\omega = f = 2$, a dash-dotted vertical line the effective wave band limit $\sigma_{\mathrm{c},l}$ according to equation (6.8).

The energy spectra for the lids plus outer cylinder libration case (figure 6.6) are more complex than those for the frustum libration case (figure 6.5), which indicates that there are different phenomena contributing to the flow.

We begin with an evaluation of the frequency dependencies of the spectra $K_{l\omega}^{(5)}(\omega)$ in the bulk and $K_{l\omega}^{(4)}(\omega)$ over the lid. The argumentation of the frustum libration case can be applied straightforwardly to the lids plus outer cylinder libration case similar to the corner beam excitation discussed in section 5.3 and we only need to take into account the lid's Ekman layer eruption frequency $\omega = f = 2$. The interaction mechanisms and, hence, the frequency dependencies given in table 6.2 should not change, but primed variables (w'_{E}, $\boldsymbol{Q}'_{\parallel}$) need to replaced by unprimed ones (w_{E}, $\boldsymbol{Q}_{\parallel}$) in accord with the notation of chapter 5. The frequency dependency providing the best fit of the simulated spectra $K_{2\omega}^{(5)}$ and $K_{3\omega}^{(5)}$ in $0.1 < \omega < \sigma_{\mathrm{c},l}$ is given by a thick solid line. (The resonance peak at $\omega \approx 0.9$ has been excluded.)

It turns out that the scaling law describing the energy response spectra in the bulk are those associated with the corner flow mechanism. This is remarkable, since the proposed frequency dependencies have been derived in full analogy to the frustum libration case implying a generality of the underlying dynamics. By contrast, one fails to fit the Ekman layer spectra $K_{l\omega}^{(4)}$ on the grounds of the mechanisms listed in table 6.2. All of the proposed frequency dependencies suggest a single global maximum at the eruption frequency $\omega = 2$, whereas the simulated spectra exhibit a global maximum at $\omega = \sigma_{\mathrm{c},l}$. This is puzzling since the effective wave band limit $\sigma_{\mathrm{c},l}$ should be relevant only for inertial waves. It seems as if the non-linearity in the oscillating Ekman layer over the lid is dominated by the waves which impinge on the boundary layer. The reason for the qualitatively different behaviour seems to be the effective Coriolis force, which is by a factor 10 stronger in the boundary layer over the lid than it is over the frustum. Hence, non-linearity is suppressed in the oscillating Ekman layer over the lid for the parameters selected.

Furthermore, the spectra $K_{l\omega}^{(5)}(\omega)$ in the bulk and $K_{l\omega}^{(4)}(\omega)$ shown in figures 6.6(a, b) exhibit notable non-monotonic behaviour in the form of resonance peaks which is in contrast to the frustum libration case. The strongest resonances occur for primary flow features $(1, 1)$ wave attractor at $\omega = 0.52$, $(1, 2, 0)$ normal mode at $\omega = 0.87$, $(1, 3)$ wave attractor at $\omega = 1.18$,

$(1,4,0)$ normal mode at $\omega = 1.38$, $(1,6,0)$ normal mode at $\omega = 1.63$, and $(1,8,0)$ normal mode at $\omega = 1.76$. Only the harmonics 2ω and 3ω of the $(1,1)$ wave attractor and the first harmonic of the $(1,2,0)$ normal mode resonance lie in the inertial wave band ('free modes'), whereas other harmonics have frequencies larger than 2 and, thus, correspond to 'bound modes' (see section 4.2). Regardless of whether the harmonic are free modes or a bound modes, resonant excitation at the forcing frequency ω is mostly accompanied by resonant excitation of the non-linear modes. However, there are a few exceptions, for example, the 3ω-harmonic does not possess a peak at $\omega = 1.18$ and 1.63 in contrast to the 2ω-harmonic. This is a very interesting property since a wave attractor and a normal mode resonance are affected. One might be able to answer the question by computing the viscous non-linear eigenmode and complex eigenvalues (frequencies), which is a task beyond the scope of this work.

The low frequency band $0 < \omega < 0.25$ yields comparably large energies for all the spectra shown in figures 6.6(a, b), but in particular for the Stokes layer, $K^{(3)}_{l\omega}(\omega)$. A sharp drop by about an order of magnitude can be observed around $\omega = 0.2$, which indicates onset of centrifugal instability of the Stokes layer (as mentioned in section 4.4; for a detailed discussion see Ghasemi V. *et al.*, 2016; Sauret *et al.*, 2012). That is, the flow near the librating outer cylinder becomes turbulent and the frequency spectrum broadens significantly so that several frequencies $l\omega$ are notably non-zero. Inertial waves are excited spontaneously by the near wall turbulence (Sauret *et al.*, 2013) due to which all energy spectra are modified. Here, the near-wall turbulence dominates the non-linear the system response only at low libration frequencies $\omega \lesssim 0.2$, which has not been in the focus of this study. In hindsight, the selection of the non-dimensional parameters $R = 0.2$ and $E = 3.19 \times 10^{-5}$ is justified also for study of non-linear inertial waves.

In conclusion, the system response is dominated by linear and non-linear inertial waves for the non-dimensional parameters $R = 0.2$ and $E = 3.19 \times 10^{-5}$. Investigating two different configurations, frustum libration and lids plus outer cylinder libration, the frequency dependencies obtained by DNS suggest that non-linear waves are dominantly driven by a non-linearity in the boundary layer which is localised in the corners. Hence, the corner flow is responsible for both linear and non-linear wave excitation. An extension of the linear theory to a weakly non-linear theory by qualitative arguments allowed parametrise the kinetic energy of the non-resonantly excited waves by the oscillating Ekman layer solution. The core assumption is weak non-linearity in the sense that the Rossby number is small ($R \ll 1$) and that the boundary layer flow is of larger amplitude than the wave field excited due to which energy of low frequencies can only deplete into higher frequencies and there is no feedback. The rudimentary theory needs to be tested further and to be put on a more solid foundation, which is seen for instance in the fact that the non-linear response of the oscillating Ekman layer over the librating lid is not correctly described.

In the next section, we will consider the system response with respect to the quality factor. This will remove the non-uniqueness of results following from the selected domain decomposition.

6.3 Quality factor

All previous analyses regarding the spectra relied on the domain decomposition (figure 6.1). The problem of that approach is its non-uniqueness, which means only the scaling exponents can be compared for a fixed set of parameters. Hence there are difficulties arising when simulation results obtained at different resolutions, at different Rossby or Ekman numbers, or by different

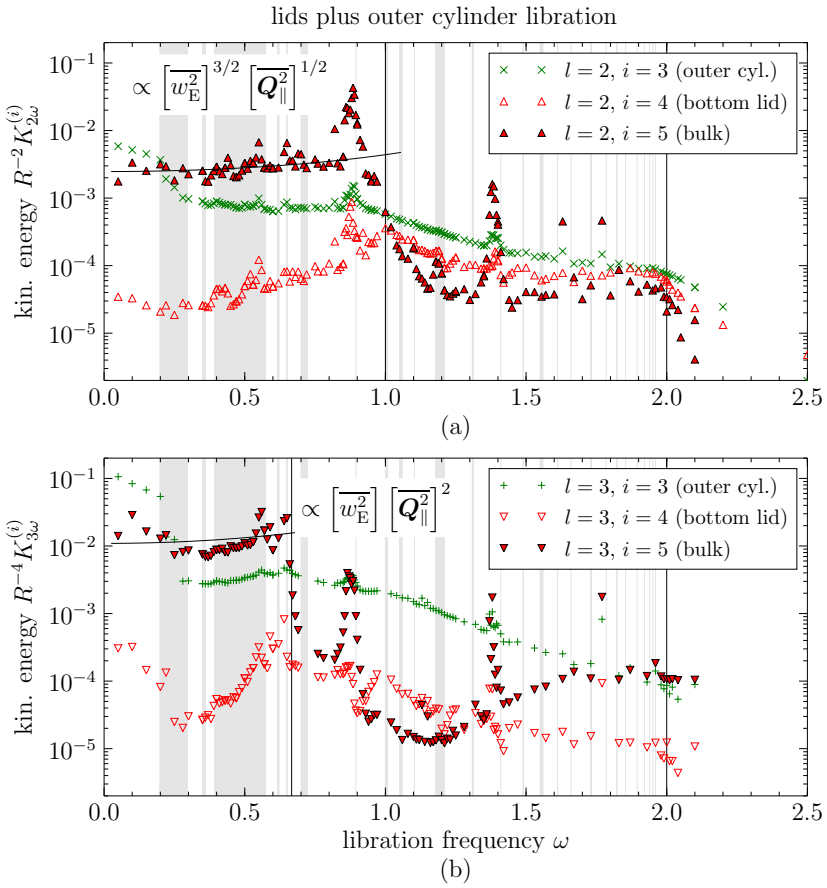

Figure 6.6: Kinetic energy response spectra at the harmonics 2ω and 3ω of the forcing frequency ω for the case of lids plus outer cylinder libration supplementing figure 6.3 ($R = 0.2$, $E = 3.19 \times 10^{-5}$). Panel (a) shows the response spectra $K_{2\omega}^{(i)}$, whereas panel (b) shows the response spectra $K_{3\omega}^{(i)}$. The simplified bifurcation diagram at frequency ω is given for orientation by grey lines and patches. A dotted vertical line marks the boundary layer eruption frequency. A dash-dotted vertical line marks the wave band limit for each harmonic.

numerical solvers are to be compared to each other. This is the motivation to define an integral quantity exhibiting the resonances, but which takes into account the whole fluid volume. The *quality factor* or simply Q *factor* fulfils the requirement by being uniquely defined as we will see shortly.

The Q factor is commonly used in oscillator theory (e.g. Jaworski & Detlaf, 1972, pp. 113–144, 473), but it has also been applied in the astrophysical context (e.g. Ogilvie & Lin, 2004, and references therein). Following this route of thought, the librating annulus (figure 1.3) is considered as a parametric resonator of presently unknown properties, one says, it has an unknown characteristic. Here, DNS is used to sample the characteristic by varying the forcing frequency. Each data points is obtained from the statistically stationary state due to continuous librational forcing (see equation (1.2)) by the frustum or the lids together with the outer cylinder. The procedure is analogous to the energy spectra discussed above, which means the libration frequency is only allowed to change quasi-stationary. Ogilvie & Lin (2004) discuss that the characteristic of such a fluid dynamical resonator results from the energy uptake and the energy dissipation and is, thus, the result of intricate internal dynamics. That study illustrates that it is feasible to compute the Q factor of a fluid dynamical system numerically. In principle, it seems possible to measure the Q factor in a laboratory experiment, though I am unaware of any such attempts.

The Q factor is a non-dimensional coefficient given by the power ratio

$$Q := \frac{\omega \bar{K}}{\bar{D}}, \tag{6.11}$$

in which ω is the libration frequency, $\bar{K}$ is the time-averaged total kinetic energy, $\bar{D}$ is the time-averaged dissipation rate. The Q factor weights the energy stored in the dynamical system with the amount of energy passing through the system per reference period in the statistically stationary state. Stationary statistics imply that the average flux of energy passing through the system is transformed completely into heat[5], where effects of heating are neglected in the present model (see chapter 2).

The reference period due to libration is $T_{\mathrm{lib}} = 2\pi\omega^{-1}$. Hence, the bar $\overline{(\cdot)}$ denotes an average over several integer libration periods MT_{lib} with $M \gtrsim 10$. The time-averaged total kinetic energy $\bar{K}$ is thus computed straightforwardly by equation (6.2). Similarly, the time-averaged dissipation rate $\bar{D}$ results from a temporal average of equation (3.74), say

$$\bar{D} = \int_V \bar{\Phi} \, \mathrm{d}V \tag{6.12}$$

with the dissipation function Φ according to equation (3.73).

[5]In the statistically stationary state, the energy flux through the system is given by the dissipation rate $\bar{D}$ or the power uptake $\bar{P}$ since the kinetic energy $\bar{K}$ is constant. For impermeable walls, $\boldsymbol{n} \cdot \boldsymbol{v} = 0$ (velocity $\boldsymbol{v}$, surface normal $\boldsymbol{n}$), the kinetic energy equation (e.g. Batchelor, 1967, pp. 151–153) reduces to

$$0 = \frac{\overline{\mathrm{d}K}}{\mathrm{d}t} = -\bar{D} + \bar{P} = -\int_V \bar{\Phi} \, \mathrm{d}V + \oint_{\partial V} \overline{(\boldsymbol{v} \cdot \boldsymbol{\tau})} \cdot \boldsymbol{n} \, \mathrm{d}S$$

with $\mathrm{d}S$ the area element, $\bar{\phi}$ the time-averaged dissipation function, $\boldsymbol{\tau}$ the strain rate tensor. The volume integral is more accurately computed by the present numerical scheme due to staggering (see chapter 3). The surface integral, however, has been used by Klein *et al.* (2014, appendix D) for an estimation by accounting only for the idealised oscillating boundary layer.

The trade-off in using the Q factor instead of the domain decomposition is that the dissipation rate D needs to be computed accurately. This is more demanding than the kinetic energy since precise velocity gradients are required. This implies that the wave attractor and the boundary layer have to be highly-resolved. Here this is ensured for the parameters $R = 0.2$, $E = 3.19 \times 10^{-5}$ according to the considerations on the resolution requirements in chapter 3 and the wave attractors shown in chapter 4.

The Q factor can be extended also to frequency-filtered fields. Let us recall the effect of weak non-linearity for $R \ll 1$ as discussed in sections 4.4 and 6.2. As we have seen already, the flow variability is localised at a few harmonics $l\omega$ ($l = 1, 2, \ldots$) of the forcing frequency and to orders R^l in the velocities relative to the laboratory frame of reference. The velocity field seen from the co-rotating frame of reference has the decomposition

$$\boldsymbol{v} = R^1 \boldsymbol{v}_{0\omega} + \sum_{l=1}^{\infty} \mathrm{Re}\left(R^{l-1} \boldsymbol{v}_{l\omega} \mathrm{e}^{\mathrm{i}l\omega t}\right), \tag{6.13}$$

which yields for the time-averaged kinetic energy density

$$\overline{v^2} = R^2 v_{0\omega}^2 + \frac{1}{2} \sum_{l=1}^{\infty} R^{2l-2} \left|\boldsymbol{v}_{l\omega}\right|^2. \tag{6.14}$$

Mixed terms vanish under the temporal average so that there is a hierarchy in the contributions to v^2 to orders R^{2l-2}. The 0ω-term corresponds to the mean flow and has kinetic energy of leading order $O\left(R^2\right)$. The mean flow exhibits complex dynamics, which is beyond the scope of this work. Further details on the matter can be found in Seelig (2014, laboratory experiments) and Ghasemi V. (2016, DNS).

The strain rate tensor $\boldsymbol{\tau}$ and the time-averaged dissipation function $\bar{\Phi}$ can be decomposed to orders of R^l analogous to equations (6.13) and (6.14) respectively. Hence, the Q factor definition given by equation (6.11) has the extension

$$Q_{l\omega} := \frac{l\omega K_{l\omega}}{D_{l\omega}} \qquad \text{for} \quad l = 1, 2, \ldots . \tag{6.15}$$

Q factor at the forcing frequency

Figure 6.7(a) shows the standard and filtered Q factor as supplement to the kinetic energy spectra and the wave excitation efficiency (section 6.1). The figure layout is similar to the kinetic energy spectra, that is, the ordinate is in logarithmic scale and low-order wave attractors (LOWAs) and neutral orbits (LONOs) obtained by ray tracing (see section 2.4) are indicated by grey patches and lines respectively. The boundary layer eruptions at $\omega = 0.2$ over the librating frustum and $\omega = 2$ over the librating lid are indicated by dotted vertical lines. The frequency limit for propagating inertial waves is at $\omega = 2$. The first aspect to note regarding the data is that the difference between Q and $Q_{1\omega}$ is smaller than the variability due to ω-variation. This reflects once again the dominance of the forcing frequency in the variability of the flow. It is therefore sufficient to consider only the spectrum for Q.

Note that the dotted horizontal line marks the value $Q_\mathrm{c} = 1/2$. $Q_\mathrm{c} = 1/2$ is the critical resonator quality of a classical (harmonic) oscillator. If we take the latter as an approximation to the fluid dynamical resonator, the value $Q = Q_\mathrm{c}$ corresponds to the aperiodic limit. Hence, $Q > Q_\mathrm{c}$ ($Q < Q_\mathrm{c}$) means the resonator is under-damped (over-damped) and there are (no) free oscillations of the system.

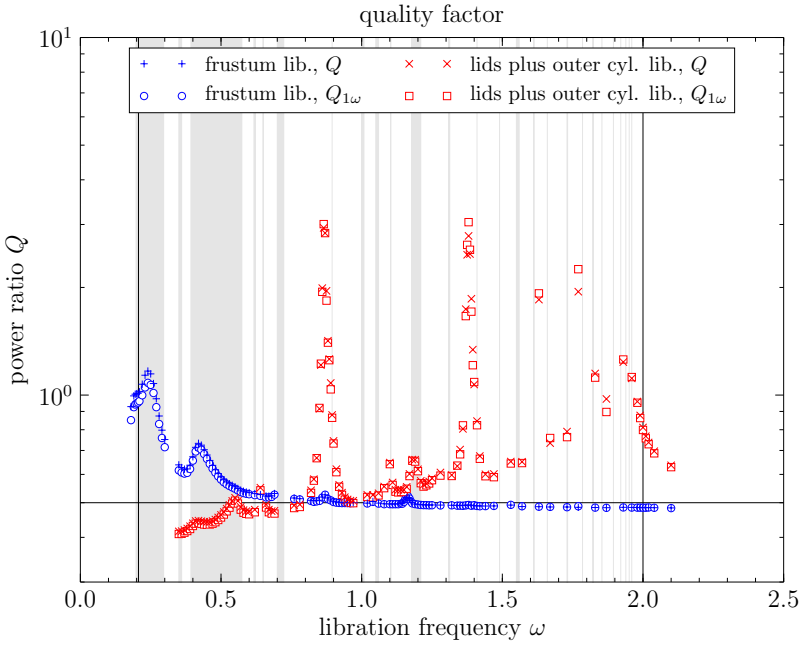

(a)

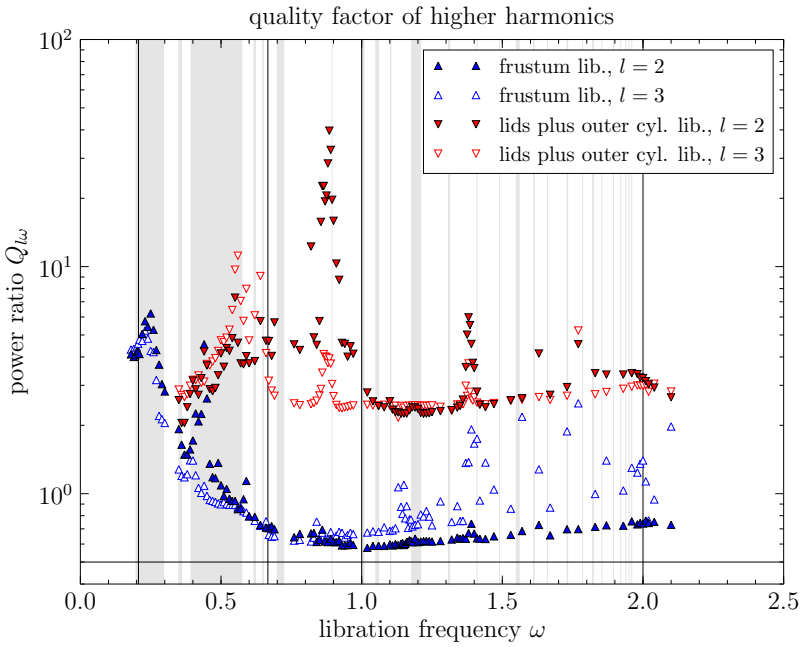

(b)

Figure 6.7: Quality factor of the annulus for the frustum and lids together with the outer cylinder in libration. Panel (a) compares the unfiltered Q and the filtered $Q_{1\omega}$. Panel (b) shows the factors $Q_{l\omega}$ of the higher harmonics $l = 2, 3$. The simplified bifurcation diagram at frequency ω is given for orientation by broken grey lines and patches. Dotted vertical lines marks the boundary layer eruption frequencies $\omega = 0.2$ (frustum) and $\omega = 2$ (lid). Solid and dash-dotted vertical lines mark the wave band limits $l\omega = 2$ for the harmonics 2ω and 3ω respectively. Fixed parameters are $R = 0.2$, $E = 3.19 \times 10^{-5}$.

In the librating annulus, $Q > Q_c$ is due to boundary layer eruptions and due to resonant excitation of (inertial) waves. Similar to the kinetic energy spectra, the boundary layer eruption affects not only a single frequency but the whole frequency spectrum and leads to a broad peak, say the global trend discussed extensively for the kinetic energy spectra. The explanation based on the boundary layer theory (see section 6.1 and chapter 5) explains also the global properties of the Q factor spectra but, as before, there are resonance peaks beyond the simple theory.

Resonances occur when LOWAs or modes (LONOs) are excited so that the Q factor increases suddenly upon variation of the forcing frequency. In figure 6.7(a) this is most notable for the modes $(2,1,0)$, $(4,1,0)$, $(6,1,0)$ and $(8,1,0)$ at $\omega = 0.88,\ 1.38,\ 1.63,\ 1.77$ excited by the librating lids and outer cylinder, as well as the $(1,1)$ LOWA at $\omega \approx 0.42$ and the $(2,1)$ LOWA at $\omega \approx 0.25$ excited by the librating frustum. The mode resonances yield an order-of-magnitude-jump in the Q factor values and are therefore much stronger than the LOWA resonances. This can be understood by computing integral values.

Modes correspond to oscillatory circulation cells on the system scale (figure 4.10), whereas wave attractors exhibit a localisation of the kinetic energy along thin shear layers (figure 4.4). Hence, the fluid mass in motion and thus integral kinetic energy is much larger in the case of a low-order mode than it is in the case of a low-order wave attractor. For the dissipation rate, however, shear is the important quantity which is potentially larger for the wave attractors. Hence, in the case of a wave attractor the numerator (denominator) in equation (6.11) is typically smaller (larger) than in the case of a mode which both lead to the expectation of smaller Q factor values associated with the wave attractor than with the mode. Hence, energy conversion (into heat) should be more efficient when a wave attractor is excited (e.g. Ogilvie, 2005; Ogilvie & Lin, 2004). We will discuss this further in section 6.4 by comparing resonance peaks of a mode and a wave attractor.

Note that $Q \simeq Q_c$ is approached when inertial wave excitation is weak and the libration frequency is far from the boundary layer eruption frequency, that is, $|\omega - f_*| \gg 1$. This is seen best for the frustum libration case for $\omega \gtrsim 1$. It is interesting that Q does not approach $Q = Q_c$, but keeps decreasing slowly, which means the system becomes critical at first and drifts to an slightly over-damped state as the boundary layer thickness keeps decreasing. This indicates that energy injection also by non-linear processes (like the non-linearity in the oscillating Ekman layers, e.g., Busse, 2011; Sauret & Le Dizès, 2013) reduces further. Dissipation is thus more and more localised at the librating wall. It is interesting that for the case of lids plus outer cylinder libration and $\omega \to 0$ values $Q < Q_c$ are reached. This happens in the inertial wave band, so even if wave excitation efficiency is weak, the drop to an over-damped state might be explained by destructive interference of the inertial waves emitted from the corners in a radial-axial section (for the related discussion see chapter 4).

Q factor at harmonics of the forcing frequency

Figure 6.7(b) shows the quality factors $Q_{l\omega}$ for the lth harmonic at $l = 2$ (filled markers) and $l = 3$ (unfilled markers) supplementing the kinetic energy spectra of section 6.2. The layout is similar to figure 6.7(a) where only the effective wave band limits $\omega = 2/l$ (see equation (6.8)) have been added by a solid and dash-dotted vertical line respectively.

For the frustum in libration and $\omega < 2/l$, both $Q_{2\omega}$ and $Q_{3\omega}$ in figure 6.7(b) are qualitatively similar to Q in figure 6.7(a). The frequency dependency is dominated by the scaling of the boundary layer eruption, that is, the non-resonantly excited corner beams. The LOWA 'resonances' at $\omega = 0.25$ and $\omega = 0.42$ of figure 6.7(a) are *not* visible in figure 6.7(b). Hence, the increase of $Q_{l\omega}$ for the libration frequency approaching the boundary layer eruption frequency

reflects the increased non-linearity of the corner flow due to a maximisation of the Ekman pumping and the Ekman flux (see figures 5.11 and 5.12). Hence, a maximisation of the wave excitation efficiency (see figure 6.4).

For the frustum in libration and $\omega > 2/l$, both $Q_{2\omega}$ and $Q_{3\omega}$ in figure 6.7(b) are qualitatively different to Q in figure 6.7(a). That is, the resonator remains under-damped and there is substantial scatter in the data points for $Q_{3\omega}$ for $\omega \gtrsim 1.3$ indicating that the numerical accuracy limit has been reached for the kinetic energy and dissipation rate oscillating with 3ω. However, with $Q_{2\omega}$ reaching its minimum at $Q \approx 0.6 > Q_\mathrm{c}$ indicates that the higher harmonics are under-damped in the corresponding time interval which is the integer fraction T_lib/l of the libration period T_lib. The interpretation is that the frequency ω has no internal sources and is injected by the boundary condition. By contrast, frequencies $l\omega$ for $l > 1$ have sources anywhere in the domain. If $l\omega > 2$, the non-linear modes excited cannot propagate which means they are bound to the spatial structures of the driving frequencies[6]. Here this is primarily the flow structures of the $(l = 1)$-component. Shear and dissipation rates are thus reduced (see the discussion in chapter 4) so that $Q_{l\omega} > Q_\mathrm{c}$ for $l > 1$.

For the lids and outer cylinder in libration the argumentation works out very similar to the frustum libration case. The quality factors $Q_{2\omega}$ and $Q_{3\omega}$ shown in figure 6.7(b) are almost indistinguishable from another for frequencies $\omega < 0.5$ and $\omega > 1$. Differences are notable only in the frequency band $0.5 \leqslant \omega \leqslant 1$, where $2\omega < 2$ corresponds to free modes but $3\omega > 2$ to bound modes. That is, the $(2, 1, 0)$ mode resonance at $\omega = 0.88$ yields a much stronger response in the 2ω component than in the 3ω component since kinetic energy can be redistributed by 2ω waves but not by the 3ω waves. This leads to different distribution of the kinetic energy of the 2ω waves than for the ω and 3ω waves. In this scenario, it is assumed that the dissipation rate remains almost constant for the harmonics.

Note further that $Q_{2\omega}$ and $Q_{3\omega}$ are by about a factor 5 larger in the lids plus outer cylinder libration case compared to the frustum libration case. This hints at a more efficient excitation of non-linear inertial modes by the lid libration Interestingly, the spectral shapes of both quality factors are otherwise similar for libration frequencies $\omega > 1$ and the two configurations investigated. The reason is unclear at present. Suitable mechanisms might be related to additional excitation by wave–wave interactions of corner beams (the 2ω component related to the mean flow mechanism described by Seelig, 2014, pp. 74–77) or even the boundary layer since the Ekman flux has a stronger radial component for $\omega < f_*$ than for $\omega > f_*$ (see figure 5.12).

In conclusion, computation of the Q factor response spectra allowed us to gather additional information about the wave excitation efficiency by removing the ambiguity of the domain decomposition but at the expense that there is no theory from which the frequency scaling laws could be inferred. For the case of weak non-linearity ($R \ll 1$), the 'traditional' Q factor computed from time-averaged quantities is only marginally different from the coefficient $Q_{1\omega}$ computed from frequency-filtered quantities (figure 6.7(a)).

Both Q and $Q_{1\omega}$ exhibit qualitatively similar properties as the wave excitation efficiency (figure 6.4). The Q factor, however, is normalised and linked to resonator theory which allows to interpret the values directly. We have seen that $Q > Q_\mathrm{c} = 1/2$ corresponds to an under-damped system obtained when waves are strongly excited. That is, in the case of boundary layer eruption and in the case of resonance. Resonance leads to small peaks in the Q factor spectra, which are stronger when normal modes are excited than in the case of wave attractors.

[6]Strictly speaking, 'bound modes' are not necessarily restricted to frequencies outside the inertial wave band, but that is where they are most relevant in the present study.

In addition, the quality factors $Q_{2\omega}$ and $Q_{3\omega}$ for the higher harmonics have been computed and exhibit an interesting property of being under-damped ($Q > Q_c$). This is by a factor 5 stronger in the case of lids and outer cylinder libration than in the case of frustum libration. The reasons is unclear and potentially related to higher harmonic generation is spread over the fluid volume for ω in the inertial wave band. In the next and last section of this chapter we will look at the system response across a resonance peak by using various quantities, including the Q factor, in order to investigate the differences when a normal mode or a wave attractor is excited.

6.4 Properties of a resonance: wave attractor *versus* normal mode

The aim of this section is to investigate the properties of the fluid-dynamical system in the case of resonance. Two types of resonances have been addressed in the previous sections: the 'classical resonances' associated with normal modes (in analogy to the considerations in Greenspan, 1969) and the wave attractor resonances.

First, in the case of a normal mode resonance, one is faced with the excitation of smooth basin-scale oscillation patterns. Corresponding linear solutions are obtained by neglecting viscosity (e.g. Greenspan, 1969). It is exceptional that the annular confinement (figure 1.3) exhibits such normal modes (see Borcia & Harlander, 2012). In the weakly viscous and non-linear setting it is assumed that the linear solution is a good approximation even for finite Rossby numbers. For librational forcing, the Rossby number R is proportional to the libration amplitude ε. Hence, for any practical situation, the limit of $R \to 0$ or $\varepsilon \to 0$ can never be realised and there is basically *no* justification for the linear wave concept. (The non-linear nature of inertial waves is not just an artefact of librational forcing; see, for example, Kerswell (1999) and Ghasemi V. (2016).) The implication is that resonance has to be extended to the excitation of viscous, non-linear waves.

Second, in the case of a wave attractor resonance the situation is worse compared to a normal mode since it is not clear what the resonance mechanism is. The usual argumentation is that small viscosity regularises singularities but leaves the basin-scale structures unaffected (see chapter 4). So, when a wave attractor exists, a corresponding *viscous* mode is found to exhibit a similar pattern of shear layers (see section 2.4 and, e.g., Harlander & Maas, 2007; Rieutord & Valdettaro, 1997). When the flow is also (weakly) non-linear, it is commonly assumed that non-linear modes exist whose structures can be approximated by the spectrum of linear waves. The non-linear waves are also independent of the boundary condition since a boundary layer will adjust the free-stream solution to the proper boundary condition.

Kinetic energy K, dissipation rate D and the Q factor were introduced above as measures for the flow activity, the energy conversion into heat and the ratio of energy stored *versus* energy dissipated respectively. Inertial waves are helical (see chapters 2.3, 4 and 5) and only recently helicity has in fact received an increasing attention in the rotating flow community (e.g. Albrecht *et al.*, 2015; Lopez & Marques, 2014, 2015). Here helicity is addressed as diagnostic quantity that supplements the discussion of resonance. The total helicity is defined as

$$H := \int_V \boldsymbol{v} \cdot \boldsymbol{\zeta} \, \mathrm{d}V \qquad \text{with} \quad \boldsymbol{\zeta} \equiv \boldsymbol{\nabla} \times \boldsymbol{v}, \tag{6.16}$$

which is quadratic in the velocity magnitude but also contains phase information so that it can take positive and negative values. The filtered helicity $H_{l\omega}$ is computed analogous to $K_{l\omega}$ from the filtered velocity components $\hat{v}_{r,l\omega}$, $\hat{v}_{\phi,l\omega}$, $\hat{v}_{z,l\omega}$ (see appendix A.3).

Helicity is not just interesting from a diagnostic point of view. It has been shown that helicity is a conserved quantity in inviscid flows and thus just as constituting to the flow evolution as the kinetic energy[7](Névir, 1998; Névir & Blender, 1993; Névir & Sommer, 2009). Here we are faced with a viscous (dissipative) flow, which means neither kinetic energy nor helicity are strictly conserved. The bulk of fluid may be viewed as *almost inviscid*, though , since viscous forces are localised in the boundary layers. In the dissipative system, however, sources of the kinetic energy and the helicity are the oscillating boundary layers and the corner flow (see chapter 5) which means inertial wave excitation is crucial for a redistribution of both quantities in geophysically relevant weakly non-linear flows.

In order to elucidate the resonance conditions highly-resolved spectra of the total kinetic energy K, the total dissipation rate D, the Q factor and the total helicity H have been computed for the rotating annulus with wall libration. In the following, a wave attractor resonance excited by frustum libration and a normal mode resonance excited by lids plus outer cylinder libration is considered for default parameter values $R = 0.2$, $E = 3.19 \times 10^{-5}$. It is also assumed that the results obtained for low-order wave attractors and modes are general in the sense that they apply also to higher-order spatial patterns and to other configurations.

Wave attractor resonance excited by frustum libration

Figures 6.8(a–d) show the system response in terms of the four variables K, D, H and Q by varying the libration frequency ω across the frequency band of the $(1,1)$ wave attractor (figure 2.7). The LOWA frequency band is shown by a grey shaded area over $[0.393, 0.574]$. The frequency resolution is $\Delta\omega = 0.01$. In each figure shows different sets of data points corresponding to the time-averaged or filtered quantities. The temporal averages are denoted $\bar{K}$, $\bar{D}$, $\bar{H}$ and Q (without the bar according due to the definition (6.11)) and marked by pluses (+). The analogous frequency-filtered at $l\omega$ and time-averaged quantities are denoted $K_{l\omega}$, $D_{l\omega}$, $H_{l\omega}$ and $Q_{l\omega}$ (see appendix A.3). The nomenclature is thus analogous to the previous sections. The differences are that the whole fluid volume is used for the analyses and that the Rossby number correction R^{2l-2} according to weakly non-linear theory is implied for $l \geqslant 2$. The computation of averages and the filtering has been performed over 32 libration periods in the statistically stationary state.

Time-averaged quantities compared to the contribution of the forcing frequency. The temporal averages are marked by pluses (+) in figures 6.8(a–d), whereas the quantities filtered at the forcing frequency ω ($l = 1$) are marked by unfilled circles ($\circ$). It is easy to see that the respective data points have almost the same values, which means the component oscillating with the forcing frequency dominates the dynamics. Hence it is sufficient to consider only the temporal averages. The wave attractor resonance occurs at $\omega \approx 0.42$ and is notable for $\bar{K}$, $\bar{H}$ and Q by a local maximum.

[7] A 3-D, incompressible, inviscid flow (which is approximately the case for the bulk flow of the annular cavity) evolves due to the vorticity equation

$$\frac{\partial \boldsymbol{\zeta}_\mathrm{a}}{\partial t} = (\boldsymbol{\zeta}_\mathrm{a} \cdot \boldsymbol{\nabla})\, \boldsymbol{v} - (\boldsymbol{v} \cdot \boldsymbol{\nabla})\, \boldsymbol{\zeta}_\mathrm{a} \qquad \text{with} \quad \boldsymbol{\zeta}_\mathrm{a} \equiv \boldsymbol{\zeta} + f\boldsymbol{e}_z.$$

Névir & Blender (1993) show that the total kinetic energy K and helicity H are conserved. In turn, the functionals $K[\boldsymbol{\zeta}]$ and $H[\boldsymbol{\zeta}]$ can be use to formulate a bracket algebra from which the equations of motion can be derived. The bracket algebra generalises the Hamiltonian dynamics and the Poisson bracket to the so-called Nambu dynamics and the Nambu bracket (Nambu, 1973).

There are global trends in the response spectra of $\bar{K}$ and $\bar{D}$ (figures 6.8(a, b)). While the spectrum of $\bar{K}$ exhibits a small peak, that of $\bar{D}$ does not. In the spectrum of Q the global trend is largely compensated and values $Q > Q_c = 1/2$ (dotted line) indicate an effect of the wave attractor on the system dynamics. However, for the selected non-dimensional parameters the dissipation rate is due to the oscillating Ekman layer and practically unaffected by the wave attractor. Considering the dissipation rate and internal heating, the present configuration is obviously boundary layer-dominated. This suggests that the integral quantities do not specifically provide information about the waves or the boundary layer alone, but merely on feedback of the waves on the boundary layer. This completes the picture of the previous analyses (chapters 5 and 6) in which the two regions have been discussed separately.

It is interesting in this regard that the resonance is strongest in the helicity $\bar{H}$. The helicity exhibits an asymmetric peak of positive sign. Remember that the sign of helicity and the direction of inertial wave propagation are correlated (section 2.3) by means of positive helicity being related to downward (in $-z$-direction) propagating waves and *vice versa*. The simulated helicity response spectrum seems a bit odd in this respect. That is, inertial waves are mainly excited at the bottom inner corner of the annular confinement (see, for example, figure 4.1) and upward propagating waves of negative helicity dominate the interior (figure 4.2).

It can be shown that the idealised frustum boundary layer (section 5.2) exhibits negative helicity toward the bulk for ω larger than the boundary layer eruption frequency $f_* = 0.2$ (though large positive values occur in the viscous layer in proximity to the wall). In analogy to $\bar{K}$, $\bar{D}$ and Q also $\bar{H}$ is certainly dominated by the boundary layer modified by the interior solution. Inertial waves excited return to the source, the librating frustum wall and the corners in particular (see chapter 4). The focusing reflection at the frustum causes a spatial compression and generates various wave numbers all belonging to the forcing frequency. Even in a completely linear setting ($R \to 0$) one is thus faced with a complicated flow structure emerging near the librating frustum wall that demands matching of at least two helical waves (incident and reflected) and the helical boundary layer flow.

To make the argumentation from above a bit clearer, figures 6.9(a, b) show the local modification of the helicity density in proximity to the frustum due to an incident wave beam. On the one hand, precisely at the resonance in panel (a) and, on the other hand, for an off-resonant situation in panel (b). In figure 6.9(b) the rhomboidal $(1, 1)$ wave attractor is excited with the libration frequency $\omega = 0.47$. Only the lower inner part of the radial-axial section is shown for a fairly wide range of contour levels so that the waves are no longer visible (compare to figure 4.2). Therefore, the wave attractor path is given by a solid black line for orientation. With the aid of the inertial ray path only a weak shade of the focused wave beam can be discerned originating from the focusing reflection at $(r, z) \approx (0.8, 2.3)$. In accord with downward wave propagation it has positive helicity. The reflection modifies the boundary layer so that it has positive helicity throughout around the reflection point. Otherwise, the unperturbed oscillating Ekman layer has mainly negative helicity toward the bulk in agreement with boundary layer theory.

Figure 6.9(a) shows the $(1, 1)$ wave attractor excited by the resonant libration frequency $\omega = 0.42$. The wave attractor is still rhomboidal but elongated as predicted by ray tracing (see figure 2.10). The reflection point has moved to $(r, z) \approx (0.9, 0.8)$, which is closer to the wave source at the bottom inner corner A. One can observe that in comparison to panel (b) the volume exhibiting positive helicity has increased in vertical and also radial direction. An investigation of the raw data reveals that the helicity values at the reflection point reach 2 in panel (a) but only 1 in panel (b). This indicates stronger interaction of the wave beam with its source in the case of resonance shown in figure 6.9(a).

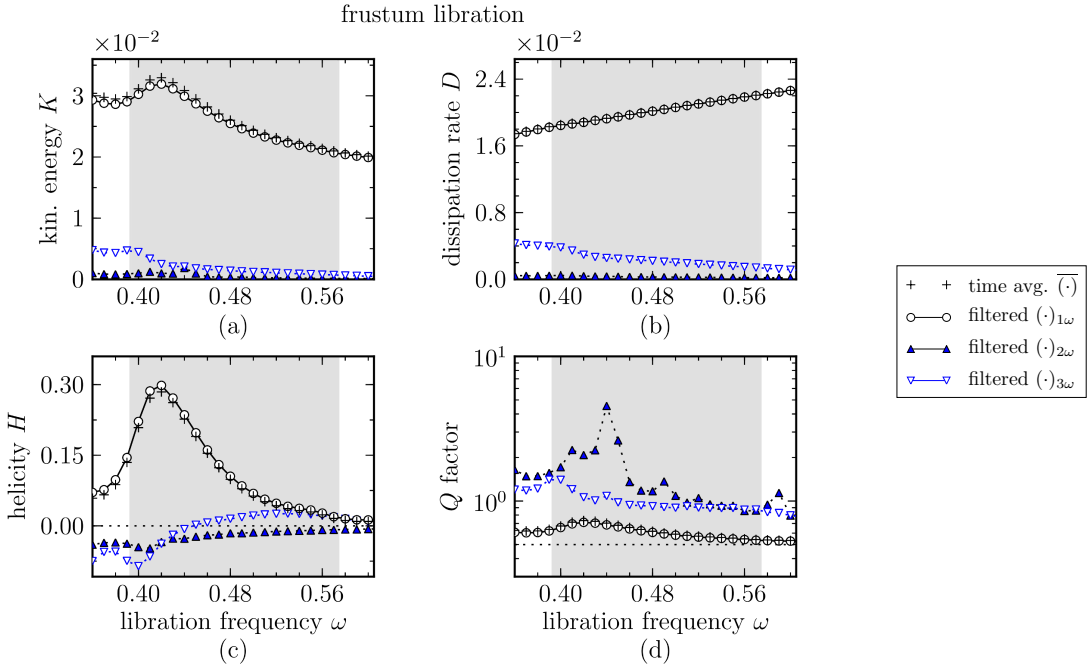

Figure 6.8: High-resolution response spectra for the case of frustum libration and libration frequencies ω covering the $(1,1)$ wave attractor interval shown by a grey shading. All quantities shown have been integrated over the whole annulus volume. Time-averages $\overline{(\cdot)}$ and frequency-filtered values $(\cdot)_{l\omega}$ have ben obtained over a time interval of 32 libration periods in the statistically stationary state. Auxiliary horizontal lines are given for $H = 0$ in panel (c) and $Q_\mathrm{c} = 1/2$ in panel (d). Default non-dimensional parameters have been used $\left(R = 0.2,\ E = 3.19 \times 10^{-5}\right)$.

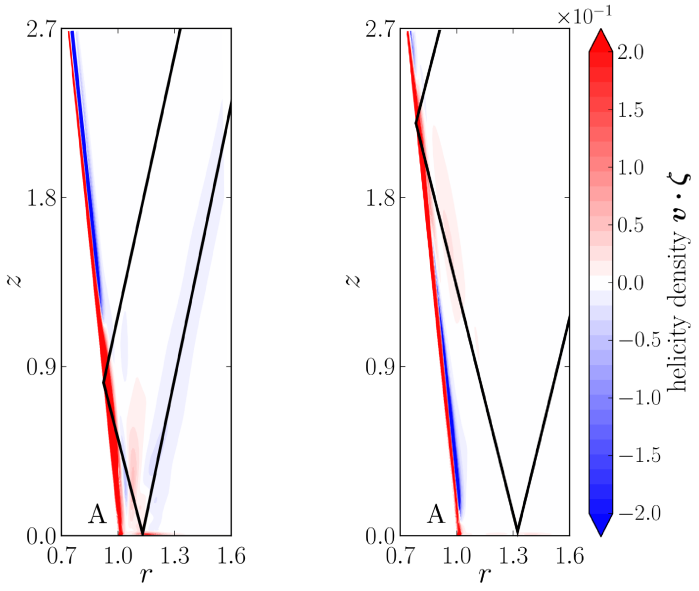

(a) $\omega = 0.42$ (b) $\omega = 0.47$

Figure 6.9: Contours of the helicity density $\boldsymbol{v} \cdot \boldsymbol{\zeta}$ in a fraction of the radial-axial section at different libration frequencies ω. The flow is excited by frustum libration with dimensionless parameters $R = 0.2$, $E = 3.19 \times 10^{-5}$. The helicity distribution remains qualitatively the same over one libration period so that only the snapshots at $\omega t = 0$ are shown. The range of contour levels has been increased to show the modification of the boundary layer flow to positive helicity due to an incident wave. The wave attractor path is given for orientation due to the lack of internal structure (compare to figure 4.2). Waves originate mainly from corner A.

The total helicity at resonance depends strongly on the dynamics and cannot be predicted by simple arguments, but the following interpretation of the wave attractor resonance observed at $\omega = 0.42$ can be given:

- the rhomboidal wave attractor has a small path length and only few reflections are required to focus the initial wave beam from corner A on the wave attractor which minimises viscous losses according to equation (2.31) or (2.33), respectively;
- the wave attractor returns to the source (corner) which yields interaction of the inertial waves in the vicinity of the wave attractor and the corner vortex, and might be the reason for the system not being able to draw more energy from the infinite energy source of wall libration;
- individual, parallel segments of the wave attractor path are sufficiently separated so that destructive interference of inertial waves does not occur.

Contributions from harmonics of the forcing frequency. Let us come back to figure 6.8 by focusing at the contributions at the harmonics 2ω and 3ω of the forcing frequency ω shown by filled and unfilled triangular markers. The filtered quantities $K_{l\omega}$, $D_{l\omega}$ and $H_{l\omega}$ $(l = 2, 3)$ have been rescaled with R^{2l-2}, which means rescaling does *not* affect the $Q_{l\omega}$. One can see

that the response at the harmonics is not as strongly affected by the boundary layer as in the 1ω component. This is notable, for example, by the slope of $D_{2\omega}$ and $D_{3\omega}$ having opposite monotonicity than $D_{1\omega}$.

Furthermore, the magnitudes of $K_{2\omega}$, $K_{3\omega}$ in panel (a) and $D_{2\omega}$, $D_{3\omega}$ in panel (b) are substantially smaller than those of $K_{1\omega}$ or $D_{1\omega}$, respectively, even though the expected Rossby number dependency has been compensated. The corrected energies and dissipation rates yield $K_{3\omega} > K_{2\omega}$ and $D_{3\omega} > D_{2\omega}$, which suggests a scaling law R^a with $a < 2l - 2$ for the quadratic quantities measured in the co-rotating frame of reference.

The helicity contributions $H_{2\omega}$ and $H_{3\omega}$ in panel (c) have a negative peak close to the resonance, though shifted to slightly lower frequencies. On the one hand, the negative peak means dominance of upward propagating waves, which is the case for the harmonics emitted by the unstable corner vortex at the lower inner corner of the radial-axial section (see sections 4.4 and 5.1). On the other hand, the helicity resonance peaks are shifted to slightly smaller libration frequencies $\omega = 0.41$ and $\omega = 0.40$, which means $2\omega = 0.82$ and $3\omega = 1.2$. The 2ω resonance is unclear, but the 3ω can be identified as non-linear excitation of the $(1, 3)$ wave attractor. By contrast, the quality factor $Q_{2\omega}$ of the 2ω harmonic shown in panel (d) yields a resonance at $\omega = 0.44$, which can be interpreted as non-linear excitation of the $(1, 2, 0)$ mode.

Normal mode resonance excited by lids plus outer cylinder libration

Figures 6.10(a–d) show the system response in terms of the four variables K, D, H and Q by varying the libration frequency ω around the $(2, 1, 0)$ mode, which is expected at $\omega = 0.89$ according to geometric ray tracing (figure 2.11). The expected resonance frequency is shown by a broken grey vertical line. Selected libration frequencies cover the interval $[0.82, 0.94]$ with a resolution of $0.005 \leqslant \Delta\omega = 0.01$ (small values in the middle, larger ones near the boundaries), which means a factor 2 finer frequency increments than in figure 6.8. Otherwise the arrangement of figure 6.10 is similar to figure 6.8 discussed above only that red colours remind us that lids and outer cylinder libration has been used to excite waves. Note also that the non-dimensional parameters have been kept at their default values, that is, $R = 0.2$ and $E = 3.19 \times 10^{-5}$.

Time-averages and contributions at the forcing frequency. The first aspect to note in figures 6.10(a–d) is that time-averaged quantities $\bar{K}$, $\bar{D}$, $\bar{H}$ and Q are only marginally different from the corresponding values $K_{1\omega}$, $D_{1\omega}$, $H_{1\omega}$ and $Q_{1\omega}$ obtained by filtering at the forcing frequency ω. As before, is it sufficient to discuss only the time-averaged quantities.

The second aspect to note is that the normal mode resonance yields about an order of magnitude larger values of $\bar{K}$, $\bar{D}$ and Q than in the case of the wave attractor resonance discussed above. This is partly related to the enhanced wave excitation in the case of lids plus outer cylinder libration compared to the case of frustum libration as discussed earlier and reflected by higher Q values.

The third aspect concerns the resonance peak, which appears narrower and symmetric in contrast to the wave attractor resonance (figure 6.8). It is also interesting that all four quantities possess an extremal value at $\omega = 0.870 - 0.005$ and a full width at half maximum of about $\delta\omega = 0.015$. This is quite narrow already and will reduce further together with the Ekman number. For practically relevant Ekman numbers $E \lesssim 10^{-10}$ the system will exhibit a very sharp resonance when the resonance frequency is met (see Ghasemi V., 2016, for further discussion). Moreover, $\bar{K}$ and Q exhibit local maxima (figures 6.10(a, d)), whereas for $\bar{D}$ and $\bar{H}$ exhibit local minima (figures 6.10(b, c)). The helicity taking negative values is an interesting point but cannot be clarified at present. We may hypothesise that either the $(2, 1, 0)$ mode

itself possess non-zero helicity (compare to Lopez & Marques, 2015), or that the total helicity is again the result of an intricate feedback of the bulk flow on the oscillating boundary layer. The flow structures are too complex here (Ekman and Stokes boundary layers, mode, four corner beams) to speculate about an answer. Instead, it is worth to discuss the dissipation rate $\bar{D}$ which is obviously affected by the resonance.

The normal mode resonance yields a *local reduction of the total dissipation rate*, which can be seen in figure 6.10(b). This is quite unexpected but in line with a recent study on normal mode excitation by libration in straight annular confinements (Ghasemi V., 2016). Ghasemi V. (2016) discusses in detail that normal modes can be excited efficiently when the 'phase pattern' formed by the corner beams becomes stationary. It corresponds then to a neutral orbit as obtained by ray tracing and is also compliant with the phase pattern of the eigenmode[8]. Hence, in the case of a mode resonance the basin-scale oscillation pattern of the mode is phase-locked with the corner beams due to which velocity gradients are reduced along the corner beams. In that way overall shear and, thus, the dissipation rate are reduced. The effect of dissipation rate reduction is small here but can become relevant when Ekman numbers become very small so that corner beams and thus energy dissipation is more localised in the fluid interior. An open question is whether or not the normal mode excited has a significant effect also on the boundary layer by interacting with the source (see the previous section). In any case, the normal mode resonance behaves qualitatively different to the wave attractor resonance since the latter always has a small cross-scale and is thus more likely to yield an increased dissipation rate (e.g. Ogilvie, 2005) which is not the case for (low-order) normal modes and their smooth spatial patterns.

The fourth aspect concerns the global trends of the kinetic energy and the dissipation rate. Namely, $\bar{K}$ and $\bar{D}$ approach the same individual values to the left and right of the resonance peak. This can be attributed to the boundary layer, namely the oscillating Ekman layer over the top and bottom lid. It has been discussed in sections 5.2 and 6.1 how the boundary layer response differs for libration frequencies ω smaller or larger than the eruption frequency f_* (here it is $f_* = 2$ for the oscillating Ekman layer over the lids).

To elucidate further the resonance condition it appears necessary to compute the spectra of (non-linear) viscous eigenmodes.

Contributions from higher-harmonics. The harmonic frequencies 2ω and 3ω are given by filled and unfilled triangular markers in figures 6.10(a–d). The reader is reminded that the filtered quantities $K_{l\omega}$, $D_{l\omega}$ and $H_{l\omega}$ $(l = 2, 3)$ have been rescaled with R^{2l-2}, which means magnitudes $Q_{l\omega}$ remain normalised. The magnitudes of $K_{2\omega}$, $K_{3\omega}$ shown in panel (a) and $D_{2\omega}$, $D_{3\omega}$ shown in panel (b) are much smaller than $K_{1\omega}$ or $D_{1\omega}$, respectively, even though the expected Rossby number dependency has been compensated. This is generally similar to the case of the wave attractor discussed above (figure 6.8), though rescaling with the Rossby number seems to work a bit better here.

The behaviour of the various quantities across the resonance frequency $\omega = 0.870$ is quite interesting. The kinetic energy $K_{2\omega}$ shown in figure 6.10(a) exhibits a broad peak with sub-structure and a local maximum at $\omega = 0.885$. This can be interpreted as non-linear excitation of the $(1, 8, 0)$ mode at $2\omega = 1.77$ (see the dashed grey line at around $\omega = 1.77$ in figure 6.7). The second harmonic yields $3\omega > 2$ for the frequency band considered here and $K_{3\omega}$ does not exhibit a notable peak.

[8] A corresponding solution has been discussed in chapter 4, figure 4.10, but not in as much detail as by Ghasemi V. (2016) due to the unknown spectrum of eigenmodes in the frustum geometry.

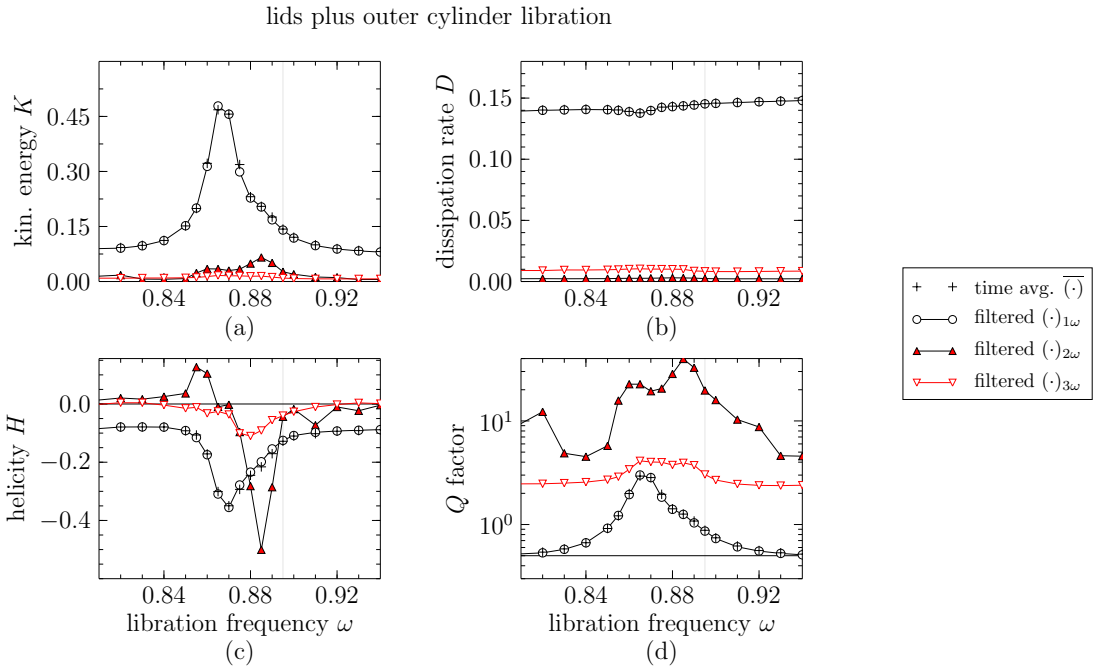

Figure 6.10: High-resolution response spectra for the case of lids and outer cylinder libration and libration frequencies ω across the $(1, 2, 0)$ normal mode resonance. The resonance frequency predicted by ray tracing is shown by a dashed grey line. All quantities shown have been integrated over the whole annulus volume. Time-averages $\overline{(\cdot)}$ and frequency-filtered values $(\cdot)_{l\omega}$ have ben obtained over a time interval of 32 libration periods in the statistically stationary state. Auxiliary horizontal lines are given for $H = 0$ in panel (c) and $Q_\mathrm{c} = 1/2$ in panel (d). Default non-dimensional parameters have been used $\big(R = 0.2,\ E = 3.19 \times 10^{-5}\big)$.

The helicity $H_{2\omega}$ shown in figure 6.10(c) exhibits an interesting substructure of the resonance peak with sign changes and a local extremal values at $\omega = 0.855$ ($H > 0$) and $\omega = 0.885$ ($H < 0$). The former peak yields $2\omega = 1.71$, which is close to a low-order wave attractor (the solid grey line at around $\omega = 1.73$ in figure 6.7), whereas the latter peak coincides with the local $K_{2\omega}$ maximum. Both helicity peaks form the substructure of the peak in the quality factor $Q_{2\omega}$, but only the negative helicity peak yields a local maximum in $Q_{2\omega}$ at $\omega = 0.885$. It is worth noting that the 3ω harmonic has a local minimum in $H_{3\omega}$ at $\omega = 0.880$ and two maxima in $Q_{3\omega}$ at $\omega = 0.865$ and $\omega = 0.885$. The 3ω frequency cannot propagate freely, so that its properties are strongly linked to the spatial pattern of the driving 1ω and 2ω waves (see section 4.2).

In summary, the largest effect of resonance with an inertial wave has been divided in two situations: a wave attractor resonance or a normal mode resonance. Highly-resolved response spectra have been computed of time-averaged and filtered values of the total kinetic energy, total dissipation rate, total helicity and the Q factor by varying the libration frequency in a small interval across a resonance peak. Filtered quantities up to the second harmonic of the libration frequency ω have been computed. The main contribution to the variability has been found at the forcing frequency. Hence it is not necessary to filter the data in a weakly non-linear moderately viscous flow regime ($R = 0.2,\ E = 3.19 \times 10^{-5}$). At the forcing frequency, the moderate viscosity yields dominance of the boundary layer so that dissipation rates remained unaffected in the case of a wave attractor resonance, but reduced in the case of a strong normal mode resonance.

Furthermore, note that the harmonics $l\omega$ ($l \geqslant 2$) of the forcing frequency ω have been considered important since they would indicate the emergence of non-linear interactions in a weakly non-linear flow. For the parameters investigated, higher harmonics are not yet strong enough to yield interactions in contrast to precessing flow (for example, Albrecht *et al.*, 2015; Lopez & Marques, 2015; Mason & Kerswell, 1999). However, it has been shown that resonance of harmonics is possible but depends strongly on the spectrum of eigenfunctions. That is, it is crucial that the multiple $l\omega$ lies close to the eigenfrequency of a low-order wave attractor or a low-order neutral orbit (or normal mode for that matter). For the wave attractor resonance at $\omega = 0.42$, a 'non-linear resonance' in the sense that harmonics of the forcing frequency are also resonantly exciting a wave attractor or normal mode, has been found for the two lowest harmonics 2ω and 3ω. For the normal mode resonance at $\omega = 0.875$, only the 2ω harmonic is able to exhibit such resonance and was also found. The 3ω harmonic in this case does not fulfil the linear wave dispersion relation and is therefore depends only on the property of its sources (the 1ω and 2ω contributions). In the present configuration, however, the harmonics of 2ω and higher contribute only by a small fraction to the total variability which prevents the investigation of secondary effects such as long-time instabilities (for example Mason & Kerswell, 1999).

7 Summary and conclusion

Three aspects of waves in rotating flows have been in the focus of the present study: (i) the identification and characterisation of flow structures related to inertial waves, (ii) the clarification of the wave excitation mechanism and its efficiency due to wall libration, and (iii) the identification of resonance conditions and their relation to inertial waves.

In the following, we begin with a few general remarks. After that, we address the three mentioned points separately in more detail. The chapter closes with an outlook.

General remarks

The flow configuration selected for this study is a 1-to-1 analogue of a laboratory experiment installed at the BTU Cottbus - Senftenberg (see Seelig, 2014). A homogeneous liquid is confined in an annular confinement that is formed by two concentric co-rotating cylinders, and two rigid lids at the top and bottom ends. More precisely, the inner cylinder was modified so that it resembles a truncated cone or frustum (see figure 1.3). Inertial waves were excited by libration, which consists in a sinusoidally modulated wall rotation rate as given by equation (1.2). Waves were excited using small libration amplitudes $\varepsilon \ll 1$ and libration frequencies ω from within the inertial wave band $[0, 2\Omega_0]$, where Ω_0 denotes the mean rotation rate.

The geometry was kept constant throughout this study, but two complementary forcing configurations were investigated: the frustum in libration and the lids together with the outer cylinder in libration. Direct numerical simulations (DNS) were performed in order to resolve the processes of wave excitation and wave propagation. The numerical solver used is written in terms of terrain-following coordinates in order to treat the frustum wall accurately. In addition, contravariant volume fluxes are used instead of velocity components to aid conservation properties in locally refined grids (see chapter 3 for further details).

The flow configuration has two non-dimensional parameters, the Rossby number $R = \varepsilon\, r_{\mathrm{lib}}\, (\Delta r)^{-1}$ and the Ekman number $E = \nu\, \Omega_0^{-1}\, (\Delta r)^{-2}$, where r_{lib} is the distance of the librating wall from the rotational axis, Δr is the minimum gap width, and ν is the kinematic viscosity of the fluid. R measures the strength of the non-linearity of the forcing relative to the Coriolis force, whereas E measures the strength of viscous forces relative to the Coriolis force. A Reynolds number can thus be defined as $Re = R/E$. In this work the range $2 \times 10^{-2} \leqslant R \leqslant 4 \times 10^{-1}$ and $10^{-5} \leqslant E \leqslant 3 \times 10^{-3}$ was investigated. Following the literature, R and E are based on the basin dimension and the forcing amplitude, which means they do *not necessarily* represent similarity parameters of the flow excited. The reasons for this deficiency are likely related to the lack of data available for most geo- and astrophysical flows. At the very least, the definitions of R and E give an impression of the scale gap between a table-top experiment and an actual planetary flow. This scale gap increases most rapidly, for example, from the lower left to the upper right in the parameter space shown in figure 1.1.

Identification and characterisation of inertial waves

The **first key result** of this work is the virtually perfect agreement between numerical solutions and the laboratory measurements of Seelig (2014). Qualitatively and quantitatively similar bulk

flow structures were obtained (see figures 4.3 and 4.9), where it is worth to point out that the DNS and the laboratory experiments were conducted for precisely the same external parameters and confinement geometry. The agreement indicates once more that the Navier–Stokes equations can accurately describe the dynamics of a fluid system. Of course, the numerical solutions obtained only approximate the real flow since the flow variables velocity and pressure are computed only at a finite set of points (nodes) solving the discretised (algebraic) system of equations. DNS ensures that the node density is high enough to resolve all relevant scales of the flow which means numerical errors are negligible. Therefore, the correspondence between laboratory measurements and DNS also validates the method, that is, the contravariant solver formulation and its implementation (see chapter 3).

In fact, when scaling back to SI units, both DNS and laboratory experiments reveal flow velocities of only 1 $\mathrm{mm\,s^{-1}}$ while the azimuthal velocity is of the order 1 $\mathrm{m\,s^{-1}}$. This indicates that the inertial waves excited are only a small perturbation to the underlying state of rigid body rotation. It is quite interesting that the finite amplitude waves excited are stable over a wide parameter range. To summarise, the bulk flow is non-linear but dominated by linear (wave) dynamics.

In addition to DNS, geometric ray tracing was applied to identify spatial structures related to waves. By ray tracing the path of an inertial wave is traced out by following the characteristics of the linearised Navier–Stokes equations (see section 2.4). A qualitative comparison to DNS results indicates that ray tracing is able to describe and to predict the flow structures corresponding to inertial waves amazingly well (see figures 4.12 and 4.13). This is in line with earlier studies (e.g. Beardsley, 1970; Borcia *et al.*, 2014; Maas, 2001; McEwan, 1970), where ray tracing seems to be successful mainly because of three reasons. First, the amplitudes of the waves excited by libration is very small so that non-linear instability is not an issue. Second, wave emission is strongly localised in the corners (edges) of the annular domain so that inertial waves form distinct shear layers from the beginning on (so-called wave beams when viewed in a radial-axial section). Third, inertial waves undergo focusing reflections at the sloping frustum wall. After several reflections at one or more oblique walls kinetic energy might be concentrated in a tiny volume fraction, this it what is called the excitation of a wave attractor. Due to this concentration, infinitely thin wave *rays* are a good approximation of finite wave *beams* due to which ray tracing is able to capture the 3-D flow patterns related to inertial wave attractors.

Inertial waves are helical shear waves which means they exhibit a 3-D structure in the velocity and the vorticity fields for which the dispersion relation constrains the orientation of the shear and the direction of the energy propagation. The excitation of inertial waves by wall libration suggests that the boundary layer flow is the source of kinetic energy and helicity. Both kinetic energy and helicity leave the boundary layer simultaneously which renders wave excitation tied to the conservation of both quantities. In fact, it can be shown that helicity enters the dynamical equations on the same level as the kinetic energy (Névir, 1998; Névir & Blender, 1993). Here it is helpful to know the helicity distribution because the sign of the helicity allows to infer the direction of kinetic energy propagation once we are certain that the flow is dominated by inertial waves. Positive (negative) helicity corresponds to downward (upward) propagating waves (see section 2.3), which was confirmed by the numerical simulations conducted (see figures 4.2 and 4.8). One could say that the kinetic energy contains the *amplitude information*, whereas helicity contains the *phase information*.

The importance of helical structures in the velocity field has been recognised earlier, but is typically associated with the vortex stretching mechanism underlying the turbulent cascade and turbulent mixing (e.g. Davidson, 2013, pp. 283). Inertial waves take part in the mixing process by redistributing momentum, kinetic energy and helicity, but inertial waves are yet

different from 'ordinary' eddy turbulence by being much more organised in space and time (e.g. Campagne *et al.*, 2015).

The wave excitation mechanism and its efficiency

The **second key result** of this work is to be seen in the uncovering of the wave excitation mechanism due to wall libration. It was shown by the aid of boundary layer theory that a mass flux difference across the corners (edges) is at heart of the conversion into wave energy. Part of the libration-induced Ekman flux in the oscillating boundary layer is redirected into the fluid bulk due to which fluid parcels are radially displaced in the vicinity of the corner (see figures 5.14 and 5.15). Based on the latter mechanism, the functional dependency of the total kinetic energy in the bulk, K^{bulk}, on the libration frequency ω has been derived (see section 5.3) and was then validated by DNS (see section 6.1). For the bulk flow dominated by inertial waves it turns out that

$$K^{\mathrm{bulk}}(\omega) \propto w_{\mathrm{E}}^2(\omega) \qquad \text{for} \quad R = \text{fix}, \quad E = \text{fix},$$

where $w_{\mathrm{E}}(\omega)$ denotes the theoretical Ekman pumping velocity amplitude at the top of the Ekman layer over the librating frustum or the lids respectively. The dependency $R^{-1}w_{\mathrm{E}}(\omega, E)$ (rescaled with R) is given by equations (5.38)–(5.40). The validity of equation (7) with respect to the libration frequency was confirmed by fitting $w_{\mathrm{E}}^2(\omega)$ in amplitude to the simulated kinetic energy spectra $K_{1\omega}^{\mathrm{bulk}}(\omega)$ to account for the unknown conversion coefficient (see figures 6.2 and 6.3). The subscript 1ω denotes filtering at the libration frequency. It is worth to emphasize that the frequency dependency given by equation (7) not only describes DNS results, but is also in very good agreement with the laboratory measurements of Seelig (2014).

The wave excitation efficiency (figure 6.4) was computed as ratio of the total kinetic energy in the bulk and the total kinetic energy trapped in the boundary layer over librating walls for the purpose of comparison of the two complementary forcing configurations. It confirms the observation of Seelig (2014, p. 95) that wave excitation by frustum libration (libration of a steeply inclined wall) excites low frequency waves most efficiently, whereas lid libration (libration of a horizontal wall) excites high frequency waves with frequency close to $2\Omega_0$ most efficiently. The wave excitation efficiency reaches a global maximum when the libration frequency equals the local Coriolis parameter, namely

$$\omega_{\max} = f_* \equiv 2\Omega_0 \sin\alpha. \tag{7.1}$$

In the latter equation α denotes the inclination of the librating wall with respect to the bottom lid. (In this setting the bottom lid is supposed to be perpendicular to the mean angular velocity vector $\Omega_0\ \boldsymbol{e}_z$.) This suggests that the confinement geometry plays a secondary role with respect to wave excitation by libration. This means that edges, ridges, or even a split-ring configuration (as used, for example, by Hollerbach & Fournier, 2004) yields localised inertial wave excitation because an Ekman flux difference emerges at any of these discontinuities of the boundary condition.

It is worth to point out that the wall does not need to librate in order to excite inertial waves. Alternatively, a boundary layer current could also be driven by an oscillating pressure gradient force or by tides. Both would lead to a boundary layer structure similar to that found over the librating wall but with the wall at rest. We expect a similar localisation of the wave excitation at discontinuities of the boundary condition since the mass flux difference argumentation can be applied straightforwardly.

An immediate question concerns the importance of details of the corner flow for with respect to wave excitation? Present DNS results in conjunction with the boundary layer analysis suggests that the details of the corner flow are actually *not* so important for wave emission. The boundary layer analysis shows that the Ekman flux difference is the key ingredient for the localisation of inertial wave excitation, irrespective of whether or not the corner flow is helical. Nevertheless, also the helicity properties appear to be in line with the assertion that the corner flow details are not essential for the wave excitation by libration.

Helicity is a signed quantity that takes into account both amplitude and phase information by projecting the vorticity vector on the velocity vector. We have shown that inertial waves of negative (positive) helicity are emitted from a corner flow of positive (negative) helicity (see figures 4.2 and 5.2), which is certainly surprising. Moreover, the magnitude of the helicity density of the waves excited is typically by about two orders of magnitude smaller than the helicity density of the corner vortex. In the case of a bulk flow resonance, though, one can see a clear peak in the total helicity which renders the volumetric contribution of the corner vortices to the total helicity negligible. The corner vortex is therefore merely a secondary phenomenon relevant for the local stabilisation of the boundary layer flow by counteracting the strong gradients imposed by the boundary condition.

Note that the latter does not mean that the generation of azimuthal vorticity in the boundary layer, for instance due to centrifugal instability, is irrelevant for wave excitation *per se*. On the contrary, azimuthal vorticity generated by an instability of the boundary layer flow was shown to emit inertial waves as well (see e.g. figures 4.14 and 4.19). This implies that non-linearity of the corner flow tends to enhances the wave excitation efficiency.

Note further that the excitation of inertial waves by wall libration requires a finite amplitude ($\varepsilon > 0$ in equation (1.2)) which means that we are faced with a non-linear flow *per se*. By restricting our attention to small Rossby numbers ($R \ll 1$) we hoped for a dominance of approximately linear wave dynamics and stable bulk flow. Both of these were met and it was quite amazing to see how well the linear wave approximation in terms of ray tracing is able to predict the dominating flow structures related to inertial waves (see section 4.3).

The **third key result** concerns additional frequency content. In addition to the prescribed libration frequency there are also other frequencies present in the DNS solutions (see section 4.4) and appear to have saturated in amplitude. No bulk flow instability could be observed in any of the present simulations, which differs from the long-time instability observed by Mason & Kerswell (1999). This is most likely due to the axisymmetric forcing employed here which cannot excite azimuthal wave numbers directly.

The additional frequencies besides the libration frequency ω are mainly located at the harmonics $l\omega$ ($l = 2, 3 \ldots$) in the weakly non-linear flow regime studied. The frequency dependency of the higher-harmonic kinetic energy $K^{\mathrm{bulk}}_{l\omega}(\omega)$ has been obtained on the grounds of qualitative arguments and by making the unknown excitation efficiency coefficient a constant parameter fixed by fitting the empirical frequency scaling to the DNS data (see figures 6.5 and 6.6). The fluid response at the harmonics $l = 2, 3$ investigated can be explained to a good deal by the Ekman pumping mechanism of the primary waves. A discussion of the possible interaction mechanisms lead to the conclusion that higher harmonics are mainly generated in the corner flow by a self-interaction mechanism. Another but less efficient mechanism is a wave–boundary-layer interaction in which the boundary layer flow interacts with a wave beam that returns to the librating wall after reflection at other walls of the confinement. For $R \geqslant 0.2$ the corner flow starts to destabilise during the centrifugally unstable phase of libration and emits higher-harmonic waves directly (see figure 5.3). For $R \geqslant 0.4$ the boundary layer over the librating frustum has turned turbulent and emits inertial waves spontaneously (as in Sauret *et al.*, 2013).

The bulk flow looks more chaotic though due to the presence of several frequencies being excited at once. A frequency decomposition (e.g. figure 4.14) shows that the bulk flow is merely a superposition of waves rather than 'wave turbulence', which would imply strong interaction of waves and wave frequencies across a range of scales.

Resonance conditions

The **fourth key result** of this study is that there are two different types of resonances in a rotating fluid, normal modes and wave attractors. Resonance means that the kinetic energy stored in the system is much larger than the amount of energy converted (dissipated) into heat during a libration period so that large velocity amplitudes are encountered. The resonance peaks appear on top of the global frequency dependency imposed by the wave excitation mechanism. More precisely, the kinetic energy contained in the system was found to increase suddenly by up to a factor of 50 in places when the libration frequency ω was incremented to $\omega + \delta\omega$ using a step of $\delta\omega/\Omega_0 = 0.05$. This indicates how sensitive even a moderately viscous fluid system reacts to a change of the forcing parameter and illustrates once more why resonance phenomena are so ubiquitously discussed in various applications.

The resonance frequencies of a system, however, are in general difficult to predict in the first place. For the rotating annulus it was shown by ray tracing that they are irregularly distributed over the inertial wave band (see figure 2.9). In the DNS, resonance conditions were found very close to frequencies of low-order modes and within frequency bands of low-order wave attractors. Only the low-order modes and wave attractors could be excited because of the relatively large Ekman number used ($E \sim 10^{-5}$). This means higher order modes or wave attractors could not be excited only because of too large dissipative losses. In practical applications with $E \lesssim 10^{-9}$ the restriction to low-order wave attractors is potentially lesser an issue, which increases the relevance of wave attractor resonances there.

The resonance mechanism of a normal mode represents the 'classical' case of resonance where losses are minimised. In a fluid, this corresponds to a minimisation of the velocity gradients and, thus, kinetic energy dissipation. The flow is organised such that it varies smoothly on the basin scale (e.g. figure 4.10). A small influx of kinetic energy into the system due to libration is sufficient for the system to accumulate a huge amount of energy in the mode until the dissipation rate equals the energy influx.

By contrast, in the case of a wave attractor resonance, a mechanism must exist that counteracts spatial concentration of kinetic energy so that gradients are smoothed and the dissipation rate is reduced again. The mechanism proposed in this study is as follows: consider a finite Ekman number flow ($E > 0$) with inertial waves and focusing reflections. In this setting, molecular diffusion will balance the spatial concentration of energy at some point and thus limits the minimum wave beam width (see section 2.3). An energetically *optimal ray pattern* may develop by constructive interference of the viscously broadened wave beams. That is, we are interested in a constructive interference of a corner beam with its reflected counterpart. Here libration provides a periodic perturbation which has a constant phase relation with the wave field excited. The corner beams excited have a dominant frequency and a unique phase distribution across the wave beam (see figure 6.2). Consequently, a stationary interference pattern is formed by the emitted wave beam and all its reflections. The *resonance frequency* is then obtained for the optimal path in which the focused wave beam overlaps and is in-phase with the neighbouring beams which have traversed the confinement geometry a round trip more or less respectively. Steep gradients are smoothed in that way (see figure 4.5) which yields a

dissipation rate smaller than in a hypothetical scenario without the focused corner beam and only the wave attractor present in the fluid.

The optimal ray pattern dictates the resonance frequency but depends heavily on the confinement geometry and the location of the wave source, viscosity (that is, the Ekman number E), and the non-linearity of the flow (that is, the Rossby number R). This is exemplified by the totally different resonance peaks around $\omega/\Omega_0 = 0.45$ in figures 6.2 and 6.3, which also shows that patterns belonging to the same wave attractor can support different resonance peaks depending on the forcing provided.

To summarise the latter points, it is interesting that the common principle between a wave attractor resonance and a normal mode (standing wave) resonance seems to be the constructive interference of propagating waves. The difference, though, is in the phase relation due to which in the case of a standing wave two waves need to propagate in *opposite* directions, whereas in the case of a wave attractor they propagate in the *same* direction. In the latter case, the constant phase is only reached by a balance of viscous broadening (in-/decrease of the phase/group velocity) and geometric focusing (de-/increase of the phase/group velocity).

The resonances simulated here manifest themselves as narrow peaks in the spectra of the kinetic energy, the quality factor and the helicity (see figures 6.8 and 6.10). Interestingly, the helicity peak is observed for both normal modes and wave attractors. The peak overshadows even the boundary layer flow which agrees with the notion that resonance in the librating annulus is tied to the excitation of low-order inertial wave patterns. In the case of resonance it is generally relevant to know if flow amplitudes are large enough to drive substantial mean flows that might feed back on the resonance condition by modifying the mean rotation rate (see e.g. Baruteau & Rieutord, 2013). The effect is of the order ε^2 so that it is negligible here given the small libration amplitudes used[1] ($\varepsilon \lesssim 10^{-1}$).

Altogether, wave attractors can be relevant in applications because of the concentration of kinetic energy and helicity. Secondary flows can be driven (e.g. Tilgner, 2008) or instabilities may develop as a result of the steep gradients and the complex flow structure (e.g. Jouve & Ogilvie, 2014). This can be relevant in the atmosphere, for example, where it might be the excitation of a wave attractor for inertial or gravity waves that seeds other non-linear phenomena such as the Quasi-Biennial Oscillation (e.g. Baldwin *et al.*, 2001; Seelig, 2014). Because of the similarity between inertial waves and gravity waves the wave attractor resonances are driven in precisely the same way in density stratified flows like the ocean and the atmosphere.

Outlook

The validation of numerical solutions against available measurements was mandatory to be confident that the simulations capture the essential phenomena. Vorticity and helicity, however, are usually not available due to insufficient measurements accuracy and therefore very rarely reported in literature. It would be interesting to obtain vorticity or helicity distributions from a laboratory experiment in a future measurement campaign. This might shed some light on the existence of the corner vortex and may help to clarify its relevance for wave excitation.

An interesting point in the clarification of the role of the corner vortex would be an analytical approach to the corner flow problem. Wang (1970) started to develop an analytical solution by a series expansion, but excluded the corner region. In the case of wall libration it is the Ekman pumping mechanism that drives a wall-tangential flow to or from the corner. Alternatively, vibrational forcing can be used that has a similar effect and yields a corner vortex as well as

[1] For an in-depth analysis of the mean flow driven by inertial waves in the present configuration see Ghasemi V. (2016).

a localisation of the wave excitation (Lopez & Marques, 2014). These settings are reminiscent of 2-D eddies discussed by (Moffatt, 1964), who considered a flow incident to various corner geometries without specifying how the flow might be driven. It seems as if a future analytical investigation might be feasible by combining Moffatt's and Wang's theory. Another option could be the application of a multi-pole expansion in analogy to Machicoane *et al.* (2015), who studied the far field of inertial waves emitted by small oscillating wave makers. We may assume that the corner flow can be expanded into a converging multi-pole series and make use of the mentioned theory. Strikingly, this would mean that the waves outside the boundary layer, which have been neglected on purpose by Wang (1970) and Busse (2011), would actually be needed to 'close' the corner flow problem.

The annular confinement used in this work with its broken mirror symmetry can be viewed as somewhere in between simple geometry and complex geometry since it exhibits wave attractors and normal modes. In the near future, it would be interesting to extend the present study by a computation of the spectrum of frequency eigenvalues and an asymptotic analysis to single out the weakly-damped eigenmodes (analogous to Rieutord *et al.*, 2001). The eigenmodes obtained in that way could then be compared to the DNS results presented here. The spatial patterns, on the one hand, can be compared directly to the spatial distribution of any dynamical variable. On the other hand, the spectrum of the damping coefficient might find its closest correspondence in the simulated Q factor spectrum (figure 6.7). It might be possible to clarify whether or not a wave attractor resonance exhibits a reduction of the damping coefficient (imaginary part of the frequency eigenvalue) independently of the boundary condition. If this would not be the case, the DNS results and laboratory experiments of Seelig (2014) would lead to the conclusion that a wave attractor resonance is different from a normal mode resonance by means of that a wave attractor resonance is rather a detached boundary layer phenomenon.

The DNS results of this study indicate that additional frequencies are strongest when a spatial coupling of low-order wave attractors occurs. This observation was very surprising, but could not be investigated further in the course of this work. However, it seems worth to address this mechanism for harmonic and anharmonic frequency generation in the future.

The linear wave solution corresponds to a 3-D zero-amplitude wave for which there is still a controversy whether or not they are non-linearly stable (e.g. Ghasemi V., 2016; Kerswell, 1999). This indicates that non-zero azimuthal wave numbers may actually play a crucial role for the long-time instability which was observed, for example, by Mason & Kerswell (1999, though for a confinement geometry that exhibits normal modes but no wave attractors).

Another extension of the present study could address the validity of the asymptotic linear theory Ogilvie (see e.g. 2005); Rieutord *et al.* (see e.g. 2001) with respect to practical applications. It is not yet clear yet whether this theory gives meaningful results for small but notably *non*-zero Rossby number when the Ekman number tends to zero ($E \lesssim 10^{-9}$). It is not unlikely that instabilities lead to turbulent collapse of wave attractors in this scenario. If is the case, asymptotic heating rates obtained by linear theory might actually never be reached in practice. If this is not the case, high-resolution numerical simulations and/or more elaborate turbulence models would be needed to accurately simulate planetary interior flows. Turbulent collapse might be an intermittent phenomenon which leads to the question about the time scale of breakdown and re-organisation of the flow.

As final remark on the relevance of this work for mankind: the present results and the open questions sketched hopefully contribute to a better understanding of the dynamics of Earth's core. Earth's magnetic field, for example, changes polarity about every 500,000 years with a flip duration of only a couple of centuries, which could be caused by a wave-driven hydrodynamical instability but this is still elusive. Given the importance of the magnetic field for life on Earth

and modern life, it appears quite important to continue uncovering the interplay between waves, resonances, instabilities, and turbulence in rotating flows and geophysical flows.

A Supplementary material

A.1 On the history of the Navier–Stokes solver HYBRID-NEW

The basis for the Navier–Stokes solver HYBRID-NEW has been laid by Choi in the early 1990s at the Center for Turbulence Research (CTR), Stanford, CA. Back then, the contravariant flux form of the momentum equation has been worked out for the stream-wise and wall-normal coordinates in order to study planar channel flow over small-scale topography (periodic span-wise direction; see Choi, 1993; Choi *et al.*, 1992, 1993). In the late 1990s and still at CTR, Kaltenbach and colleagues developed the code further for large-eddy simulations with a focus on asymmetric planar diffuser flow (Kaltenbach *et al.*, 1999; Lund & Kaltenbach, 1995).

Between 2000 and 2004 HYBRID-NEW has been extended by Kaltenbach and Hauschild at ISTA, TU Berlin, DE, for the purpose of direct numerical simulations of the flow in an axial diffuser. A comprehensive code documentation has been added at that stage, which treats the coordinate transformation in detail (Kaltenbach & Hauschild, 2004). The axial region was treated similarly to Akselvoll & Moin (1996); Verzicco & Orlandi (1996), but the implementation seems to have disappeared. The implementation up to that point has been in Fortran 77 with a focus on high-performance vector machines. Kaltenbach and colleagues also added an algebraic grid generator that allowed to construct 2-D locally orthogonal diffuser grids with a stretched wall-normal (radial) coordinate.

HYBRID-NEW has been developed further by Ghasemi V. and myself since 2011 at the Chair Environmental Meteorology, BTU Cottbus - Senftenberg, focusing on direct numerical simulations of the flow induced by libration of axisymmetric confinements. My responsibility, on the one hand, has been the implementation of the Coriolis force and the libration boundary conditions in the generalised framework (Klein, 2014a; Klein *et al.*, 2014). I have also re-introduced the factoring of the viscous terms for the implicit treatment of the second wall-bounded direction. On the technical level, I have ported the code to Fortran 95, introduced loop-level parallelism (The OpenMP ARB, 2008), developed interfaces to the FFTW library (Frigo & Johnson, 1997), and extended the script environments (Klein, 2014b) by staying close to the user interface of COSMO-CLM[1] Ghasemi V., on the other hand, added axially periodic boundary conditions, which demanded careful rearrangements in the Poisson solver for an improved performance (see Ghasemi V., 2016). He also developed online statistical tools for an in-depth study of the flow induced by wall libration (Ghasemi V., 2016; Ghasemi V. *et al.*, 2016). Ghasemi V. and me modified the algebraic grid generator by implementing different shape functions for the frustum wall and by introducing coordinate stretching also for the second direction of the 2-D grid.

[1] The COSMO-CLM community, `http://www.clm-community.eu`, last accessed: Oct. 10, 2015.

A.2 Smoothing of the frustum wall

As mentioned in section 3.1, the inner frustum (see figure 1.3) demands a modification so that the constraint of locally orthogonal grid lines can be fulfilled as it was assumed for the transformed equations of motion. Smooth slope transitions are needed in the vicinity of the lids (see figure 3.4). The piecewise shape function $r_1(z)$ needs to be two times continuously differentiable in order to avoid metrical artefacts and from the viscous terms. Curvature radii should be large in order to preserve conservation properties of the scheme as much as possible.

I have selected the smoothing such that the frustum wall has a linear central part of 92% of the entire height. Each slope transition occupies 4% of the height, which means slope transitions occupy $\Delta z = 0.2$ of the annulus height $h = 5$ with respect to the configuration in figure 3.4. Three points of the purely linear frustum are kept fix: A denoting the intersection of the frustum with the bottom lid, B denoting the intersection of the frustum with the top lid, and $\mathrm{A} + (\mathrm{B} - \mathrm{A})/2$ at mid-height. Assuming $r_\mathrm{A} \geqslant r_\mathrm{B}$ yields

$$r_1(z) = r_\mathrm{A} + (r_\mathrm{A} - r_\mathrm{B})\big[1 - f\,(z|h, \Delta z)\,\big], \tag{A.1}$$

where the normalised ramp function $f(z) \in [0, 1]$ depends on two parameters, the annulus height h and the length of a slope transition Δz.

In order to determine $f(z)$ we need to make assumptions on the type of slope transitions, for which the simplest choice consists in polynomials. Let $p(\xi)$ denote such a polynomial that is defined on the unit interval. It shall increase monotonically and be point symmetric to $(1/2, 1/2)$. We require an inflection point at $\xi = 1/2$ in order to match a linear part later. In addition, we demand terrace points at $\xi = 0, 1$ so that the lids will be approached at right angle.

Let $p' \equiv \mathrm{d}p/\mathrm{d}\xi$ denote the total derivative, where derivatives of fourth order and higher are denoted by Roman numbers, for example $p^{(\mathrm{iv})}(\xi) \equiv \mathrm{d}^4 p/\mathrm{d}\xi^4$. The conditions that determine the polynomial of lowest possible order read

$$\left.\begin{array}{lll} p(0) = 0, & p'(0) = \ldots = p^{(\mathrm{iv})}(0) = 0, & p^{(\mathrm{v})}(0) \neq 0, \\ p(1) = 1, & p'(1) = \ldots = p^{(\mathrm{iv})}(1) = 0, & p^{(\mathrm{v})}(1) \neq 0, \\ p(1/2) = 1/2, & p''(1/2) = 0, & p'''(1/2) \neq 0. \end{array}\right\} \tag{A.2}$$

Assuming that $p(\xi)$ increases monotonically, $p'(\xi) > 0$ for $\xi \in (0, 1)$, yields the solution to equations (A.2) and the first derivative as

$$p(\xi) = 6\xi^5 - 15\xi^4 + 10\xi^3, \qquad p'(\xi) = 30\xi^2\,(1 - \xi)^2\,. \tag{A.3}$$

Scaling of $p(\xi)$ and matching a linear piece in the middle yields the normalised shape function $f(z)$ as (compare to Klein *et al.*, 2014, appendix B)

$$f\,(z|h, \Delta z) = \begin{cases} A\,p\left(\dfrac{z}{2\Delta z}\right) & \text{for} \quad 0 \leqslant z \leqslant \Delta z \\ A\,\left[\dfrac{1}{2} + p'\,(1/2)\,\dfrac{z - \Delta z}{2\Delta z}\right] & \text{for} \quad \Delta z < z < h - \Delta z \\ A\,\left[p'\,(1/2)\,\dfrac{1 - 2\Delta z}{2\Delta z} + p\left(\dfrac{z - h + 2\Delta z}{2\Delta z}\right)\right] & \text{for} \quad h - \Delta z \leqslant z \leqslant h \end{cases} \tag{A.4}$$

with the scaling factor

$$A = \frac{2\Delta z}{1 + p'(1/2)\,[h - 2\Delta z]}. \tag{A.5}$$

Smoothing of the frustum exhibits a slight discrepancy in the wall inclination compared to the fully linear frustum, namely $\alpha_{\mathrm{num}} \approx 5.93^\circ$ for the smoothed frustum but $\alpha_{\mathrm{lin}} \approx 5.71^\circ$ for the linear one. As can be seen in figure 3.4(b, c) the error is largest near the inner top and bottom corners, but it remains of the order of one grid cell. This modification gives the most significant portion of the discretisation error that cannot be resolved by increasing the resolution.

A.3 Frequency filter

In order to decompose flow structures by their time scales, the simulation data is Fourier-filtered after letting the system pass a transient stage. Sometimes this is referred to as viewing the system from the 'frequency domain'.

The method applied consists in mapping first-order variables velocity, vorticity, and the strain rates to grid cell centres. After that, these are mapped to an underlying cylindrical or Cartesian basis. These interpolated and mapped diagnostic fields are filtered by a running sum. At the end, the complex amplitudes are computed.

From the filtered first-order variables, the filtered second-order quantities like kinetic energy, enstrophy or helicity are computed. The procedure can be applied also to pressure, but cross-time level interpretation is generally not possible in the present implementation.

Construction of the filter

The frequency filter is a running sum over evenly-spaced time increments (not necessarily the time steps Δt), in which time slices are summed over M_σ integer periods of the selected filter frequency σ in order to minimise leakage errors. In addition, we require

$$\frac{\sigma}{M_\sigma} < \omega, \tag{A.6}$$

which means at least one libration period $T_{\mathrm{lib}} = 2\pi/\omega$ is used as time interval to compute the statistics.

The present study focuses on libration-induced flow, which is forced only with a single frequency (see equation (1.2)) and subject to a weak non-linearity (Rossby number $R \ll 1$; see equation (2.8)). When the flow is stable (not turbulent), frequency mixing due to the non-linearity yields the variability of the flow described by a harmonic series with frequencies $\sigma_l = l\omega$ as multiples of the libration frequency ω. Is *ad hoc* assumption can be exploited for the implementation of the frequency filter to aid computational efficiency. On the one hand, we can increase the filter interval to several time steps $m\Delta t$ with $m \geqslant 1$ ensuring that the sampling theorem (see Press *et al.*, 1992, pp. 494–498) is fulfilled for the highest frequency σ_{max}. On the other hand, we only need to consider harmonics of the libration frequency $\sigma = \sigma_l$, which means M_σ can be the same ($M_\sigma \equiv M = \mathrm{const.}$) when filtering at any of the harmonic frequencies.

The projection amplitudes $a_l(\boldsymbol{r})$, $b_l(\boldsymbol{r})$ of some scalar field $\psi(\boldsymbol{r},t)$ at point $\boldsymbol{r}$ and time t are obtained with the correct scale by evaluating the discrete Fourier integrals (see Bronstein *et al.*, 2005, pp. 437–443)

$$\left.\begin{aligned} a_l &= \frac{2}{MT_{\mathrm{lib}}} \int\limits_{MT_{\mathrm{lib}}} \mathrm{d}t\, \psi(t) \cos(l\omega t) \approx \frac{2}{N} \sum_{n=0}^{N-1} \psi^n \cos\frac{2\pi nl}{N}, \\ b_l &= \frac{2}{MT_{\mathrm{lib}}} \int\limits_{MT_{\mathrm{lib}}} \mathrm{d}t\, \psi(t) \sin(l\omega t) \approx \frac{2}{N} \sum_{n=0}^{N-1} \psi^n \sin\frac{2\pi nl}{N}, \end{aligned}\right\} \tag{A.7}$$

in which $\psi^n \equiv \psi(\boldsymbol{r}, t^n)$ is taken at the discrete time level t^n with $n = 0, 1, \ldots, N-1$ recorded in the statistically stationary state. A constant time step Δt (see section 3.4) aids accuracy by using the Fourier quadrature points. Typical integration lengths used in this work have been in the range $4 \leqslant M \leqslant 16$. A longer time interval has been used for the parameters the libration-induced flow exhibits instability.

From $a_l(\boldsymbol{r})$ and $b_l(\boldsymbol{r})$ the real-valued amplitudes $A_l(\boldsymbol{r}) \geqslant 0$ and phases $\theta_l(\boldsymbol{r}) \in [-\pi, \pi)$ are obtained from

$$\left.\begin{aligned} A_l &= \sqrt{a_l^2 + b_l^2}, \quad \theta_l = \arctan\left(\frac{b_l}{a_l}\right) && \text{for} \quad l \geqslant 1, \\ A_0 &= \frac{1}{N} \sum_{n=0}^{N-1} \psi^n, \quad \theta_0 \equiv 0 && \text{for} \quad l = 0, \end{aligned}\right\} \tag{A.8}$$

where $l = 0$ corresponds to the temporal average or the mean flow. For later use, one has the complex amplitudes $\hat{c}_l(\boldsymbol{r})$ given by

$$\hat{c}_l = A_l\, \mathrm{e}^{\mathrm{i}\theta_l}. \tag{A.9}$$

Such a statistical analysis is generally feasible by an online evaluation of the filter, where frequencies need to be selected before the simulation. For stable flow, an implementation as post-processing step has been found feasible and flexible since sampling can be performed at an increased time interval. The post-processing tool developed can be applied to any series of output files stored from the simulation in the VTK format (for the VTK format description see Schroeder *et al.*, 2004, 2010).

Quadratic and second-order quantities

Let the product $\phi\psi$ denote the real-valued second-order quantity, for example, contributions to the kinetic energy (v_z^2), enstrophy (ζ_z^2) or helicity $(v_z\zeta_z)$. Let further $(\phi\psi)_\sigma$ denote the *time-averaged contribution filtered at the frequency* σ, which is real-valued and therefore lacks the hat $(\hat{})$. Using the short form $(\phi\psi)_\sigma$ implies computation of the filtered second-order quantity from purely time-harmonic (filtered) input, that is,

$$(\phi\psi)_\sigma := \frac{1}{T_\sigma} \int\limits_{T_\sigma} \mathrm{d}t\, \mathrm{Re}\left(\hat{\phi}_\sigma\, \mathrm{e}^{\mathrm{i}\sigma t}\right) \mathrm{Re}\left(\hat{\psi}_\sigma\, \mathrm{e}^{\mathrm{i}\sigma t}\right), \tag{A.10}$$

in which T_σ denotes an appropriate time interval for the computation of the statistical quantity (see the previous section).

The computation can be made more efficient when complex amplitudes are used. Substituting $\mathrm{Re}(\hat{\psi}_\sigma) = (\hat{\psi}_\sigma + \hat{\psi}_\sigma^\dagger)/2$ into equation (A.10), and using that $(\hat{\phi}_\sigma\hat{\psi}_\sigma)^\dagger = \hat{\psi}_\sigma^\dagger\hat{\phi}_\sigma^\dagger$ (Bronstein *et al.*, 2005, pp. 34–38) yields

$$(\phi\psi)_\sigma = \frac{1}{2T_\sigma}\int\limits_{T_\sigma} \mathrm{d}t\,\mathrm{Re}\left(\hat{\phi}_\sigma\hat{\psi}_\sigma\,\mathrm{e}^{\mathrm{i}2\sigma t}\right) + \frac{1}{2T_\sigma}\int\limits_{T_\sigma} \mathrm{d}t\,\mathrm{Re}\left(\hat{\phi}_\sigma^\dagger\hat{\psi}_\sigma\right) = \frac{1}{2}\mathrm{Re}\left(\hat{\phi}_\sigma^\dagger\hat{\psi}_\sigma\right). \tag{A.11}$$

The first term in the latter equation vanishes under integral over $T_\sigma = 2\pi M_\sigma/\sigma$ ($M_\sigma = 1, 2, \ldots$). As before, σ may be replaced by $l\omega$ ($l = 0, 1, 2, \ldots$) for the frequency comb, which means $T_\sigma = MT_{\mathrm{lib}}$ is an integer multiple of the libration period $T_{\mathrm{lib}} = 2\pi/\omega$.

Bibliography

K. Akselvoll & P. Moin (1996). 'An efficient method for temporal integration of the Navier–Stokes equations in confined axisymmetric geometries'. *Journal of Computational Physics*, **125**(2), pp. 454–463. DOI: 10.1006/jcph.1996.0107.

T. Albrecht, H. M. Blackburn, J. M. Lopez, R. Manasseh & P. Meunier (2015). 'Triadic resonances in precessing rapidly rotating cylinder flows'. *Journal of Fluid Mechanics*, **778**(R1), pp. 1–11. DOI: 10.1017/jfm.2015.377.

K. D. Aldridge & I. Lumb (1987). 'Inertial waves identified in the Earth's fluid outer core'. *Nature*, **325**(6103), pp. 421–423. DOI: 10.1038/325421a0.

C. D. Andereck, S. S. Liu & H. L. Swinney (1986). 'Flow regimes in a circular Couette system with independently rotating cylinders'. *Journal of Fluid Mechanics*, **164**, pp. 155–183. DOI: 10.1017/S0022112086002513.

E. Anderson, Z. Bai, C. Bischof, S. Blackford, J. Demmel, J. Dongarra, J. Du Croz, A. Greenbaum, S. Hammarling, A. McKenney & D. Sorensen (1999). *LAPACK Users' Guide*. Society for Industrial and Applied Mathematics, 3rd edn. ISBN 0-89871-447-8 (paperback). Last accessed: 2015/04/10, URL: `http://www.netlib.org/lapack/`.

A. Arakawa & V. R. Lamb (1977). 'Computational design of the basic dynamical processes of the UCLA general circulation model'. *Methods of Computational Physics*, **17**, pp. 173–265.

G. B. Arfken & H. J. Weber (2005). *Mathematical Methods for Physicists*. Elsevier, 6th edn.

M. P. Baldwin, L. J. Gray, T. J. Dunkerton, K. Hamilton, P. H. Haynes, W. J. Randel, J. R. Holton, M. J. Alexander, I. Hirota, T. Horinouchi, D. B. A. Jones, J. S. Kinnersley, C. Marquardt, K. Sato & M. Takahashi (2001). 'The Quasi-Biennial Oscillation'. *Reviews of Geophysics*, **39**(2), pp. 179–229.

C. Baruteau & M. Rieutord (2013). 'Inertial waves in a differentially rotating spherical shell'. *Journal of Fluid Mechanics*, **719**, pp. 47–81. DOI: 10.1017/jfm.2012.605.

G. K. Batchelor (1967). *An Introduction to Fluid Dynamics*. Cambridge University Press.

R. C. Beardsley (1970). 'An experimental study of inertial waves in a closed cone'. *Studies in Applied Mathematics*, **49**, pp. 187–196.

J. Boisson, C. Lamriben, L. R. M. Maas, P.-P. Cortet & F. Moisy (2012). 'Inertial waves and modes excited by the libration of a rotating cube'. *Physics of Fluids*, **24**, 076602. DOI: 10.1063/1.4731802.

I. D. Borcia, A. Ghasemi V. & U. Harlander (2014). 'Inertial wave mode excitation in a rotating annulus with partially librating boundaries'. *Fluid Dynamics Research*, **46**, 041423. DOI: 10.1088/0169-5983/46/4/041423.

I. D. Borcia & U. Harlander (2012). 'Inertial waves in a rotating annulus with inclined inner cylinder: comparing the spectrum of wave attractor frequency bands and the eigenspectrum in the limit of zero inclination'. *Theoretical and Computational Fluid Dynamics*, **27**, pp. 397–413. DOI: 10.1007/s00162-012-0278-6.

J. Boussinesq (1877). 'Essai sur la théorie des eaux courantes'. *Méemoires présent és par divers savants à l'Académie des Sciences*, **XXIII**(1), pp. 1–680.

F. P. Bretherton (1964). 'Low frequency oscillations trapped near the equator'. *Tellus*, **16**, pp. 181–185.

I. N. Bronstein, K. A. Semendjajew, G. Musiol & H. Mühlig (2005). *Taschenbuch der Mathematik*. Harri Deutsch, 6th edn.

D. L. Brown, R. Cortez & M. L. Minion (2001). 'Accurate projection methods for the incompressible Navier–Stokes equations'. *Journal of Computational Physics*, **168**(2), pp. 464–499. DOI: 10.1006/jcph.2001.6715.

E. Buckingham (1914). 'On physically similar systems; illustrations of the use of dimensional equations'. *Physical Review*, **4**, pp. 345–376. DOI: 10.1103/PhysRev.4.345.

F. H. Busse (2010). 'Mean zonal flows generated by librations of a rotating spherical cavity'. *Journal of Fluid Mechanics*, **650**, pp. 505–512. DOI: 10.1017/S0022112010000753.

F. H. Busse (2011). 'Zonal flow induced by longitudinal librations of a rotating cylindrical cavity'. *Physica D Nonlinear Phenomena*, **240**(2), pp. 208–211. DOI: 10.1016/j.physd.2010.09.010.

F. H. Busse, E. Dormy, R. Simitev & A. M. Soward (2007). *Mathematical Aspects of Natural Dynamos*. Grenoble Sciences and CRC Press.

M. A. Calkins, J. Noir, J. D. Eldredge & J. M. Aurnou (2010). 'Axisymmetric simulations of libration-driven fluid dynamics in a spherical shell geometry'. *Physics of Fluids*, **22**(8), 086602. DOI: 10.1063/1.3475817.

A. Campagne, B. Gallet, F. Moisy & P. Cortet (2015). 'Disentangling inertial waves from eddy turbulence in a forced rotating-turbulence experiment'. *Physical Review E*, **91**, 043016. DOI: 10.1103/PhysRevE.91.043016.

C. Canuto, M. Y. Hussaini, A. Quarteroni & T. A. Zang (2006). *Spectral Methods; Fundamentals in Single Domains*. Springer.

M. E. Cartan (1922). 'Sur les petites oscillations d'une masse de fluide'. *Bulletin des Sciènces Mathématiques*, **46**, pp. 317–369.

H. Choi (1993). *Turbulent drag reduction: studies of feedback control and flow over riblets*. Ph.D. thesis, Stanford University, Stanford, CA.

H. Choi, P. Moin & J. Kim (1992). 'Turbulent drag reduction: studies of feedback control and flow over riblets'. Tech. Rep. TF-55, Department of Mechanical Engineering, Stanford University, Stanford, CA.

H. Choi, P. Moin & J. Kim (1993). 'Direct numerical simulations of turbulent-flow over riblets'. *Journal of Fluid Mechanics*, **255**, pp. 503–539. DOI: 10.1017/S0022112093002575.

A. J. Chorin (1968). 'Numerical solution of the Navier–Stokes equations'. *Mathematics of Computation*, **22**(104), pp. 745–762.

R. L. Comstock & B. G. Bills (2003). 'A solar system survey of forced librations in longitude'. *Journal of Geophysical Research*, **108**(E9), pp. 5100. DOI: 10.1029/2003JE002100.

P.-P. Cortet, C. Lamriben & F. Moisy (2010). 'Viscous spreading of an inertial wave beam in a rotating fluid'. *Physics of Fluids*, **22**, 086603. DOI: 10.1063/1.3483468.

R. Courant, K. Friedrichs & H. Lewy (1928). 'Über die partiellen Differenzengleichungen der mathematischen Physik'. *Mathematische Annalen*, **100**, pp. 32–74. DOI: 10.1007/BF01448839.

O. Czarny, E. Serre, P. Bontoux & R. M. Lueptow (2003). 'Interaction between Ekman pumping and the centrifugal instability in Taylor–Couette flow'. *Physics of Fluids*, **15**(2), pp. 467–477. DOI: 10.1063/1.1534108.

P. A. Davidson (2013). *Turbulence in Rotating, Stratified and Electrically Conducting Fluids*. Cambridge University Press. ISBN 978-1-107-02686-5. DOI: 10.1007/978-1-4419-6412-0.

P. A. Davidson (2014). 'The dynamics and scaling laws of planetary dynamos driven by inertial waves'. *Geophysical Journal International*, **198**(3), pp. 1832–1847. DOI: 10.1093/gji/ggu220.

Y. Duguet, J. F. Scott & L. L. Penven (2006). 'Oscillatory jets and instabilities in a rotating cylinder'. *Physics of Fluids*, **18**(10), 104104. DOI: 10.1063/1.2357973.

D. R. Durran (2010). *Numerical Methods in Fluid Dynamics with Applications to Geophysics*. Texts in Applied Mathematics 32. Springer, 2nd edn. ISBN 978-1-4419-6411-3. DOI: 10.1007/978-1-4419-6412-0.

V. W. Ekman (1905). 'On the influence of Earth's rotation on ocean currents'. *Arkiv för Matematik, Astronomi och Fysik*, **2**, pp. 1–52.

M. Frigo & S. G. Johnson (1997). 'FFTW'. Online. Last accessed: 2015/02/25, URL: `http://www.fftw.org/`.

M. Frigo & S. G. Johnson (2005). 'The design and implementation of FFTW3'. *Proceedings of the IEEE*, **93**(2), pp. 216–231. Invited paper, Special Issue on Program Generation, Optimization, and Platform Adaptation.

T. Gal-Chen & R. C. J. Somerville (1975a). 'Numerical solution of the Navier–Stokes equations with topography'. *Journal of Computational Physics*, **17**, pp. 276–310. DOI: 10.1016/0021-9991(75)90054-6.

T. Gal-Chen & R. C. J. Somerville (1975b). 'On the use of a coordinate transformation for the solution of the Navier–Stokes equations'. *Journal of Computational Physics*, **17**, pp. 209–228. DOI: 10.1016/0021-9991(75)90037-6.

T. Gerkema (2006). 'Internal-wave reflection from uniform slopes: higher harmonics and coriolis effects'. *Nonlinear Processes in Geophysics*, **13**, pp. 265–273. URL: `www.nonlin-processes-geophys.net/13/265/2006/`.

A. Ghasemi V. (2016). *Mean flow generation in librating annular cavities*. Ph.D. thesis, Fak. 2, Brandenburgische Technische Universität Cottbus - Senftenberg, Cottbus, Germany.

A. Ghasemi V., M. Klein, U. Harlander, M. V. Kurgansky, E. Schaller & A. Will (2016). 'Mean flow generation by görtler vortices in a rotating annulus with librating sidewalls'. *Physics of Fluids*, **28**(5), 056603. DOI: 10.1063/1.4948406.

D. Goldberg (1991). 'What every computer scientist should know about floating-point arithmetic'. *ACM Computing Surveys (CSUR)*, **23**(1), pp. 5–48.

L. Gostiaux, T. Dauxois, H. Didelle, J. Sommeria & S. Viboux (2006). 'Quantitative laboratory observations of internal wave reflection on ascending slopes'. *Physics of Fluids*, **18**, 056602.

H. P. Greenspan (1969). *The Theory of Rotating Fluids*. Cambridge Monographs on Mechanics and Applied Mathematics. Cambridge University Press. Reprint with corrections.

P. M. Gresho & R. L. Sani (1987). 'On pressure boundary conditions for the incompressible Navier–Stokes equations'. *International Journal for Numerical Methods in Fluids*, **7**, pp. 1111–1145. DOI: 10.1002/fld.1650071008.

U. Grigull, J. Straub & P. Schiebener (1990). *Steam Tables in SI-Units / Wasserdampftafeln*. Springer.

U. Harlander (2008). 'Towards an analytical understanding of internal wave attractors'. *Advances in Geosciences*, **15**, pp. 3–9.

U. Harlander & L. R. M. Maas (2006). 'Characteristics and energy rays of equatorially trapped, zonally symmetric internal waves'. *Meteorologische Zeitschrift*, **15**, pp. 439–450. DOI: 10.1127/0941-2948/2006/0139.

U. Harlander & L. R. M. Maas (2007). 'Two alternatives for solving hyperbolic boundary value problems of geophysical fluid dynamics'. *Journal of Fluid Mechanics*, **588**, pp. 331–351. DOI: 10.1017/S0022112007007574.

F. H. Harlow & J. E. Welch (1965). 'Numerical calculation of time-dependent viscous incompressible flow of fluid with free surface'. *The Physics of Fluids*, **8**(12), pp. 2182–2189.

J. Hazewinkel, L. R. M. Maas & S. B. Dalziel (2008). 'Observations on the wavenumber spectrum and evolution of an internal wave attractor'. *Journal of Fluid Mechanics*, **598**, pp. 373–382. DOI: 10.1017/S0022112007000031.

G. A. Henderson & K. D. Aldridge (1992). 'A finite-element method for inertial waves in a frustum'. *Journal of Fluid Mechanics*, **234**, pp. 317–327. DOI: 10.1017/S0022112092000806.

E. Høiland (1962). 'Discussion of a hyperbolic equation relating to inertia and gravitational fluid oscillations'. *Geofysiske Publikasjoner*, **24**, pp. 211–227.

R. Hollerbach & A. Fournier (2004). 'End-effects in rapidly rotating cylindrical taylor–couette flow'. In R. Rosner, G. Rüdiger & A. Bonanno, eds., 'MHD Couette Flows: Experiments and Models', vol. 733, pp. 114–121.

R. Hollerbach & R. R. Kerswell (1995). 'Oscillatory internal shear layers in rotating and precessing flows'. *Journal of Fluid Mechanics*, **298**, pp. 327–339.

B. M. Jaworski & A. A. Detlaf (1972). *Physik Griffbereit*, vol. 1. Vieweg.

L. Jouve & G. I. Ogilvie (2014). 'Direct numerical simulations of an inertial wave attractor in linear and nonlinear regimes'. *Journal of Fluid Mechanics*, **745**, pp. 223–250. DOI: 10.1017/jfm.2014.63.

H.-J. Kaltenbach, M. Fatica, R. Mittal, T. S. Lund & P. Moin (1999). 'Study of flow in a planar asymmetric diffuser using large-eddy simulation'. *Journal of Fluid Mechanics*, **390**, pp. 151–185.

H.-J. Kaltenbach & A. Hauschild (2004). 'Documentation of an incompressible fully-conservative Navier–Stokes solver in generalized coordinates with rotational symmetry'. Documentation of HYBRID-NEW, axial diffuser version.

H.-J. Kaltenbach, A. Will, M. Klein & A. Ghasemi V. (2014). 'Documentation of an incompressible fully-conservative Navier–Stokes solver in generalized coordinates with rotational symmetry'. Documentation of HYBRID-NEW (version 3.9).

R. R. Kerswell (1995). 'On the internal shear layers spawned by the critical regions in oscillatory Ekman boundary layers'. *Journal of Fluid Mechanics*, **298**, pp. 311–325. DOI: 10.1017/S0022112095003326.

R. R. Kerswell (1999). 'Secondary instabilities in rapidly rotating fluids: inertial wave breakdown'. *Journal of Fluid Mechanics*, **382**, pp. 283–306. DOI: 10.1017/S0022112098003954.

R. R. Kerswell (2002). 'Elliptical instability'. *Annual Review of Fluid Mechanics*, **34**, pp. 83–113.

J. Kim & P. Moin (1985). 'Application of a fractional-step method to incompressible Navier–Stokes equations'. *Journal of Computational Physics*, **59**(2), pp. 308–323. DOI: 10.1016/0021-9991(85)90148-2.

M. Klein (2014a). 'Navier–Stokes equations in non-inertial systems and generalized coordinates'. Extension of the documentation of HYBRID-NEW (version 3.9).

M. Klein (2014b). 'User's Guide to HYBRID-NEW'. Technical documentation and usage of the script environment.

M. Klein, T. Seelig, M. V. Kurgansky, A. Ghasemi V., I. D. Borcia, A. Will, E. Schaller, C. Egbers & U. Harlander (2014). 'Inertial wave excitation and focusing in a liquid bounded by a frustum and a cylinder'. *Journal of Fluid Mechanics*, **751**, pp. 255–297. DOI: 10.1017/jfm.2014.304.

S. Koch, U. Harlander, C. Egbers & R. Hollerbach (2013). 'Inertial waves in a spherical shell induced by librations of the inner sphere: Experimental and numerical results'. *Fluid Dynamics Research*, **45**(3), 035504. DOI: 10.1088/0169-5983/45/3/035504.

A. N. Kolmogorov (1941). 'The local structure of turbulence in incompressible viscous fluid for very large Reynolds numbers'. *Doklady Akademii Nauk SSSR*, **30**(4), pp. 299–303.

M. V. Kurgansky (2002). *Adiabatic Invariants in Large-Scale Atmospheric Dynamics*. Taylor & Francis. ISBN 0-415-28415-5.

K. Kuttler (2011). *Calculus: Theory and Applications*, vol. 2. World Scientific.

F.-P. R. Lam & L. R. M. Maas (2008). 'Internal wave focusing revisited; a reanalysis and new theoretical links'. *Fluid Dynamics Research*, **40**, pp. 95–122. DOI: 10.1016/j.fluiddyn.2007.02.003.

L. D. Landau & E. M. Lifshitz (1987). *Fluid Mechanics*, vol. 6 of *Course of Theoretical Physics*. Pergamon Press, 2nd edn.

H. Le & P. Moin (1991). 'An improvement of fractional step methods for the incompressible Navier–Stokes equations'. *Journal of Computational Physics*, **92**(2), pp. 369–379.

R. J. LeVeque (2007). *Finite Difference Methods for Ordinary and Partial Differential Equations: Steady-State and Time-Dependent Problems*. Society for Industrial and Applied Mathematics (SIAM). ISBN 978-0-898716-29-0.

J. Lighthill (1978). *Waves in Fluids*. Cambridge University Press.

R. S. Lindzen (1990). *Dynamics in Atmospheric Physics*. Cambridge University Press. ISBN 978-0-521-01821-0.

J. M. Lopez & F. Marques (2011). 'Instabilities and inertial waves generated in a librating cylinder'. *Journal of Fluid Mechanics*, **687**, pp. 171–193. DOI: 10.1017/jfm.2011.378.

J. M. Lopez & F. Marques (2014). 'Rapidly rotating cylinder flow with an oscillating sidewall'. *Physical Review E*, **89**, 013013. DOI: 10.1103/PhysRevE.89.013013.

J. M. Lopez & F. Marques (2015). 'Precession of a rapidly rotating cylinder flow: traverse through resonance'. *Journal of Fluid Mechanics*, **782**, pp. 63–98. DOI: 10.1017/jfm.2015.524.

Lord Kelvin (1880). 'Vibrations of a columnar vortex'. *Philosophical Magazine*, **10**, pp. 155–168.

T. S. Lund & H.-J. Kaltenbach (1995). 'Experiments with explicit filtering for LES using a finite-difference method'. Tech. Rep. Annual Research Briefs 1995, Center for Turbulence Research, Stanford, CA.

H. Luo & T. R. Bewley (2004). 'On the contravariant form of the Navier–Stokes equations in time-dependent curvilinear coordinate systems'. *Journal of Computational Physics*, **199**, pp. 355–375.

L. R. M. Maas (2001). 'Wave focusing and ensuing mean flow due to symmetry breaking in rotating fluids'. *Journal of Fluid Mechanics*, **437**, pp. 13–28.

L. R. M. Maas (2003). 'On the amphidromic structure of inertial waves in a rectangular parallelepiped'. *Fluid Dynamics Research*, **33**, pp. 373–401. DOI: 10.1016/j.fluiddyn.2003.08.003.

L. R. M. Maas (2005). 'Wave attractors: linear yet nonlinear'. *International Journal of Bifurcation and Chaos*, **15**(9), pp. 2757–2782. DOI: 10.1142/S0218127405013733.

L. R. M. Maas (2009). 'Exact analytic self-similar solution of a wave attractor field'. *Physica D Nonlinear Phenomena*, **238**, pp. 502–505. DOI: 10.1016/j.physd.2008.11.006.

L. R. M. Maas, D. Benielli, J. Sommeria & F.-P. A. Lam (1997). 'Observation of an internal wave attractor in a confined stably-stratified fluid'. *Nature*, **388**, pp. 557–561.

L. R. M. Maas & F.-P. A. Lam (1995). 'Geometric focusing of internal waves'. *Journal of Fluid Mechanics*, **300**, pp. 1–41. DOI: 10.1017/S0022112095003582.

L. R. M. Maas & J. J. M. van Haren (1987). 'Observations on the vertical structure of tidal and inertial currents in the central North Sea'. *Journal of Marine Research*, **45**, pp. 293–318.

N. Machicoane, P.-P. Cortet, B. Voisin & F. Moisy (2015). 'Influence of the multipole order of the source on the decay of an inertial wave beam in a rotating fluid'. *Physics of Fluids*, 066602. DOI: 10.1063/1.4922735.

W. V. R. Malkus (1968). 'Precession of the Earth as the cause of geomagnetism'. *Science*, **160**(3825), pp. 259–264.

A. M. M. Manders & L. R. M. Maas (2003). 'Observations of inertial waves in a rectangular basin with one sloping boundary'. *Journal of Fluid Mechanics*, **493**, pp. 59–88. DOI: 10.1017/S0022112003005998.

A. M. M. Manders & L. R. M. Maas (2004). 'On the three-dimensional structure of the inertial wave field in a rectangular basin with one sloping boundary'. *Fluid Dynamics Research*, **35**, pp. 1–21. DOI: 10.1016/j.fluiddyn.2004.03.004.

P. S. Marcus (1984). 'Simulation of Taylor–Couette flow. Part 2. Numerical results for wavy-vortex flow with one travelling wave'. *Journal of Fluid Mechanics*, **146**, pp. 65–113.

D. M. Mason & R. R. Kerswell (1999). 'Nonlinear evolution of the elliptical instability: an example of inertial wave breakdown'. *Journal of Fluid Mechanics*, **396**, pp. 73–108.

A. D. McEwan (1970). 'Inertial oscillations in a rotating fluid cylinder'. *Journal of Fluid Mechanics*, **40**(3), pp. 603–640.

L. Messio, C. Morize, M. Rabaud & F. Moisy (2008). 'Experimental observation using particle image velocimetry of inertial waves in a rotating fluid'. *Experiments in Fluids*, **44**, pp. 519–528. DOI: 10.1007/s00348-007-0410-3.

H. K. Moffatt (1964). 'Viscous and resistive eddies near a sharp corner'. *Journal of Fluid Mechanics*, **18**(1), pp. 1–18.

H. K. Moffatt (1969). 'The degree of knottedness of tangled vortex lines'. *Journal of Fluid Mechanics*, **35**(1), pp. 117–129.

P. Moin & K. Mahesh (1998). 'Direct numerical simulation: A tool in turbulence research'. *Annual Review of Fluid Mechanics*, **30**, pp. 539–578. DOI: 10.1146/annurev.fluid.30.1.539.

Y. Morinishi, T. S. Lund, V. O. Vasilyev & P. Moin (1998). 'Fully conservative higher order finite difference schemes for incompressible flow'. *Journal of Computational Physics*, **143**(1), pp. 90–124. DOI: 10.1006/jcph.1998.5962.

Y. Nambu (1973). 'Generalized Hamiltonian dynamics'. *Physical Review E*, **7**(8), pp. 2405–2412.

P. Névir (1998). *Die Nambu-Felddarstellung der Hydro-Thermodynamik und ihre Bedeutung für die dynamische Meteorologie*. Habilitationsschrift, FB Geowissenschaften, Freie Universität Berlin.

P. Névir & R. Blender (1993). 'A Nambu representation of incompressible hydrodynamics using helicity and enstrophy'. *Journal of Physics A: Mathematical and General*, **26**, pp. L1189–L1193.

P. Névir & M. Sommer (2009). 'Energy-vorticity theory of ideal fluid mechanics'. *Journal of the Atmospheric Sciences*, **66**, pp. 2073–2084. DOI: 10.1175/2008JAS2897.1.

J. Noir, M. A. Calkins, M. Lasbleis, J. Cantwell & J. M. Aurnou (2010). 'Experimental study of libration-driven zonal flows in a straight cylinder'. *Physics of the Earth and Planetary Interiors*, **182**, pp. 98–106. DOI: 10.1016/j.pepi.2010.06.012.

J. Noir, D. Cébron, M. Le Bars, A. Sauret & J. M. Aurnou (2012). 'Experimental study of libration-driven zonal flows in non-axisymmetric containers'. *Physics of the Earth and Planetary Interiors*, **204–205**, pp. 1–10. DOI: 10.1016/j.pepi.2012.05.005.

J. Noir, F. Hemmerlin, J. Wicht, S. M. Baca & J. M. Aurnou (2009). 'An experimental and numerical study of librationally driven flow in planetary cores and subsurface oceans'. *Physics of the Earth and Planetary Interiors*, **173**, pp. 141–152. DOI: 10.1016/j.pepi.2008.11.012.

J. Noir, D. Jault & P. Cardin (2001). 'Numerical study of the motions within a slowly precessing sphere at low Ekman number'. *Journal of Fluid Mechanics*, **437**, pp. 283–299.

G. I. Ogilvie (2005). 'Wave attractors and the asymptotic dissipation rate of tidal disturbances'. *Journal of Fluid Mechanics*, **543**, pp. 19–44.

G. I. Ogilvie & D. N. C. Lin (2004). 'Tidal dissipation in rotating giant planets'. *The Astrophysical Journal*, **610**, pp. 477–509.

P. Orlandi (2000). *Fluid Flow Phenomena: A Numerical Toolkit*. Kluwer.

S. A. Orszag (1971). 'On the elimination of aliasing in finite-difference schemes by filtering high-wavenumber components'. *Journal of the Atmospheric Sciences*, **28**, pp. 1074.

S. A. Orszag & G. S. Patterson, Jr. (1972). 'Numerical simulation of three dimensional homogeneous isotropic turbulence'. *Physical Review Letters*, **28**, pp. 76–79.

E. Ott (1993). *Chaos in Dynamical Systems*. Cambridge University Press.

T. Peacock & A. Tabaei (2005). 'Visualization of nonlinear effects in reflecting internal wave beams'. *Physics of Fluids*, **17**, 061702. DOI: 10.1063/1.1932309.

J. Pedlosky (1987). *Geophysical Fluid Dynamics*. Springer, 2nd edn.

J. Pedlosky & H. P. Greenspan (1967). 'A simple laboratory model for the oceanic circulation'. *Journal of Fluid Mechanics*, **27**, pp. 291–304.

J. B. Perot (1993). 'An analysis of the fractional step method'. *Journal of Computational Physics*, **108**, pp. 51–58.

O. M. Phillips (1963). 'Energy transfer in rotating fluids by reflection of inertial waves'. *Physics of Fluids*, **6**(4), pp. 513–520. DOI: 10.1063/1.1706766.

R. A. Plumb & A. D. McEwan (1978). 'The instability of a forced standing wave in a viscous stratified fluid: A laboratory analogue of the Quasi-Biennial Oscillation'. *Journal of Atmospheric Sciences*, **35**, pp. 1827–1839.

S. B. Pope (2000). *Turbulent Flows*. Cambridge University Press.

D. Prandle (1982). 'The vertical structure of tidal currents and other oscillatory flows'. *Continental Shelf Research*, **1**(2), pp. 191–207.

W. H. Press, S. A. Teukolsky, W. T. Vetterling & B. P. Flannery (1992). *Numerical Recipes in Fortran 77: The Art of Scientific Computing*, vol. 1. Cambridge University Press, 2nd edn. Last accessed: 2012/12/03, URL: `http://www.nr.com/oldverswitcher.html`.

W. H. Press, S. A. Teukolsky, W. T. Vetterling & B. P. Flannery (1996). *Numerical Recipes in Fortran 90: The Art of Parallel Scientific Computing*, vol. 2. Cambridge University Press, 2nd edn. Last accessed: 2012/12/03, URL: `http://www.nr.com/oldverswitcher.html`.

A. Rabitti & L. R. M. Maas (2013). 'Meridional trapping and zonal propagation of inertial waves in a rotating fluid shell'. *Journal of Fluid Mechanics*, **729**, pp. 445–470. DOI: 10.1017/jfm.2013.310.

A. Rabitti & L. R. M. Maas (2014). 'Inertial wave rays in rotating spherical fluid domains'. *Journal of Fluid Mechanics*, **758**, pp. 621–654. DOI: 10.1017/jfm.2014.551.

M. M. Rai & P. Moin (1991). 'Direct simulations of turbulent-flow using finite-difference schemes'. *Journal of Computational Physics*, **96**(1), pp. 15–53.

M. Rieutord, B. Georgeot & L. Valdettaro (2001). 'Inertial waves in a rotating spherical shell: Attractors and asymptotic spectrum'. *Journal of Fluid Mechanics*, **435**, pp. 103–144. `arXiv:physics/0007007`.

M. Rieutord, S. A. Triana, D. S. Zimmerman & D. P. Lathrop (2012). 'On the excitation of inertial modes in an experimental spherical Couette flow'. *Physical Review E*, **86**, 026304.

M. Rieutord & L. Valdettaro (1997). 'Inertial waves in a rotating spherical shell'. *Journal of Fluid Mechanics*, **341**, pp. 77–99.

M. Rieutord & L. Valdettaro (2010). 'Viscous dissipation by tidally forced inertial modes in a rotating spherical shell'. *Journal of Fluid Mechanics*, **643**, pp. 363–394.

P. J. Roache (1998). *Fundamentals of Computational Fluid Dynamics*. Hermosa. ISBN 0-913478-09-1.

M. Roberts & J. C. Bowman (2011). 'Dealiased convolutions for pseudospectral simulations'. *Journal of Physics: Conference Series*, **318**(7), 072037. DOI: 10.1088/1742-6596/318/7/072037.

R. S. Rogallo (1981). 'Numerical experiments in homogeneous turbulence'. Tech. Rep. NASA-TM-81315, Thermosciences Division, Department of Mechanical Engineering, Stanford University, NASA Ames, CA.

M. Rosenfeld, D. Kwak & M. Vinokur (1991). 'A fractional step solution method for the unsteady incompressible Navier–Stokes equations in generalized coordinate systems'. *Journal of Computational Physics*, **94**(1), pp. 102–137. DOI: 10.1016/0021-9991(91)90139-C.

C. G. Rossby (1939). 'Relation between variations in the intensity of the zonal circulation of the atmosphere and the displacements of the semipermanent centers of action'. *Journal of Marine Research*, **2**, pp. 38–55. [Reprinted in: B. Saltzman (1962): 'Selected Papers on the Theory of Thermal Convection'. New York, Dover.].

R. Salmon (1998). *Lectures on Geophysical Fluid Dynamics*. Oxford University Press.

S. Salon & V. Armenio (2011). 'A numerical investigation of the turbulent Stokes–Ekman bottom boundary layer'. *Journal of Fluid Mechanics*, **684**, pp. 316–352. DOI: 10.1017/jfm.2011.303.

A. Sauret, D. Cébron & M. Le Bars (2013). 'Sponateous generation of inertial waves from boundary turbulence in a librating sphere'. *Journal of Fluid Mechanics*, **728**(R5), pp. 1–11. DOI: 10.1017/jfm.2013.320.

A. Sauret, D. Cébron, M. Le Bars & S. Le Dizès (2012). 'Fluid flows in a librating cylinder'. *Physics of Fluids*, **24**, 026603. DOI: 10.1063/1.3680874.

A. Sauret & S. Le Dizès (2013). 'Libration-induced mean flow in a spherical shell'. *Journal of Fluid Mechanics*, **718**, pp. 181–209. DOI: 10.1017/jfm.2012.604.

H. Schade (1997). *Tensoranalysis*. Walter de Gruyter.

W. Schroeder, K. Martin & B. Lorensen (2004). *File Formats for VTK version 4.2 (taken from VTK user's guide)*. Kitware Inc. Last accessed: 2011/11/28, URL: `http://www.vtk.org/VTK/img/file-formats.pdf`.

W. Schroeder, K. Martin & B. Lorensen (2010). *VTK User's Guide*. Kitware Inc., 11th edn. ISBN 1930934238.

T. Seelig (2014). *Inertial wave propagation, focusing and mean flow excitation: Theory and experiments*. Ph.D. thesis, Fak. 3, Brandenburgische Technische Universität Cottbus - Senftenberg, Cottbus, Germany.

K. Stewartson & J. A. Rickard (1969). 'Pathological oscillations of a rotating fluid'. *Journal of Fluid Mechanics*, **35**, pp. 759–773.

G. G. Stokes (1851). 'On the effect of the internal friction in fluids on the motion of pendulums'. *Transactions of the Cambridge Philosophical Society*, **9**, pp. 8.

A. Swart, A. Manders, U. Harlander & L. R. M. Maas (2010). 'Experimental observation of strong mixing due to internal wave focusing over sloping terrain'. *Dynamics of Atmospheres and Oceans*, **50**, pp. 16–34. DOI: 10.1016/j.dynatmoce.2009.08.003.

A. Tabaei, T. R. Akylas & K. G. Lamb (2005). 'Nonlinear effects in reflecting and colliding internal wave beams'. *Journal of Fluid Mechanics*, **526**, pp. 217–243. DOI: 10.1017/S0022112004002769.

J.-M. Teuler (1998). 'JMFFT – J.-M. Fast Fourier Transforms'. Online. Last accessed: 2015/02/24, URL: `http://www.idris.fr/data/publications/JMFFT/`.

The OpenMP ARB (2008). 'The OpenMP API: Specification for Parallel Programming'. Online. Last accessed: 2015/03/24, URL: `http://openmp.org/`.

J. E. Thompson, Z. U. A. Warsi & C. W. Mastin (1985). *Numerical Grid Generation: Foundations and Applications*. North-Holland.

R. O. R. Y. Thompson (1979). 'A mechanism for angular momentum mixing'. *Geophysical and Astrophysical Fluid Dynamics*, pp. 221–234.

H. Thorade (1928). 'Gezeitenuntersuchungen in der Deutschen Bucht der Nordsee'. *Deutsche Seewarte*, **46**(3), pp. 1–85.

A. Tilgner (1999). 'Driven inertial oscillations in spherical shells'. *Physical Review E*, **59**, pp. 1789–1794.

A. Tilgner (2007). 'Zonal wind driven by inertial modes'. *Physical Review Letters*, **99**(19), 194501. DOI: 10.1103/PhysRevLett.99.194501.

A. Tilgner (2008). 'Dynamo action with wave motion'. *Physical Review Letters*, **100**, 128501. DOI: 10.1103/PhysRevLett.100.128501.

A. Tilgner & F. H. Busse (2001). 'Fluid flows in precessing spherical shells'. *Journal of Fluid Mechanics*, **426**, pp. 387–396.

J. van Kan (1986). 'A second-order accurate pressure-correction scheme for viscous incompressible flow'. *SIAM Journal of Scientific Computing*, **7**(3), pp. 870–891. DOI: 10.1137/0907059.

O. V. Vasilyev (2000). 'High order finite difference schemes on non-uniform meshes with good conservation properties'. *Journal of Computational Physics*, **157**, pp. 746–761. DOI: 10.1006/jcph.1999.6398.

R. Verzicco & P. Orlandi (1996). 'A finite-difference scheme for three-dimensional incompressible flows in cylindrical coordinates'. *Journal of Computational Physics*, **123**(2), pp. 402–414. DOI: 10.1006/jcph.1996.0033.

M. Vinokur (1974). 'Conservation equations of gasdynamics in curvilinear coordinate systems'. *Journal of Computational Physics*, **14**, pp. 105–125.

M. Vinokur (1980). 'On one-dimensional stretching functions for finite-difference calculations'. Tech. Rep. NASA CR-3313, School of Engineering, Engineering and Applied Science Research, University of Santa Clara, Santa Clara, CA.

M. Vinokur (1983). 'On one-dimensional stretching functions for finite-difference calculations'. *Journal of Computational Physics*, **50**, pp. 215–234.

C.-Y. Wang (1970). 'Cylindrical tank of fluid oscillating about a state of steady rotation'. *Journal of Fluid Mechanics*, **41**, pp. 581–592. DOI: 10.1017/S0022112070000769.

N. P. Wedi & P. Smolarkiewicz (2004). 'Extending Gal-Chen and Somerville terrain-following coordinate transformation on time-dependent curvilinear boundaries'. *Journal of Computational Physics*, **193**, pp. 1–20. DOI: 10.1016/j.jcp.2003.07.034.

N. P. Wedi & P. Smolarkiewicz (2006). 'Direct numerical simulation of the Plumb–McEwan laboratory analog of the QBO'. *Journal of the Atmospheric Sciences*, **63**, pp. 3226–3252. DOI: 10.1175/JAS3815.1.

W. W. Wood (1966). 'An oscillatory disturbance of rigidly rotating fluid'. *Proceedings of the Royal Society A*, **293**, pp. 181–212.

K. Zhang, K. H. Chan, X. Liao & J. M. Aurnou (2013). 'The non-resonant response of fluid in a rapidly rotating sphere undergoing longitudinal libration'. *Journal of Fluid Mechanics*, **720**, pp. 212–235.

Publications and presentations

Publications in peer-reviewed journals

- A. Ghasemi V., M. Klein, U. Harlander, M. V. Kurgansky, E. Schaller & A. Will (2016). 'Mean flow generation by Görtler vortices in a rotating annulus with librating side-walls'. *Phys. Fluids*, **28**(5), 056603.

- M. Klein, T. Seelig, M. V. Kurgansky, A. Ghasemi V., I. D. Borcia, A. Will, E. Schaller, C. Egbers & U. Harlander (2014). 'Inertial wave excitation and focusing in a liquid bounded by a frustum and a cylinder'. *J. Fluid Mech.*, **751**, pp. 255–297.

Presentations at international conferences

- M. Klein, A. Ghasemi V., T. Seelig, I. D. Borcia, U. Harlander & A. Will (2015). 'DNS of inertial wave attractors in a librating annulus with height-dependent gap width'. 15$^{\text{th}}$ European Turbulence Conference, Delft, The Netherlands. (oral)

- M. Klein, A. Ghasemi V., T. Seelig, I. D. Borcia, U. Harlander & A. Will (2015). 'DNS of inertial wave attractors in a librating annular cavity with a height-dependent gap'. 19$^{\text{th}}$ International Couette–Taylor Workshop, Cottbus, Germany. (oral)

- M. Klein, A. Ghasemi V., T. Seelig, I. D. Borcia, U. Harlander & A. Will (2015). 'Mean flow generation and inertial wave attractors in a librating annulus: DNS and theory' (oral). European Geophysical Union (EGU) General Assembly 2015, Vienna, Austria.

- M. Klein, A. Ghasemi V., U. Harlander & A. Will (2014). 'Inertial wave excitation and wave attractors in a librating annulus: DNS'. European Geophysical Union (EGU) General Assembly 2014, Vienna, Austria. (poster)

- M. Klein, T. Seelig, M. V. Kurgansky, A. Ghasemi V., I. D. Borcia, A. Will, E. Schaller, C. Egbers & U. Harlander (2013). 'Inertial wave excitation and wave attractors in an annular cavity with an inclined wall: DNS'. EUROMECH Colloquium 552: *Modelling atmospheric and oceanic flows: insights from laboratory experiments and numerical simulations*, Berlin, Germany. (oral and poster)

- M. Klein, T. Seelig, M. V. Kurgansky, A. Ghasemi V., I. D. Borcia, A. Will, E. Schaller, C. Egbers & U. Harlander (2013). 'Inertial waves and wave excitation mechanisms in annular cavities: simulations, experiments and theory'. 14$^{\text{th}}$ European Turbulence Conference, Lyon, France. (oral)

- M. Klein, T. Seelig, A. Ghasemi V., A. Will, E. Schaller, C. Egbers & U. Harlander (2011). 'Wave–mean flow interaction in a rotating annulus'. KlimaCampus Workshop: *Numerical Methods for Scale Interactions*, Hamburg, Germany. (poster)

Other presentations

- M. Klein (2015). 'Inertial wave attractors and wave excitation by libration in an annulus'. MHD Coffee Seminar, Helmholtz-Zentrum Dresden - Rossendorf, Germany. (oral)
- M. Klein (2011–2015). Semi-annual PhD Seminar of the Chair Environmental Meteorology, BTU Cottbus - Senftenberg. (oral)